

THE MINISTRY OF SCIENCE AND HIGHER EDUCATION OF THE RUSSIAN FEDERATION



ST. PETERSBURG STATE
POLYTECHNICAL UNIVERSITY
JOURNAL

Physics
and Mathematics

**VOLUME 15, No.3.3,
2022**

Peter the Great St. Petersburg
Polytechnic University
2022

ST. PETERSBURG STATE POLYTECHNICAL UNIVERSITY JOURNAL. PHYSICS AND MATHEMATICS

JOURNAL EDITORIAL COUNCIL

A.I. Borovkov – vice-rector for perspective projects;
V.A. Glukhikh – full member of RAS;
D.A. Indeitsev – corresponding member of RAS;
V.A.I. Rudskoy – full member of RAS;
R.A. Suris – full member of RAS;
A.E. Zhukov – corresponding member of RAS.

JOURNAL EDITORIAL BOARD

V.K. Ivanov – Dr. Sci. (phys.-math.), prof., SPbPU, St. Petersburg, Russia, – editor-in-chief;
A.E. Fotiadi – Dr. Sci. (phys.-math.), prof., SPbPU, St. Petersburg, Russia, – deputy editor-in-chief;
V.M. Kapralova – Candidate of Phys.-Math. Sci., associate prof., SPbPU, St. Petersburg, Russia, – executive secretary;
V.I. Antonov – Dr. Sci. (phys.-math.), prof., SPbPU, St. Petersburg, Russia;
I.B. Bezprozvanny – Dr. Sci. (biology), prof., The University of Texas Southwestern Medical Center, Dallas, TX, USA;
A.V. Blinov – Dr. Sci. (phys.-math.), prof., SPbPU, St. Petersburg, Russia;
A.S. Cherepanov – Dr. Sci. (phys.-math.), prof., SPbPU, St. Petersburg, Russia;
D.V. Donetski – Dr. Sci. (phys.-math.), prof., State University of New York at Stony Brook, NY, USA;
V.V. Dubov – Dr. Sci. (phys.-math.), prof., SPbPU, St. Petersburg, Russia;
D.A. Firsov – Dr. Sci. (phys.-math.), prof., SPbPU, St. Petersburg, Russia;
P.A. Karasev – Dr. Sci. (phys.-math.), prof., SPbPU, St. Petersburg, Russia;
A.S. Kheifets – Ph.D., prof., Australian National University, Canberra, Australia;
O.S. Loboda – Candidate of Phys.-Math. Sci., associate prof., SPbPU, St. Petersburg, Russia;
J.B. Malherbe – Dr. Sci. (physics), prof., University of Pretoria, Republic of South Africa;
V.M. Ostryakov – Dr. Sci. (phys.-math.), prof., SPbPU, St. Petersburg, Russia;
V.E. Privalov – Dr. Sci. (phys.-math.), prof., SPbPU, St. Petersburg, Russia;
E.M. Smirnov – Dr. Sci. (phys.-math.), prof., SPbPU, St. Petersburg, Russia;
A.V. Solov'yov – Dr. Sci. (phys.-math.), prof., MBN Research Center, Frankfurt am Main, Germany;
A.K. Tagantsev – Dr. Sci. (phys.-math.), prof., Swiss Federal Institute of Technology, Lausanne, Switzerland;
I.N. Toptygin – Dr. Sci. (phys.-math.), prof., SPbPU, St. Petersburg, Russia;

The journal is included in the List of leading peer-reviewed scientific journals and other editions to publish major findings of theses for the research degrees of Doctor of Sciences and Candidate of Sciences.

The publications are presented in the VINITI RAS Abstract Journal and Ulrich's Periodical Directory International Database.

The journal is published since 2008 as part of the periodical edition 'Nauchno-tekhnicheskie vedomosti SPb-GPU'.

The journal is registered with the Federal Service for Supervision in the Sphere of Telecom, Information Technologies and Mass Communications (ROSKOMNADZOR). Certificate ПИ № ФС77-52144 issued December 11, 2012.

The journal is distributed through the CIS countries catalogue, the «Press of Russia» joint catalogue and the «Press by subscription» Internet catalogue. The subscription index is 71823.

The journal is in the **Web of Science** (Emerging Sources Citation Index), **Scopus**, the **Russian Science Citation Index** (RSCI) and the **Directory of Open Access Journals** (DOAJ) databases.

© Scientific Electronic Library (<http://www.elibrary.ru>).

No part of this publication may be reproduced without clear reference to the source.

The views of the authors may not represent the views of the Editorial Board.

Address: 195251 Politekhnicheskaya St. 29, St. Petersburg, Russia.

Phone: (812) 294-22-85.

<http://ntv.spbstu.ru/physics>

© Peter the Great St. Petersburg Polytechnic University, 2022

Contents

Condensed matter physics

Smirnova M. A., Bachurin V. I., Churilov A. B. <i>Influence of the initial surface state on the ripple formation induced by O_2^+ sputtering of Si</i>	8
Belov Y. D., Zimin S. P., Amirov I. I., Naumov V. V., Abramof E., Rapp P. H. O. <i>Formation of Pb-Sn Janus particles on the surface of lead-tin telluride films during ion-plasma sputtering</i>	13
Rakhmanova G. R., Sedov D. D., Iorsh I. V. <i>Transport and optical phenomena in two-dimensional dirac semimetals</i>	18
Seraya O. V., Lizunova A. A., Khabarov K. M., Nouraldeem M., Ivanov V. V. <i>In-flow laser modification of silver nanoparticles synthesized by spark discharge</i>	22
Rybin V. V., Solovyev A. A., Zuev A. D. <i>Thermal and mechanical properties of a metal-matrix composite with ceramic inclusions</i>	27
Reznik R. R., Gridchin V. O., Kotlyar K. P., Ubyivovk E. V., Dragunova A. S., Kryzhanovskaya N. V., Cirlin G. E. <i>Physical properties of InGaAs quantum dots in AlGaAs nanowires synthesized on silicon at different growth temperatures</i>	31
Shandyba N. A., Kirichenko D. V., Chernenko N. E., Eremenko M. M., Balakirev S. V., Solodovnik M. S. <i>Effect of FIB-modification of Si(111) surface on GaAs nanowire growth</i>	36
Balakirev S. V., Kirichenko D. V., Chernenko N. E., Shandyba N. A., Eremenko M. M., Solodovnik M. S. <i>Multistage droplet epitaxy for the fabrication of InAs/GaAs quantum dots with ultra-low density</i>	42
Chernenko N. E., Kirichenko D. V., Shandyba N. A., Balakirev S. V., Eremenko M. M., Solodovnik M. S. <i>Experimental study of nanoholes formation using local droplet etching of FIB-modified GaAs (001) surface</i>	48
Eremenko M. M., Balakirev S. V., Chernenko N. E., Shandyba N. A., Ageev O. A., Solodovnik M. S. <i>Effect of pregrowth annealing temperature on the subsequent epitaxial growth of GaAs on Si</i>	54
Nikitina L. S., Lakhina E. A., Eremenko M. M., Balakirev S. V., Chernenko N. E., Shandyba N. A., Ageev O. A., Solodovnik M. S. <i>Study of FIB-modified silicon areas by AFM and Raman spectroscopy</i>	59
Lomakin A. I., Baeva E. M., Titova N. A., Zolotov P. I., Kolbatova A. I., Goltsman G. N. <i>Electron phase-breaking time in ultra-thin Nb films</i>	64

Simulation of physical processes

Shamin E. S., Sharapov A. A., Skuratov I. D., Demidov S. O., Gornev E. S. <i>Sidewall roughness model for optical losses calculation in photonic integrated circuits</i>	70
Kozhevnikov V. Yu., Kozyrev A. V., Kokovin A. O., Semeniuk N. S. <i>The kinetic simulation in vacuum electronics: uncovering the fundamental nature of non-Maxwellian distribution function effects</i>	76
Tishin P. D., Shishkina D. A., Shishkin I. A., Poluektova N. A., Latukhina N. V. <i>Investigation of degradation characteristics of photosensitive structures with porous silicon</i>	82
Nizameeva G. R., Gainullin R. R., Nizameev I. R., Kadirov M. K. <i>Cetyltrimethylammonium bromide as a soft template for the synthesis of a conductometric gas sensor active substance</i>	86
Bogdanova M. V., Uvarov A. V., Gudovskikh A. S. <i>Optimization of the contact grid for the GaP/Si solar cells</i>	93



Atom physics and physics of clusters and nanostructures

- Fattakhov I. S., Trushin O. S., Popov A. A., Mazaletsky L. A.** *Growth of nanostructured cobalt thin film at oblique angle deposition* 97
- Dronova M. A., Danilov E. A., Veretennikov M. R.** *Electrical conductivity and optical properties of water-based graphene/AgNWs hybrid inks for flexible electronics* 101
- Troshkina N. N., Novikova S. A., Nasirov P. D., Volobueva M. Yu., Mukhina I. V., Popova A. A., Gribova E. D.** *Investigation of the optical properties of quantum dots depending on the nature and number of additional semiconductor layers*..... 106
- Shipovskaya A. B., Gegel N. O., Babicheva T. S.** *Comparative analysis of nanosized structures in thin hydrogel plates of chitosan L- and D-ascorbate–hydrochloride*..... 111
- Asharchuk I.M., Vovk N.A., Sokolov V.I., Goryachuk I.O., Minaev N.V., Tarkhov M.A.** *Upconversion luminescence particles based on NaYf₄ matched with passive optical devices* 118

Physical electronics

- Maksimova A. A., Uvarov A. V., Kirilenko D. A., Baranov A. I., Vyacheslavova E. A., Gudovskikh A. S.** *Plasma deposited indium phosphide and its electrophysical properties* 123
- Listyukhin V. A., Pecherskaya E. A., Golubkov P. E., Aleksandrov V. S., Shepeleva A. E.** *Monitoring of overhead power lines in real time*..... 128
- Egorkin V. I., Zemlyakov V. E., Zaitsev A. A., Chukanova O. B.** *GaN ICE-mode p-channel and n-channel transistors simulation*..... 134
- Vovk N. A., Asharchuk I. M., Timofeeva E. R., Filippov I. A., Zenova E. V., Smirnov K. V., Tarkhov M. A.** *Development of technological methods for fabrication high-density luminescent structures based on up-conversion NaYF₄:Yb³⁺, Er³⁺ particles*..... 138
- Ivanov A. E., Aladov A. V., Chernyakov A. E., Zakgeim A. L.** *A comprehensive study of electroluminescence and temperature distribution of “UX:3” AlInGaN LED*..... 142
- Kenesbay R., Enns Ya. B., Kazakin A. N., Kleimanov R., Akulshin Yu. D.** *Low-induction integral heater for temperature control of MEMS vapor cell*..... 147
- Struchkov N. S., Kozlovskaya E. A., Tsarik K. A., Lashkov A. V., Levin D. D., Romashkin A. V.** *On the mechanism of CNT network NH₃ sensitivity: modeling and experimental study of the density effect.* 151

Physical optics

- Sinitskaya O. A., Shubina K. Yu., Mokhov D. V., Uvarov A. V., Filatov V. V., Mizerov A. M., Timoshnev S. N., Nikitina E. V.** *Development of visible-blind ultraviolet photodetectors based on ultrathin GaN epitaxial layers grown on c-Al₂O₃ substrates*..... 157
- Dragunova A. S., Kryzhanovskaya N. V., Moiseev E. I., Zubov F. I., Kalyuzhnyy N. A., Mintairov S. A., Nadtochiy A. M., Guseva Yu. A., Kulagina M. M., Zhukov A. E.** *Analysis of characteristics of InGaAs/GaAs microdisk lasers bonded onto silicon board*..... 163
- Fominykh N. A., Moiseev E. I., Makhov I. S., Min'kov K. N., Nadtochiy A. M., Guseva Yu. A., Kulagina M. M., Mintairov S. A., Kalyuzhnyy N. A., Kryzhanovskaya N. V., Zhukov A. E.** *The investigation of optical coupling of microlasers with tapered fiber*..... 167

Astafiev A. A., Shakhov A. M., Syrchina M. S., Shepel D. V., Nadtochenko V. A. <i>Comparison of femtosecond laser, hydrothermal and microwave synthesis of fluorescent products from L-lysine....</i>	171
Scherbak S. A., Reshetov I. V., Lipovskii A. A. <i>Optical second-harmonic response of an axially-symmetric medium under radially polarized excitation.....</i>	177
Miropoltsev M. A., Tkach A. P., Maleeva K. A., Bogdanov K. V. <i>Fabrication of SERS-active structures via electrostatic deposition of colloidal gold nanoparticles on polymer microspheres.....</i>	182
Peretokin A. V., Stepikhova M. V., Novikov A. V., Smagina Zh. V., Dyakov S. A. <i>Peculiarities of the luminescence response of two-dimensional photonic crystals with ordered Ge(Si) nanoislands obtained using different ordering approaches.....</i>	188
Mekhtiev E. E., Gerasin I. S., Rudavin N. V., Duplinsky A. V., Kurochkin Yu. V. <i>Posterior laser-locking technique for MDI-QKD.....</i>	194
Gerasin I. S., Mekhtiev E. E., Maksimova E. I., Rudavin N. V., Duplinsky A. V., Kurochkin Yu. V. <i>Novel method for preparing high-indistinguishable coherent state.....</i>	198
Merzlinkin V. E., Khmelev A. V., Duplinsky A. V., Kurochkin V. L., Kurochkin Yu. V. <i>Polarization compensation design for free-space quantum communication transmitter.....</i>	202
Dobretsov R. K., Davydov V. V., Evstrapov A. A. <i>Creation of a device for detecting fluorescence from microfluidic chips.....</i>	207
Mikhailovskii M. S., Savelev R. S., Sidorenko M. S., Sadrieva Z. F., Bogdanov A. A., Petrov M. I. <i>Collective states with high quality factors in chains of dielectric resonators.....</i>	213
Tolkach N. M., Vishnyakov N. V., Litvinov V. G., Yakubov A. O., Trofimov E. S., Sherchenkov A. A. <i>Investigation of crystallinity degree for $Ge_2Sb_2Te_5$ films by reflection and transmission photometry..</i>	219
Kondratiev V. I., Ivanova T., Tyugaev M. D., Samusev A. K., Kravtsov V. <i>Experimental study of all-van-der-Waals waveguide polaritons at room temperature.....</i>	223
Frolov I. V., Radaev O. A., Sergeev V. A. <i>Measurement of the internal quantum efficiency of emission in the local region of the LED chip.....</i>	226
Dryazgov M. A., Korneeva Yu. P., Korneev A. A. <i>New design of a waveguide integrated photon number resolving superconducting detector with micron-wide strips.....</i>	230
Fomin A. V., Filonenko E. M., Kryukov S. A., Nazhmetov S. Kh. <i>The effect of mesa-stripe design parameters on the 975 nm laser diode output characteristics.....</i>	235

Physical materials technology

Eurov D. A., Volkova E.A., Kirilenko D. A., Kurdyukov D. A., Stovpiaga E. Yu. <i>TEM contrast enhancement by adsorption of erbium ions on the inner surface of micro-mesoporous silica particles.....</i>	239
Babich E. S., Kaasik V. P., Redkov A. V., Lipovskii A. A. <i>Optical absorption and Raman scattering mapping of nanoparticles patterns formed in glass by nanosecond laser in UV, VIS and IR.....</i>	244
Stetsyura S. V., Kharitonova P. G., Glukhovskoy E. G. <i>Langmuir-Blodgett technology to obtain semi-magnetic photosensitive materials.....</i>	250
Volkova M. G., Ivanishcheva A. P., Petrov V. V., Bayan E. M. <i>The effect of the seed layer on the TiO_2 nanotubes coatings quality grown on the glass substrates by hydrothermal synthesis.....</i>	255

Melnichenko I. A., Kryzhanovskaya N. V., Berdnikov Yu. S., Moiseev E. I., Makhov I. S. <i>Optical studies of InP nanostructures monolithically integrated in Si (100)</i>	260
Gulyaeva I. A., Ivanishcheva A. P., Volkova M. G., Bayan E. M., Petrov V. V. <i>Surface and electrophysical properties study of thin TiO₂-SnO₂ nanocomposite films</i>	265
Gulyaeva I. A., Ignatieva I. O., Bayan E. M., Petrov V. V. <i>Study of structural properties and photoconductivity of Co₃O₄ – ZnO thin films</i>	271
Malo D., Lizunova A. A., Nouraldeen M., Borisov V. I., Ivanov V. V. <i>Aluminum nanostructures produced by aerosol dry printing for ultraviolet photoluminescence enhancement</i>	276
Bondarenko D. N., Gridchin V. O., Kotlyar K. P., Baranov A. I., Maksimova A. A., Reznik R. R., Cirlin G.E. <i>Physical properties of GaN/InGaN nanowires grown by PA-MBE on silicon substrate</i>	281
Enns Y. B., Kazakin A. N., Komarevtsev I. M., Kondrateva A. S., Mishin M. V. <i>Modification of the optical and electrical properties of NiO films by thermal annealing</i>	285
Kurilova A. V., Sukhachev A. L., Shulga K. V., Bogdanov K. V., Nemtsev I. V., Dubavik A. Y., Sokolov A. E. <i>Synthesis and properties of nanostructure composites based on barium titanate and 3D metals</i>	290
Kutepov M. E., Domaratskiy I. K., Zhukov S. S., Kaidashev E. M., Lisnevskaya I. V., Abdulvakhidov K. G., Kaydashev V. E. <i>Optimizing deposition regimes to fabricate vanadium dioxide film for active metasurfaces</i>	295
Morozova E. V., Timkaeva D. A. <i>Thermoelectric properties of graphenylene nanotubes with encapsulated fullerenes</i>	300
Masharin M. A., Makarov S. V., Samusev A. K. <i>Temperature-dependent exciton-polaritons in perovskite photonic crystal slab</i>	306
Gridchin V. O., Reznik R. R., Kotlyar K. P., Shugabaev T. M., Dragunova A. S., Kryzhanovskaya N. V., Cirlin G. E. <i>Plasma assisted molecular beam epitaxy growth of InGaN nanostructures on Si substrates</i>	311
Balakirev S. V., Lakhina E. A., Kirichenko D. V., Chernenko N. E., Shandyba N. A., Eremenko M. M., Solodovnik M. S. <i>Independent control of size and shape of GaAs nanostructures during droplet epitaxy using ultra-low arsenic flux</i>	315
Miroshnichenko A. S., Deriabin K. V., Mukhin I. S., Islamova R. M. <i>Low-adhesive silicone rubbers for flexible light-emitting devices</i>	320

Physics of molecules

Tonkaev P. A., Grechaninova E. V., Pushkarev A. P., Makarov S. V. <i>Photoluminescence from lead halide perovskite superlattices</i>	326
Zhurikhina V. V. <i>Plasmonic structures for sensors</i>	330

Radiophysics

Uvarov I. V., Naumov V. V., Kupriyanov A. N., Izyumov M. O., Amirov I. I. <i>A seesaw-type MEMS switch with Pt and Ru contacts</i>	335
Lyubchak A. N., Prikhodko A. N., Andreev V. S., Shurakov A. S., Goltsman G. N. <i>A mmWave rod antenna array compatible with a PCB prototyping technology</i>	340

Prikhodko A. N., Belikov I. I., Lvov A. V., Shurakov A. S., Goltsman G. N. Millimeter wave photonic crystal waveguides fabricated via direct machining.....	345
Vosheva T. S., Bulatov N. O., Burtsev V. D., Khudykin A. A., Filonov D. S. Controlling asymmetric reflection of metasurfaces with loss.....	350
Dmitriev R. A., Grevtseva A. S., Davydov V. V. Features of microwave excitation signal formation in a quantum frequency standard.....	354

Theoretical physics

Medvedeva S. S., Gaidash A. A., Miroshnichenko G. M., Kiselev A. D., Kozubov, A. V. Dynamics of the uncertainty value of quadratures for bosonic quantum states.....	360
Petrov I. V., Menskoy D. D., Tayduganov A. S. Phase-time-encoding MDI QKD tolerant to detector imperfections.....	365

Experimental technique and devices

Kryzhanovskaya N. V., Moiseev E. I., Dragunova A. S., Maximov M. V., Mintairov S. A., Kaluzhnyy N. A., Zubov F. I., Kulagina M. M., Guseva J. A., Likhachev A. I., Zhukov A. E. Integrated optical transceiver based on III-V microdisk laser and photodiode.....	371
Uvarov I. V., Shlepakov P. S., Abramychev A. M., Svetovoy V. B. Fabrication of a micropump based on the fast electrochemical actuator with the PDMS membrane.....	376
Khakimova A. A., Pominov V. V., Babicheva T. S., Shmakov S. L., Zakharevich A. M., Shipovskaya A. B. TEM use for the study of chitosan microspheres and nanospheres obtained from its salts with several acids.....	381

CONDENSED MATTER PHYSICS

Conference materials

UDC 537.534

DOI: <https://doi.org/10.18721/JPM.153.301>

Influence of the initial surface state on the ripple formation induced by O_2^+ sputtering of Si

M. A. Smirnova ¹✉, V. I. Bachurin ¹, A. B. Churilov ¹

¹P.G. Demidov Yaroslavl State University, Yaroslavl, Russia

✉ e-mail: masha_19957@mail.ru

Abstract. Influence of the initial Si surface state on the rate of ripple nucleation under bombardment with low-energy O_2^+ ions was investigated. It was found that the creation of a defect area in the Si near-surface layer or the creation of the initial surface relief by ion bombardment with a focused Ga^+ ion beam facilitates a significant acceleration of the ripple nucleation on the Si surface during subsequent irradiation with an O_2^+ ion beam.

Keywords: ripple formation, sputtering, nanostructuring, silicon, ion beam.

Funding: This study was funded by the Ministry of Education and Science of the Russian Federation within the framework of the state assignment of the P.G. Demidov Yaroslavl State University of topic no. 0856-2020-0006.

Citation: Smirnova M. A., Bachurin V. I., Churilov A. B., Influence of the initial surface state on the ripple formation induced by O_2^+ sputtering of Si, St. Petersburg State Polytechnical University Journal. Physics and Mathematics. 15 (3.3) (2022) 8–12. DOI: <https://doi.org/10.18721/JPM.153.301>

This is an open access article under the CC BY-NC 4.0 license (<https://creativecommons.org/licenses/by-nc/4.0/>)

Материалы конференции

УДК 537.534

DOI: <https://doi.org/10.18721/JPM.153.301>

Влияние начального рельефа поверхности Si на формирование рипплов при облучении ионами O_2^+

М. А. Смирнова ¹✉, В. И. Бачурин ¹, А. Б. Чурилов ¹

¹ЯрГУ им. П.Г. Демидова, Ярославль, Россия

✉ e-mail: masha_19957@mail.ru

Аннотация. Исследовано влияние предварительно сформированного рельефа поверхности Si, облученного ионным пучком Ga^+ с энергией 30 keV на скорость зарождения рипплов при бомбардировке ионами O_2^+ . Установлено, что начальный рельеф поверхности способствует существенному ускорению процесса зарождения рипплов на поверхности Si.

Ключевые слова: формирование рипплов, распыление, наноструктурирование, кремний, ионный пучок.

Финансирование: Работа выполнена в рамках Государственного задания ЯрГУ им. П. Г. Демидова Минобрнауки РФ по теме 0856-2020-0006.

Ссылка при цитировании: Смирнова М. А., Бачурин В. И., Чурилов А. Б. Влияние начального рельефа поверхности Si на формирование рипплов при облучении ионами O_2^+ // Научно-технические ведомости СПбГПУ. Физико-математические науки. 2022. Т. 15. № 3.3. С. 8–12. DOI: <https://doi.org/10.18721/JPM.153.301>

Статья открытого доступа, распространяемая по лицензии CC BY-NC 4.0 (<https://creativecommons.org/licenses/by-nc/4.0/>)



Introduction

Ion beam sputtering is a powerful method for micro- and nanostructures formation on the surface of various materials. The main advantages of this method are the fairly short processing time of large areas and the possibility of metals, semiconductors, insulators nanostructuring. Moreover, the adjustment of irradiation parameters, such as angle of incidence, fluence, kinetic energy and ion beam diameter, allows generating a sized-controllable structure. Recently, a large number of works is devoted to the study of a periodic wavelike nanostructures (ripples) formation on the metal and semiconductor surfaces [1].

According to experiments, ripple nucleation on the Si surface occurs at a certain (critical) fluence, which depends on the energy and type of ions and the ion beam incidence angle [2-5]. At the moment, there is a small number of works [6, 7] which demonstrate that the creation of initial topographic inhomogeneity's on the Si surface leads to a marked reduction of the critical fluence required for the sputter ripple nucleation.

In the present work, we have studied an influence of the initial Si surface state on the process of ripple nucleation and evolution under bombardment with low-energy O_2^+ ions. Initial surface is defined as the Si surface irradiated by 30 keV Ga^+ ion beam.

Materials and Methods

Experiments on the formation of ripples on the Si (100) surface were carried out on the Cameca IMS 4f machine. All the samples were bombarded by separated 12,5 keV O_2^+ ion beam at an angle of 38° with respect to the surface normal.

Fig. 1 *a*) shows the geometry of the conducting experiments. At the moment of ripple nucleation, which are perpendicular to the plane of the ion beam incidence, oxygen enrichment occurs on the wave slopes facing to the incidence ion beam. The concentration of this enrichment is corresponding to SiO_2 [9]. This leads to increasing of the current of secondary Si^+ ions (Fig. 1 *b*). Reaching the plateau of the $I(t)$ dependence indicates the completion of the ripple formation process with a constant wavelength. Two series of samples were prepared. In the first series, the surface bombardment was stopped at the moment of ripple nucleation; in the second series it was stopped after final ripple formation.

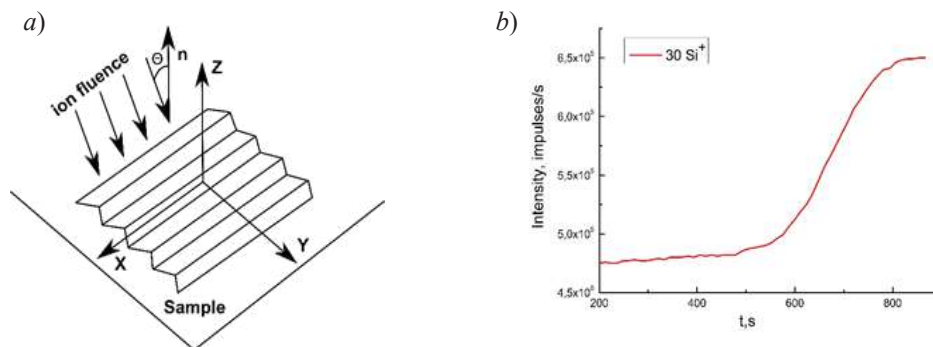


Fig. 1. Ripple formation scheme (*a*). The dependence of the secondary ion current output on the irradiation time (in this case, ion implantation of Si were carried out under $\Theta = 0^\circ$, $\Phi = 10^{17} \text{ cm}^{-2}$) (*b*)

The process of ripple nucleation was determined by an increasing the current of secondary Si^+ ions [8], which detected during ion bombardment of the surface. The depth of the sputtering crater where ripples nucleated was determined on a Talystep profilometer. The samples were pretreated by ion implantation of Si(100) surface with a 30 keV Ga^+ ion beam on a Quanta 3D 200i. Beams with a diameter of $4 \mu\text{m}$ were used. The dimensions of the irradiated area were $200 \times 200 \mu\text{m}^2$. An angles of incidence of the ion beam were $\Theta = 0^\circ, 30^\circ$, ion fluences were $\Phi = 10^{17}, 2 \cdot 10^{17}, 4 \cdot 10^{17} \text{ cm}^{-2}$. A more detailed analysis of the surface topography was carried out ex-situ using a scanning electron microscope Supra 40.

Results and Discussion

Silicon samples irradiated with a Ga^+ ions were examined by the SEM method. It was found that at a fluences of $2 \cdot 10^{17}$, $4 \cdot 10^{17} \text{ cm}^{-2}$ a noticeable surface relief in the form of grid-like structure and ripples occurs and $\Theta = 0^\circ$, 30° respectively. As the fluence increases, the surface rms roughness increases up to 30 nm at $\Theta = 30^\circ$ and $\Phi = 4 \cdot 10^{17} \text{ cm}^{-2}$. At a fluence of $\Phi = 10^{17} \text{ cm}^{-2}$, an irradiated surface stays smooth at normal incidence and a small perturbations are observed at $\Theta = 30^\circ$.

Fig. 2 demonstrates the Si surface relief before (left column) and after (right column) irradiation with an O_2^+ ion beam. In Fig. 2, *a*) there is an experiment with initial smooth Si surface, Fig. 2, *b*) shows an experiments where the initial surfaces were pretreated with a gallium ions at different ion fluences.

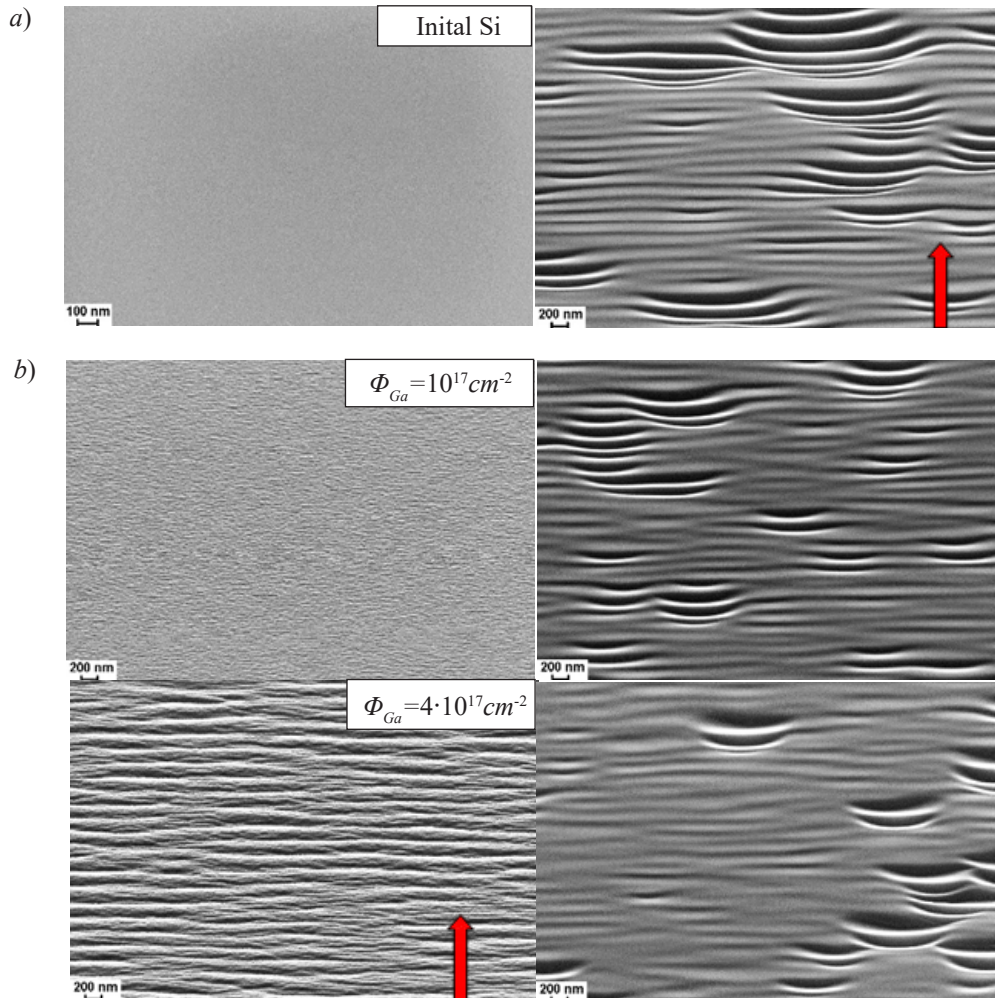


Fig. 2. The surface state before (left column) and after (right column) irradiation with an O_2^+ ion beam in cases of initial smooth (*a*) and pretreated (*b*) Si surface. The arrow indicates the direction of incidence of the ion beam

Irradiation with O_2^+ ion beam of the virgin Si surface leads to the ripple formation at a depth of $\sim 6.5 \mu\text{m}$ with an average wavelength of $\lambda = 460 \text{ nm}$, which is in good agreement with the data of [8]. The formation of ripples with wavelength $\lambda = 450 \pm 30 \text{ nm}$ was observed on the pretreated Si samples. In this case, the depth of ripple nucleation decreased significantly: practically 1.5 times at a fluence of $\Phi = 10^{17} \text{ cm}^{-2}$ and more than 2 times at $\Phi = 2 \cdot 10^{17}$ and $4 \cdot 10^{17} \text{ cm}^{-2}$, both in the case of pretreated samples with Ga^+ ions at normal and oblique beam incidence (Fig. 3). In the last case, the critical dose for ripple nucleation is lower for all ion fluences, possibly due to the shallower depth of the implanted gallium and the higher amplitude of the relief created by Ga^+ ion bombardment.

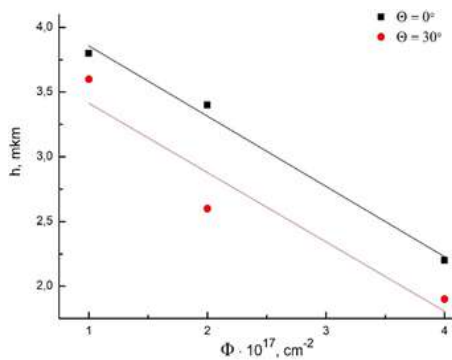


Fig. 3. The dependence of the ripple nucleation depth on the fluence of irradiation of initial Si surface with Ga^+ ions

As noted above, the presence of surface topographic inhomogeneities leads to decrease of the critical fluence required for ripple nucleation on the Si surface under ion bombardment [6, 7]. Present study established that the same effect is triggered by preliminary creation of a defect region in the Si near-surface layer without noticeable changes in the surface topography by implantation with Ga^+ ion beam at $\Phi = 10^{17} \text{ cm}^{-2}$. The apparently reason of accelerated ripple nucleation in this case is that the implanted Ga is located in the form of separate nanometer-sized precipitates lying at a depth of 10–20 nm in the Si near-surface layer (at $\Theta = 0^\circ$) [10]. During the sputtering of such samples with O_2^+ ion beam at depths of

10–20 nm a topographic instability may arise due to the difference in sputtering rates of Ga and Si, which will initiate the ripple nucleation process.

One of the first models explaining the formation of ripples [11] combines the effects of sputtering and surface diffusion and is based on the sputtering theory of Sigmund [12]. It relates the rate of atom removal to the energy deposited by incident ion into surface layer. The coefficients in proposed equation [11] are functions of the ion beam parameters and relate the sputtering yield at any point on the surface to the local curvature. Thus, the presence of the original surface local curvature is necessary. Later in the work [13] it is stated, that transition between the flat and rippled states of the surface is not possible. To explain the appearance of the initial surface topography leading to a change of the local angle of ion incidence the term $\eta(x,y,t)$ which accounts the stochastic nature of the current density of incident ions was introduced in the equation of a nonlinear model of ripple formation [14]. From a practical point of view, accounting of this summand seems to be quite difficult. Therefore, in [15] it was suggested to substitute it for an arbitrary initial relief in the modeling of the formation of the wave-like relief. This approach led the authors to the results of modeling structures that quite well consistent with the experimental results.

Thus, it is shown that both the creation of the initial relief on the Si surface and the creation of a defective region in the near-surface layer lead to a significant reduction in the critical dose of irradiation with O_2^+ ions required to initiate the formation of ripples on the Si surface.

Acknowledgments

This study was performed with financial support from the Ministry of Education and Science of the Russian Federation within the framework of the state assignment of the P.G. Demidov Yaroslavl State University of topic no. 0856-2020-0006 and using equipment of the facilities sharing centre “Micro- and Nanostructures Diagnostics”.

REFERENCES

1. Cuerno R. and Kim J.-S., A perspective on nanoscale pattern formation at surfaces by ion-beam irradiation, *Journal of Applied Physics*. 128 (2020) 180902.
2. Carter G., Vishnyakov V., Ne^+ and Ar^+ ion bombardment-induced topography on Si, *Surface and Interface Analysis*. 23 (1995) 514–520.
3. Elst K., Vandervorst W. J., Influence of the composition of the altered layer on the ripple formation, *Journal Vacuum Science and Technology A*. 12 (1994) 3205–3216.
4. Smirnov V. K., Kibalov D. S., Krivelevich S. A., Lepshin P. A., Potapov E. V., Yankov R. A., Skorupa W., Makarov V. V., Danilin A. B., Wave-ordered structures formed on SOI wafers by reactive ion beams, *Nuclear Instruments and Methods B*. 147 (1999) 310–315.
5. Bhattacharjee S., Karmkar P., Naik V., Sinha A. K., Chakrabarti A., The role of carbon in ion beam nano-patterning of silicon, *Applied Physics Letters*. 103 (2013) 181601.

6. **Smirnov V. K., Kibalov D. S., Lepshin P. A., Bachurin V. I.**, Influence of topographical irregularities on the process of formation of wave micro relief on silicon surfaces, *Izvestiya Akademii Nauk, Seriya Fizicheskaya* 64 (2000) 626–630.

7. **Karmakar P., Mollick S. A., Ghose D., Chakarabarti A.**, Role of initial surface roughness on ion induced surface morphology, *Applied Physics Letters*. 93 (2008) 103102.

8. **Smirnov V. K., Kurbatov D. A., Potapov E. V.**, Investigation of nitrogen and oxygen ion interaction with a silicon surface, *Izvestiya Akademii Nauk, Seriya Fizicheskaya*. 56 (3) (1992) 71-76.

9. **Wittmaack K.**, Local SiO₂ formation in silicon bombarded with oxygen above the critical angle for beam-induced oxidation: new evidence from sputtering yield ratios and correlation with data obtained by other techniques, *Surface and Interface Analysis*. 29 (2000) 721-725.

10. **Rommel M., Spoldi G., Yanev V., Beuer S., Amon B., Jambrech J., Petersen S., Bauer A. J.**, Comprehensive study of focused ion beam induced lateral damage in silicon by scanning probe microscopy techniques, *Journal Vacuum Science and Technology B*. 28 (2010) 595–607.

11. **Bradley R. M., Harper M. E.**, Theory of ripple topography induced by ion bombardment, *Journal Vacuum Science and Technology A*. 6 (1988) 2390–2395.

12. **Sigmund P.**, A mechanism of surface micro-roughening by ion bombardment, *Journal of Materials Science*. 8 (1973) 1545–1553.

13. **Shipman P. D., Bradley R. M.**, Theory of nanoscale pattern formation induced by normal-incidence ion bombardment of binary compounds, *Physical Review B*. 84 (2011) 085420.

14. **Cuerno R., Barbasi A. I.**, Dynamic scaling of ion-sputtered surfaces, *Physical Review Letters*. 74 (1995) 4746–4749.

15. **Kahng B., Jeong H., Barbasi A. I.**, Quantum dot and hole formation in sputter erosion, *Applied Physics Letters*. 78 (2001) 805-807.

THE AUTHORS

SMIRNOVA Mariya A.

e-mail: masha_19957@mail.ru

ORCID: 0000-0002-7241-6342

CHURILOV Anatoly B.

e-mail: abchurilov@mail.ru

ORCID: 0000-0003-0732-7025

BACHURIN Vladimir I.

e-mail: vibachurin@mail.ru

ORCID: 0000-0002-6883-252X

Received 14.07.2022. Approved after reviewing 19.07.2022. Accepted 20.07.2022.

Conference materials

UDC 538.971

DOI: <https://doi.org/10.18721/JPM.153.302>

Formation of Pb-Sn Janus particles on the surface of lead-tin telluride films during ion-plasma sputtering

Y. D. Belov ¹✉, S. P. Zimin ^{1,2}, I. I. Amirov ¹, V. V. Naumov ¹,
E. Abramof ³, P. H. O. Rappl ³

¹ Valiev Institute of Physics and Technology of RAS, Yaroslavl Branch, Yaroslavl, Russia;

² P.G. Demidov Yaroslavl State University, Yaroslavl, Russia;

³ Materials and plasma research and development group (GPDMP), National Institute for Space Research (INPE), São José dos Campos, Brazil

✉ yadbelov@gmail.com

Abstract. The formation of Janus-like particles of Pb-Sn during ion-plasma treatment of the surface of lead-tin telluride films was found. $Pb_{0.6}Sn_{0.4}Te$ films 2 μm thick were grown on (111) BaF_2 substrates by molecular beam epitaxy. The ion-plasma treatment of the samples was carried out in a high-density low-pressure radio frequency inductively coupled plasma at an ion energy of 75 eV and 25 eV. The duration of the sputtering process was 240 s. The evolution of the film surface morphology and the formation of Pb-Sn Janus particles with nano- and submicron sizes have been studied.

Keywords: lead-tin telluride, Janus particles, ion-plasma treatment, ion energy

Funding: The investigation was supported by the Program no. FFNN-2022-0017 of the Ministry of Science and Higher Education of Russia for Valiev Institute of Physics and Technology of RAS and within the framework of the initiative research work of the P.G. Demidov Yaroslavl State University. Grants: No. 305.764/2018-7 and No. 307.192/2021-0 of the National Council for Scientific and Technological Development (CNPq) of Brazil.

Citation: Belov Y. D., Zimin S. P., Amirov I. I., Naumov V. V., Abramof E., Rappl P. H. O., Formation of Pb-Sn Janus particles on the surface of lead-tin telluride films during ion-plasma sputtering, St. Petersburg State Polytechnical University Journal. Physics and Mathematics. 15 (3.3) (2022) 13–17. DOI: <https://doi.org/10.18721/JPM.153.302>

This is an open access article under the CC BY-NC 4.0 license (<https://creativecommons.org/licenses/by-nc/4.0/>)

Материалы конференции

УДК 538.971

DOI: <https://doi.org/10.18721/JPM.153.302>

Образование Pb-Sn Янус-частиц на поверхности пленок теллурида свинца-олова при ионно-плазменном распылении

Я. Д. Белов ¹✉, С. П. Зимин ^{1,2}, И. И. Амиров ¹,
В. В. Наумов ¹, Е. Абрамоф ³, Р. Н. О. Раппл ³

¹ ЯФ ФТИАН им. К.А. Валиева РАН, Ярославль, Россия;

² Ярославский государственный университет имени П.Г. Демидова, Ярославль, Россия;

³ Materials and plasma research and development group (GPDMP), National Institute for Space Research (INPE), São José dos Campos, Brazil

✉ yadbelov@gmail.com

Аннотация. Описано образование янус-подобных частиц Pb-Sn при ионно-плазменной обработке поверхности пленок $Pb_{0.6}Sn_{0.4}Te$, выращенных на подложках (111) BaF_2 методом молекулярно-лучевой эпитаксии. Ионно-плазменная обработка образцов осуществлялась в реакторе плотной аргоновой плазмы высокочастотного индукционного

разряда низкого давления при энергии ионов 75 эВ и 25 эВ. Продолжительность процесса распыления составляла 240 с. Изучена эволюция морфологии поверхности пленки и формирование Pb-Sn Янус-частиц нано- и субмикронных размеров.

Ключевые слова: теллурид свинца-олова, янус-частицы, ионно-плазменная обработка, энергия иона

Финансирование: Работа выполнена в рамках Государственного задания, код темы FFNN-2022-0017. Гранты: № 305.764/2018-7 и № 307.192/2021-0 Национального совета по научно-техническому развитию Бразилии.

Ссылка при цитировании: Белов Я. Д., Зимин С. П., Амиров И. И., Наумов В. В., Абрамоф Э., Раплл П. Образование Pb-Sn Янус-частиц на поверхности пленок теллурида свинца-олова при ионно-плазменном распылении // Научно-технические ведомости СПбГПУ. Физико-математические науки. 2022. Т. 15. № 3.3. С. 13–17. DOI: <https://doi.org/10.18721/JPM.153.302>

Статья открытого доступа, распространяемая по лицензии CC BY-NC 4.0 (<https://creativecommons.org/licenses/by-nc/4.0/>)

Introduction

Semiconductor solid solutions of lead-tin telluride ($\text{Pb}_{1-x}\text{Sn}_x\text{Te}$) are important materials for use in IR photovoltaic devices, thermoelectric devices and laser systems [1]. The band gap of the material is capable of smoothly changing in the range of 0.32–0–0.18 eV (300 K) with varying the tin content $0 \leq x \leq 1$ [2]. The x value at which band inversion is observed in $\text{Pb}_{1-x}\text{Sn}_x\text{Te}$ increases from 0.35 to 0.65 with an increase in temperature in the range 4.2–300 K. It is known that the phenomenon of band inversion in lead–tin telluride is accompanied by a transition from the trivial state to the state of a topological crystalline insulator [3], which makes it important to form and study the processes of nanostructuring of $\text{Pb}_{1-x}\text{Sn}_x\text{Te}$ materials. One of the widely used approaches to the formation of nanorods and nanowires of lead-tin telluride is a method based on the vapor-liquid-solid (VLS) mechanism, in which gold [4–6] or a gold–tin alloy is usually used as a seed catalyst [7]. In our works, we have shown that an effective method for nanostructuring the surface of lead chalcogenides crystals and films is the ion-plasma treatment method. In particular, it was shown in [8] that, during ion-plasma treatment, lead-tin telluride nanocones can grow by a modified VLS mechanism with plasma-assisted self-formation of metal nanodroplets of the seed catalyst. At the same time, the question of the chemical composition of the droplets of the seed catalyst remains unclear. The purpose of this work is to study the role of lead and tin atoms in the formation of nanostructures by the VLS mechanism during ion-plasma surface modification.

Materials and Methods

Single-crystal $\text{Pb}_{0.6}\text{Sn}_{0.4}\text{Te}$ films 2 μm thick were grown by molecular beam epitaxy on a Riber 32 P setup (INPE, Brazil) on (111) BaF_2 substrates. The energies of Ar^+ ions (E_i) were 75 eV and 25 eV, the treatment time was 240 s. The ion current density was $5.2 \text{ mA}\cdot\text{cm}^{-2}$. The surface morphology was studied by scanning electron microscopy (SEM) on a Supra 40 Carl Zeiss microscope; chemical analysis was carried out by energy dispersive X-ray (EDX) method on an INCA attachment. The technique of carrying out experiments is involved in [8]

Results and Discussion

The initial samples had a flat surface and were characterized by the presence of triangular dislocation pits. The surface density of the dislocation exit pits was $\sim 10^9 \text{ cm}^{-2}$. When the surface was treated with ions with an energy of 75 eV for 240 seconds, the surface was strongly modified. Fig. 1, a shows the appearance of an ensemble of nanocones with a quasi-spherical cap on top. The diameter of the quasi-spherical caps was 40–100 nm. The formation of such cones is explained by the growth of nanostructures by the VLS mechanism under conditions of parallel action of the ion flow [8]. Confirmation of the possibility of realizing the VLS mechanism is the formation of



nanostructures in the microgap under the mask, where there was no ion bombardment (Fig. 1, *b*). Under the mask, classical nanopillars with a quasi-spherical catalyst cap were formed [9]. The tilt of the nanopillars at an angle of 55° corresponded to the <100> orientations, which have minimal growth energy. This experiment allows us to conclude that the formation of cone-shaped structures with a quasi-spherical cap at the top (Fig. 1, *a*) can be explained by growth processes by the VLS mechanism in the presence of an accompanying flow of argon ions. After two-stage (75 eV, 240 s + 25 eV, 240 s) treatment, large hemispherical formations appeared on the surface, reaching 1 μm in diameter (Fig. 2, *c*).

The chemical composition of lead-tin telluride films in the initial state and after various conditions of plasma treatment is given in Table 1. The measurements were carried out on an area of 50×10 μm² when the sample is tilted at an angle of 70° relative to the normal to the surface. This geometry of the experiment provided an increase in the contribution of the surface compared to the volume. Microanalysis of the surface composition of Pb_{1-x}Sn_xTe showed that plasma treatment with ions led to an increase in the metal content on the surface and a decrease in the tellurium content (Table 1).

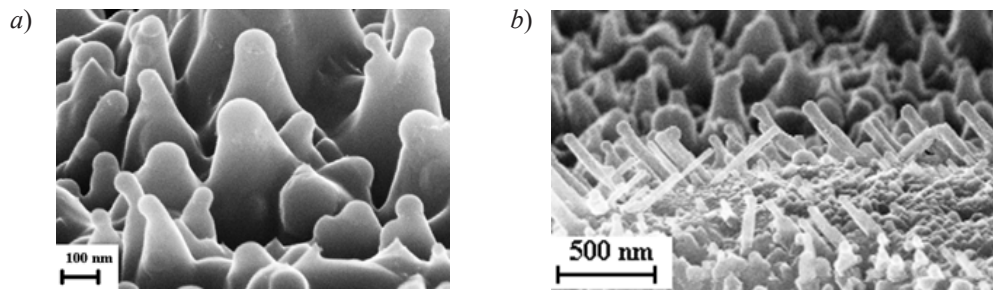


Fig. 1. Structures on the surface of the Pb_{0.6}Sn_{0.4}Te film (*a*) and under the mask (*b*) after 240 s treatment at an ion energy of 75 eV

Table 1

Chemical composition of lead-tin telluride films in the initial state and after plasma treatment

Chemical element	Quantity, at.%		
	Initial state	Processing 75 eV, 240 s	Processing 75 eV, 240 s + 25 eV, 240 s
Pb	25.43	27.22	35.24
Sn	23.46	27.53	34.87
Te	51.11	45.25	29.90

Analysis of the nanostructured surface of Pb_{0.6}Sn_{0.4}Te film in SEM in the backscattered electron mode showed that, in contrast to the analysis in secondary electrons (Fig. 2 *a, c*), it showed the presence of strongly contrasting regions (Fig. 2 *b, d*). It is known that the mode of backscattered electrons allows separating regions consisting of heavy and light elements [10], since the latter have a darker shade. In the backscattered electrons in (Fig. 2, *b*), dark “caps” are observed at the top of the nanocones, which indicates that their composition differs from that of the film. In this mode of analysis, light and dark regions are clearly distinguished on structured Pb_{0.6}Sn_{0.4}Te in the form of hemispheres (Fig. 2 *d*). This indicates that the hemispheres are Janus particles, consisting of areas with predominant localization of heavy (lead) and lighter (tin) chemical elements. It can be assumed that the quasi-spherical catalyst particles at the tops of the cones (Fig. 2, *b*) are also Janus particles. The occurrence of quasi-spherical Janus particles of the Au-Sn catalyst over SnTe nanowires was also described by Sadowski [7], where two regions consisted of Au and an Au-Sn alloy.

The size of the droplets made it possible to carry out their local EDX analysis. Analysis of the chemical composition of light and dark areas of Janus-like droplets (Fig. 3) showed that the content of tellurium in these areas is low and does not exceed 2-11 at.% for different samples. For the light region (region 1, on the Fig. 3), the content of lead and tin was 76 and 13 at.%, respectively.

For the dark region (region 2), these indicators were 3 and 95 at.%. This suggests that the submicron Janus structures observed on the surface consist of two regions with a predominant content of either lead or tin.

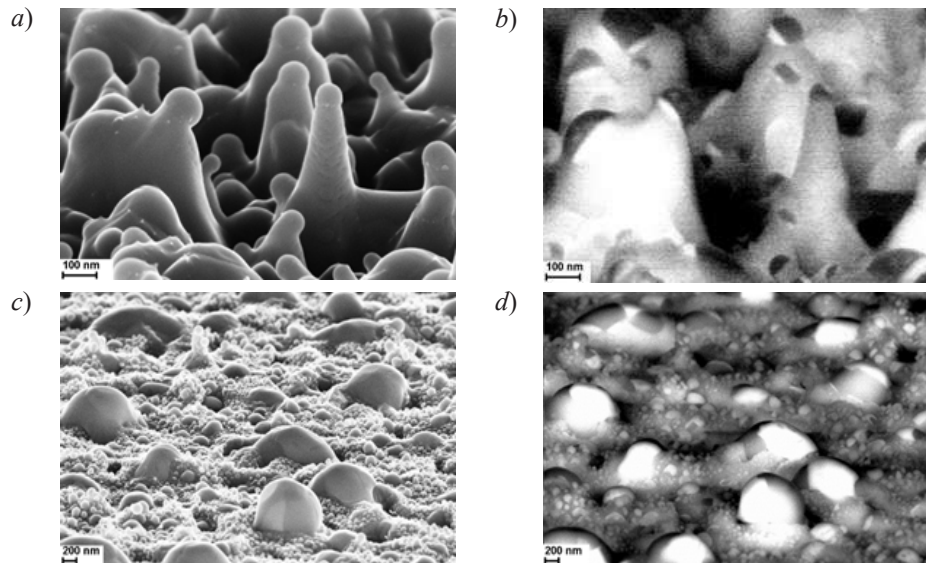


Fig. 2. SEM images of the $\text{Pb}_{0.6}\text{Sn}_{0.4}\text{Te}$ film surface after treatment with argon ions $E_i=75$ eV (*a, b*) for 240 s and after two-step processing 75 eV, 240 s+25 eV, 240 s (*c, d*) in the secondary electron mode (*a, c*) and in the backscattered electron mode (*b, d*)

The ratio of elements in two areas the Janus-like droplets (76 at.% Pb, 13 at.% Sn; 3 at.% Pb, 95 at.% Sn) is very close to the solidification of drops from the liquid phase according to the Pb–Sn phase diagram and close to the experimental values obtained in [11].

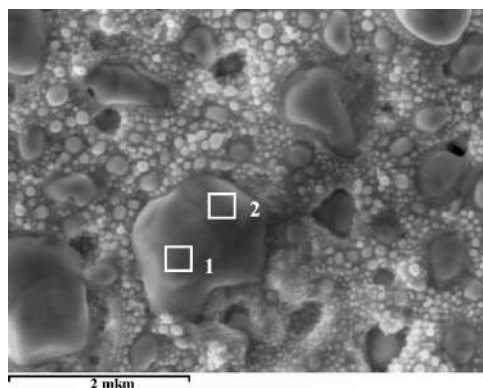


Fig. 3. Local energy-dispersive analysis of a large Janus drop at two different points

Conclusion

The results of this work showed that, as a result of plasma treatment of $\text{Pb}_{0.6}\text{Sn}_{0.4}\text{Te}$ films, nano- or submicron Pb-Sn Janus particles are formed on their surface. It is known that Janus-like Pb-Sn nanoparticles have features of transition to the liquid state [12], which should be taken into account when using them as a seed catalyst in the process of nanostructure formation by the VLS mechanism.

REFERENCES

1. Ishida A., Naruse K., Nakashima S., Takano Y., Du S., Hirakawa K., Interband absorption in PbTe/PbSnTe-based type-II superlattices, Applied Physics Letters. 113 (2018) 072103-1 – 072103-4.
2. Dimmock J. O., Melngailis I., Strauss A. J., Band structure and laser action in $\text{Pb}_x\text{Sn}_{1-x}\text{Te}$, Physical Review Letters. 16 (1966) 1193–1196.



3. **Tanaka Y., Ren Z., Sato T., Nakayama K., Souma S., Takahashi T., Segawa K., Ando Y.,** Experimental realization of a topological crystalline insulator in SnTe, *Nature Physics*. 8 (2012) 800–803.
4. **Saghir M., Lees M.R., York S.J., Hindmarsh S.A., Sanchez A.M., Walker M., McConville C.F., Balakrishnan G.,** Nanomaterials and crystals of topological insulators and topological crystalline insulators, *Journal of the Indian Institute of Science*. 96 (2) (2016) 121–130.
5. **Safdar M., Wang Q., Wang Z., Zhan X., Xu K., Wang F., Mirza M., He J.,** Weak antilocalization effect of topological crystalline insulator $\text{Pb}_{1-x}\text{Sn}_x\text{Te}$ nanowires with tunable composition and distinct {100} facets, *Nano Letters*. 15 (2015) 2485.
6. **Li Z., Shao S., Li N., McCall K., Wang J., and Zhang S. X.,** Single crystalline nanostructures of topological crystalline insulator SnTe with distinct facets and morphologies, *Nano Letters*. 13 (11) (2013) 5443–5448.
7. **Sadowski J., Dziawa P., Kaleta A., Kurowska B., Reszka A., Story T., Kret S.,** Defect-free SnTe topological crystalline insulator nanowires grown by molecular beam epitaxy on graphene, *Nanoscale*. 10 (2018) 20772–20778.
8. **Zimin S. P., Gorlachev E. S., Amirov I. I., Naumov V. V., Juskenas R., Skapas M., Abramof E., Rappl P. H. O.,** Plasma-assisted surface nanostructuring of epitaxial $\text{Pb}_{1-x}\text{Sn}_x\text{Te}$ ($0 \leq x \leq 1$) films, *Semiconductor Science and Technology*. 34 (2019) 095001–1–095001–9.
9. **Cui Y., Lauhon L. J., Gudiksen M. S., Wang J., Lieber C. M.,** Diameter-controlled synthesis of single-crystal silicon nanowires, *Applied physics letters*, 78 (15) (2001) 2214–2216.
10. **Niedrig H.,** Physical background of electron backscattering, *Scanning*. 1 (1978) 17–34.
11. **Khan P. Y., Bhattacharya V., Biswas K., Chattopadhyay K.,** Melting and solidification behavior of Pb-Sn embedded alloy nano-particles, *Journal of Nanoparticle Research*. 15 (2013) 2049–1–2049–16.
12. **Chen C. L., Lee J.-G., Arakawa K., Mori H.,** Comparative study on size dependence of melting temperatures of pure metal and alloy nanoparticles, *Applied Physics Letters*, 99 (2011) 013108–1–013108–3.

THE AUTHORS

BELOV Yaroslav D.
yadbelov@gmail.ru
ORCID: 0000-0001-9226-8108

ZIMIN Sergey P.
zimin@uniyar.ac.ru

AMIROV Ildar I.
ildamirov@yandex.ru
ORCID: 0000-0001-5273-3298

NAUMOV Victor V.
vvnau@rambler.ru

ABRAMOF Eduardo
eduardo.abramof@inpe.br
ORCID: 0000-0001-7560-7470

RAPPL Paulo
paulo.rappl@inpe.br
ORCID: 0000-0003-4548-3416

Received 04.05.2022. Approved after reviewing 05.07.2022. Accepted 05.07.2022.

Conference materials

UDC 535.015

DOI: <https://doi.org/10.18721/JPM.153.303>

Transport and optical phenomena in two-dimensional Dirac semimetals

G. R. Rakhmanova ¹✉, D. D. Sedov ¹, I. V. Iorsh ¹

¹ School of Physics and Engineering, ITMO University, Saint Petersburg, Russia

✉ gulnaz.rahmanova@metalab.ifmo.ru

Abstract. The discovery of graphene with Dirac cones at the Fermi energy attracted intense interest in the field of two-dimensional materials. However, in many two-dimensional materials, including graphene, Dirac points are gapped by spin-orbit coupling. Here we consider two-dimensional Dirac semimetals which have Dirac-like band dispersion in the presence of spin-orbit coupling protected by nonsymmorphic lattice symmetry. This is of interest because it opens a richer spectrum of optical properties than other topological materials. We choose the model of nonsymmorphic Dirac semimetal α -bismuthine containing anisotropic Dirac cones. We calculated interband and intra-band linear optical conductivity within the formalism based on the density matrix approach and Kubo formula. We show that electronic state in conduction band supports plasmons with quasi-linear anisotropic dispersion. The difference in the interband absorption spectrum can only be observed for electronic states on the Fermi surface and a width equal to the plasmon energy. The results suggest that such Dirac semimetals can be promising material for studying nonlinear optical properties.

Keywords: Dirac semimetal, plasmon, conductivity, linear response

Funding: The numerical calculations are funded by RPMA grant of School of Physics and Technology of ITMO University. The analytical calculations were supported by the Foundation for the Advancement of Theoretical Physics and Mathematics “BASIS” (No. 21-1-5-17-1).

Citation: Rakhmanova G. R., Sedov D. D., Iorsh I. V., Transport and optical phenomena in two-dimensional dirac semimetals, St. Petersburg State Polytechnical University Journal. Physics and Mathematics. 15 (3.3) (2022) 18–21. DOI: <https://doi.org/10.18721/JPM.153.303>

This is an open access article under the CC BY-NC 4.0 license (<https://creativecommons.org/licenses/by-nc/4.0/>)

Материалы конференции

УДК 535.015

DOI: <https://doi.org/10.18721/JPM.153.303>

Транспортные и оптические свойства двумерных материалов с дираковским спектром носителей заряда

Г. Р. Рахманова ¹✉, Д. Д. Седов ¹, И. В. Иорш ¹

¹ Физико-технический мегафакультет, Университет ИТМО, Санкт-Петербург, Россия

✉ gulnaz.rahmanova@metalab.ifmo.ru

Аннотация. Были изучены транспортные и оптические свойства двумерных (2D) полуметаллов Дирака. Исследован пример α -висмутена как 2D несимморфного полуметалла, содержащий анизотропные конусы Дирака, с различными скоростями Ферми вдоль направлений x и y . С помощью формализма Кубо были рассчитаны линейная внутризонная и межзонная проводимости. Было показано, что электронные состояния поддерживают 2D плазмоны с анизотропной квазилинейной дисперсией. Результаты позволяют предположить, что 2D полуметаллы Дирака несут в себе потенциал для усиленных квадратичных оптических откликов.

Ключевые слова: полуметаллы Дирака, проводимость, плазмоны, линейный отклик



Финансирование: Численные расчеты выполнены при финансовой поддержке гранта НИРМА ФТ МФ Университета ИТМО. Аналитические расчеты выполнены при финансовой поддержке Фонда развития теоретической физики и математики «БАЗИС» (№ 21-1-5-17-1).

Ссылка при цитировании: Рахманова Г. Р., Седов Д. Д., Иорш И. В. Транспортные и оптические свойства двумерных материалов с дираковским спектром носителей заряда // Научно-технические ведомости СПбГПУ. Физико-математические науки. 2022. Т. 15. № 3.3. С. 18–21. DOI: <https://doi.org/10.18721/JPM.153.303>

Статья открытого доступа, распространяемая по лицензии CC BY-NC 4.0 (<https://creativecommons.org/licenses/by-nc/4.0/>)

Introduction

The discovery of graphene with Dirac cones at the Fermi energy attracted intense interest in the field of two-dimensional (2D) materials [1]. However, Dirac points in many 2D materials, including graphene, are vulnerable to spin-orbit coupling (SOC) [2]. Recently, 2D Dirac semimetals with a nonsymmorphic symmetry has been predicted to have Dirac points not gapping by SOC [3]. Despite the long-term discovery of similar three-dimensional SOC-resistant Dirac points in several bulk materials [4], the search for realistic 2D materials that possess Dirac points at low energy remains a challenge. The article [5] discloses a family of monolayer materials of the HfGeTe as the first example of materials that support Dirac fermions robust against SOC close to the Fermi level. In [6] was shown the existence of 2D Dirac fermions in a chemically modified group-VA 2D puckered structure. In the presence of SOC Dirac nodal lines split and form an hourglass-shaped dispersion protected by a nonsymmorphic symmetry. These discoveries open the door to the study of 2D nonsymmorphic Dirac semimetal which may provide a richer spectrum of optical properties than other topological materials.

Dirac-like band dispersions have recently been described in the nonsymmorphic monolayer film, α -bismuthene (α -Bi) [7]. It is centrosymmetric and nonmagnetic material, so the time-reversal and inversion symmetries are preserved. In addition, the lattice is invariant under a glide mirror reflection that leads to protected Dirac points at the high symmetry momentum points of the Brillouin zone. In [8] theoretical analysis of the photon absorption spectrum for the model of α -Bi was investigated. In the absence of a magnetic field, the absorption coefficient is very similar to the absorption coefficient of graphene in that it is independent of frequency. In this paper, we will explore the new properties that nonsymmorphic symmetry brings to the optical conductivity.

Materials and Methods

Consider a quantum system described by the time independent Hamiltonian H_0 in equilibrium. Its eigenenergies are E_n and eigenstates are $|n\rangle$. Suppose now that a weak external perturbation is applied to the system at some time, $t = t_0$, in such a way that the Hamiltonian of the system is now written in the form:

$$\hat{H}(t) = \hat{H}_0 + \theta(t - t_0) \hat{V}(t) \quad (1)$$

Linear conductivity can be obtained within the formalism based on the density matrix approach, where the average current is given by:

$$\langle J(t) \rangle = \text{Tr}[J\rho(t)] = \sum_n \frac{e^{-\beta E_n}}{Z} \langle n(t) | \hat{J}(t) | n(t) \rangle, \quad (2)$$

where J is the current operator, $\rho(t)$ is the density matrix operator, E_n and $|n(t)\rangle$ are the eigenvalues and eigenfunctions written in the interaction picture, respectively. The time-

dependent eigenstates in the interaction picture are $|n(t)\rangle = \exp\left(-i/\hbar \int^t dt' \hat{V}(t')\right) |n\rangle$, the interaction term is given by $\hat{V}(t) = J(t, r) A(t, r')$, A is the vector potential of the perturbing field.

The current operator is introduced as $J = \frac{\partial H}{\partial A}$. The coupling to electromagnetic field is introduced via the gauge transform $k \rightarrow k - eA$.

The linear response of the current density j to the electric field E is defined in the frequency domain by

$$j(r, \omega) = \int d^3 r' \sigma(r, r', \omega) E(r', \omega) \quad (3)$$

where $\sigma(r, r', \omega)$ is the conductivity tensor. The corresponding Fourier transform can be taken in order to express the conductivity tensor in the representation $\sigma(q, \omega)$, where q is the wave vector.

Results and Discussion

1. Model

We choose the model of nonsymmorphic Dirac semimetal α -Bi containing anisotropic Dirac cones with different Fermi velocities along the x and y - directions that described by the Hamiltonian in the form [8]:

$$\hat{H} = v_x k_x (\sigma_x \cos \alpha + \sigma_y \sin \alpha) + v_y k_y \sigma_z \quad (4)$$

where σ_i are Pauli matrices for the spin degree of freedom, $v_y = v$ and $v_x = \rho v$. The anisotropy factor ρ refers to the mismatch in the Fermi velocity along x and y -direction. The angle α is the “mixing angle”, which is an intrinsic parameter of the model.

The eigenvalues are:

$$E = \pm v \sqrt{\rho^2 k_x^2 + k_y^2} \quad (5)$$

2. Linear Conductivity

We shall assume that $T \rightarrow 0$ and wave vector of plasmons is much smaller than Fermi wave vector.

We calculated x and y – components of the average current using the formula (2) and find the expression for conductivity through the formula (3).

Analytical solution for intra-band absorption coefficient in conductance band is given by:

$$\text{Re}(\sigma_x(w, \tilde{q})) = \frac{\alpha c}{\rho^2} \frac{2k_F \omega^2}{v q^2} \frac{1}{\sqrt{v^2 \tilde{q}^2 - \omega^2}} \quad (6)$$

where $\alpha = e^2 / \hbar c$ standing for the fine structure constant and $\tilde{q} = \sqrt{\rho^2 q_x^2 + q_y^2}$.

The result of eq. (6) describes 2D plasmons with anisotropic quasi-linear dispersion $\omega = v\tilde{q}$. Such plasmons are characterized by extremely long lifetimes. The (Fig. 1, a) shows the isofrequency diagram of absorption in the space of a quasi-wave vector in a 2D semimetal with a finite relaxation time, where it can be seen that the plasmons has an anisotropic dispersion. The Figure 1 (b) shows that plasmons have quasi-linear dispersion.

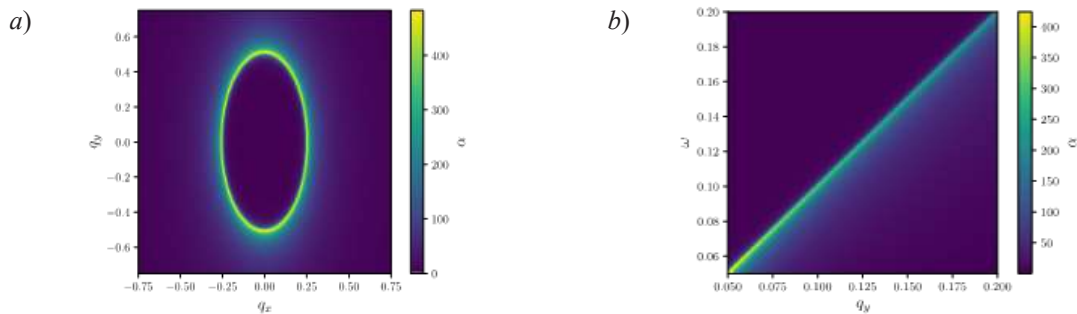


Fig. 1. The isofrequency diagram of absorption in the space of a quasi-wave vector in a 2D semimetal with a finite relaxation time (a). Absorption diagram in q, ω -space for $q_x=0$ (b)



Consider the interband conductivity. At zero temperature, plasmons, the collective oscillations of electrons, can only be excited at the Fermi surface. Therefore, the difference in the interband absorption spectrum can only be in the electronic states with the wave vector k_F . In terms of energy, the width of this region will be $2vq$, because it cannot be greater than the energy of the plasmon due to the conservation of energy and momentum. For electronic states with wave vector bigger than k_F the interband absorption coefficient is frequency-independent as in graphene:

$$\text{Re}(\sigma_x) = \frac{\pi\alpha v c}{2\rho^2}. \quad (7)$$

Conclusion

In conclusion, we demonstrate that 2D Dirac semimetals with nonsymmorphic symmetry have Dirac-like band dispersion in the presence of spin-orbit coupling that provides richer spectrum of optical properties. The electronic states in conduction band supports plasmons with quasi-linear anisotropic dispersion. The difference in the interband absorption spectrum can only be observed for electronic states on the Fermi surface and a width equal to the plasmon energy. These results suggest that 2D nonsymmorphic Dirac semimetals can be promising material for studying nonlinear optical properties. Also, such materials can be promising for tunable magneto-optical devices.

Acknowledgments

The numerical calculations are funded by RPMA grant of School of Physics and Technology of ITMO University. The analytical calculations were supported by the Foundation for the Advancement of Theoretical Physics and Mathematics “BASIS” (№ 21-1-5-17-1).

REFERENCES

1. Novoselov K. S., Geim A. K., Morozov S. V., Jiang D., Zhang Y., Dubonos S. V., Grigorieva I. V., Firsov A. A., Electric Field Effect in Atomically Thin Carbon Films, *Science*. 306 (5696) (2004) 666–669.
2. Fang C., Chen Y., Kee H.-Y., Fu L., Topological nodal line semimetals with and without spin-orbital coupling, *Phys. Rev. B*. 92 (2015) 081201.
3. Young S. M., Kane C. L., Dirac Semimetals in Two Dimensions, *Phys. Rev. Lett.* 115 (12) (2015) 126803.
4. Young S. M., Zaheer S., Teo J. C. Y., Kane C. L., Mele E. J. and Rappe A. M., Dirac Semimetal in Three Dimensions, *Phys. Rev. Lett.* 108 (2012) 140405.
5. Guan S., Liu Y., Yu Z.-M., Wang S.-S., Yao Y., and Yang S. A., Two-dimensional spin-orbit Dirac point in monolayer HfGeTe, *Phys. Rev. Materials*. 1 (2017) 054003.
6. Jin K.-H., Huang H., Wang Z., Liu F., 2D Nonsymmorphic Dirac Semimetal in Chemically Modified Group-VA Monolayer with Black Phosphorene Structure, *Nanoscale*. 11 (2019) 7256–7262.
7. Kowalczyk P. J., Brown S. A., Maerkl T., Lu Q., Chiu C.-K., Liu Y., Yang S. A., Wang X., Zasada I., Genuzio F., Mentesh T. O., Locatelli A., Chiang T.-C., Bian G., Realization of Symmetry-Enforced Two-Dimensional Dirac Fermions in Nonsymmorphic α -Bismuthene, *ACS Nano*. 14 (2) (2020) 1888–1894.
8. Chakraborty A., Bian G., Vignale G., Photon absorption of two-dimensional nonsymmorphic Dirac semimetals, *Phys. Rev. B*. 105 (2022) 085101.

THE AUTHORS

RAKHMANOVA Gulnaz R.
gulnaz.rahmanova@metalab.ifmo.ru
ORCID: 0000-0001-8750-4065

IORSH Ivan V.
i.iorsh@metalab.ifmo.ru
ORCID: 0000-0003-4992-6122

SEDOV Denis D.
denis.sedov@metalab.ifmo.ru
ORCID: 0000-0002-7241-7572

Received 12.07.2022. Approved after reviewing 14.07.2022. Accepted 14.07.2022.

Conference materials

UDC 544.032.65

DOI: <https://doi.org/10.18721/JPM.153.304>

In-flow laser modification of silver nanoparticles synthesized by spark discharge

O. V. Seraya ¹ ✉, A. A. Lizunova ¹, K. M. Khabarov ¹, M. Nouraldeen ^{1,2}, V. V. Ivanov ¹

¹ Moscow Institute of Physics and Technology, Dolgoprudny, Russia;

² Physics Department, Faculty of Science, Tartous University, Tartous, Syria

✉ seraia.ov@phystech.edu

Abstract. Silver nanoparticles have unique optical properties due to surface plasmon resonance, so they are widely used in various fields of science and technology. The synthesis of aerosol nanoparticles using a spark discharge allows to obtain submicron fractal agglomerated nanoparticles. For future application there is a need to develop new methods to produce nanoparticles with different shapes and sizes to control their optical properties. The article was devoted to the study of the processes of interaction of nanosecond laser radiation of different power (0.230 and 460 MW) and wavelength (527 and 1054 nm) with the flow of aerosol agglomerates of silver nanoparticles (10–400 ml/min) synthesized in a spark discharge, and the assessment of the effect of pulsed radiation power on the morphology of silver nanoparticles. It was shown that best modification of silver nanoparticles to spherical shape was formed at the maximum laser radiation power of the wavelength of 527 nm, close to the plasmon resonance peak for silver.

Keywords: nanoparticles, silver, spark discharge, laser radiation, modification, plasmon resonance

Funding: This research was funded by the Ministry of Science and Higher Education of the Russian Federation (State Contract No. 075-03-2022-107, Project Identifier 0714-2021-0007, Project Title: “Development of functional materials with controlled electrical, chemoresistive and catalytic properties for manufacturing sensor microsystems by using methods of printed electronics”).

Citation: Seraya O. V., Lizunova A. A., Khabarov K. M., Nouraldeen M., Ivanov V. V., In-flow laser modification of silver nanoparticles synthesized by spark discharge, St. Petersburg State Polytechnical University Journal. Physics and Mathematics. 15 (3.3) (2022) 22–26. DOI: <https://doi.org/10.18721/JPM.153.304>

This is an open access article under the CC BY-NC 4.0 license (<https://creativecommons.org/licenses/by-nc/4.0/>)

Материалы конференции

УДК 544.032.65

DOI: <https://doi.org/10.18721/JPM.153.304>

Лазерная модификация наночастиц серебра, синтезированных в газовом разряде

O. V. Seraya ¹ ✉, A. A. Lizunova ¹, K. M. Khabarov ¹, M. Nouraldeen ^{1,2}, V. V. Ivanov ¹

¹ Московский физико-технический институт, Долгопрудный, Россия;

² Кафедра физики, Факультет естественных наук, Тартусский университет, Тартус, Сирия

✉ seraia.ov@phystech.edu

Аннотация. Наночастицы серебра обладают уникальными оптическими свойствами благодаря поверхностному плазмонному резонансу и широко используются в различных областях науки и техники. С помощью газового разряда можно получить аэрозоль из фрактальных агломерированных наночастиц серебра. Для дальнейшего



применения интересны способы модификации их формы и размера для управления оптическими свойствами. Статья посвящена исследованию процессов взаимодействия наносекундного лазерного излучения различной мощности (0, 230 и 460 МВт) и длины волны (527 и 1054 нм) с потоком аэрозольных агломератов наночастиц серебра (10-400 мл/мин), синтезированных в газовом разряде, и оценке влияния мощности импульсного излучения на морфологию наночастиц серебра. Показано, что наилучшая модификация наночастиц серебра до сферической формы формируется при максимальной мощности лазерного излучения на длине волны 527 нм, близкой к пику плазмонного резонанса для серебра.

Ключевые слова: наночастицы, серебро, газовый разряд, лазерное излучение, модификация, плазмонный резонанс

Финансирование: Работа выполнена при финансовой поддержке Министерства науки и высшего образования Российской Федерации (государственное задание № 075-03-2022-107, проект «Разработка функциональных материалов с управляемыми электрическими, хеморезистивными и каталитическими свойствами для создания сенсорных микросистем с применением методов печатной электроники», идентификатор проекта 0714-2021-0007).

Ссылка при цитировании: Серая О. В., Лизунова А. А., Хабаров К. М., Нуралдин М., Иванов В. В. Лазерная модификация наночастиц серебра, синтезированных в газовом разряде // Научно-технические ведомости СПбГПУ. Физико-математические науки. 2022. Т. 15. № 3.3. С. 22–26. DOI: <https://doi.org/10.18721/JPM.153.304>

Статья открытого доступа, распространяемая по лицензии CC BY-NC 4.0 (<https://creativecommons.org/licenses/by-nc/4.0/>)

Introduction

Silver nanoparticles (NPs) have unique optical properties due to surface plasmon resonance, which can be tuned to a specific wavelength by changing the shape and size of the nanoparticles [1]. At the moment, there are several options for manufacturing volumetric micro-sized structures from nanoparticles that are used in electronics, Raman spectroscopy, photonics, solar energetics and biomedicine [2-5]. For example, such structures are obtained by lithography, inkjet printing using nanoinks or by dry aerosol printing with nanoparticles obtained in a pulsed spark discharge. The urgency of manufacturing and modifying particles in the flow for dry aerosol printing of plasmon structures is associated with ensuring a more environmentally friendly process, in contrast to the use of nanoinks, which entails environmental pollution and requires the subsequent removal of component residues from the obtained structures from nanoparticles and cleaning the nozzles from large microdrops. Moreover, the method of producing nanoparticles in a pulsed spark discharge is economically advantageous for obtaining nanoparticles of various metals, oxides and semiconductors and is devoid of difficulties associated with the synthesis, transportation and storage of components, and provides a lower electrical resistivity of sintered lines of silver nanoparticles than when annealing particles obtained from nanoinks as well [6].

Materials and Methods

The scheme of a setup describing the experiment principle is provided in Fig. 1. Nanoparticles synthesis was carried out in the discharge chamber that was made from glass (Duran glass, KF50, Millab) in which two hollow Ag electrodes were opposite mounted. An aerosol with silver nanoparticles was produced in a spark discharge (1.5 kV) in a flow of argon carrier gas (Ar 6.0) of 10-400 ml/min, then it was processed by laser radiation with a wavelengths' of 527 and 1054 nm at pulse energies up to 900 μ J and pulse repetition rate up to 500 Hz directly in the gas stream. The resulting aerosol was transported to a nozzle to focus it on a copper TEM-grid with carbon film for next TEM-characterization, cellulose filter and a substrate to form various plasmon nanostructures then. A more detailed description of the setup is provided in [7].

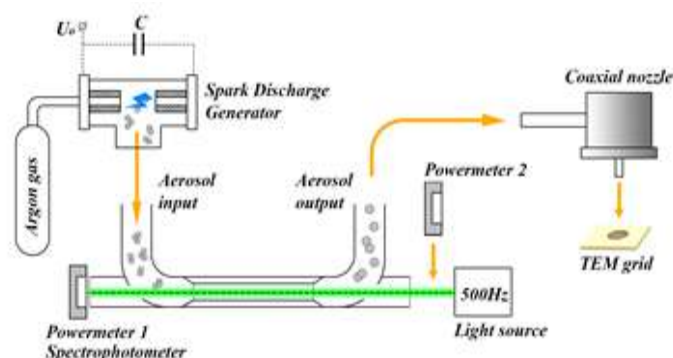


Fig. 1. Scheme of spark discharge synthesis of Ag NPs

During the project, the study of particle size parameters, morphology and phase composition was carried out using a set of methods. Transmission electron microscopy (TEM) on a JEOL JEM-2100 device with an accelerating voltage of 200 kV enforced getting images of nanoparticles and diffraction patterns for structure analyzing. Aerosol NP analyzer SMPS 3936 (TSI Inc., Shoreview, MN, USA) for measuring the particle size distribution in the flow was used. These measurements give an equivalent size of the primary nanoparticles' agglomerates. By Jasco V770 spectrophotometer extinction spectrums were obtained. ImageJ image analysis software for constructing a statistical distribution of the sizes of silver nanoparticles as well as information for analyzing diffraction patterns from the American Mineralogist Crystal Structure Database were used.

Results and Discussion

A typical TEM image of large agglomerate of primary nanoparticles obtained in the spark discharge (gas flow 50 ml/min) without laser interaction and the corresponding electron diffraction pattern are presented on figure 2. Most of the primary NPs' sizes were detected to be from 6 to 30 nm, a few single particles with sizes of 35–43 nm were observed. The average size was 16 ± 4.5 nm for primary silver nanoparticles, and 160 ± 132 nm for agglomerates (TSI data). Pursuant to SAED pattern we had concluded that all of NPs were crystallized in the silver phase of the Fm3m space group.

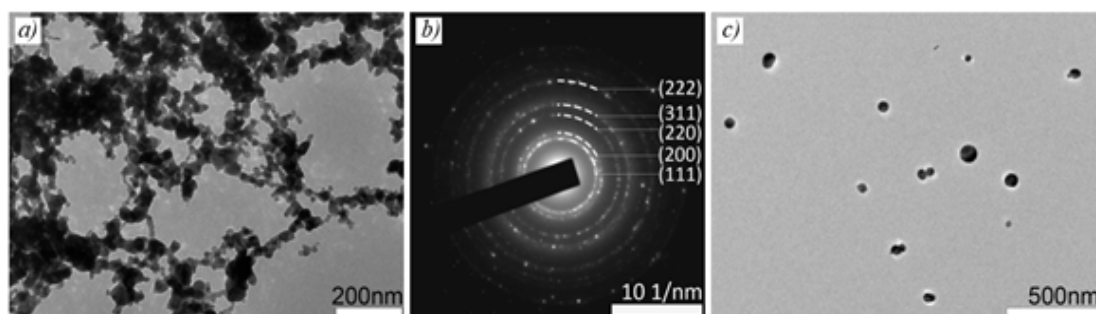


Fig. 2. TEM image of primary Ag NPs primary agglomerates (no laser) (a); SAED pattern taken from primary agglomerates area (b); TEM image of Ag NPs modified by laser radiation of wavelength of 527 nm (c)

Firstly, modification of nanoparticles with radiation of wavelength of 1054 nm was investigated. As a result of the conducted research, it turned out that the power value of pulsed laser radiation affects the size of nanoparticles and the shape of their agglomerates: smaller sizes were observed for nanoparticles that did not interact with laser radiation. Half-power red laser does not provide the sintering of all nanoparticles as well as full-power radiation. But number of sintered nanoparticles is higher in the last case. Moreover, sphere-like particles with small ones on their surface were detected. According to TEM images of Ag NPs modification by laser radiation of wavelength of 1054 nm (gas flow 50 ml/min), better modification was achieved using the full laser power (460 MW).

The observed amount of remaining agglomerates of primary nanoparticles (Fig. 4, *a*) led to the assumption that not all nanoparticles have enough time to interact with laser radiation, since they can be overlapped by others that have already interacted. In this regard, it was decided to reduce the gas flow from 50 to 10 ml/min. The flow of nanoparticles decrease affects the quality of sintering: individual spherical nanoparticles and reduction of agglomerates' groups number were observed.

During pulsed laser modification of aerosol agglomerates of nanoparticles, the sizes of sintered nanoparticles in the flow were measured by their electrical mobility, depending on the energy density of the incident radiation at pulse repetition frequencies of 50 and 500 Hz (Fig. 3, *a*). In the (Fig. 3, *a*), the black dotted line corresponds to the modal distribution size of the initial agglomerates, determined by their electrical mobility. Experimental dependences of the size of agglomerates demonstrate a NPs shrinkage that is the decrease in size as the energy density of laser pulses increases was observed. With a further increase in the pulse energy density, close shrinkage values are observed in the range of pulse energy densities, the shrinkage graph reaching a horizontal region with NPs sizes close to 100 nm at energy densities from 250 to 850 $\mu\text{J}/\text{cm}^2$ and pulse repetition frequencies of 50 and 500 Hz.

The energy required for modification depends on the size, material and extinction/absorption coefficient of nanoparticles at the laser wavelength. It is known that the maximum absorption coefficient of silver at a wavelength of 400 nm, that's why better modification by green laser than red was assumed. Absorption spectra analysis of silver agglomerated nanoparticles showed the maximum intensity peak of absorption energy at 390 nm closed to the green part of visible spectrum (Fig. 3, *b*). Shape changing by green laser impact to spherical was confirmed by TEM results (Fig. 2, *c*).

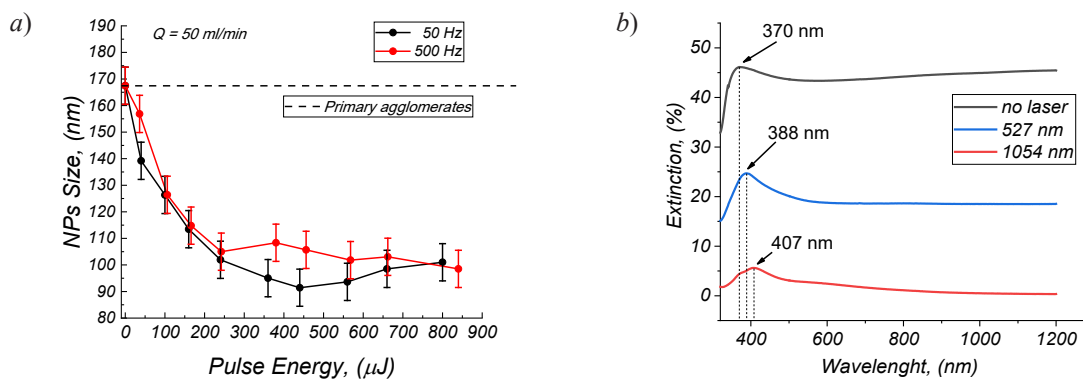


Fig. 3. Dependencies of Ag NPs size on the pulse energy density of laser radiation with the wavelength of 1054 nm at the pulse repetition rate of 50 Hz (black curve) and 500 Hz (red curve) (*a*); Absorption spectra of primary and modified NPs by laser radiation of wavelength of 1054 and 527 nm (gas flow: 50 ml/min) (*b*)

Conclusion

The best modification was achieved using the full red and green lasers' power (460 MW). All of NPs were crystallized in the silver phase of the Fm3m space group. Longer interaction time between NPs and laser radiation by decreasing the flow of nanoparticles provides better sintering quality: individual spherical silver particles were observed. Better spherical shape was obtained by full power green laser modification than red. The maximum absorption coefficient was detected at a wavelength of ~ 390 nm.

Acknowledgments

This research was funded by the Ministry of Science and Higher Education of the Russian Federation (State Contract No. 075-03-2022-107, Project Identifier 0714-2021-0007, Project Title: "Development of functional materials with controlled electrical, chemoresistive and catalytic properties for manufacturing sensor microsystems by using methods of printed electronics").

REFERENCES

1. Kelly K. L., Coronado E., Zhao L. L., Schatz G. C., The optical properties of metal nanoparticles: the influence of size, shape, and dielectric environment, *The Journal of Physical Chemistry B*, 107(3) (2003) 668–677.
2. Iskandar F., Nanoparticle processing for optical applications – A review, *Advanced Powder Technology*, 20(4) (2009) 283–292.
3. Li Y. S., Cheng J., Chung K. T., Surface-enhanced Raman spectroscopy using silver nanoparticles on a precoated microscope slide, *Spectrochimica Acta Part A: Molecular and Biomolecular Spectroscopy*, 69 (2) (2008) 524–527.
4. Catchpole K. A., Polman A., Plasmonic solar cells, *Optics express*, 16 (26) (2008) 21793–21800.
5. Ivanov V. V., Efimov A. A., Mylnikov D. A., Lizunova A. A., Synthesis of Nanoparticles in a Pulsed-Periodic Gas Discharge and Their Potential Applications, *Russian Journal of Physical Chemistry A*. 92 (3) (2018) 607–612.
6. Ivanov V. V., Efimov A. A., Mylnikov D. A., Lizunova A. A., Bagazeev A. V., Beketov I. V., Shcherbinin S. V. High-efficiency synthesis of nanoparticles in a repetitive multigap spark discharge generator, *Technical Physics Letters*. 42 (8) (2016) 876–878.
7. Khabarov K. M. , Urazov M. N., Lizunova A. A., Kameneva E. I., Efimov, A. A., Ivanov V. V., Influence of Ag Electrodes Asymmetry Arrangement on Their Erosion Wear and Nanoparticle Synthesis in Spark Discharge, *Applied Sciences*. 11 (9) (2021) 4147.

THE AUTHORS

SERAYA Olesya V.

seraia.ov@phystech.edu

ORCID: 0000-0001-6945-4818

LIZUNOVA Anna A.

lizunova.aa@mipt.ru

ORCID: 0000-0002-2895-4696

KHABAROV Kirill M.

kirill.khabarov@phystech.edu

ORCID: 0000-0002-8710-7040

NOURALDEEN Messan

messannouraldeen@phystech.edu

ORCID: 0000-0001-5437-0021

IVANOV Victor V.

ivanov.vv@mipt.ru

ORCID: 0000-0002-9149-0468

Received 04.05.2022. Approved after reviewing 05.07.2022. Accepted 05.07.2022.

Conference materials

UDC 52-334

DOI: <https://doi.org/10.18721/JPM.153.305>

Thermal and mechanical properties of a metal-matrix composite with ceramic inclusions

V. V. Rybin ¹✉, A. A. Solovyev ¹, A. D. Zuev ¹

¹ Ulyanovsk State University, Ulyanovsk, Russia

✉ vlad_rib@mail.ru

Abstract. Metal-matrix composite was a blend of fine aluminum powder serving as a matrix while neodymium or aluminium oxide with 10% of volume ratio as a ceramic inclusion. Samples of the cylinder shape were manufactured used powder metallurgy method. All samples dimensions were 12.7 mm in diameter and 4 mm in height. The aim of this study was to measure the microhardness, density, porosity and thermal conductivity of the material, as well as its SEM analysis. The metallographic analysis of the composite showed a uniform distribution of ceramic inclusions with an average size of 0.8–1.2 mm and a high porosity of 5.3–5.5% in volume. The research results of the properties of aluminum composites with various oxide inclusions were compared. Their thermal properties differ significantly, while the mechanical properties vary within the same limits. The obtained values are determined by the structure of composite and its production technology. They can be used to predict of the material behavior under external influences.

Keywords: aluminium matrix composite, aluminium oxide, neodymium oxide, thermal conductivity, microhardness

Citation: Rybin V. V., Solovyev A. A., Zuev A. D., Thermal and mechanical properties of a metal-matrix composite with ceramic inclusions, St. Petersburg State Polytechnical University Journal. Physics and Mathematics. 15 (3.3) (2022) 27–30 DOI: <https://doi.org/10.18721/JPM.153.305>

This is an open access article under the CC BY-NC 4.0 license (<https://creativecommons.org/licenses/by-nc/4.0/>)

Материалы конференции

УДК 52-334

DOI: <https://doi.org/10.18721/JPM.153.305>

Тепловые и механические свойства металло-матричного композита с керамическими включениями

В. В. Рыбин ¹✉, А. А. Соловьев ¹, А. Д. Зюев ¹

¹ Ульяновский государственный университет, Ульяновск, Россия

✉ vlad_rib@mail.ru

Аннотация. Исследуемый в работе металло-матричный композит был подготовлен методами порошковой металлургии, состоял из алюминия и 10% по объему оксида неодима или оксида алюминия. Целью исследования было измерение микротвердости, плотности, пористости и теплопроводности материала, а также изучение его микроструктуры. Проведено сравнение полученных результатов для композитов разного состава.

Ключевые слова: композит с алюминиевой матрицей, оксид алюминия, оксид неодима, теплопроводность, микротвердость

Ссылка при цитировании: Рыбин В. В., Соловьев А. А., Зюев А. Д. Тепловые и механические свойства металло-матричного композита с керамическими включениями // Научно-технические ведомости СПбГПУ. Физико-математические науки. 2022. Т. 15. № 3.3. С. 27–30. DOI: <https://doi.org/10.18721/JPM.153.305>

Статья открытого доступа, распространяемая по лицензии CC BY-NC 4.0 (<https://creativecommons.org/licenses/by-nc/4.0/>)

Introduction

Ceramic inclusions in metal-matrix composites increase their strength and hardness, chemical and thermal stability. Such materials have good resistance to elevated temperatures, therefore they are used for the production of thermal barrier coatings, turbine engines and other critical parts and assemblies.

Aluminum is a widely used matrix material due to its low weight, low cost and ease of fabrication. The reinforcing component is either oxides or carbides, and of them alumina (Al_2O_3), silicon carbide (SiC) and graphite in various configurations are widely used.

In most cases, manufacturing technology involves casting of various types and subsequent processing to give the desired geometry. Another production option is the use of powder metallurgy methods [1-2]. In this case, it is possible to obtain the required composition by simply mixing the components.

Composites used in this work based on aluminum powder with neodymium or aluminum oxide as ceramic inclusions, the volume fraction of which was 10%.

The aim of this work was to study the mechanical and thermophysical properties of the materials used.

Materials and Methods

Composites were obtained by adding Nd_2O_3 or Al_2O_3 powders at a volume ratio of 10% to Al matrix using powder metallurgy. Al powder having an average size of 30- μm as the matrix and oxide powders having an average size of 1 μm were used in the experiments.

The sintered samples were polished with various grit abrasive paper and diamond paste solution and etched also in order to conduct microstructure studies using optical microscope and scanning electron microscope (SEM). Microstructure studies were carried out using Zeiss Axio brand optical microscope, Phenom ProX brand SEM. The PMT-3M tester was used for microhardness measurements. Composite microhardness measurement method was carried out by Vickers test, which was based on ASTM standards (E. 92–82, 2003), with a Vickers hardness number

$$HV = 1.8544 \frac{P}{d^2}. \quad (1)$$

The microhardness of the produced samples was measured at room temperature for 10 s at a load of 5–20 g. After taking at least three measurements in different areas, the sample average hardness was taken.

Thermal conductivity of the composite was measured using a pulsed laser analyzer Linseis LFA 1000. Its chemical composition was determined using a micro-XRF spectrometer Bruker M4 Tornado.

Results and Discussion

The microstructure of sintered Al- Nd_2O_3 and Al- Al_2O_3 composites was characterized in order to determine if the particle distribution was consistent and the particle agglomeration occurred.

A typical microstructure of composite at high magnification is shown in Fig. 1. Locally located dark areas in the figure may be pores accumulation places and various defects in the crystal structure. The dark streaks are the result of the sample damage during the polishing process. Light areas appear to be sites of oxide accumulation.

Microstructural observations showed a homogeneous and uniform distribution of oxide particles in the composite matrix, which was noted in other researchers works [3]. The visible large light fields represent agglomerates of oxide phase particles.

The results of metallographic studies showed that the volume fraction of oxide inclusions was 2.25–2.45%, and their average size was 0.8–1.2 μm (Fig. 1). A similar structure of the composite also determined its density, which was 2.5 g/cm^3 .

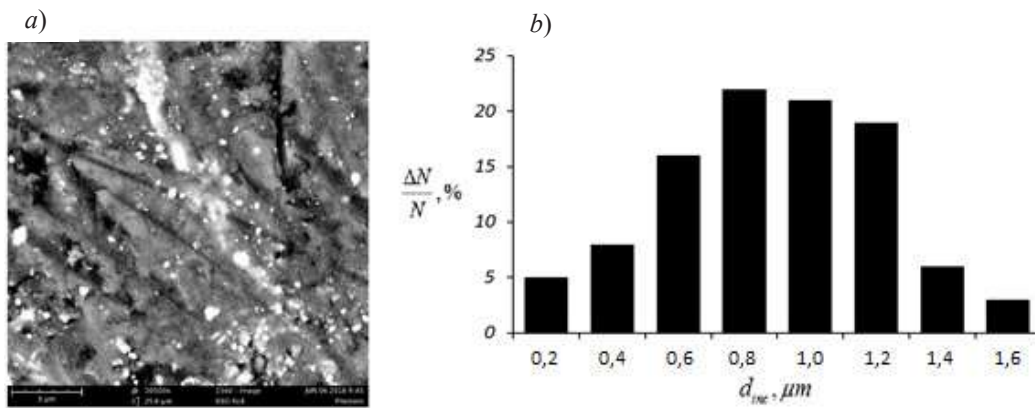


Fig. 1. SEM image (a) and oxide inclusions size distribution (b) of 10% Nd_2O_3/Al composite

The microhardness of studied composites, in comparison with cast and sintered aluminum [4], is shown in Table 1:

Table 1

Microhardness of composites and pure Al

Material	Microhardness, HV
Al+10% Nd_2O_3	54–60
Al+10% Al_2O_3	71–77
Sintered aluminum	38–42
Cast aluminum	29–31

The hardness of composites is comparable with the values obtained by other authors [5]. An increase in the hardness of the composite can be associated with a homogeneous and uniform distribution of inclusions in the aluminum matrix. Oxide particles act as a barrier to dislocation movement, strengthening the matrix by creating regions of high dislocation density. A decrease in the size of oxide particles located at the grain boundaries and distributed inside the grains causes blocking of the grain boundaries and deceleration of the movement of dislocations.

The thermal conductivity of studied composites is shown in Fig. 2.

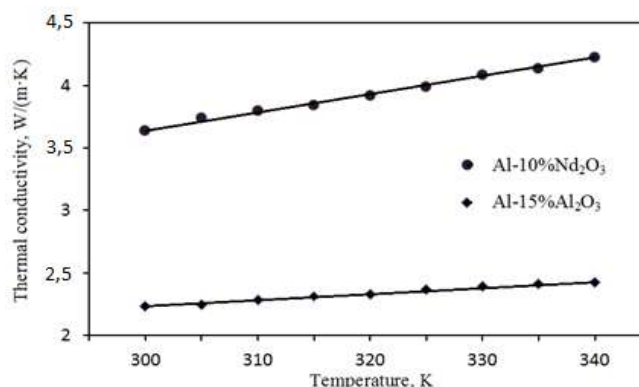


Fig. 2. The thermal conductivity of composite with inclusions of neodymium oxide and alumina

The measurement results showed that in the temperature range of 300–340 K, the materials have a thermal conductivity of 3.6–4.2 W/(m·K) for Al- Nd_2O_3 and 2.2–2.4 W/(m·K) for Al- Al_2O_3 , which is significantly lower than the values for cast and sintered powder aluminum (220 and 200 W/(m·K) at room temperature, respectively [6–7]) and even aluminum oxide (37 W/(m·K) at room temperature [8]).

Such low values of the thermophysical properties of the composite indicate poor thermal contact of various phases in its structure, a large volume of internal pores with zero thermal conductivity. In addition, aluminum powder particles are easily oxidized in air and covered with a thin oxide film with low thermal conductivity. Neodymium oxide, like oxides of other rare earth elements, also has a low thermal conductivity, not exceeding 1 W/(m·K) [9].

Conclusion

Microhardness and thermal conductivity of aluminum matrix composite with neodymium and aluminum oxide inclusions were investigated. The parameter values turned out to be low and comparable to aluminum hardened by its own oxide.

The conducted studies confirm the need for a more controlled process of composite sintering under high vacuum and increased pressing pressure. The low thermal conductivity of the material under study must be taken into account when choosing the thermal modes of operation of products made from it.

REFERENCES

1. **Tosun G., Kurt M.**, The porosity, microstructure, and hardness of Al-Mg composites reinforced with micro particle SiC/Al₂O₃ produced using powder metallurgy, *Composites Part B*. 174 (2019) 106965.
2. **Suarsana K., Soenoko R.**, Hardness, density and porosity of Al/(SiCw+Al₂O₃p) composite by powder metallurgy process without and with sintering, *Applied Mechanics and Materials*. 776 (2015) 246–252.
3. **Sadeghi B., Cavaliere P., Perrone A.**, Effect of Al₂O₃, SiO₂ and carbon nanotubes on the microstructural and mechanical behavior of spark plasma sintered aluminum based nanocomposites, *Particulate Science and Technology*. 38 (2020) 7–14.
4. **Garbiec D., Jurczyk M., Levintant-Zayonts N., Mosecicki T.**, Properties of Al–Al₂O₃ composites synthesized by spark plasma sintering method, *Archives of Civil and Mechanical Engineering*. 15 (2015) 933–939.
5. **Kamaruzaman F. F., Nuruzzaman D. M., Ismail N. M., Hamedon Z., Iqbal A. K. M. A., Azhari A.**, Microstructure and properties of aluminium-aluminium oxide graded composite materials, *IOP Conference Series: Materials Science and Engineering*. 319 (2018) 012046.
6. **Cardarelli F.**, *Materials Handbook: A Concise Desktop Reference*, second ed, Springer Verlag, London, 2008.
7. **Saheb N., Khan M. S.**, Compressive strength and thermal properties of spark plasma sintered Al–Al₂O₃ nanocomposite, *Science of Sintering*. 50 (2018) 1–14.
8. **Gudlur P., Forness A., Lentz J., Radovic M., Muliana A.**, Thermal and mechanical properties of Al/Al₂O₃ composites at elevated temperatures, *Materials Science and Engineering: A*. 531 (2012) 18–27.
9. **Predeep P., Saxena N. S.**, Effective thermal conductivity and thermal diffusivity of some rare earth oxides, *Physica Scripta*. 55 (1997) 634–636.

THE AUTHORS

RYBIN Vladislav V.
vlad_rib@mail.ru
ORCID: 0000-0001-8280-5256

ZUEV Alexander D.
cccu.73@gmail.com
ORCID: 0000-0001-9418-4311

SOLOVYEV Alexander A.
shurken@mail.ru
ORCID: 0000-0001-7317-2813

Received 04.05.2022. Approved after reviewing 05.07.2022. Accepted 05.07.2022.

Conference materials

UDC 538.975

DOI: <https://doi.org/10.18721/JPM.153.306>

Physical properties of InGaAs quantum dots in AlGaAs nanowires synthesized on silicon at different growth temperatures

R. R. Reznik ^{1, 2, 3, 4✉}, V. O. Gridchin ^{1, 2, 3}, K. P. Kotlyar ¹, E. V. Ubyivovk ¹,
A. S. Dragunova ⁵, N. V. Kryzhanovskaya ^{1, 5}, G. E. Cirlin ⁴

¹ Saint-Petersburg State University, St. Petersburg, Russia;

² Alferov University, St. Petersburg, Russia;

³ IAI RAS, St Petersburg, Russia;

⁴ ITMO University, St. Petersburg, Russia;

⁵ HSE University, St Petersburg, Russia

✉ moment92@mail.ru

Abstract. In this work, we have studied the physical properties of InGaAs quantum dots (QDs) in AlGaAs nanowires (NWs) synthesized on silicon at different temperatures. The results of the studies have shown that, a decrease in the growth temperature leads to an increase in the mole fraction of indium in the InGaAs QD solid solution. In this case, the number of defects in QDs increases significantly due to an increase in the mismatch in the crystal lattices parameters of NWs and QDs.

Keywords: III-V compounds, silicon, nanowires, quantum dots, molecular beam epitaxy

Funding: The samples were grown under financial support of the Ministry of Science and Higher Education of the Russian Federation, research project no. 2019-1442. The morphology of grown samples was studied under financial support of the Russian Science Foundation Grant № 21-72-00099. The study of grown samples optical properties was implemented in the framework of the Basic Research Program at the National Research University Higher School of Economics (HSE University). The structural properties of grown samples were carried out using equipment of St. Petersburg State University Interdisciplinary Resource Centre for Nanotechnology and St. Petersburg State University Resource Centre “Centre for Optical and Laser Materials Research” with the support of the grant from St. Petersburg University № 92591131.

Citation: Reznik R. R., Gridchin V. O., Kotlyar K. P., Ubyivovk E. V., Dragunova A. S., Kryzhanovskaya N. V., Cirlin G. E., Physical properties of InGaAs quantum dots in AlGaAs nanowires synthesized on silicon at different growth temperatures, St. Petersburg State Polytechnical University Journal. Physics and Mathematics, 15 (3.3) (2022) 31–35. DOI: <https://doi.org/10.18721/JPM.153.306>

This is an open access article under the CC BY-NC 4.0 license (<https://creativecommons.org/licenses/by-nc/4.0/>)

Материалы конференции

УДК 538. 975

DOI: <https://doi.org/10.18721/JPM.153.306>

Физические свойства InGaAs квантовых точек в AlGaAs нитевидных нанокристаллах, синтезированных на кремнии при разных ростовых температурах

Р. Р. Резник ^{1, 2, 3, 4✉}, В. О. Гридчин ^{1, 2, 3}, К. П. Котляр ¹, Е. В. Убийвовк ¹,
А. С. Драгунова ⁵, Н. В. Крыжановская ^{1, 5}, Г. Э. Цырлин ⁴

¹ Санкт-Петербургский государственный университет, Санкт-Петербург, Россия;

² Санкт-Петербургский академический университет имени Ж. И. Алферова РАН, Санкт-Петербург, Россия;

³ Институт аналитического приборостроения РАН, Санкт-Петербург, Россия;

⁴ Национальный исследовательский университет ИТМО, Санкт-Петербург, Россия;

⁵ Национальный исследовательский университет «Высшая школа экономики», Санкт-Петербург, Россия
 ✉ moment92@mail.ru

Аннотация. В работе представлены результаты экспериментальных исследований физических свойств InGaAs КТ в AlGaAs ННК, синтезированных на кремнии при различных температурах. Результаты исследований показали, что, как и ожидалось, снижение температуры роста приводит к увеличению мольной доли индия в твердом растворе InGaAs КТ. При этом количество дефектов в КТ значительно возрастает из-за увеличения несоответствия параметров кристаллических решеток ННК и КТ.

Ключевые слова: соединения III-V, кремний, нитевидные нанокристаллы, квантовые точки, молекулярно-пучковая эпитаксия

Финансирование: Министерство науки и высшего образования Российской Федерации, проект тематики научных исследований № 2019-1442. Российский Научный Фонд грант № 21-72-00099. Программа фундаментальных исследований НИУ ВШЭ. Междисциплинарный ресурсный центр СПбГУ по направлению «Нанотехнологии» и ресурсный центр СПбГУ «Оптические и лазерные методы исследования вещества» при поддержке гранта Санкт-Петербургского университета № 92591131.

Ссылка при цитировании: Резник Р. Р., Гридчин В. О., Котляр К. П., Убийвовк Е. В., Драгунова А. С., Крыжановская Н. В., Цырлин Г. Э. Физические свойства InGaAs квантовых точек в AlGaAs нитевидных нанокристаллах, синтезированных на кремнии при разных ростовых температурах // Научно-технические ведомости СПбГПУ. Физико-математические науки. 2022. Т. 15. № 3.3. С. 31–35. DOI: <https://doi.org/10.18721/JPM.153.306>

Статья открытого доступа, распространяемая по лицензии CC BY-NC 4.0 (<https://creativecommons.org/licenses/by-nc/4.0/>)

Introduction

Nowadays, semiconductor direct-gap nanostructures based on III-V compounds attract increased interest of researchers due to their unique optical, mechanical, and electrical properties [1]. Moreover, the possibility of these objects integration with silicon technology has opened up wide prospects for creating applications based on them [2]. Of particular interest are combinations of III-V materials of different dimensions on the silicon surface, for example, nanowires (NWs) with quantum dots (QDs) [3]. The development of modern methods of synthesis, such as molecular-beam epitaxy (MBE), makes it possible to controllably synthesize QDs in NWs with specified sizes and surface density. In our previous works, we successfully synthesized AlGaAs NWs with GaAs QDs on a silicon surface for the first time, and it was shown that a change in the QDs growth time leads to a shift of the corresponding photoluminescence (PL) line [4]. In addition, the results of autocorrelation measurements have shown that the formed QDs are sources of single photons, which makes them promising for quantum cryptography and other applications [4]. Nevertheless, to increase the range of applications based on such nanostructures, e.g., for telecom wavelengths, it is necessary to expand the range of QDs materials for shifting emission of single photon sources to a longer wavelength region towards 1.3–1.5 μm . At present, there is a number of papers reporting on the synthesis and properties of InGaAs QDs in GaAs NWs [5–7]. However, in most cases such nanostructures are grown on GaAs substrates and exhibit PL spectra only at low temperatures due to the low localization of charge carriers. In this case, the long-wavelength shift of the PL spectra is limited by a desorption of indium adatoms from the surface at the growth temperature of GaAs NWs (500–600 °C). In [8], we synthesized AlGaAs NWs with InGaAs QDs on a silicon surface, for the first time, at growth temperatures of 320–510 °C. Due to the fact that the band gap of AlGaAs exceeds that of GaAs, the localization of charge carriers in this case has a higher value. However, PL spectra at room temperature in the region of 1.3 μm were observed only from structures synthesized at high temperatures. Therefore, we made the assumption that as the growth temperature decreases, the number of indium adatoms embedded in QDs increases. In turn, this leads to an increase in the mismatch in lattice constants between QDs and NWs, thereby may leads to the appearance of structural defects in QDs.



In this paper we present the results of experimental studies of the structural properties of AlGaAs NWs with InGaAs QDs synthesized by MBE on a silicon surface at different temperatures.

Materials and Methods

Growth experiments were carried out using Riber 21 MBE setup equipped with the effusion Ga, Al, In and As₄ cells as well as a separate metallization chamber for Au deposition, which allows one to transfer the samples to the growth chamber with no vacuum brake. The growth procedure is described in details in [8]. Prior to the growth the fabrication of Au catalyst arrays was performed. First, the oxide-free Si surface was achieved by wet chemical treatment in HF:H₂O solution and then annealing at a temperature of 950 °C in the metallization chamber. Thereafter, the substrate temperature was decreased to 550 °C and deposition of ~1 nm thick Au film followed by 1 min exposure time to improve the droplets homogeneously. Then, the substrates were transferred to the growth chamber. Upon reaching the growth temperature, which was set at 400 °C and 510 °C in our experiments, the formation of AlGaAs NWs with nominal Al content $x = 0.3$ was initiated by simultaneous opening of Al, Ga, As sources. NWs growth processes lasted 25 min, whereas the formation of InGaAs insertion was realized at 20 min by short-term (20 s) switching of Al to In fluxes. The material fluxes from all sources were constant throughout the growth process and were corresponded to the growth rates of planar layers 0.5, 0.3 and 0.5 monolayers per second (ML/S) for Ga, Al and In fluxes, respectively, according to the preliminary calibrations on a separate substrate. The NWs growth process was controlled *in situ* by reflection high-energy diffraction (RHEED). It should be noted, that RHEED revealed the wurtzite crystal phase of AlGaAs NWs throughout their growth except at the very beginning (~1 min).

The samples obtained were characterized by scanning electron microscopy (SEM), transmission electron microscopy (TEM) combined with energy-dispersive X-ray (EDX) analysis. Optical properties of NWs were studied with the use of the macro-photoluminescence technique at room temperature.

Results and Discussion

Figure 1 shows the SEM images of the samples grown at: (a) 510 °C; (b) 400 °C. As can be seen from the figure, a decrease in the growth temperature leads to a change in the geometric parameters of NWs: a decrease in the height and an increase in the diameter. The reason for that is a significant decrease in the migration speed of Al adatoms over the surface, which restricts the migration of Ga adatoms. It should be noted that NWs are mainly formed in $\langle 111 \rangle$ direction which indicates their epitaxial relation to Si(111) substrate.

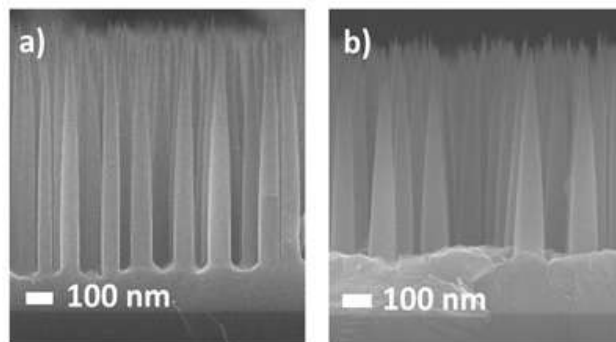


Fig. 1. Typical SEM images of AlGaAs NWs with InGaAs QDs grown on silicon at growth temperature of: (a) 510 °C; (b) 400 °C

Figure 2 shows typical PL spectra measured at room temperature from InGaAs QDs in AlGaAs NWs grown at 510 °C and 400 °C. It can be seen from the figure that the sample grown at 510 °C exhibit PL spectra at room temperature in a wide wavelength range from 850 to 1300 nm. Such a wide range of emission is associated with both the inhomogeneity of the QDs sizes in the NWs array and with the formation of several InGaAs nanoobjects in the AlGaAs NW bodies [8]. It is important to note, that the observation of PL spectra up to room temperature indicates the high optical quality of the structures. In turn, the intensity of the PL spectrum from the sample grown at 400 °C is at the noise level or is completely absent at room temperature. This may indicate a significant number of nonradiative recombination centers in QDs.

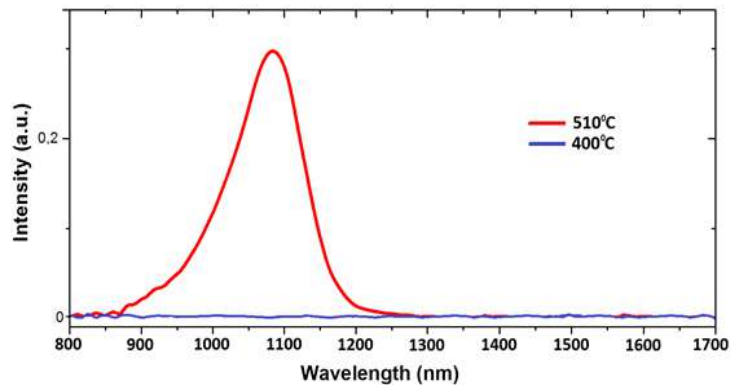


Fig. 2. Typical PL spectra measured at room temperature from InGaAs QDs in AlGaAs NWs grown on silicon at 510 °C and 400 °C

Typical TEM images of dispersed on a carbon grid single InGaAs QD in AlGaAs NW grown at the substrate temperatures of 510 °C and 400 °C are shown in figures 3, *a* and 3, *b*, respectively. It is seen that the QD grown at 510 °C contains only a few monolayers of the zinc blende structure in the wurtzite crystallographic phase of QD, which is associated with the features of the AlGaAs NWs synthesis. Studies of the grown at 510 °C InGaAs QD composition by the EDX method showed that the molar fraction of indium in QD is ~ 22%. As expected, the grown at 400 °C QD is highly dislocated and contains a large number of structural defects. The results of studies by the EDX method showed that the mole fraction of In in the solid solution of this QD is ~ 50%. Thus, the mismatch in the lattice constant parameters in the latter case increases significantly, leading to an increase in the number of nonradiative recombination centers in QDs, which is in good agreement with our pre-assumptions. One of the possible ways to overcome this problem can be the synthesis of small-size QDs. According to [9], when synthesized in a mismatched QD material with a size smaller than the critical one, the QD does not contain any structural defects. The results of corresponding studies will be presented in the following works.

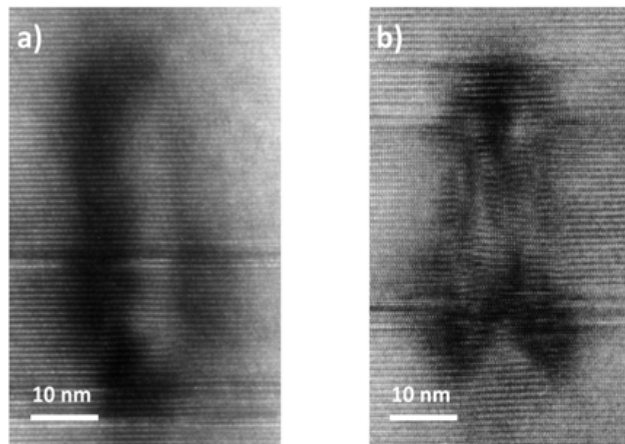


Fig. 3. Typical TEM images of single InGaAs QD in AlGaAs NW grown at the substrate temperatures of: 510 °C (*a*); 400 °C (*b*)

Conclusion

To conclude, we have studied the physical properties of InGaAs QDs in AlGaAs NWs synthesized on silicon at different temperatures. The results of the studies have shown that, as expected, a decrease in the growth temperature leads to an increase in the mole fraction of indium in the InGaAs QD solid solution. In this case, the number of defects in QDs increases significantly due to an increase in the mismatch in the crystal lattices parameters of NWs and QDs. The results of the proposed method for solving this problem will be presented in the following works.



REFERENCES

1. Dubrovskii V. G., Cirlin G. E., Ustinov V. M., Semiconductor nanowhiskers: synthesis, properties, and applications, *Semiconductors*. 43 (12) (2009) 1539–1584.
2. Mertensson T., Svensson C. P. T., Wacaser B. A., Larsson M. W., Seifert W., Deppert K., Gustafsson A., Wallenberg L. R., Samuelson L., Epitaxial III–V nanowires on silicon, *Nano Letters*. 4 (10) (2004) 1987–1990.
3. Dalacu D., Mnaymneh K., Lapointe J., Wu X., Poole P. J., Bulgarini G., Zwiller V., Reimer M. E., Ultraclean emission from InAsP quantum dots in defect-free wurtzite InP nanowires, *Nano Letters*. 12 (11) (2012) 5919–5923.
4. Leandro L., Gunnarsson C. P., Reznik R., Juns K. D., Shtrom I., Khrebtov A., Kasama T., Zwiller V., Cirlin G., Akopian N., Nanowire quantum dots tuned to atomic resonances, *Nano Letters*. 18 (11) (2018) 7217–7221.
5. Tatebayashi J., Kako S., Ho J., Ota Y., Iwamoto S., Arakawa Y., Growth of InGaAs/GaAs nanowire-quantum dots on AlGaAs/GaAs distributed Bragg reflectors for laser applications, *Journal of Crystal Growth*. 468 (2017) 144–148.
6. Heiss M., Ketterer B., Uccelli E., Morante J. R., Arbiol J., Morral A. F., Circumventing the Miscibility Gap in InGaN Nanowires Emitting from Blue to Red, *Nanotechnology*. 22 (19) (2011) 195601.
7. Makhonin M., Foster A., Krysa A., Fry P., Davies D., Grange T., Walther T., Skolnick M., Wilson L., Homogeneous array of nanowire-embedded quantum light emitters, *Nano Letters*. 13 (3) (2013) 861–865.
8. Reznik R. R., Ilkiv I. V., Kotlyar K. P., Gridchin V. O., Bondarenko D. N., Lendyashova V. V., Ubyivovk E. V., Dragunova A. S., Kryzhanovskaya N. V., Cirlin G. E., Molecular-Beam Epitaxy Growth and Properties of AlGaAs Nanowires with InGaAs Nanostructures, *Physica Status Solidi-Rapid Research Letter*. (2022) 2200056.
9. Tonkikh A. A., Tsyrlin G. E., Talalaev V. G., Novikov B. V., Egorov V. A., Polyakov N. K., Samsonenko Yu. B., Ustinov V. M., Zakharov N. D., Werner P., Room-temperature 1.5–1.6 μm photoluminescence from InGaAs/GaAs heterostructures grown at low substrate temperature, *Semiconductors*. 37 (12) (2003) 1406–1410.

THE AUTHORS

REZNIK Rodion R.
moment92@mail.ru
ORCID: 0000-0003-1420-7515

KRYZHANOVSKAYA Natalia V.
nataliakryzh@gmail.com
ORCID: 0000-0002-4945-9803

GRIDCHIN Vladislav O.
gridchinfo@gmail.com
ORCID: 0000-0002-6522-3673

UBYIVOVK Evgenii V.
moment92@mail.ru
ORCID: 0000-0003-1420-7515

KOTLYAR Konstantin P.
konstantin21kt@gmail.com
ORCID: 0000-0002-0305-0156

CIRLIN George E.
george.cirlin@mail.ru
ORCID: 0000-0003-0476-3630

DRAGUNOVA Anna S.
anndra@list.ru
ORCID: 0000-0002-0181-0262

Received 04.05.2022. Approved after reviewing 05.07.2022. Accepted 05.07.2022.

Conference materials

UDC 538.975

DOI: <https://doi.org/10.18721/JPM.153.307>

Effect of FIB-modification of Si(111) surface on GaAs nanowire growth

N. A. Shandyba ¹✉, D. V. Kirichenko ¹, N. E. Chernenko ¹,
M. M. Eremenko ¹, S. V. Balakirev ¹, M. S. Solodovnik ¹

¹ Southern Federal University, Taganrog, Russia

✉ shandyba@sfedu.ru

Abstract. The paper presents the results of experimental studies of GaAs nanowire growth on Si(111) substrate with Ga focused ion beam modified areas with different treatment doses. We observed a significant difference between the parameters of nanowires arrays formed on modified and unmodified areas. It is shown that changing the dose of Ga ions from 52 fC/ μm^2 to 1×10^4 fC/ μm^2 allows to form nanowire arrays with a different set of parameters in a single technological cycle with a high selectivity. The possibility of regulating of the NW length in the range of 1–6 μm , the density in the range of 0–7.8 μm^{-2} , the diameter in the range of 28–95 nm and the normally oriented NWs in the range of 5–70 % by focused ion beam have been experimentally demonstrated. The change of modes and mechanisms of the catalytic centers formation and the initial stage of GaAs NWs growth were revealed.

Keywords: nanowires, gallium arsenide, focused ion beam, molecular beam epitaxy, silicon

Funding: This work was supported by the Ministry of Science and Higher Education of the Russian Federation; the state task in the field of scientific activity No. FENW-2022-0001 at the Southern Federal University.

Citation: Shandyba N. A., Kirichenko D. V., Chernenko N. E., Eremenko M. M., Balakirev S. V., Solodovnik M. S., Effect of FIB-modification of Si(111) surface on GaAs nanowire growth, St. Petersburg State Polytechnical University Journal. Physics and Mathematics, 15 (3.3) (2022) 36–41. DOI: <https://doi.org/10.18721/JPM.153.307>

This is an open access article under the CC BY-NC 4.0 license (<https://creativecommons.org/licenses/by-nc/4.0/>)

Материалы конференции

УДК 538.975

DOI: <https://doi.org/10.18721/JPM.153.307>

Исследование влияния ФИП-обработки поверхности Si(111) на процессы роста нитевидных нанокристаллов GaAs

Н. А. Шандыба ¹✉, Д. В. Кириченко ¹, Н. Е. Черненко ¹,
М. М. Ерёмченко ¹, С. В. Балакирев ¹, М. С. Солодовник ¹

¹ Южный федеральный университет, Таганрог, Россия

✉ shandyba@sfedu.ru

Аннотация. В работе представлены результаты экспериментальных исследований роста нитевидных нанокристаллов GaAs. Выявлено резкое различие между нитевидными нанокристаллами, сформированными на модифицированных и немодифицированных участках подложки Si. Показано, что изменение дозы имплантации ионов Ga с 52 фКл/мкм² до 1×10^4 фКл/мкм² позволяет варьировать параметры (плотность, диаметр, длину и ориентацию относительно подложки) массива нитевидных нанокристаллов в широком диапазоне условий в едином технологическом цикле. Представлены основные закономерности, которые отображают нелинейную зависимость параметров сформированных структур от дозы имплантации ионов.



Ключевые слова: нитевидные нанокристаллы, фокусированный ионный пучок, молекулярно-лучевая эпитаксия, кремний, арсенид галлия

Финансирование: Работа поддержана Министерством науки и высшего образования Российской Федерации; Государственное задание в области научной деятельности, проект № FENW-2022-0001.

Ссылка при цитировании: Шандыба Н. А., Кириченко Д. В., Черненко Н. Е., Ерёмченко М. М., Балакирев С. В., Солодовник М. С. Исследование влияния ФИП-обработки поверхности Si(111) на процессы роста нитевидных нанокристаллов GaAs // Научно-технические ведомости СПбГПУ. Физико-математические науки. 2022. Т. 15. № 3.3 С. 36–41. DOI: <https://doi.org/10.18721/JPM.153.307>

Статья открытого доступа, распространяемая по лицензии CC BY-NC 4.0 (<https://creativecommons.org/licenses/by-nc/4.0/>)

Introduction

III–V nanowires (NWs) are promising objects for creating various elements and devices in the fields of photonics, micro- and nanoelectronics, micromechanics and sensors. This is possible due to the combination of unique electronic, optical and mechanical properties of this nanostructure type [1]. The creation of devices based on NWs requires the development of technologies for controlling their main characteristics, such as: length, diameter, shape, chemical composition, doping type, doping level, and array density [2]. The fabrication of NWs is usually carried out using the “vapor-liquid-solid” (VLS) mechanism, which makes it possible to control the main NWs parameters by changing the size and surface arrangement of metal nanodroplets which act as catalytic centers for further NWs growth.

These changes can be performed using various combinations of epitaxial and lithographic methods [3]. So, depending on the type of VLS mechanism, electron beam lithography [4], nanoimprint lithography [5] and the so-called nanospheric lithography [6] are most widely used for NWs formation with different main characteristics.

Recently, the local ion-beam surface treatment using a Ga focused ion beam (FIB) has been actively studied as an alternative method for controlling NWs parameters [7–10]. This method makes it possible minimizing the main drawbacks of the traditional technological approaches based on the optical lithography operations, chemical wet and plasma etching [11–12].

On the one hand, the focused ion beam method can be used for the formation of holes in the masking oxide layer (in SiO₂/Si structures) with subsequent localization of catalyst droplets in them [7]. On the other hand, the Ga ion beam and self-catalytic VLS growth can be used for direct local formation of catalytic centers [8]. In this case, Ga ions implanted into the substrate by FIB form Ga droplets on the surface during further annealing which promote GaAs NW catalytic growth [9]. So, this technology makes it possible to effectively control the size, density and position of the formed metal droplets by changing various technological parameters of the FIB treatment and pre-growth annealing that thereby largely predetermining the characteristics of subsequently growing GaAs NWs [10]. At the same time, issues related to the mutual influence of the main parameters of ion-beam processing and epitaxial synthesis on the key characteristics of GaAs NWs remain poorly understood. The mechanisms underlying on the FIB-induced NW growth are also have many questions.

The aim of this work is to study the effect of the Si(111) surface treatment with different Ga ion doses on the GaAs nanowire growth.

Experiment

FIB treatment of the Si(111) surface was carried out using a Nova NanoLab 600 scanning electron microscope (SEM) equipped an ion beam system with a Ga ion source. We modified square areas with a size of 5×5 μm by Ga ion beam at accelerating voltage of 30 kV and beam current of 30 pA. The dose of Ga ions varied from 52 fC/μm² to 1×10⁴ fC/μm² by changing the number of FIB passes. Ga ions are predominantly implanted into the substrate surface under the used FIB treatment modes. So, surface etching was suppressed.

Self-catalytic GaAs NWs were grown by molecular beam epitaxy (MBE) on a SemiTEq STE 35. Si(111) samples with FIB-modified surface areas were preliminarily annealed under ultrahigh vacuum conditions at a temperature of 600 °C. At this stage, the processes of implanted Ga ions segregation were initiated to form Ga catalytic centres. In this condition, native Si oxide masking layer was not removed. It allowed us to simultaneously form GaAs NWs outside the modified regions. Then, GaAs NWs were grown at the same substrate temperature (600 °C) with the equivalent GaAs deposition rate and thickness equal to 0.25 ML/s and 200 nm, respectively. The Ga and As fluxes were preliminarily calibrated by the GaAs growth rate on GaAs(001) substrates.

The control of the obtained structures morphology was carried out by SEM methods. Analysis of the geometric parameters of GaAs NWs (length, diameter, density and orientation) based on SEM images was performed using specialized software SIS Software Scandium.

Results and discussion

An analysis of the obtained SEM images of the Si(111) surface with FIB-modified areas shows a significant effect of the Ga ion dose on the formation processes and geometric parameters of GaAs NW arrays (Fig. 1).

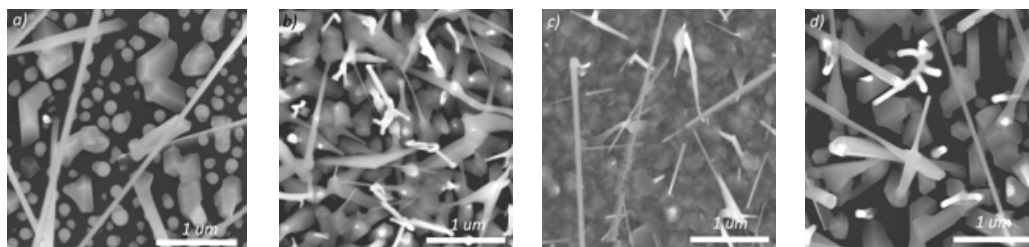


Fig. 1. SEM images of modified areas after GaAs nanowires growth for Ga ion dose of 52 fC/μm² (a), 260 fC/μm² (b), 1 × 10⁴ fC/μm² (c) and unmodified area (d)

Quantitative analysis of the GaAs NW arrays geometric parameters based on SEM images and subsequent statistical processing of the obtained data were performed (Fig. 2).

The NWs growth is significantly suppressed at the area with an ion dose of 52 fC/μm² (Fig. 1, a) and their density equal to 0.36 μm⁻² (Fig. 2, a). The NWs density value in this area is almost an order of magnitude lower than the array density formed on the unmodified surface (2.56 μm⁻²). At the same time, Ga droplets array is formed in this area with density of 13.6 μm⁻².

Increasing the FIB treatment dose leads to a sharp raising the GaAs NWs density (Fig. 1, b). The peak value of 7.8 μm⁻² is reached at the dose of 5.2 × 10³ fC/μm², which then gradually decreases to 5.76 μm⁻² (Fig. 1, c). It is also worth noting that the NWs density is more than 2 times higher than their density on the unmodified surface, excluding the data point of minimal dose value (Fig. 2, a).

The dependences of the GaAs NWs length and diameter on the FIB treatment dose (Figs. 2, b and 2, c, respectively) are quite similar. Both graphs show a sharp decrease in the NWs length and diameter with an increase in the ion dose. Starting from a dose of 1.56 × 10³ fC/μm², the values reach saturation. The NWs density in this range has a pronounced tendency to decrease (Fig. 2, a). We assume that this behaviour may be related to the intensification of the parasitic growth in the region of high doses (Fig. 1). The maximum value of normally oriented GaAs NWs is 70 % at a dose of 520 fC/μm² (Fig. 2, d). This dependence first increases, and then sharply decreases (at the dose of 5.2 × 10³ fC/μm²) with stabilization at a value in the range 6–10 % (the reference value is about 50 %).

We assumed that the use of low ion doses should suppress the formation of Ga droplets and GaAs crystallites on modify area by the following reasons. Ions are predominantly embedded into the crystal structure of the near-surface substrate layer at low doses regime. At the same time, the lattice is enriched with ions and the defects generated by them but retains its structure [13]. The concentration of defects in these areas is relatively low, so crystal structure relaxation is complicated during annealing. The presence of defects also makes it difficult for the implanted Ga ions (atoms) to reach the surface. This, in turn, affects the suppression of the catalyst

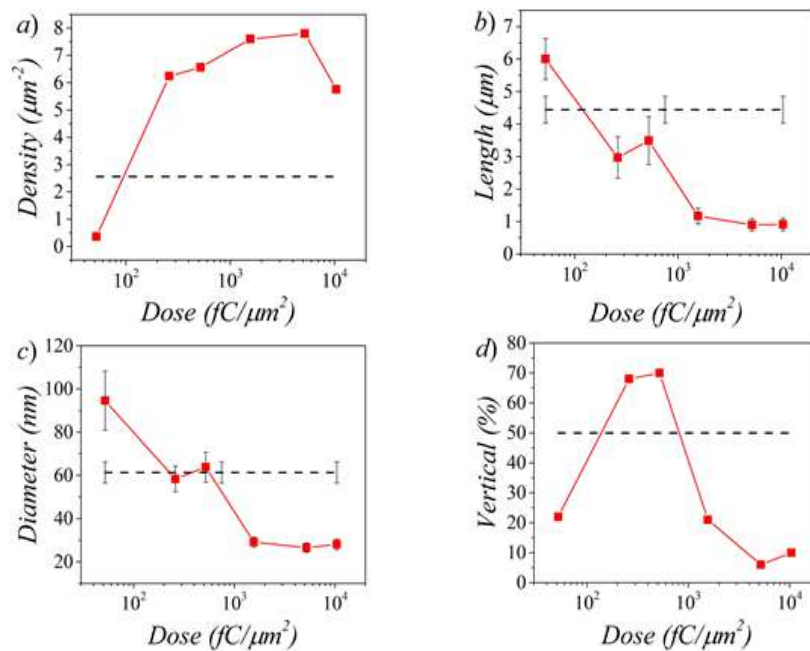


Fig. 2. Dependences of density (a), length (b), diameter (c) and vertical orientation of NWs (d) on Ga ion dose (dash lines correspond to values for unmodified areas).

droplets formation from the implanted material. While the expected result should have confirmed this assumption, this study showed that a high-density array of Ga droplets is formed in the area with a dose of 52 fC/μm² (Fig. 1, a). We believe that the droplets formed at the initial growth stage from supplied growth components. This is confirmed by the fact that there is almost complete suppression of directly catalytic growth with the participation of these droplets (Fig. 1, a; 2, a). We suppose that the reason of this behavior may be related with the NW nucleation stage. This stage was, apparently, kinetically retarded or extended in time in these areas. This led to the outflow of material to neighbouring regions, where the initial stage of NW formation proceeded much faster.

Changing the ion dose from 52 to 260 fC/μm² is accompanied by an increase in defects on the modified region. We think that this leads to enhanced of the crystal lattice relaxation processes at the annealing stage. This causes segregation of embedded Ga ions on the Si substrate surface and, as consequently, the formation of catalyst droplets [14]. The creation of the metal component excess on this area leads to an expected increase in the self-catalytic NWs density (more than 2 times) and GaAs crystallites, respectively (Figs. 1, b; 2, a). The values of NWs length and diameter decrease to 2.97 μm and 58 nm, respectively (Figs. 2, b; 2, c). It is also interesting to note that this area has a maximum fraction of GaAs NWs oriented normally to the substrate and equal to 70 %.

With a further increase in the dose up to 1×10⁴ fC/μm², the nanowire density changes insignificantly, while the diameter, length, and number of vertically oriented structures sharply decrease. We associate this system behaviour with a change in the GaAs NW nucleation mechanism. The formation of the metal component excess for the catalytic centres creation under conditions of 100 % coverage of surface with GaAs crystallites is possible only in the following case. We believe that in the process of epitaxial growth there is an additional uncompensated flow of Ga atoms due to continued segregation of embedded Ga ions. This assumption is in good agreement with the results of experimental studies. First, the NW diameter (Fig. 2, c) in the studied ion dose range is more than 2 times below reference values. We attribute this to the fact that the segregation flow of excess Ga to the surface is quite small. Consequently, the size of the formed catalytic centres and the diameter of the growing NWs is relatively small. Second, this flow should decrease with time due to the finite number of embedded Ga ions as can be seen from Fig. 1, c. GaAs NWs have a pronounced conical shape and a relatively small length (0.91 μm). Third, in this area the Ga droplets formation happen mainly not on the Si(111) surface, but on various faces of randomly oriented GaAs crystallites. So, the fraction of GaAs NWs oriented normally to the substrate decreases sharply and at doses above 1.56×10³ fC/μm² does not exceed 20 %.

Conclusion

Thus, the performed experimental studies have shown that the control of different NWs parameters by the FIB method is possible by varying the implantation dose of Ga⁺ ions into the Si(111) substrate. A sharp difference between NWs arrays formed on modified and unmodified regions of the Si substrate was revealed. It is shown that changing the dose of Ga ions from 52 fC/μm² to 1×10⁴ fC/μm² makes it possible to control the main NW parameters, such as: length (1–6 μm), density (0–7.8 μm⁻²), diameter (28–95 nm) and orientation (5–70 %). The change of modes and mechanisms of the catalytic centres formation and the initial stage of GaAs NWs growth has been experimentally demonstrated. The possibility of forming GaAs NWs arrays with significantly different geometric parameters on one sample in a single technological cycle is experimentally shown.

REFERENCES

1. Barrigon E., Heurlin M., Bi Z., Monemar B., Samuelson L., Synthesis and Applications of III–V Nanowires, *Chemical Reviews*. 119 (15) (2019) 9170–9220.
2. Ghasemi M., Leshchenko E. D., Johansson J., Assembling your nanowire: An overview of composition tuning in ternary III-V nanowires, *Nanotechnology*. 32 (7) (2021) 072001.
3. Ren D., Huh J., Dheeraj D. L., Weman H., Fimland B., Influence of pitch on the morphology and luminescence properties of self-catalyzed GaAsSb nanowire arrays, *Applied Physics Letters*. 109 (2016) 243102.
4. Plissard S., Larrieu G., Wallart X., Caroff P., High yield of self-catalyzed GaAs nanowire arrays grown on silicon via gallium droplet positioning, *Nanotechnology*. 22 (27) (2011) 275602.
5. Küpers H., Tahraoui A., Lewis R. B., Rauwerdink S., Matalla M., Krüger O., Bastiman F., Riechert H., Geelhaar L., Surface preparation and patterning by nano imprint lithography for the selective area growth of GaAs nanowires on Si(111), *Semiconductor Science and Technology*. 32 (11) (2017) 115003.
6. Madaria A. R., Yao M., Chi C. Y., Huang N., Lin C., Li R., Povinelli M. L., Dapkus P. D., Zhou C., Toward optimized light utilization in nanowire arrays using scalable nanosphere lithography and selected area growth, *Nano Letters*. 12 (6) (2012) 2839–2845.
7. Bahrami D., Mostafavi Kashani S. M., Al Hassan A., Davtyan A., Pietsch U., High yield of self-catalyzed GaAs nanowire growth on silicon (111) substrate templated by focused ion beam patterning, *Nanotechnology*. 31 (18) (2020) 185302.
8. Detz H., Kriz M., Lancaster S., MacFarland D., Schinnerl M., Zederbauer T., Andrews A. M., Schrenk W., Strasser G., Lithography-free positioned GaAs nanowire growth with focused ion beam implantation of Ga, *Journal of Vacuum Science & Technology B*. 35 (2017) 011803.
9. Hetzel M., Lugstein A., Zeiner C., Wyjcik T., Pongratz P., Bertagnolli E., Ultra-fast vapour-liquid-solid synthesis of Si nanowires using ion-beam implanted gallium as catalyst, *Nanotechnology*. 22 (39) (2011) 395601.
10. Lancaster S., Kriz M., Schinnerl M., MacFarland D., Zederbauer T., Andrews A. M., Schrenk W., Strasser G., Detz H., Focused ion beam implantation for the nucleation of self-catalyzed III-V nanowires, *Microelectronic Engineering*. 177 (2017) 93–97.
11. Za'bah N. F., Kwa K. S. K., Bowen L., Mendis B., O'Neill A., Top-down fabrication of single crystal silicon nanowire using optical lithography, *Journal of applied physics*. 112 (2) (2012) 024309.
12. Fan H. J., Werner P., Zacharias M., Semiconductor nanowires: from self-organization to patterned growth, *Small*. 2 (6) (2006) 700–717.
13. Lugstein A., Basnar B., Hobler G., Bertagnolli E., Current density profile extraction of focused ion beams based on atomic force microscopy contour profiling of nanodots, *Journal of Applied Physics*. 92 (2002) 4037–4042.
14. White C. W., Wilson S. R., Appleton B. R., Young Jr. F. W., Supersaturated substitutional alloys formed by ion implantation and pulsed laser annealing of group-III and group-V dopants in silicon, *Journal of Applied Physics*. 51 (1980) 738–749.



THE AUTHORS

SHANDYBA Nikita A.

shandyba@sfedu.ru

ORCID: 0000-0001-8488-9932

KIRICHENKO Danil V.

dankir@sfedu.ru

ORCID: 0000-0001-7476-2778

CHERNENKO Natalia E.

nchernenko@sfedu.ru

ORCID: 0000-0001-8468-7425

EREMENKO Mikhail M.

eryomenko@sfedu.ru

ORCID: 0000-0002-7987-0695

BALAKIREV Sergey V.

sbalakirev@sfedu.ru

ORCID: 0000-0003-2566-7840

SOLODOVNIK Maxim S.

solodovnikms@sfedu.ru

ORCID: 0000-0002-0557-5909

Received 19.07.2022. Approved after reviewing 27.07.2022. Accepted 28.07.2022.

Conference materials

UDC 538.9

DOI: <https://doi.org/10.18721/JPM.153.308>

Multistage droplet epitaxy for the fabrication of InAs/GaAs quantum dots with ultra-low density

S. V. Balakirev ¹, D. V. Kirichenko ¹✉, N. E. Chernenko ¹,
N. A. Shandyba ¹, M. M. Eremenko ¹, M. S. Solodovnik ¹

¹ Southern Federal University, Taganrog, Russia

✉ dankir@sfedu.ru

Abstract. In this paper, we demonstrate a novel technique enabling fabrication of small-sized InAs/GaAs quantum dots with a very low surface density during droplet epitaxy. In contrast to the traditional two-stage approach, we introduce an additional stage of exposure to the ultra-low arsenic flux which enables partial diffusion decay of droplets with a large initial size. While exposure of droplets to large arsenic fluxes leads to their transformation into rings, disks and holes, exposure to the ultra-low flux makes it possible to reduce the volume of droplets maintaining their initial surface density. At the following stages of crystallization and annealing, In droplets are converted into InAs quantum dots with an average diameter below 30 nm and a surface density below 10^8 cm⁻². The standard deviation of quantum dot diameters is found to be less than 5%. Furthermore, we demonstrate that the growth procedure is well-reproducible, which makes it a promising method of quantum dot fabrication for advanced nanophotonic devices.

Keywords: droplet epitaxy, InAs/GaAs, nanostructures, quantum dots

Funding: This study was supported by the Russian Science Foundation Grant No. 21-79-00310, at the Southern Federal University.

Citation: Balakirev S. V., Kirichenko D. V., Chernenko N. E., Shandyba N. A., Eremenko M. M., Solodovnik M. S., Multistage droplet epitaxy for the fabrication of InAs/GaAs quantum dots with ultra-low density, St. Petersburg State Polytechnical University Journal. Physics and Mathematics, 15 (3.3) (2022) 42–47. DOI: <https://doi.org/10.18721/JPM.153.308>

This is an open access article under the CC BY-NC 4.0 license (<https://creativecommons.org/licenses/by-nc/4.0/>)

Материалы конференции

УДК 538.9

DOI: <https://doi.org/10.18721/JPM.153.308>

Многостадийная капельная эпитаксия для формирования квантовых точек InAs/GaAs со сверхнизкой плотностью

С. В. Балакирев ¹, Д. В. Кириченко ¹✉, Н. Е. Черненко ¹,
Н. А. Шандыба ¹, М. М. Еременко ¹, М. С. Солодовник ¹

¹ Южный федеральный университет, Таганрог, Россия

✉ dankir@sfedu.ru

Аннотация. В данной статье демонстрируется новая методика, позволяющая получать квантовые точки InAs/GaAs малого размера с низкой поверхностной плотностью в процессе капельной эпитаксии. Особенность подхода заключается во введении дополнительной стадии экспозиции капель в ультрамалом потоке мышьяка, которая позволяет обеспечить частичный диффузионный распад капель с большим исходным размером при сохранении их исходной поверхностной плотности, после чего на стадиях кристаллизации и отжига капли In преобразуются в однородные массивы квантовых точек InAs с диаметром менее 30 нм и поверхностной плотностью менее 10^8 см⁻².

Ключевые слова. капельная эпитаксия, In/GaAs, наноструктуры, квантовые точки



Финансирование: Исследование выполнено за счет гранта Российского научного фонда № 21-79-00310, в Южном федеральном университете.

Ссылка при цитировании: Балакирев С. В., Кириченко Д. В., Черненко Н. Е., Шандыба Н. А., Ерёменко М. М., Солодовник М. С., Многостадийная капельная эпитаксия для формирования квантовых точек InAs/GaAs со сверхнизкой плотностью // Научно-технические ведомости СПбГПУ. Физико-математические науки. 2022. Т. 15. № 3.3. С. 42–47. DOI: <https://doi.org/10.18721/JPM.153.308>

Статья открытого доступа, распространяемая по лицензии CC BY-NC 4.0 (<https://creativecommons.org/licenses/by-nc/4.0/>)

Introduction

Today, studies of physical processes and phenomena in epitaxial nanostructures, such as quantum dots and rings, nanowires, tunnel-coupled heterostructures etc., are on their top because of their possible applicability in promising widely used quantum photonic and nanoelectronic devices [1]. Both fundamental and applied aspects of the nanostructure fabrication are also of great importance [2]. Although various methods of A3B5 quantum dot formation have been developed for their further use in high-efficiency semiconductor devices [3], a method of droplet epitaxy remains one of the most advantageous due to its flexibility and possibilities for the growth of various nanostructures excluding wetting layer formation [4, 5]. Because droplet epitaxial growth of nanostructures is carried out in two main stages – deposition of metal atoms forming droplets and their crystallization in the group-V vapor – it becomes possible to alter surface density and geometrical parameters of nanostructures independently [6, 7]. Low-density droplets are usually obtained at high substrate temperatures leading to a concomitant increase in their size [5, 8]. Large droplets cannot be then converted to compact quantum dots suitable for photonic and electronic applications. Meanwhile, quantum dots with ultra-low density are actively used for the fabrication of single and entangled photon emitters, in which case they must be well-isolated from each other [9].

In this paper, we demonstrate a technique of multistage droplet epitaxy which makes it possible to form single InAs quantum dots with an appropriate size (~ 25 nm) and an ultra-low density ($\sim 3 \cdot 10^7$ cm⁻²). The peculiarity of our technique consists in the introduction of an additional stage of droplet epitaxy between droplet formation and crystallization, namely exposure of indium droplets to the arsenic flux of an ultra-low value (10^{-7} – 10^{-6} Pa) which we demonstrated previously [6]. As a result of this exposure, indium atoms diffuse out of the droplets inducing their reduction in volume. Subsequent high-temperature crystallization of shrunk droplets enables formation of low-density semiconductor quantum dot arrays suitable for production of single quantum dot single and entangled photon sources on their basis.

Materials and Methods

The samples were grown in a SemiTEq STE35 molecular beam epitaxy system with solid-state sources on epi-ready GaAs substrates with the (001) orientation. The native oxide was removed by heating the substrate to 600 °C under a pressure of As₄ $P = 4 \cdot 10^{-5}$ Pa. Then, a GaAs buffer layer with a thickness of 250 nm was grown at a temperature of 580 °C at a growth rate of 1 monolayer (ML) per second. Next, the substrate was cooled down to the deposition temperature $T = 300$ °C with the arsenic valve completely closed. In order to monitor the growth process *in situ* and calibrate the growth rates, a reflection high-energy electron diffraction system was used in the growth chamber.

At the first stage of droplet epitaxy procedure, 1.5 equivalent ML of indium were deposited on the surface of the GaAs(001) substrate at a growth rate of 0.25 ML/s. At the next stage, droplets formed on samples A were exposed to an As₄ flux of various values (P/P_0 from 1 to 929 where $P_0 = 7 \cdot 10^{-8}$ Pa is a background pressure) and were kept in the growth chamber during 5 minutes after closing the arsenic valve. Substrates with droplets on samples B were brought to $T = 200$ °C, 300 °C, 400 °C and 500 °C and then exposed to the arsenic flux $P/P_0 = 714$ with immediate substrate heating to 500 °C. For two of group B samples, a period t between substrate heating

and arsenic supply was 60 and 180 seconds. Droplets on samples C were exposed to an ultra-low arsenic flux, after which they were arsenized at $T = 500\text{ °C}$ and $P/P_0 = 714$.

At the last stage, all samples were unloaded and characterized using FEI Nova Nanolab scanning electron microscope (SEM) and NT-MDT NTEGRA atomic force microscope (AFM).

Results and discussion

The average diameter of droplets obtained after deposition of 1.5 ML of indium on the GaAs(001) surface at $T = 300\text{ °C}$ is found to be 98 nm (Fig. 1, *a*). Exposure of the droplets to the arsenic flux leads to the formation of various nanostructures and their complexes [10]. A low arsenic flux is traditionally applied to transform In droplets into InAs rings [11] or to etch the surface under the droplets [12–14]. However, we use fluxes of ultra-low values (below 10^{-6} Pa) to demonstrate that droplets can be reduced in size under their exposure due to the phenomenon of diffusion decay [6]. As a result, a decrease in the droplet size from 98 to 18 nm is observed after exposure to the arsenic flux of various values P/P_0 in a range from 1 to 2.9. Because of the crystallization at a boundary of three phases, the formation of InAs ring also occurred around the original droplet circle (Fig. 1, *b*) The ring diameter does not change significantly with increasing P confirming the assumption about the nature of its formation.

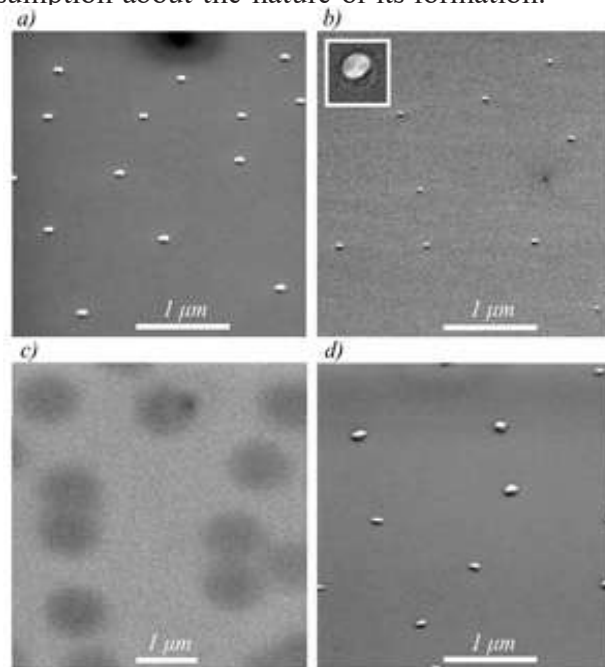


Fig. 1. SEM images of nanostructures obtained after deposition of 1.5 ML of indium and subsequent exposure to the arsenic flux P/P_0 : 1 (*a*); 1.4 (*b*); 500 (*c*); 714 with the simultaneous substrate heating up to 500 °C (*d*). Inset area is $150 \times 150\text{ nm}^2$.

An increase in the arsenic flux P/P_0 from 4 to 10 induces droplet etching of the surface leading to the formation of a hole under the initial droplet position. The droplet etching, also known as “nanodrilling”, is a process typical for high-temperature droplet epitaxy [15]. However, it is also observed in a range of low temperatures when the exposing arsenic flux is not very large [6]. The holes are found to have a diameter of about 40 nm surrounded by the original droplet ring with the depth of approximately 2 nm.

A significant increase in the arsenic flux (P/P_0 from 70 to 929) leads to the complete diffusion decay of droplets with their spreading over the surface within a disk-shaped area (Fig. 1, *c*). The average diameter of these disks ranges from 674 to 885 nm. More thorough consideration of the disk areas allows another observation of crystallized InAs rings at the place of original droplets. This indicates that the three-phase boundary crystallization has a higher rate among all the microscopic processes. At the same time, we found out previously that the droplet decay without ring formation is still possible in case of minimum arsenic fluxes when droplets have a larger size [6].



A transition to high-temperature exposure (at $T = 500\text{ }^{\circ}\text{C}$) leads to a qualitative change in the growth system. Droplets do not decay into monolayer-high disks but convert into faceted nanostructures (dots) (Fig. 1, *d*). The average diameter of dots obtained after the high-temperature arsenic exposure without a pause between the arsenic supply and substrate heating (heating expectation time $t = 0\text{ s}$) is 102 nm. However, we also study the dependence of the dot parameters on this time period. An increase in t from 0 to 60 and 180 seconds leads to a decrease in the diameter of dots from 102 to 87 nm and to 38 nm, respectively (Fig. 2). The reduction of dots with increasing expectation time is attributed to the fact that droplets decay during the arsenic exposure without heating rather than crystallize. However, as soon as the substrate reaches a certain temperature, crystallization becomes more preferable than the diffusion decay, and the remainders of droplets convert into faceted dots. The surface density of dots increases with increasing t from $3 \cdot 10^7$ to $9 \cdot 10^7\text{ cm}^{-2}$ which is associated with the fact that droplets may break up into several parts during the high-temperature exposure.

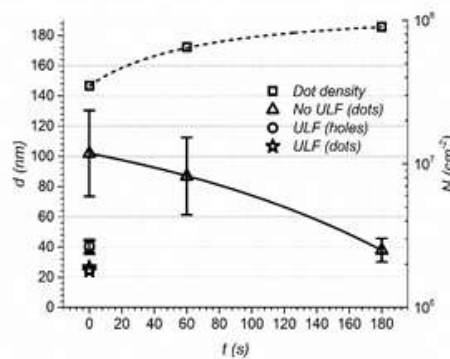


Fig. 2. Heating expectation time dependences of the diameter (triangles) and surface density (squares) of nanostructures obtained after deposition of 1.5 ML of indium and subsequent exposure to the arsenic flux $P/P_0 = 714$. Circles and stars denote diameters of holes and dots, respectively, obtained after two-stage exposure of droplets to the arsenic flux.

To obtain small-sized quantum dots with a value of the initial droplet density, we implement a two-stage exposure in the arsenic flux. At the first stage, the droplet volume is reduced to an optimal value under the influence of the ultra-low arsenic flux. At the final stage, a droplet with required parameters is crystallized into a semiconductor dot. Taking into account that the low-temperature arsenic exposure leads to the droplet decay and the high-temperature exposure allows fixation of the droplet shape with its further crystallization, we can select parameters at which dots have a size below 30 nm.

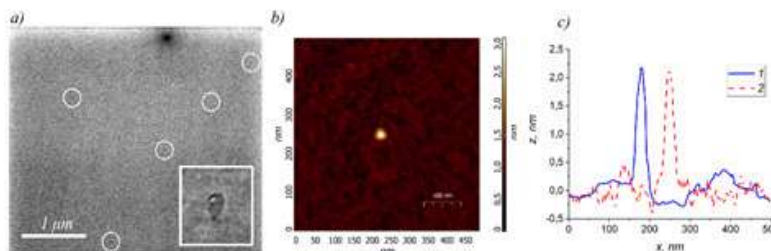


Fig. 3. SEM (*a*) and AFM (*b*) images of nanostructures obtained after deposition of 1.5 ML of indium and subsequent two-stage exposure to the arsenic flux. AFM (*c*) sections of typical nanostructures from Figure 4 *a*, *b*, *c*: 1) $P/P_0 = 2.0$, 2) $P/P_0 = 2.9$. Inset area is $150 \times 150\text{ nm}^2$

Figure 3 demonstrates our results of the two-stage exposure of droplets with various values of the ultra-low arsenic flux as an intermediate stage: $P/P_0 = 2$ (Fig. 3, *a*) and $P/P_0 = 2.9$ (Fig. 3, *b*). We observe that the resulting nanostructures represent dot-hole complexes wherein shallow holes surround nanodots. An average hole diameter is 40 nm, but it is not expected to have a significant influence on the optoelectronic properties of final structures. The main result

consists in the formation of small-sized dots located at a great distance from each other (more than 1 μm on average). The surface density of dots is found to be $3 \cdot 10^7 \text{ cm}^{-2}$ whereas their average diameter/height is 27/2.8 nm for $P/P_0 = 2$ and 24/2.5 nm for $P/P_0 = 2.9$ (Fig. 3). The dots have a small size dispersion with 4% and 5% standard deviation of their diameter for $P/P_0 = 2$ and $P/P_0 = 2.9$, respectively. Moreover, it is important to note that the technological procedure has good reproducibility which is confirmed by the fact that low-density of small-sized dots were formed on various samples with different values of the ultra-low arsenic flux.

Conclusion

Using the multistage droplet epitaxial technique, we demonstrated the possibility of fabrication of low-density arrays of droplets that can be reduced in size and then transformed into semiconductor quantum dots. In contrast to the one-stage crystallization in the arsenic vapor, nanostructures obtained after the pre-exposure of large droplets to the ultra-low arsenic flux have a small size and a small size dispersion. Because an initial droplet array is set to have a low surface density, crystallized dots are also located at a large distance from each other making it possible to easily find and separate them. Furthermore, the process is demonstrated to be well-reproducible which is especially important in semiconductor technology. Thus, the results obtained open up great opportunities for the fabrication of single quantum dots for modern quantum photonic and nanoelectronic devices.

REFERENCES

1. Wei S.-H., Jing B., Zhang X. Y., Liao J. Y., Yuan C. Z., Fan B. Y., Lyu C., Zhou D. L., Wang Y., Deng G. W., Song H. Z., Oblak D., Guo G. C., Zhou Q., Towards real-world quantum networks: a review, 16 (3) (2022) 1–29.
2. Große J., von Helversen M., Koulas-Simos A., Hermann M., Reitzenstein S., Development of site-controlled quantum dot arrays acting as scalable sources of indistinguishable photons, APL Photonics. 5 (2020) 096107.
3. Han I. S., Kim J. S., Noh S. K., Lee S. J., Hopkinson M., Tracing the two- to three-dimensional transition in InAs/GaAs sub-monolayer quantum dot growth, Applied Surface Science, 526 (2020) 146713.
4. Sanguinetti S., Watanabe K., Tateno T., Gurioli M., Werner P., Wakaki M., Koguchi N., Modified droplet epitaxy GaAs/AlGaAs quantum dots grown on a variable thickness wetting layer, Journal of Crystal Growth, 253 (2003) 71–76.
5. Balakirev S. V., Solodovnik M. S., Eremenko M. M., Konoplev B. G., Ageev O. A., Mechanism of nucleation and critical layer formation during In/GaAs droplet epitaxy, Nanotechnology, 30 (2019) 505601.
6. Balakirev S. V., Chernenko N. E., Eremenko M. M., Ageev O. A., Solodovnik M. S., Independent Control Over Size and Surface Density of Droplet Epitaxial Nanostructures Using Ultra-Low Arsenic Fluxes, Nanomaterials, 11 (2021) 1184.
7. Lee J. H., Wang Z. M., Salamo G. J., The control on size and density of InAs QDs by droplet epitaxy (april 2009), IEEE Transactions on Nanotechnology, 8 (4) (2009) 431–436.
8. Lee J. H., Wang Z. M., Salamo G. J., Observation of change in critical thickness of in droplet formation on GaAs(100), Journal of Physics: Condensed Matter, 19 (2007) 176223.
9. Wu J., Wang Z. M., Li X., Mazur Y. I., Salamo G. J., Fabrication of ultralow-density quantum dots by droplet etching epitaxy, Journal of Materials Research, 32 (2017) 4095–4101.
10. Somaschini C., Bietti S., Fedorov A., Koguchi N., Sanguinetti S., Outer zone morphology in GaAs ring/disk nanostructures by droplet epitaxy, Journal of Crystal Growth, 323 (1) (2011) 279–281.
11. Li X. L., Yang G. W., Growth mechanisms of quantum ring self-assembly upon droplet epitaxy, The Journal of Physical Chemistry C, 112 (2008) 7693–7697.
12. Heyn C., Stemmann A., Hansen W., Nanohole formation on AlGaAs surfaces by local droplet etching with gallium, Journal of Crystal Growth, 311 (7) (2009) 1839–1842.
13. Heyn C., Stemmann A., Klingbeil M., Strelow C., Köppen T., Mendach S., Hansen W., Mechanism and applications of local droplet etching, Journal of Crystal Growth, 323 (1) (2011) 263–266.



14. **Stemmann A., Heyn C., Kuppen T., Kipp T., Hansen W.**, Local droplet etching of nanoholes and rings on GaAs and AlGaAs surfaces, *Applied Physics Letters*, 93 (2008) 123108.
15. **Heyn C., Feddersen S.**, Modeling of Al and Ga droplet nucleation during droplet epitaxy or droplet etching, *Nanomaterials*, 11 (2) (2021) 1–13.

THE AUTHORS

BALAKIREV Sergey V.

sbalakirev@sfedu.ru

ORCID: 0000-0003-2566-7840

KIRICHENKO Danil V.

dankir@sfedu.ru

ORCID: 0000-0001-7476-2778

CHERNENKO Natalia E.

nchernenko@sfedu.ru

ORCID: 0000-0001-8468-7425

SHANDYBA Nikita A.

shandyba@sfedu.ru

ORCID: 0000-0001-8488-9932

EREMENKO Mikhail M.

eryomenko@sfedu.ru

ORCID: 0000-0002-7987-0695

SOLODOVNIK Maxim S.

solodovnikms@sfedu.ru

ORCID: 0000-0002-0557-5909

Received 04.05.2022. Approved after reviewing 05.07.2022. Accepted 05.07.2022.

Conference materials

UDC 538.9

DOI: <https://doi.org/10.18721/JPM.153.309>

Experimental study of nanoholes formation using local droplet etching of FIB-modified GaAs (001) surface

N. E. Chernenko ¹✉, D. V. Kirichenko ¹, N. A. Shandyba ¹,
S. V. Balakirev ¹, M. M. Eremenko ¹, M. S. Solodovnik ¹

¹ Southern Federal University, Taganrog, Russia

✉ nchernenko@sfedu.ru, insep@sfedu.ru

Abstract. In this work, we study of the effect of focused ion beam (FIB) and pre-growth treatment based on local droplet etching (LDE) techniques combination on the regular nanohole array formation on GaAs (001) surface, which can act as template for selective quantum dot formation in future. The results of the influence of the regimes of method combination on the nanohole shape and size are presented. Based on the analysis of Raman spectra, we have shown that the use of LDE-based technique makes it possible to almost restore the crystal structure of FIB-modified regions completely. The possibility of obtaining highly symmetrical, faceted by {101} and {011} planes nanoholes of various diameters and depths in selected surface points in one technological cycle is shown.

Keywords: focused ion beam, quantum dots, GaAs, molecular beam epitaxy, nanopatterning, local droplet etching

Funding: The study was supported by the Russian Science Foundation grant No. 21-79-00310 at the Southern Federal University, <https://rscf.ru/project/21-79-00310/>.

Citation: Chernenko N. E., Kirichenko D. V., Shandyba N. A., Balakirev S. V., Eremenko M. M., Solodovnik M. S., Experimental study of nanoholes formation using local droplet etching of FIB-modified GaAs (001) surface, St. Petersburg State Polytechnical University Journal. Physics and Mathematics, 15 (3.3) (2022) 48–53. DOI: <https://doi.org/10.18721/JPM.153.309>

This is an open access article under the CC BY-NC 4.0 license (<https://creativecommons.org/licenses/by-nc/4.0/>)

Материалы конференции

УДК 538.9

DOI: <https://doi.org/10.18721/JPM.153.309>

Экспериментальное исследование образования наноглублений с помощью локального капельного травления модифицированной поверхности GaAs (001) фокусированным ионным пучком

Н. Е. Черненко ¹✉, Д. В. Кириченко ¹, Н. А. Шандыба ¹,
С. В. Балакирев ¹, М. М. Еременко ¹, М. С. Солодовник ¹

¹ Южный Федеральный Университет, Таганрог, Россия

✉ nchernenko@sfedu.ru, insep@sfedu.ru

Аннотация. Вданной работе представлены результаты экспериментальных исследования влияния сочетания модификации поверхности GaAs(001) методом фокусированных ионных пучков (ФИП) и последующей предростовой обработки на основе техники локального капельного травления на процессы формирования упорядоченных массивов углублений с целью их использования в дальнейшем для селективного роста квантовых точек. Представлены результаты исследований режимов в рамках используемого подхода на размеры и форму формируемых углублений. С помощью рамановской спектроскопии показано, что капельное травление позволяет практически полностью восстановить кристаллическую структуру подложки в области ФИП-модификации.



Также продемонстрирована возможность получения высокосимметричных, ограниченных набором плоскостей $\{101\}$ и $\{011\}$ углублений различных размеров в заданных точках поверхности в рамках единого технологического цикла.

Ключевые слова: фокусированный ионный пучок, квантовые точки, GaAs, молекулярно-лучевая эпитаксия, наноструктурирование, локальное капельное травление

Финансирование: Исследование выполнено за счет гранта Российского научного фонда № 21-79-00310 в Южном федеральном университете, <https://rscf.ru/project/21-79-00310/>.

Ссылка при цитировании: Черненко Н. Е., Кириченко Д. В., Шандыба Н. А., Балакирев С. В., Еременко М. М., Солодовник М. С., Экспериментальное исследование образования наноглублений с помощью локального капельного травления модифицированной поверхности GaAs (001) фокусированным ионным пучком // Научно-технические ведомости СПбГПУ. Физико-математические науки. 2022. Т. 15. № 3.3. С. 48–53. DOI: <https://doi.org/10.18721/JPM.153.309>

Статья открытого доступа, распространяемая по лицензии CC BY-NC 4.0 (<https://creativecommons.org/licenses/by-nc/4.0/>)

Introduction

To date, research is being actively conducted aimed at the possibility of flexible control of the parameters of quantum dots (QDs), which underlie the creation of a promising elemental base of quantum communications (sources of single and entangled photons) and quantum computing (quantum registers based on quantum dots) [1–9]. The dependence of the functional characteristics of quantum dots on their composition, size, shape, and mutual arrangement in arrays requires the development of methods and technologies that allow one to effectively control the processes of formation of quantum dots and their final characteristics.

One of the most promising approaches in this respect is the use of combinations of epitaxial techniques with methods of pre-growth surface modification by forming an array of nanoholes at given points on the substrate. For pre-growth modification, electron-beam [10] and nanoimprint lithography [11] are most widely used today. However, traditional lithographic techniques are poorly compatible with subsequent epitaxial growth processes due to increased defect formation and/or surface contamination and do not provide the required quality of nanostructures.

Against this background, the technology of focused ion beams (FIB) compares favorably, which makes it possible to locally modify the sample surface under high vacuum conditions, without the use of resists, masks, and subsequent chemical surface treatment [12]. At the same time, ion bombardment of the surface during the FIB-treatment significantly damages the crystal structure of the substrate, which complicates the formation of optically active QDs in such nanoholes. Therefore, the use of FIB for these tasks requires the development of methods for reducing the defectiveness to an acceptable level or complete restoration of the substrate crystal structure.

In this work, to form ordered arrays of nanoholes for the subsequent selective QD growth, we propose to use a combination of modification of the GaAs(001) surface by the FIB method and subsequent pre-growth treatment based on the local droplet etching (LDE) technique. We have experimentally shown that, in this combination, the FIB method can be effectively used to localize the formation of Ga droplets with precision, and subsequent processing of samples based on droplet etching can be used to subsequently create highly symmetric nanoholes at modification points [13]. In this case, the droplet etching process is accompanied by the selective removal of amorphized and defects saturated near-surface regions at modification points. Experimental dependences of the influence of the dose of ion-beam treatment on the characteristics of the formed nanoholes in a single technological process are obtained.

Materials and Methods

For experimental study we used epi-ready GaAs(001) substrates. FIB-modification of GaAs surface was carried out using a Nova NanoLab 600 scanning electron microscope (SEM) equipped with a FIB system with a Ga ion source. For this we formed point arrays $5 \times 5 \mu\text{m}$ in size with distance of $1 \mu\text{m}$ between points using FIB treatment. We used ion beam with accelerating voltage

of 10 kV and beam current of 0.3 pA. The Ga ion dose was given by changing number of beam passes in each point. The passes number N was varied from 1 to 300.

Then we used pre-growth treatment based on combination of high temperature annealing and LDE technique in SemiTEq STE 35 MBE setup to obtain arrays of local nanoholes at FIB-modification points on the GaAs substrate. All samples were studied by the SEM, AFM, and Raman spectroscopy before and after pre-growth treatment.

Results and Discussion

An analysis of the AFM results showed that immediately after the FIB modification, starting from $N = 5$, an array of nanoholes is formed on the GaAs surface. In this case, the nanohole diameter increases with the increase in the number of FIB passes (and, accordingly, the dose of FIB-treatment) from 64 nm at $N = 5$ to 160 nm at $N = 300$. At same time the depth of the nanohole increases from 4.8 nm to 65.1 nm, respectively. Pre-growth treatment based on a combination of high-temperature annealing and local droplet etching leads to a transformation in the size and shape of the nanoholes. The structure diameter increases from 126 nm (at $N = 5$) to 310 nm (at $N = 300$), while the depth increases from 46 to 126 nm, respectively. In this case, as can be seen from the AFM profiles, the nanoholes become faceted. Analysis of the AFM profiles of nanoholes (Fig. 1, *a*) in different directions made it possible to determine the angle between the main faceting planes and the substrate plane, which is 45° .

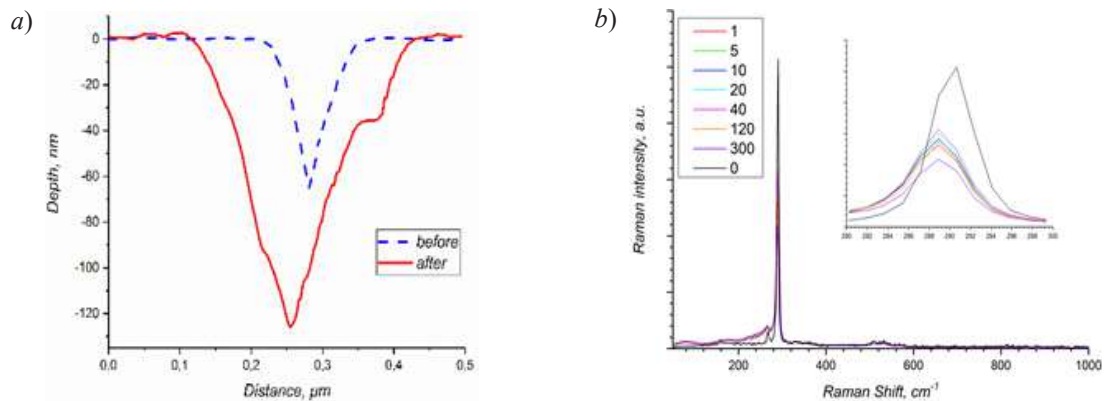


Fig. 1. AFM profiles of nanoholes before and after LDE-based treatment (*a*); Raman spectra from FIB-modified areas with different passes number (*b*)

The results of the study of samples by Raman spectroscopy are shown in Fig. 1, *b*. As can be seen from the presented spectra, an increase in the number of passes (dose of ion-beam treatment) leads to a decrease in the intensity of the LO-phonon line of crystalline GaAs 291 cm^{-1} – by about 1.5 times, which is due to saturation of the near-surface layers by defects in the crystal structure during processing. At the same time, at the points of modification, the LO-GaAs peak shifts by about 2 cm^{-1} to the left relative to the unmodified surface, which can also be associated with distortions of the crystal structure that occur in the regions adjacent to nanoholes. It is important to note that the intensity of the line decreases sharply even at the 1 pass, further decreasing insignificantly (Fig. 1, *b*). This may indicate that the main contribution to the reduction is due precisely to the defective region, and not to the amorphous layer directly on the surface at the etch points. In this case, the length of the defect regions is determined mainly by the energy of the ions, which depends on the accelerating voltage. Thus, we can say that the dose affects the concentration of defects within the region specified by the beam accelerating voltage.

Analysis of SEM images (Fig. 2) showed that after pre-growth treatment based on local droplet etching, highly symmetric nanoholed are formed on the surface at modification points, which correlates with AFM data. Taking into account the previously measured angles between the main facets and the surface plane, as well as the mutual orientation relative to the wafer base cuts, we found that the main facets of the nanoholes belong to the $\{101\}$ and $\{011\}$ plane families (Fig. 2, *a, b*). Moreover, it is important to note that as the number of passes and, as a consequence, the size of the nanohole increase, the $\{111\}$ A and $\{111\}$ B planes begin to appear additionally (Fig. 2, *c*). In addition, as can be seen from the presented SEM images, at small passes, the

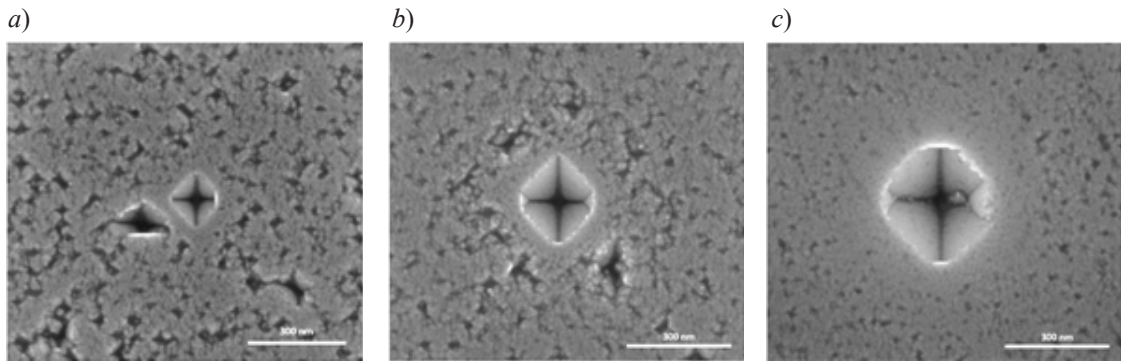


Fig. 2. SEM images of the GaAs (001) surface with nanoholes formed after LDE-based treatment of FIB-modified points with different number of FIB passes N : 5 (a), 40 (b), 300 (c)

surface around the nanoholes is inhomogeneous and has many disordered pits comparable in depth (up to 20 nm). However, as the treatment dose increases, an area of reduced roughness appears around the pits, which increases with the number of passes and the size of the hole. The high roughness of the unmodified areas is due to the processes of removal of native GaAs oxide at high temperatures. The formation of areas with reduced roughness is apparently due to the redeposition of the sputtered material during the FIB treatment, which at the LDE stage helps to remove the oxide, suppressing the etching processes on the surface.

Analysis of SEM images, taking into account information about the angles between the main faceting planes, made it possible to calculate the actual dimensions of the nanoholes and plot the corresponding dependencies (Fig. 3). As can be seen from the presented data, the nanohole diameters measured by AFM and those determined from SEM data are practically the same (Fig. 3, a). In this case, the lateral size of the structures after droplet etching increases by almost a factor of 2 compared to the initial one.

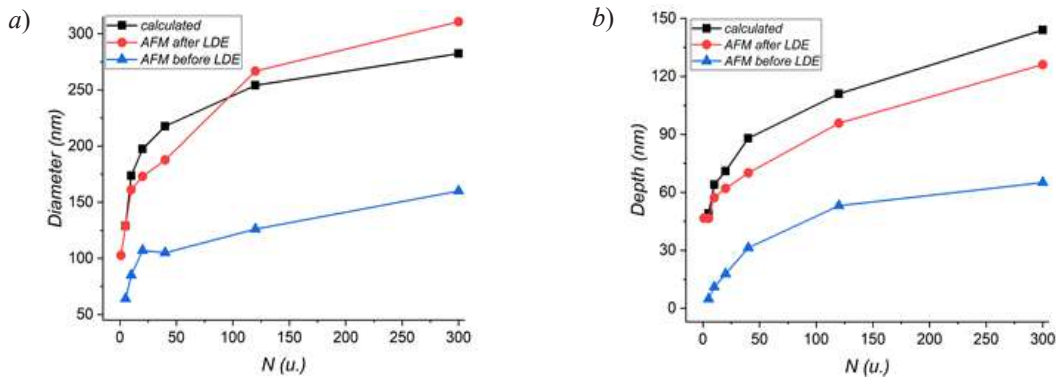


Fig. 3. Experimental dependences of the diameter (a) and depth (b) of the obtained nanoholes on the number of FIB passes before and after LDE-based treatment. Calculated – data based on SEM images analysis

We also showed a significant (many times) increase in the nanohole depth at the points of FIB-modification. If after FIB the nanohole depth changed, as mentioned earlier, from 4.8 to 65 nm (according to AFM data), then after LDE the calculated depth smoothly increases from 54 to 138 nm, i.e. 10 times – at low doses, and more than 2 times – at high ion doses. At the same time, as can be seen from the dependences, AFM underestimates the depth by approximately 10% in the entire measured range, which is due to the finite curvature of the AFM probe tip.

We attribute such a sharp and significant increase in the size of the modified cavities during pre-growth treatment to the anomalously high rate of anisotropic etching of the substrate by the Ga liquid droplet. This is due to the fact that, in contrast to the conventional LDE process, when the surface of the epitaxial layer with a high crystal structure perfection is subjected to local etching, in this case, much less stable regions with a disturbed crystal structure, saturated with defects and an excess of implanted Ga ions are etched. Thus, it can be assumed that the

pre-growth treatment based on LDE technique proposed by us makes it possible to selectively remove almost the entire defective area around the modification points. This opens broad prospects for using the proposed approach for creating templates with the aim of subsequently obtaining site-controlled optically active quantum dots. And the possibility of obtaining highly symmetric nanoholes makes this technique suitable for controlling the shape of quantum dots, which is very important for creating sources of single and entangled photons.

Conclusion

Thus, the results of experimental studies allow us to conclude that the use of a combination of the FIB and LDE methods is promising for creating ordered and highly symmetric nanoholes for obtaining regular (site-controlled) arrays of quantum dots of a given shape, size, and density. In addition, we have shown the possibility of obtaining holes of various sizes and shapes in a single technological cycle.

REFERENCES

1. Gurioli M., Wang Z., Rastelli A., Kuroda T., Sanguinetti S., Droplet epitaxy of semiconductor nanostructures for quantum photonic devices, *Nature Materials*. 18 (2019) 799–810.
2. Michler P., Kiraz A., Becher C., Schoenfeld W. V., Petroff P. M., Zhang L., Hu E., Imamoglu A., A quantum dot single-photon turnstile device, *Science* 290 (2000) 2282–2285.
3. Santori C., Fattal D., Vučković J., Solomon G. S., Yamamoto Y., Indistinguishable photons from a single-photon device, *Nature* 419 (2002) 594–597.
4. Schöll E., Hanschke L., Schweickert L., Zeuner K. D., Reindl M., Covre da Silva S. F., Lettner T., Trotta R., Finley J. J., Müller K., Rastelli A., Zwiller V., Jöns K. D., Resonance fluorescence of GaAs quantum dots with near-unity photon indistinguishability, *Nano Lett.* 19 (4) (2019) 2404–2410.
5. Akopian N., Lindner N. H., Poem E., Berlatzky Y., Avron J., Gershoni D., Gerardot B. D., Petroff P. M., Entangled photon pairs from semiconductor quantum dots, *Phys. Rev. Lett.* 96, (2006) 130501.
6. Huber D., Reindl M., Covre da Silva S. F., Schimpf C., Martín-Sánchez J., Huang H., Piredda G., Edlinger J., Rastelli A., Trotta R., Strain-Tunable GaAs Quantum Dot: A Nearly Dephasing-Free Source of Entangled Photon Pairs on Demand, *Phys. Rev. Lett.* 121 (2018) 033902.
7. Liu J., Su R., Wei Y., Yao B., Covre da Silva S. F., Yu Y., Iles-Smith J., Srinivasan K., Rastelli A., Li J., Wang X., A solid-state source of strongly entangled photon pairs with high brightness and indistinguishability, *Nat. Nanotechnol.* 14 (2019) 586.
8. Wang H., Hu H., Chung T.-H., Qin J., Yang X., Li J.-P., Liu R.-Z., Zhong H.-S., He Y.-M., Ding X., Deng Q., Dai Y.-H., Huo Y.-H., Hufiling S., Lu C.-Y., Pan J.-W., On-demand semiconductor source of entangled photons which simultaneously has high fidelity, efficiency, and indistinguishability, *Phys. Rev. Lett.* 122 (2019) 113602.
9. Kuroda T., Mano T., Ha N., Nakajima H., Kumano H., Urbaszek B., Jo M., Abbarchi M., Sakuma Y., Sakoda K., Suemune I., Marie X., and Amand T., Symmetric quantum dots as efficient sources of highly entangled photons: Violation of Bell's inequality without spectral and temporal filtering, *Phys. Rev. B* 88 (2013) 041306 (R).
10. Hugh M., Paul R., Aaron D. and Joanna M. M., Focused ion beam modification of surfaces for directed self-assembly of InAs/GaAs (001) quantum dots, *Nanotechnology* 18 (2007) 455303 (6pp).
11. Chien-Chia Cheng, Meneou K., Cheng K. Y., Effects of nano-pattern size on the property of InAs site-controlled quantum dots, *Journal of Crystal Growth* 323 (2011) 180–182.
12. Lisitsyn S.A., Balakirev S.V., Avilov V.I., Kolomytsev A.S., Klimin V.S., Solodovnik M.S., Konoplev B.G., Ageev O.A., Study of nanoscale profiling modes of GaAs epitaxial structures by focused ion beams, *Nanotechnologies in Russia*. 13 (1-2) (2018) 26–33.
13. Küster A., Heyn Ch., Ungeheuer A., Juska G., Moroni S. T., Pelucchi E. and Hansen W., Droplet etching of deep nanoholes for filling with self-aligned complex quantum structures, *Nanoscale Res. Lett.* 11 (2016) 282.



THE AUTHORS

CHERNENKO Natalia E.

nchernenko@sfedu.ru

ORCID: 0000-0001-8468-7425

KIRICHENKO Danil V.

dankir@sfedu.ru

ORCID: 0000-0001-7476-2778

SHANDYBA Nikita A.

shandyba@sfedu.ru

ORCID: 0000-0001-8488-9932

BALAKIREV Sergey V.

sbalakirev@sfedu.ru

ORCID: 0000-0003-2566-7840

EREMENKO Mikhail M.

eryomenko@sfedu.ru

ORCID: 0000-0002-7987-0695

SOLODOVNIK Maxim S.

solodovnikms@sfedu.ru

ORCID: 0000-0002-0557-5909

Received 04.05.2022. Approved after reviewing 05.07.2022. Accepted 05.07.2022.

Conference materials

UDC 538.9

DOI: <https://doi.org/10.18721/JPM.153.310>

Effect of pregrowth annealing temperature on the subsequent epitaxial growth of GaAs on Si

M. M. Eremenko ¹✉, S. V. Balakirev ¹, N. E. Chernenko ¹,
N. A. Shandyba ¹, O. A. Ageev ¹, M. S. Solodovnik ¹

¹ Southern Federal University, Taganrog, Russia

✉ eryomenko@sfedu.ru

Abstract. In this work, we studied the effect of the pregrowth annealing temperature on the epitaxial growth of GaAs on modified Si area. It is shown that an increase in the annealing temperature leads to a decrease in the selectivity of GaAs epitaxial growth, as well as to a transition from two-dimensional like growth to the growth of nanowires. At an accelerating voltage of 10 kV, 5 passes of the focused ion beam, and an annealing temperature of 600 °C, no epitaxial growth was observed on the modified areas. An increase in the accelerating voltage of the focused ion beam to 20 kV led to the onset of the formation of GaAs nanostructures at low values of the number of passes. An increase in the annealing temperature to 800 °C with the subsequent growth of GaAs leads to the activation of parasitic growth outside the modification regions over the entire range of accelerating voltages and the number of processing passes of the focused ion beam.

Keywords: silicon, gallium arsenide, molecular beam epitaxy, annealing, scanning electron microscopy, focused ion beam

Funding: This work was supported by the Russian Science Foundation Grant No. 20-69-46076 at the Southern Federal University.

Citation: Eremenko M. M., Balakirev S. V., Chernenko N. E., Shandyba N. A., Ageev O. A., Solodovnik M. S., Effect of pregrowth annealing temperature on the subsequent epitaxial growth of GaAs on Si, St. Petersburg State Polytechnical University Journal. Physics and Mathematics, 15 (3.3) (2022) 54–58. DOI: <https://doi.org/10.18721/JPM.153.310>

This is an open access article under the CC BY-NC 4.0 license (<https://creativecommons.org/licenses/by-nc/4.0/>)

Материалы конференции

УДК 538.9

DOI: <https://doi.org/10.18721/JPM.153.310>

Влияние температуры предростового отжига на последующий рост арсенида галлия на кремнии

M. M. Eremenko ¹✉, S. V. Balakirev ¹, N. E. Chernenko ¹,
N. A. Shandyba ¹, M. S. Solodovnik ¹, O. A. Ageev ¹

¹ Южный федеральный университет, Таганрог, Россия

✉ eryomenko@sfedu.ru

Аннотация. В данной работе исследовалось влияние температуры предростового отжига на эпитаксиальный рост GaAs на модифицированных участках Si. Показано, что повышение температуры отжига от 600 до 800 °C приводит к снижению селективности эпитаксиального роста GaAs, а также к переходу от двумерного роста к росту нитевидных нанокристаллов.

Ключевые слова: кремний, арсенид галлия, молекулярно-пучковая эпитаксия, отжиг, сканирующая электронная микроскопия, сфокусированный ионный пучок



Финансирование: Работа выполнена в рамках проекта Российского научного фонда № 20-69-46076 в Южном Федеральном университете.

Ссылка при цитировании: Ерёмченко М. М., Балакирев С. В., Черненко Н. Е., Шандыба Н. А., Агеев О. А., Солодовник М. С. Влияние температуры предостового отжига на последующий рост арсенида галлия на кремнии // Научно-технические ведомости СПбГПУ. Физико-математические науки. 2022. Т. 15. № 3.3. С. 54–58. DOI: <https://doi.org/10.18721/JPM.153.310>

Статья открытого доступа, распространяемая по лицензии CC BY-NC 4.0 (<https://creativecommons.org/licenses/by-nc/4.0/>)

Introduction

With its high-speed data processing capability, outstanding thermal performance, and low cost, silicon technology is the world leader in modern micro- and nanoelectronics. On the other hand, the indirect-gap nature of silicon does not allow it to be used as a basis for creating information transmission devices based on light sources. For these purposes, III-V semiconductors are used because of their outstanding optical properties. Therefore, in recent years, the task has been to find approaches for the integration of III-V semiconductors on silicon, which would allow combining the advantages of both technologies [1].

The formation of high-quality III-V structures on silicon still remains an unsolved task. One of the important tasks is the problem of mismatch of crystal lattice parameters between silicon and III-V materials, which prevents the monolithic integration of potential photonic integrated circuits based on silicon and III-V light emitting sources [2]. However, not only the difference in the lattice parameters of both materials affects the quality of resulting structures, but also the difference in thermal expansion coefficients [3], as well as the growth of a polar semiconductor on a nonpolar substrate [4].

Recently, many different growth and non-growth techniques have been used for monolithic integration: growth of nanowires (NW) [5], nanoinsertions [6], the use of misoriented substrates [7], aspect ratio trapping [8], etc. [2, 4, 9]. One such method is surface treatment with a focused ion beam (FIB). It is known from the works that this method is used to obtain NWs and makes it possible to create nucleation centers and localize the growth of structures [10, 11]. Also, by changing the parameters of FIB processing and subsequent annealing, it is possible to obtain amorphous and porous areas on a silicon substrate, which will potentially make it possible to reduce the defectiveness of the grown III-V structures [12, 13].

In this work, we study the influence of the annealing temperature of Si(100) modified by FIB on the subsequent GaAs epitaxial growth.

Materials and Methods

Experimental studies of GaAs epitaxial growth were carried out on FIB-modified Si(100) substrates. FIB modification was carried out by treating substrate areas $5 \times 5 \mu\text{m}$ in size with a Ga^+ beam with an accelerating voltage of 10 and 20 kV and beam passes varying from 5 to 200 (the implantation dose increased accordingly). Then the samples were placed in a growth chamber and subjected to annealing followed by epitaxial growth. The annealing temperature varied from 600 to 800 °C, the annealing time was 60 minutes. Next, a GaAs buffer layer 200 nm thick was deposited at a growth temperature of 600 °C and a growth rate of 0.25 ML/s. Then the samples were removed from the chamber and examined by scanning electron microscopy.

Results and Discussion

At the first stage of experimental studies, samples were obtained annealed at 600 and 800 °C. Fig. 1 shows a significant difference in the morphology of the FIB-modified areas after annealing. Upon annealing at 600 °C, the formation of GaAs structures nanosized arrays is observed on the surface of the modified areas treated at 20kV (Fig. 1, *a*), and upon annealing at 800 °C, holes are formed (Fig. 1, *b*). An explanation of this mechanism of change in the surface structure during annealing is presented in our previous work [12]. However, on surfaces treated with a 10 kV

beam, a slightly different result is observed. Annealing of such modified surfaces at 600 °C and beam passes number of 200 resulted in the formation of a high-density array with smaller GaAs crystallites (Fig. 1, *c*) than when processed with 20 kV. Increasing the annealing temperature to 800 °C did not lead to the formation of large holes in the modified 10 kV areas (Fig. 1, *d*), as in the case of beam treatment at 20 kV. This behavior is associated with a decrease in the distortion of the Si crystal lattice due to a simultaneous decrease in the ion energy and the implantation dose during FIB treatment at 10 kV.

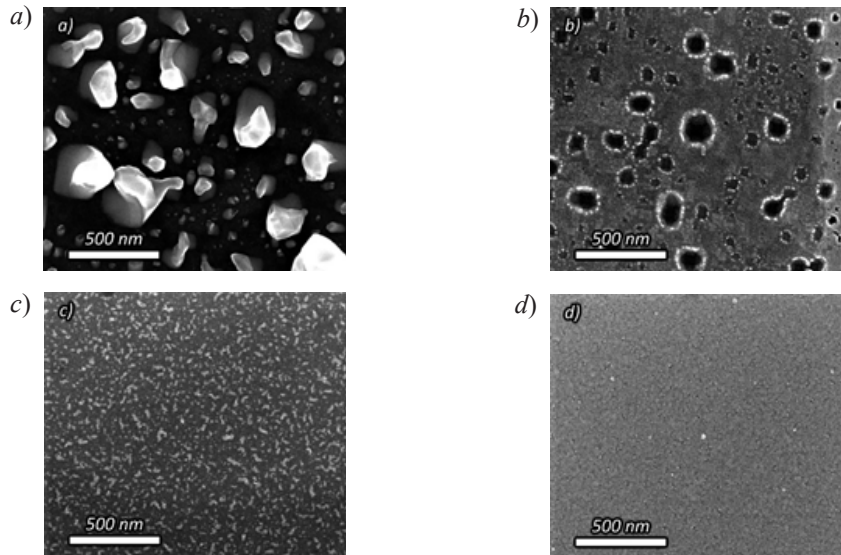


Fig. 1. SEM images of FIB-modified Si areas after annealing in arsenic flux at temperatures of 600 °C (*a*), (*c*) and 800 °C (*b*), (*d*). The accelerating voltage was 10 kV for (*a*), (*b*), and 20 kV for (*c*), (*d*). The number of beam passes was 200.

At the second stage, the epitaxial growth of GaAs on Si was performed. The results showed the possibility of achieving high selectivity of GaAs growth on FIB-modified samples annealed at 600 °C. A comparative analysis of the structures formed in areas with different FIB exposure modes (Fig. 2) allows us to conclude that the selectivity of the growth process is determined by the number of passes within one value of the accelerating voltage. This can be associated with an increased amount of implanted material. Thus, after deposition of 200 nm GaAs, structures were not formed only in the areas processed at the lowest number of passes and accelerating voltage equal to 10 kV (Fig. 2, *a*). We attribute this behavior to the fact that, at such a number of passes, the formation of nanosized holes on the silicon surface during annealing begins, which act as localization and nucleation centers for epitaxially grown structures.

Note that there is also a difference in the morphology of the obtained structures grown in the areas obtained at 10 and 20 kV. Structures grown in areas with large crystallites (Fig. 1, *a*) end up with a morphology with NWs (Fig. 2, *d*), while such a structure is not observed during growth in areas treated at 10 kV over the entire range of beam passes (Fig. 2, *a*, *b*). This is due to an increase in the total implantation dose with a change in the accelerating voltage from 10 to 20 kV due to an increase in the beam diameter during FIB treatment. This was also affected by the damage of the crystal lattice during processing with higher ion energy, since NWs tend to parasitic growth on defects. Also, by increasing the accelerating voltage to 20 kV during FIB treatment and, in fact, the total dose of implantation, the onset of epitaxial growth is shifted to the region of low beam passes. (Fig. 2, *c*).

Raising the annealing temperature to 800 °C (Fig. 3) followed by the growth of GaAs under similar conditions leads to the activation of parasitic growth outside the modification areas, which reduces the selectivity of the growth process. This change is associated with the formation of pores in the native oxide at a high annealing temperature. It should be noted that the growth of GaAs in the modified areas is accompanied by the formation of nanowires oriented in directions perpendicular to each other. Increasing the accelerating voltage to 20 kV led to a change in the GaAs morphology in the modified area and the formation of a distinct structure already

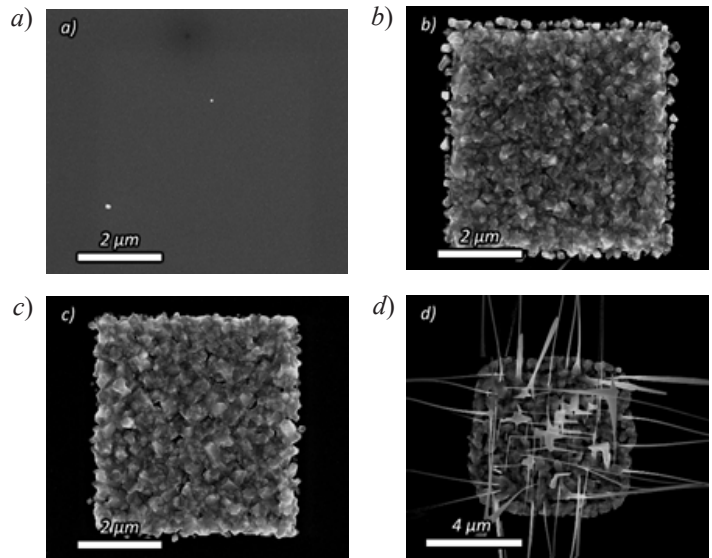


Fig. 2. SEM images of FIB-modified Si areas after annealing at $T = 600\text{ }^\circ\text{C}$ followed by deposition of 200 nm GaAs at $T = 600\text{ }^\circ\text{C}$. The number of beam passes was 5 for (a), (c) and 200 for (b), (d). The accelerating voltage was 10 kV for (a), (b), and 20 kV for (c), (d)

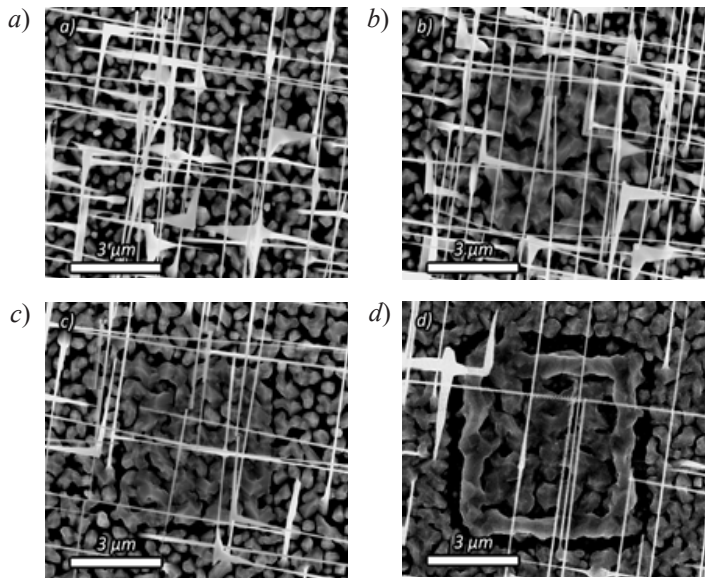


Fig. 3. SEM images of FIB-modified Si areas after annealing at $T = 800\text{ }^\circ\text{C}$ followed by deposition of 200 nm GaAs at $T = 600\text{ }^\circ\text{C}$. The number of beam passes was 5 for (a), (c) and 200 for (b), (d). The accelerating voltage was 10 kV for (a), (b), and 20 kV for (c), (d)

at low number of beam passes (Fig. 3, c). However, the presence of parasitic growth outside the modification areas is an undesirable result, so annealing at 600 °C is more optimal for the localization of the GaAs nanostructure.

Conclusion

It can be seen from the above results that changing the annealing temperature, accelerating voltage, and/or the number of passes makes it possible to obtain various kinds of morphology on the silicon surface: from the formation of a surface with GaAs crystallites to strongly disturbed with the formation of holes. The influence of these parameters on the subsequent epitaxial growth is great, since they allow one to change not only the morphology of the resulting structures, but also the type of growth. However, further research in this direction is required to identify the optimal set of GaAs growth parameters on FIB-modified Si (growth rate, V/III flux ratios, deposition thickness, etc.).

REFERENCES

1. Zhou Z., Yin B., Michel J., On-chip light sources for silicon photonics, *Light: Science & Applications*. 4 (2015) e358.
2. Tang M., Park J.-S., Wang Z., Chen S., Jurczak P., Seeds A., Liu H., Integration of III-V lasers on Si for Si photonics, *Progress in Quantum Electronics*. 66 (2019) 1–18.
3. Colombo D., Grilli E., Guzzi M., Sanguinetti S., Marchionna S., Bonfanti M., Fedorov A., von Känel H., Isella G., Müller E., Analysis of strain relaxation by microcracks in epitaxial GaAs grown on Ge/Si substrates, *Journal of Applied Physics*. 101 (2007) 103519.
4. Bolkhovityanov Yu. B., Pchelyakov O. P., GaAs epitaxy on Si substrates: modern status of research and engineering, *Physics – Uspekhi*. 51 (5) (2008) 437–456.
5. Knoedler M., Bologna N., Schmid H., Borg M., Moselund K. E., Wirths S., Rossell M. D., Riel H., Observation of Twin-free GaAs Nanowire Growth Using Template-Assisted Selective Epitaxy, *Crystal Growth and Design*. 17 (2017) 6297–6302.
6. Viazmitinov D. V., Berdnikov Yu., Kakhodazadeh S., Dragunova A., Sibirev N., Kryzhanovskaya N., Radko I., Huck A., Yvinda K., Semenova E., Monolithic integration of InP on Si by molten alloy driven selective area epitaxial growth, *Nanoscale*. 12 (2020) 23780.
7. Chand N., van Derziel J. P., Weiner J. S., Sergent A. M., Lang D. V., GaAs on Silicon Grown by Molecular Beam Epitaxy Progress and Applications for Selectively Doped Heterostructure Transistors, *Materials Science and Engineering*. B3 (1989) 485–496.
8. Shi B., Han Y., Li Q., Lau K. M., 1.55 μm lasers epitaxially grown on silicon, *IEEE Journal of Selected Topics in Quantum Electronics*. 25 (6) (2019) 1–11.
9. Alaskar Y., Arafat S., Wickramaratne D., Zurbuchen M. A., He L., McKay J., Lin Q., Goorsky M. S., Lake R. K., Wang K. L., Towards van der Waals Epitaxial Growth of GaAs on Si using a Graphene Buffer Layer, *Advanced Functional Materials*. 24 (2014) 6629–6638.
10. Hetzel M., Lugstein A., Zeiner C., Wrojcik T., Pongratz P., Bertagnolli E., Ultra-fast vapour–liquid–solid synthesis of Si nanowires using ion-beam implanted gallium as catalyst, *Nanotechnology*. 22 (2011) 395601.
11. Detz H., Kriz M., Lancaster S., MacFarland D., Schinner M., Zederbauer T., Andrews A. M., Schrenk W., Strasser G., Lithography-free positioned GaAs nanowire growth with focused ion beam implantation of Ga, *Journal of Vacuum Science & Technology B*. 35 (2017) 011803.
12. Eremenko M. M., Shandyba N. A., Chernenko N. E., Balakirev S. V., Nikitina L. S., Solodovnik M. S., Ageev O. A., Investigation of the effect of annealing on Si(100) substrate modified by Ga⁺ focused ion beam, *Journal of Physics: Conference Series*. 2086 (2021) 012027.
13. Lajnef M., Bardaoui A., Sagne I., Chtouroua R., Ezzaouia H., Atomic Layer Epitaxial Growth of GaAs on Porous Silicon Substrate, *American Journal of Applied Sciences*. 5 (5) (2008) 605–609.

THE AUTHORS

EREMENKO Mikhail M.
eryomenko@sfedu.ru
ORCID: 0000-0002-7987-0695

SHANDYBA Nikita A.
shandyba@sfedu.ru
ORCID: 0000-0001-8488-9932

BALAKIREV Sergey V.
sbalakirev@sfedu.ru
ORCID: 0000-0003-2566-7840

AGEEV Oleg A.
ageev@sfedu.ru
ORCID: 0000-0003-1755-5371

CHERNENKO Natalia E.
nchernenko@sfedu.ru
ORCID: 0000-0001-8468-7425

SOLODOVNIK Maxim S.
solodovnikms@sfedu.ru
ORCID: 0000-0002-0557-5909

Received 20.07.2022. Approved after reviewing 27.07.2022. Accepted 28.07.2022.

Conference materials

UDC 538.9

DOI: <https://doi.org/10.18721/JPM.153.311>

Study of FIB-modified silicon areas by AFM and Raman spectroscopy

L. S. Nikitina ¹✉, E. A. Lakhina ¹, M. M. Eremenko ¹, S. V. Balakirev ¹,
N. E. Chernenko ¹, N. A. Shandyba ¹, O. A. Ageev ¹, M. S. Solodovnik ¹

¹ Southern Federal University, Taganrog, Russia

✉ larnikitina@sfedu.ru

Abstract. This paper presents the results of atomic force microscopy and Raman spectroscopy studies of the effect of high-temperature annealing on the height/depth parameters of silicon areas modified by a focused ion beam. It is shown that the focused ion beam treatment with 5 beam passes leads to swelling of the surface of the modified silicon areas. It was found that the depth of the focused ion beam modified area is different after annealing at 600 and 800 °C. An increase in the number of passes in both cases led to an increase in the depth of the focused ion beam modified areas. The results of studies of Raman spectroscopy showed that with an increase in the number of passes, a decrease in the crystallinity of silicon occurs. It is also shown that annealing of such regions leads to the restoration of crystallinity upon annealing at 600 °C and almost complete restoration of crystallinity at 800 °C.

Keywords: silicon, A3B5, molecular beam epitaxy, annealing, atomic force microscopy, focused ion beam, Raman spectroscopy

Funding: This work was supported by the Russian Science Foundation Grant No. 20-69-46076 at the Southern Federal University.

Citation: Nikitina L. S., Lakhina E. A., Eremenko M. M., Balakirev S. V., Chernenko N. E., Shandyba N. A., Ageev O. A., Solodovnik M. S., Study of FIB-modified silicon areas by AFM and Raman spectroscopy, St. Petersburg State Polytechnical University Journal. Physics and Mathematics, 15 (3.3) (2022) 59–63. DOI: <https://doi.org/10.18721/JPM.153.311>

This is an open access article under the CC BY-NC 4.0 license (<https://creativecommons.org/licenses/by-nc/4.0/>)

Материалы конференции

УДК 538.9

DOI: <https://doi.org/10.18721/JPM.153.311>

Исследование областей кремния, модифицированного ФИП, методами АСМ и рамановской спектроскопии

Л. С. Никитина ¹✉, Е. А. Лахина ¹, М. М. Еременко ¹, С. В. Балакирев ¹,
Н. Е. Черненко ¹, Н. А. Шандыба ¹, М. С. Солодовник ¹, О. А. Агеев ¹

¹ Южный федеральный университет, Таганрог, Россия

✉ larnikitina@sfedu.ru

Аннотация. В данной работе представлены результаты исследований с помощью атомно-силовой микроскопии (АСМ) и рамановской спектроскопии влияния высокотемпературного отжига на параметры высоты/глубины областей кремния, модифицированных фокусированным ионным пучком (ФИП). Показано, что обработка ФИП с 5 проходами пучка приводит к «вспучиванию» участков модифицированного кремния. Установлено, что глубина модифицированных ФИП участков после отжига при 600 и 800 °C различна. Увеличение числа проходов в обоих случаях приводило к увеличению глубины ФИП-обработанных участков.

Результаты исследований рамановской спектроскопии показали, что с увеличением числа проходов происходит увеличение дефектности кремния. Показано также, что отжиг ФИП-обработанных участков приводит к восстановлению кристаллической структуры при отжиге на 600 °С и практически полному ее восстановлению при 800 °С.

Ключевые слова: кремний, АЗВ5, молекулярно-лучевая эпитаксия, отжиг, атомно-силовая микроскопия, сфокусированный ионный пучок, рамановская спектроскопия

Финансирование: Работа выполнена в рамках проекта Российского научного фонда № 20-69-46076 в Южном федеральном университете.

Ссылка при цитировании: Никитина Л. С., Лахина Е. А., Ерёменко М. М., Балакирев С. В., Черненко Н. Е., Шандыба Н. А., Агеев О. А., Солодовник М. С., Исследование областей кремния, модифицированного ФИП, методами АСМ и рамановской спектроскопии // Научно-технические ведомости СПбГПУ. Физико-математические науки. 2022. Т. 15. № 3.3. С. 59–63. DOI: <https://doi.org/10.18721/JPM.153.311>

Статья открытого доступа, распространяемая по лицензии CC BY-NC 4.0 (<https://creativecommons.org/licenses/by-nc/4.0/>)

Introduction

Today, research in the field of searching for new functional materials is gaining more attention. One of these scientific directions is the production of optoelectronic and photonic integrated circuits based on the integration of III-V semiconductors on silicon [1, 2]. Obtaining such structures is possible through monolithic integration which is a promising method that would make it possible to obtain semiconductor structures in a single technological cycle and greatly reduce the cost of their production. However, the direct growth of III-V semiconductors on Si is difficult due to a significant lattice mismatch, which leads to a high level of defectiveness of the grown layers [1, 3]. A different number of methods are used to reduce the number of dislocations: the use of nucleation layers [4, 5], two- or three-step growth of buffer layers [4, 6], as well as the growth of thick buffer layers [7, 9], substrate misorientation [1, 4], the use of dislocation filters [4, 6], aspect ratio trapping (ART) [2, 8] etc. [1, 2, 9], but it has not yet been possible to achieve a minimum dislocation density comparable to the native substrate. In turn, surface modification by a focused ion beam (FIB) is one of the most flexible, accurate, and operational tools for creating a nanoscale relief on a surface [10] similar to ART method. FIB allows not only to control the processes of self-organization of epitaxial nanostructures, but also the positioning and localization of their formation. It is also assumed that partial or complete amorphization of the surface in this way will help to avoid the occurrence of antiphase domains, improve stress relaxation and localize most of the defects in the lower, nucleation layers.

In this work, atomic force microscopy (AFM) and Raman spectroscopy studies of the effect of high-temperature annealing on the height parameter of FIB-modified silicon areas were carried out, as well as to evaluate its defectiveness.

Materials and Methods

The modification of the silicon substrates was carried out by treating the areas of 5×5 μm with a focused Ga⁺ ion beam. The processing parameters for AFM studies were: accelerating voltage – 30 kV, the number of beam passes varied from 5 to 200. The processing parameters for Raman spectroscopy studies were: accelerating voltage varied from 5 to 30 kV; the number of beam passes varied from 1 to 200. After FIB processing, the substrates were studied by AFM and Raman spectroscopy. Next, the samples were subjected to thermal annealing in an MBE chamber for 60 minutes. The annealing temperature varied from 600 to 800 °C. Then they were removed from the MBE chamber and examined by AFM and Raman spectroscopy to compare the resulting parameters.

Results and Discussion

AFM studies of the samples without annealing showed that the processing of silicon areas with a small number of beam passes results in swelling of these areas (Fig. 1, *a*). A further increase



in the number of beam passes led to etching and a gradual increase in the depth of the modified areas (Fig. 1, *b*). It should be noted that the height of the processed area was compared with the level of the substrate with the number of beam passes equal to 10. After that, the formation of a deepening was observed with an increase in the number of beam passes.

Raman spectroscopy studies have shown that an increase in the number of passes leads to a decrease in silicon crystallinity because the intensity of the main crystalline (c-Si) TO-phonon peak (521 cm^{-1}) decreases (Fig. 1, *c*). This behavior is associated with an increase in the distortion of the Si crystal lattice due to defects introduced during Ga ion implantation. It should be noted that the intensity of the c-Si peak from the area treated with 200 passes is greater than the c-Si peak from 100 passes. We attribute this behavior to the specifics of the FIB method, since simultaneous processes of saturation of the area with the implanted material and etching of the substrate occur. Thus, at 200 passes, most of the amorphous phase was etched off and the signal from crystalline silicon increased.

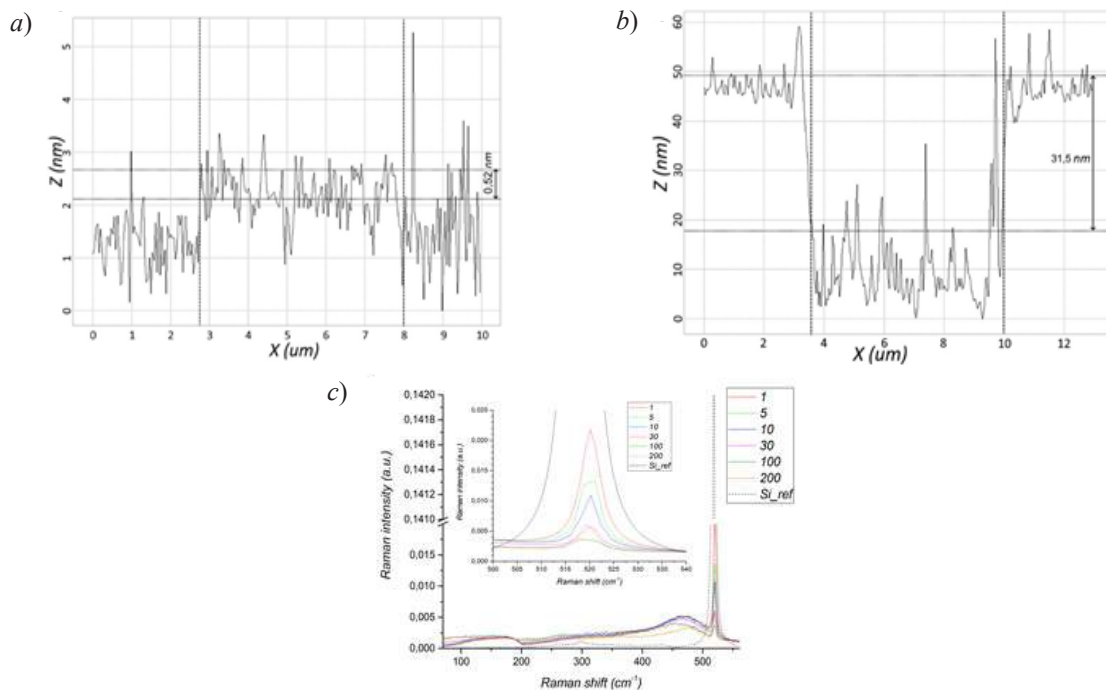


Fig. 1. AFM profiles of FIB-modified silicon areas treated with (*a*) 5 beam passes and (*b*) 200 beam passes. (*c*) Normalized Raman spectra of FIB-modified Si areas with different beam passes.

Next, the silicon samples were annealed at 600 and 800 °C. AFM studies of samples annealed at 600 °C showed that no surface swelling was observed with 1 beam pass and the height of the treated area, as in the case of processing with 10 passes without annealing, was compared with the substrate level (Fig. 2, *a*). An increase in the depth of the modified areas is also observed compared to the samples without annealing (Fig. 2, *b*). This is due to the release of the implanted material to the surface and its partial desorption. It should be noted that a significant change in depth is observed when processing with a large number of passes (100 and 200). Apparently, this is due to the fact that during FIB processing with large number of beam passes, high damage to the modified areas and, accordingly, high defectiveness occur, which contribute to a more intensive release of the implanted material and its evaporation.

The situation slightly changes in the AFM study of samples after high-temperature annealing at 800 °C. With a small number of beam passes, there is no swelling of the surface, and a deepening of the changed areas is immediately observed (Fig. 1, *a*). This indicates that during annealing, the implanted material emerges on the surface, followed by its evaporation and/or etching of the modified area, which leads to the formation of a deepening. A subsequent increase in the number of passes led to an even greater increase in the depth of the modified areas compared to annealing at a lower temperature. Moreover, the change in the height/depth

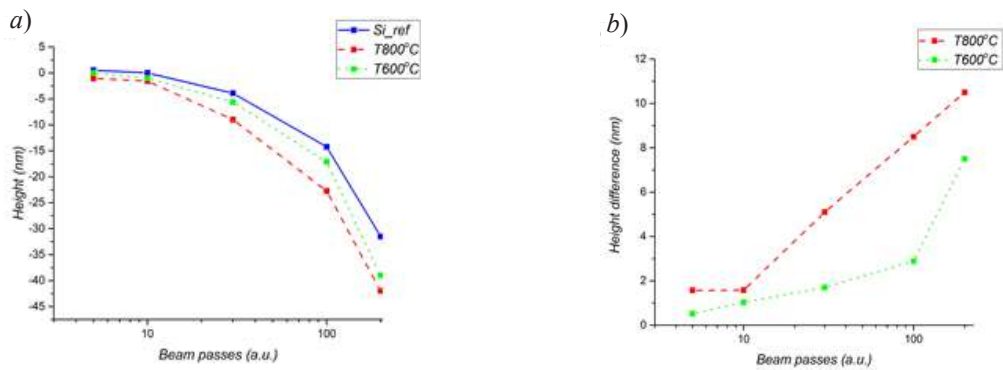


Fig. 2. Height of FIB-modified areas before and after annealing (negative height values indicate etch depth) (a); Height difference between annealed and non-annealed substrate at different annealing temperatures (b)

of the modified areas is not the same if we compare the cases of samples annealed at 600 and 800 °C (Fig. 2, b).

Raman spectroscopy studies of samples annealed at 600 °C showed that, upon annealing, the intensity of the c-Si TO-phonon peak exhibits a nonmonotonic change with increasing number of beam passes (Fig. 3, a). This minimum intensity behavior at 30 passes is possibly due to the fact that the implanted material remains embedded in the silicon lattice after annealing. Apparently, with such a set of parameters, there is no critical damage of the silicon crystal lattice, during which an intense release of the implanted material to the surface occurs, as in the cases with 100 and 200 passes. An increase in the annealing temperature to 800 °C leads to an increase in the intensity of the crystalline Si TO-phonon peak (521 cm^{-1}) for almost all beam passes to the spectral values obtained from the untreated substrate (Fig. 3, b). In this case, it can be concluded that such annealing is not suitable, since no amorphous silicon phase remains on the surface and subsequent growth will occur in exactly the same way as on a substrate not treated with FIB.

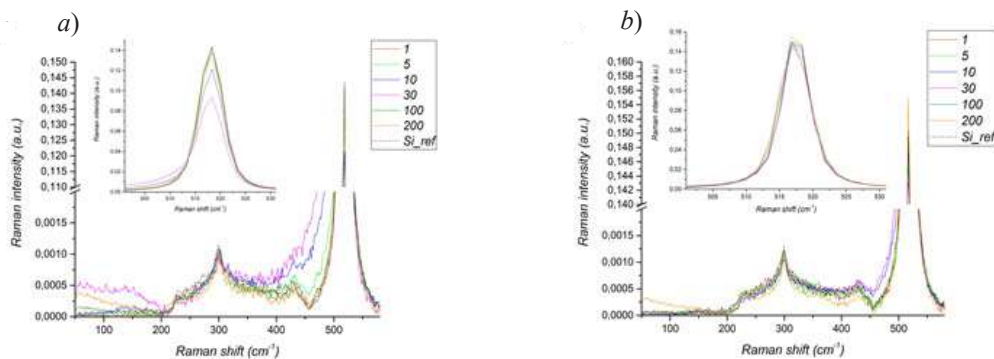


Fig. 3. Normalized Raman spectra of FIB-modified Si areas at different beam passes after annealing at 600 °C (a) and 800 °C (b)

Conclusion

As can be seen from the above results, the annealing temperature and the amount of implanted material critically determine the depth and crystallinity of the modified silicon regions. An increase in the annealing temperature led to an increase in the depth of the treated areas, as well as an increase in their crystallinity due to the etching of the amorphous layer. We concluded that the appropriate annealing temperature is annealing at 600 °C due to the incomplete removal of the amorphous phase and the presence of an implanted material on the surface, which will act as nucleation centers for subsequent growth. We believe that the growth of III-V structures on such FIB-modified substrates will lead to complete localization of the structure, and potentially such a solution will help achieve high-quality monolithic integration of III-V structures on silicon substrates.



REFERENCES

1. Park J.-S., Tang M., Chen S., Liu H., Heteroepitaxial Growth of III-V Semiconductors on Silicon, Crystals. 10 (2020) 1163.
2. Kunert B., Mols Y., Baryshnikova M., Waldron N., Schulze A., Langer R., How to control defect formation in monolithic III/V hetero-epitaxy on (100) Si? A critical review on current approaches, Semiconductor Science and Technology. 33 (2018) 093002.
3. Kroemer H., Polar-on-nonpolar epitaxy, Journal of Crystal Growth. 81 (1987) 193–204.
4. Chen S., Li W., Wu J., Jiang Q., Tang M., Shutts S., Elliott S. N., Sobiesierski A., Seeds A. J., Ross I., Snowton P. M., Liu H., Electrically pumped continuous-wave III–V quantum dot lasers on silicon, Nature photonics. 10 (2016) 307–311.
5. Lee A. D., Jiang Q., Tang M., Zhang Y., Seeds A. J., Liu H., InAs/GaAs Quantum-Dot Lasers Monolithically Grown on Si, Ge, and Ge-on-Si Substrates, IEEE Journal of Selected Topics in Quantum Electronics. 19 (4) (2013) 1901107.
6. Li K., Liu Z., Tang M., Liao M., Kim D., Deng H., Sanchez A. M., Beanland R., Martin M., Baron T., Chen S., Wu J., Seeds A., Liu H., O-band InAs/GaAs quantum dot laser monolithically integrated on exact (001) Si substrate, Journal of Crystal Growth. 511 (2019) 56–60.
7. Georgakilas A., Stoemenos J., Tsagaraki K., Kominou Ph., Flevaris N., Panayotatos P., Christou A., Generation and annihilation of antiphase domain boundaries in GaAs on Si grown by molecular beam epitaxy, Journal of Materials Research. 8 (8) (1993) 1908–1921.
8. Alcotte R., Martin M., Moeyaert J., Cipro R., David S., Bassani F., Ducroquet F., Bogumilowicz Y., Sanchez E., Ye Z., Bao X. Y., Pin J. B., Baron T., Epitaxial growth of antiphase boundary free GaAs layer on 300 mm Si(001) substrate by metalorganic chemical vapour deposition with high mobility, APL Materials. 4 (2016) 046101.
9. Bolkhovityanov Yu. B., Pchelyakov O. P., GaAs epitaxy on Si substrates: modern status of research and engineering, Physics – Uspekhi. 51 (5) (2008) 437–456.
10. Detz H., Kriz M., Lancaster S., MacFarland D., Schinner M., Zederbauer T., Andrews A. M., Schrenk W., Strasser G., Lithography-free positioned GaAs nanowire growth with focused ion beam implantation of Ga, Journal of Vacuum Science & Technology B. 35 (2017) 011803.

THE AUTHORS

NIKITINA Larisa S.
larnikitina@sfedu.ru
ORCID: 0000-0001-7397-8630

LAKHINA Ekaterina A.
lakhina@sfedu.ru
ORCID: 0000-0002-9326-2418

EREMENKO Mikhail M.
eryomenko@sfedu.ru
ORCID: 0000-0002-7987-0695

BALAKIREV Sergey V.
sbalakirev@sfedu.ru
ORCID: 0000-0003-2566-7840

CHERNENKO Natalia E.
nchernenko@sfedu.ru
ORCID: 0000-0001-8468-7425

SHANDYBA Nikita A.
shandyba@sfedu.ru
ORCID: 0000-0001-8488-9932

AGEEV Oleg A.
ageev@sfedu.ru
ORCID: 0000-0003-1755-5371

SOLODOVNIK Maxim S.
solodovnikms@sfedu.ru
ORCID: 0000-0002-0557-5909

Received 20.07.2022. Approved after reviewing 27.07.2022. Accepted 28.07.2022.

Conference materials

UDC 537.9

DOI: <https://doi.org/10.18721/JPM.153.312>

Electron phase-breaking time in ultra-thin Nb films

A. I. Lomakin ^{1,2} ✉, E. M. Baeva ², N. A. Titova ²,
P. I. Zolotov ², A. I. Kolbatova ^{1,2}, G. N. Goltsman ^{1,2}

¹ Moscow Pedagogical State University, Moscow, Russia;

² National Research University Higher School of Economics, Moscow, Russia

✉ andrey.lomakin.2021@mail.ru

Abstract. Here we study the temperature dependences of the electron phase-breaking time τ_ϕ in ultra-thin superconducting niobium (Nb) films. In Nb films, passivated with a layer of silicon (Si), the observed temperature dependence of the phase-breaking time is $\tau_\phi \sim T^{2.5}$, is resembling the electron-phonon scattering. However, in the uncovered Nb films, we observe the saturation of τ_ϕ at low temperatures, which may be a signature of the surface magnetic disorder, present in native Nb oxide on the film surface.

Keywords: magnetoresistance, thin films, inelastic scattering, magnetic disorder

Funding: This study was partially funded in the framework of RFBI 19-32-60076 “Study of influence of magnetic disorder on the transport and superconducting properties of thin epitaxial films of transition metals” and the Russian Science Foundation grant No. 19-72-10101 “Resistive state in the region of the superconducting transition as a stationary random process”.

Citation: Lomakin A. I., Baeva E. M., Titova N. A., Zolotov P. I., Kolbatova A. I., Goltsman G. N., Electron phase-breaking time in ultra-thin Nb films, St. Petersburg State Polytechnical University Journal. Physics and Mathematics, 15 (3.3) (2022) 64–69. DOI: <https://doi.org/10.18721/JPM.153.312>

This is an open access article under the CC BY-NC 4.0 license (<https://creativecommons.org/licenses/by-nc/4.0/>)

Материалы конференции

УДК 537.9

DOI: <https://doi.org/10.18721/JPM.153.312>

Время сбоя фазы в ультратонких пленках Nb

А. И. Ломакин ^{1,2} ✉, Э. М. Баева ², Н. А. Титова ²,
Ф. И. Золотов ², А. И. Колбатова ^{1,2}, Г. Н. Гольцман ^{1,2}

¹ Московский Педагогический Государственный Университет, Москва, Россия;

² Национальный Исследовательский Университет Высшая Школа Экономики, Москва, Россия

✉ andrey.lomakin.2021@mail.ru

Аннотация. В данной работе мы представляем результаты экспериментального исследования времени сбоя фазы волновой функции электрона в ультратонких сверхпроводящих пленках ниобия (Nb). В Nb пленках, пассивированных слоем кремния (Si), наблюдается сильная зависимость времени сбоя фазы от температуры $\tau_\phi \sim T^{2.5}$, вероятно, обусловленная электрон-фононным рассеянием. Однако в непокрытых кремнием Nb пленках наблюдается насыщение времени сбоя фазы при низких температурах, что может быть обусловлено наличием поверхностного магнитного беспорядка, возникающий в естественном окисле Nb на поверхности пленки.

Ключевые слова: магнетосопротивление, тонкие пленки, неупругое рассеяние, магнитный беспорядок

Финансирование: Работа выполнена в рамках грантов Российского фонда фундаментальных исследований 19-32-60076 «Исследование влияния магнитного



беспорядка на транспортные и сверхпроводящие свойства тонких эпитаксиальных пленок переходных металлов» и Российского научного фонда № 19-72-10101 «Резистивное состояние в окрестности сверхпроводящего перехода как стационарный случайный процесс».

Ссылка при цитировании: Ломакин А. И., Баева Э. М., Титова Н. А., Золотов Ф. И., Колбатова А. И., Гольцман Г. Н., Время сбоя фазы в ультратонких пленках Nb // Научно-технические ведомости СПбГПУ. Физико-математические науки. 2022. Т. 15. № 3.3. С. 64–69. DOI: <https://doi.org/10.18721/JPM.153.312>

Статья открытого доступа, распространяемая по лицензии CC BY-NC 4.0 (<https://creativecommons.org/licenses/by-nc/4.0/>)

Introduction

Magnetic disorder, potentially present in the native oxides on the surface of thin superconducting films, can crucially suppress superconductivity due to breaking of the time-reversal symmetry in superconductors [1, 2]. However, distinction this mechanism from other mechanisms of superconductivity suppression is not straightforward. For example, it is well known that the native oxide of Nb is conductive and, hence, it can diminish superconducting properties due to the inverse proximity effect [3]. Meanwhile some experimental observations show signatures of magnetic disorder on the surface of Nb [4–5], one can to obtain additional information with magnetoresistance transport measurements. In particular, one can expect the saturation of phase-breaking time of the electron wavefunction in case of scattering on magnetic disorder [6–7]. In this work we investigate the dependence of phase-breaking time upon temperature by measuring magnetoresistance in ultrathin superconducting Nb films. We observed a strong dependence of the phase-breaking time on temperature in Nb films, passivated with a layer of silicon (Si). Meanwhile, in uncovered Nb films, we observe the saturation of the electron phase-breaking time at low temperatures.

Materials and Methods

Ultrathin Nb films are sputtered using the magnetron sputtering system (AJA International Inc.) with a background pressure of 9×10^{-8} torr. The samples are deposited on r-cut Al_2O_3 and Si substrates by sputtering of the Nb target with diameter of 50.8 mm and purity of 99.95% in argon atmosphere (99.998% purity). The working pressure is 3.1 mTorr. During deposition the substrates are heated up to $T_{\text{dep}} = 400$ °C. This heating is controlled with a built-in PID controller, and T_{dep} is pre-calibrated using an analog thermometer (PTC Instruments). The rotation of substrates during deposition and the relatively large distance between substrates and the target (~ 10 cm) allows for fabrication on Nb films with high uniformity. The acquisition of thin Nb films is controlled by piezoelectric microweighting in the test process. The film growth rate is 0.11 nm/s, and the thickness is determined by the time of film deposition. The films investigated have thicknesses in the range of 3–6 nm. To prevent unintentional oxidation of Nb films in the atmosphere, two films are passivated with a 5-nm thick silicon (Si) layer. In this study, we prepare two passivated Nb samples (A1, A2) and two uncovered samples (B1, B2). In the latter case, the films are exposed to strong unintentional oxidation [8].

To study transport properties, we patterned the films into 500- μm wide and 1000- μm long Hall-bars. Electrical transport measurements are carried out with a 370 AC LakeShore resistance bridge at a bias current less than 1 μA . Normal-state resistance R_s is measured in a four-probe configuration. The measurements are carried out on a custom ^4He cryogenic insert immersed in a dewar in a wide temperature range (from 300 K to 1.7 K). At low temperatures we measure the magnetoresistance $R_s(B)$, the temperature dependencies of the second critical magnetic field $B_{c2}(T)$ and the Hall resistance R_H at 25 K by applying perpendicular magnetic field B up

to 4 T. The latter allows to determine the carrier density $n = B / (edR_H)$. We determine the slope dB_{c2}/dT at T_c by measuring $R(T)$ -dependencies on different values of B (not shown here). The latter allows to estimate the critical magnetic field $B_{c2}(0)$, the electron diffusivity D using the following expressions $B_{c2}(0) = -0.69T_c(dB_{c2}/dT)$, $D = -4k_B / (\pi e) (dB_{c2}/dT)^{-1}$.

For samples B1 and B2 we estimate the diffusion D coefficient by extrapolation from data for thicker films (not presented here). Here, the critical temperature T_c is determined as the temperature at $R_s = R_s^{10K} / 2$. The parameters of the studied samples are presented in Table 1.

Table 1

Characteristics of niobium films

	With a Si layer		Without a Si layer	
	A1	A2	B1	B2
d , nm	6	3	5	3
Substrate	Al_2O_3	Al_2O_3	Al_2O_3	Si
T_c , K	7.53	3.26	1.10	0.92
R_s^{10K} , Ohm	20.0	137.3	186.4	363.8
R_s^{300K} , Ohm	48.57	181.9	186.8	363.8
D , cm^2/s	3.56	1.59	1.3	1.2
n , cm^{-3}	4.85×10^{22}	4.06×10^{22}	3.03×10^{22}	3.25×10^{22}
$B_{c2}(0)$, T	2.32	2.25	0.93	0.84
τ_p , fs	14.3	6.4	5.2	4.8
α_{e-e}^{-1} , ps	203	97	227	165
α_{e-ph}^{-1} , ps	7.5	20	100	20
p	2.5	1.5	0	0
τ_c , ps	inf	10	2.4	6.7

Theory

To determine the electron phase-breaking time τ_ϕ in thin films, one should experimentally study contribution of quantum corrections to magnetoconductance [9]. The dimensionless change in magnetoconductance at a fixed temperature T can be determined from the measured sheet resistance $R_s(B, T)$ using the expression:

$$\delta G(B, T) = \frac{2\pi^2 \hbar}{e^2} [R_s(B, T)^{-1} - R_s(0, T)^{-1}]. \quad (1)$$

There are different contributions to the magnetoconductance: weak localization [10] and superconducting fluctuations (Maki-Thompson (MT), Aslamazov-Larkin (AL), and renormalization of density of states (DOS) contributions) [9]. Since the superconducting fluctuations are stronger than the weak localization in our samples, we refer only to the contribution of the superconducting fluctuations:

$$R_s(B, T)^{-1} = \sigma(B, T) = \sigma^{AL}(B, T) + \sigma^{DOS}(B, T) + \sigma^{MT}(B, T) + \sigma^{WL}(B, T), \quad (2)$$

where

$$\begin{aligned} \sigma^{AL}(B, T) &= \frac{\pi^2 \varepsilon}{4h^2} \left[\psi \left(\frac{1}{2} + \frac{\varepsilon}{2h} \right) - \psi \left(1 + \frac{\varepsilon}{2h} \right) + \frac{\varepsilon}{h} \right], \\ \sigma^{DOS}(B, T) &= -\frac{28\zeta(3)}{\pi^2} \left[\ln \left(\frac{1}{2h} \right) - \psi \left(\frac{1}{2} + \frac{\varepsilon}{2h} \right) \right], \\ \sigma^{MT}(B, T, \tau_\phi) &= -\beta_{MT}(T, \tau_\phi) \left[\psi \left(\frac{1}{2} + \frac{B_\phi}{B} \right) - \psi \left(\frac{1}{2} + \frac{B_\phi}{B} \frac{\varepsilon}{\gamma_\phi} \right) \right], \\ \sigma^{WL}(B, T) &= \frac{3}{2} \psi \left(\frac{1}{2} + \frac{B_2}{B} \right) - \psi \left(\frac{1}{2} + \frac{B_2}{B} \right) - \frac{1}{2} \psi \left(\frac{1}{2} + \frac{B_3}{B} \right). \end{aligned}$$

Here $\psi(x)$ is the Digamma function, $\varepsilon = \ln(T/T_c)$ and $h = 0.69B/B_{c2}(0)$ are the reduced temperature and magnetic field, respectively, $\gamma_\phi = \pi\hbar / (8k_B T \tau_\phi)$ is the phase-breaking parameter



with τ_ϕ , which is used as a fitting parameter here. The characteristic fields are defined as $B_1 = B_0 + B_{so}$, $B_2 = B_\phi + 4B_{so}/3 + 2B_s/3$, $B_3 = B_\phi + 2B_s$, $B_{so} = \hbar/4eD\tau_{so}$, $B_o = \hbar/4eD\tau$. The coefficient in MT term $\beta_{MT}(T, \tau_\phi)$ can be found in [11].

In order to analyze the dependence of the phase breaking time upon temperature, it is useful to represent τ_ϕ as the sum of four different contributions, namely the scattering on superconducting fluctuations, the electron-electron scattering, the electron-phonon scattering and the scattering on magnetic moments:

$$\tau_\phi^{(-1)}(T) = \tau_{SC}^{-1} + \tau_{e-e}^{-1} + \tau_{e-ph}^{-1} + \tau_s^{-1}. \quad (3)$$

While magnetic scattering is independent of temperature, other terms are dependent on T in the following way:

$$\tau_{SC}^{-1} = \frac{\pi g k_B T}{\hbar} \frac{2 \ln 2}{\varepsilon + \beta},$$

$$\tau_{e-e}^{-1} = \frac{\pi g k_B T}{\hbar} \ln \frac{1}{2\pi g} = \alpha_{e-e} \frac{T}{T_C},$$

$$\tau_{e-ph}^{-1} = \alpha_{e-ph} \left(\frac{T}{T_C} \right)^p,$$

where $\beta = 4 \ln 2 / [\sqrt{\ln^2(2\pi g) + 64 / (\pi^2 g)} + \ln(2\pi g)]$, $g = e^2 R_s / (2\pi^2 \hbar)$, α_{e-e} and α_{e-ph} are material-dependent constants, p is the power index, which is in the range of 2-3 for Nb films, as shown previously in Ref. [12].

Results and Discussion

Fig. 1, *a* shows the dependence of the sheet resistance R_s upon temperature for all samples. One can see that the passivated samples have lower R_s and higher values of the critical temperature T_c than the uncovered samples. This observation means that 5 nm-Si layer protects films from unintentional oxidation.

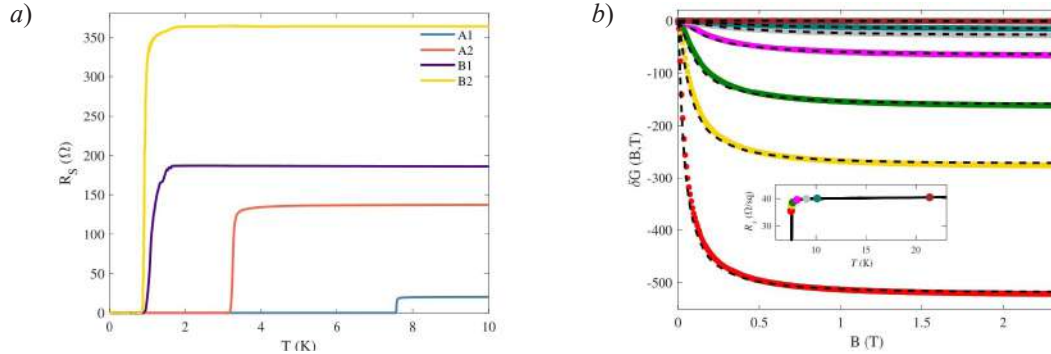


Fig. 1. The dependence of the sheet resistance R_s upon temperature for all investigated samples (*a*); The normalized magnetoconductance $\delta G(B, T)$ versus magnetic field for a representative sample (A1) (*b*); Different colors of the curves correspond to different operating temperatures marked on the $R_s(T)$ -curve in the inset. The dashed black lines represent the fits by Eq.(2).

In Fig. 1, *b* we plot the normalized magnetoconductance for a representative sample A1. The magnitude of the phase-breaking time at each operating temperature is deduced from the fits of the experimental data by Eq.(2) (the dashed black lines in Fig. 1).

Fig. 2 shows the phase-breaking time τ_ϕ as a function of temperature for all studied samples. We fit the experimental dependence $\tau_\phi(T)$ with Eq.(3) (dashed black lines) using α_{e-ph} , p , and τ_s as fitting parameters. The best-fit values, which defined the electron-phonon time τ_{e-ph} (α_{e-ph}^{-1} and p), are listed in Table 1. One can see that the best-fit values of electron-phonon time at the T range under study are much smaller than the estimated values of the electron-electron time. Thus we exclude electron-electron scattering from further analysis. Since τ_s is supposed to be a temperature independent parameter and $\tau_{SC} \sim \ln(T)/T$, we assume that the increase in τ_ϕ with

against decreasing of T is determined by the electron-phonon inelastic scattering time. First of all, we observe the close power-law T -dependence of τ_ϕ for the passivated samples ($\tau_\phi(T) \sim T^{2.5}$ for A1 and $\tau_\phi(T) \sim T^{1.5}$ for A2), meanwhile τ_ϕ for the uncovered samples does not show a pronounced dependence on T . The observed results for $\tau_{e-ph}(T)$ in the passivated samples are also close to previous reported data for thin Nb films [12]. The sign of saturation in T -dependence of τ_ϕ is observed for A2, B1, and B2 samples and can be explained by the finite value of τ_s (see Table 1). Now, we can compare τ_s derived from τ_ϕ with τ_s obtained from the quantitative analysis of suppression of T_c in Nb films [13].

The estimated value of τ_s for passivated sample A2 is an order of magnitude longer than value of τ_s reported in [13], which indicates that the magnetic disorder cannot be the dominant factor in this film. In additional, we assume that the suppression of T_c with the film thickness in the passivated samples can be related to the inverse proximity effect due to metallic silicide at the Nb-Si interface [3] rather than the magnetic disorder [13].

In contrast, we observe the enhanced phase-breaking rate τ_ϕ^{-1} for the uncovered samples B1 and B2, which evidences an additional phase-breaking mechanism. We also notice that the low-temperature value of $\tau_\phi \approx 1.5$ ps is consistent with the spin-flip scattering time τ_s in Nb reported in [13]. This result, together with the observed decrease of τ_ϕ and the saturation in $\tau_\phi(T)$ -dependence, indicates that the electron dephasing in the uncovered samples may be caused by the magnetic disorder in the native oxide layer [6]. It is the worth remark that the magnetic disorder concentrated in native Nb oxide is known to be a source of parasitic magnetic flux noise in uncovered Nb-based superconducting quantum interference devices [14] and power-independent losses in Nb-based resonators [15].

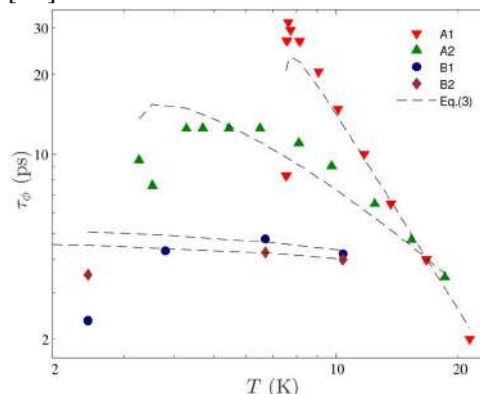


Fig. 2. Temperature dependence of the phase-breaking time τ_ϕ upon temperature extracted from the magnetoconductance measurements. The data are plotted with symbols on a log-log scale

Conclusion

We investigated the influence of the Si passivating layer on the electron phase-breaking rate in ultrathin Nb films. We observed the power-law type $\tau_\phi(T)$ -dependence in the passivated Nb samples and a tendency towards saturation in the $\tau_\phi(T)$ -dependence for the uncovered Nb samples. The latter may indicate the presence of the magnetic disorder in the native niobium oxide on the Nb surface. The study can be useful for the design of microelectronic Nb-based devices.

REFERENCES

1. Tamir I., Trahms M., Gorniaczyk F., F. von Oppen, Shahar D., Franke K. J., Direct observation of intrinsic surface magnetic disorder in amorphous superconducting films, *Physical Review B*, 105 (2022) L140505.
2. Abrikosov A., Gorkov L., Contribution to the theory of superconducting alloys with paramagnetic impurities, *Sov. Phys. JEPT* 12, 1243 (1961).
3. Delacour C., Ortega L., Faucher M., Crozes T., Fournier T., Pannetier B., Bouchiat V., Persistence of superconductivity in niobium ultrathin films grown on r-plane sapphire, *Physical Review B*, 83 (2011) 144504.
4. Rogachev A., Wei T.-C., Pekker D., Bollinger A.T., Goldbart P., Bezryadin A., Magnetic-field enhancement of superconductivity in ultranarrow wires, *Physical Review Letters*, 97 (2006) 137001.



5. Proslir T., Zasadzinski J. F., Cooley L., Antoine C., Moore J., Norem J., Pellin M., Gray K.E., Tunneling study of cavity grade Nb: Possible magnetic scattering at the surface, Applied Physics Letters, 92 (2008) 212505.
6. Vranken G., C. Van Haesendonck, Bruynseraede Y., Enhanced magnetic surface scattering of weakly localized electrons, Physical Review B, 37 14 (1988) 8502.
7. Pierre Y F. Birge N.O., Dephasing by Extremely Dilute Magnetic Impurities Revealed by Aharonov-Bohm Oscillations, Physical Review Letters 89, 20 (2002) 206804.
8. Hikita M., Tajima Y., Tamamura T., Weak localization, fluctuation, and superconductivity in thin Nb films and wires, Physical Review B, 42 (1) (1990) 118.
9. Glatz A., Varlamov A. A., Vinokur V. M., Fluctuation spectroscopy of disordered two-dimensional superconductors Physical Review B, 84 (2011) 104510.
10. Rosenbaum R., Superconducting fluctuations and magnetoconductance measurements of thin films in parallel magnetic fields, Physical Review B, 32 4 (1985) 2190.
11. Lopes dos Santos J. M. B., Abrahams E., Superconducting fluctuation conductivity in a magnetic field in two dimensions, Physical Review B, 31 (1985) 172.
12. Gershenson E. M., Gershenson M. E., Gol'tsman G. N., Lyul'kin A.M., Semenov A. D., Sergeev A. V., Electron-phonon interaction in ultrathin Nb films, JETP, 70 3 (1990) 505.
13. Samsonova A. S., Zolotov P. I., Baeva E. M., Lomakin A. I., Titova N. A., Kardakova A. I., Goltsman G. N., Signatures of Surface Magnetic Disorder in Niobium Films, IEEE Transactions on Applied Superconductivity, 31 5 (2021) 7000205.
14. Kumar P., Sendelbach S., Beck M. A., Freeland J. W., Wang Zhe, Wang Hui, Yu Clare C., Wu R. Q., Pappas D. P., McDermott R., Origin and reduction of 1/f magnetic flux noise in superconducting devices, Physical Review Applied, 6 (2016) 041001.
15. Altoé M. V. P., et al., Localization and Mitigation of Loss in Niobium Superconducting Circuits, PRX Quantum, 3 (2022) 020312.

THE AUTHORS

LOMAKIN Andrey I.
andrey.lomakin.2021@mail.ru
ORCID: 0000-0002-7576-9223

BAEVA Elmira M.
baeva.elm@gmail.com
ORCID: 0000-0002-6805-2670

TITOVA Nadezhda A.
titovana@mail.ru

ZOLOTOV Philipp I.
pizolotov@ya.ru

KOLBATOVA Anna I.
anna_kardakova@mail.ru
ORCID: 0000-0002-3441-3968

GOLTSMAN Gregory N.
goltsman@rplab.ru
ORCID: 0000-0002-1960-9161

Received 14.08.2022. Approved after reviewing 17.08.2022. Accepted 09.09.2022.

SIMULATION OF PHYSICAL PROCESSES

Conference materials

UDC 539.2

DOI: <https://doi.org/10.18721/JPM.153.313>

Sidewall roughness model for optical losses calculation in photonic integrated circuits

E. S. Shamin ^{1,2}✉, A. A. Sharapov ^{1,2}, I. D. Skuratov ^{1,2},
S. O. Demidov ^{1,2}, E. S. Gornev ^{1,2}

¹ Moscow Institute of Physics and Technology, Moscow, Russia;

² Molecular Electronics Research Institute, Zelenograd, Russia

✉ yevgeniy.shamin@phystech.edu

Abstract. One of the key performance indicators of photonic circuits is the value of optical propagation losses. Among several factors which impact these losses, the sidewall roughness is considered as the primary focus of this work. The optical signal, propagating along the photonic device, scatters on roughness of its element's surfaces. This decreases the output power, as well as leads to the higher heating and worse transmission characteristics, which in its turn increases the noise ratio and creates undesired phase deviations. Thus, the problem of sidewall roughness simulation (and consequently, losses estimation in microwave photonic circuits caused by it) is relevant at the design stage of the devices. Therefore, a new, highly efficient model of sidewall roughness based on a photolithography simulation and imitational modelling of photoresist exposure is presented. Principles of operation and implementation features of the model are described. Simulation results, obtained using the new roughness model, are demonstrated and an approach on their verification with experimental data is suggested. Additionally, theoretical estimations for the optical losses caused by sidewall roughness in ridge Si waveguides are discussed.

Keywords: sidewall roughness, photolithography modeling, random close packing, photoresist exposure modeling, integral photonics, optical losses

Funding: This work was funded by a grant by the Fund for Assistance to Small Innovative Enterprises No. 075-15-2020-791 40ГУРЭС14/72785 dated Dec 26, 2021.

Citation: Shamin E. S., Sharapov A. A., Skuratov I. D., Demidov S. O., Gornev E. S., Sidewall roughness model for optical losses calculation in photonic integrated circuits, St. Petersburg State Polytechnical University Journal. Physics and Mathematics, 15 (3.3) (2022) 70–75. DOI: <https://doi.org/10.18721/JPM.153.313>

This is an open access article under the CC BY-NC 4.0 license (<https://creativecommons.org/licenses/by-nc/4.0/>)

Материалы конференции

УДК 539.2

DOI: <https://doi.org/10.18721/JPM.153.313>

Модель шероховатости для расчета оптических потерь в фотонных интегральных схемах

Е. С. Шамин ^{1,2}✉, А. А. Шарапов ^{1,2}, И. Д. Скуратов ^{1,2},
С. О. Демидов ^{1,2}, Е.С. Горнев ^{1,2}

¹ Московский физико-технический институт, Москва, Россия;

² Научно-исследовательский институт молекулярной электроники, Зеленоград, Россия

✉ yevgeniy.shamin@phystech.edu

Аннотация. Оптические потери радиофотонных схем является одним из важнейших показателей качества их работы. Среди множества эффектов, влияющих на оптические потери, можно выделить шероховатость боковых стенок оптических элементов



таких схем (далее шероховатость). В данной работе предлагается к рассмотрению высокоэффективная модель появления шероховатости, состоящая из расчета оптической части фотолитографии, а также имитационного моделирования резиста. Описаны принципы функционирования и особенности реализации представленной модели. Продемонстрированы результаты моделирования, полученные с помощью новой модели шероховатости, а также предложен метод их экспериментальной верификации. Приводится теоретическая оценка потерь в волноводной структуре, связанных с шероховатостью.

Ключевые слова: шероховатость, моделирование фотолитографии, случайная плотная упаковка, моделирование проявления фоторезиста, интегральная фотоника, оптические потери

Финансирование: Работа выполнена при финансовой поддержке Фонда содействия развитию малых форм предприятий в научно-технической сфере. Грант № 075-15-2020-791 40ГУРЭС14/72785 от 26 декабря, 2021.

Ссылка при цитировании: Шамин Е. С., Шарапов А. А., Скуратов И. Д., Демидов С., Горнев Е. С., Модель шероховатости для расчёта оптических потерь в фотонных интегральных схемах // Научно-технические ведомости СПбГПУ. Физико-математические науки. 2022. Т. 15. № 3.3. С. 70–75. DOI: <https://doi.org/10.18721/JPM.153.313>

Статья открытого доступа, распространяемая по лицензии CC BY-NC 4.0 (<https://creativecommons.org/licenses/by-nc/4.0/>)

Introduction

The research activity in the field of integrated photonics is growing steadily. As a result, some aspects of microelectronics technology which were earlier ignored, are becoming more relevant. One of such aspects is a problem of sidewall roughness, which is assumed to be one of the main components contributing to the energy efficiency of photonic integrated circuits [1]. The signal propagating along the photonic device, scatters on roughness of its element's surfaces. This decreases the output power, as well as leads to the higher heating and worse transmission characteristic, which in its turn increases the noise ratio and creates undesired phase deviations. This hinders the use of photonic devices in radiolocation and RF transmission circuits.

Most often, due to the low availability of roughness modeling tools, as well as the high computational complexity of the algorithms used in them, the described problems are identified only at the stage of testing of the final devices. Thus, the problem of estimating losses in photonic circuits caused by sidewall roughness is relevant at the design stage. In this work a highly efficient sidewall roughness model is proposed, which could allow to fill this gap.

Materials and Methods

Roughness simulation, in terms of the model presented, consists of two steps. First step is a modelling of the photolithography which allows to take the effect of photon shot noise on the formation of roughness into account [2]. Second step is an application of the original imitational model of the resist exposure. It is assumed that the etching process used for manufacturing integrated photonic elements is chosen to be highly anisotropic, which results in inheritance of roughness features from the resist to the formed structure.

Based on the photolithography modelling data (Fig. 1, *a*), a region of “Unreliable illumination” is calculated [3] (Fig. 1, *b*). In this region there might be statistical deviations in energy, transferred to resist which may lead to local under- or over-exposures. Thus, it is assumed that sidewall roughness will be localized inside the “Unreliable illumination” region. Formally this region could be defined as by equation (1) on the aerial image plane (distribution of intensity over the resist, obtained as a result of modeling the optical part of photolithography). Here $I_{imaging}$ is defined as an average intensity over which photoresist becomes exposed and σ_I is defined by (2). $E(I)$ denotes an expected value of intensity, which could be substituted with intensity, obtained from CAD simulations. This reflects the statistical nature of roughness modeling.

$$\begin{cases} I + 3\sigma_I(I) \geq I_{\text{imaging}}, & I \leq I_{\text{imaging}} \\ I - 3\sigma_I(I) \leq I_{\text{imaging}}, & I > I_{\text{imaging}} \end{cases} \quad (1)$$

$$\sigma_I(I) = \sqrt{\frac{E(I)}{TA \frac{\lambda}{hc}}} \quad (2)$$

where I is intensity, T is exposure time, A is an elementary area unit on the XY simulation plane and λ is a photolithography wavelength.

The contribution of photoresist effects to sidewall roughness is taken into account by applying an imitational model of the resist exposure. In terms of this model, the macromolecules of the photoresist material are represented as tightly packed spheres or as referred further – grains. The resist grains mass (and, accordingly, size) variations are taken into account by specifying the grains radii distribution. If resist grain is partially or completely located within “Unreliable illumination” region, its exposure occurs only with some probability, which contributes to the roughness of the final structure.

After processing the initial data and obtaining the “Unreliable illumination” region, a smooth buffer region is built around it on a distance of two maximum radii from given grain radii distribution (Fig. 1, *b*). This ensures that every placed grain would give noticeable impact to final roughness modeling result as well as there would be minimal number of grains to be processed. Over the smooth buffer region, a grid data structure and a grid-based buffer are built with cell size of four maximum radii from given radii distribution (Fig. 1, *c*). The former one allows to address placed grain’s location by their number and numbers of placed grains by the number of grid cell. This allows the close packing algorithm to compute in linear time with respect to the number of balls to be processed. The latter one allows to efficiently calculate if placed grain is inside valid region and thus is used as a shape to be filled. The close packing algorithm, used in this work is a highly optimized for photoresist modeling 2D realization of 3D version of algorithm, presented at [4]. The result of the application of this algorithm could be seen at Fig. 1, *c*.

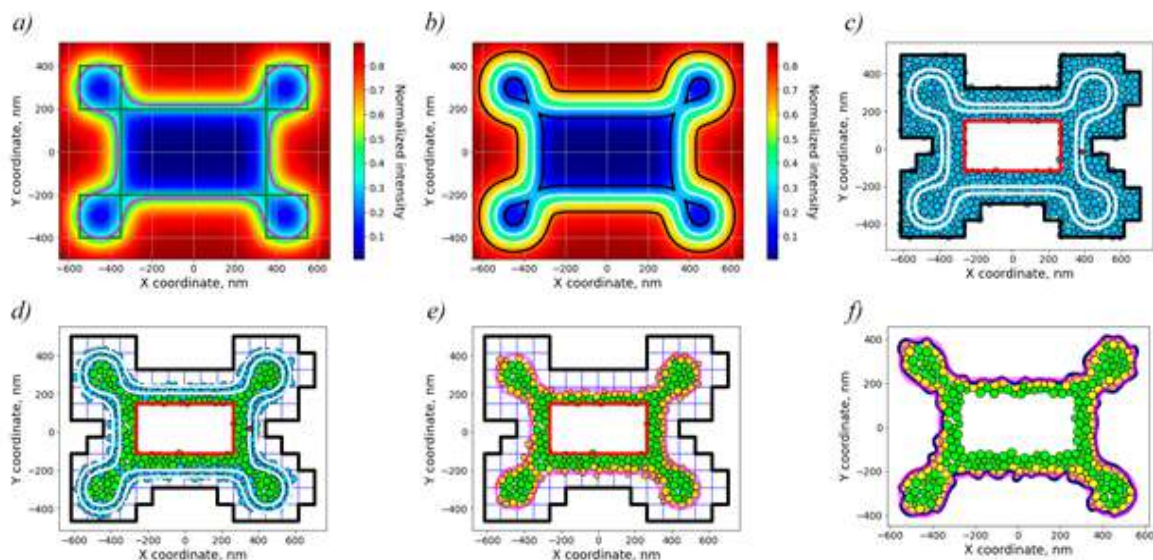


Fig. 1. Initial data for unreliable exposure model: aerial image and exposed resist contour (marked as purple). Initial topology polygons are presented with green lines (*a*); Buffer region (marked as black) is built around “Unreliable illumination” region (marked as white) (*b*); Result of the close packing algorithm application on a grid-based region (marked as black), built around buffer region, shown on Fig. 1, *b*) (*c*); Grains labeling: blue ones (in contrast to green ones) are exposed by chance (*d*); Exposed grains (marked as yellow). Initial resist contour (marked as transparent purple) is presented for comparison (*e*); Result of the patching and smoothing algorithms application. Initial resist contour (marked as transparent purple) is presented for comparison (*f*)



The final step before exposure simulation is grains labeling (Fig. 1, *d*) – algorithm defines, which grains from close packed ones fall into “Unreliable illumination” region and which ones are definitely exposed. Consequently, unreliable grains are processed using the criterion, described further in this work. Remaining (exposed) grains could be seen at Fig. 1, *e*. Finally – patching algorithm is applied between each neighboring grain which returns their convex hull – this and an additional spline interpolation algorithm allows for overall smoothness of the final result (Fig 1, *f*).

To simulate the exposure process – an exposure probability function is calculated for each of the unreliable grains, which could be expressed as (3). Each unreliable grain is split into 3 parts – reliable one, which is located in the definitely exposed region, unreliable one – according to the name, and underexposed one, as shown in Fig 2, *a*. Those correspond to values A_{in} , A_{ur} , and A_{out} in (3) – which represent the fractions of overall grain area. Important to note that sum of this values equals to one.

$$P(Exposure) = A_{in} + A_{ur} \cdot P(I) + 0 \cdot A_{out} \quad (3)$$

where $P(I)$ is derived from Poisson cumulative distribution function and A_{in} , A_{ur} and A_{out} are fractions of grain area, defined by Fig. 2, *a*.

For photoresist that becomes exposed over low intensity values, $P(I)$ in (3) has the meaning of probability that less than the threshold number of photons (proportional to $I_{imaging}$) strikes the grain in average over its area. This probability is calculated using the Poisson cumulative distribution function (Fig. 2, *b*), which is built for each grain by the average number of photons over all yellow points shown in Fig. 2, *a*. Respectively, for photoresist that becomes exposed over high intensity values, $P(I)$ should be calculated as $1 - P(I)$ for low intensity resist.

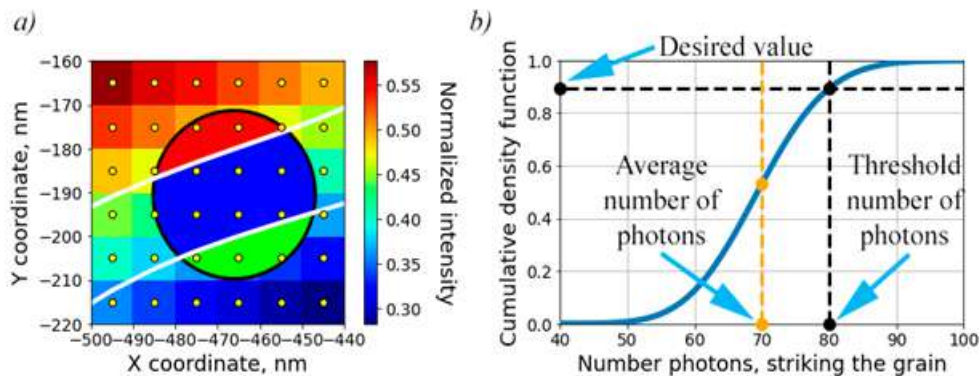


Fig. 2. Location of intensity points (yellow) that are averaged for each grain for probability calculation. Additionally, 3 split parts, calculated for each grain are shown – each corresponding to one of three fractions of area, used in (3): red part corresponds to A_{out} fraction of grain area, blue part corresponds to A_{ur} fraction and green part corresponds to A_{in} fraction (*a*); Probability calculation that less than threshold number of photons will strike the grain on average (*y* axis value, corresponding to horizontal black dotted line). Calculation is performed with the use of Poisson cumulative distribution function (*b*)

Results and Discussion

As could be seen on Fig. 3, *a* – resulting distribution of grain sizes (grains are shown on Fig. 1, *c*) is closely matched with initial one. It is also worth noting that overall running time of all applied algorithms is close to linear in respect to number of grains needed to be processed (as shown in Fig. 3, *b*). Results of high-precision modeling are shown on Fig. 3, *c*. Initial number of resist grains was about 3.5k. Full computation time needed to achieve the result presented was about 13s.

Sidewall roughness inflict and therefore highly correlated with optical losses. In agreement with Yap-form Payne-Lacey model [5], losses caused by sidewall roughness scattering in ridge optical waveguide can be expressed as (4):

$$\alpha_{PL}(TE / TM) = \frac{4.34\sigma^2}{\sqrt{2}d^4\beta_{TE/TM}} g(V) \cdot f_e(x, \gamma) \quad (4)$$

where σ is root-mean-square roughness, d is ridge waveguide half width, $\beta_{TE/TM}$ is a propagation constant. $g(V)$ and $f_e(x, \gamma)$ are functions described in [5].

By measuring these losses one can calculate device sidewall roughness and, consequently, verify new roughness model. On this basis, we propose a verification methodology that could be divided to three steps:

- Fabrication of test waveguide structures;
- Evaluation of numerical roughness characteristics by using a scanning electron microscope [6];
- Measurement of the transmission characteristic of the devices obtained.

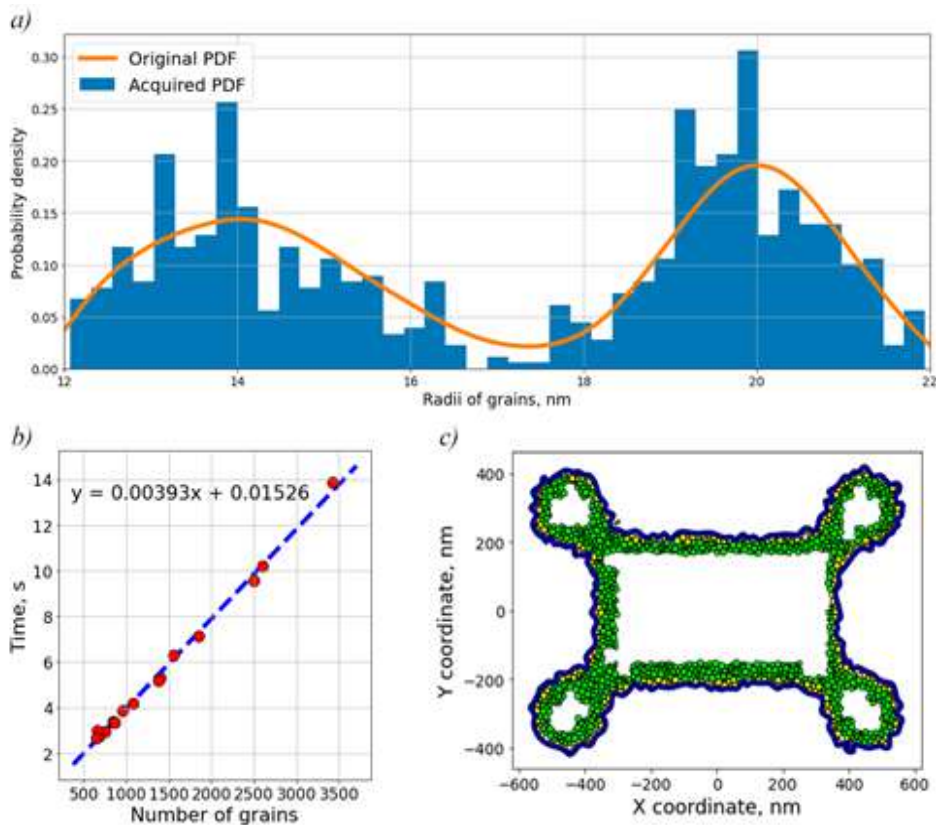


Fig. 3. Acquired probability density function (shown with histogram) and original probability density function (shown as orange curve) of grain's radii distribution (a); Time vs resulting number of grains processed by all applied algorithms (b); Results of high-precision modeling. Initial number of grains was about 3.5k. Running time was about 13s (c)

Conclusion

In this work simulation results, obtained using the new, highly efficient sidewall roughness model, were demonstrated. Principles of operation and implementation features of the model were described. An approach on their verification with experimental data was suggested. Additionally, theoretical estimations for the optical losses caused by sidewall roughness in Si waveguide are discussed.

REFERENCES

1. **Guiana B., Zadehgol A.**, Characterizing THz Scattering Loss in Nano-Scale SOI Waveguides Exhibiting Stochastic Surface Roughness with Exponential Autocorrelation, *Electronics*, 11.3 (2022) 307.



2. **Mack C.**, Fundamental principles of optical lithography: the science of microfabrication. John Wiley & Sons, 2008.
3. **Sharapov A. A., et al.**, Grounds and problem statement for software complex for photolithography optimization for minimization of losses in optical structures of photonic integrated circuits, IOP Conference Series: Materials Science and Engineering, IOP Publishing, 939 (1) (2020).
4. **Lozano E., Roehl D., Celes W., Gattass M.**, An efficient algorithm to generate random sphere packs in arbitrary domains. Computers & Mathematics with Applications, 71 (8) (2016) 1586–1601.
5. **Shang H., Sun D., Yu P., Wang B., Yu T., Li T. Jiang H.**, Investigation for sidewall roughness caused optical scattering loss of silicon-on-insulator waveguides with confocal laser scanning microscopy. Coatings, 10 (3) (2020) 236.
6. **Sharapov A., Baranov G.**, Comparative analysis of estimation techniques for qualitative roughness characteristics of nanostructures. Proceedings of MIPT, 2 (38) (2018) 72–79.

THE AUTHORS

SHAMIN Evgeniy S.

yevgeniy.shamin@phystech.edu
ORCID: 0000-0002-0470-350X

SHARAPOV Andrey A.

andrey.sharapov@phystech.edu
ORCID: 0000-0001-9945-3875

SKURATOV Ilya D.

ilya.skuratov@phystech.edu
ORCID: 0000-0002-4045-2883

DEMIDOV Stanislav O.

demidov.so@phystech.edu
ORCID: 0000-0003-0115-8822

GORNEV Evgeniy S.

egornev@niime.ru
ORCID: 0000-0003-1706-4142

Received 14.07.2022. Approved after reviewing 19.07.2022. Accepted 02.09.2022.

Conference materials

UDC 533.9.02

DOI: <https://doi.org/10.18721/JPM.153.314>

The kinetic simulation in vacuum electronics: uncovering the fundamental nature of non-Maxwellian distribution function effects

V. Yu. Kozhevnikov ¹✉, A. V. Kozyrev ¹, A. O. Kokovin ¹, N. S. Semeniuk ¹

¹Institute of High Current Electronics SB RAS, Tomsk, Russia

✉ Vasily.Y.Kozhevnikov@ieee.org

Abstract. This paper presents main theoretical results obtained in vacuum explosive-emission electronics by using of the numerical methods aimed to the direct solution of Vlasov Poisson kinetic equations. It was shown that computational physical kinetics makes it possible to explain a number of important physical laws occurring in vacuum diodes unlike widely used Particle-in-Cell or hydrodynamic simulation. The kinetic approach makes it possible to take into account nonequilibrium non-Maxwellian effects mainly associated with the “tails” of distribution functions. The advantages of kinetic simulation are shown on two highly relevant problems of vacuum electronics are considered in details.

Keywords: vacuum electronics, physical kinetics, numerical simulation

Funding: The work was carried out within the framework of the state assignment of the Ministry of Science and Higher Education of the Russian Federation on the topics FWRM 2021 0007, FWRM-2021-0014.

Citation: Kozhevnikov V. Yu., Kozyrev A. V., Kokovin A. O., Semeniuk N. S., The kinetic simulation in vacuum electronics: uncovering the fundamental nature of non-Maxwellian distribution function effects, St. Petersburg State Polytechnical University Journal. Physics and Mathematics, 15 (3.3) (2022) 76–81. DOI: <https://doi.org/10.18721/JPM.153.314>

This is an open access article under the CC BY-NC 4.0 license (<https://creativecommons.org/licenses/by-nc/4.0/>)

Материалы конференции

УДК 533.9.02

DOI: <https://doi.org/10.18721/JPM.153.314>

Кинетическое моделирование в вакуумной электронике: раскрытие фундаментальной природы эффектов немаквелловской функции распределения

В. Ю. Кожевников ¹✉, А. В. Козырев ¹, А. О. Коковин ¹, Н.С. Семенюк ¹

¹ Институт сильноточной электроники СО РАН, Томск, Россия

✉ Vasily.Y.Kozhevnikov@ieee.org

Аннотация. В статье представлены основные теоретические результаты, полученные в вакуумной взрывоэмиссионной электронике с использованием численных методов решения системы кинетических уравнений Пуассона-Власова. Было показано, что именно вычислительная физическая кинетика позволяет объяснить ряд важных физических закономерностей, происходящих в вакуумных диодах. Кинетический подход согласованно учитывает неравновесные немаквелловские эффекты, определяемые т.н. «хвостами» функций распределения. Подробно показаны преимущества кинетического моделирования на примере двух актуальных задач вакуумной электроники.

Ключевые слова: вакуумная электроника, физическая кинетика, численное моделирование

Финансирование: Работа выполнена в рамках Государственных заданий «Разряды в газах высокого и низкого давления и применения низкотемпературной газоразрядной



плазмы в электрофизических устройствах и технологиях» (код темы FWRM 2021 0007) и «Высокоинтенсивные источники спонтанного и индуцированного излучения оптического диапазона спектра и их применение для решения научных и технологических задач» (код темы FWRM 2021 0014).

Ссылка при цитировании: Кожевников В. Ю., Козырев А. В., Коковин А. О., Семенюк Н. С., Кинетическое моделирование в вакуумной электронике: раскрытие фундаментальной природы эффектов немаквелловской функции распределения // Научно-технические ведомости СПбГПУ. Физико-математические науки. 2022. Т. 15. № 3.3. С. 76–81. DOI: <https://doi.org/10.18721/JPM.153.314>

Статья открытого доступа, распространяемая по лицензии CC BY-NC 4.0 (<https://creativecommons.org/licenses/by-nc/4.0/>)

Introduction

For decades, vacuum electronics has remained an area of plasma physics attracting a great interest which is explained by its wide practical application [1]. From a theoretical point of view, vacuum electronics is a self-consistent description of space-charge limited (SCL) flows of charged particles. The SCL can be clearly explained by the example of a simple two-electrode system (vacuum diode) to which a certain voltage is applied. Even if the charges injection from cathode is assumed to be unlimited, the total current through the diode is always limited to

$$j_{SCL} = \frac{4\epsilon_0}{9} \sqrt{\frac{2q}{m}} \frac{U^{3/2}}{D^2}, \quad (1)$$

w.r.t. the voltage U applied to the infinite parallel plates located at a distance D from each other (m is the electron rest mass, q is the electron charge, ϵ_0 is the vacuum dielectric permittivity). The expression of (1) is called the Child's law [2]. It involves many assumptions, e.g. zero initial electron velocities, electrons only emission and a steady-state approximation, however the Child's law provides an ideal theoretical understanding of the SCL phenomenon and the tendency limiting the maximum current that can be carried through the vacuum device. Subsequently [3], Child's law was significantly corrected to relax the approximations used in (1).

In the beginning of the computational plasma physics era, the particle-in-cell (PIC) method was introduced for studying many transient processes in plasma [4]. Another more fundamental and much more computationally difficult principle is based on simultaneous solution of Boltzmann equations together with the electromagnetic field equations. The primary objects of kinetic numerical simulation are the electron and ion distribution functions (EDF and IDF), which provide more information about the system of charged particles than the characteristics of macroparticles in PIC approach. As an example, a pair of one-dimensional (1D) problems of non-stationary current flow in planar vacuum diodes are considered below. The 1D makes it possible to exclude from consideration geometric factors, which are usually referred to for the phenomenological explanation of complex phenomena. Thus, physical kinetics is used in this paper to simulate problems that are simple in terms of computational performance, but at the same time, the methods reveal non-trivial features that can only be described using a more fundamental approach.

Materials and Methods

Let us denote f_e the EDF and f_i the single-charge IDF. Thus, in 1D formulation the EDF and IDF depend on spatial variable x , momentum p_x , and time variable t . Both distribution functions obey collisionless kinetic (Vlasov) [5] equations

$$\begin{cases} \frac{\partial f_e}{\partial t} + \frac{p_x}{m_e} \frac{\partial f_e}{\partial x} - qE_x \frac{\partial f_e}{\partial p_x} = 0 \\ \frac{\partial f_i}{\partial t} + \frac{p_x}{m_i} \frac{\partial f_i}{\partial x} + qE_x \frac{\partial f_i}{\partial p_x} = 0 \end{cases} \quad (2)$$

where m_e and m_i are rest masses of electron and ion, respectively.

Neglecting the magnetic field influence, the system of Vlasov equations (2) describes the electrons and ion motion in the electric field E_x . The electric field equation has to be solved mutually with (2) in order to obtain a self-consistent solution, so we complement (2) with 1D Poisson's equation for electric potential φ

$$\frac{\partial^2 \varphi}{\partial x^2} = -\frac{q}{\varepsilon_0}(n_i - n_e), \quad E_x = -\frac{\partial \varphi}{\partial x}, \quad n_{e,i}(x, t) = \int_{-\infty}^{\infty} f_{e,i}(x, p_x, t) dp_x, \quad (3)$$

where ε_0 is dielectric permittivity of vacuum, n_e and n_i are electron and ion number densities, respectively.

The cathode is maintained at the point of $x = 0$ with the electric potential $\varphi = 0$, and the anode is at a distance D in the point $x = D$ with the electric potential $U(t)$. Thus, the Poisson's equation (3) can be solved in quadratures in the form of the following expressions:

$$E_x(x, t) = -\frac{U(t)}{D} - \frac{q}{\varepsilon_0 D} \int_0^x [n_e(x', t) - n_i(x', t)] dx' + \frac{q}{\varepsilon_0 D} \int_0^D \int_0^x [n_e(x', t) - n_i(x', t)] dx' dx, \quad (4)$$

$$\varphi(x, t) = U(t) \frac{x}{D} + \frac{qx}{\varepsilon_0 D} \int_0^D \int_0^x [n_e(x', t) - n_i(x', t)] dx' dx - \frac{q}{\varepsilon_0} \int_0^x \int_0^{x'} [n_e(x'', t) - n_i(x'', t)] dx'' dx'.$$

The initial conditions for the equations (2)-(4) are chosen to be zero $f_e = f_i = 0$, $U = 0$. The system of equations (2)-(4) is solved numerically using semi-Lagrangian methods [5] at a rectangular uniform phase-space grid (x, p_x) .

The "Anomalous" Electrons in Nanosecond Vacuum Diode

One of the novel physical phenomena regarding vacuum diodes became the effect of fast electrons generation with energies ε exceeding the maximum voltage U_{max} applied to the diode (multiplied by an elementary charge q) $\varepsilon > qU_{max}$. This group of electrons are also known as electrons with the "anomalously high" energies. Depending on experimental conditions fairly large groups of electrons with "anomalously" high kinetic energies can exist.

To elucidate the conditions for the "anomalous electrons" appearance, we posed the problem of a non-stationary current flow in planar vacuum diode with predominant electron emission from the cathode during the applying to it a voltage pulse $U(t)$ with a short leading edge t_{rise} and a constant amplitude of U_{max} . The term "short leading edge" suggests that the front duration is comparable to the electrons time of flight on their way from the cathode to the anode. By setting the cathode electron emission condition with the boundary condition at $x = 0$ for the

EDF $f_e(x=0, p_x, t) = n_0 / \sqrt{2\pi m W_0} e^{-\frac{p_x^2}{2mW_0}}$, where W_0 is the electron temperature, n_0 is emission electron number density, and $f_i = 0$, for short anode voltage rise time we obtain the relaxation oscillation of the collector current (Fig. 1) as it was shown in [6]. No oscillations are observed at the large lengths of the anode voltage rise time, and in the case of intermediate values (~ 0.5 ns), the oscillations have a lower amplitude and decay more intensively than at short rise times (below or equal to 0.1 ns). The establishment of a stationary current flow leads to that the collector current density becomes equal to j_{SCL} , regardless of the duration of the anode voltage pulse duration.

The collector current peak arises when the electron beam reaches the anode. The relaxation oscillations buildup is caused by the irregularity of charge inflow and outflow into the interelectrode gap. However, the computational physical kinetics allows to look at the process of the peak collector current density formation from the more fundamental point of view. Fig. 2 shows the comparison of the EDF density plots corresponding to the shortest anode voltage rise time ($t_{rise} = 0.1$ ns) in the case of stationary current flow (a) and at the time point corresponding to the maximum collector current density (b).

The electron beam reaches anode at this time point (Fig. 2, b) have mean energy exceeding qU_{max} by more that 20 percent with respect to steady-state value equal exactly to qU_{max} . If the rise time is relatively longer (here ~ 2 ns), the electron beam mean energy doesn't override qU_{max} value during the whole voltage pulse duration. Its EDF is similar to Fig. 2, a. The electrons with "anomalously high" energies form anode current density relaxation oscillations peaks.

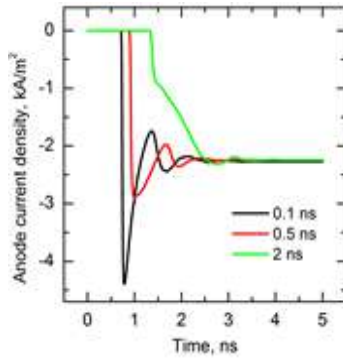


Fig. 1. The collector current density given for different risetimes ($D = 1$ cm, $U_{max} = 2$ kV)

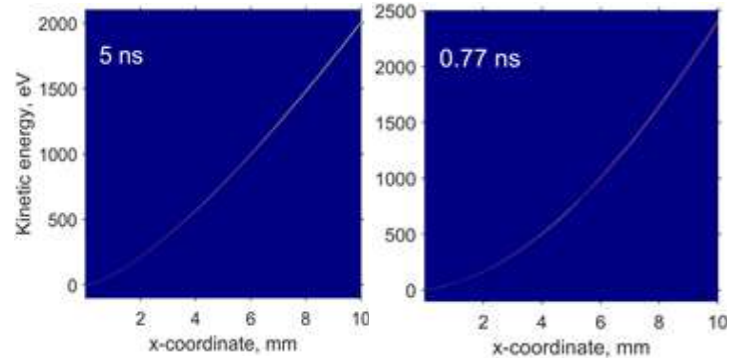


Fig. 2. The EDF density plots corresponding to a steady-state ($t = 5$ ns) and to the maximum of the collector current ($t = 770$ ps)

The “Anomalous” Ion Transport in Nanosecond Vacuum Diode

Another problem of vacuum electronics is connected to an explosive emission generating a dense quasi-neutral cathode plasma [7]. Explosive cathode plasma consists of electrons and a group of multiple-charged metal ions located in a thin near-cathode sheath. In various experiments it was convincingly shown that the critical role in the vacuum breakdown plays the existence of directed ion flows from cathode to anode [8]. Numerous experiments indicate that ions not only move towards the anode, but also their kinetic energies are exceeding the typical vacuum discharge combustion voltage (multiplied by q), e.g. see [9]. These ions are called the “anomalous”, and their transfer processes in vacuum diodes are called the “anomalous ion transport”, due to an ability to travel from cathode to anode. Here we give the simplest self-consistent explanation to this phenomenon from a standpoint of physical kinetics. The simplified case of a cathode plasma composition consisting of electrons and single-charged metal (carbon) ions is considered in planar 1D case here.

At $t = 0$ emission plasma enter the vacuum diode from the cathode as a nonequilibrium ($T_i = 3$ eV, $T_e = 1$ eV) quasi-neutral plasma with average number density of $n_e \approx n_i = n_0$. The regular plasma flow from cathode into the gap is modeled by simple boundary conditions

$$f_{e,i}(x=0, p_x, t) = n_0 / \sqrt{2\pi m q T_{e,i}} e^{-\frac{p_x^2}{2mqT_{e,i}}}.$$

Fig. 3 shows the EDF dynamics f_e at the initial stage of vacuum breakdown. The very first frame shows that the EDF looks similar to the case of stationary current flow in a vacuum diode (Fig. 2). Fig. 4 illustrates the phenomenon of the “anomalous ions acceleration” as is. Fast electron plasma component displacement is accompanied by slower ion dynamics also moving towards the anode. Fig. 5 shows the true electrodynamic cause of the “anomalous” ion acceleration. Starting from the first time points, electrons move towards the anode forming a region of negative electric potential near the cathode (“virtual cathode”). This forces ions to accelerate towards the anode. During the ion motion between the physical and the “virtual” cathode the displacement of a negative potential region occurs, and the cathode plasma starts to fill the near-cathode space. This process continues until the plasma fills the entire diode. These later stages of a vacuum breakdown are shown in details in [10] both for two- and multi-component cathode plasma.

The ion plasma component motion occurs at velocities that are significantly higher than the average value corresponding to a “virtual cathode” depth. One can say that “anomalous” ion acceleration is a motion of ions having an “anomalously” high energies. The IDF “tail” prolongs from near to thermal energies of several electron-volts up to 100 eV, while the instant electric potential minimum doesn’t exceed -25 V. The reason of why ions are moving in the “anomalous transport” mode acquire higher energies is in the nonstationary influence of the electric field due to the formation and subsequent displacement of the “virtual cathode” region towards anode. The ions turn into the continuous electrodynamic acceleration regime. This physical mechanism is similar to the formation of runaway electron beams [11].

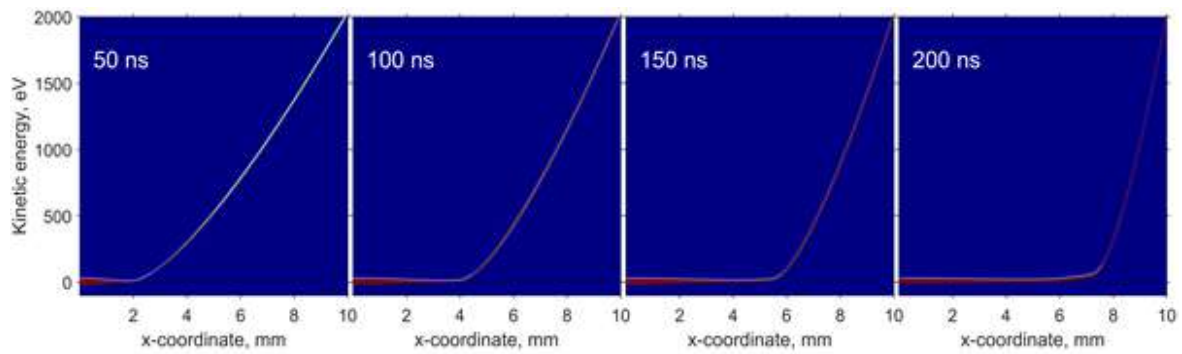


Fig. 3. The EDF f_e density plots computed for selected time steps. In arbitrary units normalized to boundary maximal value

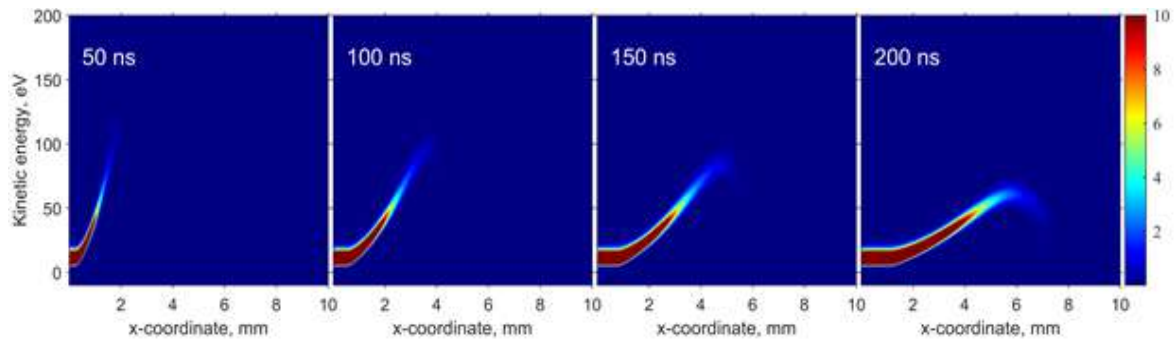


Fig. 4. The IDF f_i density plots computed for selected time steps. Plot is given in arbitrary units; the absolute values have to be multiplied by 10^{39} s/(kg·m⁴)

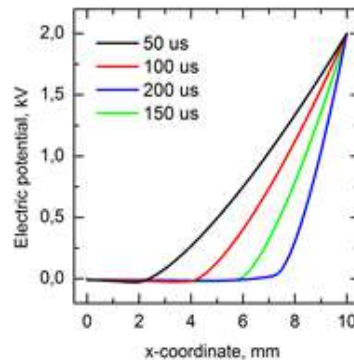


Fig. 5. The electrostatic potential evolution for selected time steps

The results of this paper convincingly show key advantages of computational physical kinetics with respect to the fundamental problems of vacuum electronics.

REFERENCES

1. Beck A. H., Marton L., Handbook of Vacuum Physics, Vol. 2: Physical Electronics. Physics Today, 23.5 (1970).
2. Child C. D., Discharge from Hot CaO, Physical Review (Series I), 32 (5) (1911) 492–511.
3. Ragan-Kelly B., Explorations of Space-Charge Limits in Parallel-Plate Diodes and Associated Techniques for Automation, PhD Thesis, UCLA, Berkley, 2013.
4. Birdsall C. K., Langdon A. B., Plasma Physics via Computer Simulation, 1991.
5. Kozhevnikov V. Y., Kozyrev A. V., Semeniuk N. S., Modeling of Space Charge Effects in Intense Electron Beams: Kinetic Equation Method Versus PIC Method, IEEE Transactions on Plasma Science, 45(10) (2017) 2762–2766.



6. **Airapetov A. Sh., Feoktistov A. L.**, Current limit in a non-stationary flat diode, *Kratkie Soobshchenia po Fizike*, 2 (18) (1990) 18–20.
7. **Litvinov E. A., Mesyats G. A., Proskurovskii D. I.**, Field Emission and Explosive Electron Emission Processes in Vacuum Discharges, *Soviet Physics Uspekhi*, 26 (2) (1983) 138–159.
8. **Krinberg I. A.**, Three modes of plasma expansion in a vacuum arc. The Proceedings of XXI International Symposium on Discharges and Electrical Insulation in Vacuum (ISDEIV), Yalta, Russia, (2004) 178-181.
9. **Oks E. M., Savkin K. P., Yushkov G. Y., Nikolaev A. G., Anders A., Brown I. G.**, Measurement of total ion current from vacuum arc plasma sources. *Review of Scientific Instruments*, 77(3) (2006) 03B504.
10. **Kozhevnikov V., Kozyrev A., Kokovin A., Semeniuk N.**, The Electrodynamic Mechanism of Collisionless Multicomponent Plasma Expansion in Vacuum Discharges: From Estimates to Kinetic Theory. *Energies*, 14 (22) (2021) 7608.
11. **Zubarev N. M., Kozhevnikov V. Y., Kozyrev A. V., Mesyats G. A., Semeniuk N. S., Sharypov K., Shunailov S. A., Yalandin M. I.**, Mechanism and dynamics of picosecond radial breakdown of a gas-filled coaxial line. *Plasma Sources Science and Technology*, 29 (12) (2020) 125008.

THE AUTHORS

KOZHEVNIKOV Vasily Yu.
Vasily.Y.Kozhevnikov@ieee.org
ORCID: 0000-0001-7499-0578

KOKOVIN Aleksandr O.
kokovin.alexandr@mail.ru
ORCID: 0000-0003-2068-7674

KOZYREV Andrey V.
kozyrev@to.hcei.tsc.ru
ORCID: 0000-0002-7078-7991

SEMENIUK Natalia S.
viliiskoeozero@yandex.ru
ORCID: 0000-0002-5972-2839

Received 04.05.2022. Approved after reviewing 05.07.2022. Accepted 05.07.2022.

Conference materials

UDC 004.942

DOI: <https://doi.org/10.18721/JPM.153.315>

Investigation of degradation characteristics of photosensitive structures with porous silicon

P. D. Tishin ¹, D. A. Shishkina ¹✉, I. A. Shishkin ¹,
N. A. Poluektova ¹, N. V. Latukhina ¹

¹ Samara National Research University, Samara, Russia

✉ shishkina.da@ssau.ru

Abstract. In this paper, the effect of porous silicon on the characteristics of photosensitive structures in open space is investigated. For this purpose, photovoltaic converters based on polished silicon of various configurations were created: a sample with a porous layer and a coating of zinc sulfide; a sample without a porous layer with a coating of zinc sulfide and a sample with a porous layer and a combined coating of zinc sulfide and dysprosium fluoride. The porous layer is less susceptible to environmental factors harmful to solar cells that reduce their service life, in particular, cosmic radiation. Also, porous surface contributes to higher electrical and optical properties of solar cells. And the antireflection coatings of zinc sulfide and dysprosium fluoride can reduce the number of recombination centers and increase light absorption, which also has a positive effect on the characteristics of structures. The results of the study of volt-ampere characteristics of silicon photosensitive devices are presented. An increase in the radiation resistance of structures using porous silicon is shown.

Keywords: photosensitive structures, porous silicon, radiation resistance

Citation: Tishin P. D., Shishkina D. A., Shishkin I. A., Poluektova N. A., Latukhina N. V., Investigation of degradation characteristics of photosensitive structures with porous silicon, St. Petersburg State Polytechnical University Journal. Physics and Mathematics, 15 (3.3) (2022) 82–85. DOI: <https://doi.org/10.18721/JPM.153.315>

This is an open access article under the CC BY-NC 4.0 license (<https://creativecommons.org/licenses/by-nc/4.0/>)

Материалы конференции

УДК 004.942

DOI: <https://doi.org/10.18721/JPM153.315>

Исследование деградации характеристик фоточувствительных структур с пористым кремнием

П. Д. Тишин ¹, Д. А. Шишкина, ¹✉, И. А. Шишкин ¹,
Н. А. Полуэктова ¹, Н. В. Латухина ¹

¹ Самарский национальный исследовательский университет имени академика С.П. Королева, Самара, Россия

✉ shishkina.da@ssau.ru

Аннотация. В данной работе исследуется влияние наноструктурированного кремния на характеристики фоточувствительных структур в открытом космосе. Для этого были созданы солнечные элементы различной конфигурации: с пористым слоем и покрытием из сульфида цинка; без пористого слоя с покрытием из сульфида цинка; с пористым слоем и комбинированным покрытием из сульфида цинка и фторида диспрозия. Представлены результаты исследования вольт-амперных характеристик полученных структур. Показано увеличение радиационной стойкости пористых структур.

Ключевые слова: фоточувствительные структуры, пористый кремний, радиационная стойкость.

Ссылка при цитировании: Тишин П. Д., Шишкина Д. А., Шишкин И. А., Полуэктова Н. А., Латухина Н. В., Исследование деградации характеристик



фоточувствительных структур с пористым кремнием // Научно-технические ведомости СПбГПУ. Физико-математические науки. 2022. Т. 15. № 3.3. С. 82–85. DOI: <https://doi.org/10.18721/JPM.153.315>

Статья открытого доступа, распространяемая по лицензии CC BY-NC 4.0 (<https://creativecommons.org/licenses/by-nc/4.0/>)

Introduction

Solar cells are a fairly promising option for a power source for space nanosatellites by many factors [1]. In particular, the rarefied atmosphere contributes to an increase in the service life of solar cells, and also contributes to an increase in the efficiency of such structures by 10–20% compared to terrestrial analogues. When choosing the substrate material for future photosensitive structures, preference is given to silicon because of its cheapness, as well as the width of its band gap, which contributes to greater generation of free charge carriers [2]. However, recent studies show that the use of porous silicon instead of a flat surface improves the characteristics of solar cells [3]. The porous surface is a pyramid, which reduces the reflection of sunlight and increases the radiation resistance of structures.

Materials and Methods

To prepare the flight experiment, 14 silicon samples with different surface types were taken on board the Aist-2D [4]. Phosphoric (*n*-type) and boric (*p*-type) diffusants were applied to the samples to create a p-n transition. Diffusion was carried out in a diffusion furnace at a temperature of 1000 °C for 40 minutes. Further, using electrochemical etching in a vertical cell [5]. The final stage of creating photosensitive structures is the application of titanium-palladium silver compound contacts and reflective coatings of zinc sulfide and dysprosium fluoride by thermal vacuum spraying on a magnetron sputtering unit.

Results and Discussion

Tests of the obtained silicon photosensitive structures were carried out on the Aist-2D small spacecraft directly in outer space, in order to investigate the radiation resistance of the obtained photoelectronic converters to cosmic radiation, as well as to mechanical and climatic influences.

For clarity, three samples were selected: a polished silicon wafer with pores and a ZnS coating (No. 1); a polished silicon wafer without pores with a ZnS coating (No. 3); a polished silicon wafer with pores and a combined ZnS+DyF₃ coating (No. 10).

To construct the current-voltage characteristics (Fig. 1-3), the data obtained were processed in the MATLAB Simulink graphical programming environment.

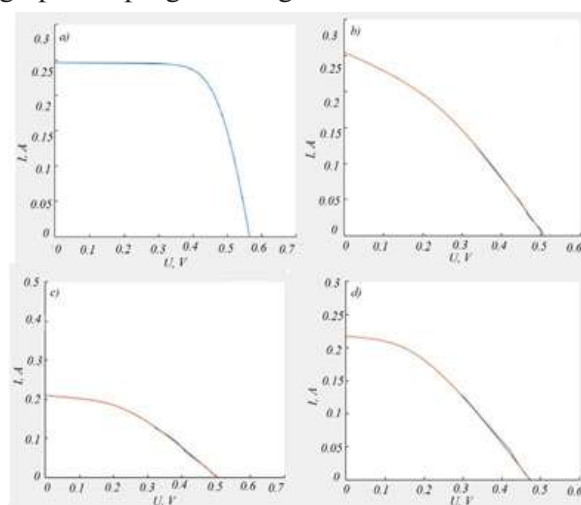


Fig. 1. Current-voltage characteristics of solar cell No.1: ground tests (a); 02.10.2017 (b); 23.11.2017 (c); 11.01.2018 (d)

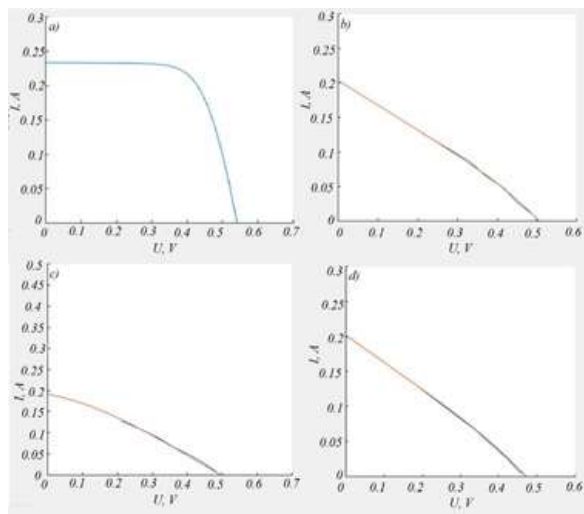


Fig. 2. Current-voltage characteristics of solar cell No.3: ground tests (a); 02.10.2017 (b); 23.11.2017 (c); 11.01.2018 (d)

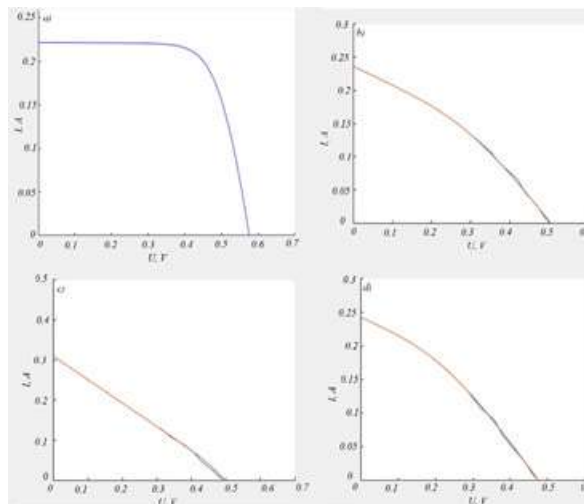


Fig. 3. Current-voltage characteristics of solar cell No.10: ground tests (a); 02.10.2017 (b); 23.11.2017 (c); 11.01.2018 (d)

From the graphs obtained, one can see the influence of radiation effects on the parameters of a solar cell with pores. The short-circuit current of solar cell No. 10 on 23.11.2017 increased to 0.3 A, and the open-circuit voltage decreased noticeably from 0.58 to 0.48 V. On solar cell No. 3, after radiation exposure, the current and voltage parameters decreased and further fluctuated near the marks of 0.2 A and 0.5 V. It can be concluded that solar cell No. 10 with a porous layer and a double coating has a higher short-circuit current compared to the others.

Conclusion

Thus, solar cells with silicon nanostructures and ZnS+DyF3 double coating are more radiation resistant compared to solar cells made according to classical technology and are promising for space applications.

REFERENCES

1. Nelson J. A., The physics of solar cells, World Scientific Publishing Company, 2003.
2. Yu, P., Wu, J., Liu, S., Xiong, J., Jagadish, C., Wang, Z. M., Design and fabrication of silicon nanowires towards efficient solar cells: Nano Today. 11 (6) (2016) 704–737.



3. **Shishkina D. A., Poluektova N. A., Shishkin I. A.**, Photovoltaic characteristics of structures with porous silicon obtained by various technological plans, Journal of Physics: Conference Series: IOP Publishing. 2086 (1) (2021) 012102.

4. **Gurtov A. S., Ivkov S. V., Lizunkova D. A., Shishkin I. A., Latukhina N. V.**, Operational characteristics of photovoltaic converters based on porous silicon, participating in the flight experiment on spacecraft “AIST-2D”, XIV Korolev Readings: mater. International conf. (2017) 503.

5. **Shishkin I. A., Lizunkova D. A., Latukhina N. V.**, The process of pore formation on a textured silicon substrate during electrochemical etching: a 3D model, Information Technologies and Nanotechnologies (2020) 27–30.

THE AUTHORS

TISHIN Pavel D.

tishin.pavel1999@gmail.com

ORCID: 0000-0002-9420-1852

POLUEKTOVA Natalia A.

natapolivekt37@gmail.com

ORCID: 0000-0003-4189-6192

SHISHKINA Daria A.

daria.lizunkova@yandex.ru

ORCID: 0000-0003-4118-1429

LATUKHINA Natalia V.

natalat@yandex.ru

ORCID: 0000-0003-2651-056

SHISHKIN Ivan A.

shishkinivan9@gmail.com

ORCID: 0000-0002-8413-9661

Received 25.07.2022. Approved after reviewing 26.07.2022. Accepted 26.07.2022.

Conference materials

UDC 544.723

DOI: <https://doi.org/10.18721/JPM.153.316>

Cetyltrimethylammonium bromide as a soft template for the synthesis of a conductometric gas sensor active substance

G. R. Nizameeva ^{1,2✉}, R. R. Gainullin ¹, I. R. Nizameev ^{1,3}, M. K. Kadirov ¹

¹ A. E. Arbuzov Institute of Organic and Physical Chemistry, Kazan, Russia;

² Kazan National Research Technological University, Kazan, Russia;

³ Kazan National Research Technical University named after A.N. Tupolev, Kazan, Russia

✉ guliya.riv@gmail.com

Abstract. This paper presents the investigation of cetyltrimethylammonium bromide (CTAB) molecules self-organization at the glass substrate, which is used as a micellar template in the synthesis of metal nanonetworks. These nanonetworks can be used as an active substance of gas sensors for detection of toxic gases. The free surface energy of glass which is used in the work as a substrate, and the free energy of the glass-CTAB interface are calculated.

Keywords: micellar template, metal nanonetworks, gas sensors, cetyltrimethylammonium bromide, surface energy, atomic force microscopy

Funding: The reported study was funded by the government assignment for FRC Kazan Scientific Center of RAS.

Citation: Nizameeva G. R., Gainullin R. R., Nizameev I. R., Kadirov M. K., Cetyltrimethylammonium bromide as a soft template for the synthesis of a conductometric gas sensor active substance, St. Petersburg State Polytechnical University Journal. Physics and Mathematics, 15 (3.3) (2022) 86–92. DOI: <https://doi.org/10.18721/JPM.153.316>

This is an open access article under the CC BY-NC 4.0 license (<https://creativecommons.org/licenses/by-nc/4.0/>)

Материалы конференции

УДК 544.723

DOI: <https://doi.org/10.18721/JPM153.316>

Цетилтриметиламмония бромид как мицеллярный шаблон для синтеза активного элемента газового сенсора

Г. Р. Низамеева ^{1,2✉}, Р. Р. Гайнуллин ¹, И. Р. Низамеев ^{1,3}, М. К. Кадиров ¹

¹ Институт органической и физической химии имени А. Е. Арбузова КазНЦ РАН, Казань, Россия;

² Казанский национальный исследовательский технологический университет, Казань, Россия;

³ Казанский национальный исследовательский технический университет

им. А. Н. Туполева, Казань, Россия

✉ guliya.riv@gmail.com

Аннотация. В данной работе представлены результаты исследования процессов самоорганизации молекул цетилтриметиламмония бромида (СТАВ), который используется в качестве мицеллярного шаблона при синтезе ориентированных наносетей металлов. Полученные наносети могут использоваться в качестве активного элемента для обнаружения токсичных газов в газовых сенсорах. Рассчитана свободная поверхностная энергия стекла, которое используется в работе в качестве основы для газового сенсора, и свободная энергия границы раздела стекло – раствор СТАВ, на котором формируется мицеллярный шаблон.

Ключевые слова: мицеллярный шаблон, металлические нанопровода, газовый сенсор, цетилтриметиламмония бромид, поверхностная энергия, атомно-силовая микроскопия



Финансирование: Работа выполнена в рамках государственного задания ФИЦ КазНЦ РАН.

Ссылка при цитировании: Низамеева Г. Р., Гайнуллин Р. Р., Низамеев И. Р., Кадиров М. К., Цетилтриметиламмония бромид как мицеллярный шаблон для синтеза активного элемента газового сенсора // Научно-технические ведомости СПбГПУ. Физико-математические науки. 2022. Т. 15. № 3.3. С. 86–92. DOI: <https://doi.org/10.18721/JPM.153.316>

Статья открытого доступа, распространяемая по лицензии CC BY-NC 4.0 (<https://creativecommons.org/licenses/by-nc/4.0/>)

Introduction

Atmospheric pollution has become one of the most serious problems faced by mankind. In recent years, this problem has attracted more and more attention from a significant part of the scientific community and pushes for the study of various issues of environmental safety. The main cause of air pollution is the release of harmful gases, liquids and chemicals into the air. Air pollutants adversely affect human health and can lead to serious consequences if the maximum allowable concentration is increased. Therefore, to control the content of toxic gases in the atmosphere and monitor the environment, there is a practical need to create productive, accurate and cheap sensors for detecting and measuring the maximum allowable concentration of toxic gases. The importance of creating such devices is quite obvious, because they will solve the problems of atmospheric monitoring and control of factory conditions, medical problems and problems of the food industry.

To date, nanometer-sized materials are widely used in gas sensors as an active element for detecting harmful gases in the atmosphere. Of particular interest are one-dimensional nanomaterials such as oriented nanonetworks and metal oxide nanowires. Such structures have superior physical and chemical properties compared to thin-film and bulk materials [1]. At present, gas sensors based on nanowires of metal oxides of n-type conductivity are widely studied. However, until recently, insufficient attention has been paid to semiconductor p-type metal oxides. Meanwhile, they have a high specific surface area, sensitivity to toxic gases, low cost and environmental friendliness. Of greatest interest among p-type metal oxides is nickel oxide [2–4]. Oriented nanowires based on nickel oxide NiO, as one of the few materials, are able to detect gases such as ammonia and nitrogen oxides at room temperature, which is the most significant advantage in their application.

Oriented nickel oxide nanowires are obtained by various methods, but from the point of view of economy and scalability, the most promising is the synthesis of nickel nanowires by chemical deposition from a liquid phase using a “soft” micellar template followed by oxidation of the obtained nanowires. Molecules of surface-active substances (surfactants) act as such a template, which, as a result of self-organization, form cylindrical micelles at the “solid-liquid” interface. These cylinders can be used as templates for the synthesis of metal nanonetworks. The characteristics of the micellar template will determine the length, width, and repetition period of metallic nanowires. In this regard, studies of the properties of a micellar template formed at the “solid-liquid” interface are of great practical importance.

In this work, we study the processes of self-organization of CTAB molecules at the glass–surfactant solution interface and the micellar template of CTAB on the surface of a glass substrate made of silicate glass. The obtained data on the processes of self-organization of STAB at the interface “solid body – liquid” allow to more effectively control the chemical deposition of metal networks.

Materials and Methods

In this work, a Levenhuk G 100 round cover glass with a thickness of 0.13–0.17 mm and a diameter of 11 mm was used as the basis for the sensor. The glass substrate was preliminarily cleaned and degreased. Cleaning and degreasing were carried out with distilled water and ethyl alcohol, which can be replaced with isopropyl alcohol. The process of final cleaning consisted in immersing the substrate in ethanol and washing due to translational movements in the liquid bulk.

After that, the surface of the glass substrate was washed with distilled water. The surface was dried with an air jet.

Visualization of the surface of the glass substrate was carried out on a scanning probe microscope MultiMode V manufactured by Veeco (USA) in a discontinuous contact mode. For scanning, RTESP (Veeco) rectangular cantilevers with silicon probes were used. The resonant frequency of these cantilevers is in the region of 250–350 kHz, and the radius of curvature of the probe is 10–13 nm. Microscopic images were obtained with a resolution of 512×512 pixels per frame at a scanning speed of 1 Hz. To eliminate distortions associated with the “trembling” of the microscope under the influence of external noise, we used the SG0508 anti-vibration system, which is capable of smoothing vibrations with a frequency of up to 0.5 Hz (lower limit).

To obtain oriented nickel nanowires on the glass surface, we used the method of chemical metal deposition from the liquid phase using a CTAB micellar template. To form a micellar surfactant template, an aqueous solution of CTAB with a concentration of 1 mM was applied to the glass surface. After that, waited for 10 minutes to form a micellar template. Nickel chloride (nickel (II) chloride 6-aqueous) was used as a nickel precursor. Nickel nanowires were synthesized in the presence of a magnetic field.

Microscopic images of the CTAB micellar template on the glass surface were obtained in an AFM liquid cell. Before each experiment, the liquid cell was cleaned initially with bidistilled water and then with acetone. The feedback setting of the integral component during the experiment was in the range of 0.5–1, and the proportional component was in the range of 5–10. The scanning speed was maintained in the range of 1–2 Hz. The calibration of transverse dimensions was performed by scanning a special calibration grid (STR3-1800P, VLSI Standards Inc.) in a temperature range of 20–60 °C. The nonlinearity of the piezo crystal in this range is not observed. The images were obtained by contact AFM. In this case, the pressure force of the probe to the surface of the adsorbed micellar structures of STAB, at the interface of the liquid-substrate transition, was chosen as the smallest possible, at which the micelle structure is not disturbed and, at the same time, clear images can be obtained. Adsorbed CTAB structures have always been studied in regions that did not have surface topology irregularities.

Results and Discussion

Surfactant solutions, which at certain concentrations form cylindrical aggregates at the “solid body – surfactant solution” interface, are of particular interest. They can be used as a “soft template” for metal nanonetworks, which have recently become the subject of intensive research, due to the possibility of using them in many applications. Both anionic and cationic surfactants can be used for the micellar template. The choice of a specific surfactant is determined by the nature of the solid on which the surfactant molecules are adsorbed and a micellar template is formed. Depending on the type of substrate, cylindrical and semi-cylindrical structures of surfactant molecules may form at the “solid-liquid” interface, or they may not form at all. In our case, glass is used as a solid body. The shape of adsorbed surfactant structures, as well as the functional characteristics of gas sensors, will largely depend on the type and quality of the glass working surface, on which oriented nickel oxide nanowires are deposited as an active element. To assess the quality of the substrate surface, a parameter such as roughness is used.

To determine the roughness, the surface morphology of the selected glass substrate was examined by atomic force microscopy (AFM). The surface morphology of the glass substrate, which is used in this work as the basis for the sensor, and the topographic histogram are shown in Figure 1.

According to the obtained data, the surface roughness R_a (arithmetic mean of the absolute values of the profile deviations within the baseline) of the glass substrate is approximately 3.24 nm.

For a more detailed understanding of the processes of self-organization of CTAB molecules at the “glass-liquid” interface, we studied the wetting angles of the glass used in the work as a substrate with water and aqueous solutions of CTAB at various concentrations. As a result of the research, it was found that the contact angle of the glass substrate when wetted with water is 19.30, which indicates the hydrophilicity of the glass substrate.

The properties of glass strongly depend on the density of OH groups on its surface, and their density, in turn, is determined by the concentration of silicon on the surface. The SiOH groups play an important role in the adsorption of organic substances on the glass surface.

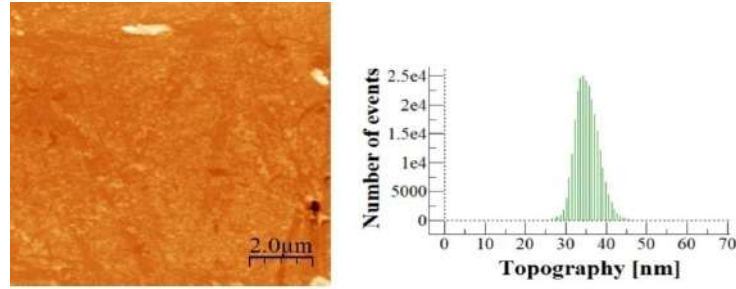


Fig. 1. AFM image of a small area of the glass substrate and the histogram corresponding to the topography

For the numerical characterization of the physicochemical properties of a solid surface, the value of the free surface energy is used. Measuring this value directly is a difficult task. Usually, indirect methods are used (for example, by measuring the contact angle).

Glass has a polar surface. The free surface energy is determined by two components: van der Waals interactions (interparticle interaction) and acid-base interactions:

$$\gamma_{SV} = \gamma_{SV}^{LW} + \gamma_{SV}^{AB}, \quad (1)$$

where γ_{SV} is free surface energy of a rigid body, γ_{SV}^{LW} is Lifshitz-van der Waals component, γ_{SV}^{AB} is acid-base interaction component (includes electron-acceptor and electron-donor parameters of the acid-base free energy component of a solid or liquid).

Various approaches are used to calculate the value of the free surface energy of a solid body. The most common approach in modern literature is the method of Neumann et al. [5, 6]. In these works, the ratio is used to calculate the value γ_{SV}

$$\frac{\cos \theta + 1}{2} = \sqrt{\frac{\gamma_{SV}}{\gamma_{LV}} e^{-\beta(\gamma_{LV} - \gamma_{SV})^2}}, \quad (2)$$

θ is contact angle of wetting of a solid surface by the liquid under consideration (for polar surfaces it must be polar, and for non-polar surfaces it must be non-polar), γ_{LV} is surface tension of a liquid, β is constant independent of surface type ($\beta = 0.000115 \text{ (m}^2/\text{mJ)}^2$ [265]).

Equation (2) makes it possible to calculate the value γ_{SV} provided that the values and θ are known. However, this equation has no analytical solution. To determine the approximate value

γ_{SV} appropriate substitutions are introduced into equation (2) and reduced to the form $f(x) = 0$. Next, Newton's iterative method is used [5].

Let's introduce substitutions:

$$x^2 = \frac{\gamma_{SV}}{\gamma_{LV}}; a = \frac{\cos \theta + 1}{2}; b = \beta \cdot \gamma_{LV}^2, \quad (3)$$

Equation (2) is transformed into the form

$$a = x \cdot e^{-b(1-x^2)^2} \text{ or } x = a \cdot e^{b(1-x^2)^2} \quad (4)$$

Because θ is obtained by measuring the system {solid - liquid - gas} with the condition $\gamma_{SV} < \gamma_{LV} \Rightarrow 0 \leq x \leq 1$. Then the problem is reduced to finding a solution to the equation:

$$f(x) = x - a \cdot e^{b(1-x^2)^2} = 0, \quad (0 \leq x \leq 1) \quad (5)$$

Newton's method is reduced to finding by successive approximation

$$x_{n+1} = x_n - \frac{f(x_n)}{f'(x_n)}, (n = 1, 2, \dots) \quad (6)$$

Approximations (iterations) continue until the required degree of accuracy is obtained. In our case, to obtain the accuracy of the value to one decimal place in mJ/m², it is enough to reach x₃.

$$x_{n+1} = x_n - \frac{x_n - a \cdot e^{b(1-x_n^2)^2}}{1 + 4abx_n(1-x_n^2)e^{b(1-x_n^2)^2}}, \quad (7)$$

For pure water $\gamma_{LV} = 72.8 \frac{mJ}{m^2}$, $\theta = 19.3^\circ$.

$$a = \frac{\cos 19.3 + 1}{2} = 0.973; \quad b = 0.000115 \cdot 72.8^2 = 0.6095. \quad (8)$$

We choose the initial seed value x equal to 1.0:

$$x_2 = x_1 - \frac{1 - a \cdot e^0}{1 + 0} = a = 0.973, \quad (9)$$

$$x_3 = x_2 - \frac{x_2 - a \cdot e^{b(1-x_2^2)^2}}{1 + 4abx_2(1-x_2^2)e^{b(1-x_2^2)^2}} = 0.9745, \quad (10)$$

$$\gamma_{SV} = x_3^2 \cdot \gamma_{LV} = 69.1 \frac{mJ}{m^2}. \quad (11)$$

According to the calculated data, the free surface energy of the glass turned out to be 69.1 mJ/m².

For comparison, similar calculations were carried out for the glass used in the work ($\theta = 47^\circ$) [7, 8]:

$$\gamma_{SV} = x_3^2 \cdot \gamma_{LV} = 55.2 \frac{mJ}{m^2}. \quad (12)$$

From the data obtained, it can be concluded that the free surface energy depends on the type of glass.

Further, to determine the concentration of CTAB at which a stable micellar pattern is formed on the surface of the glass substrate, we studied the concentration dependence of the wetting angle of the selected brand of glass with aqueous solutions of CTAB. The results obtained are presented in table 1.

Table 1

Concentration dependence of the contact angle of wetting a glass substrate with CTAB solutions

Concentration, mM	Contact angle θ , °
0.1	19.7
0.25	20
0.5	23.93
1	25.2
2	23.26
5	21.67
10	20.9

In the course of studies on the contact angle of wetting, it was revealed that wetting inversion is observed for the glass substrate. At concentrations below 1 mM, hydrophobization of the glass substrate is observed, and at concentrations above this, hydrophilization is observed. At a CTAB concentration of 1 mM, a transition from hydrophobicity to hydrophilicity is observed, and the formation of a micellar pattern is observed at the glass-CTAB solution interface.



The micellar template is a repeating cylindrical strip suitable for further deposition of oriented nickel nanonetworks. It was determined that the micellar pattern is formed 10 minutes after applying the STAB solution to the glass surface; the band repetition period in such a system is 4.5–5 nm.

To estimate the change in the surface energy of glass after the formation of a micellar template, the free energy of the glass–CTAB solution interface was calculated using the Yang equation (13) ($C = 1 \text{ mmol/l}$) γ_{SL} :

$$\gamma_{SV} - \gamma_{SL} = \gamma_{LV} \cdot \cos \theta. \quad (13)$$

For CTAB concentration 1 mmol/l $\gamma_{LV} = 41 \frac{\text{mJ}}{\text{m}^2}$ and $\theta = 25.2^\circ$. Then

$$\gamma_{SL} = 69.1 \frac{\text{mJ}}{\text{m}^2} - 0.905 \cdot 41 \frac{\text{mJ}}{\text{m}^2} \approx 32 \frac{\text{mJ}}{\text{m}^2}. \quad (14)$$

The value of the interfacial energy of the glass-surfactant solution calculated by the Yang equation turned out to be 32 mJ/m².

Conclusion

The dependences of the wetting contact angle of CTAB solutions on glass on a concentration were studied. It was found that the application of a CTAB solution with a concentration of 1 mM on the surface of silicate glass leads to the formation of a micellar system in the form of repeating cylindrical bands which is suitable for obtaining oriented nickel oxide nanonetworks. The free surface energy of the glass used in this work as the basis for the sensor was calculated. The value of free surface energy is 69.1 mJ/m². The free energy of the glass–CTAB solution interface was calculated using obtained for glass data. The value is 32 mJ/m². The results show that adsorption of surfactant molecules actually occurs at the glass–CTAB solution interface leading to a decrease in the free surface energy of the glass.

Acknowledgments

The reported study was funded by the government assignment for FRC Kazan Scientific Center of RAS. Nizameeva G. R. performed measurements of contact angle at Arbuzov Institute of Organic and Physical Chemistry and AFM studies at Kazan National Research Technological University. Gainullin R. R. performed liquid sample preparations at Arbuzov Institute of Organic and Physical Chemistry. Nizameev I.R. performed measurements of contact angle at Arbuzov Institute of Organic and Physical Chemistry and topographic studies at Kazan National Research Technical University. Kadirov M. K. performed calculations of surface tension constants at Arbuzov Institute of Organic and Physical Chemistry.

REFERENCES

1. Barsan N., Weimar U., Conduction model of metal oxide gas sensors, *Journal of electroceramics*, 7 (3) (2001) 143–167.
2. Hu Z., Chen D., Yang P., Yang L., Qin L., Huang Y., Zhao X., Sol-gel processed yttrium doped NiO as hole transport layer in inverted perovskite solar cells for enhanced performance, *Appl. Surf. Sci.*, 441 (2018) 258–264.
3. Yu Y., Xia Y., Zeng W., Liu R., Synthesis of multiple networked NiO nanostructures for enhanced gas sensing performance, *Mater. Lett.*, 206 (2017) 80–83.
4. Zhang Y., Zeng W., New insight into gas sensing performance of nanoneedle-assembled and nanosheet-assembled hierarchical NiO nanoflowers, *Mater. Lett.*, 195 (2017) 217–219.
5. Spelt J. K., Li D., Neumann A. W., The equation of state approach to interfacial tensions, *Modern approaches to wettability*, (1992) 101–142.
6. Szymczyk K., Zdziennicka A., Jańczuk B., Adsorption and wetting properties of cationic, anionic and nonionic surfactants in the glass-aqueous solution of surfactant-air system, *Materials Chemistry and Physics*, 162 (2015) 166–176.

7. Nizameev I. R., Muscat A. J., Motyakin M. V., Grishin M. V., Zakharova Ya L., Nizameeva G. R., Kadirov M. K., Surfactant templated oriented 1-D nanoscale platinum and palladium systems on a modified silicon surface, *Nano-Structures & Nano-Objects*, 17 (2019) 1–6.

8. Kadirov M. K., Litvinov A. I., Nizameev I. R., Zakharova L. Y., Adsorption and pre-micellar aggregation of CTAB molecules and fabrication of nanosized platinum lattice on the glass surface, *J. Phys. Chem. C.*, 118 (2014) 19785–19794.

THE AUTHORS

NIZAMEEVA Guliya R.

guliya.riv@gmail.com

ORCID: 0000-0002-4991-0502

NIZAMEEV Irek R.

irek.rash@gmail.com

ORCID: 0000-0002-5420-6181

GAINULLIN Radis R.

radis.g@mail.ru

ORCID: 0000-0002-0602-0470

KADIROV Marsil K.

kamaka59@gmail.com

ORCID: 0000-0003-3204-8431

Received 10.08.2022. Approved after reviewing 11.08.2022. Accepted 12.08.2022.

Conference materials

UDC 538.91

DOI: <https://doi.org/10.18721/JPM.153.317>

Optimization of the contact grid for the GaP/Si solar cells

M. V. Bogdanova ¹✉, A. V. Uvarov ¹, A.S. Gudovskikh ^{1,2}

¹ St. Petersburg Academic University of RAS, St. Petersburg, Russia;

² St. Petersburg Electrotechnical University ("LETI"), St. Petersburg, Russia

✉ bogdanovamilanav@mail.com

Abstract. In this paper, the calculation of electrical properties for (n)GaP–p(Si) solar cells was performed for different contact grid design. The influence of annealing temperature on the current-voltage curves of solar cells was shown via the Hall measurements and the simulation respectively. For calculations 20 μm and 200 μm width contact bars were used. First group corresponds to lithography. The second one could be appropriate for mass-scalable screen-printing metallization technique. The distance between contacts was varied in the range from 50 μm to 4000 μm in case for 20 μm contact width and in the range from 200 μm to 4000 μm in case for 200 μm contact width. According to the results of calculation, the thermal annealing at 600–700 °C is optimal for 20 μm configuration of contact grid. The predicted conversion efficiency is approximately 21.5%. Relative to contact grid with 200 μm width of bars, the optimal annealing temperature is 700 °C. These conditions lead to 19% conversion efficiency.

Keywords: solar cells, heterojunction GaP/Si, screen-printing, contact grid

Funding: This work was supported by Ministry of Science and Higher Education of the Russian Federation (research project 0791-2020-0004).

Citation: Bogdanova M. V., Uvarov A. V., Gudovskikh A. S., Optimization of the contact grid for the GaP/Si solar cells, St. Petersburg State Polytechnical University Journal. Physics and Mathematics, 15 (3.3) (2022) 93–96. DOI: <https://doi.org/10.18721/JPM.153.317>

This is an open access article under the CC BY-NC 4.0 license (<https://creativecommons.org/licenses/by-nc/4.0/>)

Материалы конференции

УДК 538.91

DOI: <https://doi.org/10.18721/JPM153.317>

Оптимизация контактной сетки для солнечных элементов на основе GaP/Si

М. В. Богданова ¹✉, А. В. Уваров ¹, А. С. Гудовских ^{1,2}

¹ Академический университет им. Ж.И. Алфёрова, Санкт-Петербург, Россия;

² Санкт-Петербургский государственный электротехнический университет («ЛЭТИ»), Санкт-Петербург, Россия

✉ bogdanovamilanav@mail.com

Аннотация. В данной работе проведен расчет электрических свойств солнечных элементов (n)GaP–p(Si) для различных конфигураций контактной сетки. Было показано влияние температуры отжига на вольтамперные характеристики солнечных элементов при помощи измерений методом Холла и моделирования. Для расчетов использовались ширина контактов 20 мкм и 200 мкм. Первая группа соответствует нанесению контактов при помощи литографии. Вторая группа может подойти для масштабируемого метода трафаретной печати. Расстояние между контактами варьировалось в диапазоне от 50 мкм до 4000 мкм при ширине контакта 20 мкм и в диапазоне от 200 мкм до 4000 мкм при ширине контакта 200 мкм. По результатам расчетов термический отжиг при 600–700 °C оптимален для конфигурации контактной сетки 20 мкм. Прогнозируемый КПД преобразования составляет приблизительно 21.5%. При ширине контактов

200 мкм оптимальная температура отжига составляет 700 °С. Эти условия соответствуют эффективности преобразования 19%.

Ключевые слова: солнечные элементы, гетеропереход GaP/Si, трафаретная печать, контактная сетка

Финансирование: Работа выполнена при поддержке Министерства Науки и Образования Российской Федерации (код проекта 0791-2020-0004).

Ссылка при цитировании: Богданова М. В., Уваров А. В., Гудовских А. С., Оптимизация контактной сетки для солнечных элементов на основе GaP/Si // Научно-технические ведомости СПбГПУ. Физико-математические науки. 2022. Т. 15. № 3.3. С. 93–96. DOI: <https://doi.org/10.18721/JPM.153.317>

Статья открытого доступа, распространяемая по лицензии CC BY-NC 4.0 (<https://creativecommons.org/licenses/by-nc/4.0/>)

Introduction

The formation of contact systems is an important technological process in the design of solar cells. Materials, structure, and geometry of contacts affect the distribution of currents [1–2].

Depending on the contact position relative to the propagation of light (front or rear), they have different requirements. In the front contact system, an optimum must be observed between the shading effect and the contact resistance losses [3–4]. If the contact grid area is small, then the optical losses associated with shading will decrease, but the electrical resistance will increase. Therefore, in industrial solar cells, one can often find a configuration of mutually perpendicular current-carrying bars and strips. It is the optimal ratio between light and electrical losses.

In this work, we will calculate contact systems for the (n)GaP/(p)Si structure, we will search for the optimal distance between contacts at fixed annealing temperatures.

Materials and Methods

In our simulations, we varied the distance between contact bars and estimated its influence on the conversion efficiency. We calculated the electrical properties of GaP/Si solar cells using Silvaco software. For calculation we used spectra in the wavelength range from 0.3 μm to 1.2 μm, the spectral density distribution corresponds to the AM1.5G standard. For numerical calculations, we divided this range into 50 bands of equal width. The radiation propagated along the normal on the sample, while we considered the condition of complete bleaching with GaP (there is no reflection at the interface with GaP). For electrical calculation the Shockley-Read-Hall model was used.

The influence of the thermal annealing on electrical properties was analyzed using experimental data obtained for (n)GaP/(p)Si structures. Various annealing temperature was applied in range from 500 °C to 800 °C. Via the Hall method, we measured the concentration and the mobility of charge carriers in the (n)GaP layer and inversion layer at the (n)GaP/(p)cSi interface. Using the database [5] the lifetime was taken as a parameter for further calculations. Further, the influence of annealing temperature and the searching of the optimal distance between the contacts was considered.

Results and Discussion

The Hall measurements results are shown below.

Table 1

The electrical properties of inversion layer

Annealing temperature, °C	Without	500	600	700	750	800
Concentration, cm ⁻³	8·10 ¹⁷	1·10 ¹⁹	8·10 ¹⁹	5·10 ²⁰	3·10 ²¹	7·10 ²²
Mobility, cm ² ·V ⁻¹ ·s ⁻¹	108	25	29	26	30	0.5
Lifetime, s	5·10 ⁻⁵	1·10 ⁻⁷	1·10 ⁻⁸	1·10 ⁻⁸	1·10 ⁻⁹	1·10 ⁻⁹



The thicknesses and electrical properties of the remaining layers are given in the table below. The GaP-Si junction is designed to generate and spatially separate electron-hole pairs and the BSF (back surface field) is used to reduce the surface recombination of charge carriers.

Table 2

Electrical properties of layers in GaP/Si solar cell

Parameter	(n)GaP	(p)c-Si	BSF
Thickness, μm	0.05	300	1
Concentration, cm^{-3}	10^{18}	10^{16}	10^{19}
Mobility, $\text{cm}^2 \cdot \text{V}^{-1} \cdot \text{s}^{-1}$	1	holes: 300; electrons: 1000	holes: 300; electrons: 1000
Lifetime, s	10^{-6}	10^{-4}	10^{-4}

The calculated conversion efficiency dependency for 20 μm is shown in Fig. 1. This width of contact provides higher efficiency. However, the lithography of contact grid deposition is more complicated in comparison with the screen-printing method

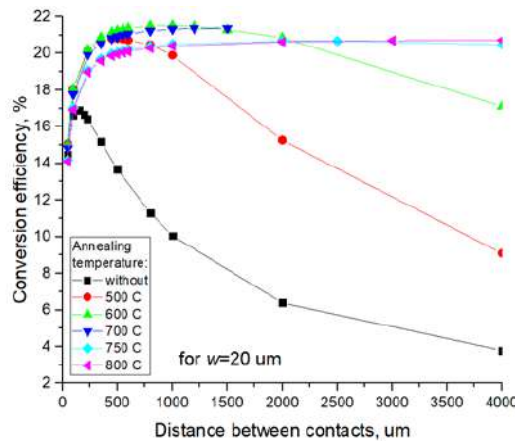


Fig. 1. Dependence of the simulated conversion efficiency of a solar cell on the distance between the contacts for a contact width of 20 μm for GaP/Si structures annealed at different temperatures

Based on the data obtained, we can notice that in the absence of annealing, the conversion efficiency is lower by several percent, which can be associated with a low concentration of charge carriers. For annealing temperature of 500 $^{\circ}\text{C}$ an increase in efficiency is noticed. However, at a distance between contacts of 1 μm a significant decrease is observed. From a practical point of view, this is not convenient since the implementation of the possibility of reducing shadow losses is limited.

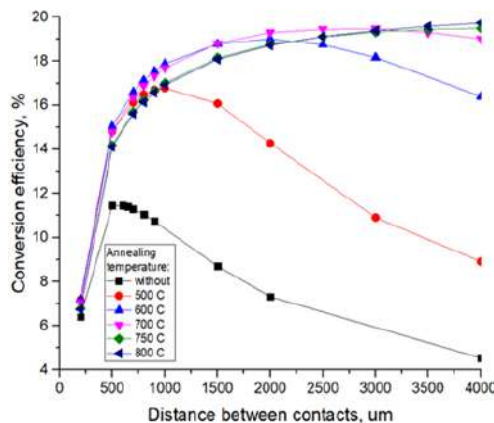


Fig. 2. Dependence of the simulated conversion efficiency of a solar cell on the distance between the contacts for a contact width of 200 μm for GaP/Si structures annealed at different temperatures

The simulation results show that at an annealing temperature of 600–700 °C the solar cell has high and stable conversion efficiency values of about 21.5%. This can be related to the fact that there is an optimum between the values of the concentration and the carrier lifetime. For annealing temperature of 800 °C, the experiment shows a low mobility of the inversion layer (an order of magnitude lower than at other temperatures). This may be due to the large number of capture traps caused by phosphorus diffusion. However, the simulation shows an increase in efficiency with saturation as the distance between the contacts increases. Here there is a discrepancy between the computer model and experiment.

Now we will focus on the contact widths of 200 μm, which is preferred for screen printing technology (Fig. 2).

For a contact width of 200 μm, a similar nature of the dependences is observed except that the maximum efficiency under these conditions is about 19%. Of particular note are the results that correspond to an annealing temperature of 700 °C. In this case, with lengths between contacts from 2 to 3.5 mm, it is possible to maintain an efficiency of 19%. This allows to use the screen printing taking into account inhomogeneities in the application of contacts.

Conclusion

In case for 20 μm width of contacts, the calculated conversion efficiency could exceed 21% under the annealing temperatures 600–700 °C with distance between contacts in range 0.7–1.5 mm (Fig. 1). The maximum efficiency for the optimal conditions in 200 μm configuration is about 19%. These results correspond to an annealing temperature of 700 °C with lengths between contacts in range from 2 to 3.5 mm, which is an appropriate condition for the using the screen-printing method.

REFERENCES

1. Zhang C., Vadiie E., King R. R., Honsberg C. B., Carrier-selective contact GaP/Si solar cells grown by molecular beam epitaxy, *Journal of Materials Research*, 33 (8) (2018), 414–423. DOI: 10.1557/jmr.2018.14.
2. Saive R., Emmer H., Chen C. T., Zhang C., Honsberg C., Atwater H., Study of the Interface in a GaP/Si Heterojunction Solar Cell, *IEEE Journal of Photovoltaics*, 8 (6) 1568–1676. DOI: 10.1109/JPHOTOV.2018.2861724.
3. Uvarov A. V., Baranov A. I., Vyacheslavova E. A., Kalyuzhnyi N. A., Kudryashov D. A., Maksimova A. A., Morozov I. A., Mintairov S. A., Salii R. A., Gudovskikh A. S., Formation of Heterostructures of GaP/Si Photoconverters by the Combined Method of MOVPE and PEALD, *Technical Physics Letters*, 47 (2021) 730–733. DOI: 10.1134/S1063785021070270.
4. Uvarov A. V., Gudovskikh A. S., Nevedomskiy V. N., Baranov A. I., Kudryashov D. A., Morozov I. A., Kleider J. P., Low temperature epitaxial growth of GaP on Si by atomic-layer deposition with plasma activation, *Journal of Physics D: Applied Physics*, 53 (345105) (2020) 1–4. DOI: 10.1088/1361-6463/ab8bfd.
5. Electrical properties of Silicon // *New Semiconductor Materials. Biology systems. Characteristics and Properties*. URL: http://www.matprop.ru/Si_electric.

THE AUTHORS

BOGDANOVA Milana V.
 bogdanovamilanav@mail.com
 ORCID: 0000-0002-6813-7201

GUDOVSKIKH Alexander S.
 gudovskikh@spbau.ru
 ORCID: 0000-0002-7632-3194

UVAROV Alexander V.
 lumenlight@mail.ru
 ORCID: 0000-0002-0061-6687

Received 19.09.2022. Approved after reviewing 20.09.2022. Accepted 20.09.2022.

Conference materials

UDC 29.19.22

DOI: <https://doi.org/10.18721/JPM.153.318>

Growth of nanostructured cobalt thin film at oblique angle deposition

I. S. Fattakhov ^{1, 2}✉, O. S. Trushin ¹, A. A. Popov ¹, L. A. Mazaletsky ²

¹ Valiev Institute of Physics and Technology of Russian Academy of Sciences,
Yaroslavl Branch, Yaroslavl, Russia;

² P. G. Demidov Yaroslavl State University, Yaroslavl, Russia

✉ 33ychenikan@mail.ru

Abstract. Nanocolumnar Co thin films growth by oblique angle deposition on Si substrate is experimentally studied. Formation of regular arrays of vertical Co nanocolumns has been observed at incidence angles more than 80 degrees with rotation of substrate. Such films might be perspective material for applications as a magnetic recording media for next generations of hard disks.

Keywords: Co thin films, nanocolumns, oblique angle deposition

Funding: Reported study was carried out under State Programs No. FFNN-2022-0018 of the Ministry of Science and Higher Education of Russia on the equipment of the center for collective use of the scientific equipment “Diagnostics of micro- and nanostructures”.

Citation: Fattakhov I. S., Trushin O. S., Popov A. A., Mazaletsky L. A., Growth of nanostructured cobalt thin film at oblique angle deposition, St. Petersburg State Polytechnical University Journal. Physics and Mathematics, 15 (3.3) (2022) 97–100. DOI: <https://doi.org/10.18721/JPM.153.318>

This is an open access article under the CC BY-NC 4.0 license (<https://creativecommons.org/licenses/by-nc/4.0/>)

Материалы конференции

УДК 29.19.22

DOI: <https://doi.org/10.18721/JPM.153.318>

Рост наноструктурированной плёнки кобальта при наклонном напылении

И. С. Фаттахов ^{1, 2}✉, О. С. Трушин ¹, А. А. Попов ¹, Л. А. Мазалецкий ²

¹ Ярославский филиал Физико-технологического института имени
К. А. Валиева Российской академии наук, Ярославль, Россия;

² Ярославский государственный университет им. П. Г. Демидова, Ярославль, Россия

✉ 33ychenikan@mail.ru

Аннотация. Экспериментально исследован рост тонких пленок Co при наклонном напылении на подложку Si. Образование массивов наноколонн Co наблюдалось при углах падения более 80 градусов при вращении подложки. Такие плёнки могут быть перспективным материалом для применения в качестве носителей магнитной записи для следующих поколений жестких дисков.

Ключевые слова: тонкие плёнки из кобальта, наноколонны, напыление под углом

Финансирование: Работа выполнена в рамках Государственной программы № ФФНН-2022-0018 Министерства науки и высшего образования России на оборудовании центра коллективного пользования научным оборудованием «Диагностика микро- и наноструктур».

Ссылка при цитировании: Фаттахов И. С., Трушин О. С., Попов А. А., Мазалецкий Л. А., Рост наноструктурированной плёнки кобальта при наклонном напылении //

Introduction

Magnetic thin films with easy axis normal to the substrate surface are of considerable interest as a promising material for ultrahigh density magnetic recording. However thin film growth at standard conditions leads to magnetization vector oriented in the plane of the surface. By controlling the texture parameters of the films during their growth, one can change their properties in a targeted manner, thereby achieving the required functional characteristics [1]. A promising method for the formation of films with special properties is their nanostructuring during growth. The formation of homogeneous and well-ordered arrays of nanostructures on the surface makes it possible to change significantly the electrophysical, magnetic, and optical properties of the films. One of the well-known technological methods allowing to ensure the growth of nanostructures is oblique angle deposition. It is a relatively inexpensive technology that can be easily implemented in conditions of mass production. This method of producing films has attracted considerable interest in recent years, and many works are devoted to it [2, 3]. It is known that this method can be used to obtain nanostructures of various shapes and sizes, from inclined nanowires and nanospirals to vertical nanocolumns [2]. It has been found that by varying the angle of incidence one can change the direction of magnetic anisotropy [4]. Besides that chiral nanostructured thin films can be produced through precise control of the angle of incidence of a vapor flux concurrent with substrate rotation [5]. It was found that the reason for nanostructuring of films under oblique deposition is the shading effect, which consists in the fact that crystallites, which received a random advantage in growth at the initial stages, further suppress the growth of neighbors, intercepting the flux of atoms incident on the surface and, thereby, forming pores. Main goal of this work was finding optimal conditions for the formation of perpendicular magnetic anisotropy in Co films using this method.

Experiment

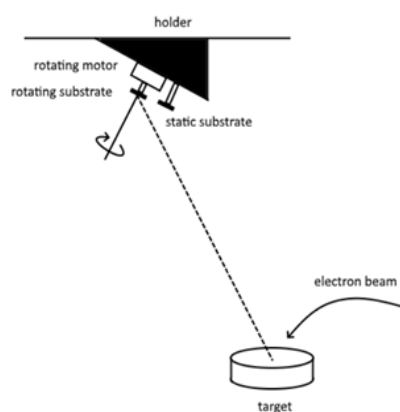


Fig. 1. Schematic of the experiment for the oblique angle deposition

Electron beam evaporation is a suitable technology for oblique angle deposition experiments. This method combines a sufficiently high working vacuum and a homogeneous flow of the evaporated material. Experiments on the deposition of Co films on an inclined substrate were carried out on an Oratoria-9 electron beam evaporation unit. The deposition conditions were as follows: base vacuum $4 \cdot 10^{-6}$ Torr, electron beam voltage 8 kV, current 0.5 A. A standard single-crystal silicon wafer with a thermal oxide layer 300 nm thick was used as a substrate. During deposition substrate inclination angle was fixed to be equal to 85° . The distance from the evaporator to the substrate was about 1 m. This significant distance from the source of the evaporated material provided a high level of flow uniformity. Besides that the substrate was rotating around its vertical axis with variable rate. All experiments were done at room temperature. The growth rate of the film at

these conditions was equal to 1 nm/s. The schematic of the experiment is shown in Figure 1. We used a collector motor to rotate the substrate at a controlled speed. The static sample was located as close as possible to the rotating one and is needed to compare with the results obtained on the rotating sample. The surface morphology of the obtained films was investigated by scanning electron microscopy (SEM) (Supra 40).

Results and Discussion

Cross-section of the film deposited at incidence angle $\varphi = 85^\circ$ and rotation rate of 30 rpm is shown at fig. 2, *a*. One can see that fibrous nanostructure is formed at these conditions. A rotation of the substrate during growth leads to vertical alignment of nanocolumns. More complete information about the morphology of the film is obtained from the analysis of top view on its surface shown at fig. 2, *b*. One can see that separate Co fibers have shape of nanocolumns extending upwards with the width less than 70 nm.

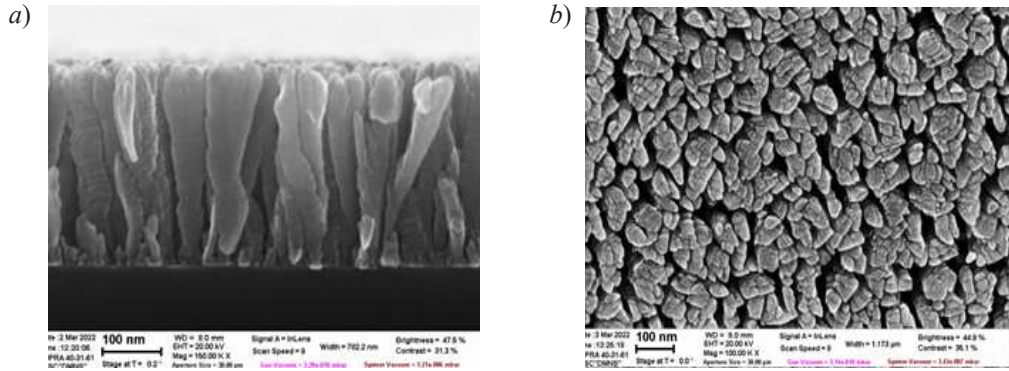


Fig.2: Cross-section of the Co film (*a*) and top view on its surface (*b*). The images were obtained using electron scanning microscopy (SUPRA-40)

The next experiment was carried out at the speed of rotation of 0.6 rpm and at incidence angle $\varphi = 85^\circ$. Cross-section of the film is shown at fig. 3, *a*. One can see that vertical spiral nanocolumns are formed at these conditions. The analysis of the top view from fig. 3, *b* shows that separate Co fibers have shape of nanocolumns extending upwards with the width less than 100 nm. The fig. 3, *c*. and fig. 3, *d*. show the cross-section and top view of the static sample. These images confirm that spiral form of nanocolumns is the result of substrate rotation.

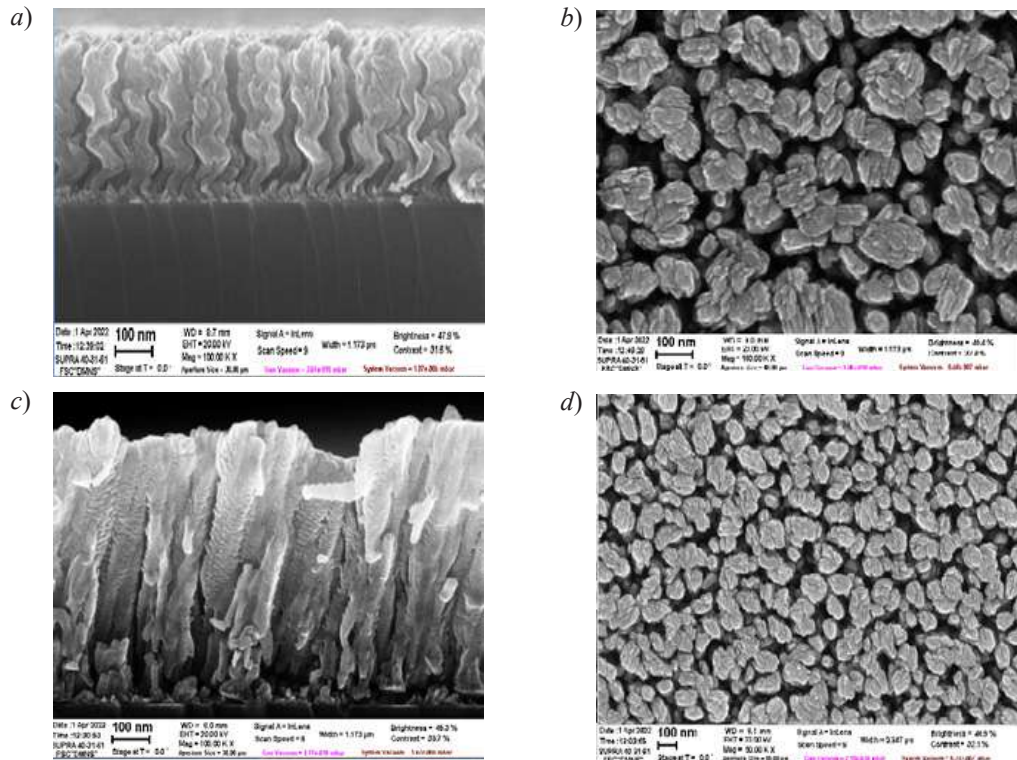


Fig. 3: Cross-section of the Co film (*a*) and top view on its surface (*b*). The images were obtained using electron scanning microscopy (SUPRA-40)

Conclusion

In summary, as the results of experimental studies of the growth of Co thin films by oblique angle deposition with rotation of substrate it was found that optimal conditions for regular arrays formation of nanocolumns and nanospirals, are achieved at the angle of 85°. By varying substrate rotation rate it is possible to change shape of nanocolumns from spiral to rod. Studies of magnetic properties of the films are currently in progress. Such films might be perspective for application in ultrahigh density magnetic recording.

REFERENCES

1. **Amirov I. I., Selyukov R. V., Naumov V. V., Gorlachev E. S.**, Russian Microelectronics, 50 (1) (2021) 1.
2. **Barranco A., Borrás A., Gonzalez-Elipé A., Palmero A.**, Perspectives on oblique angle deposition of thin films: From fundamentals to devices, Progress in Materials Science, 76 (2016) 59–153.
3. **Hawkeye M., Taschuk M., Brett M.**, Glancing Angle Deposition of Thin Films, UK: John Wiley & Sons Ltd, 2014. Pp. 1–299.
4. **Akulov A. A., Trushin O. S., Popov A. A., Pestova A. N., Mazaletsky L. A.**, Nanostructuring at oblique incidence deposition of cobalt, J. Phys. Conf. Ser., 2086 (2021) 012001.
5. **Liu F., Umlor M. T., Shen L., Weston J., Eads W., Barnard J. A., Mankey G. J.**, The growth of nanoscale structured iron films by glancing angle deposition, Journal of Applied Physics, 85 (1999) 5486.

THE AUTHORS

FATTAKHOV Ilya S.
33ychenikan@mail.ru
ORCID: 0000-0002-6671-9179

TRUSHIN Oleg S.
otrushin@gmail.com

POPOV Aleksandr A.
aapopov@mail.ru

MAZALETSKY Leonid A.
boolvinkl@ya.ru

Received 20.07.2022. Approved after reviewing 22.07.2022. Accepted 22.07.2022.

Conference materials
UDC 661.666.2; 544.774.3
DOI: <https://doi.org/10.18721/JPM.153.319>

Electrical conductivity and optical properties of water-based graphene/AgNWs hybrid inks for flexible electronics

M. A. Dronova ^{1,2} ✉, E. A. Danilov ¹, M. R. Veretennikov ¹

¹ Research Institute for Graphite-Based Structural Materials "NIIgraphite", Moscow, Russia;

² Bauman Moscow State Technical University (BMSTU), Moscow, Russia

✉ mariadv277@gmail.com

Abstract. The present study provides the description of water-based inks made of hybrid graphene-silver nanoparticles conductive fillers in a wide concentration range for printed electronics applications. Aqueous graphene suspensions were manufactured via ultrasonic exfoliation of pristine graphite, whereas polyol synthesis was used to obtain silver nanowires. Hybrid suspensions were centrifuged to improve transmittance while retaining electrical conductivity. As a result, we successfully manufactured conductive transparent films with transmittance up to 96%.

Keywords: conductive ink, graphene, silver nanowires, flexible electronics

Citation: Dronova M. A., Danilov E. A., Veretennikov M. R., Electrical conductivity and optical properties of water-based graphene/AgNWs hybrid inks for flexible electronics, St. Petersburg State Polytechnical University Journal. Physics and Mathematics, 15 (3.3) (2022) 101–105. DOI: <https://doi.org/10.18721/JPM.153.319>

This is an open access article under the CC BY-NC 4.0 license (<https://creativecommons.org/licenses/by-nc/4.0/>)

Материалы конференции
УДК 661.666.2; 544.774.3
DOI: <https://doi.org/10.18721/JPM.153.319>

Электропроводность и оптические свойства гибридных чернил на основе графена и серебряных наностержней в водной среде для гибкой электроники

М. А. Дронова ^{1,2} ✉, Е. А. Данилов ¹, М. Р. Веретенников ¹

¹ Научно-исследовательский институт конструкционных материалов на основе графита «НИИГрафит», Москва, Россия;

² Московский государственный технический университет имени Н.Э. Баумана, Москва, Россия

✉ mariadv277@gmail.com

Аннотация. В настоящем исследовании представлено описание гибридных чернил, изготовленных из проводящих графеновых частиц и наночастиц серебра в широком диапазоне концентраций. Водные суспензии графена были изготовлены путем ультразвуковой эксфолиации исходного графита; для получения серебряных наностержней был использован процесс полиольного синтеза. Гибридные суспензии подвергались центрифугированию для повышения оптического пропускания при сохранении уровня электропроводности. В результате были успешно изготовлены проводящие прозрачные плёнки с коэффициентом пропускания до 96%.

Ключевые слова: электропроводящие чернила, графен, серебряные наностержни, гибкая электроника

Ссылка при цитировании: Дронова М. А., Данилов Е. А., Веретенников М. Р., Электропроводность и оптические свойства гибридных чернил на основе графена и серебряных наностержней в водной среде для гибкой электроники // Научно-

технические ведомости СПбГПУ. Физико-математические науки. 2022. Т. 15. № 3.3. С. 101–105. DOI: <https://doi.org/10.18721/JPM.153.319>

Статья открытого доступа, распространяемая по лицензии CC BY-NC 4.0 (<https://creativecommons.org/licenses/by-nc/4.0/>)

Introduction

Flexible electronics have shown great potential for applications in various areas of human life. Applications include flexible printed circuit boards [1], flexible electrodes for displays [2–4], antennas [5], wearable skin sensors [6], etc [7]. The growing need in printed electronics causes increased interest in manufacturing of new materials that meet optical and electrical requirements.

Since the most common and simple method for flexible electronics production is inkjet printing technology, there are also specific requirements for inks in terms of particle size and other important parameters to consider, such as viscosity, adhesion, sintering temperature and so on [8]. In particular, the solvent must dry sufficiently quickly, but not so fast as to clog the nozzle.

Thus, manufacturing inks with suitable properties is a challenging task. Firstly, the choice of conductive filler must be made. Among suitable materials are conducting polymers, carbon nanotubes (CNTs), graphene and metal nanoparticles (MNPs) of various shapes [9]. Despite its advantages, all of the abovementioned inks have their shortcomings.

Currently, the most widely used inks are based on silver nanoparticles or nanowires due to their excellent electrical conductivity [10]. Another commonly used option is graphene-based ink because of its excellent electronic and mechanical properties [11]. However, both of these ink types have limitations as well. Specifically, high concentration of AgNPs and high sintering temperature are required to achieve desired conductivity values, or low conductivity of pure graphene ink that limits its widespread use. Moreover, high cost of Ag increases processing cost. Combination of graphene and AgNWs solves cost-effectiveness problems by reducing the concentration of AgNWs. Simultaneously, it increases conductivity, and graphene improves the mechanical performance of AgNWs for flexible electronic applications.

Further questions arise regarding the solvent used in inks. This choice can serve as a separate topic for research because of its importance [12], since the ability to use inkjet printing technology depends mostly on the properties of the solvent. For example, it must have the required viscosity and surface energy. Moreover, it is necessary for the solvent to have low boiling point in order to apply inks on plastic substrates. Many options are often limited by toxicity and cost, therefore, the use of water is most environmentally friendly and economically viable way. Thereby, in this work water was chosen as a suitable option for graphene exfoliation, while polyol synthesis in particular requires ethylene glycol.

Experimental section

Graphene suspensions were obtained using the ultrasonic exfoliation technique described in [13]. As a precursor, 300 mg of pristine graphene GE-1 (GOST 17022-81) was used and added to 50 ml of water. Due to the hydrophobic nature of graphene, exfoliating graphite in water is particularly challenging and requires the aid of surfactants. Therefore, in the obtained graphite suspension (6 mg/ml) has been added 0.6 mg/ml of ZONYL BA-L surfactant. The suspension was then subjected to a 7.5-hour ultrasonic exfoliation on an ultrasonic homogenizer with an acoustic power of 100 W at a frequency of 22.5 kHz, which led to stable conductive suspensions of graphene. Further sonication hardly changes particle size distributions.

Suspensions of AgNWs were manufactured via polyol process. The main advantage of this process is the ability to vary wide number of parameters to obtain the required result [14]. In this study, 150 mg of silver nitrate was reduced with ethylene glycol (EG) at 178 °C in the presence of KBr, AgCl and polyvinylpyrrolidone (10^6 g/mol).

In order to determine the effect of the mass ratio of graphene on the characteristics of the resulting suspensions, 7 hybrid suspensions were made with different mass graphene loadings: 15, 25, 35, 50, 75, 85 wt.%, the volume of each was 20 ml. All hybrid suspensions were then placed

in an ultrasonic bath with operating frequency of 35 kHz and sonicated for 30 minutes in order to achieve homogeneity.

For the purpose of transparent and free of agglomerates hybrid suspensions, 10 mL of suspensions were sonicated in an ultrasonic bath for 10 minutes and subjected to centrifugation for 45 minutes on centrifuge Hettich EBA 280 with 2000 rpm. Transparent suspensions and the sediment remaining on the walls of the flasks were separated from each other.

Conductivity measurements were made using SevenCompact Cond meter S230 and conductivity sensor InLab 710 (Mettler Toledo). Measurements of initial suspensions of graphene and silver were taken immediately after the synthesis. Initial hybrid suspensions were measured after sonication, while centrifuged suspensions' conductivity measurements were made directly after centrifugation in order to eliminate the influence of agglomeration on conductivity.

Before measuring properties, suspensions were sonicated in an ultrasonic bath for 10 minutes in order to reduce possible agglomeration. Particle size distributions for initial suspensions were measured using laser diffraction method on Microtrac SYNC (Microtrack MRB). For measuring size of smaller particles of suspensions after centrifugation Zetasizer Nano (Malvern) was used.

Thin films were made by drop-casting 0.4 ml of ink on glass substrate with dispenser and drying for 1 hour at 100 °C. Sheet resistance was calculated using precision source-measuring unit b2901a (Agilent) from current-voltage curves (linear region slopes) in a four point-probe cell.

Optical characteristics, e.g. transmittance and absorbance, were measured for centrifuged suspensions, both in liquid and in films, via UV-Vis absorption spectrophotometry (Agilent Cary 60).

Results and discussion

Graphene/AgNWs hybrid inks with graphene content 0, 15, 25, 35, 50, 75, 85 and 100 wt.% were prepared and then centrifuged in order to achieve satisfactory transparency and dispose of agglomerates. The resulting properties for initial and centrifuged inks are shown in table 1.

Table 1

Graphene/AgNWs hybrid inks conductivity

Graphene content, wt.%		0	15	25	35	50	65	75	85	100
Conductivity, $\mu\text{S}/\text{cm}$	Initial	110.7	161.0	192.2	222.6	240.1	278.9	300.1	264.3	67.9
	Centrifuged	105.9	188.2	231.1	274.0	327.4	356.0	348.4	280.8	121.3

As can be seen from the Table 1, centrifugation increases the conductivity of suspensions, apart from AgNWs' suspension. This may be due to the removal of agglomerates and thus obtaining smaller and better conducting particles. The best conductivity among the initial suspensions is observed at a mass content of graphene of 75%. However, after centrifugation this peak shifts to 65%, although the difference in conductivity is rather small.

Results (Fig.1) show that the particle size obtained is small enough to meet the basic requirements necessary for a non-clogging printer nozzle. Centrifugation reduces the particle size by several times and at the same time increases the conductivity of the suspensions.

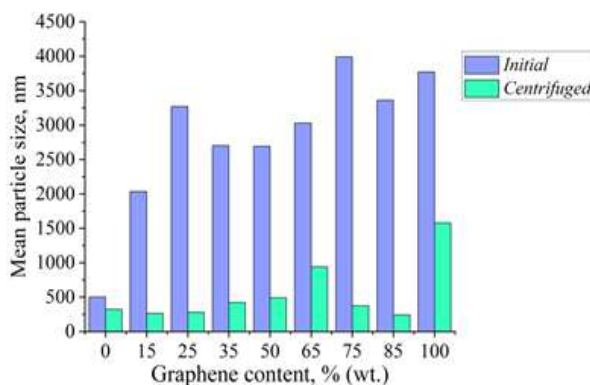


Fig. 1. Particle size distribution depending on graphene content for initial and centrifuged suspensions

In addition to reducing the size and increasing the conductivity, centrifugation provided sufficient transparency; Figure 2 presents UV-visible absorption spectra of the produced inks. The results for optical characteristics are given for the most conductive of the suspension, as well as for centrifuged AgNWs and graphene.

As can be seen from the spectra and Table 1, although transparency is lowest for 75 wt.% suspension, its conductivity is the highest of all hybrid suspensions. However, the 65 wt.% suspension that differs fairly little in conductivity, has excellent transparency.

Although it is expected that the absorption of the films will correlate with the absorption of suspensions, the obtained results (Fig. 3) show a different dependency.

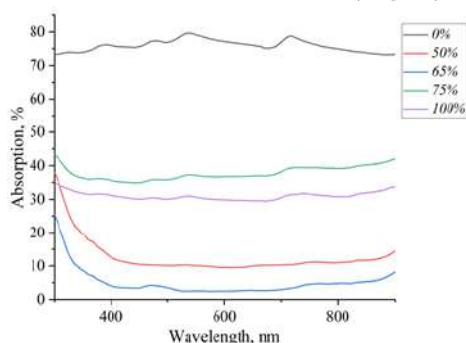


Fig. 2. Suspensions' absorption depending on graphene content

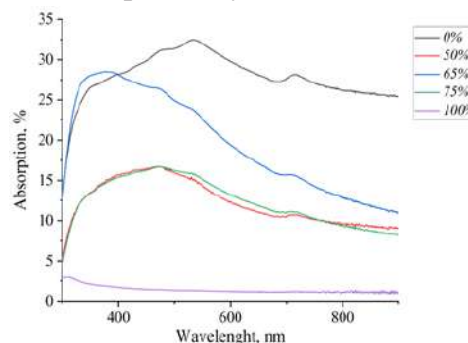


Fig. 3. Films absorption depending on graphene content

For example, better transmittance instead of 65% hybrid is obtained for hybrids with 50 and 75 wt.% graphene content. In general, obtaining hybrids in the form of films increases their transmission, although it should be taken into account that one layer is not enough for printed paths to be conductive.

Hybrids in the form of films are distinguished by the presence of an absorption peak in the region of 400–450 nm. This local maximum of absorbance indicates the presence of silver nanoparticles. The obtained absorption spectra are similar to the spectra obtained by the authors [15] for similar graphene-silver hybrids.

This difference in absorption for films and suspensions can be explained by the obvious drawbacks of the film deposition method. Despite the fact that the same amount of ink is applied to the substrate, the distribution of the liquid over the surface is always different. This leads to the need to work on improving the adhesion of suspensions to the substrate.

Sheet resistance was measured for films obtained from initial suspensions, since even multilayer deposition of centrifuged suspensions has not yet given satisfactory results in terms of conductivity. Obtained characteristics are shown in the table below.

Table 2

Sheet resistance of films from initial suspensions

Graphene content, wt.%	15	25	35	50	65	75	85
Sheet resistance, $10^{-3} \cdot \Omega/\text{sq}$	48.0	28.6	3.1	4.5	11.3	48.9	5.7

Despite the fact that suspensions with a graphene content of 65–75% have the highest conductivity, we obtained the best sheet resistance of $3.1 \cdot 10^3 \Omega/\text{sq}$ for film with 35 wt.% graphene content. An inconsistent result may be associated with the measurement method that damages the films. This, in turn, leads to the conclusion that ways to increase film adhesion for more adequate measurement results are needed.

Conclusion

In this work, we manufactured water-based graphene/AgNWs hybrid inks. Their electrical conductivity and optical transmittance were measured. Best conductivity value of $356 \mu\text{S}/\text{cm}$ and excellent transparency up to 96% obtained for centrifuged suspension with 65% graphene mass content. However, the highest transparency in the form of films has the one made from 75% hybrid suspension, that is only 2.5% less conductive than 65 wt.% graphene content hybrid. The best sheet resistance for drop casted thin films of $3.1 \cdot 10^3 \Omega/\text{sq}$ is observed in the film with 35% graphene mass content.

REFERENCES

1. **Phung T. H., Jeong J., Gafurov A. N., Kim I., Kim S. Y., Chung H. J., Lee T. M.**, Hybrid fabrication of LED matrix display on multilayer flexible printed circuit board, *Flexible and Printed Electronics*, 6 (2) (2021) 024001.
2. **Street R. A., Wong W. S., Ready S. E., Chabinyc M. L., Arias A. C., Limb S., Lujan R.**, Jet printing flexible displays, *Materials Today*, 9 (4) (2006) 32–37.
3. **Kwon O. E., Shin J. W., Oh H., Kang C. M., Cho H., Kwon B. H., Lee J. I.**, A prototype active-matrix OLED using graphene anode for flexible display application, *Journal of Information Display*, 21 (1) (2020) 49–56.
4. **Zhang Q., Di Y., Huard C. M., Guo L. J., Wei J., Guo J.**, Highly stable and stretchable graphene–polymer processed silver nanowires hybrid electrodes for flexible displays, *Journal of Materials Chemistry C*, 3 (7) (2015) 1528–1536.
5. **Park M., Im J., Shin M., Min Y., Park J., Cho H., Kim K.**, Highly stretchable electric circuits from a composite material of silver nanoparticles and elastomeric fibres, *Nature nanotechnology*, 7 (12) (2012) 803–809.
6. **Zeng W., Shu L., Li Q., Chen S., Wang F., Tao X. M.**, Fiber-based wearable electronics: a review of materials, fabrication, devices, and applications. *Advanced materials*, 26 (31) (2014) 5310–5336.
7. **Htwe Y. Z. N., Mariatti M.**, Printed Graphene and Hybrid Conductive Inks for Flexible, Stretchable, and Wearable Electronics: Progress, Opportunities, and Challenges. *Journal of Science: Advanced Materials and Devices*, (2022) 100435.
8. **Cummins G., Desmulliez M. P.**, Inkjet printing of conductive materials: a review, *Circuit world*, 38 (4) (2012) 193–213.
9. **Kamyshtny A., Magdassi S.**, Conductive nanomaterials for printed electronics, *Small*, 10 (17) (2014) 3515–3535.
10. **Fernandes I. J., Aroche A. F., Schuck A., Lamberty P., Peter C. R., Hasenkamp W., Rocha T. L.**, Silver nanoparticle conductive inks: Synthesis, characterization, and fabrication of inkjet-printed flexible electrodes, *Scientific reports*, 10 (1) (2020) 1–11.
11. **Capasso A., Castillo A. D. R., Sun H., Ansaldo A., Pellegrini V., Bonaccorso F.**, Ink-jet printing of graphene for flexible electronics: an environmentally-friendly approach, *Solid State Communications*, 224 (2015) 53–63.
12. **Htwe Y. Z. N., Abdullah M. K., Mariatti M.**, Optimization of graphene conductive ink using solvent exchange techniques for flexible electronics applications, *Synthetic Metals*, 274 (2021) 116719.
13. **Samoilov V. M., Danilov E. A., Nikolaeva A. V., Yerpuleva G. A., Trofimova N. N., Abramchuk S. S., Ponkratov K. V.**, Formation of graphene aqueous suspensions using fluorinated surfactant-assisted ultrasonication of pristine graphite, *Carbon*, 84 (2015) 38–46.
14. **Fiévet F., Ammar-Merah S., Brayner R., Chau F., Giraud M., Mammeri F., Viau G.**, The polyol process: a unique method for easy access to metal nanoparticles with tailored sizes, shapes and compositions. *Chemical Society Reviews*, 47 (14) (2018) 5187–5233.
15. **Htwe Y. Z. N., Abdullah M. K., Mariatti M.**, Water-based graphene/AgNPs hybrid conductive inks for flexible electronic applications, *Journal of Materials Research and Technology*, 16 (2022) 59–73.

THE AUTHORS

DRONOVA Maria A.
 mariadv277@gmail.com
 ORCID: 0000-0002-9791-4583

VERETENNIKOV Mikhail R.
 MiklVeretennikov@gmail.com
 ORCID: 0000-0001-8990-0782

DANILOV Egor A.
 danilovegor1@gmail.com
 ORCID: 0000-0002-1986-3936

Received 21.07.2022. Approved after reviewing 26.07.2022. Accepted 26.07.2022.

Conference materials
UDC 544.77, 541.64
DOI: <https://doi.org/10.18721/JPM.153.320>

Investigation of the optical properties of quantum dots depending on the nature and number of additional semiconductor layers

N. N. Troshkina ¹✉, S. A. Novikova ¹, P. D. Nasirov ¹, M. Yu. Volobueva ¹,
I. V. Mukhina ¹, A. A. Popova ¹, E. D. Gribova ¹

¹ Dubna State University, Moscow region, Dubna, Russia
✉ natik.faiier@gmail.com

Abstract. The present study aims to investigate the properties of quantum dots (QDs) depending on the nature and number of additional semiconductor layers. The analysis of spectral data showed that when CdTe QDs are coated with a ZnS shell, a bathochromic shift of the exciton peak and maximum of fluorescence is observed due to the restriction of charge carriers in the nucleus. However, the build-up of the additional shell leads to a decrease in the quantum yield, which may be due to the difference in the parameters of the crystal lattices to CdS and ZnS and the occurrence of defects in the crystal structure. In contrast, CdTe QDs coated with a CdS shell increased the quantum yield and shifted the peak of fluorescence to a longer wavelength region.

Keywords: quantum dots, nanoparticles, bandgap, synthesis, core, shell

Funding: This research was carried out with the financial support of The Foundation for Assistance to Small Innovative Enterprises in Science and Technology (No. 16271ГУ/2021).

Citation: Troshkina N. N., Novikova S. A., Nasirov P. D., Volobueva M. Yu., Mukhina I. V., Popova A. A., Gribova E. D., Investigation of the optical properties of quantum dots depending on the nature and number of additional semiconductor layers. St. Petersburg State Polytechnical University Journal. Physics and Mathematics, 15 (3.3) (2022) 106–110. DOI: <https://doi.org/10.18721/JPM.153.320>

This is an open access article under the CC BY-NC 4.0 license (<https://creativecommons.org/licenses/by-nc/4.0/>)

Материалы конференции
УДК 544.77, 541.64
DOI: <https://doi.org/10.18721/JPM.153.320>

Исследование оптических свойств квантовых точек в зависимости от природы и количества дополнительных полупроводниковых слоев

Н. Н. Трошкина ¹✉, С. А. Новикова ¹, П. Д. Насиров ¹, М. Ю. Волобуева ¹,
И. В. Мухина ¹, А. А. Попова ¹, Е. Д. Грибова ¹

¹ Государственный университет «Дубна», Московская область, Дубна, Россия
✉ natik.faiier@gmail.com

Аннотация. Данное исследование направлено на изучение свойств квантовых точек (КТ) в зависимости от природы и количества дополнительных полупроводниковых слоев. Анализ спектральных данных показал, что при покрытии CdTe КТ оболочкой из ZnS наблюдается bathochromic сдвиг экситонного пика и максимума флуоресценции из-за ограничения носителей заряда в ядре. Однако наращивание дополнительной оболочки приводит к снижению квантового выхода, что может быть связано с различием параметров кристаллических решеток CdS и ZnS и наличием дефектов в кристаллической структуре. Напротив, у CdTe КТ после покрытия оболочкой CdS, увеличивается квантовый выход и сдвигается пик флуоресценции в более длинноволновую область.

Ключевые слова: квантовые точки, наночастицы, запрещенная зона, синтез, ядро, оболочка

Финансирование: This research was carried out with the financial support of The Foundation for Assistance to Small Innovative Enterprises in Science and Technology (No. 16271ГУ/2021).

Ссылка при цитировании: Трошкина Н. Н., Новикова С. А., Насиров П. Д., Волобуева М. Ю., Мухина И. В., Попова А. А., Грибова Е. Д., Исследование оптических свойств квантовых точек в зависимости от природы и количества дополнительных полупроводниковых слоев // Научно-технические ведомости СПбГПУ. Физико-математические науки. 2022. Т. 15. № 3.3. С. 106–110. DOI: <https://doi.org/10.18721/JPM.153.320>

Статья открытого доступа, распространяемая по лицензии CC BY-NC 4.0 (<https://creativecommons.org/licenses/by-nc/4.0/>)

Introduction

Currently, semiconductor nanostructured materials are much in demand due to their unique properties. Nanostructured materials exhibit specific optical and electronic properties when their size changes in the range of 1–100 nm. Depending on the dimension, they can be classified as twodimensional (thin films or quantum wells); one-dimensional (quantum wires); zero-dimensional (quantum dots) ones [1]. Thus, a QD is a zero-dimensional system and has a limited number of atoms forming discrete energy states. QDs have a surface effect and a quantum restriction which affect their atomic-like properties [2]. The quantum restriction results in specific size- and shapedependent optoelectronic properties.

Colloidal chemistry techniques allow the synthesis of multicomponent QDs from semiconductors with different characteristics, primarily with different band gap widths. A special place in this group is occupied by core/shell QDs, consisting of a core of one semiconductor covered by a shell of another [3]. Due to the low luminescence of the QD nuclei themselves, hybrid structures consisting of a nanoscale semiconductor core and their shell are often created for practical purposes. By selecting the type of shell material and its thickness, the maximum luminescence enhancement effect can be achieved [4]. Such a QD structure is called a “core/shell” structure. Additional shell build-up significantly improves the fluorescence quantum yield and photostability of quantum dots. The proper choice of the shell material and its thickness are important factors affecting the overall properties of QDs. If the core and shell structures have a huge lattice mismatch, this leads to lattice deformation and defective states occur inside or at the core/shell interface. In addition, a thicker semiconductor shell creates mismatch dislocations, which also reduces the fluorescence quantum yield due to the non-radiative process [5].

The present study aims to investigate the properties of quantum dots depending on the nature and number of additional semiconductor layers. QDs with a CdTe core and additional semiconductor shells were synthesised in the study. The material of the semiconductor shells is selected so that the difference between the crystal lattices of the core-shell-shell is minimal. The layer size is controlled by the synthesis time. As the size of the semiconductor layer increases, the quantum yield increases to a certain size, then decreases sharply with a further increase in the layer size, which is demonstrated in [6]. In order to increase stability, additional shells from wider-band ZnS and CdS semiconductors were built up on CdTe QDs. The analysis of spectral data showed that when CdTe QDs are coated with a ZnS shell, a bathochromic shift of the exciton peak and maximum of fluorescence is observed due to the restriction of charge carriers in the nucleus. However, the build-up of the additional shell leads to a decrease in the quantum yield, which may be due to the difference in the parameters of the crystal lattices to CdS and ZnS and the occurrence of defects in the crystal structure. In contrast, CdTe QDs coated with a CdS shell increased the quantum yield and shifted the peak of fluorescence to a longer wavelength region.

Synthesis of CdTe/CdS/ZnS-TTK-(L-cys) QDs

The synthesis of multilayer CdTe/CdS/ZnS-TGA-(L-cys) QDs was carried out in three steps in an inert atmosphere and at 98 °C.

To obtain CdTe QDs a solution of cadmium precursor with stabilizer was prepared and a freshly prepared solution of sodium hydrotelluride NaHTe (tellurium precursor) was quickly added under

constant stirring, with Cd:Te ratio of 1:0.3. Powder of tellurium Te (0.387 mmol) and sodium borohydride NaBH_4 (1.692 mmol) were mixed, and cadmium chloride CdCl_2 (0.2 mmol) was dissolved in water with added stabilizer to obtain tellurium precursor. TGA (0.6 mmol) was used as stabilizer. The pH of the solutions obtained was adjusted to 9.2 with a sodium hydroxide solution with a concentration of 0.5 M to obtain the TGA salt.

To cover CdTe QDs with CdS layer, Cd precursor and S precursor were slowly added to the solution stabilized by TGA QDs using syringes, the reaction mixture was boiled under stirring with reflux for 2 hours (borate buffer (5 mmol) with $\text{pH} = 10$ was used as reaction medium).

The synthesis of CdTe/CdS-TGA QDs with a CdTe:CdS ratio of 1:1.5 was carried out as follows. To prepare the Cd precursor, a 0.15 mmol sample of CdCl_2 was placed in a 25 ml beaker and dissolved in 10 ml of deionized water. To the obtained solution 0.45 mmol of TGA was added and the mixture was stirred for 5 min. Then the pH of the resulting solution was adjusted to 10 with 0.5 M NaOH. Precursor S was prepared by dissolving 0.150 mmol of thiourea in 5 ml of deionized water. QDs with a CdTe:CdS ratio of 1:3 and 1:3.75 were prepared according to the same algorithm.

The synthesised CdTe/CdS QDs were coated with ZnS, where L-cys was used as a stabiliser for further use of the QDs in bioassay. The order of ZnS coating is similar to that of CdS coating. To prepare the Zn precursor, a suspension of L-cys (0.300 mmol) was placed in a beaker, dissolved in 10 ml of deionized water, and diluted with 0.5 M NaOH to $\text{pH} = 9$. To the obtained stabilizer solution, 1 ml of solution containing (0.150 mmol) ZnCl_2 was slowly added under stirring and the mixture was stirred for 5 min. After that the pH of the resulting solution was adjusted to 10. The precursor S was prepared by dissolving 0.150 mmol of thiourea in 5 ml of deionized water.

Purification of QDs

The resulting QDs were precipitated with isopropanol in a centrifuge at 8000 rpm for 15 minutes, and the liquid was decanted. The procedure was carried out twice. After that, the deposited QDs were dried at 50 °C in air.

Results and Discussion

The key to the use of QDs in bioassays is that they must have hydrophilic properties. Importantly, QDs produced by high-temperature organometallic synthesis are hydrophobic, and further application in aqueous media requires additional hydrophilization of their surface, which is usually accompanied by deterioration of optical properties.

QDs produced by aqueous colloidal synthesis (ACS) are hydrophilic and immediately suitable for use. Also, this synthesis is carried out at low temperatures and using relatively environmentally friendly reagents.

CdTe QDs obtained by ACS were used as nuclei for multilayer QDs, where TGA was chosen as a stabilizer. The synthesis was carried out for 60 minutes. The mole ratios of Cd:Te, Cd:TGA are given in Table 1.

Table 1

The mole ratios of Cd:Te, Cd:TGA

	Mole ratios	
	Synthesis of CdTe-TGA QDs	Cd:Te
Cd:TGA		1:3
Synthesis of CdTe/CdS-TGA QDs	CdTe:CdS	1:1.5
		1:3
		1:3.75

Cadmium sulphide was used as a second layer in order to eliminate defects that may appear as a result of the large mismatch of CdTe and ZnS crystal lattices. The mole ratios of CdTe:CdS during the QDs syntheses were 1:1.5, 1:3 and 1:3.75 (Table 1). The CdS precursor concentrations were varied to study the effect of layer thickness on the optical properties of the QDs.

The third layer was the wide band semiconductor ZnS. The bandgap width of zinc sulphide is larger than that of the core, which allows the charge carriers to be kept inside the core without allowing them to interact with the dispersion medium, which has a positive effect on the quantum yield. In addition, zinc sulphide is more resistant to oxidation and has a

higher affinity to thiolcontaining stabilizers, which improves the colloidal stability of QDs [7].

The synthesis revealed that, after coating CdTe/1.5CdS-TGA QDs with ZnS shell, the luminescence of QDs completely disappeared. Therefore, a decision was made to increase the thickness of the CdS shell to move the crystal lattices of CdTe and ZnS further away from each other.

The synthesized CdTe/1.5CdS-TGA, CdTe/3CdS-TGA и CdTe/3.75CdS-TGA QDs were studied by spectral methods of analysis. From the fluorescence spectra (Figure 1), it can be observed that the fluorescence peak of CdTe/3.75CdS-TGA QDs is flatter and narrower compared to the peaks of CdTe/1.5CdS-TGA and CdTe/3CdS-TGA QDs, indicating high dispersion of QDs in size [4].

One of the most important characteristics of a QD is the quantum yield of luminescence.

Therefore, the quantum yield of QDs was calculated. The quantum yield of luminescence was determined by comparison method, where Rhodamine 6J was used as a reference. The quantum yield of luminescence of CdTe/1.5CdS-TGA, CdTe/3CdS-TGA and CdTe/3.75CdS-TGA QDs was 8%, 10% and 13%, respectively. From which it can be concluded that the quantum yield increased when the shell thickness was increased.

The successful coating of QDs with ZnS layer and the improved QDs characteristics depend on the thickness of the second layer - CdS. The synthesized CdTe/1.5CdS-TGA, CdTe/3CdS-TGA and CdTe/3.75CdS-TGA QDs were further coated with a ZnS layer.

The spectral studies showed that the CdTe/1.5CdS-TGA QDs after coating with an additional layer of ZnS completely disappeared fluorescence, while QDs with CdTe:CdS ratios of 1:3 did not lose fluorescence due to the reduced effect of CdTe and ZnS lattice mismatch. The presented spectra (Figure 2) show that the additional ZnS envelope leads to a bathochromic shift of the exciton peak and the fluorescence maximum.

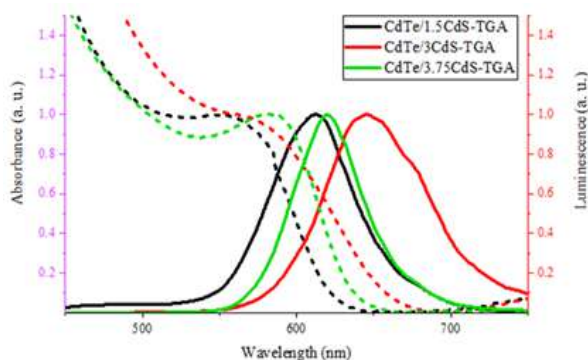


Fig. 1. Normalized absorption and fluorescence spectra of CdTe/1.5CdS-TGA, CdTe/3CdS-TGA and CdTe/3.75CdS-TGA QDs

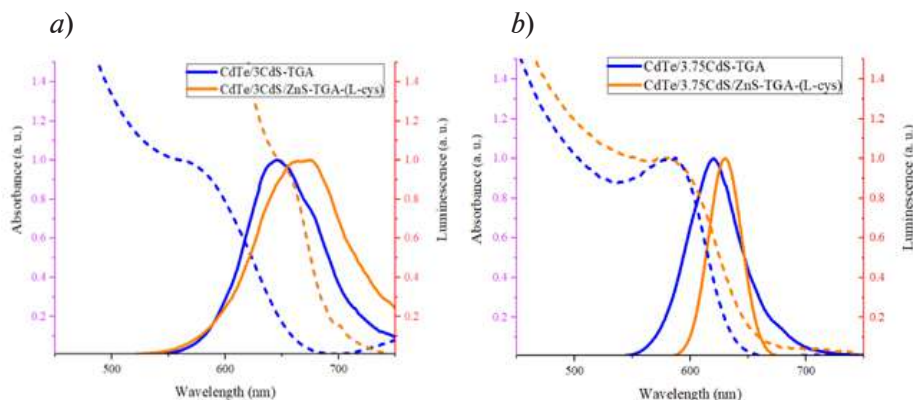


Fig. 2. Normalized absorption and fluorescence spectra of a) CdTe/3CdS-TGA, CdTe/3CdS/ZnS-TGA-(L-cys) QDs, b) CdTe/3.75CdS-TGA и CdTe/3.75CdS/ZnS-TGA-(L-cys) QDs

When coated with a ZnS layer, the quantum yield of CdTe/3CdS/ZnS-TGA-(L-cys) and CdTe/3.75CdS/ZnS-TGA-(L-cys) QDs luminescence was strongly reduced in both cases, which was 3.8% and 1.3%.

Thus, in further studies, it is proposed to continue increasing the CdS shell to improve the optical properties of QDs. But it should be considered that the effects of crystal lattice mismatch between the two materials begin to affect at high shell thicknesses, which leads to the appearance of mechanical stresses that relax with the formation of structural defects, reducing the quantum yield of particles [8].

Conclusion

The influence of CdS layer thickness on QDs optical properties was studied. The results of this study showed that the optimum thickness of CdS layer was obtained with CdTe:CdS ratio of 1:3.75 because these QDs have better optical characteristics, and also have the highest quantum yield of luminescence in comparison with QDs with other ratios.

REFERENCES

1. **Ramalingam G. et al.**, Quantum confinement effect of 2D nanomaterials, Quantum Dots-Fundamental and Applications. IntechOpen, 2020.
2. **Kumar D. S., Kumar B. J., Mahesh H. M.**, Quantum nanostructures (QDs): an overview, Synthesis of Inorganic Nanomaterials. 2018. Pp. 59–88.
3. **Speranskaya E. S. et al.**, Synthesis of hydrophobic and hydrophilic core-shell quantum dots, Izvestia of Saratov University. New series. Chemistry. Biology. Ecology. 12 (2012).
4. **Shamilov R. R. et al.**, Peculiarities of luminescence of multilayer quantum dots produced by water-organic synthesis method, Vestnik of Kazan Technological University. 19 (4) (2016).
5. **Xia M. et al.**, Surface passivation of CdSe quantum dots in all inorganic amorphous solid by forming Cd_{1-x}Zn_xSe shell, Scientific reports. 7 (1) (2017) 1–9.
6. **Romanova K. A., Galyametdinov Y. G.**, Theoretical study of the properties of core/shell/envelope quantum dots CdSe/CdS/ZnS and CdSe/ZnS/ZnS, Vestnik of Kazan University of Technology. 20 (18) (2017).
7. **Saikia D. et al.**, CdTe/ZnS core/shell quantum dot-based ultrasensitive PET sensor for selective detection of Hg (II) in aqueous media, Sensors and Actuators B: Chemical. 230 (2016) 149–156.
8. **McBride J. Treadway J., Feldman L. C., Pennycook S. J., Rosenthal S. J.**, Structural basis for near unity quantum yield core/shell nanostructures, Nano Letters. 6 (7) (2006) 1496–1501.

THE AUTHORS

TROSHKINA Natalia N.
natik.faiier@gmail.com
ORCID: 0000-0001-9722-4155

NOVIKOVA Sagila A.
sagila@uni-dubna.ru

NASIROV Pavel D.
CHemBioslne@gmail.com

VOLOBUEVA Margarita Yu.
gutairlesson@gmail.com

MUKHINA Irina V.
musha08_@mail.ru

POPOVA Anna A.
anpopova@gmail.com

GRIBOVA Elena D.
elena_g67@gmail.ru

Received 12.08.2022. Approved after reviewing 21.08.2022. Accepted 05.09.2022.

Conference materials
UDC 547.458.1:[539.25+539.26]
DOI: <https://doi.org/10.18721/JPM.153.321>

Comparative analysis of nanosized structures in thin hydrogel plates of chitosan L- and D-ascorbate–hydrochloride

A. B. Shipovskaya ¹✉, N. O. Gegel ¹, T. S. Babicheva ¹

¹ Saratov State University, Saratov, Russia

✉ Shipovskayaab@yandex.ru

Abstract. Transmission electron microscopy and small-angle X-ray scattering were used to explore the supramolecular structure of thin hydrogel plates of chitosan L- and D-ascorbate–hydrochloride. The objects reveal dendritic formations and structures of fractal dimension at the macrolevel and nanolevel of organization of polymeric substance, respectively. A comparative analysis of the morphology and average size of phase inhomogeneities and their bulk distribution in the material depending on the ascorbic acid isomer (L or D) was carried out.

Keywords: L- (D-) chitosan ascorbate hydrochloride, hydrogel plates, transmission electron microscopy, small-angle X-ray scattering

Funding: The work was carried out within the framework of the grant of the Russian Science Foundation No. 22-23-00320. <https://rscf.ru/project/22-23-00320/>.

Citation: Shipovskaya A. B., Gegel N. O., Babicheva T. S., Comparative analysis of nanosized structures in thin hydrogel plates of chitosan L- and D-ascorbate–hydrochloride. St. Petersburg State Polytechnical University Journal. Physics and Mathematics, 15 (3.3) (2022) 111–117. DOI: <https://doi.org/10.18721/JPM.153.321>

This is an open access article under the CC BY-NC 4.0 license (<https://creativecommons.org/licenses/by-nc/4.0/>)

Материалы конференции
УДК 547.458.1:[539.25+539.26]
DOI: <https://doi.org/10.18721/JPM.153.321>

Сравнительный анализ наноразмерных структур в тонких гидрогелевых пластинах L- и D-аскорбата-гидрохлорида хитозана

А. Б. Шиповская ¹✉, Н. О. Гегель ¹, Т. С. Бабичева ¹

¹ Саратовский национальный исследовательский государственный университет имени Н. Г. Чернышевского, Саратов, Россия

✉ Shipovskayaab@yandex.ru

Аннотация. Методами просвечивающей электронной микроскопии и малоуглового рентгеновского рассеяния изучена надмолекулярная структура тонких гидрогелевых пластин L- и D-аскорбата-гидрохлорида хитозана. На макроуровне организации полимерного вещества обнаруживаются дендритные образования, наноуровне – структуры фрактальной размерности. Проведен сравнительный анализ морфологии и среднего размера фазовых неоднородностей и их объемного распределения в материале в зависимости от изомера аскорбиновой кислоты (L или D).

Ключевые слова: L- (D-) аскорбат-гидрохлорида хитозана, гидрогелевые пластины, просвечивающая электронная микроскопия, малоугловое рассеяние рентгеновских лучей

Финансирование: Работа выполнена в рамках гранта Российского научного фонда № 22-23-00320. <https://rscf.ru/project/22-23-00320/>.

Ссылка при цитировании: Шиповская А. Б., Гегель Н. О., Бабичева Т. С., Сравнительный анализ наноразмерных структур в тонких гидрогелевых пластинах

L- и D-аскорбата-гидрохлорида хитозана // Научно-технические ведомости СПбГПУ. Физико-математические науки. 2022. Т. 15. № 3.3. С. 111–117. DOI: <https://doi.org/10.18721/JPM.153.321>

Статья открытого доступа, распространяемая по лицензии CC BY-NC 4.0 (<https://creativecommons.org/licenses/by-nc/4.0/>)

Introduction

In recent years, along with the dynamically developing biomedical lead of using the aminopolysaccharide chitosan, there is great interest in obtaining thin-film nanocomposite materials based thereon for solving applied problems of optoelectronics and optosensorics, in particular, for designing highly sensitive and highly selective planar waveguides, detectors, and optical sensors for analytical applications [1–6]. Such optical materials are used to diagnose biological macromolecules (DNA, proteins), cells and genetic markers [1], to monitor small organic molecules [2, 3], to analyze trace amounts of heavy metal ions [4], to design sensors for gaseous hydrogen sulfide [5] and integrated optical humidity sensors [6]. The choice of chitosan for creating an optically sensitive layer is determined not only by the formation of thin film substrates, encapsulation and stabilization of various microobjects and nanoparticles therein, but also by the possibility of making hydrogel coatings with nanosized supramolecular ordering. In addition, this aminopolysaccharide is soluble in a slightly acidic aqueous medium, including aqueous solutions of biologically active carboxylic acids, and is obtained from annually renewable natural resources. In this connection, the use of chitosan as an alternative to synthetic and even inorganic materials in optics contributes to the development of environmentally friendly technologies.

Transmission electron microscopy (TEM) is widely used to assess the geometric characteristics and topology of the nanosized structure of chitosan-containing hydrogel materials; while small-angle X-ray scattering (SAXS) is employed for structural diagnostics of condensed phased of polymeric substance at a nanometer scale, obtaining information of the molecular order of a polydisperse system, evaluation of the size of scattering nanosized inhomogeneities [7–11]. The TEM method provides for direct visualization of nanostructures in thin objects, but characterizes their surface morphology only within a limited area of the test sample. The SAXS method significantly complements and extends TEM, since it allows analyzing the nature and fractal dimension of scattering objects, as well as to obtain averaged characteristics of scattering aggregates and their size distribution.

Previously, the authors of this paper prepared hydrogel thin-film plates based on chitosan L-(D-)ascorbate by template sol-gel synthesis, considered the rheokinetics of the process, and estimated the deformation-strength characteristics of the material [12–14]. It was found that the gelation time during the formation of such plates decreases with a decrease in the polymer concentration and an increase in the reaction temperature. The load-elongation curves obtained for all samples are typical for soft elastic materials with macroscopic plasticity. Chitosan D-ascorbate retarded gelation and raised the strength-elastic properties of sol-gel plates in comparison with chitosan L-ascorbate. In addition, chitosan L- and D-ascorbates differed in the condensed macrophase morphology, as well as in the conformation and chiroptic characteristics of macromolecules: the maximum wavelength of the dichroic band and the values of its specific ellipticity, the sign of specific optical rotation, and the type of dispersion curves. It seems that the differences found in the chiral organization of the spatial structure of our hydrogel plates based on chitosan L-(D-)ascorbate, as well as the differences (described in Ref. [15]) in the reactivity of L- and D-ascorbic acid with respect to chitosan and in the parameters of the monoclinic cell of anhydrous crystals of chitosan L- and D-ascorbate may also have a significant effect on the supramolecular structure of the chitosan-containing hydrogel system at the nanoscale level of its organization.

The purpose of this work was to explore the structure and supramolecular ordering of thin hydrogel sheets of chitosan L- and D-ascorbate-hydrochloride using TEM and SAXS methods.

Materials and Methods

The following reagents were used: chitosan hydrochloride (CS·HCl) with a viscosity average molecular weight of 38 kDa and a degree of deceleration DD = 80 mol.% (Bioprogress Ltd., RF); L-ascorbic acid (L-AscA, ZAO FP Meligen, RF), D-isoascorbic acid (D-AscA, ZAO Khimreaktiv, RF); polyvinyl alcohol (PVA, structurant) with a weight average molecular weight of 89–98 kDa (Sigma Aldrich, USA); a solution of silicon tetraglycerolate in glycerol (Si(C₃H₇O₃)₄·3C₃H₈O₃, a gelling agent) with a concentration of 58.7 wt.%, obtained in the laboratory of organic materials, Institute of Organic Synthesis named after I. Ya. Postovsky, Ural Branch of the Russian Academy of Sciences (RF) according to the method from Ref. [16]; Milli-Q distilled water. All reagents were chemically pure and were used without further purification.

Aqueous solutions CS·HCl in L-AscA and D-AscA of a concentration of 4 wt.% were prepared in a –NH₂:AscA equimolar ratio and used in our experiments. To prepare solutions a sample of CS·HCl powder was suspended in the calculated amount of water on a magnetic stirrer, followed by addition of an air-dry L-(D-)AscA powder. The system was left at 20 ± 2 °C for one day until complete dissolution. Aqueous PVA solutions of a concentration of 10 wt.% were prepared by suspending a sample of polymer powder in the calculated amount of water on a magnetic stirrer for 5 min, followed by 850 W microwave treatment in a laboratory microwave system Mars-5 (CEM Corporation, USA) during 30–50 s.

TEM images were obtained on a transmission electron microscope A Libra 120 (Carl Zeiss, Germany) at 120 kV. Hydrogel plates were fixed with glutaraldehyde for 12 h, dehydrated in increasing concentrations of ethyl alcohol (30, 50, 70, 80, and 96%), absolute acetone and propylene oxide, then embedded with EPON-812[®] epoxy resin and kept at 37, 45 and 57 °C for 24 h at each temperature. Ultrathin sections were obtained on an LKB-III microtome (Sweden) and applied to a formvar-coated copper grid.

SAXS measurements were carried out on a Hecus S3-MICRO small-angle diffractometer (Austria) with a Kratky collimation system, Cu K α radiation at a voltage of 50 kV and a current of 1 mA, using a 1D-PSD 50 M detector with a resolution of 1024 pixels. The distance from the quartz cell with the hydrogel plate to the detector was 281 mm. The measurements were carried out in vacuum at 295 K, exposure time 1,000 sec. Scattering intensity $I(q)$ was recorded in the range of the scattering wave vector modulus $q = 0.01–0.65 \text{ \AA}^{-1}$, where $q = 4\pi \sin \theta/\lambda$, 2θ being the scattering angle (deg), λ the radiation wavelength (1.542 Å). Scattering curves were normalized using Lupolen software. The structural parameter n , which characterizes the morphology of scattering inhomogeneities, was calculated from the slope of the straight sections of the scattering curve in the $(\ln I; q)$ coordinates, the average radius of gyration R_g of scattering inhomogeneities (in our case, having the physical meaning of the average size of scattering domains) was calculated from the dependence in Guinier coordinates $(\ln I; q^2)$ [11, 17]. The size distribution function of inhomogeneities $D_V = f(R)$, where R is the average size of scattering domains, was calculated using the GNOM software [18].

Results and Discussion

Fig. 1 shows the TEM images of ultrathin sections of hydrogel plates of chitosan L- and D-ascorbate-hydrochloride, hereinafter referred to as CS·HCl·L-AscA and CS·HCl·D-AscA. Analysis of these TEM photos shows the presence of two phases in the structure of the samples, namely: an optically “inert” denser phase of the structurant and gelation agent and an optically less dense condensed phase of chitosan ascorbate, represented by supramolecular aggregates of a dendritic-like type. The dendritic structures have a center and relatively extended branches up to ~3–5 μm in length. However, the structure and morphology of dendrites, the size and number of side branches depend on the AscA isomer used to obtain the hydrogel plates (Table 1).

For example, a highly branched dendritic structure with dense symmetrical filamentous branches was observed for the CS·HCl·L-AscA samples. The width of the main and lateral branches was ~0.3–0.4 μm and ~0.2–0.3 μm , respectively. The angle between the axes of the main branches varied in a range of ~60–70°. The geometry and topological characteristics of the dendritic structure of the CS·HCl·D-AscA sample differed significantly. First of all, the supramolecular formations were less branched and less regular. Almost no formation of symmetrical branches was observed. The width of the main and side branches, as well as the angle between the axes of the main branches, increased and amounted to ~0.9–1.2 μm , ~0.5–0.8 μm , and ~80–90°, respectively.

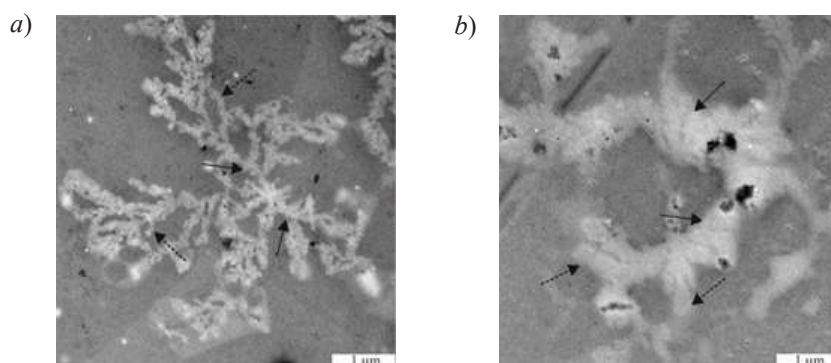


Fig. 1. TEM images of ultrathin sections of our hydrogel plates based on CS·HCl·L-AscA (a) and CS·HCl·D-AscA (b); smooth arrows mark the main branches of dendritic structures, while dotted arrows mark lateral branches

Table 1

Structural and dimensional characteristics of the supramolecular ordering of hydrogel plates of chitosan L- and D-ascorbate-hydrochloride from TEM and SAXS data

Parameter CS·HCl·L-AscA	Sample		
	CS·HCl·D-AscA	CS·HCl·D-AscA	
TEM			
Branch index	5 ± 1	3 ± 1	
Main branch length (μm)	3.5 ± 0.5	4.5 ± 0.5	
Main branches width (μm)	0.35 ± 0.05	1.05 ± 0.15	
Side branch width (μm)	0.25 ± 0.05	0.65 ± 0.15	
Angle between the axes of the main branches (deg)	65 ± 5	80 ± 5	
SAXS			
Power decay exponent in the dependence $\ln I(q) = f(q)$, n	I	2.4	2.1
	II	1.8	1.7
Fractal dimension	2.4	2.1	
Average radius of gyration of scattering inhomogeneities, R_g (\AA)	15–170	25–190	
Average size of the dominant fraction of scattering domains, R (\AA)	15–85	25–70	
Volume fraction of the predominant fraction of scattering domains, $D_v \cdot 10$	3.8	6.0	

Besides, the dendrite morphostructure was looser, and the number of side branches was significantly less compared to the sample obtained using the AscA L-isomer.

The intensity curves of small-angle X-ray scattering by CS·HCl·L-AscA and CS·HCl·D-AscA hydrogel plates in semilogarithmic coordinates smoothly decreased with the scattering wave vector modulus and had no Bragg peaks, which indicated scattering by loose-packed inhomogeneity domains and amorphous structure of the samples (Fig. 2). The scattering indicatrices $\ln I(q) = f(q)$ can be divided into two rectilinear sections (I and II), differing in the nature of the angular dependence of the radiation intensity $I(q) \sim q^{-n}$. The first and second corresponded to the scattering coordinate range $q < 0.02 \text{ \AA}^{-1}$ and $q \sim 0.02 - 0.11 \text{ \AA}^{-1}$, respectively. $q \sim 0.02 \text{ \AA}^{-1}$ can be considered as the crossover point. The decay exponent at low values q , equal to $n = 2.4$ and 2.1 for CS·HCl·L-AscA and CS·HCl·D-AscA, respectively (Table 1), indicates the presence of

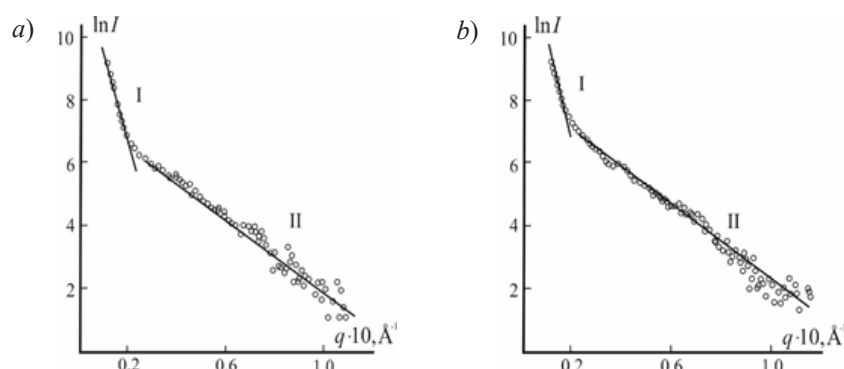


Fig. 2. Curves of small-angle X-ray scattering for hydrogel plates based on CS·HCl·L-AscA (a) and CS·HCl·D-AscA (b)

scattering bulk domains with a fractal structure in the hydrogel spatial network (bulk fractals) [8, 11]. In the range of higher q values, the slope of the SAXS curve for the same samples is $n = 1.8$ and $n = 1.7$, respectively. This means that polymer coils in scattering inhomogeneities have the conformation of self-avoiding semi-rigid chains [11]. The fractal dimension, which for bulk fractal clusters is evaluated by the $\ln I(q) = f(q)$ slope in the region of small q , is most pronounced for the CS·HCl·L-AscA sample. Quantitative indicators of the average radius of gyration of phase inhomogeneities of the supramolecular structure of the CS·HCl·L-AscA and CS·HCl·D-AscA plates also differ (Table 1). E.g., the CS·HCl·D-AscA sample is characterized by a larger average size of scattering domains and a wider range of R_n values.

The volume size distribution functions of scattering domains calculated from the SAXS curves for the CS·HCl·L-AscA (a) and CS·HCl·D-AscA plates show a bimodal character with two maxima. The average size R of the dominant fraction of domains (Fig. 3, first maximum) correlates with the average radius of gyration of scattering inhomogeneities (Table 1).

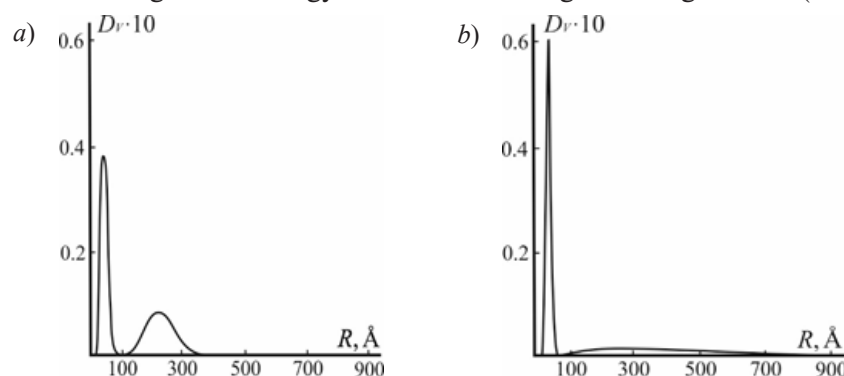


Fig. 3. Volume size distribution functions of scattering domains for our hydrogel plates based on CS·HCl·L-AscA (a) and CS·HCl·D-AscA (b)

The wider range of R_n is due to the fact that when calculating the average values of the radius of gyration, all scattering domains are taken into account, including the largest ones, whose weight fraction in the total supramolecular structure of the samples under study is relatively small (the second maximum). It is noteworthy that the amplitude of the $D_v(R)$ function, which is proportional to the electron density of scattering objects and, accordingly, the volume fraction of the main fraction of scattering domains, is much higher for CS·HCl·D-AscA. A narrower width of the distribution of the predominant fraction of scattering domains by R is also a distinctive feature of this sample.

Conclusion

Our comparative analysis of the structure of thin hydrogel plates of chitosan L- and D-ascorbate-hydrochloride carried out in this work by TEM and SAXS gives grounds to conclude that the materials differ in their supramolecular ordering and dimensional characteristics of phase inhomogeneities. The TEM images of plates made from CS·HCl·L-AscA reveal more branched

dendrite-like structures with a smaller branch width than those made from CS·HCl·D-AscA. The SAXS indicatrices show the fractal organization of nanosized inhomogeneities of the hydrogel spatial network with the largest average size of scattering objects for the CS·HCl·D-AscA sample. The volume size distribution functions of scattering domains have a bimodal character with the larger amplitude and the narrower distribution of the main fraction of nanostructures for CS·HCl·D-AscA.

The experiments performed, as well as our previous studies [12–14], indicate the important role of the (L-, D-) ascorbic acid isomer used to dissolve chitosan in the design of polymeric materials with a given spatial organization. Hydrogel plates made from CS·HCl·L-AscA and CS·HCl·D-AscA can be very promising in creating a sensitive layer of optical sensors for recognizing enantiomers of biologically active and medicinal compounds, separating racemic mixtures of optically active substances, detecting chiral molecules and even chiral nanoparticles and quantum dots.

REFERENCES

1. Huang W. C., Chi H. S., Lee Y. C., Lo Y. C., Liu T. C., Chiang M. Y., Chen H. Y., Li S. J., Chen Y. Y., Chen S. Y., Gene-embedded nanostructural biotic–abiotic optoelectrode arrays applied for synchronous brain optogenetics and neural signal recording, *ACS Appl. Mater. Interfaces*. 11(12) (2019) 11270–11282.
2. Wang X., Wolfbeis O. S., Fiber-optic chemical sensors and biosensors (2015–2019), *Anal. Chem.* 92(1) (2019) 397–430.
3. Rehmat Z., Mohammed W. S., Sadiq M. B., Somarapalli M., Anal A. K., Ochrotoxin A detection in coffee by competitive inhibition assay using chitosan-based surface plasmon resonance compact system, *Colloids Surf. B*. 174 (2019) 569–574.
4. Boruah B. S., Biswas R., In-situ sensing of hazardous heavy metal ions through an ecofriendly scheme, *Optics and Laser Technology*. 137 (2021) 106813.
5. Mironenko A. Yu., Sergeev A. A., Nazirov A. E., Modin E. B., Voznesenskiy S. S., Bratskaya S. Yu., H₂S optical waveguide gas sensors based on chitosan/Au and chitosan/Ag nanocomposites, *Sensors and Actuators B: Chemical*. 225 (2016) 348–353.
6. Jang J., Kang K., Raeis-Hosseini N., Ismukhanova A., Jeong H., Jung C., Kim B., Lee J.-Y., Park I., Rho J., Self-powered humidity sensor using chitosan-based plasmonic metal–hydrogel–metal filters, *Adv. Opt. Mater.* 8 (2020) 1901932.
7. Mashile P. P., Nomngongo P. N., Magnetic cellulose-chitosan nanocomposite for simultaneous removal of emerging contaminants: adsorption kinetics and equilibrium studies, *Gels*. 7 (4) (2021) 190–210.
8. Lin Y.-J., Chuang W.-T., Hsu, S.-H., Gelation mechanism and structural dynamics of chitosan self-healing hydrogels by in situ saxs and coherent x-ray scattering, *ACS Macro Lett.* 8 (11) (2019) 1449–1455.
9. Postnova I., Silant'ev V., Sarin S., Shchipunov Yu., Chitosan hydrogels and bionanocomposites formed through the mineralization and regulated charging, *Chem. Rec.* 18 (7-8) (2018) 1247–1260.
10. Ashrafi H., Azadi A., Chitosan-based hydrogel nanoparticle amazing behaviors during transmission electron microscopy, *Inter. J. Biolog. Macromolec.* 84 (2016) 31–34.
11. Ventura I., Bianco-Peled H., Small-angle X-ray scattering study on pectin–chitosan mixed solutions and thermoreversible gels, *Carbohydr. Polym.* 123 (2015) 122–129.
12. Shipovskaya A. B., Malinkina O. N., Gegel N. O., Zudina I. V., Lugovitskaya T. N., Structure and properties of chitosan salt complexes with ascorbic acid diastereomers, *Russ. Chem. Bull.* 70 (2021) 1765–1774.
13. Shipovskaya A. B., Zhuravleva Yu. Yu., Khonina T. G., Malinkina O. N., Gegel N. O., Influence of the ascorbic acid isoform on the sol-gel synthesis kinetics and properties of silicon–chitosan-containing glycerohydrogel plates, *J. Sol-Gel Sci. Technol.* 92 (2) (2019) 349–358.
14. Gegel N. O., Zhuravleva Yu. Yu., Shipovskaya A. B., Malinkina O. N., Zudina I. V., Influence of chitosan ascorbate chirality on the gelation kinetics and properties of silicon–chitosan-containing glycerohydrogels, *Polymers*. 10 (3) (2018) 259–275.
15. Ogawa K., Nakata K., Yamamoto A., Nitta Y., Yui T., X-ray study of chitosan L- and D-ascorbates, *Chem. Mater.* 8 (9) (1996) 2349–2351.

16. **Larchenko E. Yu., Shadrina E. V., Khonina T. G., Chupakhin O. N.**, New hybrid chitosan–silicone containing glycerohydrogels, *Mendeleev Commun.* 4 (24) (2014) 201–202.
17. **Feigin L., Svergun D. I.**, Structure analysis by small angle X-ray and neutron scattering. Plenum Press, New York, 1987.
18. **Svergun D. I.**, Determination of the regularization parameter in indirect-transform methods using perceptual criteria, *J. Appl. Cryst.* 25 (1992) 495–503.

THE AUTHORS

SHIPOVSKAYA Anna B.

Shipovskayaab@yandex.ru

ORCID: 0000-0003-1916-4067

BABICHEVA Tatyana S.

tatyana.babicheva.1993@mail.ru

ORCID: 0000-0002-6655-8483

GEGEL Natalia O.

gegeln@yandex.ru

ORCID: 0000-0001-5724-7571

Received 15.07.2022. Approved after reviewing 05.08.2022. Accepted 05.08.2022.

Conference materials

UDC 53.08

DOI: <https://doi.org/10.18721/JPM.153.322>

Upconversion luminescence particles based on NaYF₄ matched with passive optical devices

I. M. Asharchuk ¹✉, N. A. Vovk ², V. I. Sokolov ²,
I. O. Goryachuk ², N. V. Minaev ², M. A. Tarkhov ¹

¹ Institute of Nanotechnologies of Microelectronics of the RAS, Moscow, Russia;

² Federal Scientific Research Center "Crystallography and Photonics" RAS, Moscow, Russia

✉ ilyaasharchuk@gmail.com

Abstract. The work is aimed at creating matching passive elements with optical planar devices. A three-dimensional structure-interface was made to match the position of the center of the optical fiber with active optical elements. NaYF₄ microparticles doped with rare-earth ions Yb³⁺, Tm³⁺, Er³⁺ with a diameter of 2.2 μm and 1.65 μm were synthesized. The formation of hemispherical lenses with radii from 0.75 to 25 μm has been demonstrated for optical matching with optical fiber by IR (infrared) photopolymerization.

Keywords: upconversion, two-photon polymerisation, rare-earths

Funding: The work was supported by GK No. 20411.1950192501.11.003. Code "Progress".

Citation: Asharchuk I. M., Vovk N. A., Sokolov V. I., Goryachuk I. O., Minaev N. V., Tarkhov M. A., Upconversion luminescence particles based on NaYF₄ matched with passive optical devices St. Petersburg State Polytechnical University Journal. Physics and Mathematics, 15 (3.3) (2022) 118–122. DOI: <https://doi.org/10.18721/JPM.153.322>

This is an open access article under the CC BY-NC 4.0 license (<https://creativecommons.org/licenses/by-nc/4.0/>)

Материалы конференции

УДК 53.08

DOI: <https://doi.org/10.18721/JPM153.322>

Апконверсионные люминесцентные частицы на основе NaYF₄ совмещенные с пассивными оптическими устройствами

И. М. Ашарчук ¹✉, Н. А. Вовк ², В. И. Соколов ²,
И. О. Горячук ², Н. В. Минаев ², М. А. Тархов ¹

¹ Институт нанотехнологий микроэлектроники РАН, Москва, Россия;

² Федеральный научно-исследовательский центр «Кристаллография и фотоника» РАН, Москва, Россия

✉ ilyaasharchuk@gmail.com

Аннотация. Работа направлена на создание согласования пассивных элементов с оптическими планарными устройствами. Создана трехмерная структура-интерфейс для согласования положения центра оптоволокна с активными оптическими элементами. Синтезированы микрочастицы NaYF₄, легированные редкоземельными ионами Yb³⁺, Tm³⁺, Er³⁺, диаметром 2.2 мкм и 1.65 мкм. Было продемонстрировано формирование полусферических линз радиусом от 0.75 до 25 мкм при оптическом согласовании с оптическим волокном путем ИК (инфракрасной) фотополимеризации. Продемонстрирована зависимость сигнала от позиции ввода в согласующий элемент.

Ключевые слова: апконверсия, двухфотонная полимеризация, редкоземельные элементы

Финансирование: Работа выполнена в рамках проекта ГК № 20411.1950192501.11.003. Код «Прогресс».

Ссылка при цитировании: Ашарчук И. М., Вовк Н. А., Соколов В. И., Горячук И. О., Минаев Н. В., Тархов М. А., Апконверсионные люминесцентные частицы на основе NaYF_4 совмещенные с пассивными оптическими устройствами // Научно-технические ведомости СПбГПУ. Физико-математические науки. 2022. Т. 15. № 3.3. С. 118–122. DOI: <https://doi.org/10.18721/JPM.153.322>

Статья открытого доступа, распространяемая по лицензии CC BY-NC 4.0 (<https://creativecommons.org/licenses/by-nc/4.0/>)

Introduction

Today, the directions for creating single-photon radiation sources necessary for quantum computing, quantum cryptography, etc. are relevant [1]. However, an equally important problem is the manufacture of matching elements for detecting and delivering radiation to single-photon sources and detectors, respectively [2]. Upconversion nanoparticles (UCNPs) doped with Er^{3+} , Tm^{3+} , Yb^{3+} lanthanides can serve as single-photon emitters; they have anti-Stokes emission, manifested by the generation of high-energy photons through multiphoton absorption of low-energy photons [1]. Compared to traditional phosphors such as fluorescent dyes and quantum dots, UCNPs are resistant to photobleaching, they are photostable and have real intermediate energy levels [3–5]. Such features of UCNPs with matching technology become attractive for the development of single-photon radiation sources necessary for quantum computing.

Materials and techniques

To obtain fluoride microcrystals of the composition $\text{NaY}_{0.78}\text{F}_4:\text{Yb}_{0.2}, \text{Er}_{0.02}, \text{NaY}_{0.78}\text{F}_4:\text{Yb}_{0.2}, \text{Tm}_{0.006}$ with a hexagonal crystal lattice (β -form), commercial reagents were used: oxides of yttrium, ytterbium, erbium, sodium carbonate, oleic acid 90%, 1-octadecene 90% (Sigma-Aldrich), and trifluoroacetic acid 99% (PanReac). Synthesis was carried out by thermal decomposition of trifluoroacetates of rare earth elements and sodium in an oxygen-free environment in a mixture of oleic acid and 1-octadecene. To determine the phase of the crystals, X-ray diffraction analysis (XRD - X-Ray Diffractometry) was used. The electron microscopy (SEM) method was used to analyze the shape and size of the particles. To form polymer microlenses, we used an original approach, NIR photopolymerization [6] based on lanthanide-doped upconversion microparticles (UCMPs) $\text{NaYF}_4:\text{Yb}, \text{Tm}$. UCMPs convert NIR light into ultraviolet (UV) or visible (VIS) light, which in turn triggers the photopolymerization reaction in Dental Clear photopolymer (HARZLabs, Russia). The microparticles were deposited on the substrate by centrifugation at a speed of 1800 min⁻¹ for 30 s. For the photopolymerization process, a continuous laser with a wavelength of 975 nm (PL980P330J, Thorlabs) and an incident power of 50 mW was used. The radiation was focused using an Olympus UPlanSApo 60x/1.2 NA objective. W.

We used a setup [7], based on a submicron three-dimensional positioning system ABL1000 (Aerotech, USA) air-bearing direct-drive linear stage and high-speed galvano-scanner ‘HurrySCAN II 14’ (ScanLab). The second harmonic of the TEMA-100 femtosecond laser (Avesta-Proekt, Russia), with $\lambda = 525$ nm, 70 MHz, 200 fs and power up to 200 mW, was used as the light source. An acousto-optic modulator at operational frequencies up to 1 MHz was used as the optical shutter. The NFOL process was used to create the microadapter. Polymethyl methacrylate (PMMA) 495K A2 is used as a spin-coated resistive material. The typical average power of femtosecond laser radiation for the implementation of the NFOL process on PMMA with a thickness of 800 microns was 18–22 mW [8]. Determination of the morphology of microlenses with a radius of 1.55 μm was carried out using atomic force microscopy in the contact mode of the probe.

For hollows formation were applied are next technological processes. The first step of creating a pattern of was formed in the photoresist (AZ4999) using a laser lithograph, followed by development in a 0.7% KOH solution. When applying the photoresist, the thermal oxide plate was processed in GMDS to improve the adhesion characteristics. The thickness of the photoresist was 600 nm. Next, the thermal oxide was etched through the formed mask by plasma-chemical etching in C_4F_8 gas. To further fill the hollows formed in thermal silicon oxide, an aqueous suspension of $\text{NaYF}_4:\text{Yb}^{3+}, \text{Tm}^{3+}$ particles and hexane was formed. The weight ratio of particles to hexane

was 1:10,000 times, respectively. The next step was to place a 4" mm plate with formed hollows into the suspension and keep it there for several hours. Due to the natural settling of particles on the surface, a uniform layer was formed, the technology is similar to the deposition of carbon nanotubes [8]. Part of the $\text{NaYF}_4: \text{Yb}^{3+}, \text{Tm}^{3+}$ particles also fell into pre-prepared wells. The final technological step in the formation of the final structure was the removal of "extra" particles by the method of hydrodynamic cleaning under the action of a high-pressure water jet. Particles that got into the hollows due to surface forces are kept in them, and the rest of the particles are removed.

To determine the response when combining the fiber through a microoptical adapter, an installation was assembled where the signal from the detector arrived at a UCMPs located on planar detector. The input signal at a wavelength of 975 nm with a power of 500 uW was fed through a fiber to fiber U-bench system (Thorlabs) for a single-mode fiber with a core of 7 um and a core diameter of 125 um. A chopper was inserted into the fiber to fiber U-bench system to modulate the signal at a frequency of 7 Hz. The electrical signal from the detector was sent to the lock-in amplifier. Alignment before insertion of a single-mode fiber was performed using a 3-axis micrometric shift.

Results and discussion

As a demonstration, the process of supplying an optical fiber to a hemispherical microlens made by IR photopolymerization was implemented. The principle of formation of microlenses is shown in Fig. 1 (I, II-a), UCMPs are re-emit absorbed quanta from a wavelength of 975 nm to the visible and UV wavelengths (345.360, 450.475, 645 nm), and the photoinitiator dissolved in the monomer has an absorption spectrum in the short wavelength range (Fig. 1(I), blue line). This starts the IR photopolymerization reaction. Microstructures in the form of microlenses were formed on a cover glass substrate. By varying the exposure time, several sizes of microlenses of different diameters were obtained (Fig. 1(II-c)). At an exposure of 30 s under the action of laser radiation with a wavelength of 975 nm, the diameter of the hemispherical microlenses was $\sim 50 \mu\text{m}$. Since spincoating was used at the initial stage in the deposition of UCMPs, their ordered distribution over the substrate was not achieved. A deterministic particle arrangement process has been proposed and described in Materials and Methods above. Next, a microadapter was fabricated over the formed microlenses with UCMPs (Fig. 1(III)). Figure 1 (II-b) shows an electron photograph of the synthesized particles. Synthesized microparticles with a hexagonal crystal lattice and low dispersion of diameter $d = 1.65 \pm 0.1$ and $2.2 \pm 0.13 \mu\text{m}$ for $\text{NaYF}_4: \text{Yb}^{3+} \text{Er}^{3+}$ and $\text{NaYF}_4: \text{Yb}^{3+}, \text{Tm}^{3+}$, respectively. Hemispherical microlenses with radii from 0.75 to 25 um were obtained.

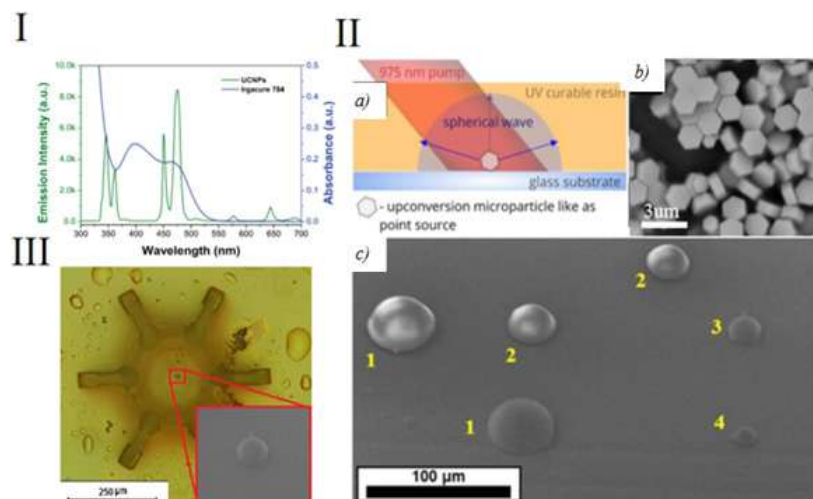


Fig. 1. I Luminescence spectra of an upconversion NaYF_4 microparticle: $\text{Yb}^{3+}, \text{Tm}^{3+}$ (green curve) and absorption spectra of the Irgacure 784 photoinitiator (blue curve). II (a) schematic representation of the principle of IR photopolymerization, (b) SEM image $\text{NaYF}_4: \text{Yb}^{3+}, \text{Tm}^{3+}$ particles, (c) SEM photograph of hemispherical microlenses formed by IR photopolymerization with different exposure times by 975 nm radiation pump power 50 mW (1) 30 s (2) 20 s (3) 10 s (4) 5 s III Three-dimensional structure of the optical fiber interface formed above the microlens, top view

It can be seen that the passive optical device, consisting of a microparticle and a particle formed on top of it, is located in the center of the microadapter. The Fig. 2, *a* shows a schematic representation of signal acquisition from a microparticle located above a planar detector. Point -350 is taken as the position when the fiber is near the front plane of the adapter. Point 0 was determined by the position of the fiber close to the microparticle.

The Fig. 2, *b* shows the dependence of the detector signal on the position of the injected fiber. It can be seen that as the fiber approaches the detector, the signal level increases and, reaching a certain level, does not change – it reaches a plateau. This happens at around -150 microns. The relative plateau level is 1.4 micro volts.

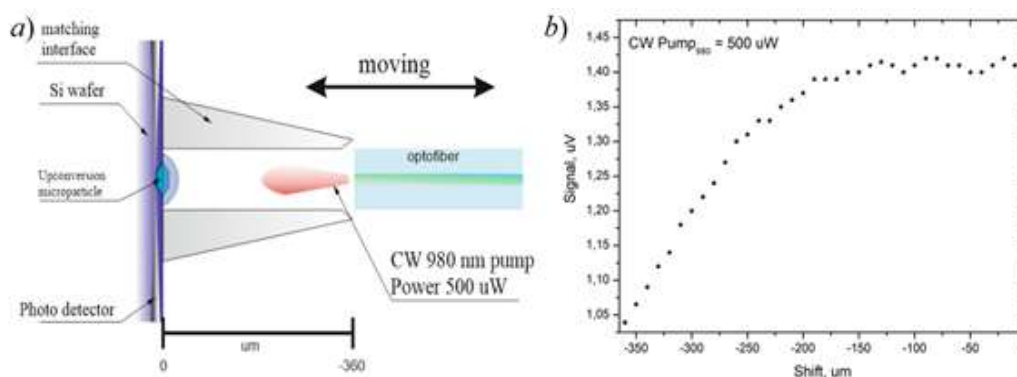


Fig. 2. Scheme describing the process of introducing an optical fiber into the optofiber matching interface (*a*); dependence of the signal from the photodetector on the depth of fiber insertion (*b*)

Fluctuations in the signal from the detector are visible. The authors hypothesized that these fluctuations are related to the temperature instability of the detector associated with its heating. Since the calculated intensity at the output of a fiber with a thickness of 7 microns and a radiation power of 500 microwatts is 1.2 kW/cm². However, further experiments are expected to confirm or refute this hypothesis.

Conclusion

The hemispherical microlenses formed by IR photopolymerization with different exposure times by 975 nm radiation pump power 50 mW, minimal microlens diameter were reached 1.5 μm. The developed technological approach to the creation of a microoptical holder for standard single-mode and multimode fibers is demonstrated. This type of holder can be used to manufacture an optical matching unit for optical fibers with sensitive optical elements. Which allows you to combine the position of the center of the optical fiber with active optical elements. The resulting interface unit can be used in planar integrated optical microdevices.

REFERENCES

1. Thomas S., Senellart P., The race for the ideal single-photon source, *Nature Nanotechnology*, 12 (2021) 367–368.
2. Mäntynen H., Anttu N., Zhipei Sun and Harri Lipsanen, Single-photon sources with quantum dots in III–V nanowires, *Nanophotonics*. 8 (5) (2019) 747–769.
3. Zhou B., Shi B., Jin D., Liu X., Controlling upconversion nanocrystals for emerging applications. *Nat. Nanotechnol.* 10 (2015) 924–936.
4. Liu Y. et al., Amplified stimulated emission in upconversion nanoparticles for super-resolution nanoscopy. *Nature*, 543 (2017) 229–233.
5. Karimov D. N., Demina P. A., Koshelev A. V., Rocheva V. V., Sokovikov A. V., Generalova A. N., Zubov V. P., Khaydukov E. V., Koval'chuk M. V., Panchenko V. Y., Upconversion nanoparticles: synthesis, photoluminescence properties, and applications, *Nanotechnologies in Russia*, 15 (2020) 655–678.
6. Demina P., Arkharova N., Asharchuk I., Khaydukov K., Karimov D., Rocheva V., Nechaev A., Grigoriev Y., Generalova A., Khaydukov E., Polymerization assisted by upconversion nanoparticles under NIR light *Molecules*, 24 (2019) 2476.

7. **Minaev N. V., Tarkhov M. A., Dudova D. S., Timashev P. S., Chichkov B. N., Bagratashvili V. N.**, Fabrication of superconducting nanowire single-photon detectors by nonlinear femtosecond optical lithography, *Laser Phys. Lett.*, 15 (2018) 1–6.

8. **Minaev N. V. et. al.**, Fabrication of micro-optical connectors for electro-optical sensor devices by a combined femtosecond laser system, *Laser Phys. Lett.*, 18 (2018) 1–7.

9. **Bishop M. D., Hills G., Srimani T., Lau C., Murphy D., Fuller S., Shulaker M. M.**, Fabrication of carbon nanotube field-effect transistors in commercial silicon manufacturing facilities, *Nature Electronics*, 3 (8) (2020) 492–501.

THE AUTHORS

ASHARCHUK Ilya M.
ilyaasharchuk@gmail.com
ORCID: 0000-0001-6445-0009

VOVK Nikolay A.
vovkolg2011@gmail.com

SOKOLOV Viktor I.
visokol@rambler.ru

GORYACHUK Ivan O.
ivolgor@yandex.ru

MINAEV Nikita V.
minaevn@gmail.com

TARKHOV Michael A.
tmafuz@mail.ru

Received 01.08.2022. Approved after reviewing 01.08.2022. Accepted 02.08.2022.

PHYSICAL ELECTRONICS

Conference materials

UDC 621.315.592

DOI: <https://doi.org/10.18721/JPM.153.323>

Plasma deposited indium phosphide and its electrophysical properties

A. A. Maksimova ^{1,2}✉, A. V. Uvarov ², D. A. Kirilenko ³,
A. I. Baranov ², E. A. Vyacheslavova ², A. S. Gudovskikh ^{1,2}

¹ St. Petersburg Electrotechnical University "LETI", St.
Petersburg, Russia;

² St. Petersburg Academic University, St. Petersburg, Russia;

³ Ioffe Physical Technical Institute, St. Petersburg, Russia

✉ maksimova_alina@spbau.ru

Abstract. In this article, indium phosphide (InP) layers were grown using the method of plasma-chemical atomic layer deposition on crystalline silicon substrates for the first time. Trimethylindium (TMI) was used as a source of indium, and phosphine (PH₃) was used as a source of phosphorus. Properties of InP layers were evaluated, such as structural properties, electrical conductivity, type of conductivity and carrier concentration to integrate them into a c-Si-based solar cell. Root-Mean-Square (RMS) roughness measurements showed that the use of intermediate annealing in Ar plasma after the stage of deposition of a phosphorus monolayer leads to a significant decrease in roughness to the level of fractions of nanometers. The composition of the InP layers according to the energy dispersive X-ray spectroscopy (EDX) was close to stoichiometric. The measurements of dark IV characteristics showed that the InP layer has a donor type of conductivity. I–V characteristics of InP/p-Si structure under solar spectrum illumination, show open circuit voltage of $V_{oc} = 0.48$ V. Van der Pauw measurements demonstrate high concentration of carriers and their high mobility. Thus, the possibility of using InP-based layers for solar cells was shown.

Keywords: silicon, solar cells, indium phosphide, plasma enhanced chemical vapor deposition, atomic layer deposition

Funding: This study was funded by Ministry of Science and Higher Education of the Russian Federation (research project 0791-2020-0004).

Citation: Maksimova A. A., Uvarov A. V., Kirilenko D. A., Baranov A. I., Vyacheslavova E. A., Gudovskikh A. S., Plasma deposited indium phosphide and its electrophysical properties. St. Petersburg State Polytechnical University Journal. Physics and Mathematics, 15 (3.3) (2022) 123–127. DOI: <https://doi.org/10.18721/JPM.153.323>

This is an open access article under the CC BY-NC 4.0 license (<https://creativecommons.org/licenses/by-nc/4.0/>)

Материалы конференции

УДК 621.315.592

DOI: <https://doi.org/10.18721/JPM.153.323>

Плазменно-осажденный фосфид индия и его электрофизические свойства

А. А. Максимова ^{1,2}✉, А. В. Уваров ², Д. А. Кириленко ³,
А. И. Баранов ², Е. А. Вячеславова ², А. С. Гудовских ^{1,2}

¹ Санкт-Петербургский электротехнический университет «ЛЭТИ», Санкт-Петербург, Россия;

² Санкт-Петербургский Академический Университет, Санкт-Петербург, Россия;

³ Физико-технический Институт им. Иоффе, Санкт-Петербург, Россия

✉ maksimova_alina@spbau.ru

Аннотация. Впервые методом плазмохимического атомно-слоевого осаждения были выращены слои фосфида индия (InP). В качестве источника индия выступал триметиллиндий (ТМИ), а в качестве источника фосфора – фосфин (PH₃). Были оценены структурные свойства слоев InP, а также электропроводность, тип проводимости и концентрация носителей. Состав слоев InP по данным энергодисперсионной рентгеновской спектроскопии (EDX) близок к стехиометрическому. Выращенные слои имеют донорный тип проводимости, световые ВАХ продемонстрировали напряжение холостого хода Voc=0.48 В. Таким образом, была оценена возможность использования слоев на основе InP для создания солнечных элементов.

Ключевые слова: кремний, солнечные элементы, фосфид индия, плазмохимическое осаждение, атомно-слоевое осаждение

Финансирование: Работа выполнена в рамках Госзадания № 0791-2020-0004 «Исследования по разработке новых физико-технологических подходов формирования фотоэлектрических преобразователей солнечной энергии на основе кремния».

Ссылка при цитировании: Максимова А. А., Уваров А. В., Кириленко Д. А., Баранов А. И., Вячеславова Е. А., Гудовских А. С., Плазменно-осажденный фосфид индия и его электрофизические свойства // Научно-технические ведомости СПбГПУ. Физико-математические науки. 2022. Т. 15. № 3.3. С. 123–127. DOI: <https://doi.org/10.18721/JPM.153.323>

Статья открытого доступа, распространяемая по лицензии CC BY-NC 4.0 (<https://creativecommons.org/licenses/by-nc/4.0/>)

Introduction

Indium phosphide (InP) is a promising material for applications in various areas of electronics due to its distinctive properties such as high electron mobility (higher than that of silicon, germanium and gallium arsenide) and high band gap value (1.3 eV). In this regard, InP has found application in power and high-frequency electronics. InP-based solid solutions are widely used to create light emitting diodes (LEDs), laser diodes, and avalanche photodiodes. InP has good optical and electronic properties, it is also a direct-gap semiconductor, due to which it has found application in the creation of photonic integrated circuits. The above properties also make indium phosphide an attractive material in solar cells (SCs) fabrication. According to [1], the efficiency of SCs based on InP under standard conditions reaches 21.9%.

Recently, research has been actively conducted on the creation of solar cells based on the integration of third group elements A₃B₅ compounds with silicon (Si) in order to reduce the cost and increase the efficiency of solar cells. Thus, it is possible to create solar cells based on the InP/Si heterojunction.

Materials and Methods

In this work, we propose to use the method of plasma-chemical vapor deposition (PECVD) for the growth of InP films. It is a reliable industrial method, which allows the growth of electronic quality films at low temperatures over large areas. Plasma-chemical deposition methods make it possible to form layers several nanometers thick, which play the role of both passivating and highly doped layers at relatively low temperatures on an industrial scale. A low-temperature (250–380 °C) plasma-chemical technology for the synthesis of thin GaP layers on Si [2] and the possibility of their donor doping [3] have recently been developed.

Phosphide layers were grown by atomic layer deposition (ALD) using an Oxford Plasmalab 100 PECVD setup. The InP films were deposited on p- and n-type silicon substrates at a temperature of 380 °C. Trimethylindium (TMI) was used as a source of indium and phosphine (PH₃) was used as a source of phosphorus. The decomposition of TMI was due to temperature, and the decomposition of phosphine was due to RF plasma with a power of 200 W (Fig. 1). Annealing in argon plasma was performed at the end of each cycle. The growth rate was 0.17 nm/cycle, which corresponds to the growth of 0.7 monolayers per cycle.

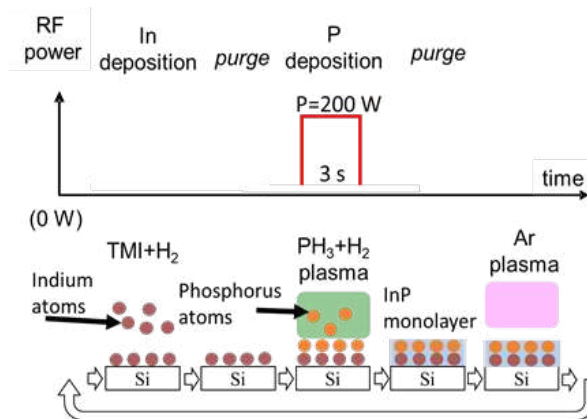


Fig. 1. Scheme of the deposition process

Results and Discussion

InP layers have a fairly rough surface with a root mean square (RMS) roughness of 3–5 nm, which is due to their microcrystalline structure. The use of intermediate annealing in Ar plasma after the stage of deposition of a phosphorus monolayer immediately before deposition of indium leads to a significant decrease in the roughness to the level of fractions of nanometers. The use of additional annealing in the Ar plasma does not lead to an increase in the growth rate. The composition of the InP layers according to energy dispersive X-ray diffraction (EDX) data was close to stoichiometric within the measurement errors.

The Raman spectra distinguish the LO peak at 341.9 cm^{-1} , which is characteristic of crystalline InP. Another L- peak characteristic of InP at 303.7 cm^{-1} merges with the response from the Si substrate at 303.44 cm^{-1} , which greatly complicates its identification [4].

Transmission electron microscopy (TEM) measurements (Fig. 2) showed that the InP film has thickness about 50 nm. A preferred orientation of the film grains is observed, consistent with the structure of the substrate. High angle annular dark-field scanning transmission microscopy (HAADF STEM) image is presented on Fig. 2, c), the sample position is on the left and on the right is the sample holding carbon glue. The EDX maps show high In and P content in deposited layer, which indicates successful InP layer growth. In addition, a layer at the interface with a small amount of O and C was detected, which can be connected with the insufficient treatment of the Si substrate before deposition process.

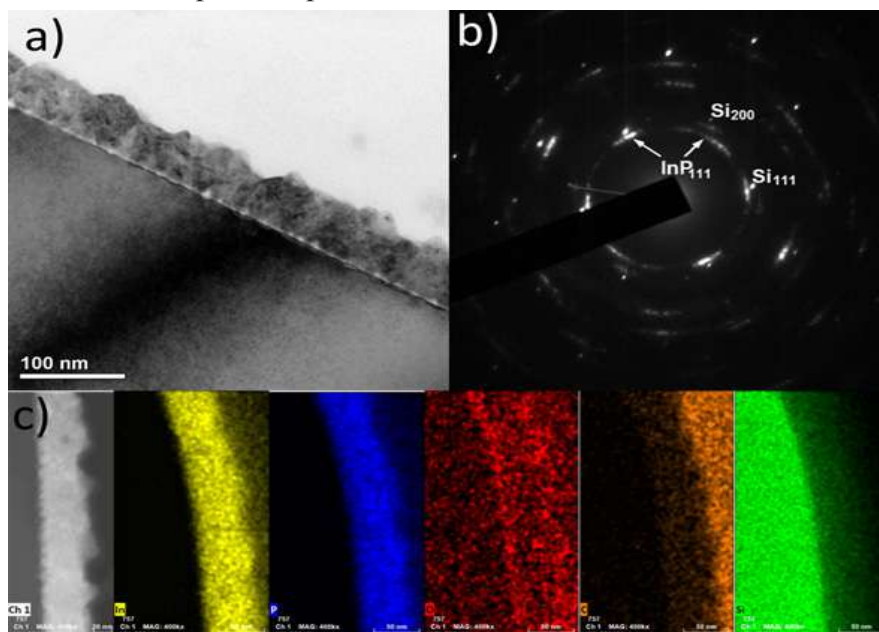


Fig. 2. TEM film images (a); electron diffraction pattern image (b); HAADF STEM image and distribution maps of the main elements (c)

To study the electrical properties of the resulting InP/Si heterojunctions to InP layers and silicon substrates, metal contacts were formed and the current-voltage characteristics (I-V) of the obtained structures were measured. An ohmic back contact to n-Si (10^{15} cm^{-3}) was formed by successive deposition of a highly doped n-GaP layer 5 nm thick and indium, while on p-Si (10^{16} cm^{-3}) indium was directly deposited without additional layers. Indium dot contacts were deposited on the front side of the InP layers.

As a result, the I-V characteristic across the InP/n-Si heterojunction has a ohmic linear form (Fig. 3), characteristic of a low resistance value, and not of a diode: this means that the resulting InP layer has a donor type of conductivity with a high concentration of free electrons. On the contrary, the dark I-V curves of InP/p-Si structure has an asymmetrical behavior: a low reverse bias current and an exponential increase in current at forward bias, which proves the presence of a p-n junction and confirms the donor type of InP layer conductivity. Further, the I-V characteristics of InP/p-Si structure under solar radiation spectrum illumination were measured, as a result of which open circuit voltage of $V_{oc} = 0.48 \text{ V}$ was obtained, which confirms the possibility of using InP-based layers for solar cells fabrication.

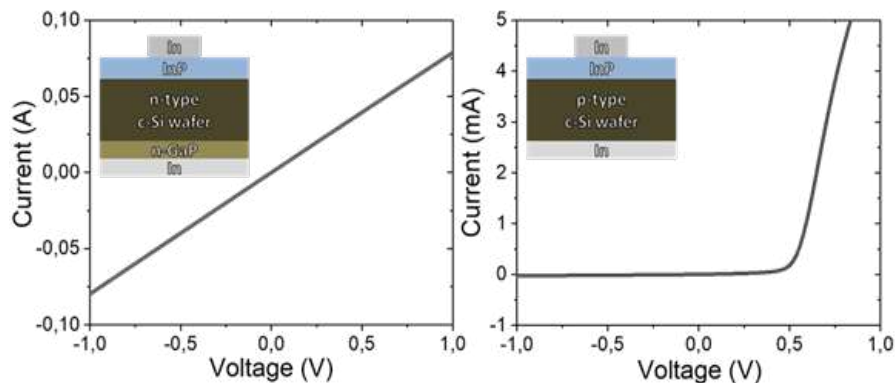


Fig. 3. Dark current-voltage characteristics for InP on n-type Si structure (a); InP on p-type Si structure (b)

Studies of electrical conductivity, type of conductivity and carrier concentration were carried out by the Van der Pauw 4-probe method at a temperature of $25 \text{ }^\circ\text{C}$ [5]. To do this, the obtained structures were divided into square samples at the corners of which point ohmic contacts to the InP layer were formed. The measurements were carried out using a measuring bench based on a Keithley 2401 precision source-meter and NdFeB permanent magnets with a uniform magnetic field of 0.56 T . Results are presented in Table 1.

Table 1

Van der Pauw measurements

	Surface resistance of the layer, Ohm/sq	Surface concentration of carriers, cm^{-2}	Carrier concentration (for $d = 50 \text{ nm}$), cm^{-3}	Carrier mobility, $\text{cm}^2/(\text{V}\cdot\text{s})$
InP/p-Si	$8.82 \cdot 10^3$	$-5.25 \cdot 10^{12}$	$-1.04 \cdot 10^{18}$	136
InP/quartz	$1.66 \cdot 10^6$	$-8.55 \cdot 10^{11}$	$-1.71 \cdot 10^{17}$	3.7

The surface resistance of InP layers on silicon and quartz substrates was $8.82 \cdot 10^3 \text{ Ohm/sq}$ and $1.66 \cdot 10^6 \text{ Ohm/sq}$, respectively. Large values of conductivity on silicon substrates are due either to the better structural properties of the InP layer or to the presence of leakage currents through the silicon substrate. The surface concentration and mobility of carriers in the InP layer are: $-5.25 \cdot 10^{12} \text{ cm}^{-2}$ and $136 \text{ cm}^2/(\text{V}\cdot\text{s})$ on silicon substrates; $-8.55 \cdot 10^{11} \text{ cm}^{-2}$ and $3.7 \text{ cm}^2/(\text{V}\cdot\text{s})$ on quartz substrates.

InP layers both on p-Si and quartz substrates have predominantly electronic type of conductivity, which indicates the absence of leakage currents through the silicon substrate with p-type conductivity. The mobility of layers on different substrates differs significantly, which also indicates the best structural properties of InP on silicon substrates. It should be noted that the resistivity of InP ($8.3 \text{ } \Omega \text{ cm}$) on quartz substrates is much lower than the resistance of GaP on quartz substrates (more than $5 \cdot 10^3 \text{ } \Omega \text{ cm}$) obtained by the same method.



Conclusion

In this work, a technology was developed to deposit layers of indium phosphide (InP) by plasma-chemical atomic layer deposition using trimethylindium (TMI) and phosphine as precursors.

RMS measurements showed that the use of intermediate annealing in Ar plasma after the stage of deposition of a phosphorus monolayer leads to a significant decrease in roughness to the level of fractions of nanometers and does not lead to an increase in the growth rate. A preferred orientation of the film grains is observed, consistent with the structure of the substrate by TEM measurements.

The measurements of dark IV characteristics showed that the InP layer has a donor type of conductivity. I–V characteristics of InP/p-Si structure under solar radiation spectrum illumination were measured, as a result of which open circuit voltage of $V_{oc} = 0.48$ V was obtained. Comparative measurements of the conductivity of InP layers on quartz and silicon indicate better mobility on silicon substrates than on quartz, which indicates their best structural properties. Thus, it is possible to use InP-based layers to create solar cells.

REFERENCES

1. Green M.A. et al., Solar cell efficiency tables (version 27), Prog. Photovolt.: Res. and Appl. 14 (2006) 45–57.
2. Gudovskikh A. S., Morozov I. A., Uvarov A. V., Kudryashov D. A., Nikitina E. V., Bukatin A. S., Kleider J.-P., Low temperature plasma enhanced deposition of GaP films on Si substrate, Journal of Vacuum Science & Technology A: Vacuum, Surfaces, and Films. 36 (2) (2018) 021302.
3. Gudovskikh A. S., Uvarov A. V., Morozov I. A., Baranov A. I., Kudryashov D. A., Zelentsov K. S., Kleider J.-P., Interface Properties of GaP/Si Heterojunction Fabricated by PE-ALD, Physica Status Solidi (a). (2018) 1800617.
4. Pierścińska D., Pierściński K., Sobczak G., Krajewska K., Chmielewski K., Kuźmicz A., Piskorski K., Gutowski P., In-Depth Experimental Analysis of Influence of Electroplated Gold Thickness on Thermal and Electro-Optical Properties of Mid-IR AlInAs/InGaAs/InP Quantum Cascade Lasers. Materials. 14 (2021) 7352.
5. van der Pauw L. J., Philips Res. Rep. 13 1 (1958).

THE AUTHORS

MAKSIMOVA Alina A.
maksimova_alina@spbau.ru
ORCID: 0000-0002-3503-7458

UVAROV Alexander V.
lumenlight@mail.ru
ORCID: 0000-0002-0061-6687

KIRILENKO Demid A.
demid.kirilenko@mail.ioffe.ru
ORCID: 0000-0002-1571-209X

BARANOV Artem I.
itiomchik@yandex.ru
ORCID: 0000-0002-4894-6503

VYACHESLAVOVA Ekaterina A.
cate.viacheslavova@yandex.ru
ORCID: 0000-0001-6869-1213

GUDOVSKI KH Alexander S.
gudovskikh@spbau.ru
ORCID: 0000-0002-7632-3194

Received 01.08.2022. Approved after reviewing 05.08.2022. Accepted 05.08.2022.

Conference materials

UDC 681.2

DOI: <https://doi.org/10.18721/JPM.153.324>

Monitoring of overhead power lines in real time

V. A. Listyukhin ¹✉, E. A. Pecherskaya ¹, P. E. Golubkov ¹,
V. S. Alexandrov ¹, A. E. Shepeleva ¹

¹ Penza State University, Penza, Russia

✉ nauka-fpите@mail.ru

Abstract. Based on the application of quality control methods, an analysis of the technological disturbances (accidents) causes on overhead power lines with a voltage in the range from 0.4 to 110 kV AC was made. The main causes of accidents on overhead lines were systematized. The need to control the operational parameters of overhead lines that affect the sustainable functioning of electric power systems has been proved. The structure of the information-measuring system for monitoring the overhead lines parameters has been developed. The purpose of its implementation is to ensure a reliable power supply to consumers, improve the level of operational and technological control of networks and reduce the economic costs of eliminating the consequences of accidents in electrical networks.

Keywords: overhead power lines, electric power systems, accelerometer, information-measuring systems, automation, digitalization, monitoring, parameter control, reliability

Funding: Rector's grant of Penza State University "Development of an information and measurement system for monitoring parameters of overhead power lines" No. ХП-213/22 dated 03/31/2022.

Citation: Listyukhin V. A., Pecherskaya E. A., Golubkov P. E., Aleksandrov V. S., Shepeleva A. E., Monitoring of overhead power lines in real time. St. Petersburg State Polytechnical University Journal. Physics and Mathematics, 15 (3.3) (2022) 128–133. DOI: <https://doi.org/10.18721/JPM.153.324>

This is an open access article under the CC BY-NC 4.0 license (<https://creativecommons.org/licenses/by-nc/4.0/>)

Материалы конференции

УДК 681.2

DOI: <https://doi.org/10.18721/JPM.153.324>

Мониторинг воздушных линий электропередачи в режиме реального времени

В. А. Листюхин ¹✉, Е. А. Печерская ¹, П. Е. Голубков ¹,
В. С. Александров ¹, А. Е. Шепелева ¹

¹ Пензенский Государственный Университет, Пенза, Россия

✉ nauka-fpите@mail.ru

Аннотация. На основе применения методов контроля качества выполнен анализ причин технологических нарушений (аварий) на воздушных линиях электропередачи напряжением в диапазоне от 0.4 до 110 кВ переменного тока. Систематизированы основные причины аварий на воздушных линиях. Доказана необходимость контроля эксплуатационных параметров воздушных линий, оказывающих влияние на устойчивое функционирование электроэнергетических систем. Разработана структура информационно-измерительной системы контроля параметров воздушных линий. Целью ее внедрения является обеспечение надёжного электроснабжения потребителей, усовершенствование уровня оперативно-технологического управления сетями и снижение экономических затрат на ликвидацию последствий аварий в электрических сетях.



Ключевые слова: воздушные линии электропередачи, электроэнергетические системы, акселерометр, информационно-измерительные системы, автоматизация, цифровизация, мониторинг, контроль параметров, надежность

Финансирование: Ректорский грант Пензенского государственного университета «Разработка информационно-измерительной системы контроля параметров воздушных линий электропередачи» № ХП-213/22 от 31.03.2022 года.

Ссылка при цитировании: Листюхин В. А., Печерская Е. А., Голубков П. Е., Александров В. С., Шепелева А. Э., Мониторинг воздушных линий электропередачи в режиме реального времени // Научно-технические ведомости СПбГПУ. Физико-математические науки. 2022. Т. 15. № 3.3. С. 128–133. DOI: <https://doi.org/10.18721/JPM.153.324>

Статья открытого доступа, распространяемая по лицензии CC BY-NC 4.0 (<https://creativecommons.org/licenses/by-nc/4.0/>)

Introduction

The current development pace of science and technology makes it possible to create conditions for the sustainable functioning of electric power systems (EPS). Network companies introduce modern types of equipment, elements, devices that have high technical and economic indicators at their facilities [1]. Also, today in a number of the Russian Federation regions there is a tendency to increase the volume of electricity consumption in rural areas. This is due to the development of agricultural enterprises, an increase in the number of consumer electronic devices, the growth of tourist bases and recreation centers. Based on the foregoing, not only the technological development of power supply systems, but also ensuring their reliability becomes relevant.

To date, the main part of the equipment in operation in rural distribution networks has a high level of wear and tear [2–4], which excludes guarantees of reliable power supply to consumers from grid organizations. The high level of accidents in the EPS, in turn, leads to significant economic costs. In view of the design, overhead power lines (OHL) are the most vulnerable elements of the EPS, which have the greatest impact on the reliability of power supply to consumers [5]. A lot of research has been directed to solving the problems of ensuring the stable functioning of overhead lines. For example, in [14], the authors proposed an intelligent system for melting ice on the wires of overhead power lines. In [15], the authors considered the use of sensor networks technology to increase the observability and controllability of overhead power lines during operation. Research [16] is aimed at applying technologies and techniques based on the radar method and ice detection equipment on overhead power lines, first introduced at electrical substations in Russia. A method for controlling wires of overhead lines by analyzing their twisting is proposed in [17]. Based on the analysis of statistical data on the causes and consequences of accidents on overhead lines, the authors propose the development and implementation of an information-measuring system for monitoring parameters that affect the stable operation of overhead lines.

Materials and Methods

When developing a block diagram of the proposed information-measuring system for monitoring the parameters of overhead power transmission lines, methods of the theory of electrical circuits, circuitry, and metrological analysis were used.

Results and Discussion

The authors analyzed the accident rate in the power grid complex [6]. Figure 1 shows a diagram of the distribution of electrical equipment damage by electrical installations types.

Based on the analysis of the damage distribution to electrical equipment by electrical installations types, it can be concluded that overhead lines are the most damaged elements of the EPS, which is about 94% of the total number of accidents. Figure 2 shows a diagram of the causes of the main accidents on overhead lines.

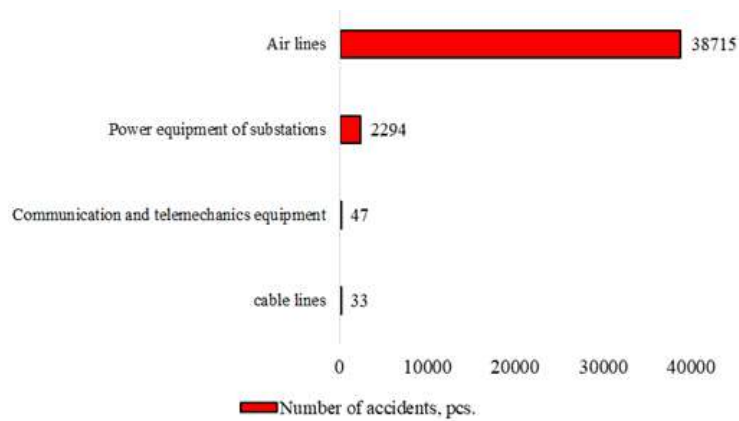


Fig.1. Diagram of electrical equipment damage distribution by electrical installations types

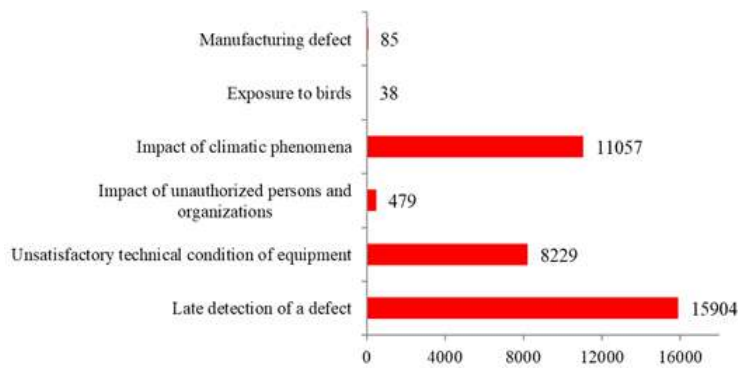


Fig.2. Diagram of the main causes of accidents on overhead lines

Based on the analysis of the number and causes of technological disturbances (accidents) in electrical networks with voltage in the range from 0.4 to 110 kV AC, the following main causes of overhead line failures were identified:

- 44.43% of the total number of accidents occur due to late defects detection;
- 31% of the total number of accidents occur due to the impact of climatic phenomena;
- 23% of the total number of accidents occur due to the unsatisfactory technical condition of the equipment due to aging, changes in the properties and the material structure.

Figure 3 shows a histogram of the percentage distribution of damage causes from the total number of accidents on overhead lines.

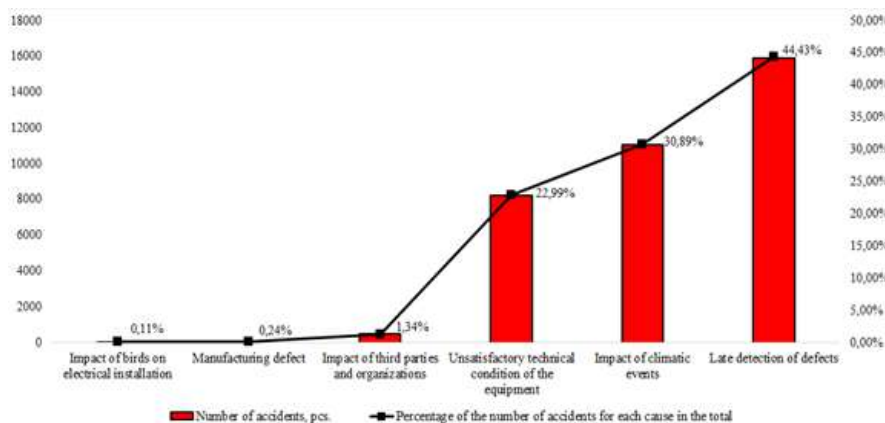


Fig.3. Histogram of the percentage distribution of damage causes from the total number of accidents on overhead lines



In order to reduce the number of technological disturbances at the facilities of the power grid complex, improve network monitoring indicators, as well as to improve the services quality provided to consumers for the transmission of electrical energy, the authors propose the development and implementation of an information-measuring system (IMS) for monitoring the overhead lines parameters.

During the overhead lines operation, the IMS monitors the parameters that affect its stable operation, namely: control of the wire sag; ambient temperature control; wind speed control. In parallel, short circuit indicators (SIC) on the line can be used to determine the overhead line operation mode and increase the network observability. Table 1 presents the characteristics of the IMS measuring channels.

Table 1

Characteristics of the IMS measuring channels

Channel name	Measuring device name	Measured value	Measurement range	Limits of permissible absolute error
Distance measurement channel	Laser distance meter	Distance	0.5–35 m	± 0.1
Ambient temperature measurement channel	Hot-wire anemometer	Ambient temperature	-45–+45 °C	± 0.5
Channel for measuring the wind loads speed	Hot-wire anemometer	Speed	0–30 m/s	± 1
Fault location	Fault indicator	Short circuit direction	20–120 A	± 1

The authors analyzed the possibility of controlling the wire sag using the following methods: 3D modeling, optical, capacitive, mechanical, frequency, thermodynamic, inclinometric. Based on the results of the analysis, a device was selected based on the inclinometric method. The device proposed earlier in [5] based on the optical method (laser rangefinder) has a number of disadvantages, namely, in terms of installation complexity and dependence on external natural factors (fog, heavy rain and snowfall). Thus, it is proposed to use the MPU-6050 device, which includes a three-axis gyroscope and a three-axis accelerometer on a single silicon chip, as well as an integrated Digital Motion Processor (DMP) as a primary measuring transducer for monitoring the wire position.

The functionality of this device allows to control the position and movement of the controlled object (overhead line wires) in space (tilt angles, trim) based on the vector of gravity and rotation speed.

Table 2

The MPU-6050 characteristics

Characteristic name	Measurement range	Unit
Supply voltage	3.7–5.5	V
Current consumption	≤ 10	mA
Maximum I2C interface frequency	400	kHz
Gyro Range	$\pm 250 - \pm 2000$	deg/s
Accelerometer range	$\pm 2, \pm 4, \pm 8$ and ± 16	g
Data output	16	bit
Resonance frequency	27	kHz
Distance between contacts	2.54	mm
Size	20×16	mm

At the same time, the temperature is measured. When moving, linear acceleration and angular velocity along three axes are determined. The MPU-6050 chip contains two devices: an accelerometer and a gyroscope. Their data is pre-processed and transmitted via the I2C serial interface to the microcontroller. A complex of a gyroscope and an accelerometer is used to stabilize an object in a required position under external influences. The MPU-6050 device characteristics are presented in the table.

Conclusion

Improving the power supply reliability to consumers is possible through the use of the proposed information-measuring network, which includes the following measuring channels: a channel for measuring the wind loads speed, a channel for measuring distance, a channel for measuring ambient temperature, a channel for determining the location of a fault. The information-measuring system enables electric grid companies to solve a number of operational tasks, namely:

- identify defective areas in a timely manner;
- reduce the time of power supply restoration to consumers.

The IMS use is expedient in the operational maintenance and electrical networks management.

REFERENCES

1. **Khlebtsov A. P., Zaynutdinova L. K., Shilin A. N.**, Research into the current state of accident rate of electric networks in agriculture using the example of Astrakhan region, IOP Conference Series: Earth and Environmental Science, 723 (5) (2021) 052015.
2. **Kondrateva O., Myasnikova E., Loktionov O.**, Analysis of the Climatic Factors Influence on the Overhead Transmission Lines, Reliability Environmental and Climate Technologies, 24 (3) 201-214.
3. **Kuchanskyy V., Malakhatka D., Zaporozhets A.**, Operating Modes Optimization of Bulk Electrical Power Networks: Structural and Parametrical Methods, Power Systems Research and Operation. Studies in Systems, Decision and Control 388, 2022.
4. **Feng D., Yu Q., Sun X., Zhu H., Lin S., Liang J.**, Risk Assessment for Electrified Railway Catenary System Under Comprehensive Influence of Geographical and Meteorological Factors, IEEE Transactions on Transportation Electrification, 7 (4) (2021) 3137–3148.
5. **Listyuhin, V. A., Pecherskaya, E. A., Timokhina, O. A., Smogunov, V. V.**, System for monitoring the parameters of overhead power lines, Journal of Physics: Conference Series, 2086 (1) (2021) 012059.
6. **Listyukhin V. A., Pecherskaya E. A., Safronova O. A., Artamonov D. V.**, Systematization and monitoring of quality parameters of overhead power transmission lines functioning, IOP Conf. Series: Earth and Environmental Science, 990 (2022) 012058. doi:10.1088/1755-1315/990/1/012058.
7. **Gupta S. D., Kundu S., Mallik A.**, Monitoring of sag & temperature in the electrical power transmission lines, International Journal of Recent Technology and Engineering (IJRTE), 1 (4) (2012) 43–45.
8. **Khasanov S. R. et al.**, Reliability modeling of high-voltage power lines in a sharply continental climate, E3S Web of Conferences. EDP Sciences, 178 (2020) 01051.
9. **Wydra M. et al.**, Overhead transmission line sag estimation using a simple optomechanical system with chirped fiber bragg gratings. Part 1: Preliminary measurements, Sensors, 18 (1) (2018) 309.
10. **Zangl H., Bretterkieber T., Brasseur G.**, A feasibility study on autonomous online condition monitoring of high-voltage overhead power lines, IEEE Transactions on Instrumentation and Measurement, 58 (5) (2009) 1789–1796.
11. **Golubkov P., Pecherskaya E., Karpanin O., Safronov M., Shepeleva J. Bibarsova A.**, 2019 “Intelligent Automated System of Controlled Synthesis of MAO-Coatings”. 24th Conference of Open Innovations Association (FRUCT), 2019, 96–103.
12. **Li V., Demina L., Vlasenko S.**, Determination of the Current State and Forecast of the Remaining Life of the Catenary Supports of Electrified Railways In: Shamtsyan M., Pasetti M., Beskopylny A. (eds). Robotics, Machinery and Engineering Technology for Precision Agriculture. Smart Innovation, Systems and Technologies 247, 2022.
13. **Zakharov S. et al.**, Analysis of accidents in 6-110 kV electric networks of Kuzbass power system, E3S Web of Conferences. EDP Sciences, 41 (2018) 03015.



14. **Levchenko I. I., Satsuk E. I., Shovkoplyas S. S.**, “Intellectual Ice Melting System on Wires of Overhead Transmission Lines of Distribution Electric Networks”, International Russian Automation Conference (RusAutoCon), 2019, pp. 1–7. doi: 10.1109/RUSAUTOCON.2019.8867692.

15. **Ivanov D. et al.**, The application of the technology of sensor networks for the intellectualization of the overhead power transmission lines, E3S Web of Conferences. – EDP Sciences, 220 (2020) 01071.

16. **Minullin R. G., Kasimov V. A., Yarullin M. R.**, “Multichannel radar control of icing on wires overhead transmission lines”, 2016 2nd International Conference on Industrial Engineering, Applications and Manufacturing (ICIEAM), 2016, pp. 1–6. doi: 10.1109/ICIEAM.2016.7911425.

17. **Yaroslavsky D. A., Ivanov D. A., Nguyen V.**, “Wire Torsion Measurement for the Tasks of Monitoring of the Mechanical State of Overhead Power Transmission Line”, International Conference on Industrial Engineering, Applications and Manufacturing (ICIEAM), 2020, pp. 1–5. doi: 10.1109/ICIEAM48468.2020.9111999.

THE AUTHORS

LISTYUKHIN Vladislav A.

Vladyan4iklist@yandex.ru

ORCID: 0000-0002-5885-9403

ALEXANDROV Vladimir S.

vsalexrus@gmail.com

ORCID: 0000-0002-1300-7901

PECHERSKAYA Ekaterina A.

peal@list.ru

ORCID: 0000-0001-5657-9128

SHEPELEVA Anastasiya E.

eduard.shepelev.67@mail.ru

ORCID: 0000-0002-8600-084X

GOLUBKOV Pavel E.

golpavpnz@yandex.ru

ORCID: 0000-0002-4387-3181

Received 12.07.2022. Approved after reviewing 15.07.2022. Accepted 08.09.2022.

Conference materials
UDC 621.382.323
DOI: <https://doi.org/10.18721/JPM.153.325>

GaN IC E-mode p-channel and n-channel transistors simulation

V. I. Egorkin¹, V. E. Zemlyakov¹, A. A. Zaitsev¹, O. B. Chukanova¹✉

¹ National Research University of Electronic Technology, Moscow, Russia

✉ Kukhtuaeva@mail.ru

Abstract. This article demonstrates TCAD simulation of normally-off p-channel and n-channel transistors based on a p-GaN gate power platform and estimates interconnections between the key parameters of the heterostructure and device behavior, in other words the type of transistor. GaN platform with p-GaN layer has been developed. It will allow to form n-channel and p-channel, normally-on and normally-off transistors on the same wafer in the same technological cycle and to create GaN complementary pair.

Keywords: GaN, high electron mobility transistor, normally-off transistor, complementary pair, integrated circuit

Funding: This work was supported by FASIE (agreement No. 68ГУРЭС14/72798 from 29.12.2021).

Citation: Egorkin V. I., Zemlyakov V. E., Zaitsev A. A., Chukanova O. B., GaN IC E-mode p-channel and n-channel transistors simulation. St. Petersburg State Polytechnical University Journal. Physics and Mathematics, 15 (3.3) (2022) 134–137. DOI: <https://doi.org/10.18721/JPM.153.325>

This is an open access article under the CC BY-NC 4.0 license (<https://creativecommons.org/licenses/by-nc/4.0/>)

Материалы конференции
УДК 621.382.323
DOI: <https://doi.org/10.18721/JPM.153.325>

Моделирование GaN n-канальных и p-канальных нормально-закрытых транзисторов для монолитных схем

В. И. Егоркин¹, В. Е. Земляков¹, А. А. Зайцев¹, О. Б. Чуканова¹✉

¹ Национальный исследовательский университет «МИЭТ», Москва, Россия

✉ Kukhtuaeva@mail.ru

Аннотация. В данной статье продемонстрировано моделирование нормально закрытых p-канальных и n-канальных транзисторов на основе GaN платформы с p-GaN слоем, а также предложена методика оценки типа прибора по его ключевым параметрам гетероструктуры. Разработана конструкция гетероструктуры для формирования GaN платформы с p-GaN слоем, которая позволит формировать приборы различного типа в едином технологическом цикле на единой подложке, а также создать комплементарную пару на основе GaN приборов.

Ключевые слова: GaN, нормально-закрытый транзистор, НЕМТ, комплементарная пара, монолитная интегральная схема

Финансирование: Работа выполнена в рамках договора с Фондом содействия инновациям (соглашение № 68ГУРЭС14/72798 от 29.12.2021 г.).

Ссылка при цитировании: Егоркин В. И., Земляков В. Е., Зайцев А. А., Чуканова О. Б., Моделирование GaN n-канальных и p-канальных нормально-закрытых транзисторов для монолитных схем // Научно-технические ведомости СПбГПУ. Физико-математические науки. 2022. Т. 15. № 3.3. С. 134–137. DOI: <https://doi.org/10.18721/JPM.153.325>



Статья открытого доступа, распространяемая по лицензии CC BY-NC 4.0 (<https://creativecommons.org/licenses/by-nc/4.0/>)

Introduction

In the past time GaN-based devices have been widely used in electronics due to development of GaN technology. Many of the challenges have been decided, for example, formation of normally-off GaN transistor. But there are still problems with high inductance between the gate electrode and driver circuit and power consumption in power electronic systems and circuits. To overcome this problem monolithic integration of driver circuit and power transistor on the same chip is offered in this article.

There has been a number of articles which demonstrate GaN-based power integrated circuits (IC) [1], but they demonstrate integration of two types – normally-on and normally-off – n-channel transistors. These circuits have disadvantage namely static power dissipation. A complementary circuit technology is needed. The technology advantages are reduction of the circuit complexity, zero power consumption, higher noise immunity and linearity [2]. This article demonstrates simulation of epitaxial structure based on p-GaN gate GaN-on-Si platform that have many advantages, such as large wafer size and low cost.

The GaN ICs allow to form high-frequency reliable power supplies with high efficiency and low cost. Also, the circuits can be widely used in AC/DC and DC/DC converters, increasing their efficiency and power density. Developed product will be used in radar systems, equipment for cellular communication systems, radio relay communication lines, navigation, telecommunications.

Materials and Methods

Based on [3–4] the constructions have been simulated. Simulation has been done with Sentaurus Technology Computer Aided Design (TCAD). The heterostructure pre-analysis was carried out on the solution of statistical problem of the charge carrier distribution in the structure basis. In such systems conduction channel is formed in quantum well on the GaN/AlGaN interface. To calculate carrier channel concentration it is needed to solve quantum-mechanical problem, but quite acceptable accuracy is obtained using the simplest approach based on classical equations in the diffusion-drift approximation. Preliminary estimates can be made based only on a static one-dimensional problem solving the Poisson equation. Thus, we can find normally-off transistor behavior conditions, estimate the transistor threshold voltage V_{th} at which conduction channel is formed.

The problem current transfer is decided to describe the current-voltage characteristics in details [5]. It is known, that calculation of structures including wide gap semiconductor layers, like GaN, has poor convergence. Calculations taking into account the charge carrier heating and the lattice temperature increase are managed to do only in rather narrow range of voltages at the contacts. At the same time results of calculations considering carrier heating have a little differences from results obtained in diffusion–drift approximation at the stage of linear growth of I_d (V_d) up to saturation. In our task we will use diffusion–drift approximation and consider relatively low voltages V_d .

First of all, p-GaN gate n-channel transistor has been simulated. The critical thickness of p-GaN layer is about 70 nm. Choosing p-GaN thickness about 100 nm dependence of type n-channel transistor on AlGaN barrier layer (t_b) and Al mole fraction (x) of this layer has been estimated (Fig. 1) as parameters of AlGaN barrier layer are key parameters determining the type of transistor – normally-on or normally-off. The thickness of AlGaN layer should be as small as possible to provide normally-off behavior.

The heterostructure p-GaN (80 nm)/ $Al_{0.23}GaN$ (15 nm)/ GaN channel / AlGaN buffer/ AlN / Si has been chosen as basic. Mg concentration in p-GaN layer is about $10^{18}sm^{-2}$. These parameters provide normally-off behavior of n-channel p-gate transistor.

To form normally-off p-channel GaN FET n+-GaN is grown on top of p-GaN layer. It's structure with two channels of different carriers. Hole-channel is basic and electron-channel is closed as this transistor works at negative voltages. Space charge region (SCR) of n+-GaN/p-GaN

junction provides normally-off behavior of the device but for certain construction. Thickness of n+-GaN layer and its concentration weakly influence on SCR width. The n+-GaN thickness is 50 nm and impurity concentration in it is about 10^{19}sm^{-2} . Dependence of type p-channel device on p- layer thickness and its activated impurity concentration also has been estimated (Fig. 2). Red region is region in which parameters of p-GaN layer might be chosen to form normally-off p-channel transistor so n-channel transistor is normally-off too. Thus, evaluation methodology of device behavior has been developed and optimal heterostructure for complimentary pair has been chosen.

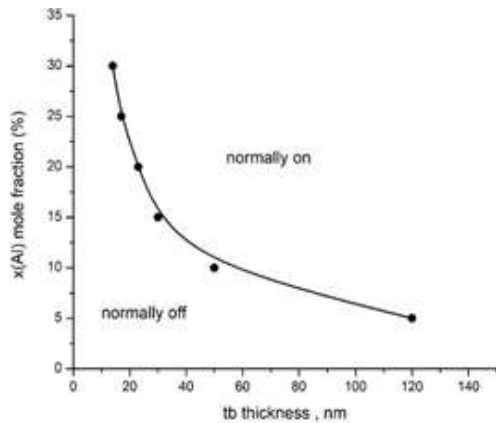


Fig. 1. Dependence of type n-channel transistor on AlGaN barrier layer (t_b) and Al mole fraction (x) of this layer

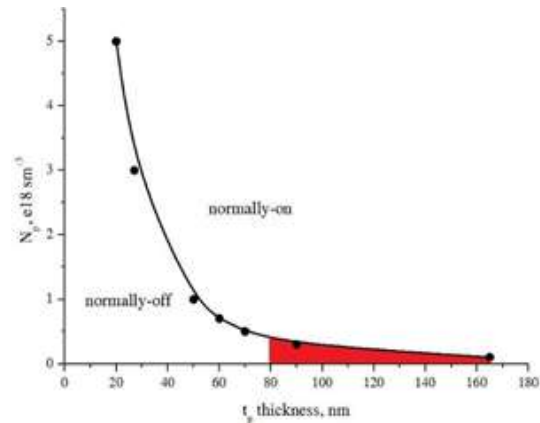


Fig. 2. Dependence of type p-channel device on p-layer thickness and its activated impurity concentration

Results and Discussion

According to the methodology heterostructure design of p-GaN (80 nm)/ $\text{Al}_{0.23}\text{GaN}$ (15 nm)/ GaN channel / AlGaN buffer/ AlN / Si has been chosen. P-GaN gate power platform will include normally-on n-channel transistor, normally-off n-channel p-gate transistor and normally-off p-channel transistor. Simulation of devices shows that the n-channel device with gate length and gate-to-source length about 1 μm ($L_g = L_{gs} = 1 \mu\text{m}$) and gate-to-drain length about 6 μm ($L_{gd} = 6 \mu\text{m}$) has threshold voltage V_{th} is about 1.5 V and maximum drain current in open state is about 400 mA/mm at 4 V on the gate that doesn't contradict our previous result [3]. The p-channel device with gate, gate- to-source and gate-to-drain lengths about 1 μm ($L_g = L_{gs} = L_{gd} = 1 \mu\text{m}$) has threshold voltage V_{th} is about -1V and maximum drain current in open state is about -0.9 mA/mm at -3 V on the gate (Fig. 4).

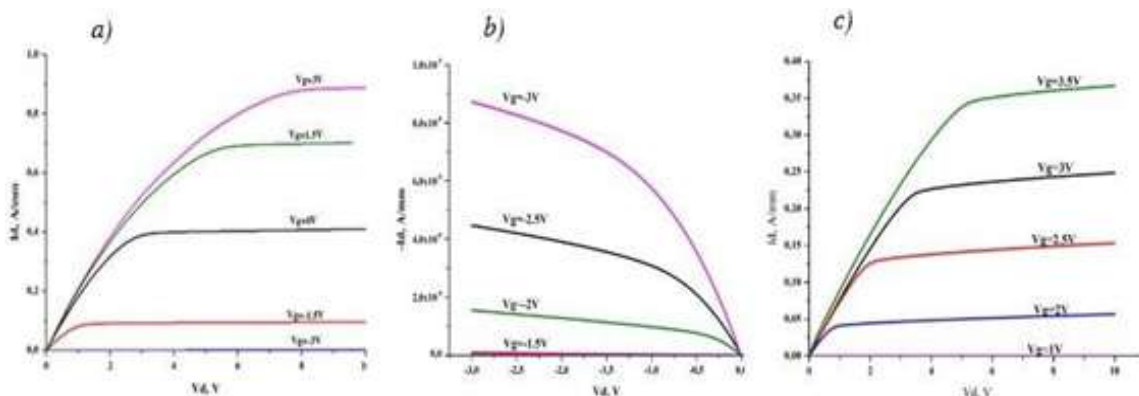


Fig. 4. Current-voltage characteristics of developed devices: *a*) normally-on n-channel HEMT, *b*) normally-off p-channel FET, *c*) normally-off n-channel p-gate HEMT.



Conclusion

Thus simulation of p-gate GaN platform has been demonstrated. It is shown that design of transistor heterostructure can be chosen with proposed methodology. Simulated transistors have an acceptable characteristic and don't contradict our previous result. Such approach allows form different type transistors on the same wafer in a single technological cycle and reduces assembly circuit time.

REFERENCES

1. Li X., Geens K., Guo W., You Sh., Zhao M., Fahle D., Odnoblyudov V., Groeseneken G., Decoutere St., Demonstration of GaN Integrated Half-Bridge With On-Chip Drivers on 200-mm Engineered Substrates, IEEE Electron Device Letters, 40 (9) (2019) 1499–1502.
2. Chowdhury N., Xie Q., Yuan Q., Cheng K., Then H., Palacois T., Regrowth-Free GaN-Based Complementary Logic on a Si Substrate, IEEE Electron Device Letters, 41 (99) (2020) 99–102.
3. Kukhtyaeva O. B., Egorkin V. I., Zemlyakov V. E., Kapaev V. V., Zaitsev A. A., Tsatsulnikov A. F., Nikolaev A. E., Sakharov A. V., Developing of normally-off p-GaN gate HEMT, In: Journal of Physics Conference Series, Saint-Petersburg, 22–25 April 2019. 1410 (2019) 012192.
4. Kukhtyaeva O. B., Egorkin V. I., Zemlyakov V. E., Kapaev V. V., Zaitsev A. A., GaN power IC normally-on and normally-off transistors technology and simulation, In: Journal of Physics Conference Series, Saint-Petersburg, 25–28 May 2021. 2086 (2021) 012058.
5. Synopsys Sentaurus TCAD, Synopsys Inc., Sentaurus Device User Guide, 2016.

THE AUTHORS

EGORKIN Vladimir I.
egorkinvi1962@mail.ru
ORCID: 0000-0002-2458-662X

ZEMLYAKOV Valery E.
vzml@rambler.ru
ORCID: 0000-0001-5681-9603

CHUKANOVA Olga B.
Kukhtuaeva@mail.ru
ORCID: 0000-0001-5726-630X

ZAITSEV Alexey A.
ziko27@yandex.ru

Received 12.08.2022. Approved after reviewing 15.08.2022. Accepted 16.08.2022.

Conference materials

UDC 53

DOI: <https://doi.org/10.18721/JPM.153.326>

Development of technological methods for fabrication high-density luminescent structures based on up-conversion NaYF₄:Yb³⁺, Er³⁺ particles

N. A. Vovk ^{1,2}✉, I. M. Asharchuk ², E. R. Timofeeva ², I. A. Filippov ²,
E. V. Zenova ², K. V. Smirnov ^{1,2}, M. A. Tarkhov ²

¹ National Research University Higher School of Economics, Moscow, Russia;

² Institute of Nanotechnologies of Microelectronics Russian Academy of Sciences, Moscow, Russia

✉ navovk_1@edu.hse.ru

Abstract. In this paper, we present a technological method for creating high-density luminescent structures based on up-conversion NaYF₄:Yb³⁺, Er³⁺ particles and experimentally demonstrate the possibility of their creation. This technology is applicable for large-scale fabrication of patterned media with a level of filling with microparticles of more than 96% for the fabrication of planar structures applicable in photonics and optoelectronics.

Keywords: up-conversion, luminescence, microparticles

Funding: The work was supported by GK No. 20411.1950192501.11.003. Code “Progress”.

Citation: Vovk N. A., Asharchuk I. M., Timofeeva E. R., Filippov I. A., Zenova E. V., Smirnov K. V., Tarkhov M. A., Development of technological methods for fabrication high-density luminescent structures based on Up-conversion NaYF₄:Yb³⁺, Er³⁺ particles. St. Petersburg State Polytechnical University Journal. Physics and Mathematics, 15 (3.3) (2022) 138–141. DOI: <https://doi.org/10.18721/JPM.153.326>

This is an open access article under the CC BY-NC 4.0 license (<https://creativecommons.org/licenses/by-nc/4.0/>)

Материалы конференции

УДК 53

DOI: <https://doi.org/10.18721/JPM.153.326>

Разработка технологических методов для создания высокоплотных люминесцентных структур на основе ап-конверсионных NaYF₄:Yb³⁺, Er³⁺ частиц

Н. А. Вовк ^{1,2}✉, И. М. Ашарчук ², Е. Р. Тимофеева ², И. А. Филиппов ²,
Е. В. Зенова ², К. В. Смирнов ^{1, 2}, М. А. Тархов ²

¹ Национальный исследовательский университет “Высшая школа экономики”, Москва, Россия;

² Институт нанотехнологий микроэлектроники Российской академии наук, Москва, Россия

✉ navovk_1@edu.hse.ru

Аннотация. В данной работе представлен технологический метод создания высокоплотных люминесцентных структур на основе ап-конверсионных NaYF₄:Yb³⁺, Er³⁺ частиц и экспериментально продемонстрирована возможность их создания. Данная технология применима для крупномасштабного изготовления патернированных сред с уровнем заполнения микрочастицами более 96% для изготовления планарных структур, применимых в фотонике и оптоэлектронике.

Ключевые слова: апконверсия, люминесценция, микрочастицы

Финансирование: Работа выполнена в рамках ГК № 20411.1950192501.11.003. Код «Прогресс».



Ссылка при цитировании: Вовк Н. А., Ашарчук И. М., Тимофеева Е. Р., Филиппов И. А., Зенова Е. В., Смирнов К. В., Тархов М. А., Разработка технологических методов для создания высокоплотных люминесцентных структур на основе ап-конверсионных $\text{NaYF}_4:\text{Yb}^{3+}, \text{Er}^{3+}$ частиц // Научно-технические ведомости СПбГПУ. Физико-математические науки. 2022. Т. 15. № 3.3. С. 138–141. DOI: <https://doi.org/10.18721/JPM.153.326>

Статья открытого доступа, распространяемая по лицензии CC BY-NC 4.0 (<https://creativecommons.org/licenses/by-nc/4.0/>)

Introduction

Up-conversion nanoparticles doped with lanthanides are capable of converting excitation in the near infrared region into visible and ultraviolet radiation [1]. Their unique optical properties are a promising class of materials for a wide range of applications such as fluorescence microscopy, deep tissue bioimaging, nanomedicine, optogenetics, security labeling, and volumetric imaging. When microparticles are pumped with IR radiation at a wavelength of 980 nm, a pixel for a display can be obtained, the luminescence wavelength of which will depend on the chemical element with which NaYF_4 particles are doped [2]. In this work, methods have been developed that make it possible to deterministically place $\text{NaYF}_4:\text{Yb}^{3+}, \text{Er}^{3+}$ microparticles in a patterned environment matrix with a high filling density. The small dispersion of microparticles by size allows filling the patterned environment with a high fill rate of $> 96\%$.

Experimental technique

The method of forming high-density luminescent structures is based on the principle of filling with $\text{NaYF}_4:\text{Yb}^{3+}, \text{Er}^{3+}$ particles pre-prepared arrays of holes on arbitrary substrates. To demonstrate the possibilities of creating luminescent structures, silicon wafers with thermal oxide 100 mm in diameter were chosen as substrates. At the first stage of creating a high-density luminescent structure, a pattern of the patterned environment was formed in the AZ4999 photoresist using a Heidelberg DWL 2000 laser lithograph, followed by development in a 0.7% KOH solution. When applying the photoresist, the thermal oxide plate was processed in GMDS to improve the adhesion characteristics during the process of applying the photoresist by spin coating. The thickness of the photoresist was 600 nm. Next, the thermal oxide was etched through the formed mask by plasma-chemical etching in C_4F_8 gas. To further fill the wells formed in thermal silicon oxide, an aqueous suspension of $\text{NaYF}_4:\text{Yb}^{3+}, \text{Er}^{3+}$ particles and hexane was formed. The weight ratio of particles to hexane was 1:10,000 times, respectively. The next step in the formation of a high-density luminescent structure was to place a 100 mm plate with holes formed in thermal oxide into the suspension and keep it there for several hours (Fig. 1). Due to the natural settling of particles on the surface, a uniform layer was formed; the technology is similar to the deposition of carbon nanotubes [3]. Part of the $\text{NaYF}_4:\text{Yb}^{3+}, \text{Er}^{3+}$ particles also fell into pre-prepared wells. The final technological step in the formation of the final structure was the removal of “extra” particles by the method of hydrodynamic cleaning under the action of a high-pressure water jet. Particles that got into the holes due to surface forces were kept in them, and the rest of the particles are removed.

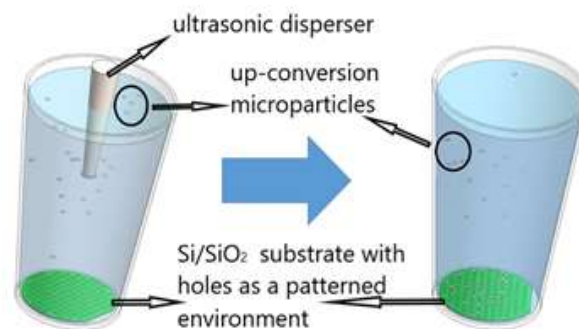


Fig. 1. Method of particle deposition in suspension by gravity on a 100 mm Si/SiO_2 substrate

To demonstrate the effect of luminescence of the structures, we used an installation consisting of a 20X magnification objective with a focal length of 20 mm. For quasi-dimensional luminescence of the obtained structures, the pump radiation was focused into the rear focal plane of the lens. A CMOS camera was used to detect particle radiation. To cut off the pump radiation, a filter was used to cut off the pump radiation at 980 nm 50 mW, which passes the radiation of up-conversion microparticles.

Results and Discussion

In the work, up-converting particles with a narrow size distribution were used (Fig. 2). It can be seen from the figure that the average particle size is 1.65 μm . The average deviation from the diameter is ± 0.1 nm. At instet shown SEM image of up-conversion microparticle. It have hexagonal form. Heigh microparticle is about 1 μm .

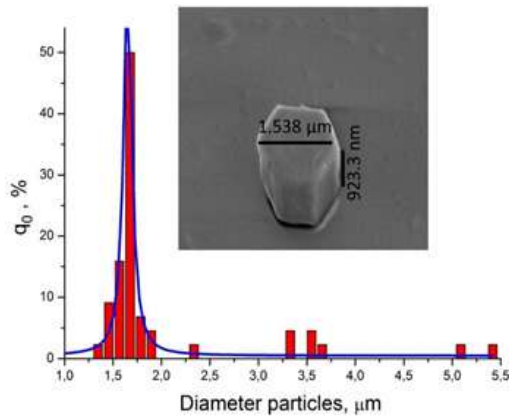


Fig. 2. Size distribution of $\text{NaYF}_4:\text{Yb}^{3+}-\text{Er}^{3+}$ up-conversion particles

Fig. 3, *c* shows the photoluminescence map of $\text{NaYF}_4:\text{Yb}^{3+}, \text{Er}^{3+}$ up-conversion microparticles in pre-prepared well arrays. The up-conversion luminescence was excited by a CW (continuous wave) laser with a wavelength of 980 nm power of ~ 50 mW. The number of particles that fell into the wells was also determined, depending on the diameters of the wells. The paper also shows that the method using plasma-chemical etching of thermal oxide as the creation of high-density luminescent structures has a significantly higher filling index with microparticles than the method using a photoresist mask with holes as a patterned environment. Our studies have shown that the filling density is at least 96% (Fig. 3, *a*).

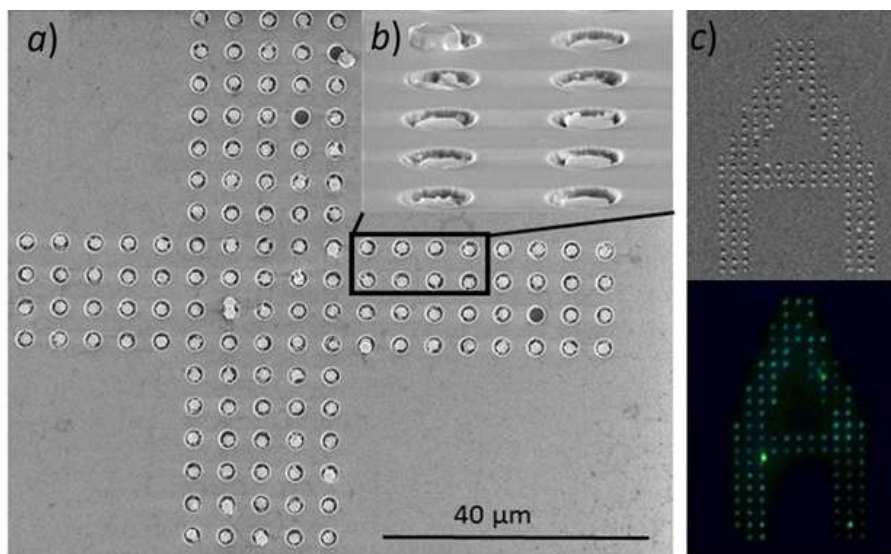


Fig. 3. Demonstration by scanning electron microscopy of the entry of microparticles into the patterned environment (*a*); magnified view of (*a*) the surface of the patterned environment at an angle (*b*); photoluminescence of up-conversion microparticles based on $\text{NaYF}_4:\text{Yb}^{3+}, \text{Er}^{3+}$ at a laser wavelength of 980 nm (*c*)



The technique of creating an array of depressions by plasma-chemical etching allows to control the depth of particles in the hole, which is necessary for the creation of photonic integrated circuits. Fig. 3, *b* demonstrates that single particles do not escape from the upper plane of the SiO₂, except when two particles stick together.

Conclusion

The technology of particle deposition by suspension deposition into patterned media produced by plasma-chemical etching is a universal technology for deposition of particles of different sizes and geometries. This allows for scalable technology and the possibility of deterministic placement of different particles over a large area. Such possibilities are an advantage over technologies using a polymer as a layer for recesses [4], using probes of an atomic force microscope to create a patterned environment [5], or particle transfer technology using optical tweezers [6].

REFERENCES

1. Wen S., Zhou J., Zheng K., Bednarkiewicz A., Liu X., Jin D., Advances in highly doped upconversion nanoparticles, *Nature Communications*. 9 (1) (2018).
2. Nie Z., Ke X., Li D., Zhao Y., Zhu L., Qiao R., Zhang X. L., NaYF₄:Yb,Er,Nd@NaYF₄:Nd Upconversion Nanocrystals Capped with Mn:TiO₂ for 808 nm NIR-Triggered Photocatalytic Applications, *The Journal of Physical Chemistry C*, 123 (37) (2019) 22959–22970.
3. Bishop M. D., Hills G., Srimani T., Lau C., Murphy D., Fuller S., Shulaker M. M., Fabrication of carbon nanotube field-effect transistors in commercial silicon manufacturing facilities, *Nature Electronics*, 3 (8) (2020) 492–501.
4. Rose M. A., Vinod T. P., Morin S. A., Microscale screen printing of large-area arrays of microparticles for the fabrication of photonic structures and for optical sorting, *Journal of Materials Chemistry C*, 1 (6) (2018) 12031–12037.
5. Rosenberger M. R., Dass C. K., Chuang H.-J., Sivaram S. V., McCreary K. M., Hendrickson J. R., Jonker B. T., Quantum Calligraphy: Writing Single Photon Emitters in a Two-Dimensional Materials Platform, *ACS Nano*. 1 (13) (2019) 904–912.
6. Paiè P., Zandrini T., Vázquez R., Osellame R., Bragheri F., Particle Manipulation by Optical Forces in Microfluidic Devices, *Micromachines*. 9 (5) (2018) 200–221.

THE AUTHORS

VOVK Nikolay A.
vovkolg2011@gmail.com
ORCID: 0000-0002-8687-3202

ASHARCHUK Ilya M.
ilyaasharchuk@gmail.com
ORCID: 0000-0001-6445-0009

TIMOFEEVA Ekaterina R.
timofeeva.e@inme-ras.ru

FILIPPOV Ivan A.
ivn.filippov@gmail.com

ZENOVA Elena V.
zenova.e@inme-ras.ru

SMIRNOV Konstantin V.
skv2050@mail.ru
ORCID: 0000-0003-1562-0520

TARHOV Michael A.
tmafuz@mail.ru

Received 04.08.2022. Approved after reviewing 05.08.2022. Accepted 15.08.2022.

Conference materials

UDC 628.9.038

DOI: <https://doi.org/10.18721/JPM.153.327>

A comprehensive study of electroluminescence and temperature distribution of “UX:3” AlInGaN LED

A. E. Ivanov ^{1, 2✉}, A. V. Aladov ¹, A. E. Chernyakov ¹, A. L. Zakgeim ¹

¹ Submicron Heterostructures for Microelectronics Research and Engineering Center of the RAS, St. Petersburg, Russia;

² Saint Petersburg Electrotechnical University “LETI”, St. Petersburg, Russia

✉ a-e-ivano-v@yandex.ru

Abstract. Comprehensive analysis of current spreading, temperature distribution and near-field electroluminescence of high-power “UX:3” AlInGaN emitting chips with a distributed system of reflective contacts, located on the back of the chip, has been performed by combination of different experimental methods. Current dependences of power and spectral characteristics, including their distribution (mapping) over the emitting surface, were studied in a wide range of operating currents. A thermal resistance evaluation was based on transient electrical processes under heating by direct current and analysis of thermal equivalent circuit (the Cauer’s model). The high resolution mapping of electroluminance and thermal radiation was obtained by optical microscope and infrared images technique. It has been established distribution pattern of light and temperature at different levels of excitation. The conclusions were drawn about the degree of uniformity of the current and light spreading and their influence on the power characteristics of devices.

Keywords: LED, light and temperature mapping, light-current characteristic, external quantum efficiency

Citation: Ivanov A. E., Aladov A. V., Chernyakov A. E., Zakgeim A. L., A comprehensive study of electroluminescence and temperature distribution of “UX:3” AlInGaN LED. St. Petersburg State Polytechnical University Journal. Physics and Mathematics, 15 (3.3) (2022) 142–146. DOI: <https://doi.org/10.18721/JPM.153.327>

This is an open access article under the CC BY-NC 4.0 license (<https://creativecommons.org/licenses/by-nc/4.0/>)

Материалы конференции

УДК 628.9.038

DOI: <https://doi.org/10.18721/JPM.153.327>

Комплексное исследование распределения светового и температурного полей в мощных AlInGaN светодиодах конструкции «UX:3»

А. Е. Иванов ^{1, 2✉}, А. В. Аладов ¹, А. Е. Черняков ¹, А. Л. Закгейм ¹

¹ Научно-технологический центр микроэлектроники и субмикронных гетероструктур Российской академии наук, Санкт-Петербург, Россия;

² Санкт-Петербургский государственный электротехнический университет «ЛЭТИ» им. В.И. Ульянова (Ленина), Санкт-Петербург, Россия

✉ a-e-ivano-v@yandex.ru

Аннотация. Исследованы токовые зависимости светового и температурного распределения (мэппинг) в наиболее совершенных на сегодняшний день AlInGaN светодиодах конструкции «UX:3» с распределенной системой отражающих контактов. Анализ ближнего поля собственного излучения совместно с ИК тепловым излучением выявил высокую однородность распределения тока по площади кристалла при всех уровнях возбуждения.



Ключевые слова: светодиод, световой и температурный мэппинг, характеристика свет-ток, внешний квантовый выход

Ссылка при цитировании: Иванов А. Е., Аладов А. В., Черняков А. Е., Закгейм А. Л., Комплексное исследование распределения светового и температурного полей в мощных AlInGaN светодиодах конструкции «UX:3» // Научно-технические ведомости СПбГПУ. Физико-математические науки. 2022. Т. 15. № 3.3. С. 142–146. DOI: <https://doi.org/10.18721/JPM.153.327>

Статья открытого доступа, распространяемая по лицензии CC BY-NC 4.0 (<https://creativecommons.org/licenses/by-nc/4.0/>)

Introduction

To date, AlInGaN LEDs from leading manufacturers, primarily OSRAM Opto Semiconductors, Cree, Philips Lumileds and some others, are great performance by a high level of design excellence and emitting characteristics. An optimized Multiple Quantum Well (MQW) heterostructure, a system of distributed reflective contacts, low values of electrical and thermal resistance ensured the achievement of watt optical powers per square millimeter at a high, more than 50% efficiency [1]. Most of the research on AlInGaN LEDs refers to continuous operation used in lighting. At the same time, interest has recently increased for the use of AlInGaN LEDs in the visible blue-green range of the spectrum, not only “for the eye”, but also in working with physical receivers, in particular, for pumping solid-state lasers [2] or in open Visible Light Communication (VLC) [3]. New applications require the use of LEDs in pulse mode with duration from tens of nanoseconds to units of milliseconds upon reaching the maximum possible radiation power (or energy per pulse). In this regard, of particular scientific and practical interest is the task of identifying the main factors limiting the energy capabilities of the LED. They are either thermal or electrical in nature. The latter can be associated both with “external” design factors: (current crowding under the contact, shadowing of light by contacts), and with “internal” processes: “efficiency droop” determined by the transport and recombination of carriers in the active region [4].

In this work, we aim to reveal the main factors limiting the performance of LEDs at high levels of excitation, using as an object of study the best to date emitting chips of the “UX:3” design. An important advantage of “UX:3” chip is a multi-point geometry of reflective n-contacts, which, thanks to a special “isolated well” technology, are transferred and distributed evenly over the p-contact area on the back of the chip. The complexity of the technology pays off with ideal conditions for uniform current distribution and light output without loss due to shading.

Experiment: Object and Methods

The object of the study is the most advanced AlInGaN LEDs OSRAM OSTAR LE B Q8WP [5] based on the emitting chip “UX:3” [6] with a distributed system of reflective p- and n-contacts located on the back side of device (Fig. 1). The implementation of the design required the development of a complex technology of isolated “wells” crossing the p-n-junction, with metal “columns” inside forming a multipoint n-contact. Thereby chip had a unilateral arrangement of contacts and the light output through the n-area without shadow effect. LEDs had $1500 \times 1200 \mu\text{m}^2$ chip mounted by “flip-chip” method on the AlN substrate.

As has been shown previously, the near field of own electroluminance (EL), as a first approximation, correlated with the current density distribution in the active region [7]. The uniformity of the current distribution can be estimated by the uniformity of the near field EL.

The near field EL was mapped by a Mitutoyo optical microscope equipped with a digital camera (12 Mpxl CMOS matrix) and Avantes AvaSpec-2048 spectrometer. Profiles of EL intensity are shown in Fig. 2, *b*. In addition, for revealing the mechanisms of current redistribution with an excitation, the dependence light output and thermal resistances on current was measured. General light-current characteristics (optical power dependence, external quantum efficiency and emission spectrum from the current) at direct current were obtained using the automated OL 770-LED Test and Measurement System [8].

To obtain the temperature distribution across the area of chip (temperature mapping), the

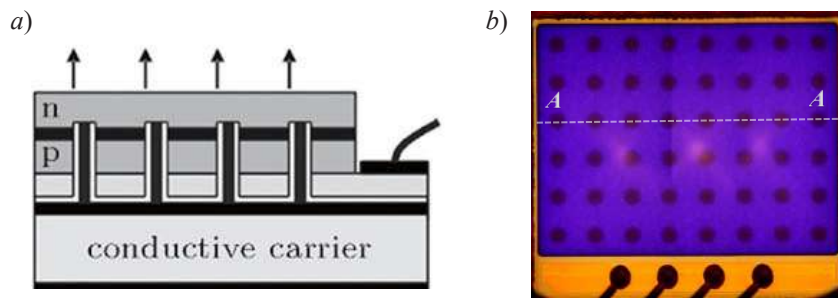


Fig. 1. The emitting chip “UX:3”: cross-section with a diagram of the formation of distributed n-contacts (a); photo of the emitting surface, dark dots correspond to the location of the n-contacts (b)

infrared (IR) micro-thermography was used, which allows to estimate not only device average heating, but also to establish the temperature distribution over the area with the detection of overheat spots and temperature gradients. Thermal radiation in the spectral range of 2.5–3 μm was mapped by a specially designed IR microscope. The use of short wavelength IR radiation as compared to conventional radiation (8–12 μm) made it possible to reduce the diffraction blurring and, consequently, to improve of the spatial IR mapping resolution to $\sim 3 \mu\text{m}$ at a temperature resolution of about 1 degree [9].

In addition, the total thermal resistance of the LED $R_{th\Sigma}$ and the thermal resistance of the individual elements of the thermal circuit (chip layers, soldering, heat sink) R_{thi} were measured using temperature-sensitive parameters, namely the forward-voltage relaxation method with a Thermal tester T3Ster [10].

Results and Discussion

In Fig. 2, a the current dependences of emitting power P_{opt} and external quantum efficiency EQE in a wide range of currents from units of milliamps to 3 A are presented. As it can be seen from Fig. 2 the above dependences have a characteristic typical for AlInGaN LEDs: deviation from the linearity of the light-current dependence due to the “efficiency droop” from EQE = 70% to EQE = 50% (drop in conversion efficiency to $\sim 40\%$). It should be noted high absolute magnitudes the above-mentioned values, which indicates the high structure perfection of devices.

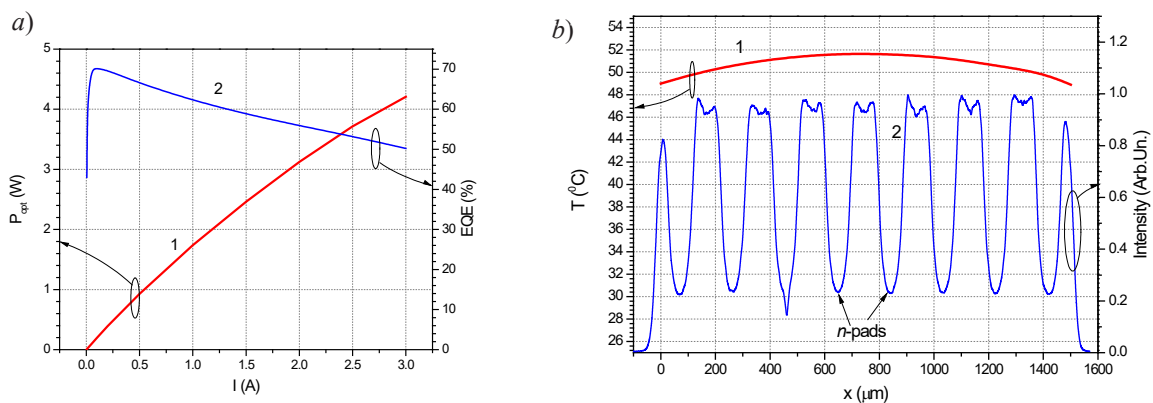


Fig. 2. LED optical power P_{opt} (curve 1) and external quantum efficiency EQE (curve 2) dependences on current (a); temperature distributions (curve 1) and EL intensity profile (curve 2) in the cross-section AA at $I = 3 \text{ A}$ (b)

The question is whether this drop is “purely” electronic in nature or the effects of self-heating and the occurrence of temperature and current density gradients over the area of the p-n junction are added and enhance efficiency loss [11]. To clarify this issue the temperature distribution over the chip area in cross section AA (Fig. 1, b) was obtained by mapping the IR thermal radiation at different operating current.

In Fig. 2, b, curve 1 shows temperature distribution in the cross-section AA at maximum direct current of $I = 3 \text{ A}$ (input power $P_{in} \sim 10.5 \text{ W}$). As can be seen in Fig. 2, b the temperature distribution remains almost uniform over the area of the chip and is not related to the location



of the n-contacts (there is no local overheating near the contacts as it could be assumed from the current crowding near them). On the other hand, there is some tendency to a concave temperature profile can be recognized in the distributions. It can be explained by the fact that the heat transfer from the center of the chip to the ambient environment is worse than at the periphery. The absolute overheating of the active region is about $\Delta T \approx 30 \text{ }^\circ\text{C}$ (the temperature of heat-sink is $20 \text{ }^\circ\text{C}$) which, taking into account the input power of 10.5 W and “optical cooling” at high conversion efficiency of 40% gives the value of the total real thermal resistance $R_{th\Sigma} \approx 4.1 \text{ K/W}$, which coincides with the thermal resistance measurement data obtained using the T3Ster.

The map of distribution near field EL intensity on the chip surface at $I = 3 \text{ A}$ was obtained by optical microscopy and shown in Fig. 2, *b*, curve 2. It can be seen that there is a uniform distribution of itself emission takes place. The minimum of curve indicates the n-contact pads, which pass through the *p-n*-junction and, accordingly, there is no radiation generation. At the same time, the light background of $\sim 20\%$ of the maximum indicates the multiple pass of radiation through the chip and the reflective properties of the n-contacts.

The results of the thermal resistance measurement of the LED are presented as cumulative structure functions in Fig. 3. In the figure, the horizontal axis shows thermal resistance R_{th} measured from the *p-n* – junction towards the heatsink. The vertical axis represents thermal capacity C_{th} from the heat source to the heatsink, shown in logarithmic scale. The total thermal resistance $R_{th\Sigma} = R_{chip} + R_{case} + R_{substrate}$ obtained at the current $I = 3 \text{ A}$. From the Fig. 3 it can be seen that the values of “electrical” thermal resistance (without “optical cooling”) amount: junction/ bottom of chip $R_{j-chip} = 0.5 \text{ K/W}$, junction/solderpoint $R_{j-sp} = 0.9 \text{ K/W}$ and junction/heat-sink $R_{j-hs} = 2.9 \text{ K/W}$.

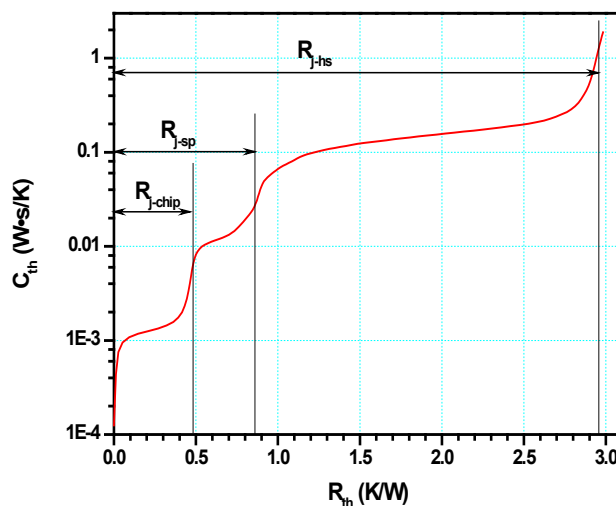


Fig. 3. Cumulative structure functions of the LED at the current $I = 3 \text{ A}$

Conclusion

High-power AlInGaN blue LED of “UX:3” design were studied by advanced experimental techniques including measurement of optical power and external quantum efficiency dependences on current, high-resolution mapping of EL and IR radiation and transient thermal analysis.

EL variation and temperature distribution were studied as well as thermal resistance for high-power LED with the driving current. For LED chip was established uniform temperature distribution of the central. The little temperature gradient $\Delta T \sim 3 \text{ K}$ of distribution in the cross-section was associated with the deterioration of the conditions of heat removal from the center to the periphery. The real material thermal resistance of the LED taking into account that part of the heat is carried away by light is $\sim 4 \text{ K/W}$.

It is concluded that in “UX:3” there are no significant current density and temperature gradients over the area up to currents $\sim 3 \text{ A}$, and the behavior of the optical characteristics is due to internal processes in the active region.

Acknowledgments

This work was carried out at the Center of Multi-User Facilities “Element Base of Microwave Photonics and Nanoelectronics: Technology, Diagnostics, and Metrology”.

REFERENCES

1. **Karpov S. Yu.**, Light-emitting diodes for solid-state lighting: searching room for improvements. Light-Emitting Diodes: Materials, Devices, and Applications for Solid State Lighting XX, Proc. SPIE 9768. 2016, 97680C. DOI: 10.1117/12.2207265.
2. **Aladov A. V., Zakgeim A. L., Ivanov A. E., Chernyakov A. E.**, JAS, 89 (3) (2022) 336–341.
3. **Pichon P., Barbet A., Blanchot J.-P., Druon F., Balembois F.**, Optica, 5 (10) (2018) 1236–1239. DOI: 10.1364/OPTICA.5.001236.
4. **Karpov S. Yu.**, Opt. Quantum Electron, 47 (6) (2015) 1293–1303. DOI: 10.1007/s11082-014-0042-9.
5. Osram Datasheet LE B Q8WP, https://www.osram.com/ecat/OSRAM%20OSTAR%C2%AE%20Projection%20Compact%20LE%20B%20Q8WP/com/en/class_pim_web_catalog_103489/prd_pim_device_2191200/.
6. **Laubsch A., Sabathil M., Baur J., Peter M., Hahn B.**, IEEE Transaction on Electron Devices, 57 (1) (2010) 79–87. DOI: 10.1109/TED.2009.2035538.
7. **Chernyakov A. E., Bulashevich K. A., Karpov S. Yu., Zakgeim A. L.**, Phys. Status Solidi A, 3 (210) (2013) 466–469. DOI: 10.1002/pssa.201200658.
8. **Zakgeim A., Chernyakov A.**, Light & Engineering, 21 (4) (2013) 64–70.
9. **Zakgeim A. L., Kuryshev G. L., Mizerov M. N., Polovinkin V. G., Rozhansky I. V., Chernyakov A. E.**, Semiconductors, 44 (3) (210) 373.
10. **Lasance C., Poppe A.**, Thermal management for LED applications. Solid State Lighting Technology and Application Series. Springer, 2014.
11. **Zakgeim A. L., Ivanov A. E., Chernyakov A. E.**, Technical Physics Letters, 47 (8) (2021) 823–826.

THE AUTHORS

IVANOV Anton E.
a-e-ivanov@yandex.ru
ORCID: 0000-0003-2819-1534

CHERNYAKOV Anton E.
chernyakov.anton@yandex.ru
ORCID: 0000-0002-8153-9512

ALADOV Andrey V.
aaladov@mail.ioffe.ru
ORCID: 0000-0001-8009-7647

ZAKGEIM Alexander L.
zakgeim@mail.ioffe.ru
ORCID: 0000-0002-1887-2064

Received 04.08.2022. Approved after reviewing 05.08.2022. Accepted 14.08.2022.

Conference materials

UDC 53

DOI: <https://doi.org/10.18721/JPM.153.328>

Low-induction integral heater for temperature control of MEMS vapor cell

R. Kenesbay ¹✉, Ya. B. Enns ¹, A. N. Kazakin ¹, R. Kleimanov ¹, Yu. D. Akulshin ¹

¹ Peter the Great Saint-Petersburg Polytechnic University, St. Petersburg, Russia

✉ ramazan.kenesbay.1999@gmail.com

Abstract. This paper describes a solution to the problem of temperature control and the occurrence of a magnetic field created by a resistive heater in a gas cell of an atomic clock. A low-induction integral heater was developed in the form of a two-layer metallization system that mutually compensates for each other's magnetic fields. Numerical simulation was carried out, based on the results of which a prototype of a low-induction integral heater was developed using precision photolithography and technologies for applying thin-film conductive and dielectric coatings. Static and dynamic tests of the fabricated integral heater were carried out.

Keywords: integral heater, MEMS, vapor cell

Funding: This work was carried out in Peter the Great St.Petersburg Polytechnic University and was supported by a grant of Russian Science Foundation (project No. 20-19-00146).

Citation: Kenesbay R., Enns Ya. B., Kazakin A. N., Kleimanov R., Akulshin Yu. D., Low-induction integral heater for temperature control of MEMS vapor cell. St. Petersburg State Polytechnical University Journal. Physics and Mathematics, 15 (3.3) (2022) 147–150. DOI: <https://doi.org/10.18721/JPM.153.328>

This is an open access article under the CC BY-NC 4.0 license (<https://creativecommons.org/licenses/by-nc/4.0/>)

Материалы конференции

УДК 53

DOI: <https://doi.org/10.18721/JPM.153.328>

Малоиндукционный интегральный нагреватель для термостатирования МЭМС газовой ячейки

Р. Кенесбай ¹✉, Я. Б. Эннс ¹, А. Н. Казакин ¹, Р. Клейманов ¹, Ю. Д. Акульшин ¹

¹ Санкт-Петербургский политехнический университет Петра Великого, Санкт-Петербург, Россия

✉ ramazan.kenesbay.1999@gmail.com

Аннотация. В данной работе описано решение проблемы термостатирования и возникновения магнитного поля, созданного резистивным нагревателем, в газовой ячейке атомных часов. Был разработан малоиндукционный интегральный нагреватель в виде двухслойной системы металлизации, которая взаимно компенсирует магнитные поля друг друга. Было проведено численное моделирование, по результатам которого был разработан прототип малоиндукционного интегрального нагревателя с применением прецизионной фотолитографии и технологий нанесения тонкоплёночных проводящих и диэлектрических покрытий. Были проведены статические и динамические испытания полученного интегрального нагревателя.

Ключевые слова: интегральный нагреватель, МЭМС, газовая ячейка

Финансирование: Работа выполнена в Санкт-Петербургском политехническом университете Петра Великого и поддержана грантом Российского научного фонда (проект № 20-19-00146).

Ссылка при цитировании: Кенесбай Р., Эннс Я. Б., Казакин А. Н., Клейманов Р., Акульшин Ю. Д., Малоиндукционный интегральный нагреватель для термостатирования

МЭМС газовой ячейки // Научно-технические ведомости СПбГПУ. Физико-математические науки. 2022. Т. 15. № 3.3. С. 147–150. DOI: <https://doi.org/10.18721/JPM.153.328>

Статья открытого доступа, распространяемая по лицензии CC BY-NC 4.0 (<https://creativecommons.org/licenses/by-nc/4.0/>)

Introduction

Atomic frequency standards based on the absorption of alkali metal vapors (Cs or Rb) are the most precision standards of frequency and time. The development of microelectronics and microsystem technology provides technical opportunities for their integrated production, miniaturization, reduction of power consumption and cost. These devices include a cell in the form of a sealed capsule filled with alkali metal vapors. However, the disadvantage of reducing the overall sizes of the atomic clock cell is a decrease in the optical path, and therefore a decrease in the intensity of the output signal. An increase in the temperature of alkali metal vapors (80–200 °C), leading to an increase in the atomic density of vapors, is a key aspect of increasing the intensity of the output signal [1]. In addition, thermal stabilization has a high value, since temperature fluctuations can lead to changes in atomic density, relaxation rate and polarization [2]. Thus, the system of temperature setting and controlling is one of the key components of the atomic clock system.

Typical power for atomic clock cells is approximately 1 mW – 50 W, depending on the size and materials of the cell, as well as the casing [3, 4]. However, the use of typical resistive heaters leads to the formation of a parasitic magnetic flux density, due to the flowing current of the heater. The use of traditional heaters is impossible due to the extreme sensitivity of atomic cells to magnetic flux.

One of the ways to create a non-inductive heating and thermal stabilization is the using of hot air flow [5]. This method of heating the vapor cell is non-magnetic and allows to achieve high heating power. But its application requires high power consumption and has a low integration ability. An alternative method is the sequential combination of two parallel resistive heaters in the form of meanders [2]. This arrangement leads to compensation of the magnetic flux density, which is generated by each heater. However, the distance between the metal lines is on the order of a millimeter and its reduction is necessary to enhance the effect of magnetic flux suppression [6].

This project is aimed at solving the problem of creating a low-induction integral heater and a resistive thermometer for atomic clock cells. The solution of the problem is based on the formation of a two-layer metallization system mutually compensating magnetic fields of each other. In the course of the work, numerical modeling methods will be used to optimize the thermal stabilization system and the following production of prototypes using thin-film conductive and dielectric coating technologies and will be used precision photolithography.

Experimental

Before manufacturing the integral heater, numerical simulation was carried out in the COMSOL Multiphysics software. The purpose of the numerical simulation was to determine the configuration of the parasitic magnetic field and minimize it. The results of numerical simulation (Fig. 1) showed the possibility of reducing the magnetic field density to 10^{-12} T. Based on the obtained results, the construction of the integral low-induction integral heater was designed and produced.

The integral heater and thermistor are a two-layer metallization of chromium, made in the form of meanders (Fig. 2, *a*). SiO₂ was chosen as the insulation between the layers. The heater is made in the form of two turns of metallization with a width of 150 microns, and the thermometer in the form of six turns with a width of 30 microns.

The heater and thermistor were made by magnetron sputtering of Cr and SiO₂ layers on a LK-5 type glass substrate. The thickness of the metallization layer and the SiO₂ insulation layer was 100 nm and 400 nm, respectively. The resistances of the manufactured heater and thermistor under normal conditions are 280 ohms and 13.5 kOhms, respectively.

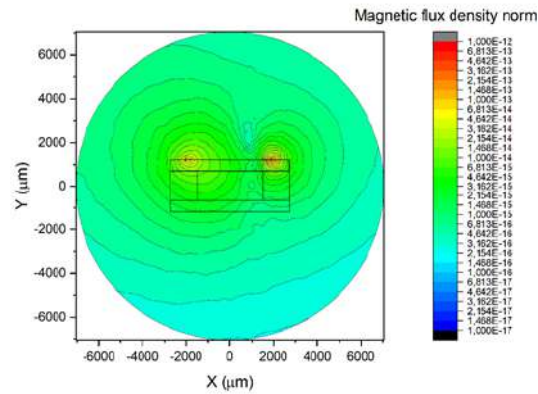


Fig. 1. Results of numerical simulation of the magnetic field density distribution

A fabricated low-induction integral heater was placed at the bottom of the vapor cell. The temperature of the vapor cell was controlled by an additional platinum microthermometer mounted on top of it. The resulting assembly was mounted on a ceramic suspension to reduce heat leakage. The ceramic suspension was made by laser scribing. Figure 2, *b* shows a schematic diagram of the resulting test block. Static and dynamic tests were carried out to determine the properties of the integral heater and thermistor.

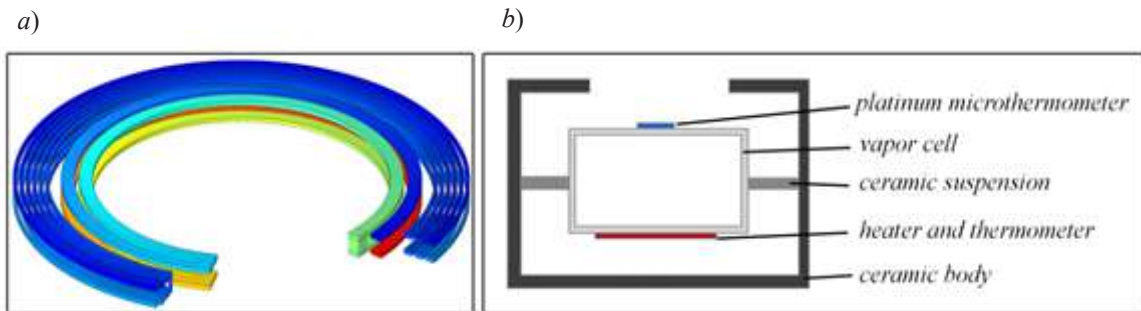


Fig. 2. Double-layer heater and thermistor (*a*); schematic diagram of test block (*b*)

During the static tests, the test block was placed on the hot plate. After reaching thermal equilibrium between the hotplate and the test block, the heating was turned off. As it cooled down, the resistances of the heater and the thermistor were measured. The determination of the temperature of the vapor cell was determined using a platinum microthermometer.

For dynamic tests were assembled a measuring circuits for a heater, a thermistor and a platinum microthermometer. A signal was applied to the thermistor and platinum microthermometer using the generator AKIP series AKIP-3409/2 (China). A voltage was applied to the heater using the power supply QJE series QJ3005P (China). Turning off the heating led to a change in the signals that were transmitted to the thermistor and the platinum microthermometer. power supply. The signal was measured using the digital oscilloscope AKIP series AKIP-4109/2 (China). The time constant for the thermistor and the heating time of the heater were determined by changes in the signal.

Results

During static tests the dependences of the resistance of the heater and the thermistor on the temperature were determined (Fig. 3, *a*, *b*). The temperature dependence on the heating power was also determined (Fig. 3, *c*). Due to the linear dependence of the resistances on temperature, the integrated heater can easily provide thermal stabilization up to 100 °C at a heating power of 700 mW. As part of the dynamic tests, the time constant for the thermistor and the heating time of the heater were obtained. The time constant of the thermistor is 800 ms, and the time of the heater is 20 ms. The results of dynamic tests show that the integrated heater has a high level of response time.

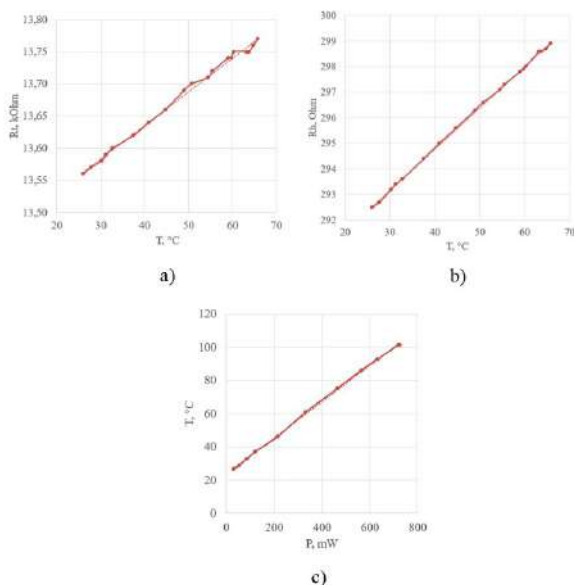


Fig. 3. A graph of the dependence of the resistance of the thermistor on the temperature (a); a graph of the dependence of the resistance of the heater on the temperature (b); graph of the dependence of the temperature on the heating power (c)

Conclusion

The characteristics of an integral heater and a thermistor were studied. The manufactured integral heater has the possibility of thermal stabilization up to 100 °C at a heating power of 700 mW.

REFERENCES

1. Seltzer S. J., Developments in alkali-metal atomic magnetometry, Ph.D. Princeton University, Princeton, 2008.
2. Wyllie R., The Development of a Multichannel Atomic Magnetometer Array for Fetal Magnetocardiography, Ph.D. University of Wisconsin-Madison, Wisconsin, 2012.
3. Shah V., Knappe S., Schwindt P. D. D., Kitching J., Subpicotesla atomic magnetometry with a microfabricated vapour cell, Nature Photonics. 1 (11) (2007) 649–652.
4. Vasilakis G., Precision measurements of spin interactions with high density atomic vapors, Ph.D. Princeton University, Princeton, 2011.
5. Allred J. C., Lyman R. N., Kornack T. W., Romalis M. V., High-sensitivity atomic magnetometer unaffected by spinexchange relaxation, Physical review letters. 89 (13) (2002) 130801.
6. Schwindt P. D., Knappe S., Shah V., Hollberg L., Kitching J., Liew L. A., Moreland J., Chip-scale atomic magnetometer, Applied Physics Letters. 85 (26) (2004) 6409–6411.

THE AUTHORS

KENESBAY Ramazan
ramazan.kenesbay.1999@gmail.com
ORCID: 0000-0001-9002-3924

KLEIMANOV Roman
kleimanovrv@mail.ru
ORCID: 0000-0003-3485-7961

ENNS Yakov B.
ennsjb@gmail.com
ORCID: 0000-0003-4396-2368

AKULSHIN Yuri D.
akulshin_yud@spbstu.ru

KAZAKIN Alexey N.
kazakin75@gmail.com
ORCID: 0000-0001-8762-1587

Received 11.08.2022. Approved after reviewing 12.08.2022. Accepted 12.08.2022.

Conference materials
UDC 621.315.5:681.586.72
DOI: <https://doi.org/10.18721/JPM.153.329>

On the mechanism of CNT network NH₃ sensitivity: modeling and experimental study of the density effect

N. S. Struchkov ¹✉, E. A. Kozlovskaya ¹, K. A. Tsarik ¹,
A. V. Lashkov ¹, D. D. Levin ¹, A. V. Romashkin ¹

¹ National Research University of Electronic Technology, Zelenograd, Moscow, Russia
✉ struchkov.nikolaj@gmail.com

Abstract. A carbon nanotubes (CNT) network is a promising gas sensing material for “e-nose” development due to the vast methods of cross-sensitivity modification. However, the dominant sensitivity mechanism remains unclear since both the CNTs and junctions between CNTs can be gas-sensitive. In this paper to estimate the contributions of both mechanisms, we simulated CNT networks with varied densities using an equivalent electrical circuit. Density variation alters the junction’s and CNT’s contribution to the network resistance, and hence the total resistive response. We compared the results with the experimental resistive response of the spray-coated CNT networks toward ammonia (NH₃). A decrease in the network density results in a higher response, which indicates a likely significant role of CNTs junctions in sensitivity of a sparse networks. We also studied the effect of formic acid treatment on CNT networks, which increases both conductivity and sensitivity by removing residual solvent.

Keywords: carbon nanotube, gas sensor, spray-coating, electric circuit simulation

Funding: This study was supported by grant of President of the Russian Federation grant No МК-4010.2022.4 (sensors fabrication, electrical simulation) and RFBR project No. 19-38-60034 (samples characterization, gas sensing measurement).

Citation: Struchkov N. S., Kozlovskaya E. A., Tsarik K. A., Lashkov A. V., Levin D. D., Romashkin A.V., On the mechanism of CNT network NH₃ sensitivity: modeling and experimental study of the density effect. St. Petersburg State Polytechnical University Journal. Physics and Mathematics, 15 (3.3) (2022) 151–156. DOI: <https://doi.org/10.18721/JPM.153.329>

This is an open access article under the CC BY-NC 4.0 license (<https://creativecommons.org/licenses/by-nc/4.0/>)

Материалы конференции
УДК 621.315.5:681.586.72
DOI: <https://doi.org/10.18721/JPM.153.329>

Механизм чувствительности сеток из УНТ к NH₃: моделирование и экспериментальное исследование влияния плотности

Н. С. Стручков ¹✉, Е. А. Козловская ¹, К. А. Царик ¹,
А. В. Лашков ¹, Д. Д. Левин ¹, А. В. Ромашкин ¹

¹ Национальный исследовательский университет «МИЭТ», Зеленоград, Москва, Россия
✉ struchkov.nikolaj@gmail.com

Аннотация. В работе было проведено моделирование эквивалентной электрической схемы сетки из углеродных нанотрубок (УНТ) для оценки влияния плотности сетки УНТ на вклад различных механизмов резистивного отклика на воздействие аммиака. Методом аэрозольного нанесения были изготовлены газочувствительные сетки УНТ с различной плотностью и измерена их чувствительность. Сравнение данных моделирования и экспериментальных результатов указывает на то, что изменение контактного сопротивления между УНТ, может является одним из механизмов сенсорного отклика в разреженных сетках.

Ключевые слова: углеродная нанотрубка, газовый детектор, аэрозольное нанесение, моделирование электрических схем

Финансирование: Работа выполнена при поддержке гранта Президента РФ № МК 4010.2022.4 и проекта РФФИ № 19-38-60034.

Ссылка при цитировании: Стручков Н. С., Козловская Е. А., Царик К. А., Лашков А. В., Левин Д. Д., Ромашкин А. В. Механизм чувствительности сеток из УНТ к NH_3 : Моделирование и экспериментальное исследование влияния плотности // Научно-технические ведомости СПбГПУ. Физико-математические науки. 2022. Т. 15. № 3.3. С. 151–156. DOI: <https://doi.org/10.18721/JPM.153.329>

Статья открытого доступа, распространяемая по лицензии CC BY-NC 4.0 (<https://creativecommons.org/licenses/by-nc/4.0/>)

Introduction

Development of “e-nose” technology promotes interest toward gas-sensitive nanomaterials. To efficiently mimic the olfactory system, an array of sensors with varied cross-sensitivity should be fitted on a single substrate. Therefore, key e-nose requirements for sensitive layers are the adjustable sensitivity toward selected gas species, miniaturization and integrability. Carbon nanotubes (CNT) fulfill these requirements and considered as a promising gas-sensing material.

Since the pioneering works in the early 2000s, the CNT’s sensitivity mechanism remains a matter of argument. A large number of studies of single CNT based field-effect transistors assert the existence of both sensitivities of CNT [1] and Schottky barrier between CNT and the electrode [2]. The apparent inconsistency of the known results rises from number of factors that determine the dominance of one of the mechanisms on the overall sensitivity in selected works. For example: presence of defects and functional groups in CNT [3], the work function of the metal that determines the height of the Schottky barrier [4, 5], the measuring temperature [6]. When studying CNT networks, the identification of the dominant mechanism is even more complicated since we should consider the presence of both metallic (m-CNT) and semiconducting CNTs (s-CNT), as well as their junctions which are also gas sensitive [7]. Sensitivity mechanisms can be localized in: 1) contact between CNT and electrode, 2) CNT channel (intra-CNT) and 3) CNT-CNT junction (inter-CNT). Taking into account that the resistance of the junctions dominates in total resistance of the low density CNT networks, especially for short CNTs [8, 9], the role of inter-CNT gas sensitivity can be essential. The dominant effect of CNT junctions in short CNT channels was already demonstrated by Boyd et al. [7] for nonfunctionalized CNTs. Inoue et al. [10] also suggest FIT model-based theory associating adsorption and contacts resistance. However, a deeper understanding of inter- and intra-CNT sensitivity contribution in large area networks of functionalized CNTs is still required since it will allow to focus on increasing the sensitivity of the dominant mechanism or vary cross-selectivity by changing different mechanisms’ contribution.

In this work, we simulated the resistive response of the resistor-based model of CNT networks and experimentally measured the resistive response of the spray-coated network to ammonia exposure. We compared simulation and experimental result to evaluate which sensitivity mechanisms prevails in fabricated gas sensing layers.

Materials and Methods

To fabricate the CNT sensor we used P3-SWCNT (“Carbon Solutions”) dispersion in a mixture of N-Methyl-2-pyrrolidone (NMP) (for HPLS “Acros Organics”) and deionized water (for HPLC, “Component-Reactive”). A multisensory chip with Ti/Au electrodes with a 50 μm gap on Si/SiO₂ substrate was spray-coated with CNT dispersion by a self-designed automated spray-coating system. To achieve uniformity of the CNT network we used ultralow dispersion flow [11]. The density of the network was varied in different segments of the chip by transferring the shadow mask while spray-coating. After deposition, chip was mounted into the PCB holder.

The morphology of obtained CNT networks was studied by atomic force microscope (AFM) Solver-Pro (“NT-MDT”) in tapping mode. The electrical characterization was carried by 2450 SourceMeter (“Keithley Instruments”). To measure CNT response to gas exposure device was preliminarily annealed in dry air by heaters integrated into the chip at 100 °C.

The gas mixture was prepared by evaporating the required volume of ammonia solution to obtain concentration of 50–400 ppm, then pumped through the device chamber with a 200 sccm flow. Chip was recovered in dry air in two steps: at first gas flow was a 2000 sccm to enhance the recovery rate, and in the second step at 200 sccm to avoid the effect of the flow rate on the response. The response was calculated as $S = (R_{gas} - R_{air}) / R_{air} \cdot 100\%$, where R_{air} and R_{gas} are the resistances of the segments before and after 15 min exposure, respectively. Resistance was evaluated at 8 segments simultaneously by measuring current at a bias voltage of 5 V, the segments denoted as CNT-1–CNT-8 from the most conductive to the least one. After studying response of the as-prepared CNT network, the substrate was immersed in formic acid (FA) to reduce the residue NMP content. The CNT layers after FA treatment are hereinafter denoted as FA-CNT.

To simulate the CNT network resistive response, we randomly generated a 2-D network of randomly distributed 1-D sticks of two types denoting m- and s-CNT. The average length was $0.8 \mu\text{m}$ and the standard deviation was 0.4 similar to AFM evaluated values, the m-CNT to s-CNT ratio was 0.33 (Fig. 1, a). The resulting network was converted into a SPICE model of an equivalent resistor circuit. We used the following approach for equivalent circuit generation: CNT was divided into segments in intersections with other CNTs and substituted with resistors with values $R_{S,M} = \rho_{S,M} \cdot L$, where L is a segment length, $\rho_M = 6 \text{ k}\Omega/\mu\text{m}$ and $\rho_S = 9 \text{ k}\Omega/\mu\text{m}$ are resistivity of m-CNT and s-CNT, respectively (Fig. 1, b). The ρ_M corresponds to experimental results for non-sorted HNO_3 treated single-walled CNTs [12], while ρ_S is slightly higher which is observed at least for as-synthesized CNTs [13]. Since the minimal resistance of CNT is limited by resistance quantum $1/2G_0$, where $G_0 = 7.7 \cdot 10^{-5} \text{ S}$ is quantum conductance, the resistors with $R_0 = 1/4G_0$ were added to each junction with other CNTs. For model simplification, the junctions were also simulated with resistors, despite the non-linearity of s- and m-CNT heterojunction [14] and junctions of s-CNTs with different chirality or diameter [13]. The values $R_{M-M} = 40 \text{ k}\Omega$, and $R_{S-S} = 60 \text{ k}\Omega$ corresponds to acid-treated CNTs [12]. $R_{S-M} = 200 \text{ k}\Omega$ a few times higher than R_{S-S} as for non-treated CNTs [13]. We estimated CNT network response using a simulated circuit resistance as R_{air} , and simulated resistance with doubled values of the R_S , R_{S-S} , R_{S-M} or all of them as R_{gas} , representing a gas-induced increase of resistance of CNT junctions or s-CNT body, respectively. The doubling of the resistance corresponds in order of magnitude to CNT-metal heterojunction response to 100 ppm NH_3 exposure [6].

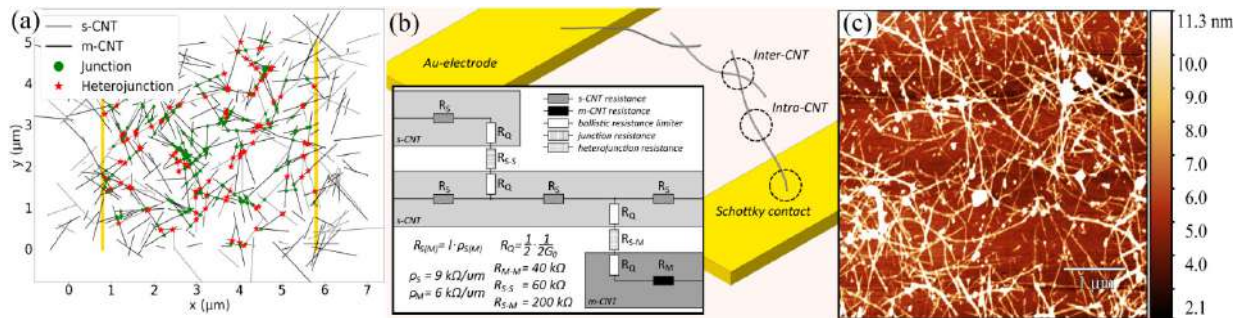


Fig. 1. Randomized CNT network (a); Equivalent resistor circuit of CNT and junctions (b); AFM image of low-density CNT network (c)

Results and discussion

Earlier reported method of CNT spray coating ensured high uniformity of CNT layer according to the AFM results (Fig. 1, c). Although, a significant number of CNT bundles was observed along with single CNTs with diameter about 3–6 nm, which were not disrupted by ultra-sonic treatment and were remaining in dispersion. It was not taken into account in the model used and may lead to overestimation of heterojunctions contribution, since the bundles may include CNTs of both types forming ohmic contacts. This effect probably was shown by A. Znidarsic et.al [12], when high-resistance junctions, which we consider to be heterojunctions, were only found for small diameter nanotubes, but not the bundles.

We counted the approximate number of CNTs in the segment with a sparse network and calculated the number in high density segments, as it is proportional to the sprayed volume. The calculated density was varied in a range $7\text{--}25 \mu\text{m}^{-2}$ from CNT-8 to CNT-1, respectively.

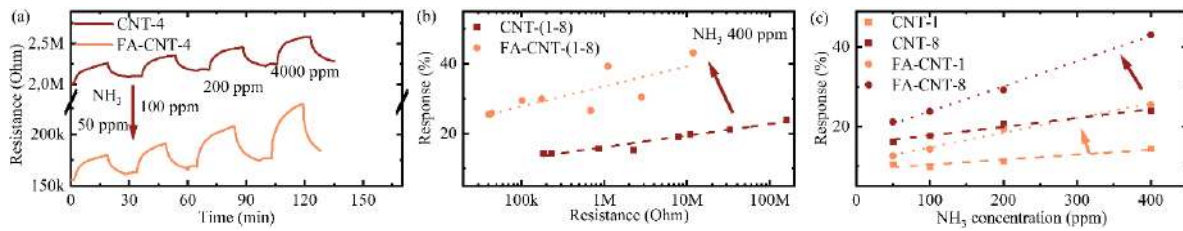


Fig. 2. CNT network response toward NH_3 exposure (a); Response dependence on CNT network resistance (b) and NH_3 concentration (c)

A gas sensing study has revealed a significant room temperature resistive response of CNT to NH_3 (Fig. 2, a). The response/recovery dynamics are close to an exponential with a time constant of about 250 s. Despite the airflow during the recovery was high, we don't observe a complete recovery in the used intervals, however, extrapolation allows us to expect a complete recovery in longer intervals. The response has a logarithmic dependence on segment resistance (Fig. 2, b) and linear on NH_3 concentration (Fig. 2, c).

FA treatment resulted in a significant decrease in network resistance. The before/after resistance ratio was 3 for high-density networks, and exceeded 10 for low-density networks. We consider that FA have strong hydrogen bonding with NMP [15] and therefore probably efficiently removes NMP residual thin layer from the interface between CNTs [16]. A decrease in the gap between CNTs, according to the thermal activation carrier hopping mechanism [17], leads to a resistance decrease. Greater resistance drop after FA treatment in sparse networks may correlate with greater contribution of junctions in their resistance. Removal of the solvent also leads to an increase of response up to two times, which correlates with both inter- and intra-CNT mechanisms. Intra-CNT response can be promoted by a decrease of junction' resistance contribution, while junction sensitivity also increases speculatively due to increase in changing barrier height with NH_3 adsorption at contact area.

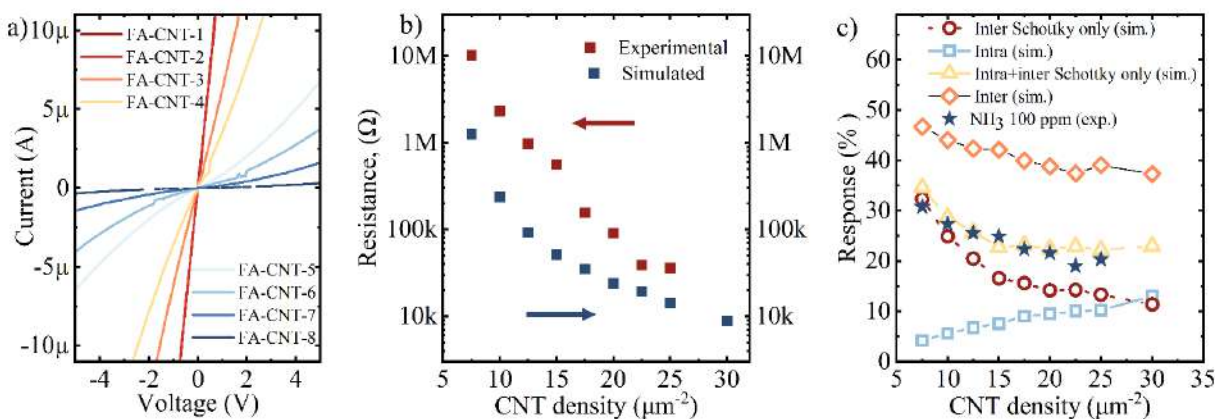


Fig. 3. (a) CNT networks current–voltage characteristic (a); Resistance dependence on CNT network density (b); Simulated and experimental dependence of response on CNT density (c)

Despite the non-linear current–voltage characteristic (Fig. 3, a), we exclude the influence of CNT metal contact since the same dependences are also observed in large area networks. The calculated resistance is several orders of magnitude less than experimental values (Fig. 3, b), probably, due to not taking into account the bending of CNTs or imprecise density approximation, higher contact resistances or influence of m-CNT on s-CNT at contact. However, both the experimental and modelled resistance have alike power dependence on density. Therefore, we plot the dependencies of the response on the density of the network (Fig. 3, c).

Experimental resistive response to ammonia exponentially decays with increasing network density. The same pattern is observed in simulated inter-CNT response with only heterojunction sensitivity. It originates from a growing number of heterojunctions participating in conductivity of sparse networks in the absence of bypassing by low-resistance similar-type CNT junctions.



For biosensors this effect has been already demonstrated by Thanahaichelvan et al. [18]. Inter-CNT response with both sensitive heterojunctions and s-CNT junctions also decrease but close to linear. Intra-CNT sensitivity in the opposite increases with the density, since each CNT adds only one parallel conductive channel but a growing number of parallel junctions. This leads to lowering the heterojunctions' role in a total conductivity and higher intra-CNT response. Therefore, junctions play a dominant role in sensitivity of sparse networks in the proposed model. There are just few factors improving intra-CNT sensitivity at sparse density, for example, the violation of m-CNT network percolation leading to higher s-CNT contribution into conductivity, but it is not sufficient at least in the proposed model with the taken inter-CNT and intra-CNT resistances.

For a deeper understanding, it is required to study the sensitivity of networks with different density and with a variable ratio of m- and s-CNT. Ham et al. [19] demonstrated superior sensitivity of a 90% s-CNT network over a 60% s-CNT. An increase in gas sensitivity with enrichment with s-CNT was also demonstrated by Nokano [20]. However, it can be both due to inter- and intra- s-CNT sensitivity, therefore, further study is required.

Conclusion

We have developed an equivalent circuit of carbon nanotube networks and simulated the resistive response to ammonia to evaluate the response dependence on the network density. We simulated the sensitivity of s-CNTs, the junctions of s-CNTs and heterojunctions between s-CNT and m-CNT. We have shown that a decrease in the network density should increase the contribution of the inter-CNT response and reduce the intra-CNT response. The same response dependence on density is observed in the experimental study, which hints at the dominant role of the junction's response.

REFERENCES

1. **Bradley K., Gabriel J. C. P., Star A., Gruner G.,** Short-channel effects in contact-passivated nanotube chemical sensors, *Applied Physics Letters*. 83 (18) (2003) 3821–3823.
2. **Zhang J., Boyd A., Tselev A., Paranjape M., Barbara P.,** Mechanism of NO₂ detection in carbon nanotube field effect transistor chemical sensors, *Applied Physics Letters*. 88 (12) (2006) 123112.
3. **Hankins A., Willard T. C., Liu A. Y., Paranjape M.,** Role of defects in the sensing mechanism of CNTFET gas sensors, *Journal of Applied Physics*. 128 (8) (2020) 084501.
4. **Sacco L., Forel S., Florea I., Cojocaru C. S.,** Ultra-sensitive NO₂ gas sensors based on single-wall carbon nanotube field effect transistors: Monitoring from ppm to ppb level, *Carbon*. 157 (2020) 631–639.
5. **Dube I., Jimenez D., Fedorov G., et al,** Understanding the electrical response and sensing mechanism of carbon-nanotube-based gas sensors, *Carbon*. 87 (2015) 330–337.
6. **Peng N., Zhang Q., Chow C. L., Tan O. K., Marzari N.,** Sensing mechanisms for carbon nanotube based NH₃ gas detection, *Nano Letters*. 9 (4) (2009) 1626–1630.
7. **Boyd A., Dube I., Fedorov G., Paranjape M., Barbara P.,** Gas sensing mechanism of carbon nanotubes: From single tubes to high-density networks, *Carbon*. 69 (2014) 417–423.
8. **Hecht D., Hu L. B., Gruner G.,** Conductivity scaling with bundle length and diameter in single walled carbon nanotube networks, *Applied Physics Letters*. 89 (13) (2006) 133112.
9. **Lee J., Stein I. Y., Devoe M. E., et al,** Impact of carbon nanotube length on electron transport in aligned carbon nanotube networks, *Applied Physics Letters*. 106 (5) (2015) 053110.
10. **Inoue S., Kokabu T., Matsumura Y.,** Effects of physical and chemical adsorption on the electric conductance of carbon nanotube films, *AIP Advances*. 8 (1) (2018) 015222.
11. **Polikarpov Y. A., Romashkin A. V., Struchkov N. S., Levin D. D.,** High uniform carbon nanotube thin films spray deposition on substrates with patterned structures having height difference, 2019 IEEE Conference of Russian Young Researchers in Electrical and Electronic Engineering, IEEE, (2019) 1980–1985.
12. **Znidarsic A., Kaskela A., Laiho P., et al,** Spatially resolved transport properties of pristine and doped single-walled carbon nanotube networks, *The Journal of Physical Chemistry C*. 117 (25) (2013) 13324–13330.

13. **Lee E. J., Balasubramanian K., Burghard M., Kern K.**, Spatially resolved potential distribution in carbon nanotube cross-junction devices, *Adv. Mater.* 21 (2009) 2720–2724.
14. **Fuhrer M. S., Nygard J., Shih L., et al**, Crossed nanotube junctions, *Science*. 288 (5465) (2000) 494–497.
15. **Mu L. W., Shi Y. J., Chen L., et al**, N-Methyl-2-pyrrolidone C1-C4 carboxylic acid: a novel solvent system with exceptional lignin solubility, *Chemical Communications*. 51 (70) (2015) 13554–13557.
16. **Mac Kernan D., Blau W.**, Exploring the mechanisms of carbon-nanotube dispersion aggregation in a highly polar solvent, *Europhysics Letters*. 83 (6) (2008) 66009.
17. **Ling Y. F., Gu G. R., Liu R. Y., et al**, Investigation of the humidity-dependent conductance of single-walled carbon nanotube networks, *Journal of Applied Physics*. 113 (2) (2013) 024312.
18. **Thanishaichelvan M., Browning L. A., Dierkes M. P., et al**, Metallic-semiconducting junctions create sensing hot-spots in carbon nanotube FET aptasensors near percolation, *Biosensors & Bioelectronics*. 130 (2019) 408–413.
19. **Ham S. W., Hong H. P., Kim J. W., et al**, Comparison of gas sensors based on oxygen plasma-treated carbon nanotube network films with different semiconducting contents, *Journal of Electronic Materials*. 44 (5) (2015) 1344–1350.
20. **Nakano M., Fujioka M., Mai K., et al**, Dielectrophoretic assembly of semiconducting carbon nanotubes separated and enriched by spin column chromatography and its application to gas sensing, *Japanese Journal of Applied Physics*. 51 (4R) (2012) 045102.

THE AUTHORS

STRUCHKOV Nikolay S.
struchkov.nikolaj@gmail.com
ORCID: 0000-0002-7382-8058

LASHKOV Andrey V.
lav.lab-sm.sstu@rambler.ru
ORCID: 0000-0001-6794-8523

KOZLOVSKAYA Ekaterina A.
k89296190714@gmail.com
ORCID: 0000-0003-0235-3101

LEVIN Denis D.
vkn@miee.ru
ORCID: 0000-0002-8414-6191

TSARIK Konstantin A.
tsarik_kostya@mail.ru
ORCID: 0000-0002-8218-7774

ROMASHKIN Alexey V.
romaleval@gmail.com
ORCID: 0000-0002-0101-6122

Received 12.08.2022. Approved after reviewing 12.08.2022. Accepted 15.08.2022.

PHYSICAL OPTICS

Conference materials

UDC 621.383.526

DOI: <https://doi.org/10.18721/JPM.153.330>

Development of visible-blind ultraviolet photodetectors based on ultrathin GaN epitaxial layers grown on c-Al₂O₃ substrates

O. A. Sinitskaya ¹✉, K. Yu. Shubina ¹, D. V. Mokhov ¹, A. V. Uvarov ¹,
V. V. Filatov ¹, A. M. Mizerov ¹, S. N. Timoshnev ¹, E. V. Nikitina ^{1,2}

¹ Alferov University, St. Petersburg, Russia;

² Ioffe Institute, St. Petersburg, Russia

✉ olesia-sova@mail.ru

Abstract. In this work, the prototypes of visible-blind ultraviolet metal-semiconductor-metal photodetectors based on GaN epitaxial layers were implemented. For this purpose, ultrathin GaN epitaxial layers were synthesized by plasma assisted molecular beam epitaxy on sapphire substrates. The morphology and electrical properties of the obtained samples were studied. To form electric contacts with the Schottky barrier, an interdigitated electrode design with Ni/Au metallization was chosen and standard lift-off laser lithography procedure was used. It has been established that the formed photodetectors have the highest sensitivity to radiation with a wavelength of 350–360 nm. It was found that rapid thermal annealing of photodetector structures at a temperature of 500 °C made possible to reduce the dark current by a maximum of 30 times. In addition, it was shown that high temperature annealing led to the increase in Schottky barrier height and decrease in the ideality factor. Thus, it was confirmed that use rapid thermal annealing method can improve the characteristics of metal-semiconductor-metal visible-blind ultraviolet photodetectors based on GaN.

Keywords: GaN, molecular beam epitaxy, ultraviolet range, photodetector, metal-semiconductor-metal, annealing

Funding: The work was supported by the Ministry of Education and Science (grant No. FSRM-2020-0008).

Citation: Sinitskaya O. A., Shubina K. Yu., Mokhov D. V., Uvarov A. V., Filatov V. V., Mizerov A. M., Timoshnev S. N., Nikitina E. V., Development of visible-blind ultraviolet photodetectors based on ultrathin GaN epitaxial layers grown on c-Al₂O₃ substrates. St. Petersburg State Polytechnical University Journal. Physics and Mathematics, 15 (3.3) (2022) 157–162. DOI: <https://doi.org/10.18721/JPM.153.330>

This is an open access article under the CC BY-NC 4.0 license (<https://creativecommons.org/licenses/by-nc/4.0/>)

Материалы конференции

УДК 621.383.526

DOI: <https://doi.org/10.18721/JPM.153.330>

Разработка видимослепых ультрафиолетовых фотодетекторов на основе ультратонких эпитаксиальных слоев GaN выращенных на подложках c-Al₂O₃

О. А. Синицкая ¹✉, К. Ю. Шубина ¹, Д. В. Мохов ¹, А. В. Уваров ¹,
В. В. Филатов ¹, А. М. Мизеров ¹, С. Н. Тимошнев ¹, Е. В. Никитина ^{1,2}

¹ Санкт-Петербургский национальный исследовательский Академический университет имени Ж. И. Алферова Российской академии наук, Санкт-Петербург, Россия;

² Физико-технический институт имени А. Ф. Иоффе, Санкт-Петербург, Россия

✉ olesia-sova@mail.ru

Аннотация. В данной работе были изготовлены прототипы видимослепых ультрафиолетовых фотодетекторов конструкции металл-полупроводник-металл (МРМ)

на основе эпитаксиальных слоев GaN, которые были синтезированы методом молекулярно-пучковой эпитаксии с плазменной активацией азота на сапфировых подложках. Для формирования контактов с барьером Шоттки была выбрана встречно-штыревая геометрия контактных площадок с металлизацией Ni/Au. Было показано, что сформированные фотодетекторы имеют максимальную чувствительность к излучению с длиной волны 350–360 нм. Было обнаружено, что быстрый термический отжиг структур со сформированными МПМ фотодетекторами при температуре 500 °С позволяет уменьшить темновой ток максимум в 30 раз. Кроме того, было показано, что высокотемпературный отжиг привел к увеличению высоты барьера Шоттки и уменьшению коэффициента неидеальности. Таким образом, было продемонстрировано, что данный метод может использоваться для улучшения характеристик видимослепых ультрафиолетовых фотодетекторов типа металл-полупроводник-металл на основе GaN.

Ключевые слова: GaN, молекулярно-пучковая эпитаксия, ультрафиолетовый диапазон, фотодетектор, металл-полупроводник-металл, отжиг

Финансирование: Работа выполнена при поддержке Министерства образования и науки (Государственное задание № FSRM-2020-0008).

Ссылка при цитировании: Синицкая О. А., Шубина К. Ю., Мохов Д. В., Уваров А. В., Филатов В. В., Мизеров А. М., Тимошнев С. Н., Никитина Е. В., Разработка видимослепых ультрафиолетовых фотодетекторов на основе ультратонких эпитаксиальных слоев GaN выращенных на подложках c-Al₂O₃ // Научно-технические ведомости СПбГПУ. Физико-математические науки. 2022. Т. 15. № 3.3. С. 157–162. DOI: <https://doi.org/10.18721/JPM.153.330>

Статья открытого доступа, распространяемая по лицензии CC BY-NC 4.0 (<https://creativecommons.org/licenses/by-nc/4.0/>)

Introduction

In recent years, the development of visible-blind ultraviolet (UV) photodetector (PD) technology has sparked interest in generating innovative ideas to improve these devices and create efficient visible-blind UV PDs. There is a wide range of UV PD applications. These devices are used in environmental, industrial, military, biological and medical fields [1]. One of the most popular PD designs is metal-semiconductor-metal (MSM) structure due to the ease of fabrication, low noise level and high detection capability [2]. UV PDs can be fabricated based on various semiconductor materials, such as Si, SiC, ZnO and others. Among them, wide bandgap semiconductors, especially (Al,Ga)N, are one of the most prospective materials for this purpose. The advantages of (Al,Ga)N are: a wide band gap corresponding to the UV spectral range ($E_g \sim 3.4 - 6.2$ eV), high mobility of charge carriers, high breakdown voltage, as well as excellent mechanical, thermal and chemical stability [3]. In this work, the prototypes of MSM UV photodetectors based on epitaxially grown on c-Al₂O₃ substrates undoped GaN layers were developed and their characteristics were studied.

Materials and Methods

The 300 nm thick GaN layers were grown by plasma-assisted molecular-beam epitaxy (PA MBE) using Veeco GEN 200 industrial type MBE setup on annealed and nitrided c-Al₂O₃ substrates. The morphology of synthesized GaN epitaxial layers was studied using scanning electron microscope (SEM) (see Fig. 1, *a, b*). Using Hall measurements, it was found that the undoped GaN epitaxial layers have n-type conductivity, which is typical for III-N materials [4, 5], with a carrier concentration of $n \sim 1.5 \times 10^{18} \text{ cm}^{-3}$ and mobility of $\mu \sim 40 \text{ cm}^2 / (\text{V}\cdot\text{s})$.

The MSM structure with semitransparent Ni/Au (15 nm thick) interdigitated electrodes (see Fig. 1, *c*) was formed using standard laser lithography technique, e-beam and thermal vacuum evaporation, and standard lift-off process. The Ni/Au contact metallization was chosen because of its low ideality factor, large Schottky barrier height (SBH, 1.04 eV [6]), and simple fabrication process.

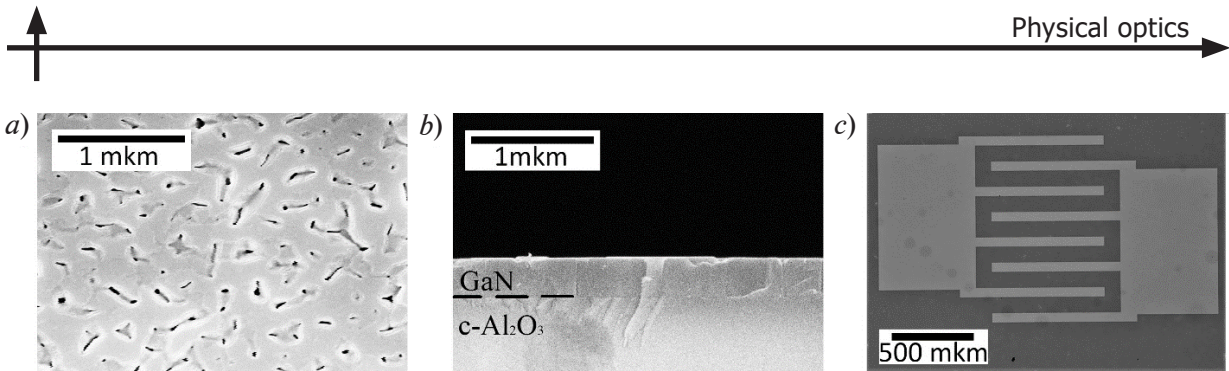


Fig. 1. SEM image of the GaN/c-Al₂O₃ epitaxial structure: plan view (a) and cross-section (b), photomicrograph of metal electrodes (c)

Results and Discussion

The UV PD I–V characteristics were obtained both in the dark, under visible range and 365 nm UV LED illumination (see Fig. 2, a). As can be seen, the I–V curves almost coincided for the measurements in dark and under normal illumination. Thus, visible radiation indeed has little effect on the operation of the fabricated UV PD. The appearance of additional photocurrent was observed under 365 nm LED illumination. At the same time, as can be seen from spectral characteristic (Fig. 2, b) the highest photoresponse was observed at wavelength range of 350–60 nm, that corresponds to GaN bandgap (3.4 eV) and confirms the reliability of the obtained I–V curves. However, as can be seen from Fig. 2, a, obtained photodetectors have a high dark current (6 mA at a bias of 2 V). It can be explained by both high dislocation density in the ultrathin epitaxial GaN layer grown on mismatched c-Al₂O₃ substrate and imperfection of contact formation procedure. It can be noted, that the dark current largely determines the sensitivity of

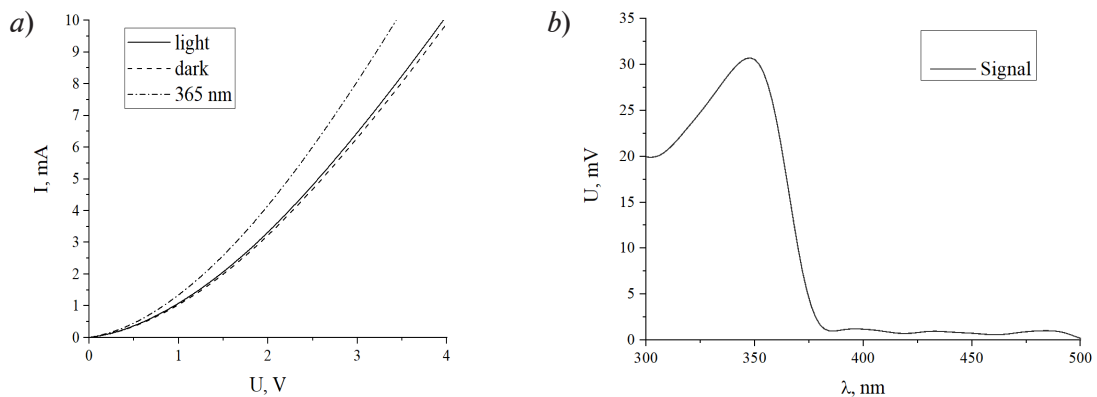


Fig. 2. I–V characteristics (a) and spectral response (b) of the formed PDs based on GaN/c-Al₂O₃

the photodetector and depends on the parameters of the Schottky barrier [7]. In a number of works, photodetectors based on GaN with Ni/Au contacts were subjected to high-temperature annealing (400–700 °C) [8–12], which led to an increase in the height of the Schottky barrier, as well as to a decrease in the level of dark current. Therefore, it was decided to carry out a series of experiments with rapid thermal annealing (RTA) of the samples using Jipelec Jetfirst 100 system. PDs based on GaN/c-Al₂O₃ epitaxial structures were annealed for 90 seconds at 400, 500 and 600 °C in the N₂ atmosphere. As expected, this resulted in a decrease in the dark current (see Fig. 3, a). It was found that the smallest dark current and the highest I_{ph}/I_d ratio consequently (see Fig. 3, b) was achieved with annealing temperature of 500 °C.

At the same time, as can be seen from Fig. 3, a, after annealing of PD structures at 600 °C, the dark current increased compared to the sample annealed at 500 °C. It can be the result of mixing Ni and Au or the Ga-Ni intermetallic formation [15–17]. Moreover, the SEM studies of the samples after annealing showed that the annealing at 600 °C leads to the formation of metal islands in the contact pad area (Fig. 3, c, d). Such phenomenon is usually observed at the interface between thin metal films and ceramics [18]. This can be explained by the fact that ceramics has very low surface energy, while the metal is quite high. To minimize the total surface energy of the system, the metal is collected in droplets to minimize the surface area and expose a large area of the ceramic surface. From this we can conclude that GaN has low surface energy, as also reported in the literature [18].

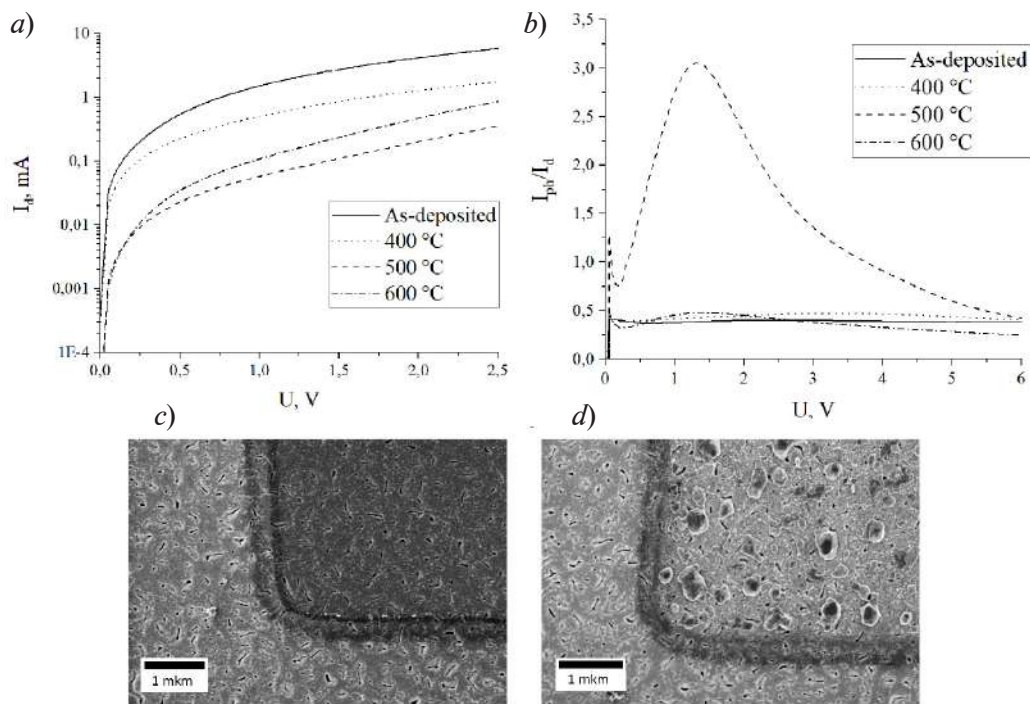


Fig. 3. Dark current of the obtained PDs before and after annealing at different temperatures (a), SEM image of the contact Ni/Au before (b) and after annealing (c)

From the I–V data for annealed and non-annealed samples, the ideality factor and the height of the Schottky barrier were determined by the Rhoderick method (Table 1) [19]. It was found that RTA actually led to an increase in the height of the Schottky barrier. An increase in the height of the Schottky barrier at higher annealing temperatures may be associated with the interfacial reactions between the metals and the semiconductor and phase transition [9]. In addition, RTA can lead to the accumulation of Ga vacancies near the metal/GaN interface which can contribute to an increase in the height of the Schottky barrier [8]. The last always corresponds to a decrease in the reverse leakage current [13, 14].

Table 1

Calculated ideality factor and height of the Schottky barrier of Ni/Au contacts for the obtained PDs

Annealing temperature, °C	Ideality factor	Height of the Schottky barrier, eV
Without annealing	2.8	0.85
400	2.7	0.88
500	2.2	1.12
600	2.1	1.16

According to the results of the study, it was found that RTA leads to a decrease in a dark current (by a maximum of 30 times). Nevertheless, its value remains relatively high. To further reduce the dark current, it is necessary to improve the crystalline quality of GaN and reduce the dislocation density in the epitaxial layers, for example, by use of various buffer layers or different types of templates for epitaxial growth of ultrathin GaN layers (SiC/substrate, GaN/substrate etc.). At the same time, the use of dielectric surface passivation (with SiO₂, Al₂O₃, etc.) and mesa etching also can provide the improvement of the characteristics of the proposed MSM PDs (including significant dark current reduce) and requires further investigation.

Conclusion

In this work, it was shown that wide-bandgap semiconductors (Al)GaN are promising materials for the creation of UV PDs due to their insensitivity to visible spectrum and sunlight, as well as high mobility of the charge carriers, and high resistance to harsh environments. UV MSM PDs



were implemented based on the ultrathin GaN epitaxial layers synthesized by the PA MBE. Interdigitated semitransparent Ni/Au Schottky contacts were formed. It was found that the RTA of the MSM PD structures at a temperature of 500 °C allows to reduce the dark current by a maximum of 30 times and to achieve significant increase in I_{ph}/I_d ratio. In addition, it was shown that high temperature annealing led to the increase in Schottky barrier height and decrease in the ideality factor. Thus, RTA can be used to improve the characteristics of the PD. However, the level of dark current in comparison with the photocurrent remains quite high. Therefore, it is necessary to improve the technology of the epitaxial synthesis of the III-N layers, as well as to use additional post-growth methods, such as the mesa structures etching and the use of surface passivation coatings.

Acknowledgments

Authors would like to thank Ya. B. Enns for fruitful discussions.

REFERENCES

1. **Munoz E., Monroy E., Pau J. L., Calle F., Omnes F., Gibart P.**, III nitrides and UV detection, *Journal of Physics: Condensed Matter*. 13 (2001) 7115–7137.
2. **Shi L., Chen K., Zhai A., Li G., Fan M., Hao Y., Zhu F., Zhang H., Cui Y.**, Status and Outlook of Metal–Inorganic Semiconductor–Metal Photodetectors, *Laser Photonics Rev.* 15 (2021) 2000401.
3. **Wengang B.**, Handbook of GaN semiconductor materials and devices, Boca Raton: Taylor & Francis, CRC Press, 2017.
4. **Baranov P. G., Bardeleben H. J., Jelezko F., Wrachtrup J.**, Magnetic Resonance of Semiconductors and Their Nanostructures: Basic and Advanced Applications, Wien, Springer-Verlag, 2017.
5. **Monish M., Mohan S., Sutar D. S., Major S. S.**, Gallium nitride films of high n-type conductivity grown by reactive sputtering, *Semiconductor Science and Technology*. 35 (4) (2020).
6. **Monroy E., Calle F., Ranchal R., Palacios T., Verdu M., Sanchez F.J., Montojo M. T., Eickhoff M., Omnes F., Bougrioua Z., Moerman I.**, Thermal stability of Pt- and Ni-based Schottky contacts on GaN and $Al_{0.31}Ga_{0.69}N$, *Semiconductor Science and Technology*. 17 (2002) L47–L54.
7. **Averin S. V., Kuznetsov P. I., Zhitov V. A., Alkeev N. V., Kotov V. M., Zakharov L. Y., Gladysheva N. B.** Metal-semiconductor-metal photodiodes based on ZnCdS/GaP wide-gap heterostructures, *Technical Physics*. 57 (11) (2012) 1514–1518.
8. **Akkaya A., Esmer L., Boyarbay Kantar B., Cetin H., Ayyıldız E.**, Effect of thermal annealing on electrical and structural properties of Ni/Au/n-GaN Schottky contacts, *Microelectronic Engineering*. 130 (2014) 62–68.
9. **Sun Y., Schen X. M., Wang J., Zhao D. G., Feng G., Fu Y., Zhang S. M., Zhang Z. H., Feng Z. H., Bai Y. X., Yang H.**, Thermal annealing behaviour of Ni/Au on n-GaN Schottky contacts, *Journal of Physics D: Applied Physics*. 35 (2002) 2648–2651.
10. **Wang C. Y., Shiao H. P., Shieh P. W., Chang H. H.**, Thermal Annealing effects study on electrical and structural properties for Ni-Au/n-GaN Schottky Contacts, *Applied Mechanics and Materials*. 284–287 (2013) 241–244.
11. **Li D., Sun X., Song H., Li Z., Chen Y., Miao G., Jiang H.**, Influence of threading dislocations on GaN-based metal-semiconductor-metal ultraviolet photodetectors, *Applied Physics Letters*. 98 (2011) 011108.
12. **Chen T. P., Young S. J., Chang S. J., Huang B. R., Wang S. M., Hsiao C. H., Wu S. L.**, Low-Frequency Noise Characteristics of GaN Schottky Barrier Photodetectors Prepared With Nickel Annealing, *IEEE Sensors Journal*. 12 (9) (2012) 282–2829.
13. **Sze S. M.**, Physics of Semiconductor Devices, Wiley – New York, 1981.
14. **Rhoderick E. H., Williams R. H.**, Metal-Semiconductor Contacts, Oxford: Clarendon Press, 1988.
15. **Kim J. K., Je J. H., Lee J. L., Park Y. J., Lee B. T.**, Microstructural Investigation of Ni/Au Ohmic Contact on p-Type GaN, *Journal of The Electrochemical Society*. 147 (12) (2000) 4645–4651.
16. **Sheu J. K., Su Y. K., Chi G. C., Chen W. C., Chen C. Y., Huang C. N., Hong J. M., Yu Y. C., Wang C. W., Lin E. K.**, The effect of thermal annealing on the Ni/Au contact of p-type GaN, *Journal of Applied Physics*. 83 (1998) 3172–3175.

17. **Jung Y., Mastro M.A., Hite J., Eddy C. R., Kim J.**, Post-annealing behavior of Ni/Au Schottky contact on non-polar a-plane GaN, Thin Solid Films. 518 (2010) 5810–5812.
18. **Duxstad K. J., Haller E. E., Yu K. M.**, High temperature behavior of Pt and Pd on GaN // Journal of Applied Physics. 81 (7) (1997) 3134–3137.
19. **Rhoderick E. H., Williams R.H.**, Metal-Semiconductor Contacts, Oxford: Clarendon Press, 1988.

THE AUTHORS

SINITSKAYA Olesya A.
olesia-sova@mail.ru
ORCID: 0000-0001-6561-0334

SHUBINA Kseniia Yu.
rein.raus.2010@gmail.com
ORCID: 0000-0003-1835-1629

MOKHOV Dmitry V.
mokhov@spbau.ru
ORCID: 0000-0002-7201-0713

UVAROV Alexander V.
lumenlight@mail.ru
ORCID: 0000-0002-0061-6687

FILATOV Vladimir V.
filatovbigfan@icloud.com
ORCID: 0000-0002-7495-1269

MIZEROV Andrey M.
andreyimizerov@rambler.ru
ORCID: 0000-0002-9125-6452

TIMOSHNEV Sergey N.
timoshnev@mail.ru
ORCID: 0000-0002-9294-3342

NIKITINA Ekaterina V.
mail.nikitina@mail.ru
ORCID: 0000-0002-6800-9218

Received 04.05.2022. Approved after reviewing 05.07.2022. Accepted 05.07.2022.

Conference materials

UDC 538.958

DOI: <https://doi.org/10.18721/JPM.153.331>

Analysis of characteristics of InGaAs/GaAs microdisk lasers bonded onto silicon board

A. S. Dragunova ¹✉, N. V. Kryzhanovskaya ^{1,2}, E. I. Moiseev ¹, F. I. Zubov ^{1,2},
N. A. Kalyuzhnyy ³, S. A. Mintairov ³, A. M. Nadtochiy ^{1,3},
Yu. A. Guseva ³, M. M. Kulagina ³, A. E. Zhukov ¹

¹ HSE University, St. Petersburg, Russia;

² Alferov University, St. Petersburg, Russia;

³ Ioffe Institute, St Petersburg, Russia

✉ anndra@list.ru

Abstract. In this work we study characteristics of the III-V microdisk lasers bonded onto silicon board. The bonding of microdisk lasers to the silicon substrate reduces their thermal resistance. Here we show improvement in output power, lasing threshold, dynamic characteristics and energy consumption in microdisk lasers with diameters of 31 μm and 19 μm by comparison of the characteristics obtained before and after bonding. Also, estimation of energy-to-data ratio was performed at 13 °C and 20 °C for a 19 μm microdisk lasers after bonding.

Keywords: hybrid integration, microlaser, quantum well dots, energy-to-data ratio, thermal resistance

Funding: This study was supported by Russian Science Foundation grant No. 18-12-00287, <https://rscf.ru/project/18-12-00287/>. Support of optical measurements was implemented in the framework of the Basic Research Program at the National Research University Higher School of Economics (HSE University).

Citation: Dragunova A. S., Kryzhanovskaya N. V., Moiseev E. I., Zubov F. I., Kalyuzhnyy N. A., Mintairov S. A., Nadtochiy A. M., Guseva Yu. A., Kulagina M. M., Zhukov A. E., Analysis of characteristics of InGaAs/GaAs microdisk lasers bonded onto silicon board. St. Petersburg State Polytechnical University Journal. Physics and Mathematics, 15 (3.3) (2022) 163–166. DOI: <https://doi.org/10.18721/JPM.153.331>

This is an open access article under the CC BY-NC 4.0 license (<https://creativecommons.org/licenses/by-nc/4.0/>)

Материалы конференции

УДК 538.958

DOI: <https://doi.org/10.18721/JPM.153.331>

Анализ характеристик InGaAs/GaAs микродисковых лазеров перенесенных на кремниевую подложку

A. С. Драгунова ¹✉, Н. В. Крыжановская ^{1,2}, Э. И. Моисеев ¹, Ф. И. Зубов ^{1,2},
Н. А. Калюжный ³, С. А. Минтаиров ³, А. М. Надточий ^{1,3},
Ю. А. Гусева ³, М. М. Кулагина ³, А. Е. Жуков ¹

¹ Национальный исследовательский университет «Высшая школа экономики», Санкт-Петербург, Россия;

² Академический университет им. Ж. И. Алфёрова, Санкт-Петербург, Россия;

³ Физико-технический институт им. А. Ф. Иоффе, Санкт-Петербург, Россия

✉ anndra@list.ru

Аннотация. В данной работе исследуются характеристики микродисковых лазеров, перенесенных на кремниевую подложку. Перенос микродисковых лазеров на кремниевую подложку снижает их тепловое сопротивление, что приводит к улучшению порога генерации, выходной оптической мощности, динамических характеристик и

энергопотребления в микродисковых лазерах диаметром 19 мкм и 31 мкм.

Ключевые слова: гибридная интеграция, микролазер, квантовые яма-точки, энергопотребление, тепловое сопротивление

Финансирование: Исследование выполнено при поддержке гранта РНФ18-12-00287, <https://rscf.ru/project/18-12-00287/>. Оптические измерения осуществлены в рамках Программы фундаментальных исследований НИУ ВШЭ.

Ссылка при цитировании: Драгунова А. С., Кръжановская Н. В., Моисеев Э. И., Зубов Ф. И., Калюжный Н. А., Минтаиров С. А., Надточий А. М., Гусева Ю. А., Кулагина М. М., Жуков А. Е., Анализ характеристик InGaAs/GaAs микродисковых лазеров перенесенных на кремниевую подложку // Научно-технические ведомости СПбГПУ. Физико-математические науки. 2022. Т. 15. № 3.3. С. 163–166. DOI: <https://doi.org/10.18721/JPM.153.331>

Статья открытого доступа, распространяемая по лицензии CC BY-NC 4.0 (<https://creativecommons.org/licenses/by-nc/4.0/>)

Introduction

In recent years, much attention has been paid to the development of microlasers based on III-V materials, which could be placed on a silicon substrate and thus allow the integration of light emitting devices with elements of silicon microelectronics and/or silicon photonics [1]. Whispering gallery mode (WGM) microlasers, such as microdisk and microring lasers, are one of the promising microlasers due to the simplicity of their manufacture, high quality factor and low optical losses. It is known [2–4], that thermal resistance increases with decreasing laser cavity size. This effect is quite critical for small devices such as microdisk lasers (MDL), because it has a great influence on their characteristics and performance due to various temperature-dependent processes [5]. It was shown in work [6] that the bonding of microdisk lasers to a silicon substrate improve thermal resistance. In [7] was reported that thermal resistance of 31 μm GaAs microdisk laser bonded on Si board reduces from 0.59 to 0.32 K/mW.

In this work we analyze the effect of reducing thermal resistance on output power, high-frequency characteristics, modulation properties and energy-to-data ratio (EDR) in microdisk lasers.

Materials and Methods

The laser heterostructure was grown by metalorganic vapour-phase epitaxy on an $n^{\pm}\text{GaAs}$ substrate misoriented by 6° toward [111] direction. The laser active region consists of 6 layers of InGaAs/GaAs quantum well-dots separated from each other with 40 nm thick GaAs spacer layers. The active region was placed at the center of an undoped GaAs waveguide with a thickness of 0.78 μm . The waveguide was clamped between two $\text{Al}_{0.4}\text{Ga}_{0.6}\text{As}$ cladding layers 1.5 μm thick doped with p- and n-types.

Microdisk lasers with a diameter of 19 and 31 μm were formed by photolithography and dry etching through the active region and two cladding layers to the substrate. The side walls of the microdisk lasers were not passivated. The n-contact was formed on the back surface of a GaAs substrate thinned to $\approx 100 \mu\text{m}$. Round-shaped AgMn/Ni/Au p-contacts were formed individually to each microdisk on top of $p^{\pm}\text{GaAs}$ top layer (Fig. 1, *a*). Then the substrate with ready-made microdisk lasers was cleaved onto chips containing 10 microlasers each.

The thermocompression bonding of microdisk lasers on the silicon surface was performed using a Finetech FINEPLACER lambda2 die bonder (Fig. 1, *b, c*). Electroluminescence was collected with a x50 Mitutoyo M Plan Apo NIR objective and detected by a Yokogawa AQ6370C optical spectrum analyzer or by Thorlabs FDG1010 $1 \times 1 \text{ cm}^2$ photodiode. Dynamic characteristics were carried out using a New Focus 1434 photodetector with the range from 50 MHz to 20 GHz and an Agilent E8364B network analyzer.

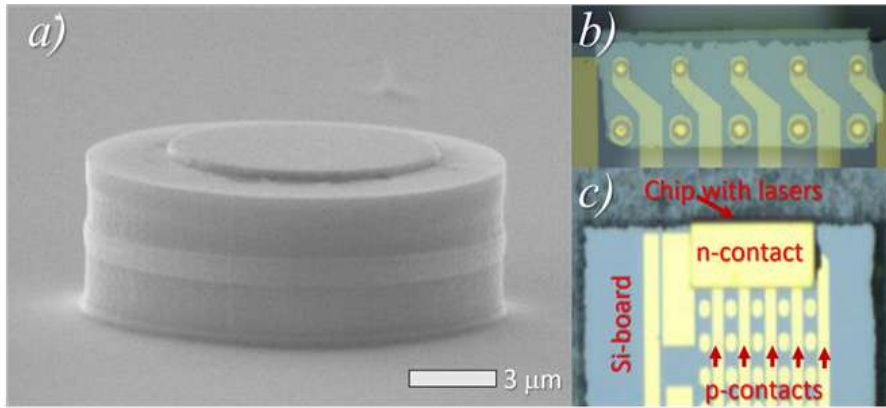


Fig. 1. Image of microdisk laser obtained by scanning electron microscopy (a), top-view of microdisk lasers placed on Si board in infra-red illumination during thermocompression bonding (b), top-view of chip with bonded microdisk lasers on Si board (c)

Results and Discussion

Characteristics of the microdisk lasers with a diameter of 19 and 31 μm were compared before and after bonding. Thermal resistance of bonded MDL decreases in 2.3 and 1.8 times for 19 μm and 31 μm , respectively. The decrease in thermal resistance in microdisk lasers bonded onto a silicon substrate is due to the higher thermal conductivity of the substrate, as well as to a decrease in the thickness of the intermediate layers. The threshold current after bonding decreased from 9.4 to 7.6 mA for 19 μm microdisk and from 21.4 to 17.4 for 31 μm microdisk (Fig. 2, a). Better heat removal from the active region results in the higher output optical power, slope of dependence of optical power on bias current and thermal roll-over.

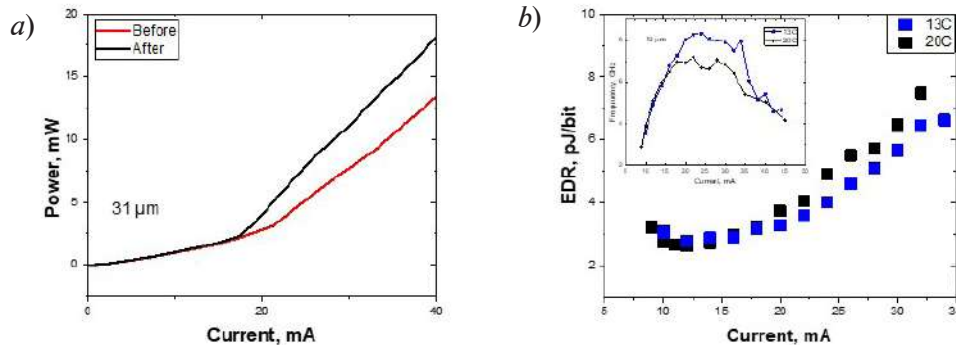


Fig. 2. The output power versus the injection current of 31 μm MDL before and after bonding (a). The dependence of EDR on the bias current for 13 $^{\circ}\text{C}$ and 20 $^{\circ}\text{C}$ and the 3dB bandwidth versus the pumping current (inset) for 19 μm MDL (b)

We also observe improvement in dynamic characteristics of the bonded lasers. The 3dB modulation bandwidth ($f_{3\text{dB}}$) of 6.9 GHz and 8 GHz for 19 μm in diameter device was obtained 20 $^{\circ}\text{C}$ and 13 $^{\circ}\text{C}$ degrees, respectively (inset in Fig.2, b). A noticeable dependence of the peak bandwidth on temperature indicates that the microlaser overheating has a significant effect on its dynamic performance. To estimate the energy efficiency of the microdisk laser intended for optical data transmission one can use energy-to-data ratio (EDR), i.e. the electrical energy consumed per bit of transmitted information, $\text{EDR} = UI/B$, where U – is voltage, I – bias current, B – bit rate [8]. The value of bit rate (B) can be estimate as twice the modulation bandwidth $B = 2f_{3\text{dB}}$. The smallest EDR value of 2.5 pJ/bit is achieved in 10–15 mA bias current range. At the current of maximum $f_{3\text{dB}}$ (25 mA) for 13 $^{\circ}\text{C}$ the EDR value is 4 pJ/bit.

Conclusion

In this work we study characteristics of the III-V microdisk lasers bonded onto silicon board. The bonding of microdisk lasers to a silicon substrate reduces their thermal resistance. Here

we show improvement in output power, lasing threshold, dynamic characteristics and energy consumption in microdisk lasers with diameters of 31 μm and 19 μm by comparison of the characteristics obtained before and after bonding. Also estimation of energy-to-data ratio was performed for a 19 μm microdisk lasers after bonding at 13 °C and 20 °C.

REFERENCES

1. Cornet C., Lreger Y., Robert C., Integrated Lasers on Silicon, ISTE Press – Elsevier, 2016.
2. Kryzhanovskaya N. V. et al., Microdisk injection lasers for the 1.27- μm spectral range, Semiconductors. 50 (3) (2016) 390–393.
3. Moiseev E., Kryzhanovskaya N., Maximov M., Zubov F., Nadtochiy A., Kulagina M., et al., Highly efficient injection microdisk lasers based on quantum well-dots, Optics Letters. 43 (19) (2018) 4554–4557.
4. Zhukov A. E., Kryzhanovskaya N. V., Moiseev E. I., Nadtochiy A. M., Dragunova A. S., Maximov M. V., et al., Impact of self-heating and elevated temperature on performance of quantum dot microdisk lasers, IEEE Journal of Quantum Electronics. 56 (5) (2020) 1–8.
5. Joyce W. B., Dixon, R. W., Thermal resistance of heterostructure lasers, Journal of Applied Physics. 46 (2) (1975) 855–862.
6. Kryzhanovskaya N., Moiseev E., Nadtochiy A., Maximov M., Dragunova A., Fetisova M., et al., Monolithic and hybrid integration of InAs/GaAs quantum dot microdisk lasers on silicon, In Integrated Optics: Design, Devices, Systems and Applications. VI 1775 (2021) 117750P.
7. Zubov F., Maximov M., Moiseev E., Vorobyev A., Mozharov A., Berdnikov Y., et al., Improved performance of InGaAs/GaAs microdisk lasers epi-side down bonded onto a silicon board, Optics Letters. 46 (16) (2021) 3853–3856.
8. Moser P., Hofmann W., Wolf P., Lott J. A., Larisch G., Payusov A., et al., 81 fJ/bit energy-to-data ratio of 850 nm vertical-cavity surface-emitting lasers for optical interconnects, Applied Physics Letters. 98 (23) (2011) 231106.

THE AUTHORS

DRAGUNOVA Anna S.

anndra@list.ru

ORCID: 0000-0002-0181-0262

KRYZHANOVSKAYA Natalia V.

nataliakryzh@gmail.com

ORCID: 0000-0002-4945-9803

MOISEEV Eduard I.

emoiseev@hse.ru

ORCID: 0000-0003-3686-935X

ZUBOV Fedor I.

fedyazu@mail.ru

ORCID: 0000-0002-3926-8675

KALYUZHNYI Nikolay A.

Nickk@mail.ioffe.ru

ORCID: 0000-0001-8443-4663

MINTAIROV Sergey A.

mintairov@scell.ioffe.ru

ORCID: 0000-0002-6176-6291

NADTOCHIY Alexey M.

al.nadtochy@mail.ioffe.ru

ORCID: 0000-0003-0982-907X

GUSEVA Yulia A.

Guseva.Julia@mail.ioffe.ru

ORCID: 0000-0002-7035-482X

KULAGINA Marina M.

Marina.Kulagina@mail.ioffe.ru

ORCID: 0000-0002-8721-185X

ZHUKOV Alexey E.

zhukale@gmail.com

ORCID: 0000-0002-4579-0718

Received 13.07.2022. Approved after reviewing 14.07.2022. Accepted 15.07.2022.

Conference materials

UDC 535.015

DOI: <https://doi.org/10.18721/JPM.153.332>

The investigation of optical coupling of microlasers with tapered fiber

N. A. Fominykh ^{1,2}✉, E. I. Moiseev ¹, I. S. Makhov ¹, K. N. Min'kov ³,
A. M. Nadtochiy ^{1,4}, Yu. A. Guseva ⁴, M. M. Kulagina ⁴, S. A. Mintairov ⁴,
N. A. Kalyuzhnyy ⁴, N. V. Kryzhanovskaya ^{1,2}, A. E. Zhukov ¹

¹ HSE University, St. Petersburg, Russia;

² Alferov University, St. Petersburg, Russia;

³ Russian Quantum Center, Moscow, Russia;

⁴ Ioffe Institute, St. Petersburg, Russia

✉ fominy-nikita@yandex.ru

Abstract. We present an investigation of optical coupling of injection microdisk and microring lasers with different diameters with a tapered fiber. We studied the dependences of the laser dominant mode intensity on the distance between the tapered fiber and the microlaser's sidewall. For every studied laser a sharp intensity growth by 2–3 orders of magnitude was observed when the tapered fiber came in contact with the microlaser. We compared lasing spectra received by the tapered fiber and by the microobjective. Though the intensity of the electroluminescence signal received by the tapered fiber was lower than that coupled by the microobjective, the ratio of the dominant (lasing) mode intensity to spontaneous emission was noticeably higher for the case of the tapered fiber.

Keywords: quantum well-dots, microlasers, microdisk resonators, tapered fiber, whispering gallery modes

Funding: The fabrication of the lasers was supported by Russian Foundation for Basic Research, project № 20-02-00334. The study of the output power was implemented in the framework of the Basic Research Program at the National Research University Higher School of Economics (HSE University). The studies of laser's spectral characteristics were supported by the Ministry of Science and Higher Education of the Russian Federation, project № 0791-2020-0002.

Citation: Fominykh N. A., Moiseev E. I., Makhov I. S., Min'kov K. N., Nadtochiy A. M., Guseva Yu. A., Kulagina M. M., Mintairov S. A., Kalyuzhnyy N. A., Kryzhanovskaya N. V., Zhukov A. E., The investigation of optical coupling of microlasers with tapered fiber. St. Petersburg State Polytechnical University Journal. Physics and Mathematics, 15 (3.3) (2022) 167–170. DOI: <https://doi.org/10.18721/JPM.153.332>

This is an open access article under the CC BY-NC 4.0 license (<https://creativecommons.org/licenses/by-nc/4.0/>)

Материалы конференции

УДК 535.015

DOI: <https://doi.org/10.18721/JPM.153.332>

Исследование оптической связи микролазеров с утоненным волокном

Н. А. Фоминых ^{1,2}✉, Э. И. Моисеев ¹, И. С. Махов ¹, К. Н. Миньков ³,
А. М. Надточий ^{1,4}, Ю. А. Гусева ⁴, М. М. Кулагина ⁴, С. А. Минтаиров ⁴,
Н. А. Калюжный ⁴, Н. В. Крыжановская ^{1,2}, А. Е. Жуков ¹

¹ Национальный исследовательский университет «Высшая школа экономики», Санкт-Петербург, Россия;

² Алфёровский университет, Санкт-Петербург, Россия;

³ Российский квантовый центр, Москва, Россия;

⁴ Физико-технический институт им. А. Ф. Иоффе, Санкт-Петербург, Россия

✉ fominy-nikita@yandex.ru

Аннотация. В данной работе представлено исследование оптической связи инжекционных микродисковых и микрокольцевых лазеров различного диаметра с утоненным оптическим волокном. Были исследованы зависимости интенсивности доминирующей моды лазера от расстояния между утоненным волокном и боковой стенкой микролазера. Для каждого исследованного лазера наблюдался резкий рост интенсивности на 2–3 порядка при контакте волокна с микролазером. Проведено сравнение спектров лазерной генерации, полученных через утоненное волокно и микрообъектив. Интенсивность сигнала электролюминесценции в случае утоненного волокна была меньше, чем у сигнала с микрообъектива, но отношение интенсивности доминирующей лазерной моды к спонтанному излучению для утоненного волокна заметно выше.

Ключевые слова: квантовые яма-точки, микролазеры, микродисковый резонатор, утоненное волокно, моды шепчущей галереи

Финансирование: Изготовление лазеров было поддержано Российским фондом фундаментальных исследований, проект № 20-02-00334. Исследование выходной мощности выполнено в рамках программы фундаментальных исследований НИУ ВШЭ (Университет ВШЭ). Исследование спектральных характеристик лазеров было поддержано Министерством науки и высшего образования РФ, проект № 0791-2020-0002.

Ссылка при цитировании: Фоминых Н. А., Моисеев Э. И., Махов И. С., Миньков К. Н., Надточий А. М., Гусева Ю. А., Кулагина М. М., Минтаиров С. А., Калюжный Н. А., Крыжановская Н. В., Жуков А. Е., Исследование оптической связи микролазеров с утоненным волокном // Научно-технические ведомости СПбГПУ. Физико-математические науки. 2022. Т. 15. № 3.3. С. 167–170. DOI: <https://doi.org/10.18721/JPM.153.332>

Статья открытого доступа, распространяемая по лицензии CC BY-NC 4.0 (<https://creativecommons.org/licenses/by-nc/4.0/>)

Introduction

In recent years, the investigation of semiconductor microdisk (MD) and microring (MR) lasers draws a lot of attention because microlasers of this design can be used as building blocks in future microphotonic and nanophotonic devices [1]. MD and MR lasers support whispering gallery modes (WGM) with high quality factor and, accordingly, low output losses [2]. WGM microlasers are promising candidates for optically coupled systems due to lateral light output. Coupling of microlaser emission by tapered fiber has already been investigated for the cases of passive WGM microresonators [3] and WGM microlasers with optical pumping [4]. In this work we study the optical coupling of injection semiconductor MD and MR lasers with different diameters (15–50 μm) with tapered fiber.

Materials and Methods

The studied injection microlasers were fabricated from a laser epitaxial heterostructure synthesized on a n^+ -GaAs substrate by MOCVD with an active region representing a 5-layer array of InGaAs/GaAs quantum well-dots. MD and MR lasers a height of about 5 μm and diameters varied in range from 15 μm to 50 μm were formed by photolithography and dry etching. We used AgMn/Ni/Au metallization to form ring contacts to the p^+ -GaAs layer at the tops of the mesas. The GaAs substrate was thinned to approximately 100 μm , and a solid electrical AuGe/Ni/Au n -contact was fabricated on its reverse surface.

Horizontal and vertical visualization was achieved by Mitutoyo M Plan Apo NIR 20x objective and CCD camera. Electroluminescence (EL) of MD and MR lasers was excited by a stabilized

DC current with a Keithley 2400 Series SourceMeter® power supply. The EL spectra were analysed with a Yokogawa AQ6370C optical spectrum analyser.

The tapered fiber was fabricated by adiabatic stretching method which allows setting a shape and parameters of the tapered section [5]. In this work we used the fiber with 2 μm diameter of the thinnest part. The tapered fiber was cleaved in the thinned part. To achieve more careful positioning near microlaser we mounted the fiber on a 3-dimensional translation stage. The coupling scheme is represented in Fig. 1.

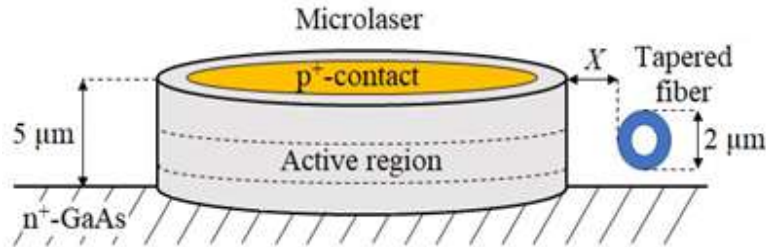


Fig. 1. The coupling scheme

Results and Discussion

We located the tapered fiber near the active region of the structures as shown in figure 1 to study the dependencies of the dominant mode intensity on the distance between the tapered fiber and the microlaser's side wall (X). We observed a sharp intensity growth by 2–3 orders of magnitude when the tapered fiber came in contact with the microlaser (Fig. 2). Any changes of the resonant line full width at half maximum were not found at the contact of the microlaser with fiber probably due to the low spectral resolution of the optical spectrum analyser used.

To receive lasing spectra by the tapered fiber we located it in contact with the sidewall ($X = 0$) of the studied microlasers and opposite their active region (Fig. 1). Such careful positioning allowed us to obtain lasing spectra with maximum intensity (Fig. 2). The lasing spectra above the threshold of the MD laser with 40 μm diameter received by the tapered fiber and by the microobjective are shown in Fig. 3. Despite lower intensity of the spectra received by the tapered fiber in comparison with that received by the microobjective the ratio of the dominant mode intensity to spontaneous emission was noticeably higher in the case of the fiber. The coupling of the lasing mode to the tapered fiber can be the reason of the higher resonant mode intensity. We also studied the evolution of the emission spectra received by the tapered fiber and by the microobjective with increasing injection current to determine a threshold current. There were no differences in the threshold currents determined by the two methods.

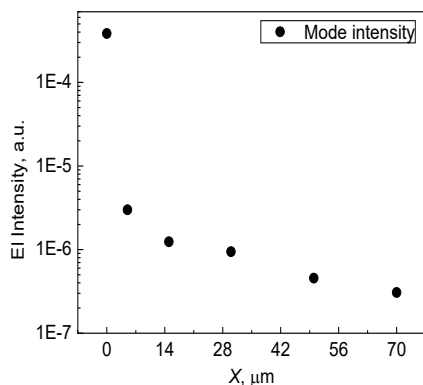


Fig. 2. The dependence of the dominant mode intensity on the distance between the tapered fiber and the 20 μm MR laser

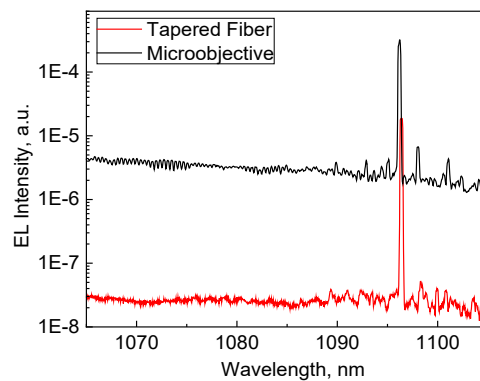


Fig. 3. EL spectra of 40 μm MD laser at 10 mA current received by the tapered fiber and by the microobjective

Conclusion

The outcoupling of the lasing emission from an injection MD and MR lasers into a tapered fiber without the evidence of the lasing parameters deterioration was realized for the first time. A sharp intensity growth by 2–3 orders of magnitude was observed when the tapered fiber came in

contact with the microlaser. In comparison with the spectra received by the microobjective the ratio of the dominant lasing mode intensity to spontaneous emission was noticeably higher for the case of the tapered fiber.

Acknowledgments

The tapered fiber was fabricated using the equipment of the Center for Collective Use VNIIOFI (ckp.vniiofi.ru).

REFERENCES

1. Schmidt C., Chipouline A., Käsebier T., Kley E.-B., Tünnermann A., Pertsch T., Shuvayev V., Deych L. I., Observation of optical coupling in microdisk resonators, *Physical Review A*. 80 (4) (2009) 043841.
2. Kryzhanovskaya N. V. et al., Evaluation of energy-to-data ratio of quantum-dot microdisk lasers under direct modulation, *Journal of Applied Physics*. 126 (6) (2019) 063107.
3. Srinivasan K., Painter O., Mode coupling and cavity-quantum-dot interactions in a fiber-coupled microdisk cavity, *Physical Review A*. 75 (2) (2007) 023814.
4. Cai M., Painter O., Vahala K. J., Sercel P. C., Fiber-coupled microsphere laser, *Optics letters*. 25 (19) (2000) 1430–1432.
5. Ivanov A. D., Min'kov K. N., Samoilenko A. A., Method of producing tapered optical fiber, *Journal of Optical Technology*. 84 (7) (2017) 500–503.

THE AUTHORS

FOMINYKH Nikita A.
fominy-nikita@yandex.ru
ORCID: 0000-0003-3919-6410

MOISEEV Eduard I.
emoiseev@hse.ru
ORCID: 0000-0003-3686-935X

MAKHOV Ivan S.
imahov@hse.ru
ORCID: 0000-0003-4527-1958

MIN'KOV Kirill N.
k.n.minkov@yandex.ru
ORCID: 0000-0002-6462-2453

NADTOCHIY Alexey M.
al.nadtochy@mail.ioffe.ru
ORCID: 0000-0003-0982-907X

GUSEVA Yulia A.
Guseva.Julia@mail.ioffe.ru
ORCID: 0000-0002-7035-482X

KULAGINA Marina M.
Marina.Kulagina@mail.ioffe.ru
ORCID: 0000-0002-8721-185X

MINTAIROV Sergey A.
mintairov@scell.ioffe.ru
ORCID: 0000-0002-6176-6291

KALYUZHNYI Nikolay A.
Nickk@mail.ioffe.ru
ORCID: 0000-0001-8443-4663

KRYZHANOVSKAYA Natalia V.
nataliakryzh@gmail.com
ORCID: 0000-0002-4945-9803

ZHUKOV Alexey E.
zhukale@gmail.com
ORCID: 0000-0002-4579-0718

Received 13.07.2022. Approved after reviewing 14.07.2022. Accepted 29.07.2022.

Conference materials

UDC 544.536

DOI: <https://doi.org/10.18721/JPM.153.333>

Comparison of femtosecond laser, hydrothermal and microwave synthesis of fluorescent products from L-lysine

A. A. Astafiev ¹✉, A. M. Shakhov ¹, M. S. Syrchina ¹, D. V. Shepel ¹, V. A. Nadtochenko ¹

¹ N. N. Semenov Federal Research Center of Chemical Physics
of the Russian Academy of Sciences, Moscow, Russia

✉ astafiev.artyom@gmail.com

Abstract. Femtosecond laser synthesis of fluorescent products from essential amino acids in living cells and tissues can be exploited in fluorescent bioimaging. To gain insight into reaction mechanism and a role of thermal processes we examine synthesis of fluorescent products from L-lysine by femtosecond laser irradiation, hydrothermal and microwave synthesis and perform comparative analysis of reaction products. Our results indicate that compared with purely thermal synthetic routes femtosecond laser synthesis favours formation of carbon dots-type fluorescent nanomaterials.

Keywords: femtosecond laser pulses, nonlinear absorption, laser treatment, nanomaterials, luminescent carbon dots, photobleaching, photostability

Funding: This study was funded by Russian Scientific Foundation grant No. 21-72-20169. The measurements were performed in the FRCCP shared research facilities No. 506694 and large-scale research facilities No. 1440743.

Citation: Astafiev A. A., Shakhov A. M., Syrchina M. S., Shepel D. V., Nadtochenko V. A., Comparison of femtosecond laser, hydrothermal and microwave synthesis of fluorescent products from L-lysine. St. Petersburg State Polytechnical University Journal. Physics and Mathematics, 15 (3.3) (2022) 171–176. DOI: <https://doi.org/10.18721/JPM.153.333>

This is an open access article under the CC BY-NC 4.0 license (<https://creativecommons.org/licenses/by-nc/4.0/>)

Материалы конференции

УДК 544.536

DOI: <https://doi.org/10.18721/JPM.153.333>

Сравнение лазерного фемтосекундного, гидротермального и микроволнового синтеза флуоресцентных продуктов из L-лизина

A. A. Астафьев ¹✉, А. М. Шахов ¹, М. С. Сырчина ¹,
Д. В. Шепель ¹, В. А. Надточенко ¹

¹ Федеральный исследовательский центр химической физики им. Н. Н. Семенова
Российской Академии Наук, Москва, Россия

✉ astafiev.artyom@gmail.com

Аннотация. В настоящей работе проведен сравнительный анализ механизмов получения люминесцентных углеродных точек, а также основных физико-химических характеристик продуктов, полученных в результате трех различных методов синтеза – лазерного фемтосекундного, микроволнового и гидротермального.

Ключевые слова: фемтосекундные лазерные импульсы, нелинейное поглощение света, лазерная модификация материалов, наноматериалы, люминесцентные углеродные точки, фотовыцветание, фотостабильность

Финансирование: Работа выполнена при финансовой поддержке РФФИ, грант № 21-72-20169. Измерения были выполнены в центре коллективного пользования № 506694 и на уникальной научной установке № 1440743.

Ссылка при цитировании: Астафьев А. А., Шахов А. М., Сырчина М. С., Шепель Д. В., Надточенко В. А., Сравнение лазерного фемтосекундного, гидротермального и микроволнового синтеза флуоресцентных продуктов из L-лизина // Научно-технические ведомости СПбГПУ. Физико-математические науки. 2022. Т. 15. № 3.3. С. 171–176. DOI: <https://doi.org/10.18721/JPM.153.333>

Статья открытого доступа, распространяемая по лицензии CC BY-NC 4.0 (<https://creativecommons.org/licenses/by-nc/4.0/>)

Introduction

Production of fluorescent species from biomolecules in living cells and tissues in situ by femtosecond laser irradiation offers many unique advantages in fluorescent bioimaging [1–2]. We demonstrated that femtosecond laser synthesis of fluorescent carbon dots from essential amino acid L-lysine provides a potential route of fluorescent species formation in living cells [3]. Laser-induced heating can be one of mechanisms responsible for carbon dots synthesis and fluorescent carbon dots can be also produced from amino acids, including L-lysine, by a more conventional thermal-driven reactions using solvothermal or microwave synthesis [4, 5]. In order to gain a better understanding of the role of thermal mechanisms and peculiarities of femtosecond laser synthesis we analysed optical properties, morphology and chemical composition of products obtained from L-lysine aqueous solution by three different routines: femtosecond laser, hydrothermal and microwave synthesis (hereafter samples Lys-FS, Lys-HT and Lys-MW respectively).

Materials and Methods

1. Synthesis and purification of products.

Lys-FS: 2 ml of L-lysine aqueous solution (0.1 g/mL) in a quartz cuvette was irradiated with trains of femtosecond laser pulses focused by a spherical lens ($f = 8$ mm, 0.5NA). Central wavelength of laser pulses was 800 nm, repetition rate – 1 kHz, duration – 50 fs, pulse energy – 1.4 mJ. Lys-HT: 10 ml of 0.5 g/mL L-lysine solution in a PTFE container was heated in an oven for 30 hours at 220 °C. Lys-MW: 5 ml of 0.1 g/mL L-lysine solution in a glass vial was heated in a domestic microwave oven for 1 min at 800 W. In order to remove unreacted L-lysine the samples were dialyzed for 72 hours in 2,000 MWCO dialysis units.

2. Samples characterization.

UV-Vis absorption and photoluminescence spectra of aqueous solutions of the samples in a 3.5-ml quartz cuvette were recorded with Shimadzu UV-3600 spectrophotometer and Shimadzu RF-5031PC spectrofluorometer. Fluorescence quantum yield at 356 nm excitation wavelength was estimated with the slope method using ethanol solution of anthracene ($\Phi = 0.27$) as a reference sample. Fluorescence decay curves of samples aqueous solutions were recorded at 450 nm emission wavelength by the a Beckr-Hickl SPC-150N time-correlated single photon counting system using excitation with laser pulses of the femtosecond laser oscillator (Tsunami, Spectra-Physics) with 360 nm central wavelength and 60 MHz repetition rate. For measurement of fluorescence anisotropy decay we recorded two fluorescence decay curves for emission with polarization parallel and perpendicular to the excitation laser and calculated emission anisotropy as a function of time.

Samples diluted in ethanol and dried on a cover slip were analyzed with an atomic-force microscopy (AFM) unit (SMENA-B, NT MDT) in an intermittent contact mode. High resolution transmission electron microscopy (HRTEM) images were recorded on a JEM 2100F high-resolution transmission electron microscope (JEOL Co. Ltd., Japan). Infrared absorption spectra were collected using a Bruker Lumos II FTIR microscope-spectrometer in a reflection mode from drops the samples aqueous solutions dried on the surface of Ag mirror. Raman spectra were collected with a Bruker Senterra Raman microscope-spectrometer using gold nanoparticles photocatalytically grown from HAuCl₄ aqueous solution for surface enhancement of the Raman scattering signal. Elemental analysis with energy-dispersive (EDS) X-ray spectroscopy was performed using a Prisma-E electron microscope (Thermo-Fisher), using L-lysine with a known C:N:O ratio (3:1:1) as a calibration sample.

Results and Discussion

Originally colorless L-lysine aqueous solution became dark red or black after laser, hydrothermal or microwave treatment and exhibited strong blue fluorescence, which indicated formation of colored and luminescent products from L-lysine. After dialysis versus a 2,000 MWCO dialysis membrane **Lys-FS** solution retained most (55%) of original integral UV-Vis absorption, whereas **Lys-HT** and **Lys-MW** retained only 5.5 and 8% of integral absorption respectively. This result suggests that hydrothermal or microwave treatment of L-lysine mostly resulted in formation of colored products with small molecular weight, which could pass through pores of the dialysis membrane. At the same time Lys-FS contained nanosized particles which were retained by the membrane. Presence of nanosized products in Lys-FS was confirmed by AFM and HRTEM images which visualized irregular-shaped nanoparticles with characteristic sizes in the range from nanometers to ca. 10–20 nanometers (Fig. 1). Also HRTEM images of the nanoparticles revealed onion-type structure consisting of concentric layers with the interlayer distance of ca. 0.35 nm (Fig. 1, *b*). This distance almost coincides with the graphite [002] lattice fringe (0.335 nm), suggesting that these nanoparticles were so-called carbon onions, consisting of concentric fullerene-type shells [6].

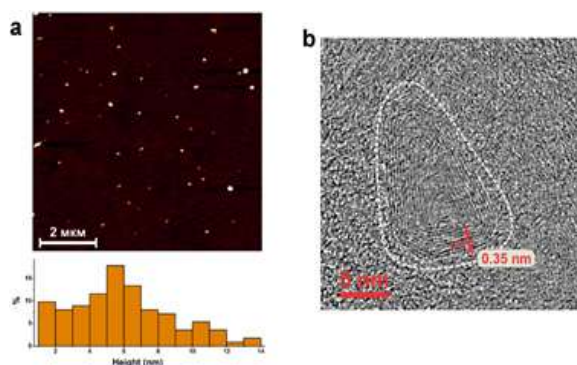


Fig. 1. AFM image of Lys-FS nanoparticles on a glass substrate and their height distribution (*a*); HRTEM image of a single Lys-FS nanoparticle (*b*)

FTIR reflectance spectra of all the purified samples exhibited characteristic secondary amide bands at ca. 1650–1650, 1550 and 1300 cm^{-1} (Fig. 2, *a*), indicative of peptide bonds formation. Thus products of the thermal or laser treatment contained peptide chains formed by polycondensation of L-lysine molecules. Second derivative analysis reveals position of Lys-FS amide I and amide III bands at 1547 and 1302 cm^{-1} , which is indicative of the α -helix peptide conformation [7, 8]. At the same time in Lys-HT the position of amide I (1666 cm^{-1}) and amide III (1311 cm^{-1}) show a more disordered secondary structure consisting of a combination of extended P_{II} helix and turns. Additionally FTIR spectra exhibited CH_2 stretching and bending vibrations from the lysine side chains, COO^- stretching vibrations from peptide terminal residues, NH , OH and CH stretching vibrations.

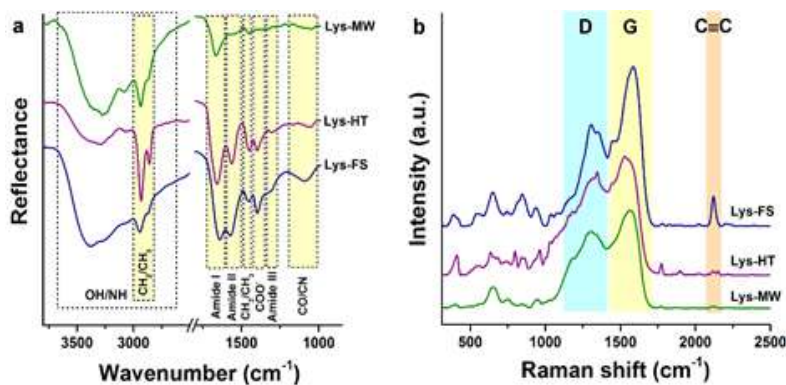


Fig. 2. FTIR (*a*) and Raman (*b*) spectra of Lys-FS, Lys-HT and Lys-MW

Raman spectra of all the three samples demonstrated broad bands centered at 1310 and 1580 cm^{-1} , which are D and G bands typical for carbonaceous materials and are indicative of sp^2 -hybridized carbon forming $\text{C}=\text{C}$ bonds and honeycomb structures of fused benzene rings. Another band at 2120 cm^{-1} attributed to $\text{C}\equiv\text{C}$ stretching was especially strong in Lys-FS spectra. Thus, in addition to the peptide chains with sp^3 -hybridized carbon all the samples contained unsaturated fragment with sp^2 and sp^3 -hybridized carbon.

Polycondensation of L-lysine molecules into peptide chains removes one oxygen atom from each residue and therefore must result in decrease of O and increase of C and N elemental content compared with L-lysine. EDS measurements for Lys-HT confirm these changes and show that its elemental content was similar to poly-lysine (Table 1), thus it mostly consists of lysine oligomers (polymers). At the same time Lys-FS and Lys-MW exhibited much larger oxygen content than poly-lysine, probably due to oxidation in presence of the atmospheric air, which compensated for a loss of oxygen in the polycondensation reaction. This oxidation is confirmed by a stronger OH stretching band on the FTIR spectra of Lys-FS and Lys-MW compared with Lys-HT. C:N atomic ratio for all the three samples was larger than 3:1 ratio expected for L-lysine or poly-L-lysine. This change is indicative of the onset of carbonization and removal of nitrogen. The C:N ratio and consequently the scale of carbonization was the largest for Lys-FS.

Table 1

CNO Elemental composition of the samples compared with L-lysine and poly-lysine

Sample	C (at. %)	N (at. %)	O (at. %)	C:N ratio	N:O ratio
L-lysine	60	20	20	3	1
Poly-L-lysine	66.7	22.2	11.1	3	2
Lys-FS	61.1	17.8	21.2	3.43	0.84
Lys-HT	65.5	20.8	13.7	3.15	1.52
Lys-MW	61.2	20.0	18.8	3.06	1.06

In summary, the chemical analysis revealed that products of L-lysine heating or laser treatment are formed by processes of L-lysine polycondensation, oxidation and partial carbonization of resulting poly-(olygo-)peptides. Carbonization converts peptide fragments to unsaturated moieties with sp^2 - and sp^3 -hybridized carbon, which is a probable mechanism for formation of light-absorbing chromophore groups. Whereas hydrothermal and microwave treatment mostly produces relatively short L-lysine oligomers, femtosecond laser treatment tends to produce larger polymer nanoparticles and induces larger oxidation and carbonization effect. Carbonization and graphitization of polymer nanoparticles can produce carbon onion structures revealed by the HRTEM.

All the three samples had strong absorption with absorption peaks and shoulders in the ultraviolet range, whereas their visible absorption was relatively weak and structureless (Fig. 3). Presence of near-UV and visible absorption demonstrates effective formation of chromophores with conjugated systems from L-lysine. All the samples exhibited strong photoluminescence with emission maxima in the blue range (at 430–440 nm) and excitation maxima near 350 nm (Table 2). Excitation maxima did not coincide with peaks and shoulders on the absorption spectrum, indicating that most UV-absorbing chromophores were nonfluorescent.

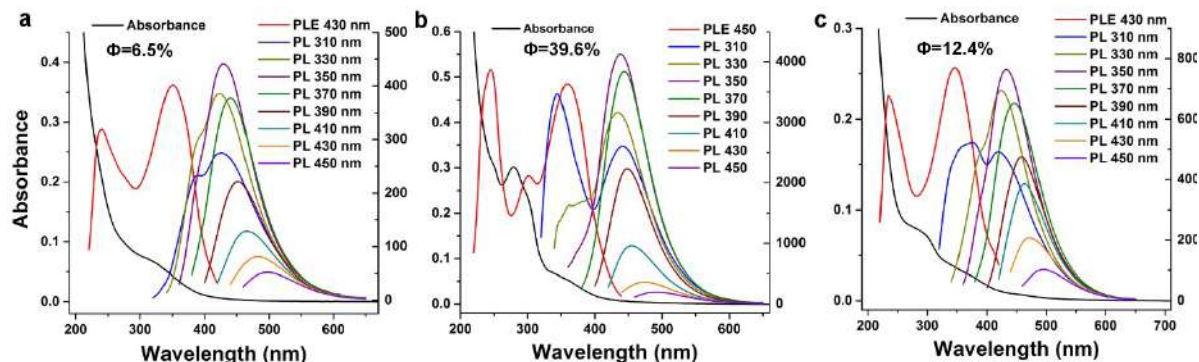


Fig. 3. UV-Vis absorbance, photoluminescence emission (PL) and excitation (PLE) spectra of Lys-FS (a), Lys-HT (b) and Lys-MW (c) in aqueous solution. Φ – fluorescence quantum yield.



Visible photoluminescence was excitation-dependent: its emission peak shifted to longer wavelengths with increase of the excitation wavelength. The large shift (from ca. 430 to 500 nm for Lys-FS) suggests a multicomponent emission from several blue- and green-emitting fluorescent chromophores. The shift of the emission maximum was accompanied by attenuation of the emission intensity corresponding to excitation of green-emitting instead of blue-emitting chromophores. This attenuation, expressed as I_{450}/I_{350} ratio in the Table 2 was the smallest and the spectral shift was the largest for the Lys-FS demonstrating that the laser-treated L-lysine had the largest population of green-emitting chromophores.

Table 2

Principal photoluminescence parameters of aqueous solutions of Lys-FS, Lys-HT and Lys-MW. Em.Max and Ex.Max – emission and excitation maximum wavelength, Φ – fluorescence quantum yield, T_{rot} – fluorescence anisotropy decay time (rotation time), I_{450}/I_{350} – ratio of integral luminescence intensity excited at 450 and 350 nm

Sample	Em.Max. (nm)	Ex.Max (nm)	Φ (%)	Lifetime (ns)	T_{rot} (ns)	I_{450}/I_{350}
Lys-FS	429	341	6.5	1.73	1.39	0.150
Lys-HT	439	359	39.6	5.19	0.37	0.046
Lys-MW	433	346	12.4	1.60	0.26	0.119

In accordance with its higher quantum yield Lys-HT demonstrated larger fluorescence lifetime, while similar decay kinetics and lifetimes of Lys-FS and Lys-MW suggests that they comprise similar chromophore groups. A large anisotropy decay time of Lys-FS corresponding to a hydrodynamic volume of 5.7 nm³ indicates that its luminescent chromophores are embedded in slowly rotating rigid nanosized poly-lysine particles. At the same time chromophore groups of Lys-HT and Lys-MW are evidently attached to shorter (and probably flexible) peptide chains, leading to their faster rotation in solution.

Conclusion

Thermal treatment of L-lysine aqueous solution under hydrothermal, microwave or femtosecond laser irradiation conditions yields products with visible absorption and bright excitation-dependent visible fluorescence. Fluorescence characteristics depend on the synthesis method and femtosecond synthesis produced products with stronger green emission. Chemical transformation of L-lysine includes polycondensation, oxidation and carbonization and results in formation of a combination of lysine oligomers (polymers) and unsaturated chromophore groups. Femtosecond laser exposure yields luminescent nanoparticles (carbon dots), which are highly oxidized and carbonized, frequently exhibit carbon onion structure and have a large content of triple C \equiv C bond. Our results confirm that luminescent species can be formed from amino acids and peptides in material of cells and tissues under pulsed laser irradiation and shed light on their formation mechanism.

REFERENCES

1. Sun Q., Qin Z., Wu W., Lin Y., Chen C., He S., Li X., Wu Z., Luo Y., Qu J., In vivo imaging-guided microsurgery based on femtosecond laser produced new fluorescent compounds in biological tissues, *Biomedical Optics Express*. 9 (2018) 581–590.
2. Astafiev A. A., Shakhov A. M., Osychenko A. A., Syrchina M. S., Karmenyan A. V., Tochilo U. A., Nadtochenko V. A., Probing intracellular dynamics using fluorescent carbon dots produced by femtosecond laser in situ, *ACS Omega*. 5 (21) (2020) 12527–12538.
3. Astafiev A. A., Shakhov A. M., Gulin A. A., Vasin A. A., Gubina M. V., Syrchina M. S., Nadtochenko V. A., Femtosecond laser synthesis and comparative analysis of fluorescent carbon dots from L-lysine aqueous solution, *Journal of Physics: Conference Series*. 2086 (2021) 012121.
4. Sahiner N., Suner S. S., Sahiner M., Nitrogen and Sulfur Doped Carbon Dots from Amino Acids for Potential Biomedical Applications. *Journal of Fluorescence*, 29 (2019) 1191–1200.
5. Bartelmess J., Giordani S., Carbon nano-onions (multi-layer fullerenes): chemistry and applications, *Beilstein Journal of Nanotechnology*, 5 (2014) 1980–1998.

6. **Yang J., Chen W., Liu X., Zhang Y., Bai Y.**, Hydrothermal synthesis and photoluminescent mechanistic investigation of highly fluorescent nitrogen doped carbon dots from amino acids, *Materials Research Bulletin*. 89 (2017) 26–32.

7. **Mirtič A., Grdadolnik J.**, The structure of poly-l-lysine in different solvents, *Biophysical Chemistry*. 175–176 (2013) 47–53

8. **Grdadolnik J., Mohacek-Grosev V., Baldwin R. L., Avbelj, F.**, Populations of the three major backbone conformations in 19 amino acid dipeptides, *Proceedings of the National Academy of Sciences*. 108 (5) (2011) 1794–1798.

THE AUTHORS

ASTAFIEV Artyom A.
astafiev.artyom@gmail.com
ORCID: 0000-0001-9269-414X

SHEPEL Denis V.
d.shepel@technoinfo.ru
ORCID: 0000-0003-2437-7219

SHAKHOV Aleksander M.
physics2007@yandex.ru
ORCID: 0000-0002-0958-2903

NADTOCHENKO Victor A.
nadtochenko@gmail.com
ORCID: 0000-0002-6645-692X

SYRCHINA Maria S.
wrongclue@gmail.com
ORCID: 0000-0002-5318-8903

Received 18.07.2022. Approved after reviewing 20.07.2022. Accepted 09.09.2022.

Conference materials

UDC 535.135

DOI: <https://doi.org/10.18721/JPM.153.334>

Optical second-harmonic response of an axially-symmetric medium under radially polarized excitation

S. A. Scherbak^{1,2}✉, I. V. Reshetov^{1,2}, A. A. Lipovskii^{1,2}

¹ Alferov University, St. Petersburg, Russia;

² Peter the Great St. Petersburg Polytechnic University, St. Petersburg, Russia

✉ Sergeygtn@yandex.ru

Abstract. We simulated optical second harmonic response, both surface and bulk, of axially symmetric media excited by tightly focused radially polarized fundamental beams. The modeling showed a highly localized character of second harmonic generation. We estimated decrease of overall second harmonic signal for defocusing of fundamental beam relatively to a sample's surface. Radiation patterns of second harmonic waves were compared for different numerical apertures of a focusing objective, for different focus shift relatively to the sample's surface and for surface and bulk second harmonic responses. The model developed is applicable for second harmonic generation by interfaces, films and poled glasses.

Keywords: nonlinear optics, second harmonic generation, radial polarization, axisymmetric medium, modeling

Funding: This study was funded by within the framework of the Russian Science Foundation project No. 21-72-00048 “Non-synchronous nonlinear optical phenomena in micro- and nano-structures using light waves with non-trivial polarizations”, research project No. 21-72-00048.

Citation: Scherbak S. A., Reshetov I. V., Lipovskii A. A., Optical second-harmonic response of an axially-symmetric medium under radially polarized excitation. St. Petersburg State Polytechnical University Journal. Physics and Mathematics, 15 (3.3) (2022) 177–181. DOI: <https://doi.org/10.18721/JPM.153.334>

This is an open access article under the CC BY-NC 4.0 license (<https://creativecommons.org/licenses/by-nc/4.0/>)

Материалы конференции

УДК 535.135

DOI: <https://doi.org/10.18721/JPM.153.334>

Генерация второй оптической гармоники осесимметричной средой под воздействием радиально поляризованного излучения

С. А. Щербак^{1,2}✉, И. В. Решетов^{1,2}, А. А. Липовский^{1,2}

¹ Санкт-Петербургский национальный исследовательский Академический университет имени Ж. И. Алферова Российской академии наук, Санкт-Петербург, Россия;

² Санкт-Петербургский Политехнический университет Петра Великого, Санкт-Петербург, Россия

✉ Sergeygtn@yandex.ru

Аннотация. Проведено моделирование генерации второй гармоники поверхностью и объемом осесимметричного образца, освещенного сильно сфокусированным радиально поляризованным световым лучом. Исследованы влияния числовой апертуры фокусирующего объектива, толщины нелинейного слоя и положения фокуса относительно поверхности образца на генерацию второй гармоники. В частности, проведено сравнение диаграмм направленности излучения в этих случаях, показан высоко локализованный характер генерации второй гармоники. Разработанная модель подходит для анализа генерации второй гармоники интерфейсами, тонкими нелинейными пленками и поляризованной областью стекла.

Ключевые слова: нелинейная оптика, генерация второй гармоники, радиальная поляризация, осесимметричная среда, моделирование

Финансирование: Работа выполнена в рамках проекта РНФ № 21-72-00048 «Несинхронные нелинейно-оптические явления в микро- и наноструктурах при использовании световых волн с нетривиальными поляризациями».

Ссылка при цитировании: Щербак С. А., Решетов И. В., Липовский А. А. Генерация второй оптической гармоники осесимметричной средой под воздействием радиально поляризованного излучения // Научно-технические ведомости СПбГПУ. Физико-математические науки. 2022. Т. 15. № 3.3. С. 177–181. DOI: <https://doi.org/10.18721/JPM.153.334>

Статья открытого доступа, распространяемая по лицензии CC BY-NC 4.0 (<https://creativecommons.org/licenses/by-nc/4.0/>)

Introduction

It is known that radially polarized light waves focused with a high numerical aperture (NA) objective acquire a significant longitudinal component of electric field near the focal plane [1]. This allows applications of vector light beams in nanoparticles' trapping and delivering [2, 3], dark-field imaging and visualization down to a single molecule [4, 5], laser material processing [6]. Also, this peculiar distribution of electric field can provide a nonlinear optical response that differs significantly from that typical for trivially polarized excitations. Particularly, this allows observation of second order nonlinearity of highly symmetrical (e.g., axial) structures under normal incidence. In nonlinear optics of vector light beams, studies of second harmonic generation (SHG) by a material with symmetry $\bar{4}3m$ [7], surface and bulk SHG, including spatially resolved experiments, by glasses [8, 9] and thin nonlinear films [10] were reported.

In this study, we developed a model that describes both surface and bulk second harmonic (SH) response of an axially symmetric medium under tightly focused radially polarized excitation. The model is applicable for SH generation by interfaces, films and poled glasses.

Theory

We consider a radially polarized light beam falling normally (along z -axis) to a focusing objective and then to the interface between two media with indices n_1 and n_2 . Resulting equations (in cylindrical coordinates) for components of the second harmonic electric field in the far-field zone in the direction defined by the polar angle θ are:

$$E_{\rho}^{2\omega}(\theta) = P_1 \sin \theta \cos \theta - P_2 \sin^2 \theta + P_2 \quad (1)$$

$$E_z^{2\omega}(\theta) = P_1 \cos^2 \theta - P_2 \sin \theta \cos \theta - P_1 \quad (2)$$

where parameters P_1 and P_2 are:

$$P_1 = 2\pi \int_0^{+\infty} r dr \int_{z_0}^{z_1} dz P_{\perp}(r, z) J_0(Kr \sin \theta) e^{iKz \cos \theta} \quad (3)$$

$$P_2 = 2\pi i \int_0^{+\infty} r dr \int_{z_0}^{z_1} dz P_{\parallel}(r, z) J_1(Kr \sin \theta) e^{iKz \cos \theta} \quad (4)$$

z_0 is the sample interface coordinate, z_1 is the coordinate of the rare side of the nonlinear layer, K – wavenumber vector of the SH wave. Components of nonlinear polarizability \mathbf{P} are connected with components of the fundamental electric field via nonlinear constitutive equations. For axially symmetric media, these are:

$$P_{\perp} = \chi_{\perp\perp\perp} E_z^2 + \chi_{\perp\parallel\parallel} E_r^2 \quad (5)$$

$$P_{\parallel} = \chi_{\parallel\perp\perp} E_z E_r \quad (6)$$

where $\chi_{\perp\perp\perp}$, $\chi_{\parallel\perp\perp}$, and $\chi_{\perp\parallel\perp}$ are nonzero components of the second order susceptibility tensor χ . Surface nonlinearity can be considered using substitution $\chi \rightarrow \chi^{surf} \delta(z-z_0)$, where $\delta(z-z_0)$ is the Dirac δ -function. Expressions for the distribution of the fundamental electric field of a radially polarized light wave, E_z and E_r , near the focal plane are presented in Ref. [7].

Squared modulus of SH field, which components are described by Eqs. (1-2), gives intensity of the radiated SH signal:

$$I_{2\omega}(\theta_2) = |T_p^{n_2 \rightarrow n_1}(\theta_2)|^2 \left(|E_r^{2\omega}(\theta_2)|^2 + |E_z^{2\omega}(\theta_2)|^2 \right) \quad (7)$$

In Eq. (7) we took into account that output SH radiation refracts at the rear side of the sample. Thus, we added the Fresnel's transmission coefficient $T_p^{n_2 \rightarrow n_1}$ and represented the intensity as a function of the refraction angle θ_2 , which related to θ via the refraction law: $n_2 \sin \theta = n_1 \sin \theta_2$. Integration of Eq. (7) over θ_2 allows obtaining total SH intensity.

Results and Discussion

In calculations, we considered fundamental wavelength of 1064 nm, $n_1 = 1$, $n_2 = 1.51$,

$z_0 = z_f = 0$, where z_f is the objective focus coordinate, and suppose $\chi_{\perp\perp\perp} = 3\chi_{\parallel\perp\perp} = 3\chi_{\perp\parallel\perp}$. This relation between the components of χ is a so-called "1/3 rule" which is common for poled glasses [11]. For surface nonlinearity we calculated SH radiation patterns for different NA's of focusing objective, see Fig. 1.

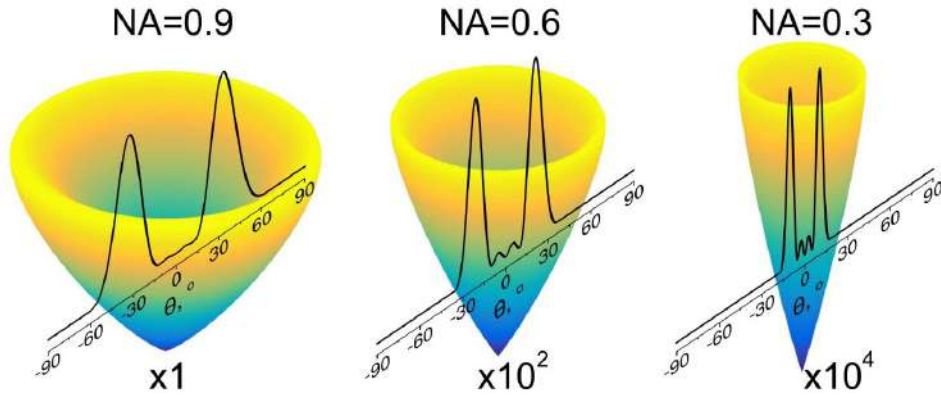


Fig. 1. SH radiation patterns for NA's of focusing objective: 0.9 (left), 0.6 (middle), 0.3 (right). Intensity scaling factor is denoted below each pattern. Overlying curves – patterns cross-sections

In Fig. 1 we observe characteristic SH radiation patterns for the case of "1/3 rule". The patterns, expectedly axially symmetric, represent a single empty cone, which corresponds to a two-lobed pattern in a cross-section (see overlaying curves in Fig. 1). For tight focusing (NA = 0.9) the pattern is relatively broad with cone's full angle about 33°. For weaker focusing (NA = 0.6 and NA = 0.3) the pattern is noticeably narrower – for NA = 0.6 angle is ~ 23°, for NA = 0.3 – about 10°. Note, these angles decrease with the aperture angles of the objectives, which are about 65°, 37° and 17°, respectively, for NA = 0.9, 0.6 and 0.3. Also, inner (closer to normal) lobes, which are barely seen for NA = 0.9, becomes more evident, though still about an order lower in magnitude than the outer ones. The overall SH radiation intensity for NA = 0.3 is about four orders of magnitude less than for NA = 0.9.

For tight focusing (NA = 0.9) we calculated SH signal depending on focus shift z_f relatively to the nonlinear interface. The dependence presented in Fig. 2, *a* demonstrates a symmetric peak with a half-width of ~ 2 μm , i.e. 1- μm focus shift from the surface results in two-fold decrease of the overall SH signal. For 3- μm focus shift, the decrease is 10-fold. Note, for smaller NAs this dependence is broader and the SH signal – lower. This was expected for lower intensity in focus and longer caustic produced by weaker objectives. Also, we estimated evolution of radiation patterns with focus shift (see insets in Fig. 2). The radiation pattern for exact focusing ($z_f = 0$) is the same as one presented in Fig. 1. For higher focus shifts (e.g., $z_f = 4 \mu\text{m}$), the pattern broadens and obtains a noticeable inner shoulder. Because of this changes, for a material with a known

relation of components of χ , the shape of the SH radiation pattern can be another criterion of the focusing. Similar dependence for bulk subsurface nonlinear layer of thickness $d_{NL} = 8 \mu\text{m}$ is presented in Fig. 2, *b* with radiation patterns as insets. The dependence of SH signal on focus shift in this case has a shape of an asymmetric peak, which is, expectedly, broader than in the case of surface nonlinearity. Also, focus position providing the maximal SH signal, $z_f \approx 1.4 \mu\text{m}$, is closer to the surface ($z_0 = 0$) than to the rear border of the nonlinear layer ($z_1 = 8 \mu\text{m}$). This is because of the refraction of the fundamental beam at the interface ($n_1 = 1/n_2 = 1.51$). Half-width of this dependence is $\sim 4 \mu\text{m}$. Thus, such dependencies can allow estimating thickness of nonlinear layers. In this case, the radiation pattern also changes with focus shift: for the optimal focusing ($z_f \approx 1.4 \mu\text{m}$) it is similar to one of surface nonlinearity, for a higher focus shift (e.g., $z_f = 6 \mu\text{m}$) the pattern broadens and obtains an outer shoulder (see the insets in Fig. 2, *b*).

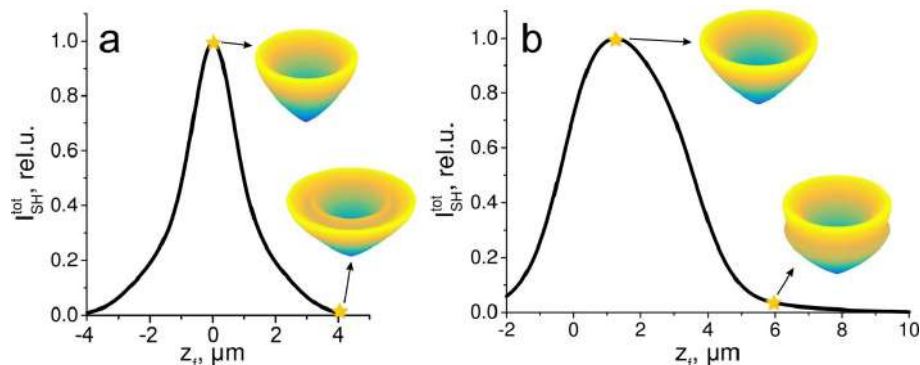


Fig. 2. Total signal of SH generation by surface nonlinearity (*a*) and subsurface nonlinear layer of thickness $d_{NL} = 8 \mu\text{m}$ vs focus shift from the surface (*b*)

In Fig. 3, *a* we demonstrate total SH signal for nonlinear layer vs thickness of this layer, d_{NL} , for the tight focusing case ($\text{NA} = 0.9$). The signal expectedly increases with the thickness and then saturates, since the excitation is localized. Note, for the non-localized regime of SHG under unfocused excitation, total SH signal depends on the thickness of nonlinear layer quadratically. Dependence of SH intensity vs. $(d_{NL})^2$ for $\text{NA} = 0.3$, which is presented in Fig. 3, *b*, is close to a linear one that confirms the latter statement. The calculated dependence slightly bends relatively to an exact line (dashed one). This is probably because the objective with $\text{NA} = 0.3$ provides rather weakly focused beam than unfocused. In the insets in Fig. 3, *a* we schematically present radiation patterns of SH waves for different thickness of the nonlinear layer. The patterns are similar to one of surface nonlinearity, though, for thicker layers, they broaden. Cones angles are denoted in the insets. This broadening can allow distinguishing surface nonlinearity from bulk one.

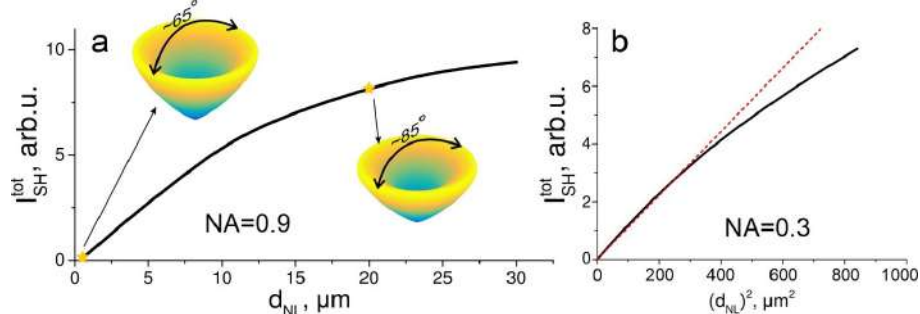


Fig. 3. Total signal of SH generation by differently thick subsurface nonlinear layers for $\text{NA} = 0.9$ (*a*) and $\text{NA} = 0.3$ (*b*). Dotted line in (*b*) represents an exact quadratic dependence and no more than guide for eyes

Conclusion

We developed a model for surface and bulk optical second harmonic response of axially symmetric medium under tightly focused radially polarized excitation. For relation between components of second order susceptibility tensor, we calculated SH radiation patterns for different NA of the focusing objective. It is demonstrated that the patterns have a shape of an empty cone and for higher NA (tighter focusing) magnitude of overall SH signal increases and the pattern



significantly broadens. For tight focusing, we estimated decrease of SH signal when the focus position shifts from the surface – 3 μm shift corresponds to an order drop in the SH intensity. We showed that for tight focusing intensity of SH saturates with increase in the thickness of nonlinear layer, that corresponds to local excitation of SHG.

REFERENCES

1. **Hao B., Leger J.**, Experimental measurement of longitudinal component in the vicinity of focused radially polarized beam, *Optics Express*. 15 (2007) 3550.
2. **Zhan Q.**, Trapping metallic Rayleigh particles with radial polarization, *Optics Express*. 12 (2004) 3377.
3. **Kawauchi H., Yonezawa K., Kozawa Y., Sato S.**, Calculation of optical trapping forces on a dielectric sphere in the ray optics regime produced by a radially polarized laser beam, *Optics Letters*. 32 (2007) 1839.
4. **Biss D. P., Youngworth K. S., Brown T. G.**, Dark-field imaging with cylindrical-vector beams, *Applied Optics*. 45 (2006) 470.
5. **Novotny L., Beversluis M. R., Youngworth K. S., Brown T. G.**, Longitudinal Field Modes Probed by Single Molecules, *Physical Review Letters*. 86 (2001) 5251–5254.
6. **Drevinskas R., Zhang J., Beresna M., Gecevičius M., Kazanskii A. G., Svirko Y. P., Kazansky P. G.**, Laser material processing with tightly focused cylindrical vector beams, *Applied Physics Letters*. 108 (2016) 221107.
7. **Ohtsu A.**, Second-harmonic wave induced by vortex beams with radial and azimuthal polarizations, *Optics Communications*. 283 (2010) 3831–3837.
8. **Wang X., Fardad S., Das S., Salandrino A., Hui R.**, Direct observation of bulk second-harmonic generation inside a glass slide with tightly focused optical fields, *Physical Review B*. 93 (2016) 1–5.
9. **Wang X., Shen S., Sun J., Fan F., Chang S.**, Surface and bulk second-harmonic responses from a glass slide using tightly focused radially polarized light, *Optics Letters*. 41 (2016) 5652.
10. **Biss D. P., Brown T. G.**, Polarization-vortex-driven second-harmonic generation, *Optics Letters*. 28 (2003) 923.
11. **Kazansky P. G., Russel P. S. J.**, Thermally poled glass: frozen-in electric field or oriented dipoles?, *Optics Communications*. 110 (1994) 611–614.

THE AUTHORS

SCHERBAK Sergey A.
sergeygtn@yandex.ru
ORCID: 0000-0002-0507-5621

LIPOVSKII Andrey A.
lipovskii@mail.ru
ORCID: 0000-0001-9472-9190

RESHETOV Ilya V.
reshetov_iv@spbstu.ru
ORCID: 0000-0002-8661-3654

Received 22.07.2022. Approved after reviewing 27.07.2022. Accepted 30.07.2022.

Conference materials

UDC 53.043

DOI: <https://doi.org/10.18721/JPM.153.335>

Fabrication of SERS-active structures via electrostatic deposition of colloidal gold nanoparticles on polymer microspheres

M. A. Miropoltsev ¹✉, A. P. Tkach ¹, K. A. Maleeva ¹, K. V. Bogdanov ¹

¹ Center of Optical Information Technologies, ITMO University, St. Petersburg, Russia

✉ miropoltsev_m@niuitmo.ru

Abstract. In the present study, we report on the fabrication and investigation of SERS active structures based on the polystyrene microspheres functionalized with gold nanoparticles. Successful deposition of the gold nanoparticles on the microsphere surface has been confirmed using the scanning electron microscopy and the zeta potential measurements. The proof-of-concept experiments have demonstrated the SERS effect with the average enhancement factor of about 10^3 . The studied structures are stable, easy to fabricate, and ready for application in sensing.

Keywords: gold nanoparticles, plasmonic nanoparticles, microspheres, surface-enhanced Raman scattering (SERS), layer-by-layer deposition

Funding: The study is funded by RPMA grant of School of Physics and Engineering of ITMO University.

Citation: Miropoltsev M. A., Tkach A. P., Maleeva K. A., Bogdanov K. V., Fabrication of SERS-active structures via electrostatic deposition of colloidal gold nanoparticles on polymer microspheres. St. Petersburg State Polytechnical University Journal. Physics and Mathematics, 15 (3.3) (2022) 182–187. DOI: <https://doi.org/10.18721/JPM.153.335>

This is an open access article under the CC BY-NC 4.0 license (<https://creativecommons.org/licenses/by-nc/4.0/>)

Материалы конференции

УДК 53.043

DOI: <https://doi.org/10.18721/JPM.153.335>

Изготовление SERS-активных структур методом электростатического нанесения коллоидных наночастиц золота на полимерные микросферы

М. А. Миропольцев ¹✉, А. П. Ткач¹, К. А. Малеева ¹, К. В. Богданов ¹

¹Центр «Информационные оптические технологии», Университет ИТМО, Санкт-Петербург, Россия

✉ miropoltsev_m@niuitmo.ru

Аннотация. В настоящей работе были разработаны и исследованы SERS-активные структуры на основе полистирольных микросфер, функционализированных наночастицами золота. Успешное осаждение золотых наночастиц на поверхность микросфер было подтверждено с помощью сканирующей электронной микроскопии и измерений дзета-потенциала. В ходе предварительных экспериментов наблюдался эффект SERS со средним коэффициентом усиления около 10^3 . Изучаемые структуры стабильны, просты в изготовлении и готовы к применению в сенсорике.

Ключевые слова: золотые наночастицы, плазмонные наночастицы, микросферы, комбинационное рассеяние с усилением поверхности (SERS), послойное нанесение

Финансирование: Исследование выполнено при финансовой поддержке гранта НИРМА Физико-технического мегафакультета Университета ИТМО.

Ссылка при цитировании: Миропольцев М. А., Ткач А. П., Малеева К. А., Богданов К. В. Изготовление SERS-активных структур методом электростатического



нанесения коллоидных наночастиц золота на полимерные микросферы // Научно-технические ведомости СПбГПУ. Физико-математические науки. 2022. Т. 15. № 3.3. С. 182–187. DOI: <https://doi.org/10.18721/JPM.153.335>

Статья открытого доступа, распространяемая по лицензии CC BY-NC 4.0 (<https://creativecommons.org/licenses/by-nc/4.0/>)

Introduction

Surface-Enhanced Raman Scattering (SERS) is a promising tool for the analysis of chemical composition and structural features of molecular and crystalline materials. The SERS method has a high selectivity for an analyte adsorbed on the surface of a plasmonic nanoparticle or located in the near field of a plasmon. For sensing applications, plasmonic nanoparticles are often assembled into more complex SERS-active structures or SERS substrates which provide higher enhancement and broader functionality [1]. Thereby, the development and fabrication of SERS-active structures from plasmonic nanoparticles have become subjects of great interest among researchers due to the high demand for ultra-sensitive detectors of environmental pollutants, pesticides, toxic or radioactive ions, and more [2].

To date, a wide variety of methods exists that allow to create SERS structures. They include direct synthesis or post-synthetic deposition of metallic nanoparticles on planar substrates and in matrices [1], nanoparticle self-assembly with the help of different stabilizing agents [3], nanostructure fabrication directly on solid substrates by nanolithography [4], and screen printing [5]. However, there is still an ongoing search for the new types of SERS structures that would be cost-effective and provide better functionality at the same time. Most of the currently available structures are two-dimensional, hence they require collection and deposition of the analyte on the planar slides. Despite common use, this approach might not be the best option for some scenarios, especially in biology, where the study of fluids is frequently performed. For these purposes, three dimensional SERS structures are more suitable, such as nanoparticle-decorated hollow fibers [6], membranes [7], and microspheres [8], that allow direct investigation of the analytes in liquid samples. Furthermore, three-dimensional architecture can provide larger Raman signal enhancement due to additional contribution from the plasmonic hotspots located in various places along the z-axis within the excitation focal volume.

Polymer microspheres (PMS) can be effectively used as the three-dimensional supports for plasmonic nanoparticles. Three approaches can be used to prepare microspheres covered with nanoparticles: (1) *in-situ* nanoparticle synthesis in the presence of microspheres [9]; (2) polymerization in the presence of nanoparticles [8]; (3) self-assembly of nanoparticle layers on the microsphere surface *via* electrostatic layer-by-layer deposition [10]. The latter approach can be very promising as it enables formation of dense nanoparticle layers with high reproducibility. In this method, oppositely charged polyelectrolytes (PE) are deposited on the surface of the PMS to produce a smooth charged coating which electrostatically attracts nanoparticles from the solution. This method has already been successfully used to deposit colloidal quantum dots and gold nanoparticles (AuNPs) on the surface of the PMS for applications in cytometry and catalysis [10, 11]. However, the possibilities of utilizing such structures for the SERS-based applications have not been widely considered.

The goal of this research is the formation of SERS-active structures from commercially available polystyrene microspheres and colloidal gold nanoparticles *via* electrostatic layer-by-layer deposition. A high stability of the prepared structures was achieved by precoating the microspheres with multiple PE layers and by using thiols as stabilizing ligands for AuNPs. The proof-of-concept measurements of the organic dye (pseudoisocyanine iodide) Raman spectra revealed that the AuNP-coated PMS structures provide sufficient enhancement and can be used in the field of SERS-based sensing.

Materials and Methods

Materials. Chloroauric acid (99.995%), trisodium citrate, pseudoisocyanine iodide (97%), 3-mercaptopropionic acid (99%) (MPA), poly(sodium 4-styrenesulfonate) ($M_w \sim 70,000$) (PSS),

poly(allylamine hydrochloride) ($M_w \sim 50,000$) (PAH) were purchased from Sigma Aldrich. Polystyrene microspheres (carboxylated, 4 μm in diameter) were obtained from Kisker Biotech. Deionized water (conductivity < 6 mS/cm) was used throughout the experiments.

Synthesis of AuNPs and ligand exchange. The synthesis of colloidal gold nanoparticles was carried out by the common citrate reduction method described in the reference [3]. After the synthesis, the ligand exchange procedure on AuNPs with mercaptopropionic acid was carried out according to the following protocol. First, a solution of MPA (10^{-5} M) was prepared in water with pH ~ 10 – 11 adjusted by NaOH to deprotonate the thiol groups. This solution was then added to AuNPs, and the obtained mixture was vigorously stirred for 20 minutes at room temperature, followed by addition of acetone and centrifugation. Finally, a purple-colored precipitate containing MPA-capped AuNPs was redissolved in pure water.

Preparation of AuNP-coated PMS. The electrostatic layer-by-layer deposition technique was adapted from the reference [11]. The first step of the standard protocol is the deposition of a smooth positively charged coating on the surface of carboxylated microspheres. This preliminary coating is composed of the three layers of polyelectrolytes added sequentially: PAH, PSS, PAH. Each layer was deposited by mixing a solution of homogenized suspension of PMS and a corresponding polyelectrolyte (3 mg/ml) in a 0.5M NaCl solution. After stirring the mixture for 20 minutes at room temperature, three centrifugation/washing cycles were performed to remove excess PE, followed by a final redispersion of PMS in water. The PE deposition and washing procedure was repeated until the PMS with three layers (PAH/PSS/PAH) were formed. For the deposition of AuNPs, the solution of MPA-capped AuNPs was added to the obtained suspension of microspheres with three layers of PE and stirred for 24 hours. The resulting suspension was washed three times to remove the unattached nanoparticles.

Equipment. The UV-VIS absorption spectra were recorded using a UV-Probe 3600 spectrophotometer (Shimadzu, Japan). Scanning electron microscopy (SEM) images were obtained on Merlin (Zeiss, Germany) by depositing samples on silicon substrates. Measurements of Raman spectra were performed with a confocal Raman microscope inVia (Renishaw, United Kingdom). Raman spectra were excited at 514 nm and recorded using a 50 \times objective lens. SERS mapping was performed using 1995 points per sample area (35 \times 55 μm) with an exposition time of 1 s per point. The hydrodynamic diameter and the zeta potential measurements of the AuNPs and the microspheres were performed on Zetasizer Nano (Malvern, United Kingdom).

Results and Discussion

In this work, gold nanoparticles were selected for the fabrication of SERS structures because of their high stability, ease of production, and suitable energy position of the plasmonic band [12]. In the common synthesis of AuNPs, chloroauric acid is reduced to gold with the help of sodium citrate in the aqueous medium [3]. Citrate ions work as stabilizing agents for the synthesized nanoparticles, favoring their long-term colloidal stability. However, during preliminary experiments we have found that the deposition of the as-prepared citrate-capped AuNPs on the microsphere surface results in instability and aggregation. It is plausible, that the weakly bound citrate ions detach from the nanoparticle surface in the presence of the functional groups of polyelectrolytes (i.e., amines, as the outer PE shell consists of PAH), leading to the uncontrollable cross-linking between AuNPs and microspheres. Therefore, to create uniform layers of nanoparticles on the surface of microspheres, we have performed the ligand exchange on AuNPs with 3-mercaptopropionic acid. As expected, the stronger bond between the metal and the thiol group of MPA significantly reduces the possibility of ligand detachment and prevents the system from aggregation.

The absorbance spectrum and the SEM image of the AuNPs prior to deposition on the PMS surface are shown in Fig. 1. As seen in Fig. 1, *a*, gold nanoparticles exhibit a plasmonic band at 525 nm, consistently with the other reports. Based on the particle size distribution obtained from the SEM images (see Fig. 1, *b*), the average size of AuNPs was estimated to be 22 ± 3 nm. The hydrodynamic diameter and the zeta-potential measurements revealed that the nanoparticles were well-dispersed and had an average zeta potential of ca. -25 mV, indicating a net negative charge due to the ionized carboxylic groups of the organic stabilizing shell.

Polystyrene microspheres are cheap, robust, and possess narrow size distribution. Therefore, we have selected them as the three-dimensional supports for the fabrication of SERS-active structures.

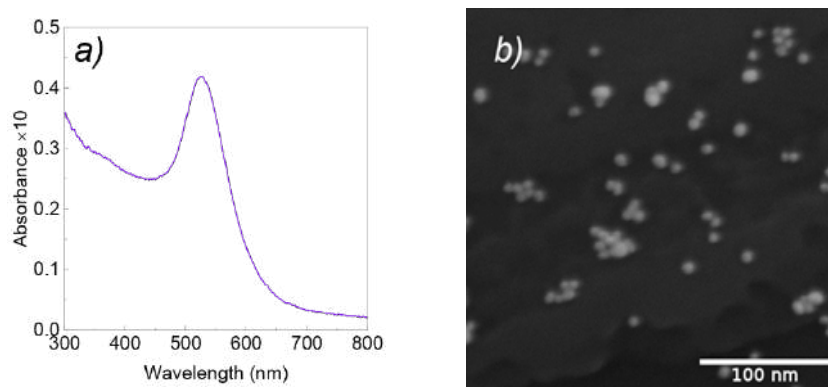


Fig. 1. Absorbance spectrum of the AuNPs solution with a plasmonic band at 525 nm (a); The SEM image of AuNPs (b)

For nanoparticles to be assembled on the microsphere surface by electrostatic forces, the components must have strong opposite charges. According to previous reports, at least three polyelectrolyte layers are necessary to facilitate a denser packing of PE and provide a stable charge on the PMS surface [13]. Since the carboxylate-modified polystyrene microspheres bear a negative charge, the first deposited layer was a positively charged polyelectrolyte PAH. Next, two more layers of the oppositely charged polyelectrolytes (PSS and PAH) were deposited in accordance with the protocol, so that the outer coating is charged positively. The average value of the zeta potential for the PMS with three layers of PE was ca. +45 mV measured directly after the deposition of the final layer. This value retained for at least one week after the coating procedure, which demonstrates a good stability of the polyelectrolyte layers.

Next, the MPA-capped AuNPs were self-assembled on the surface of the positively charged microspheres in a same manner as polyelectrolytes. The utilization of MPA as a strong stabilizing agent for gold nanoparticles ensured that the electrostatic interaction is primarily responsible for the deposition of AuNPs. After purification from the unbound nanoparticles, the functionalized microspheres were characterized by scanning electron microscopy and zeta-potential measurements.

Fig. 2 shows a SEM image of the PMS-AuNP structures, where AuNPs can be observed on the surface of the microspheres. As seen from the SEM image, the nanoparticle coverage is relatively sparse, which might be due to low nanoparticle concentration used during the assembly process. At the same time, the zeta-potential values of the prepared structures showed a significant shift from ca. +45 mV to ca. -10 mV (not shown). This demonstrates a successful adsorption of AuNPs on the PMS surface. It is also worth noting that the prepared AuNP-coated microspheres remained stable and retained negative zeta potential for more than a week.

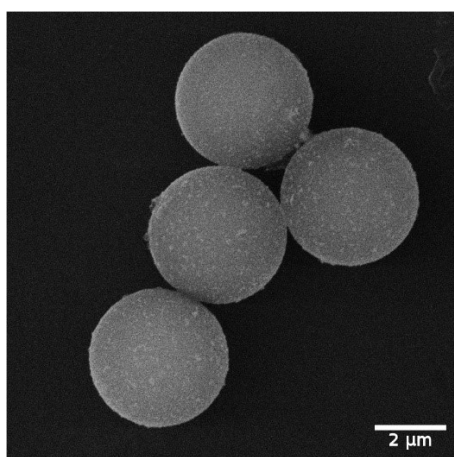


Fig. 2. SEM image of the PMS/PAH/PSS/PAH/AuNP structures

drop-casted on top of it. Then, the Raman scattering map for the 1365 cm^{-1} dye band was recorded. As seen from Fig. 3, a, the intensity enhancement is observed in those regions where the nanoparticle-decorated microspheres are located.

For further analysis, we measured the Raman spectra of the pure dye, as well as in the presence of PMS with and without AuNPs on the surface, respectively (Fig. 3, b). As follows from Fig. 3, b, only the spectrum corresponding to the sample with the PMS-AuNP structures clearly shows the characteristic dye Raman band at 1364 cm^{-1} . This band is absent in other spectra, which

confirms the enhancement effect. To estimate the efficiency of our structures, we have calculated the analytical enhancement factor (AEF) [14]:

$$AEF = \frac{I_{SERS}}{I_R} \cdot \frac{c_R}{c_{SERS}}, \quad (1)$$

where I_{SERS} and I_R are the intensities of the dye, with and without AuNPs, respectively, and c_{SERS} and c_R are the concentrations of the dye, with and without AuNPs, respectively.

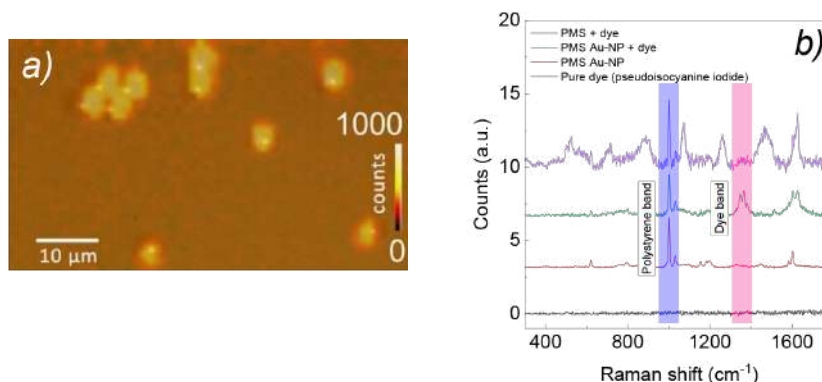


Fig. 3. Raman scattering intensity map recorded for 1365 cm^{-1} band of pseudoisocyanine iodide (a); A set of Raman spectra demonstrating the SERS effect of the prepared PMS-AuNP structures (b)

The value of AEF calculated using equation 1 has the order of ca. 10^3 . These values are somewhat lower than those reported for other SERS-active structures [15]. This indicates the need to improve the synthesis to reach a more compact packing density of gold nanoparticles.

Conclusion

In the present work, we have fabricated three-dimensional SERS-active structures by coating polymer microspheres with three layers of polyelectrolytes followed by the electrostatic deposition of AuNPs from aqueous solutions. We have characterized the morphology of the prepared structures and estimated the Raman scattering enhancement by using pseudoisocyanine iodide as an analyte. The analytical enhancement factor on the order of 10^3 has been reached, which is comparable to more complex SERS structures. The fabrication procedure is easy to upscale, and the prepared samples remain stable for more than a week. This opens wide possibilities for using such structures in analytical and sensing applications.

REFERENCES

1. Ouyang L., Ren W., Zhu L., Irudayaraj J., Prosperity to challenges: recent approaches in SERS substrate fabrication, *Reviews in Analytical Chemistry*. 36 (1) (2017).
2. Mosier-Boss P. A., Review of SERS substrates for chemical sensing, *Nanomaterials*. 7 (6) (2017) 142.
3. Khnykina K., Baranov M., Babaev A., Baranov A., Bogdanov K., Key Factors for Tuning Au Self-Assembling SERS Films: from Properties to Structure, *Optics and Spectroscopy*. 129 (4) (2021) 495–504.
4. Syed H., Podagatlapalli G. K., Mohiddon M., Soma V. R., SERS studies of explosive molecules with diverse copper nanostructures fabricated using ultrafast laser ablation, *Adv. Mater. Lett.* 6 (2015) 1073–1080.
5. Qu L.-L., Li D.-W., Xue J.-Q., Zhai W.-L., Fossey J. S., Long Y.-T., Batch fabrication of disposable screen printed SERS arrays, *Lab on a Chip*. 12 (5) (2012) 876–881.
6. Eftekhari F., Lee A., Kumacheva E., Helmy A. S., Examining metal nanoparticle surface chemistry using hollow-core, photonic-crystal, fiber-assisted SERS, *Optics letters*. 37 (4) (2012) 680–682.
7. Ouyang L., Dotzauer D. M., Hogg S. R., Macanóns J., Lahitte J.-F., Bruening M. L., Catalytic hollow fiber membranes prepared using layer-by-layer adsorption of polyelectrolytes and metal nanoparticles, *Catalysis Today*. 156 (3) (2010) 100–106.



8. Trojanowska A., Pazos-Perez N., Panisello C., Gumi T., Guerrini L., Alvarez-Puebla R. A., Plasmonic-polymer hybrid hollow microbeads for surface-enhanced Raman scattering (SERS) ultradetection, *Journal of Colloid and Interface Science*. 460 (2015) 128–134.
9. Li S., Yang X., Huang W., Synthesis of Monodisperse Polymer Microspheres with Mercapto Groups and Their Application as a Stabilizer for Gold Metallic Colloid, *Macromolecular Chemistry and Physics*. 206 (19) (2005) 1967–1972.
10. Liu Y., Li M., Chen G., A new type of raspberry-like polymer composite sub-microspheres with tunable gold nanoparticles coverage and their enhanced catalytic properties, *Journal of Materials Chemistry A*. 1 (3) (2013) 930–937.
11. Kuznetsova V., Osipova V., Tkach A., Miropoltsev M., Kurshanov D., Sokolova A., Cherevko S., Zakharov V., Fedorov A., Baranov A., Lab-on-Microsphere – FRET-Based Multiplex Sensor Platform, *Nanomaterials*. 11 (1) (2021) 109.
12. Liu J., He H., Xiao D., Yin S., Ji W., Jiang S., Luo D., Wang B., Liu Y., Recent Advances of Plasmonic Nanoparticles and their Applications, *Materials*. T. 11 (10) (2018) 1833.
13. Wang D., Rogach A. L., Caruso F., Semiconductor Quantum Dot-Labeled Microsphere Bioconjugates Prepared by Stepwise Self-Assembly, *Nano Letters*. 2 (8) (2002) 857–861.
14. Le Ru E. C., Etchegoin P. G., Quantifying SERS enhancements, *MRS bulletin*. 38 (8) (2013) 631–640.
15. Barbillon G., Latest Novelties on Plasmonic and Non-Plasmonic Nanomaterials for SERS Sensing, *Nanomaterials*. 10 (6) (2020) 1200.

THE AUTHORS

MIROPOLTSEV Maksim A.
miropoltsev_m@niuitmo.ru
ORCID: 0000-0001-5199-9502

MALEEVA Kseniya A.
khnykina@itmo.ru
ORCID: 0000-0003-2520-7561

TKACH Anton P.
aptkach@itmo.ru
ORCID: 0000-0003-3370-6248

BOGDANOV Kirill V.
kirw.bog@itmo.ru
ORCID: 0000-0003-4243-1354

Received 30.07.2022. Approved after reviewing 03.08.2022. Accepted 15.08.2022.

Conference materials

UDC 535-15

DOI: <https://doi.org/10.18721/JPM.153.336>

Peculiarities of the luminescence response of two-dimensional photonic crystals with ordered Ge(Si) nanoislands obtained using different ordering approaches

A. V. Peretokin ^{1, 2}✉, M. V. Stepikhova ¹, A. V. Novikov ¹,
Zh. V. Smagina ³, S. A. Dyakov ⁴

¹ Institute for Physics of Microstructures Russian Academy of Sciences, Nizhny Novgorod, Russia;

² Lobachevsky University, Nizhny Novgorod, Russia;

³ Rzhanov Institute of semiconductor physics Siberian Branch of Russian Academy of Sciences, Novosibirsk, Russia;

⁴ Skolkovo Institute of Science and Technology, Moscow, Russia

✉ aperetokin@ipmras.ru

Abstract. In this work, we investigated the luminescent properties of two-dimensional photonic crystals (PhCs) with ordered Ge(Si) nanoislands obtained using one- and two-stage approaches to ordering. The features of the luminescent response of such structures and their relationship with the ordering processes of nanoislands are considered. It is shown that the incorporation of Ge(Si) nanoislands into a two-dimensional PhC makes it possible to increase the intensity of their luminescent response by more than an order of magnitude, which makes the structures under consideration promising for practical applications.

Keywords: photonic crystals, Ge(Si) nanoislands, ordering, photoluminescence

Funding: Project FASO No. 0030-2021-0019 and No. FWGW-2022-0011

Citation: Peretokin A. V., Stepikhova M. V., Novikov A. V., Smagina Zh. V., Dyakov S. A., Peculiarities of the luminescence response of two-dimensional photonic crystals with ordered Ge(Si) nanoislands obtained using different ordering approaches. St. Petersburg State Polytechnical University Journal. Physics and Mathematics, 15 (3.3) (2022) 188–193. DOI: <https://doi.org/10.18721/JPM.153.336>

This is an open access article under the CC BY-NC 4.0 license (<https://creativecommons.org/licenses/by-nc/4.0/>)

Материалы конференции

УДК 535-15

DOI: <https://doi.org/10.18721/JPM.153.336>

Особенности люминесцентного отклика двумерных фотонных кристаллов с упорядоченными nanoостровками Ge(Si) полученных с использованием разных подходов к упорядочению

А. В. Перетокин ^{1, 2}✉, М. В. Степихова ¹, А. В. Новиков ¹,
Ж. В. Смагина ³, С. А. Дьяков ⁴

¹ Институт Физики Микроструктур РАН, Нижний Новгород, Россия;

² Национальный исследовательский Нижегородский государственный университет им. Н. И. Лобачевского, Нижний Новгород, Россия;

³ Институт физики полупроводников им. А. В. Ржанова СО РАН, Новосибирск, Россия;

⁴ Сколковский институт науки и технологий, Москва, Россия

✉ aperetokin@ipmras.ru

Аннотация. В работе изучены люминесцентные свойства двумерных фотонных кристаллов (ФК) с упорядоченными nanoостровками Ge(Si), полученных с использованием одно- и двухстадийного подходов к их упорядочению. Рассмотрены особенности люминесцентного отклика таких структур и их взаимосвязь с процессами



упорядочения наностроек. Показано, что встраивание наностроек в двумерный ФК позволяет более чем на порядок величины увеличить интенсивность сигнала ФЛ.

Ключевые слова: фотонные кристаллы, наностроек Ge(Si), фотолюминесценция

Финансирование: Государственное задание темы № 0030-2021-0019 и № FWGW-2022-0011.

Ссылка при цитировании: Перетокин А. В., Степихова М. В., Новиков А. В., Смагина Ж. В., Дьяков С. А., Особенности люминесцентного отклика двумерных фотонных кристаллов с упорядоченными наностройками Ge(Si), полученных с использованием разных подходов к упорядочению // Научно-технические ведомости СПбГПУ. Физико-математические науки. 2022. Т. 15. № 3.3. С. 188–193. DOI: <https://doi.org/10.18721/JPM.153.336>

Статья открытого доступа, распространяемая по лицензии CC BY-NC 4.0 (<https://creativecommons.org/licenses/by-nc/4.0/>)

Introduction

Today, the problem of creating efficient radiation sources for optical connections in the processor architecture remains unsolved [1]. Such connections will reduce the power consumption of processors and increase the speed of information processing. One of the main requirements for sources is their technological compatibility with silicon, which, as is known, is the main material of microelectronics, however, due to its indirect band gap, it has poor emitting properties.

Ge(Si) nanoislands are one of the options for such radiation sources, having a number of significant advantages: they are compatible with CMOS technology [2]; emit in the wavelength range of 1.2–1.6 μm , which is the main one for telecommunication systems [3]; they are relatively easy to produce and compact [2]; and, what is important in this work, there is the possibility of their spatial ordering on a silicon substrate [4]. The main disadvantage of Ge(Si) nanoislands is their relatively low emissivity. In order to increase the radiative efficiency of nanoislands, various options for their incorporation into low-dimensional cavities are currently being considered [5].

A large number of works [6] are devoted to photonic crystal cavities, in which an increase in the photoluminescence (PL) intensity of nanoislands is observed, reaching more than an order of magnitude, and the quality factor of the observed resonances exceeds 10^4 . It was shown that due to the precise embedding of the nanoislands in the maximum of the cavity mode field, it is possible to achieve an even higher signal amplification [6]. However, such structures have a small emitting volume and require high manufacturing precision, therefore it is much more profitable to use photonic crystals (PhCs) themselves, without a cavity, where all nanoislands are involved in the radiation processes, and not just those located in the small cavity.

For PhCs, it is also natural to think about the possibility to increase the amplification of nanoislands luminescence response due to their precise incorporation into field maxima of PhC modes. However, to date there is only one work where this idea was discussed [7], i.e., this task remains relevant.

Materials and Methods

The samples grown on SOI substrates with a Si layer thickness over the oxide of 80–90 nm were studied. For the ordered growth of nanoislands, the preliminary formation of seed pits in the substrate was used [4]. It's known that, depending on the parameters of the pits and the parameters of the formed lattice, the nucleation of nanoislands can occur both inside the pits and around them [8]. Therefore, two approaches to the nanoislands ordering in a PhC are possible: two-stage and one-stage.

To analyze the features of both approaches, 2 samples were grown. The first one was obtained using the classical two-stage ordering approach. With this approach, the fabrication of a sample occurs in two stages: I) – formation of an array of spatially ordered Ge(Si) nanoislands, and II) – formation of a PhC. At the first stage, square arrays of shallow, small in size, seed pits with a period of 1–4 μm were created on the substrate. Next, 4.5 Ge monolayers were deposited by

molecular beam epitaxy (MBE), forming Ge(Si) nanoislands inside the seed pits. Then, a silicon layer 15 nm thick was deposited by the MBE method, and a layer of nanoislands was again grown. The silicon thickness of 15 nm ensured the vertical ordering of nanoislands in the direction of growth. Thus, a structure with 10 layers of Ge(Si) nanoislands was obtained, with a total thickness above the oxide layer of ~ 300 nm; the upper layer of nanoislands was not overgrown for visual control of nanoislands location. At the second stage, in the obtained multilayer structure, in regions with ordered nanoislands, PhCs with a hexagonal lattice of holes were formed, with periods $a = 525 \div 600$ nm and the ratio $r/a = 0.14 \div 0.17$ (where r is the radius of the holes), the depth of the holes was ~ 220 nm. The growth technology and the fabrication process of this sample are described in more detail in [9].

In the one-stage approach to the nanoislands ordering, deep seed pits with vertical walls etched through the entire thickness of the active layer were used. Arrays of seed pits 200 nm in diameter were formed, arranged in a square lattice with a period of 500–2000 nm. Further, as in the previous case, a multilayer structure was grown with 4 layers of Ge(Si) nanoislands, with a total thickness of ~ 255 nm above the oxide layer. In contrast to the previous structure, the ordering of nanoislands in this case occurred around seed pits or between them. Under certain conditions, during growth, such pits did not overgrow, acting as holes of the PhC. The process of formation of such a sample is described in more detail in the article [10].

The studies in this work were carried out using a standard micro-photoluminescence (micro-PL) technique, which provides the possibility of measurements with high spatial (up to 2 μm) and spectral (up to 0.01 cm^{-1}) resolution [11]. All measurements were performed at a temperature of 77 K. The PL signal was excited by a solid-state laser with a wavelength of 532 nm, the laser power was varied from 3 to 4 mW.

The theoretical analysis of the formed PhCs was performed by the Fourier modal method in the scattering matrix formalism [12].

Results and Discussion

Fig. 1, *a* shows: the micro-PL spectra of PhC obtained using the two-stage approach, and, for comparison, of the initial, unprocessed region of the sample, without ordered Ge(Si) nanoislands. PhC period was 525 nm, $r/a = 0.17$. PhC was formed in the ordering region of nanoislands with a period of 1 μm . For this PhC, the maximum enhancement (η) of the luminescent response of Ge(Si) nanoislands was observed. At the maximum, PL signal increased almost 40 times, with respect to the signal measured in the unprocessed sample region, the increase in the integral intensity of the signal exceeded an order of magnitude ($\eta_{\text{integral}} = 12$). This enhancement of PL signal is explained by the interaction of Ge(Si) nanoislands with the optically active PhC modes, as evidenced by the presence of narrow peaks in the PL spectrum. As we showed earlier, the formation of photonic crystals in regions with long ordering periods of Ge(Si) nanoislands leads to a weaker increase in signal intensity, which is explained by a decrease in the surface density of nanoislands and, as a consequence, the number of ones interacting with PhC modes and contributing to PL signal [9].

The micro-PL spectrum of photonic crystal obtained using the one-stage approach is shown in Fig. 1, *b*, period of PhC is $a = 700$ nm. For the PhC presented, the maximum enhancement of luminescence response related with Ge(Si) nanoislands was observed. As in the two-stage approach, PL signal of photonic crystals obtained by this method exceeded by an order of magnitude the signal observed in the unprocessed region ($\eta_{\text{peak}} = 12$). The main feature of these PhCs is the strong dependence of their luminescence properties on the conditions of nanoislands formation. As the results of studies have shown, in photonic crystals with a small lattice period, under the growth conditions used, Ge(Si) nanoislands are not formed and have poor radiating properties. At large lattice periods of PhCs, nanoislands turned out to be completely formed, but the spectral range of their emission began to overlap with the high-order PhC modes, which are characterized by the low efficiency and a high degree of degeneracy, as evidenced by low-intense PL spectra observed for such PhCs, represented by broad PL lines [10]. The most optimal in this case are the lattice periods of PhCs $a = 700\text{--}900$ nm.

Fig. 2 shows the results of numerical simulation of the dispersion characteristics of emissivity carried out for the studied PhCs and the calculated field patterns of the most intense modes. The results of numerical simulation show that in PhCs with a hexagonal lattice of holes obtained by

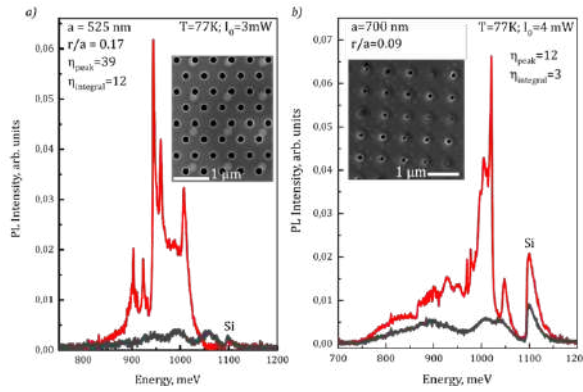


Fig. 1. Micro-PL spectra of photonic crystals obtained using (a) two- and (b) one-stage approaches to the ordering of Ge(Si) nanoislands. For comparison, in both figures, the micro-PL spectra of the original, unprocessed regions of the corresponding sample are shown in dark gray. The insets to the figures show SEM images of the studied PhCs. The values η_{peak} and $\eta_{integral}$ are the PL signal amplification at the maximum and the integral signal amplification observed in the PhCs compared to the signal in the initial unprocessed region of the sample

the two-stage method, the most intense PL line corresponds to the doublet E_2 mode [11], which is characterized by the presence of a symmetry-protected bound state in the continuum (BIC) at the Γ point of the Brillouin zone (Fig. 2, a). The emission maximum of this mode, observed in experiment, turns out to be shifted to the region of large wave-vectors in the Γ -K direction of the Brillouin zone, which may be due to the shallow depth of the holes formed in these PhCs. In a PhC with a square lattice obtained by a one-stage method, the most intense line in PL spectrum is represented by two closely spaced singlet modes A_2 and B_2 , which also show the features of BICs (Fig. 2, c). The bound-states in the continuum are characterized by a discontinuity in the dispersion curves of the emissivity at the Γ point, as it follows from the numerical simulation data (Fig. 2, a, c), and by extremely high values of the quality factor when compared with conventional radiative modes [12, 13].

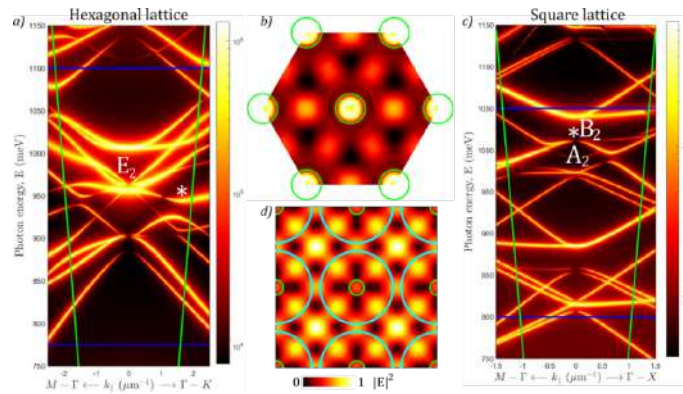


Fig. 2. Results of numerical simulation of the emissivity of studied PhCs near the Γ -point of Brillouin zone (a, c). The calculations were performed for PhCs shown in Fig. 1. The asterisks mark position of the maximum of PL signal observed in the experiment. The blue lines in the figures indicate emission range of the nanoislands, green lines indicate the collection angles of PL signal. Are the results of numerical simulation of field distribution carried out for PhC modes (b, d), indicated by asterisks in figures (a, c), respectively. The green circles indicate position of PhC holes, the blue circles in Fig. (d) indicate location of Ge(Si) nanoislands

Analyzing both approaches used in this work to the ordering of Ge(Si) nanoislands in photonic crystals, and considering the possibilities of embedding nanoislands in the maxima of the field of PhC modes, let us focus on the following. As mentioned above, in the two-stage approach, the ordering of nanoislands and the formation of PhCs occur at different stages, which makes it possible to form PhCs with any parameters and good hole quality, since this technology is well developed.

However, the main limitation here is the size of the nanoislands formed and the values of the minimum periods at which their ordering is possible. As follows from the field simulations carried out for the most intense mode (Fig. 2, *b*), it is optimal to build nanoislands between PhC holes, i.e. form a lattice of nanoislands with a period corresponding to S of PhC period, which is not feasible, since, according to literature, the minimum ordering period of Ge(Si) nanoislands is 425–500 nm [2, 4]. The incorporation of nanoislands into PhCs with a longer period should lead to a shift in the spectrum of optically active modes coinciding in energy with the emission range of Ge(Si) nanoislands into the range of high-order modes.

In the one-stage approach, due to the simultaneous formation of a PhC and the ordering of nanoislands, it becomes possible to form a PhC with any lattice parameters with ordered groups of Ge(Si) nanoislands. Ge(Si) nanoislands can be formed both around holes and between them [2, 10], which is true for square and hexagonal lattices. As can be seen in Fig. 2, *d*, the field distribution of the most intense mode in PhC with the square hole lattice obtained by one-stage formation method is even more complex than in the case of PhC considered in two-stage approach, however, due to the ordering of nanoislands around PhC holes, here we observe a stronger correlation in the spatial arrangement of the nanoislands with the field maxima of optically active PhC mode. Since the nanoislands are ordered in the same way around all holes, a high degree of periodicity of nanoislands incorporating into PhCs is achieved. To implement such an approach with two-stage ordering, it is necessary to separately solve the problem of combining arrays of nanoislands and PhCs, which, as discussed above, is not always possible. The main drawback of one-stage approach is the fact that during the growth process, holes that form photonic crystal can be partially or completely overgrown, due to which the PhC periodicity worsens, and, as a result, the quality factor of spectral lines. This is clearly seen in the SEM images shown in Fig. 1. Another consequence of the hole overgrowth is the small values of r/a ratio, which leads to the involvement of high-order modes in PL signal (Fig. 2, *c*). Nevertheless, despite such a non-ideal PhC, a spectrum of narrow lines is experimentally observed for it, exceeding the intensity of the PL signal in the unprocessed region of the sample by more than an order of magnitude.

Conclusion

As discussed above, both approaches considered by us to the ordering of Ge(Si) nanoislands in PhCs have their own advantages and disadvantages. Obviously, in order to minimize the disadvantages, it makes sense to combine these approaches: using a single-stage approach, one can achieve ordering of nanoislands between or around PhC holes, and then, using the second step from the two-stage approach, “once again” form a PhC with the same lattice parameters, but with better hole settings. Thus, it can be assumed that it will be possible to obtain a good-quality PhCs with ordered nanoislands around each hole, or between them. From the point of view of further research, here we should also once again pay attention to the two-stage approach, bearing in mind the possibility of combining the ordering lattices of Ge(Si) and PhC nanoislands. For the same (or multiple) periods of the lattices, it is possible to consider the possibility of their different mutual arrangement, which makes it possible to embed nanoislands in the selected PhC regions, maximally matching their position with the field maxima of the electromagnetic modes. Such studies can give a deeper understanding of the nanoislands interaction processes with PhC modes and of the ordering effects of nanoislands in PhCs on their luminescence response.

REFERENCES

1. Rickman. A., The commercialization silicon photonics, *Nature Photonics*. 8 (8) (2014) 579–582.
2. Brehm M., Grydlik M., Site-controlled and advanced epitaxial Ge/Si quantum dots: fabrication, properties, and applications. *Nanotechnology*, 28 (39) (2017) 392001.
3. Aleshkin V. Ya., Bekin N. A., Kalugin N. G., Krasil'nik Z. F., Novikov A. V., Postnikov V. V., Seyringer H., Self-organization of germanium nanoislands obtained in silicon by molecular-beam epitaxy. *Journal of Experimental and Theoretical Physics Letters*, 67 (1) (1998) 48–53.
4. Grydlik M., Langer G., Fromherz T., Schäffler F., Brehm M., Recipes for the fabrication of strictly ordered Ge islands on pit-patterned Si(001) substrates, *Nanotechnology*, 24 (2013) 105601.
5. Valhala K. J., Optical microcavities. *Nature*, 424 (2003) 839–846.



6. Schatzl M., Hackl F., Glaser M., Rauter P., Brehm M., Spindlberger L., Simbula A., Galli M., Fromherz T., Schäffler F., Enhanced Telecom Emission from Single Group-IV Quantum Dots by Precise CMOS-Compatible Positioning in Photonic Crystal Cavities. *ACS Photonics*, 4 (3) (2017) 665–673.
7. Jannesari R., Schatzl M., Hackl F., Glaser M., Hinger K., Fromherz T., Schäffler F., Commensurate germanium light emitters in silicon-on-insulator photonic crystal slabs. *Optics Express*, 22 (21) (2014) 25426–25435.
8. Smagina Z. V., Zinovyev V. A., Rudin S. A., Novikov P. L., Rodyakina E. E., Dvurechenskii A. V., Nucleation sites of Ge nanoislands grown on pit-patterned Si substrate prepared by electron-beam lithography. *Journal of Applied Physics*, 123 (2018) 165302.
9. Smagina Zh. V., Novikov A. V., Stepikhova M. V., Zinovyev V. A., Rodyakina E. E., Nenashev A. V., Sergeev S. M., Peretokin A. V., Kuchinskaya P. A., Shaleev M. V., Gusev S. A., Dvurechenskii A. V., Luminescence of Spatially Ordered Self-Assembled Solitary Ge(Si) Nanoislands and their Groups Incorporated into Photonic Crystals. *Semiconductors*, 54 (8) (2020) 853–859.
10. Novikov A. V., Smagina Z. V., Stepikhova M. V., Zinovyev V. A., Rudin S. A., Dyakov S. A., Rodyakina E. E., Nenashev A. V., Sergeev S. M., Peretokin A. V., Dvurechenskii A. V., One-Stage Formation of Two-Dimensional Photonic Crystal and Spatially Ordered Arrays of Self-Assembled Ge(Si) Nanoislands on Pit-Patterned Silicon-On-Insulator Substrate. *Nanomaterials*, 11 (4) (2021) 909–923.
11. Dyakov S. A., Stepikhova M. V., Bogdanov A. A., Novikov A. V., Yurasov D. V., Krasilnik Z. F., Tikhodeev S. G., Gippius N. A., Photonic bound states in the continuum in Si structures with the self-assembled Ge nanoislands. *Laser & Photonics Reviews*. 15 (2021) 2000242.
12. Tikhodeev S. G., Yablonskii A. L., Muljarov E. A., Gippius N. A., Ishihara T., Quasiguidded modes and optical properties of photonic crystal slabs. *Phys. Rev. B*, 66 (64) (2002) 045102.
13. Joseph S., Pandey S., Sarkar S., Joseph J., Bound states in the continuum in resonant nanostructures: an overview of engineered materials for tailored applications. *Nanophotonics*, 10 (17) (2021) 4175–4207.

THE AUTHORS

PERETOKIN Artem V.
aperetokin@ipmras.ru
ORCID: 0000-0003-4729-5646

SMAGINA Zhanna V.
smagina@isp.nsc.ru
ORCID: 0000-0003-0778-5894

STEPIKHOVA Margarita V.
mst@ipmras.ru
ORCID: 0000-0001-8269-0348

DYAKOV Sergey A.
s.dyakov@skoltech.ru
ORCID: 0000-0002-3729-6621

NOVIKOV Alexey V.
anov@ipmras.ru
ORCID: 0000-0002-6667-8098

Received 08.08.2022. Approved after reviewing 11.08.2022. Accepted 30.08.2022.

Conference materials

UDC 53

DOI: <https://doi.org/10.18721/JPM.153.337>

Posterior laser-locking technique for MDI-QKD

E. E. Mekhtiev ^{1, 2✉}, I. S. Gerasin ^{2, 3}, N. V. Rudavin ^{3, 4},
A. V. Duplinsky ^{3, 4}, Yu. V. Kurochkin ³

¹ LLC "QRate", Moscow, Russia;

² Moscow Institute of Physics and Technology, Dolgoprudny, Russia;

³ National University of Science and Technology MISiS, Moscow, Russia;

⁴ HSE University, Moscow, Russia

✉ mekhtiev@phystech.com

Abstract. We present a novel soft-ware based method to ensure independent lasers mutual coherence required for practical realization of advanced Measurement Device Independent Quantum Key Distribution (MDI-QKD) protocols. Proof of principle experiment has proved validity of the method, providing mutual coherence time while upper bound dictated by uncontrollable phase drift in optical fiber being $\sim 100 \mu\text{s}$.

Keywords: MDI-QKD, mode-pairing protocol, asynchronous protocols, mutual phase stabilization, mutual coherence

Funding: The study was commissioned by JSCo "RZD".

Citation: Mekhtiev E. E., Gerasin I. S., Rudavin N. V., Duplinsky A. V., Kurochkin Yu. V., Posterior laser-locking technique for MDI-QKD. St. Petersburg State Polytechnical University Journal. Physics and Mathematics, 15 (3.3) (2022) 194–197. DOI: <https://doi.org/10.18721/JPM.153.337>

This is an open access article under the CC BY-NC 4.0 license (<https://creativecommons.org/licenses/by-nc/4.0/>)

Материалы конференции

УДК 53

DOI: <https://doi.org/10.18721/JPM.153.337>

Метод обеспечения взаимной когерентности двух независимых лазеров на этапе постобработки для реализации протоколов КРК с использованием НЦУ

Э. Э. Мехтиев ^{1, 2✉}, И. С. Герасин ^{2, 3}, Н. В. Рудавин ^{3, 4},
А. В. Дуплинский ^{3, 4}, Ю. В. Курочкин ³

¹ ООО «КуРЭйт», Москва, Россия;

² Московский физико-технический институт, Долгопрудный, Россия;

³ Национальный исследовательский технологический университет «МИСиС», Москва, Россия;

⁴ Национальный исследовательский университет «Высшая школа экономики», Москва, Россия

✉ mekhtiev@phystech.com

Аннотация. В работе описан метод обеспечения взаимной когерентности независимых лазерных источников, необходимой для практической реализации определенного класса протоколов Квантового Распределения Ключей (КРК) с использованием Недоверенного Центрального Узла (НЦУ). Экспериментальная проверка подтвердила эффективность предложенного метода, обеспечившего время взаимной когерентности ~ 10 мкс. Максимально достижимое время взаимной когерентности определяется фазовым шумом в оптическом волокне и составляет ~ 10 мкс.

Ключевые слова: КРК с НЦУ, асинхронные протоколы КРК с НЦУ, стабилизация относительно фазы, взаимная когерентность

Финансирование: Исследовательская работа выполнена по заказу ОАО «РЖД».

Ссылка при цитировании: Мехтиев Э. Э., Герасин И. С., Рудагин Н. В., Дуплинский А. В., Курочкин Ю. В., Метод обеспечения взаимной когерентности двух независимых лазеров на этапе постобработки для реализации протоколов КРК с использованием НЦУ // Научно-технические ведомости СПбГПУ. Физико-математические науки. 2022. Т. 15. № 3.3. С. 194–197. DOI: <https://doi.org/10.18721/JPM.153.337>

Статья открытого доступа, распространяемая по лицензии CC BY-NC 4.0 (<https://creativecommons.org/licenses/by-nc/4.0/>)

Introduction

Measurement device independent quantum key distribution (MDI-QKD) is a promising step towards secure quantum key distribution networks [1]. The motivation for developing device independent protocols arises from inevitable gap between theoretical description of a protocol and its real device realisation. This gap can be used by eavesdropper (Eve) to obtain additional information about secret key. The most vulnerable part of real-life QKD systems are single photon detectors, since they are exposed to the majority of quantum hacking attacks [2, 3]. MDI-QKD protocols allow Eve to control measurement device, still guaranteeing security of key distribution.

With all mentioned advantages, present experimental realizations of MDI protocols does not enjoy as high security key rate as prepare-and-measure protocols. Recently so-called asynchronous or mode-pairing MDI-QKD protocols have been proposed [4, 5] to make up for this shortcoming. The main feature of these protocols is a drastic improvement of the secure key rate over longer distances. However, Asynchronous MDI-QKD requires high degree of sender lasers mutual coherence. Usually this problem is solved via various hard-ware based laser locking techniques [6]. In this work we present easy soft-ware based approach to solve this problem. We refer to this approach as posterior laser-locking technique.

Problem statement

The mode-pairing MDI-QKD essentially is a generalization of time-bin encoding MDI-QKD. Namely, instead of two using fixed time bins to encode qubit, some pairing strategy between several time bins is applied to detection events at post-processing stage. This approach allows to achieve $O(\sqrt{\eta})$ instead of standard MDI asymptotic $O(\eta)$ for a secure key rate R , where $\eta \rightarrow +\infty$ is total channel transmittance [5].

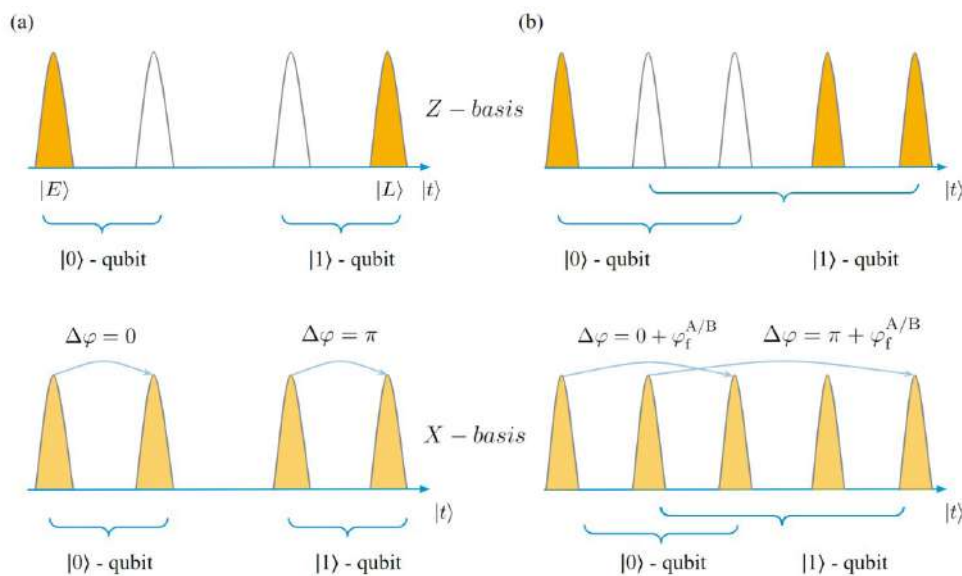


Fig. 1. MDI-QKD encoding schematics. Standard time-bin encoding (a). Mode-pairing encoding (b)

The schematic of mode-pairing encoding method is present on Fig. 1, *b*. The pairing time bin is chosen during post-processing which allow to efficiently use almost every detector “click”, despite transmittance losses. However increasing the pairing time (blue-arrows) may lead to unexpected phase difference between chosen time bins induced by optical fiber $\varphi_f^{A/B}$. This phase term is totally random and may be different for sender A and B. This fact prevents senders from matching their encoding phases $\varphi \in \{0, \pi\}$ which is a must according to MDI- protocol. The next two sections describe our approach to overcome this problem.

Setup and Methods

1. Setup

Equations should be formatted in MathType (please AVOID MS Word Equation Editor). Equations are numbered consecutively beginning with (1) to the end of the paper, e.g.: We investigate interference of two independent continuous light beams. Fig. 2. represents experimental setup. Laser A is Keysight 81950A with spectral width < 100 kHz, Laser B is Keysight 81608A with spectral width < 100 kHz. Central wavelength of the two lasers adjusted so that their mean mutual beat frequency $\langle \Delta\omega_{AB} \rangle \sim 250$ MHz. Communication link is established with standard single-mode optical fibers. We use two fiber-coupled photodetectors at detection side to register lasers interference pattern. Signal photodetector PD_s is Thorlabs PDA8GS, compensating photodetector PD_c is Thorlabs RXM40AF. Interference traces are captured by Teledyne LeCroy WaveMaster 808Zi-A oscilloscope. We investigate communication links of $L = 0, 25, 50$ and 75 km lengths to test robustness of a proposed method.

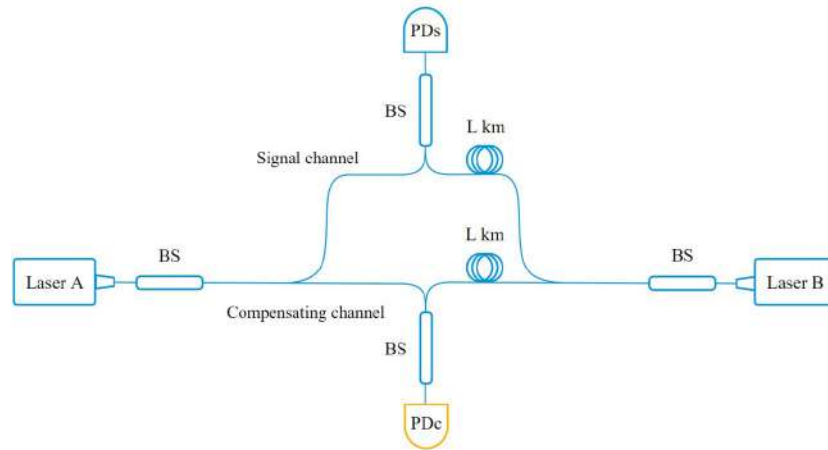


Fig. 2. Experimental setup. PD – photodetector, BS – 50:50 beamsplitter, L – optical fiber spool

2. Method

We aim to use frequency beat measured on PD_c to post-compensate phase difference on detector PD_s arising from lasers wavelength difference. Intensities on PD_s and PD_c are respectively:

$$J_s(t) \sim e^{i[\Delta\varphi_{AB}^0 + \Delta\varphi_{fs} + \Delta\omega_{AB}(t-t_s) \cdot t]} \quad (1)$$

$$J_c(t) \sim e^{i[\Delta\varphi_{AB}^0 + \Delta\varphi_{fc} + \Delta\omega_{AB}(t-t_c) \cdot t]} \quad (2)$$

where $\Delta\varphi_{AB}^0$ is initial phase difference between two laser sources; $\Delta\varphi_{fs}, \Delta\varphi_{fc}$ are random phase differences induced by optical fibers of signal and compensating channels; $\Delta\omega_{AB}(t-t_s) \cdot t, \Delta\omega_{AB}(t-t_c) \cdot t$ are phase differences on detectors PD_s and PD_c at time t due to lasers mutual incoherence; $|t_c - t_s| \cdot c$ path difference between signal and compensating channels. The proposed method works as follows:

1. Collect interference traces with detectors PD_s and PD_c ;
2. Find $\Delta\omega_{AB}(t)$ from $J_c(t)$ with Fast Fourier Transform;
3. Subtract $\Delta\omega_{AB}(t)$ from the phase of $J_s(t)$;
4. Search to find delay $|t_c - t_s| \cdot c$ minimizing final phase error $\Delta\varphi_{err}(t)$.



Results and Discussion

Table 1 shows phase error rate of the two posteriorly-locked lasers. For detection node remote at 25 km mutual lasers coherence of $\sim 100 \mu\text{s}$ is achieved with 0.15 rad certainty. We note that the upper time limit for Lasers A and B mutual coherence, imposed by random phase noise in optical fiber, $\sim 100 \mu\text{s}$ [7].

Table 1

Phase error rate against communication link length

L, km	$\Delta\varphi_{\text{err}}, \text{rad}\cdot\mu\text{s}^{-1}$
0	0.004
25	0.015
50	0.027
75	0.059

Further improvement can be achieved with using higher sample rates on oscilloscope and greater lasers detuning. Also it should be noticed that proof-of-principle experiment does not require to send weak coherent laser pulses instead of continuous beam, since these pulses inherit the phase of continuous wave from which they are “cut” with intensity modulator.

Conclusion

Altogether the degree of mutual coherence provided with new technique looks promising for effective realisation of asynchronous MDI-QKD protocols.

REFERENCES

1. Lo H. K., Curty M., Qi B., Measurement-device-independent quantum key distribution. *Physical review letters*. 108 (13) (2012) 130503.
2. Xu F., Ma X., Zhang Q., Lo H. K., Pan J. W., Secure quantum key distribution with realistic devices, *Reviews of Modern Physics*. 92 (2) (2020) 025002.
3. Jain N., Stiller B., Khan I., Elser D., Marquardt C., Leuchs, G., Attacks on practical quantum key distribution systems (and how to prevent them), *Contemporary Physics*. 57 (3) (2016) 366–387.
4. Xie Y. M., Lu Y. S., Weng C. X., Cao X. Y., Jia Z. Y., Bao Y., Chen Z. B., Breaking the Rate-Loss Relationship of Quantum Key Distribution with Asynchronous Two-Photon Interference, arXiv. (2021) preprint arXiv:2112.11635.
5. Zeng P., Zhou H., Wu W., Ma X., Quantum key distribution surpassing the repeaterless rate-transmittance bound without global phase locking, arXiv. (2022) preprint arXiv:2201.04300.
6. Khabarova K. Y., Kuderyarov K. S., Vishnyakova G. A., Kolachevsky N. N., Short-haul fibre-optic communication link with a phase noise compensation system for optical frequency signal transmission, *Quantum Electronics*. 47 (9) (2017) 794.
7. Fang X. T., Zeng P., Liu H., Zou M., Wu W., Tang Y. L., Pan J. W., Implementation of quantum key distribution surpassing the linear rate-transmittance bound, *Nature Photonics*. 14 (7) (2020) 422–425.

THE AUTHORS

MEKHTIEV EI E.
mekhtiev@phystech.edu
ORCID: 0000-0002-9756-7016

DUPLINSKY Alexander V.
a.duplinsky@goqrates.com
ORCID: 0000-0003-2222-0752

GERASIN Ilia S.
i.gerasin@goqrates.com
ORCID: 0000-0001-5084-7056

KUROCHKIN Yury V.
yk@goqrates.com
ORCID: 0000-0001-5376-6358

RUDAVIN Nikita V.
n.rudavin@goqrates.com
ORCID: 0000-0003-0264-5710

Received 12.08.2022. Approved after reviewing 18.08.2022. Accepted 24.08.2022.

Conference materials

UDC 53

DOI: <https://doi.org/10.18721/JPM.153.338>

Novel method for preparing high-indistinguishable coherent states

I. S. Gerasin^{1,2,3}, E. E. Mekhtiev^{1,2,3}, E. L. Maksimova¹, N. V. Rudavin^{3,4}✉,
A. V. Duplinsky^{1,3}, Yu. V. Kurochkin^{1,2,3}

¹ LLC "QRate", Moscow, Russia;

² Moscow Institute of Physics and Technology, Dolgoprudny, Russia;

³ National University of Science and Technology MISiS, Moscow, Russia;

⁴ HSE University, Moscow, Russia

✉ n.rudavin@goqrates.com

Abstract. The preparation of indistinguishable quantum states by remote users is one of the crucial tasks in MDI-QKD. To solve this problem, laser injection techniques or modulation of the CW laser on the transceiver side are used. These techniques require a complex setup or a pair of modulators. Here we present a different setup for generating coherent states, using one modulator and one gain-switched laser per transceiver, to find a balance between the complexity of the setup and its cost. The level of indistinguishability achieved allows our scheme to be used in high-speed MDI-QKD protocols.

Keywords: MDI-QKD, Hong-Ou-Mandel interference, Weak Coherent Pulses with Randomized Phase, Indistinguishable quantum states

Funding: The study was commissioned by JSCo "RZD".

Citation: Gerasin I. S., Mekhtiev E. E., Maksimova E. I., Rudavin N. V., Duplinsky A. V., Kurochkin Yu. V., Novel method for preparing high-indistinguishable coherent states. St. Petersburg State Polytechnical University Journal. Physics and Mathematics, 15 (3.3) (2022) 198–201. DOI: <https://doi.org/10.18721/JPM.153.338>

This is an open access article under the CC BY-NC 4.0 license (<https://creativecommons.org/licenses/by-nc/4.0/>)

Материалы конференции

УДК 53

DOI: <https://doi.org/10.18721/JPM.153.338>

Новый способ получения слаборазличимых когерентных состояний

И. С. Герасин^{1,2,3}, Э. Э. Мехтиев^{1,2,3}, Е. Л. Максимова¹, Н. В. Рудавин^{3,4}✉,
А. В. Дуплинский^{1,3}, Ю. В. Курочкин^{1,2,3}

¹ ОАО «КуРэйт», Москва, Россия;

² Московский физико-технический институт, Долгопрудный, Россия;

³ Национальный исследовательский технологический университет «МИСиС», Москва, Россия;

⁴ Национальный исследовательский университет «Высшая школа экономики», Москва, Россия

✉ n.rudavin@goqrates.com

Аннотация. Подготовка неразличимых квантовых состояний различными пользователями является одной из важнейших задач в КРК с НЦУ. Для решения этой проблемы используются методы лазерной инъекции или модуляции непрерывного лазера на стороне передатчика. Эти методы требуют сложной настройки или нескольких оптических модуляторов. В данной работе мы представляем новую установку для генерации когерентных состояний, использующую один модулятор и один лазер на стороне каждого из отправителей, чтобы найти баланс между сложностью установки и ее стоимостью. Достигнутый уровень неразличимости позволяет использовать нашу схему приготовления состояний в высокоскоростных протоколах КРК с НЦУ.



Ключевые слова: КРК с НЦУ, интерференция Хонга-У-Манделя, слабые когерентные импульсы с рандомизированной фазой (СКИРФ), неразличимые квантовые состояния.

Финансирование: Исследовательская работа выполнена по заказу ОАО «РЖД».

Ссылка при цитировании: Герасин И. С., Мехтиев Э. Э., Максимова Е. И., Рудавин Н. В., Дуплинский А. В., Курочкин Ю. В. Новый способ получения слаборазличимых когерентных состояний // Научно-технические ведомости СПбГПУ. Физико-математические науки. 2022. Т. 15. № 3.3. С. 198–201. DOI: <https://doi.org/10.18721/JPM.153.338>

Статья открытого доступа, распространяемая по лицензии CC BY-NC 4.0 (<https://creativecommons.org/licenses/by-nc/4.0/>)

Introduction

Quantum interference is one of the key experiments in quantum information technologies. It is useful for quantum teleportation, quantum computing, and quantum cryptography. Usually, the visibility of interference at the beamsplitter (Hong-Ou-Mandel interference) serves as a measure of indistinguishability of quantum states. Measurement device independent quantum key distribution (MDI-QKD) protocols require the interference at the central untrusted node of two weak coherent pulses with random phase (WCPRP) prepared by two remote users [1, 2]. There are two main approaches to generate such indistinguishable states by remote users: (a) modulating a CW laser with an intensity modulator (IM) and a phase modulator, (b) using a gain-switched semiconductor laser. The first approach allows to easily prepare almost indistinguishable states by two remote users in cost of additional optical devices and lasers with high stability [3]. The second approach implies only semiconductor lasers, however the states produced by two users are more distinguishable due to the temporal and spectral properties of two different laser diodes [4]. To increase mode match, in recent work the laser injection technique was adopted to prepare WCPRP by two remote users [5]. On the one hand, laser injection allows to achieve better mode overlap between independent gain switch laser sources, but on the other hand, it increases the complexity of the setup, and one needs to drive laser with high stability current. In our work, we propose a novel method to prepare WCPRP using gain-switched lasers without injection and only one modulator.

Materials and Methods

While building MDI-QKD system high visibility of Hong-Ou-Mandel interference [6] (Fig. 1.) must be achieved. For pure Fock single photon states best visibility $V = 1$. In case of WCPRP maximal visibility $V = 0.5$ [7]. To push experimental results close to theoretical limits interfering states, must be indistinguishable in each degree of freedom.

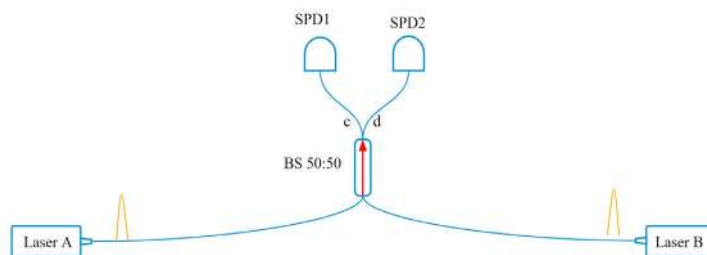


Fig.1. Basic two single photons interference scheme

Using single-mode optical fiber guarantees indistinguishability of transversal special modes, synchronization system and optical delay line should provide simultaneity of two WCPRP arrival time to the beam splitter, beam splitter with polarizer eliminates distinguishability over polarization. However, one also should adjust spectral and temporal shapes of the pulses itself, for which we use variable optical filter and intensity modulator.

To characterize the quality of preparation of indistinguishable states we calculate second order correlation function g^2 which has simple relation with visibility:

$$V = 1 - g^2 \tag{1}$$

The definition of g^2 is

$$g^2 = \frac{\langle I_c I_d \rangle}{\langle I_c \rangle \langle I_d \rangle} \tag{2}$$

where I_c, I_d are intensities of WCPRP at reseaving detectors SPD1 and SPD2 in Fig. 1. The expression for g^2 can be transformed to the more convinient form if we consider conservation of energy and the symmetry of the setup:

$$\begin{aligned} I_d(t) + I_c(t) &= 2I \\ \langle I_c \rangle &= \langle I_d \rangle = I \end{aligned} \tag{3}$$

Thus, we have for g^2 :

$$g^2 = 2 - \frac{\langle I_c^2 \rangle}{\langle I_c \rangle^2} = 1 - \left(\frac{\sigma_{I_c}}{\langle I_c \rangle} \right)^2 \tag{4}$$

which proves that measuring a distribution of only one of intensities is sufficient for calculating g^2 .

The goal of our experiment is to find filtration setup which minimizes g^2 preparing the ground for building full-fledged MDI-QKD system.

Results and Discussion

By configuring our experimental setup, we can observe the interference of different preparation schemes. We compare 4 preparation setups: **GS-laser** (Gain Switched); **GS-laser + filter**; **GS-laser + IM**; **GS-laser + filter + IM** (Fig. 2.). First, we consider the **GS-laser** scheme, where IM is turned off and the filter bandwidth is opened to its maximum value (3 nm) around the central peak of the lasers.

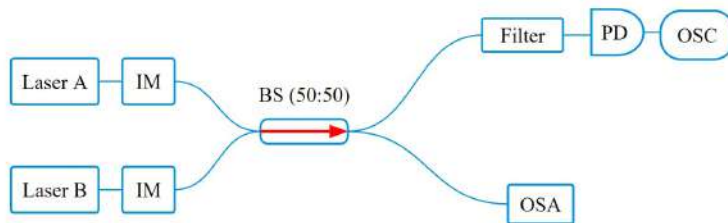


Fig. 2. Different preparation setups compared in our work

In this mode, we calculate the indistinguishability of two directly modulating semiconductor lasers. The second setup is **GS-laser + filter**. Also, in this case IM is not driven, however the filter bandwidth has its narrowest value (0.05 nm). Another setup **GS-laser + IM** is to drive IM with opened filter. The last scheme **GS-laser + filter + IM** includes the driving of IM and the filter with its narrowest bandwidth. The results of the measured second order correlation function are presented in Table 1. The results show that the proposed scheme with proper time and frequency filtering achieves values close to the theoretical minimum $g^2 = 0.5$ and can be used to prepare states in high-speed MDI-QKD setups. Moreover, the same intensity modulator can be used to prepare decoy states in MDI-QKD.

Table 1

Values of g^2 obtained for different setups of optical shemes for WCPRP preparation

Setup	g^2
GS-Laser	0.728
GS-Laser + Filter	0.588
GS-Laser + IM	0.534
GS-Laser + Filter + IM	0.508



Conclusion

Our time and spectral filtering scheme provide highly indistinguishable WCPRP states. In order to prove that we provide a Hong-Ou-Mandel experiment. Results of the experiment show the visibility close to theoretical value 0.5. Such results allow to reduce complexity of high-speed MDI QKD device and thus reduce the device cost making MDI QKD closer to commercial use.

REFERENCES

1. **Hoi-Kwong L., Curty M., Qi B.**, Measurement-device-independent quantum key distribution, Physical review letters. 108 (13) (2012) 130503.
2. **Tang Z., Wei K., Bedroya O., Qian L., Lo H. K.**, Experimental measurement-device-independent quantum key distribution with imperfect sources, Physical Review A. 93 (4) (2016) 042308.
3. **Tang Zhiyuan, et al.**, Experimental demonstration of polarization encoding measurement-device-independent quantum key distribution, Physical review letters. 112 (19) (2014) 190503.
4. **Yuan Z. L., et al.**, Interference of short optical pulses from independent gain-switched laser diodes for quantum secure communications, Physical Review A. 2 (6) (2014) 064006.
5. **Comandar L. C., et al.**, Near perfect mode overlap between independently seeded, gain-switched lasers, Optics express. 24 (16) (2016) 17849–17859.
6. **Hong Chong-Ki, Zhe-Yu Ou, Mandel L.**, Measurement of subpicosecond time intervals between two photons by interference. Physical review letters. 59 18 (1987) 2044.
7. **Hoi-Kwong L., Curty M., Qi B.**, Measurement-device-independent quantum key distribution. Physical review letters. 108 13 (2012) 130503.

THE AUTHORS

GERASIN Ilia S.

i.gerasin@goqrates.com

ORCID: 0000-0001-5084-7056

MEKHTIEV El E.

mekhtiev@phystech.edu

ORCID: 0000-0002-9756-7016

MAKSIMOVA Elizaveta I.

e.maksimova@goqrates.com

ORCID: 0000-0002-1600-0377

RUDAVIN Nikita V.

n.rudavin@goqrates.com

ORCID: 0000-0003-0264-5710

DUPLINSKY Alexander V.

a.duplinsky@goqrates.com

ORCID: 0000-0003-2222-0752

KUROCHKIN Yury V.

yk@goqrates.com

ORCID: 0000-0001-5376-6358

Received 12.08.2022. Approved after reviewing 05.09.2022. Accepted 05.09.2022.

Conference materials

UDC 535.51

DOI: <https://doi.org/10.18721/JPM.153.339>

Polarization compensation design for free-space quantum communication transmitter

V. E. Merzlinkin^{1, 2, 3}✉, A. V. Khmelev^{1, 2, 4, 5}, A. V. Duplinsky^{1, 2, 6},
V. L. Kurochkin^{1, 2, 3, 4}, Yu. V. Kurochkin^{1, 2, 3, 4, 5}

¹ LLC "QSpace Technologies", Moscow, Russia;

² LLC "QRate", Moscow, Russia;

³ National University of Science and Technology MISiS, Moscow, Russia;

⁴ Russian Quantum Center, Moscow, Russia;

⁵ Moscow Institute of Physics and Technology, Dolgoprudny, Russia;

⁶ National Research University Higher School of Economics, Moscow, Russia

✉ v.merzlinkin@goqr.com

Abstract. Quantum communication is a transmission technology that allows legitimate users to share a secret key. The BB84 protocol employs four linear polarization states for encoding in our quantum key distribution system. However, the optical elements affect the polarization features of quantum state, which leads to errors in decoded key. To reduce mistakes and increase device encoding performance, a polarization controller is included in the optical circuit. An algorithm identifying the angles of the polarization controller's wave plates has been developed. We conclude that using a polarization controller and the method of finding angles has improved the polarization extinction ration for all encoding channels of designed free-space transmitter. Finding angles of the plates is a problem of optimizing the search for parameters where the trace of matrix is maximum in the Stokes-Muller formalism. We used the gradient descent approach to determine the angles of the plates and we were able to obtain optical part of QBER values of 0.12 percent, so decreasing its values by 185 times.

Keywords: quantum communications, quantum key distribution, BB84 protocol, polarization controller, phase shift, the Poincare sphere, polarimetry

Funding: The strategic academic leadership program "Priority 2030", indicating number of the financial support of K1-2022-027.

Citation: Merzlinkin V. E., Khmelev A. V., Duplinsky A. V., Kurochkin V. L., Kurochkin Yu. V., Polarization compensation design for free-space quantum communication transmitter. St. Petersburg State Polytechnical University Journal. Physics and Mathematics, 15 (3.3) (2022) 202–206. DOI: <https://doi.org/10.18721/JPM.153.339>

This is an open access article under the CC BY-NC 4.0 license (<https://creativecommons.org/licenses/by-nc/4.0/>)

Материалы конференции

УДК 535.51

DOI: <https://doi.org/10.18721/JPM.153.339>

Квантовый передатчик в открытом пространстве с компенсацией искажений поляризации

В. Е. Мерзлинкин^{1, 2, 3}✉, А. В. Хмелев^{1, 2, 4, 5}, А. В. Дуплинский^{1, 2, 6},
В. Л. Курочкин^{1, 2, 3, 4}, Ю. В. Курочкин^{1, 2, 3, 4, 5}

¹ ООО «КуСпейс Технологии», Москва, Россия;

² ООО «КуРэйт», Москва, Россия;

³ Национальный исследовательский технологический университет МИСиС, Москва, Россия;

⁴ Российский Квантовый Центр, Москва, Россия;



⁵ Московский физико-технический институт, Долгопрудный, Россия;

⁶ Национальный исследовательский университет «Высшая школа экономики», Москва, Россия
✉ v.merzlinkin@goqrates.com

Аннотация. Квантовая коммуникация – это технология передачи, позволяющая обмениваться секретным ключом авторизованным пользователям. Протокол квантового распределения ключа BB84 использует четыре состояния линейной поляризации для кодирования, но оптические элементы влияют на поляризацию, что приводит к ошибкам в квантовом ключе при его декодировании. Поляризационный контроллер позволяет снизить величину такой ошибки в ключе. В результате, мы разработали алгоритм определения углов волновых пластин контроллера поляризации, позволяющий компенсировать влияние оптических элементов на поляризационные состояния фотонов. Поиск углов пластинок был осуществлен через решение задачи оптимизации нахождения параметров, где матрица в формализме Стокса-Мюллера имела максимальный след. Найденные углы позволили снизить оптическую часть QBER'a до значения 0.12%, что в 185 раз ниже, чем изначальный.

Ключевые слова: квантовые коммуникации, квантовое распределение ключей, BB84 протокол, контроллер поляризации, фазовый сдвиг, сфера Пуанкаре, поляриметрия

Финансирование: Программа стратегического академического лидерства «Приоритет-2030», проект № К1-2022-027.

Ссылка при цитировании: Мерзлинкин В. Е., Хмелев А. В., Дуплинский А. В., Курочкин В. Л., Курочкин Ю. В. Квантовый передатчик в открытом пространстве с компенсацией искажений поляризации // Научно-технические ведомости СПбГПУ. Физико-математические науки. 2022. Т. 15. № 3.3. С. 202–206. DOI: <https://doi.org/10.18721/JPM.153.339>

Статья открытого доступа, распространяемая по лицензии CC BY-NC 4.0 (<https://creativecommons.org/licenses/by-nc/4.0/>)

Introduction

Quantum communication is studied by a large number of scientific groups as one of the reliable and promising methods in the information security [1, 2]. Significant progress has been achieved in the development of systems and their theoretical analysis for the quantum key distribution (QKD) since the first concept was proposed [3]. However, practical realization of quantum key distribution systems are imperfect, and this fact opens up many opportunities for eavesdropping [4]. To achieve a high-secure communication, researchers propose different protocols and optical schemes to share secret key [5].

The high losses of single photons that propagates across a medium are also one of the main problems for the quantum cryptography implementation for a long distance. Nowadays, cutting-edge QKD experiment provides an adequate key rate at distance up to 250 km in an optical fiber [6]. To perform a long-distance quantum key distribution, the most preferable realization is a free-space system using polarization coding method of photon states [7]. Commonly, the BB84 decoy-state protocol is the most practically useful for free-space quantum communication based on the linear polarization states: $|H\rangle$, $|V\rangle$, $|D\rangle = \frac{1}{\sqrt{2}}(|H\rangle + |V\rangle)$, $|A\rangle = \frac{1}{\sqrt{2}}(|H\rangle - |V\rangle)$.

The transmitter using polarization encoding has to provide high linearity and unbiased bases output photon states. However, the polarization light can be affected by the imperfection of the optical elements and their dependence on incident angle of the polarization light. Therefore, polarization compensation of photons is one of the essential technology to decrease the level of errors while decoding quantum states. We report the results of polarization characteristics of designed transmitter for free-space quantum communication. The polarization properties of optical elements in transmitter have been investigated and algorithm for a polarization controller made up of one half-wave plate (HWP) and two quarter-wave plate (QWP) has been developed.

Optical systems can introduce dissipative and phase losses. Dissipative polarization losses are the rotation of one of the bases relative to the other, for example due to the large absorption of “s” or “p” polarization. Phase loss is the phase shift between the “s” or “p” of polarization, which

leads to ellipticity of polarization in the diagonal basis [8]. Dissipative losses are insignificant in our QKD optical systems, therefore, as part of the work, measures were taken to eliminate the phase error.

Incorrect measurements in QKD can be associated with two reasons, with imperfect equipment and an attacker's intrusion in the quantum channel. To evaluate the first, we introduce such a concept as a quantum bit error rate (QBER). The QBER is affected of two parts: noise counts and optical part.

Method

The transmitter using polarization encoding has to provide high linearity and unbiased bases output photon states. However, the polarization light can be affected by the imperfection of the optical elements and their dependence on incident angle of the polarization light. As a result, one of the most important ways to decrease quantum bit error rate (QBER) is a method of photon polarization compensation for the transmitter.

Laboratory measurements of the optical transmitter were shown strong polarization distortions caused by MEMS and two dichroic mirrors. These mirrors perform important functions, such as accurate alignment of the system and separation of communication channels. To compensate for the error caused by them, we utilize a polarization controller with one half-wave plate (HWP) and two quarter-wave plates (QWP). The algorithm of working with it was written based on the Stokes-Mueller formalism and include solving the optimization problem. The algorithm for finding the angles of wave plates finds the maximum of the function (1) using the gradient descent method.

$$\frac{1}{4} \text{Tr}[SM_{\lambda/4}(x)M_{\lambda/2}(y)M_{\lambda/4}(z)] = 1 \quad (1)$$

where S is matrix describing the effect of an optical system on polarization;

M is wave plate matrix;

x, y, z are angles of the plates.

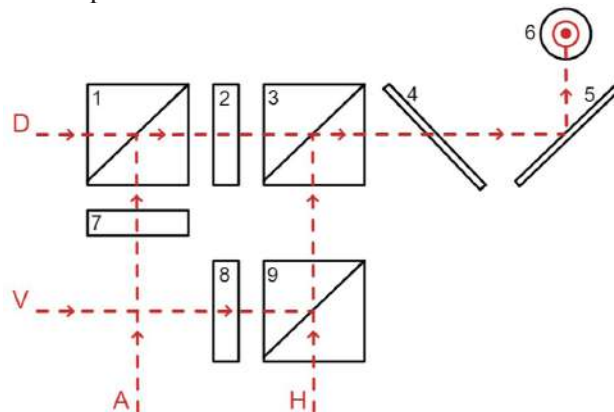


Fig. 1. The scheme of the quantum communication transmitter: 1, 9 – polarizing beam splitters; 2 – half-wave plate; 3 – beam splitters 50:50; 4 – dichroic mirror DLMP805R; 5 – dichroic mirror DMSP805T; 6 – MEMS mirror; 7, 8 – linear polarizers; V, H, D, A – vertical, horizontal, diagonal, antidiagonal polarization of the photons; dotted line – optical path of the laser beam with wavelength 850 nm

The quantum transmitter circuit, as shown in Fig. 1, was created for the QKD nanosatellite, where there is an acute problem with the size and efficient use of volume. The polarization controller was placed between the beam splitter and the dichroic mirror.

Results

Table 1 shows the improvements in the polarization parameters of the QKD transmitter that we have achieved in our work. It is possible to notice worsening in the parameters in the direct basis (horizontal and vertical polarization), this is due to the fact that the wave plates are not ideal and have their own permissions. Optical part of QBER was calculated using the equation (2).

Fig. 2 demonstrates a visual interpretation of the results obtained through the Poincare sphere and the polarization ellipse.

$$QBER_{opt} = \frac{1}{4} \sum_{i=V,H,A,D} \frac{1}{\text{tg}^{-2}\theta_i + 1} \quad (2)$$

where θ is ellipticity of polarization.

Table 1

Results of measurements of polarization's ellipticity and calculated $QBER_{opt}$

	Θ_V	Θ_H	Θ_D	Θ_A	$QBER_{opt}$
Without polarization controller	2.3°	1.6°	40.3°	42.7°	22%
With polarization controller	3.01°	2.13°	1°	1°	0.12%

Notations: θ_i – ellipticity of state polarization, $QBER_{opt}$ – optical part of $QBER$.

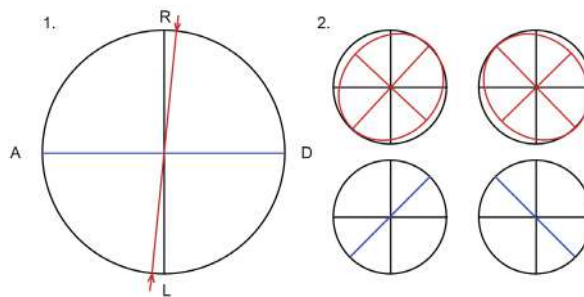


Fig. 2. Visualization of the light polarization in a diagonal basis. The initial polarization at the system's output is depicted in red; and after compensation procedure using controller is shown in blue.

1 – Section of the Poincare sphere; 2 – Polarization ellipse

Conclusion

We have reported the results of polarization characteristics of designed transmitter for free-space quantum communication. The polarization properties of optical elements in transmitter have been investigated and algorithm for a polarization controller made up of one half-wave plate (HWP) and two quarter-wave plate (QWP) has been developed. We have obtained the improvement of the $QBER_{opt}$ at 185 times.

REFERENCES

1. **Dowling Jonathan P., Gerard J. Milburn.**, Quantum technology: the second quantum revolution. Philosophical Transactions of the Royal Society of London. Series A: Mathematical, Physical and Engineering Sciences 361. 1809 (2003) 1655–1674.
2. **Sidhu, J. S., et al.**, Advances in space quantum communications. IET Quant. Comm. 2 (4) (2021) 182–217.
3. **Bennett C. H., Brassard G.**, Quantum cryptography: public key distribution and coin tossing, Proceedings of the IEEE International Conference on Computers, Systems & Signal Processing, (1984) 175–179.
4. **Sun Shihai, Anqi Huang**, A Review of Security Evaluation of Practical Quantum Key Distribution System, Entropy. 24 (2) (2022) 260.
5. **Bedington R., Arrazola J. M., Ling A.**, Progress in satellite quantum key distribution. npj Quantum Information. 3.1 (2017) 1–13.
6. **Zhang, Yichen, et al.**, Long-distance continuous-variable quantum key distribution over 202.81 km of fiber. Physical review letters. 125.1 (2020) 010502.
7. **Toyoshima Morio, et al.**, Polarization-basis tracking scheme in satellite quantum key distribution. International Journal of Optics, 2011.
8. **Wu Jincai, et al.**, Polarization study about a telescope-based transmitter for quantum communication. Applied Optics. 56.30 (2017) 8501–8506.

THE AUTHORS

MERZLINKIN Vitalii E.

v.merzlinkin@goqrata.com

ORCID: 0000-0002-4310-2619

KHMELEV Aleksandr V.

a.khmelev@goqrata.com

ORCID: 0000-0003-1511-1128

DUPLINSKY Alexey V.

a.duplinsky@gmail.com

ORCID: 0000-0002-2964-1800

KUROCHKIN Vladimir L.

v.kurockin@goqrata.com

ORCID: 0000-0002-1599-9801

KUROCHKIN Yury V.

yk@goqrata.com

ORCID: 0000-0001-5376-6358

Received 15.08.2022. Approved after reviewing 24.08.2022. Accepted 24.08.2022.

Conference materials

UDC 53.083

DOI: <https://doi.org/10.18721/JPM.153.340>

Creation of a device for detecting fluorescence from microfluidic chips

R. K. Dobretsov ¹✉, V. V. Davydov ^{1, 2, 3}, A. A. Evstrapov ⁴

¹Peter the Great Saint-Petersburg Polytechnic University, St. Petersburg, Russia;

²The Bonch-Bruевич Saint Petersburg State University of Telecommunications, St. Petersburg, Russia;

³All-Russian Research Institute of Phytopathology, Moscow Region, Russia;

⁴Institute for Analytical Instrumentation of the Russian Academy of Sciences, St. Petersburg, Russia

✉ rody99@gmail.com

Abstract. In this paper, we consider the creation and testing of a prototype for recording fluorescence from microfluidic chips during the polymerase chain reaction (PCR). The paper presents the characteristics of the main elements used to create the layout of the device for fluorescence detection. The results of experiments in testing the performance of mock-up elements and microfluidic chips are presented. The operability of the assembled layout was demonstrated during the real-time PCR reaction.

Keywords: polymerase chain reaction (PCR), microfluidic chip, DNA, fluorescence, dyes, thermal cycler, optical fiber, amplification.

Citation: Dobretsov R. K., Davydov V. V., Evstrapov A. A., Creation of a device for detecting fluorescence from microfluidic chips. St. Petersburg State Polytechnical University Journal. Physics and Mathematics, 15 (3.3) (2022) 207–212. DOI: <https://doi.org/10.18721/JPM.153.340>

This is an open access article under the CC BY-NC 4.0 license (<https://creativecommons.org/licenses/by-nc/4.0/>)

Материалы конференции

УДК 53.083

DOI: <https://doi.org/10.18721/JPM.153.340>

Создание устройства регистрации флуоресценции от микрофлюидных чипов

Р. К. Добрецов ¹✉, В. В. Давыдов ^{1, 2, 3}, А. А. Евстратов ⁴

¹Санкт-Петербургский Политехнический университет Петра Великого, Санкт-Петербург, Россия;

²Санкт-Петербургский государственный университет телекоммуникаций им. профессора М. А. Бонч-Бруевича, Санкт-Петербург, Россия;

³Всероссийский научно-исследовательский институт фитопатологии, Московская область, Россия;

⁴Институт Аналитического приборостроения РАН, Санкт-Петербург, Россия

✉ rody99@gmail.com

Аннотация. В данной работе рассматривается создание и проверка на работоспособность макета для регистрации флуоресценции от микрофлюидных чипов при проведении полимеразной цепной реакции (ПЦР). В работе приведены характеристики основных элементов, использованных при создании макета устройства для детектирования флуоресценции. Представлены результаты экспериментов при проверке работоспособности элементов макета и микрофлюидных чипов. Продемонстрирована работоспособность собранного макета при проведении ПЦР реакции в реальном времени.

Ключевые слова: полимеразная цепная реакция (ПЦР), микрофлюидный чип, ДНК, флуоресценция, красители, термоциклер, оптоволокно, амплификация

Ссылка при цитировании: Добрецов Р. К., Давыдов В. В., Евстрапов А. А. Создание устройства регистрации флуоресценции от микрофлюидных чипов // Научно-технические ведомости СПбГПУ. Физико-математические науки. 2022. Т. 15. № 3.3. С. 207–212. DOI: <https://doi.org/10.18721/JPM.153.340>

Статья открытого доступа, распространяемая по лицензии CC BY-NC 4.0 (<https://creativecommons.org/licenses/by-nc/4.0/>)

Introduction

Currently, the leading tool for chemical and biological research is the PCR polymerase chain reaction [1–5]. Other methods, mainly spectrometric, which are used for research in chemistry, biology and physics, based on the use of nuclear magnetic resonance, laser radiation, and others [6–15], cannot replace it. A small part of the PCR results can be obtained using refraction or magnetic resonance imaging (MRI) [16–23]. With PCR, specific sequences in a DNA template or to DNA can be copied or “amplified” a thousand or a million times using sequence-specific oligonucleotides, thermostable DNA polymerase, and thermal cycling techniques. Real-time PCR [2, 3, 24–26]. This is a type of PCR method that is commonly used to quantify DNA or RNA in a sample. Using sequence-specific primers, the copy number of a particular DNA or RNA sequence can be determined. Quantification is possible by measuring the amount of amplified product at each step of the PCR cycle. Quantification is possible by measuring the amount of amplified product at each step of the PCR cycle. Amplification will be observed in earlier cycles if a certain sequence (DNA or RNA) is present in the sample, and if the sequence is insufficient, amplification will be observed in later cycles or not recorded at all. Quantification of the amplified product is obtained using fluorescent probes or fluorescent DNA-binding dyes and real-time PCR tools that measure fluorescence while performing the thermal cycling required for the PCR reaction.

Most currently available devices for PCR analysis use test tubes or microtiter plates, and they have a number of serious drawbacks [24–26], which are also used in NMR and X-ray spectroscopy [27–30]. Disadvantages are uneven heating/cooling of volumetric systems, analysis speed does not meet the requirements of modern medicine, biology, environmental services, etc., namely, the requirement for rapid analysis. The solution to this problem is microfluidic chips, since they are planar systems. Using microfluidic chips, more samples can be analyzed in less time. Thus, the development and creation of devices for real-time PCR analysis using microfluidic technologies is essential for extremely important.

Design and manufacture of microfluidic chips

The transition to a microchip format when conducting analyzes based on real-time PCR reactions allows you to automate the analysis and reduce the influence of the human factor on its results. In recent years, polymers have taken the leading position as substrate materials for microfluidic devices. They have superior physical and chemical properties enabling the creation of micro-sized structures with desired characteristics that provide microscopic design features that cannot be realized in any other class of materials.

Three types of plastics are most commonly used to create microchips: polypropylene (PP), polycarbonate (PC), and polymethyl methacrylate (PMMA). Their main advantages are high heat resistance, good light transmission in the visible part of the spectrum. Polypropylene is more resistant to acids and solvents than polycarbonate and has lower water sorption (0.01–0.1% versus 0.23% for polycarbonate). The microchip design (Fig. 1, dimensions are given in mm), which consists of three chambers with supply channels, was obtained by thermal pressing in MM-100 hydraulic press (MTDI, Korea) on a stainless-steel master mold made by laser micromachining. The microchip is 38 mm long, 25 mm wide and 1 mm thick. The distance between the loading ports of neighboring cameras is 11 mm. The width of the channels is 1 mm, and the depth of the chambers is ~ 0.3 mm with a bottom thickness of ~ 0.7 mm.

Images of microfluidic chips obtained by the above method are shown in Fig. 2. The chips are filled with water. The first chip is made of polycarbonate PK Novattro (Kazan), the second one is made of polypropylene PP 44455 (RF).

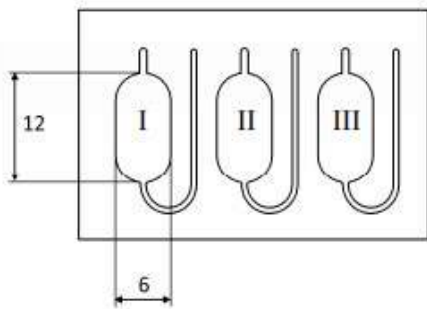


Fig. 1. Microchip design with numbering of reaction chambers

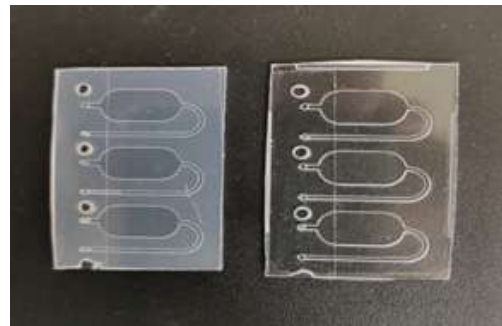


Fig. 2. Microfluidic chips made from PC (left) and PP (right)

On Fig. 3 shows the developed layout of the device for detecting fluorescence from microfluidic chips.

The main elements of the device layout are: a microfluidic chip, a LED, a photodetector (camera), a fiber optic bundle, a thermal cycler, optical lenses and filters. The light source in the device is an SMD type LED with a wavelength of emitted light of 480 nm, a power of 3 W, with a maximum control current of 700 mA and a luminous flux of up to 70 lm. From the source, light enters a system of plano-convex lenses and an excitation filter with a wavelength of 490 nm. Next, the light enters the triple optical fiber (fiber optic bundle). One channel is for excitation, the other two are for registration of the fluorescence/emission signal. Light passing through the optical fiber enters the solution in the microfluidic chip and excites fluorescence. The chip is located in a thermal cycler with which the PCR reaction is carried out. The thermal cycler also has a device for fixing the optical fiber, which allows not only to fix the lighting bundle in the thermal cycler, but also to control the distance from it to the chip. Fluorescence detection occurs with the help of a photodetector (camera), on which light enters after passing through an emission filter with a wavelength of 520 nm and plano-convex lenses.

The operability of the mock-up device was tested by performing a PCR reaction on it with specially set parameters and using a microfluidic chip filled with a reagent, under which the parameters of the PCR reaction were selected. The fluorescence signal from the chip was recorded using a camera and then processed by a computer program to obtain a PCR reaction graph. After that, it was possible to analyze the resulting graph.

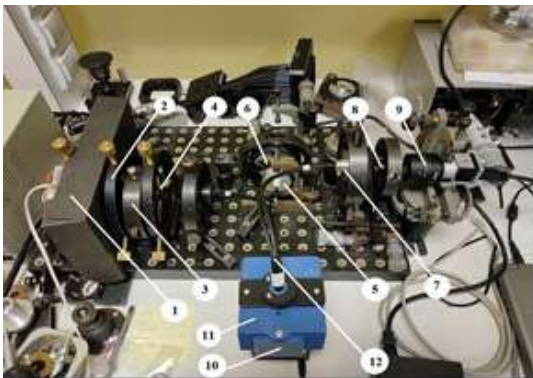


Fig. 3. Mock-up of the device for registration of fluorescence:

- 1 – source (LED);
- 2, 4, 6, 8 – lenses;
- 3 – excitation filter;
- 5, 7 – emission filters;
- 9 – photodetector;
- 10 – location of the chip;
- 11 – thermal cycler;
- 12 – optical fiber (optical fiber bundle)

The results of experimental studies of the assembled layout

For the experiment, the following PCR parameters were set:

- Primary denaturation: 91 °C and duration 1 minute;
- Cycle parameters:
 - Denaturation per cycle: 60 °C and duration 20 seconds;
 - Cycle synthesis: 75 °C and duration 10 seconds;
 - Annealing per cycle: 90 °C and duration 10 seconds;
- Number of cycles: 30;
- Final incubation: 36 °C and duration 2 minutes.

To fill the microfluidic chip, we used a set of reagents for the detection of plant DNA in food products, food raw materials, seeds and feed by real-time polymerase chain reaction “Plant Universal”. Cy5 dye was used.

A graph of the dependence of the signal level on the PCR time was obtained, shown in Fig. 4.

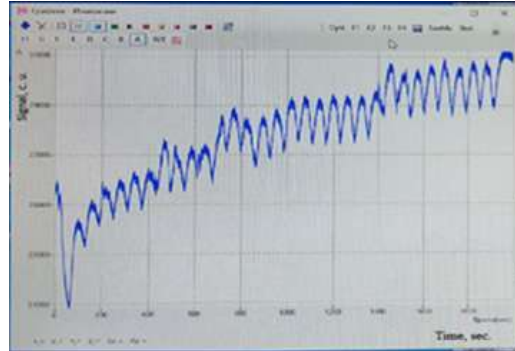


Fig. 4. Graph of the dependence of the signal level on the PCR time

On the graph (Fig. 4) one can observe the passage of the real-time PCR reaction, namely the real-time amplification process. Jumps in the signal level with reaching the peak at approximately equal intervals of time and with an increase in the signal level of the peak with each new jump, express cycles of the PCR reaction during the amplification process. That is, after each cycle, the amount of product in the chip increases and, consequently, the fluorescence signal increases.

Conclusion

As a result of experimental studies on the assembled layout, graphs were obtained reflecting the processes of thermal cycling, amplification and reaching a plateau in real time, that is, the real-time PCR process was recorded. The device model assembled in this way can be further used for biological and chemical studies on microfluidic chips during real-time PCR.

REFERENCES

1. **Reznik V. S., Kruglov V. A.**, Using of «bubble sensors» to control the quality of sequencing by the Illumina / Solexa method, *Journal of Physics: Conference Series*. 2086 (1) (2021) 012120.
2. **Kruglov V. A., Reznik V. S., Glinushkin A. P.**, Development of a hydraulic system for bridge amplification, *Journal of Physics: Conference Series*. 1695 (1) (2020) 012067.
3. **Reznik V. S., Kruglov V. A., Petrov A. I., Glinuchkin A. P., Rud V. Y.**, Development of a measuring device for the study of thermal processes during the polymerase chain reaction, *Journal of Physics: Conference Series*. 1410 (1) (2019) 012078.
4. **Mazing M. S., Zaitceva A. Yu., Kislyakov Yu. Ya., Kondakov N. S., Avdushenko S. A., Davydov V. V.**, Monitoring of Oxygen Supply of Human Tissues Using A Noninvasive Optical System Based on A MultiChannel Integrated Spectrum Analyzer, *International Journal of Pharmaceutical Research*. 12 (2) (2020) 1974–1978.
5. **Kislyakov Yu. Ya., Avdyushenko S. A., Kislyakova I. P., Zaitceva A. Yu.**, Analytical multisensory trainable system for diagnosing vocational aptitude of military medical specialists by ion content in the expired breath condensate, *Journal of Computational and Theoretical Nanoscience*. 16 (11) (2019) 4502–4507.
6. **Gryaznova E. M., Rud V. Y.**, On the possibility of using the optical method for express quality control of fruits, *Journal of Physics: Conference Series*. 2086 (1) (2021) 012143.
7. **Davydov R. V., Yushkova V. V., Stirmanov A. V., Rud V. Yu.**, A new method for monitoring the health condition based on nondestructive signals of laser radiation absorption and scattering, *Journal of Physics: Conference Series*. 1410 (1) (2019) 012067.
8. **Dyumin V., Smirnov K., Myazin N.**, Charge-coupled Device with Integrated Electron Multiplication for Low Light Level Imaging, *Proceedings of the 2019 IEEE International Conference on Electrical Engineering and Photonics, EExPolytech*. 8906868 (2019) 308–310.



9. **Davydov V. V., Kruzhalov S. V., Grebenikova N. M., Smirnov K. J.**, Method for Determining Defects on the Inner Walls of Tubing from the Velocity Distribution of the Flowing Fluid, *Measurement Techniques*. 61(4) (2018) 365–372.
10. **Davydov R. V., Rud V. Yu., Yushkova V. Y.**, On the possibility of analysis using the wavelet transform of the pulse waveform from the bloodstream, *Journal of Physics: Conference Series*. 1695 (1) (2020) 012064.
11. **Grevtseva A. S., Smirnov K. J., Rud V. Yu.**, Development of methods for results reliability raise during the diagnosis of a person's condition by pulse oximeter, *Journal of Physics: Conference Series*. 1135 (1) (2018) 012056.
12. **Makeev S. S., Grevtseva A. S., Glinushkin A. P., Matorin D. N.**, Possibilities of using spectral analysis in method of nuclear magnetic spectroscopy for condensed media investigation, *Journal of Physics: Conference Series*. 1695 (1) (2020) 012112.
13. **Davydov V. V.**, Determination of the Composition and Concentrations of the Components of Mixtures of Hydrocarbon Media in the Course of its Express Analysis, *Measurement Techniques*. 62 (2) (2020) 1090–1098.
14. **Davydov V. V., Davydova T. I.**, A nondestructive method for express testing of condensed media in ecological monitoring, *Russian Journal of Nondestructive Testing*. 53 (7) (2017) 520–529.
15. **Myazin N. S., Dudkin V. I., Grebenikova N. M.**, On the Possibility of Express Recording of Nuclear Magnetic Resonance Spectra of Liquid Media in Weak Fields, *Technical Physics*. 63(12) (2018) 1845–1850.
16. **Murzakhanov F. F., Mamin G. V., Goldberg M. A., Gafurov M. R., Orlinskii S. B.**, EPR of Radiation-Induced Nitrogen Centers in Hydroxyapatite: New Approaches to the Study of Electron-Nuclear Interactions, *Russian Journal of Coordination Chemistry/Koordinatsionnaya Khimiya*. 46 (11) (2020) 729–737.
17. **Davydov V. V., Grebenikova N. M., Smirnov K. Y.**, An Optical Method of Monitoring the State of Flowing Media with Low Transparency That Contain Large Inclusions, *Measurement Techniques*. 62 (6) (2019) 519–526.
18. **Marusina M. Y., Karaseva E. A.**, Automatic segmentation of MRI images in dynamic programming mode Asian Pacific, *Journal of Cancer Prevention*. 19 (10) (2018) 2771–2775.
19. **Kuzmin M. S., Rogov S. A.**, On the use of a multi-raster input of one-dimensional signals in two-dimensional optical correlators, *Computer Optics*. 43 (3) (2019) 391–396.
20. **Grebenikova N. M., Smirnov K. J., Rud V. Yu., Artemiev V. V.**, Features of monitoring the state of the liquid medium by refractometer, *Journal of Physics: Conference Series*. 1135 (1) (2018) 012055.
21. **Grebenikova N. M., Davydov R. V., Rud V. Yu.**, Features of the signal registration and processing in the study of liquid flow medium by the refraction method, *Journal of Physics: Conference Series*. 1326 (1) (2019) 012012.
22. **Myazin N. S., Yushkova V. V., Rud V. Y.**, On the possibility of recording absorption spectra in weak magnetic fields by the method of nuclear magnetic resonance, *Journal of Physics: Conference Series*. 1038 (1) (2018) 012088.
23. **Grebenikova N. M., Smirnov K. J.**, Features of optical signals processing for monitoring the state of the flowing liquid medium with a refractometer, *Journal of Physics: Conference Series*. 1368 (2) (2019) 022057.
24. **Matvienko I. V., Bayramov V. M., Parygina N. A., Kurochkin V. E., Alekseev Y. I.**, Synthesis of Dihydroquinoline-Based Derivatives of Fluorescent Rhodamine Dyes for Nucleic Acid Analysis by a Real-Time Polymerase Chain Reaction, *Russian Journal of Bioorganic Chemistry*. 46 (3) (2020) 349–359.
25. **Fedorov A. A., Berdnikov A. S., Kurochkin V. E.**, The polymerase chain reaction model analyzed by the homotopy perturbation method, *Journal of Mathematical Chemistry*. 57 (4) (2019) 971–985.
26. **Natyrov A. N., Vlasova N. A., Matvienko I. V., Kurochkin V. E., Alexeev J. I.**, Synthesis of Unsymmetrical Polymethine Cyanine Fluorescent Dyes for Nucleic Acid Analysis by Real-Time PCR, *Russian Journal of Bioorganic Chemistry*. 44 (5) (2018) 562–571.
27. **Myazin N. S.**, Features of formation of structure of a nuclear magnetic resonance signal in weak magnetic field, *Journal of Physics: Conference Series*. 1135 (1) (2018) 012061.
28. **Marusina M. Ya., Karaseva E. A.**, Application of fractal analysis for estimation of structural changes of tissues on MRI images *Russian Electronic Journal of Radiology*. 8 (3) (2018) 107–112.

29. **Logunov S. E., Vysoczky M. G.**, New method of researches of the magnetic fields force lines structure, Journal of Physics: Conference Series. 1038 (1) (2018) 012093.

30. **Kiryakova T. N., Marusina M. Ya., Fedchenkov P. V.**, Automatic methods of contours and volumes determination of zones of interest in MRI images, Russian Electronic Journal of Radiology. 7 (2) (2017) 117–127.

THE AUTHORS

DOBRETSOV Rodion K.

rody99@gmail.com

ORCID: 0000-0002-1960-2306

EVSTRAPOV Anatoly A.

an_evs@mail.ru

ORCID: 0000-0003-4495-8096

DAVYDOV Vadim V.

davydov_vadim66@mail.ru

ORCID: 0000-0001- 9530- 4805

Received 14.08.2022. Approved after reviewing 15.08.2022. Accepted 24.08.2022.

Conference materials

UDC 535.417.2

DOI: <https://doi.org/10.18721/JPM.153.341>

Collective states with high quality factors in chains of dielectric resonators

M. S. Mikhailovskii ¹✉, R. S. Savelev ¹, M. S. Sidorenko ¹,
Z. F. Sadrieva ¹, A. A. Bogdanov ¹, M. I. Petrov ¹

¹ ITMO University, St. Petersburg, Russia

✉ m.mikhailovskii@metalab.ifmo.ru

Abstract. Coupled dielectric subwavelength resonators supporting collective states with high quality factors are of interest due to potential in the enhancement of the light-matter interaction at the nanoscale and high versatility and tunability of such structures. Recently, it was theoretically shown that coupling between two or more collective modes via radiation continuum that can occur under variation of the parameters of such structures could significantly boost the quality factor of one of the eigenmodes. In this work, we have studied such effect numerically and experimentally for a chain of ceramic cylinders operating in the microwave spectral range. We have investigated how the present channels of losses, namely material losses, and additional scattering due to variation in geometrical and materials parameters, influence the considered effect. We have developed a feasible design that allows for observation of mode interaction. Experimental measurements of the spectral response of the proposed structures confirmed the main predicted results.

Keywords: dielectric resonators, band edge states, interaction of resonances, nanophotonics, microwave prototyping

Funding: Numerical simulations were supported by the Russian Foundation for Basic Research, grant No. 20-52-12062. Experimental measurements were supported by the Russian Science Foundation, Grant No. 22-72-10047.

Citation: Mikhailovskii M. S., Savelev R. S., Sidorenko M. S., Sadrieva Z. F., Bogdanov A. A., Petrov M. I., Collective states with high quality factors in chains of dielectric resonators. St. Petersburg State Polytechnical University Journal. Physics and Mathematics, 15 (3.3) (2022) 213–218. DOI: <https://doi.org/10.18721/JPM.153.341>

This is an open access article under the CC BY-NC 4.0 license (<https://creativecommons.org/licenses/by-nc/4.0/>)

Материалы конференции

УДК 535.417.2

DOI: <https://doi.org/10.18721/JPM.153.341>

Коллективные состояния с высокой добротностью в цепочках диэлектрических резонаторов

М. С. Михайловский ¹✉, Р. С. Савельев ¹, М. С. Сидоренко ¹,
З. Ф. Садриева ¹, А. А. Богданов ¹, М. И. Петров ¹

¹ Университет ИТМО, Санкт-Петербург, Россия

✉ m.mikhailovskii@metalab.ifmo.ru

Аннотация. Цепочки связанных диэлектрических субволновых резонаторов, поддерживающие коллективные резонансные состояния с большими добротностями, представляют интерес благодаря усилению взаимодействия света с веществом, а также возможности по настройке параметров таких структур. Недавно было теоретически показано, что взаимодействие между двумя или более коллективными модами через излучение континуума, которое может возникать при изменении параметров таких структур, значительно повышает добротность одной из мод. В данной работе мы исследовали такой эффект численно и экспериментально для цепочки керамических

цилиндров, функционирующих в микроволновом диапазоне спектра. Экспериментальные измерения спектрального отклика разработанных структур позволили пронаблюдать взаимодействием мод и подтвердили основные теоретически предсказанные результаты.

Ключевые слова: диэлектрические резонаторы, коллективные моды, взаимодействие резонансов, нанофотоника, прототипирование в микроволновом диапазоне спектра

Финансирование: Численное моделирование было выполнено при поддержке гранта РФФИ № 20-52-12062. Экспериментальные измерения были выполнены при поддержке гранта РНФ № 22-72-10047.

Ссылка при цитировании: Михайловский М. С., Савельев Р. С., Сидоренко М. С., Садриева З. Ф., Богданов А. А., Петров М. И. Коллективные состояния с высокой добротностью в цепочках диэлектрических резонаторов // Научно-технические ведомости СПбГПУ. Физико-математические науки. 2022. Т. 15. № 3.3. С. 213–218. DOI: <https://doi.org/10.18721/JPM.153.341>

Статья открытого доступа, распространяемая по лицензии CC BY-NC 4.0 (<https://creativecommons.org/licenses/by-nc/4.0/>)

Introduction

All-dielectric optical resonant structures supporting resonances with high quality factors and allowing to localize electromagnetic fields in a small volume are of both fundamental and applied interest due to significant increase of light-matter interaction strength. One type of such structures are ensembles of coupled dielectric subwavelength resonators [1, 2]. Due to the interference of radiation from individual elements, such structures support collective resonant oscillations, characterized by suppressed radiative losses and consequently high quality factors. It has been experimentally shown that such systems allow to enhance the nonlinear response of the material of which they are made [2], to enhance the photoluminescence intensity of the quantum dots integrated into them [3], to achieve regime of laser generation [4], and act as a platform for on chip sensing [5].

Besides destructive interference between radiation from individual particles in an ensemble, coupling between two or more modes via radiation continuum can occur under variation of the parameters of such structures. In this case the quality factor of one of the eigenmodes can be substantially increased. For example, this can be achieved by precision control of the gap between individual resonators in the chain [6]. This mechanism can be explained by a change of the dispersion curve of the corresponding infinite chain of particles, namely, by the appearance of an inflection point near the edge of the Brillouin zone, which leads to the destructive mode interference of the corresponding finite chain. However, this effect has been predicted only theoretically and not investigated experimentally.

In this work, we have investigated the possibility of experimental realization of the chain of dielectric resonators that support eigenmodes with high quality factors that appear due to interaction of two collective modes of the chain via radiation continuum. We have analyzed what kind of geometrical and material parameters allow to achieve such regime. We have investigated how the present channels of losses, namely material losses, and additional scattering due to variation in geometrical and materials parameters, affect the considered effect. Based on the performed analysis we have developed several feasible designs of the chains of ceramic resonators, that support high- Q modes in microwave spectral range. We have performed experimental measurements of the spectral response of the proposed structures, which confirmed the main predicted results.

Materials and Methods

In order to analyze the spectral response of an individual block of a chain of dielectric resonator we have performed multipole decomposition using the method proposed by [7], which allows one to consider resonators of arbitrary shape. In this work, we employ subwavelength ceramic resonators with high permittivity ($\epsilon \approx 44.8$), which allows us to use fundamental dipole resonances supported by these resonators.



Analysis of the dispersion properties of the infinite chain and eigenmodes of the finite chain is performed via full-wave numerical simulations. In the case of infinite chain, we are interested in the waveguide modes supported by the chain, which are characterized by real-valued eigenfrequencies (in case of zero material losses). In contrast, in finite chain the eigenmodes always lose energy through radiative losses, and therefore, eigenfrequencies are complex. The ratio of real and imaginary part determines the quality factor, which is the main characteristic in this study.

For experimental verification, scattering parameters (S -parameters) of a finite chain were measured. To control the gap between the individual cylinders in the chain, we have fabricated a sample holder made from Penoplex foam material ($\varepsilon \approx 1$) by a computer numerical control machine drilling. The holder consisted of a set of circular wells with different distances between the centers of the wells a , ranging from 33 mm to 45 mm in 0.5 mm increments. Excitation of modes in chain was done via near-field coupling of the source to the chain. The antennas were connected to the corresponding ports on the Rohde & Schwarz vector network analyzer. Next, the S_{21} parameter was measured for different values of the distance a .

Deviations in the dielectric permittivity values of individual cylinders lead to changes in the resonant frequencies of the respective cylinders. In turn, for the case of the finite chain, this affects both the maximum possible values of the quality factor of the collective mode and the corresponding optimal values of the distance a . In order to reduce the influence of disorder in the dielectric permittivity of the individual cylinders, scattering parameters were measured for all cylinders, allowing 5 cylinders with the closest resonance frequencies to be selected.

Results and Discussion

We have developed a potential design based on the ceramic cylinders with the following parameters: height of the cylinders $h = 20$ mm, and diameter of the cylinders $d = 30$ mm. The period of the chain was varied in the range $a \approx 30$ –45 mm. As it will be shown further the resonant wavelength of the considered mode will be $\lambda_0 \approx 200$ mm, which makes the considered values of period approximately 5–6 times less. The relative permittivity of the ceramic material was $\varepsilon \approx 44.8$. The material losses in ceramics were described by the dissipation factor (or loss tangent) $\tan \delta = \text{Im}(\varepsilon) / \text{Re}(\varepsilon)$, taking characteristic values in the range from 1×10^{-5} to 1×10^{-4} . A schematic representation of the cylinder chain is shown in Fig. 1, *a*.

At the first step, we have analyzed the response of the individual cylinder. Multipole decomposition performed for a single cylinder has shown that at least first few resonances, which are well separated in frequency, are characterized each by a single dominant multipole contribution. The example of the multipole decomposition performed for a spectral dependence of a scattering cross section of a cylinder excited by a plane wave incident along the diameter of the cylinder with magnetic field polarized along the cylinders axis is shown in Fig. 1, *b*. Given the negligible response of all multipole terms except for one at each of the resonances, we expect the modes of the chain of the cylinders to be formed by coupled multipoles of a single type.

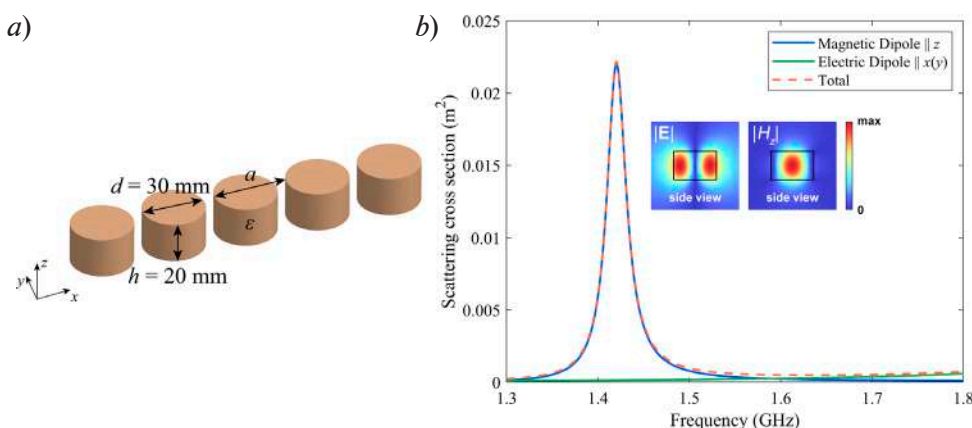


Fig. 1. Schematic of the chain of ceramic cylinders studied in this work (*a*). Multipole decomposition performed for a single cylinder (*b*). The inset shows the distribution of the total electric field and the absolute value of the out-of-plane component of the magnetic field corresponding to the magnetic dipole resonance

At the second step, we have performed numerical calculations of the dispersion curves of the infinite chain, in order to find the range of values of the chain period, in which they exhibit non-monotonic behaviour. The dispersion diagram for an infinite chain for a period $a = 32$ mm is shown in Fig. 2, *a*. The black dashed line is the light line. We observe that the chain supports a lot of waveguide modes of different types. At least first three modes are well separated spectrally below the light line. This is achieved due to rather large quality factor of the resonances in a single cylinder and rather strong coupling between the cylinders in the chain. Such behaviour helps us to distinguish the modes of different type in the corresponding finite chains in experiment. The variation of the period revealed that few of these modes can have non-monotonic character. We have focused on the fundamental mode that is formed due to coupling magnetic dipole resonances in individual cylinders. Dispersion diagrams for this mode, calculated for different values of period a , are shown in Fig. 2, *b*. The inset of Fig. 2, *b* shows the distribution of the absolute value of the out-of-plane magnetic field component and the absolute value of the electric field in the lateral cross-section of the cylinder. As one can see from Fig. 2, *b*, when the period of the chain is greater than a_{cr} , the dispersion curve of the first resonant mode is monotonic. Then, as the period of the chain decreases, the dispersion curve changes its behaviour, becoming non-monotonic, starting from some value of period $a < a_{cr}$.

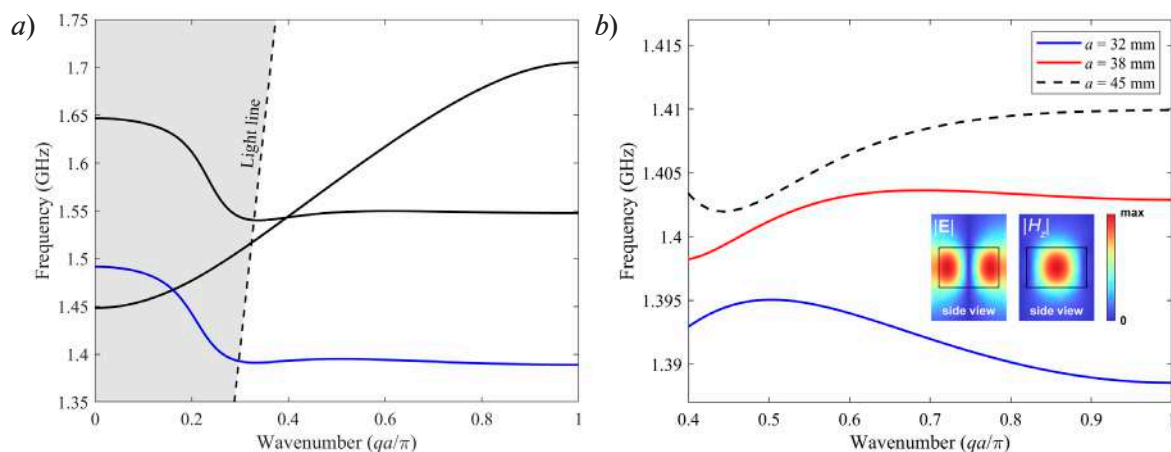


Fig. 2. Dispersion diagram for an infinite chain of ceramic cylinders for the period $a = 32$ mm (*a*). First dispersion branch of the chain of ceramic cylinders for different values of the period a (*b*). The inset shows the distribution of the total electric field and the absolute value of the out-of-plane component of the magnetic field at the edge of the Brillouin zone

After estimation of the parameters of the chain that allow for observation of the interacting collective modes, we have performed the calculations of the quality factor of the finite chain eigenmodes. For finite chains consisted of N resonators one expects to observe Fabry–Perot resonances at the frequencies related to the Bloch wavenumbers q through the dispersion of the infinite chain as follows: $qa / \pi = 1 - \xi / (N + 1)$, where ξ is the number of resonance [8]. Therefore, for the period $a = 38$ mm, the inflection point of the dispersion curve corresponds to $qa / \pi \approx 0.7$, which allows us to expect the appearance of the high- Q mode in a finite chain of 5–6 resonators for the corresponding second resonance.

In order to find the parameters at which the formation of high- Q collective mode is observed, we have calculated the dependence of the total Q -factor on the period of the chain a in the range 30–45 mm near the value 38 mm expected from the analysis of the infinite chain. The results for a chain consisting of 5 cylinders are shown in Fig. 3, *a*. One can observe that for a certain value of the period the radiation losses become suppresses and the Q -factor reaches the maximal value, which according to the theory [6] indicates the interference between two collective states. Calculations made for $\tan \delta = 1 \times 10^{-4}$ show that such level of losses still allows to observe the studied effect.

To confirm the predicted results experimentally we have performed the measurements of the spectral response of the chain of 5 cylinders according to the method described above. The excitation of the chain was performed by the magnetic loop antenna placed above the central



cylinder, which allowed us to excite only modes of specific parity. Since other two modes of this parity were well separated in frequency, in experiment we have seen a dominant Lorentzian-type response, which allowed us to easily extract a quality factor of this mode. The results of the measured Q -factors for different values of the period are shown in Fig. 3, *b*. The main qualitative result, namely the presence of the maximum in $Q(a)$ dependence was confirmed. The discrepancy between the optimal value of the period and the maximal value of Q -factor can be explained by slight difference between the spectral response of the cylinders as well as slight deviations of the real values of periods from the optimal ones.

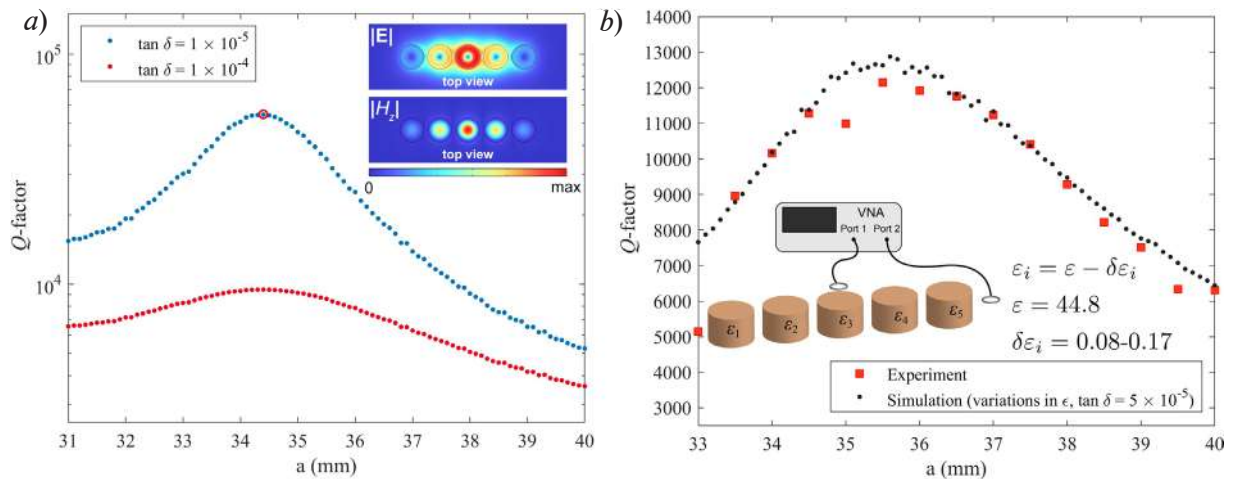


Fig. 3. Dependence of the Q -factor of the mode with the highest Q of the chain with 5 cylinders on the period of the chain. The inset shows the distribution of the total electric field and the absolute value of the out-of-plane component of the magnetic field in the chain for the parameters at which the Q -factor takes the highest value (the corresponding point is marked with a red circle) (*a*). Dependence of the Q -factor of the chain of 5 cylinders on the period extracted from the experimental data and the calculated data with introduced deviations in dielectric permittivity of individual cylinders, the inset shows the schematic of the experimental setup (*b*)

Conclusion

In conclusion, we have developed the design of the chain of ceramic cylinders that support eigenmodes with high quality factors, that is enhanced due to interaction of two collective modes of the chain via radiation continuum. We have experimentally shown that the quality factor of one of the modes of the chain exhibits a maximum in the dependence on the period of the chain, indicating the presence of interacting resonances. We have revealed that even slight change of the parameters of the chain significantly reduce the strength of the considered effect. We believe that the obtained results will allow for the design of high- Q dielectric resonators based on the collective modes in compact dielectric structures.

Acknowledgments

Numerical simulations were supported by the Russian Foundation for Basic Research, grant No. 20-52-12062. Experimental measurements were supported by the Russian Science Foundation, Grant No. 22-72-10047.

REFERENCES

1. Blaustein G. S., Gozman M. I., Samoylova O., Polishchuk, I. Y., Burin A. L., Guiding optical modes in chains of dielectric particles, *Optics Express*, 15 (25) (2007) 17380–17391.
2. Ding L., Morits D., Bakker R., Li S., Eschimese D., Zhu S., Paniagua-Dominguez R., Kuznetsov A. I., All-optical modulation in chains of silicon nanoantennas, *ACS Photonics*, 7 (4) (2020) 1001–1008.
3. Rutckaia V., Heyroth F., Schmidt G., Novikov A., Shaleev M., Savelev R. S., Schilling J., Petrov M., Coupling of Germanium Quantum Dots with Collective Sub-radiant Modes of Silicon

Nanopillar Arrays, ACS Photonics, 8 (1) (2020) 209–217.

4. Hoang T. X., Ha S. T., Pan Z., Phua W. K., Paniagua-Domínguez R., Png C. E., Chu H.-S., Kuznetsov A. I., Collective Mie resonances for directional on-chip nanolasers, Nano Letters, 20 (8) (2020) 5655–5661.

5. Ding L., Eschimese D., Ang T. Y., Morits D., Chu H. S., Lim S. T., Png C. E., Gorelik S., Paniagua-Domínguez R., Kuznetsov A. I., One-Dimensional High- Q Silicon Nanoparticle Chain Resonators for Refractive Index Sensing. ACS Applied Nano Materials, 5 (3) (2022) 3170–3176.

6. Kornovan D. F., Savelev R. S., Kivshar Y., Petrov M. I., High- Q localized states in finite arrays of subwavelength resonators, ACS Photonics, 8 (12) (2021) 3627–3632.

7. Evlyukhin A. B., Fischer T., Reinhardt C., Chichkov B. N., Optical theorem and multipole scattering of light by arbitrarily shaped nanoparticles, Physical Review B, 94 (20) (2016) 205434.

8. Asenjo-Garcia A., Moreno-Cardoner M., Albrecht A., Kimble H. J., Chang D. E., Exponential improvement in photon storage fidelities using subradiance and “selective radiance” in atomic arrays, Physical Review X, 7 (3) (2017) 031024.

THE AUTHORS

MIKHAILOVSKII Mikhail S.
m.mikhailovskii@metalab.ifmo.ru
ORCID: 0000-0002-6042-0408

SADRIEVA Zarina F.
z.sadrieva@metalab.ifmo.ru
ORCID: 0000-0001-8299-3226

SAVELEV Roman S.
r.savelev@metalab.ifmo.ru
ORCID: 0000-0002-7810-960X

BOGDANOV Andrey A.
a.bogdanov@metalab.ifmo.ru
ORCID: 0000-0002-8215-0445

SIDORENKO Mikhail S.
mikhail.sidorenko@metalab.ifmo.ru
ORCID: 0000-0002-0942-9941

PETROV Mihail I.
m.petrov@metalab.ifmo.ru
ORCID: 0000-0001-8155-9778

Received 14.08.2022. Approved after reviewing 17.08.2022. Accepted 19.08.2022.

Conference materials

UDC 535.417, 544.015.4, 536.331, 538.958, 538.975

DOI: <https://doi.org/10.18721/JPM.153.342>

Investigation of crystallinity degree for $\text{Ge}_2\text{Sb}_2\text{Te}_5$ films by reflection and transmission photometry

N. M. Tolkach ¹✉, N. V. Vishnyakov ², V. G. Litvinov ², A. O. Yakubov ¹,
E. S. Trofimov ², A. A. Sherchenkov ¹

¹ National Research University of Electronic Technology (MIET), Zelenograd, Moscow, Russia;

² Ryazan State Radio Engineering University named after V. F. Utkin, Ryazan, Russia

✉ n.m.tolkach@gmail.com

Abstract. To assess the crystallinity degree for $\text{Ge}_2\text{Sb}_2\text{Te}_5$ (GST) films the method of reflection and transmission photometry and the approximation of an effective medium of the Brueggemann type were used. It was found that the changes in the energy and duration of the laser pulse lead to the change in the ratio of crystalline and amorphous fractions and change in crystallinity degree. It was found that an increase of crystalline fraction leads to an increase of refractive index and extinction coefficient at telecommunication wavelength of 1550 nm, which also leads to changes of reflectivity and transmissivity of the GST film and can be used to perform modulation and switching of signals.

Keywords: crystallinity degree, photometry, $\text{Ge}_2\text{Sb}_2\text{Te}_5$, phase change material, phase transition, phase state, amorphous, crystalline

Funding: The reported study was funded by RFBR according to the research project No. 19-37-60023 “A study of optical switching processes in alternating structures based on crystal-amorphous materials of Ge-Sb-Te system for optical switches”.

Citation: Tolkach N. M., Vishnyakov N. V., Litvinov V. G., Yakubov A. O., Trofimov E.S., Sherchenkov A. A., Investigation of crystallinity degree for $\text{Ge}_2\text{Sb}_2\text{Te}_5$ films by reflection and transmission photometry. St. Petersburg State Polytechnical University Journal. Physics and Mathematics, 15 (3.3) (2022) 219–222. DOI: <https://doi.org/10.18721/JPM.153.342>

This is an open access article under the CC BY-NC 4.0 license (<https://creativecommons.org/licenses/by-nc/4.0/>)

Материалы конференции

УДК 535.417, 544.015.4, 536.331, 538.958, 538.975

DOI: <https://doi.org/10.18721/JPM.153.342>

Исследование степени кристалличности пленок $\text{Ge}_2\text{Sb}_2\text{Te}_5$ методами фотометрии отражения и пропускания

Н. М. Толкач ¹✉, Н. В. Вишняков ², В. Г. Литвинов ², А. О. Якубов ¹,
Е. С. Трофимов ², А. А. Шерченков ²

¹ Национальный исследовательский университет «МИЭТ», Зеленоград, Москва, Россия;

² Рязанский государственный радиотехнический университет им. В. Ф. Уткина, Рязань, Россия

✉ n.m.tolkach@gmail.com

Аннотация. Для оценки степени кристалличности $\text{Ge}_2\text{Sb}_2\text{Te}_5$ (GST) в данной работе мы использовали метод фотометрии отражения и пропускания и приближение эффективной среды типа Брюйгемана. Установлено, что изменение энергии и длительности лазерного импульса приводит к изменению соотношения кристаллической и аморфной фракций, что наблюдается по изменению степени кристалличности. Также установлено, что увеличение доли кристаллитов приводит к увеличению показателя преломления и коэффициента экстинкции для телекоммуникационной длины волны 1550 нм, что также приводит к изменению отражательной и пропускательной способностей пленки GST и будет использовано для осуществления модуляции и переключения сигналов.

Ключевые слова: степень кристалличности, фотометрия, $\text{Ge}_2\text{Sb}_2\text{Te}_5$, материал с фазовым переходом, фазовый переход, фазовое состояние, аморфный, кристаллический

Финансирование: Работа выполнена при финансовой поддержке РФФИ в рамках научно-исследовательского проекта № 19-37-60023.

Ссылка при цитировании: Толкач Н. М., Вишняков Н. В., Литвинов В. Г., Якубов А. О., Трофимов Е. С., Шерченков А. А. Исследование степени кристалличности пленок $\text{Ge}_2\text{Sb}_2\text{Te}_5$ методами фотометрии отражения и пропускания // Научно-технические ведомости СПбГПУ. Физико-математические науки. 2022. Т. 15. № 3.3. С. 219–222. DOI: <https://doi.org/10.18721/JPM.153.342>

Статья открытого доступа, распространяемая по лицензии CC BY-NC 4.0 (<https://creativecommons.org/licenses/by-nc/4.0/>)

Introduction

Semiconductor materials with first kind phase transition (Phase Change Material – PCM), in particular, chalcogenide glassy semiconductors, have found their application in non-volatile radiation-resistant memory elements for creating dynamic storage devices. Currently, PCM material $\text{Ge}_2\text{Sb}_2\text{Te}_5$ (GST) is actively used for this purpose. GST has a fast and low-energy phase transition, which can be excited by both an electric and a laser pulse [1–3]. In addition to the main phase states (amorphous and crystalline) of GST, there can be additional intermediate states due to the presence of nanosized fractions of the material in both these states. Controlling the ratio of the amorphous and crystalline fractional composition (crystallinity degree) of GST opens up wide possibilities in fine-tuning its optical parameters, but at the same time, it requires studying the processes and peculiarities that occur when laser radiation is applied to the GST material. Therefore, the aim of the work is to investigate in the GST thin films the amorphous and crystalline fraction ratio, which is characterized by the crystallinity degree.

Materials and Methods

To estimate the crystallinity degree of GST films in this work, we used the method of reflection and transmission photometry and the approximation of an effective medium of the Bruggemann type. Such approximation represents a medium in the form of amorphous matrix with growing quantity of spherical crystallites. Fraction of crystals in the matrix (crystallinity degree) is equal to [4]:

$$C = (\bar{n}^2 - \bar{n}_a^2) (2\bar{n}^2 + \bar{n}_c^2) / (3\bar{n}(\bar{n}_c^2 - \bar{n}_a^2)), \quad (1)$$

where \bar{n} , \bar{n}_a and \bar{n}_c are the complex refractive index of GST film in the current, amorphous and crystalline state respectively. The complex refractive index \bar{n} is found from the model expressions determined by the Airy formulas for reflectivity \mathfrak{R} and transmissivity \mathfrak{T} of the GST structure taking into account processes of multiple re-reflection of electromagnetic waves in the film and their interference.

System of nonlinear equations is solved to search the complex refractive index:

$$\begin{cases} f_1 = \mathfrak{R}_e - \mathfrak{R}(n, k) = 0 \\ f_2 = \mathfrak{T}_e - \mathfrak{T}(n, k) = 0 \end{cases}, \quad (2)$$

where n and k are a refractive index and an extinction ratio of the researched medium; \mathfrak{R}_e and \mathfrak{T}_e are experimental data on reflectivity and transmissivity; $\mathfrak{R}(n, k)$ and $\mathfrak{T}(n, k)$ – model expressions for reflectivity and transmissivity of the thin film structure taking into account processes of multiple re-reflection of electromagnetic waves in the film and their interference, are determined according to the Airy and Fresnel formulas [5].

Solution of simultaneous equations (2) is performed numerically according to the nonlinear system optimization method. This solution is the global minimum of the objective function of $F = (f_1 / \Delta f_1)^2 + (f_2 / \Delta f_2)^2$. Here Δf_1 and Δf_2 are scale coefficients of f_1 and f_2 function calculated as the average of experimental and model data ($\Delta f_1 = (\mathfrak{R}_e + \mathfrak{R}(n, k)) / 2$, $\Delta f_2 = (\mathfrak{T}_e + \mathfrak{T}(n, k)) / 2$).



More generally, the objective function is the following:

$$F(\mathfrak{R}_e, \mathfrak{I}_e, n, k) = ((\mathfrak{R}_e - \mathfrak{R}(n, k)) / (\mathfrak{R}_e + \mathfrak{R}(n, k)))^2 + ((\mathfrak{I}_e - \mathfrak{I}(n, k)) / (\mathfrak{I}_e + \mathfrak{I}(n, k)))^2. \quad (3)$$

The GST thin film with the thickness of 24 nm were deposited by magnetron sputtering. The measurement setup based on the NTEGRA Spectra (NT-MDT SI, Russia) was used and allowed to carry out investigations using methods of Raman spectroscopy, atomic force microscopy, optical microscopy, photometry, laser modification.

Laser modification of the GST film (see square regions in Figure 1a) has been performed by radiation with the 405 nm wavelength, with the focused spot diameter of about 1 μm and with various duration values (from 4 ns to 1 microseconds), repetition intervals T (from 20 ns to 1 microseconds) and radiant exposures (from 0.02 nJ/μm² to 20 nJ/μm²) of the pulse.

Photometry was used to measure the reflectivity and transmissivity of the GST film at 405, 532, 638 and 1550 nm wavelengths. Reflection and transmission photometry maps (see Fig. 1) obtained by scanning the GST film with the focused laser with a wavelength of 532 nm and a power of 5.3 μW (energy exposure 1.44 nJ/μm²).

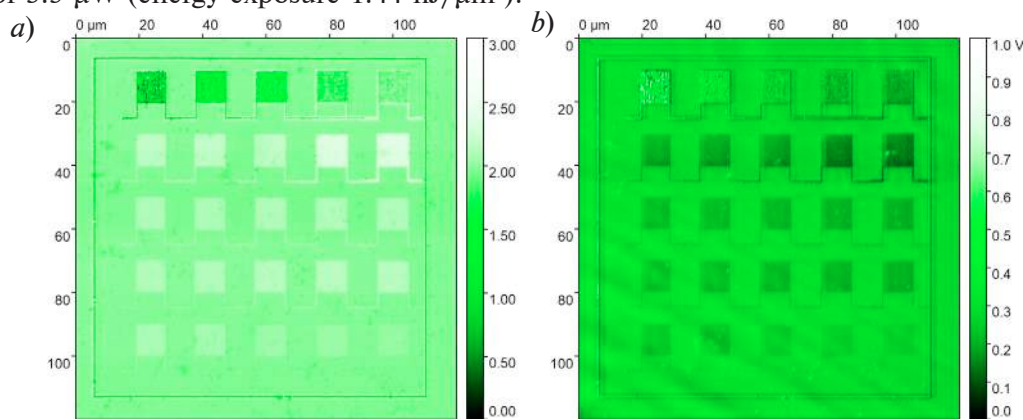


Fig. 1. Reflection (a) and transmission (b) photometry maps

Results and Discussion

Crystallinity degree of the local film area was determined using the obtained values of the complex refractive index at the wavelengths of 405, 638, and 1550 nm. As can be seen from Fig. 2, a, when films are exposed to laser pulses with wavelength of 405 nm at energy exposure of pulse from 2.92 to 3.26 nJ/μm², the crystallinity degree changes from 1 to 0.

The evaluation of crystallinity degree showed that amorphization of the film is observed when exposed to laser pulses with wavelength of 405 nm at energy exposure of pulse from 3.26 to 3.37 nJ/μm², with pulse durations up to 12 ns (see Fig. 2, b).

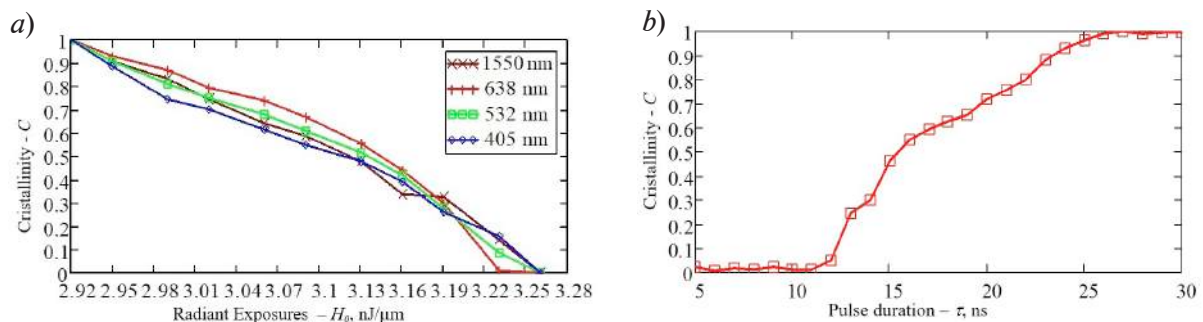


Fig. 2. Changes in the crystallinity degree of the local region in the GST film: depending on the energy exposure of the 405 nm laser pulse (a); depending on the laser pulse duration (b)

Partial crystallization of amorphous GST at these energy exposures is observed at the pulse durations from 12 to 25 ns, while full crystallization is observed at the pulse durations from 25 to 78 ns. An increase in the proportion of crystalline fractions leads to an increase of refractive index and extinction coefficient at telecommunication wavelength of 1550 nm, which also leads

to changes of reflectivity and transmissivity of the GST film and can be used to perform multilevel recording, and amplitude modulation or routing of signals.

Conclusion

Thus, it was found that a change in the energy and duration of a laser pulse leads to a change in the crystallinity degree and, so, to a change in the ratio of crystalline and amorphous fractions.

Acknowledgments

The study was performed with the equipment of Region Centre of probe microscopy of Ryazan State Radio Engineering University named after V. F. Utkin.

REFERENCES

1. Wen S., Meng Y., Jiang M. Wang Y., Multi-level coding-recoding by ultrafast phase transition on $\text{Ge}_2\text{Sb}_2\text{Te}_5$ thin films. Scientific Reports. 8 (1) (2018) 4979.
2. Kozyukhin S. A., Lazarenko P. I., Vorobyov Y. V., Savelyev M. S., Polokhin A. A., Glukhenkaya V. B., Sherchenkov A. A., Gerasimenko A. Y., Laser-induced modification of amorphous GST225 phase change materials. Matériaux & Techniques. 180070 (2018) 1–6.
3. Tolkach N. M., Vishnyakov N. V., Lazarenko P. I., Sherchenkov A. A., Sudakova A. U., Nazimov D. R., Optical switching in multilayer structures based on $\text{Ge}_2\text{Sb}_2\text{Te}_5$. Journal of Physics: Conference Series, 1695 (2020) 012075.
4. Kim D.-H., Merget F., Laurenzis M., Bolivar P. H., Kurz H., Electrical percolation characteristics of $\text{Ge}_2\text{Sb}_2\text{Te}_5$ and Sn doped $\text{Ge}_2\text{Sb}_2\text{Te}_5$ thin films during the amorphous to crystalline phase transition. Journal of Applied Physics. 97 (8) (2005) 83538.
5. Born M., Wolf E., Principles of Optics. Cambridge University Press. (2003) 753–754.

THE AUTHORS

TOLKACH Nikita M.
n.m.tolkach@gmail.com
ORCID: 0000-0001-9183-7348

YAKUBOV Alexey O.
alexsey007@mail.ru
ORCID: 0000-0003-0530-7186

VISHNYAKOV Nikolay V.
rcpm-rgtu@yandex.ru
ORCID: 0000-0002-1270-3446

TROFIMOV Egor S.
egor_trofimov.ru@mail.ru
ORCID: 0000-0002-1516-9154

LITVINOV Vladimir G.
vglit@yandex.ru
ORCID: 0000-0001-6122-8525

SHERCHENKOV Alexey A.
aa_sherchenkov@rambler.ru
ORCID: 0000-0002-5596-4363

Received 15.08.2022. Approved after reviewing 24.08.2022. Accepted 15.09.2022.

Conference materials

UDC 53.05

DOI: <https://doi.org/10.18721/JPM.153.343>

Experimental study of all-van-der-Waals waveguide polaritons at room temperature

V. I. Kondratiev ¹✉, T. Ivanova ¹, M. D. Tyugaev ¹, A. K. Samusev ¹, V. Kravtsov ¹

¹ITMO University, St. Petersburg, Russia

✉ valeriy.kondratiev@metalab.ifmo.ru

Abstract. In this work, we experimentally investigate guided polaritons utilizing only 2D van der Waals materials, with hexagonal boron nitride (hBN) as the waveguide layer and WS₂ monolayer as the excitonic medium. We place the WS₂ monolayer at the maximum of the waveguide mode electromagnetic field, therefore reaching optimal conditions for the strong coupling between the exciton resonance and waveguide mode. To excite and detect the non-radiating waveguide polariton modes, we use the back focal plane microscopy with a high-index solid immersion lens. Polaritons in such all-van-der-Waals structures observed in ambient conditions reveal new possibilities for studying fundamental aspects of light-matter interaction and provide strong advantages in terms of miniaturization and integrability of future photonic devices.

Keywords: van der Waals materials, 2D semiconductors, exciton-polaritons, waveguide polaritons

Funding: This work is supported by Russian Science Foundation (Project No. 22-22-00663).

Citation: Kondratiev V. I., Ivanova T., Tyugaev M. D., Samusev A. K., Kravtsov V., Experimental study of all-van-der-Waals waveguide polaritons at room temperature. St. Petersburg State Polytechnical University Journal. Physics and Mathematics, 15 (3.3) (2022) 223–225. DOI: <https://doi.org/10.18721/JPM.153.343>

This is an open access article under the CC BY-NC 4.0 license (<https://creativecommons.org/licenses/by-nc/4.0/>)

Материалы конференции

УДК 53.05

DOI: <https://doi.org/10.18721/JPM.153.343>

Экспериментальное исследование Ван-дер-Ваальсовых волноводных поляритонов при комнатной температуре

В. И. Кондратьев ¹✉, Т. Иванова ¹, М. Д. Тюгаев ¹, А. К. Самусев ¹, В. Кравцов ¹

¹ Санкт-Петербургский национальный исследовательский университет информационных технологий, механики и оптики, Санкт-Петербург, Россия

✉ valeriy.kondratiev@metalab.ifmo.ru

Аннотация. В этой работе мы экспериментально исследуем волноводные поляритоны, используя только двумерные Ван-дер-Ваальсовы материалы, с гексагональным нитридом бора (hBN) в качестве волноводного слоя и монослоем WS₂ в качестве экситонной среды. Мы помещаем монослой WS₂ в максимум электромагнитного поля волноводной моды, тем самым достигая оптимальных условий для сильной связи между экситонным резонансом и волноводной модой. Для возбуждения и обнаружения неизлучающих волноводных поляритонных мод мы используем метод микроскопии задней фокальной плоскости с высокоиндексной твердотельной иммерсионной линзой. Поляритоны в таких полностью Ван-дер-Ваальсовых структурах, наблюдаемые при комнатных условиях, открывают новые возможности для изучения фундаментальных аспектов взаимодействия света с веществом и открывают новые возможности для миниатюризации и интегрируемости будущих фотонных устройств.

Ключевые слова: Ван-дер-Ваальсовы материалы, двумерные полупроводники, экситон-поляритоны, волноводные поляритоны

Финансирование: Работа выполнена при поддержке гранта РФФИ (проект № 22-22-00663).

Ссылка при цитировании: Кондратьев В. И., Иванова Т., Тюгаев М. Д., Самусев А. К., Кравцов В. Экспериментальное исследование Ван-дер-Ваальсовых волноводных поляритонов при комнатной температуре // Научно-технические ведомости СПбГПУ. Физико-математические науки. 2022. Т. 15. № 3.3. С. 223–225. DOI: <https://doi.org/10.18721/JPM.153.343>

Статья открытого доступа, распространяемая по лицензии CC BY-NC 4.0 (<https://creativecommons.org/licenses/by-nc/4.0/>)

Introduction

Over the last several years, polaritonics has attracted substantial attention as a promising approach to developing non-linear optical and opto-electronic devices. Polaritons arise from strong coupling between light and resonance transitions in matter and manifest themselves in the energy spectrum as Rabi splitting between the transition and optical mode. One promising class of materials for polaritonics is the family of transition metal dichalcogenides (TMDCs). In the monolayer limit, TMDCs are direct bandgap semiconductors [1], and their optical response is dominated by the excitonic resonance. Excitons in TMDCs have large oscillator strengths and large binding energies; moreover, they are stable in ambient conditions, which makes monolayer TMDCs ideal candidates for room-temperature polaritonic devices [2].

Strong light-matter interaction can be achieved through coupling of excitonic resonances in TMDCs to resonant optical modes supported by stand-alone resonators, such as distributed Bragg reflector mirrors [3], plasmonic nanoparticles [4], or subwavelength gratings [5]. Despite the associated chip-compatible planar geometries, such systems often require complicated fabrication processes, which limits their tunability and creates challenges for applications in real devices.

Here, we study excitons in monolayer WS_2 strongly interacting with a waveguide mode in a subwavelength-thickness hBN waveguide. To excite and detect intrinsically non-radiating polaritons propagating below the light line, we use the back focal plane microscopy approach with a high-index solid immersion lens [6]. The complete device can be fabricated in a straightforward way with the dry transfer technique. The geometry of the studied structure allows us to position the WS_2 monolayer precisely at the maximum of the waveguide mode's electromagnetic field by controlling the thickness of the hBN layers. Our results provide a basis for future investigations of waveguide polaritons in devices fabricated entirely from van der Waals 2D materials.

Results and Discussion

The fabricated all-van-der-Waals polariton waveguide is schematically shown in Fig. 1, *a*. A WS_2 monolayer and hBN flakes were mechanically exfoliated from bulk crystals and then dry transferred onto a SiO_2 substrate. In order to place the WS_2 monolayer at the maximum field strength of the waveguide mode with account for the presence of SiO_2 substrate, the bottom hBN layer had a thickness of ~ 30 nm, and the top layer had a thickness of ~ 70 nm. The black solid curve in Fig. 1, *b* represents the electromagnetic field distribution along the out-of-plane direction in the sample. We used atomic force microscopy to accurately determine the thickness of the constituent hBN layers and the final assembled structure.

In Fig. 1, *d*, one can see the experimentally measured angle-resolved reflectivity spectra, which exhibit mode anticrossing at ~ 2.01 eV arising from the strong coupling between the excitonic resonance in monolayer WS_2 and the waveguide mode in hBN. To support the experimental observations, we performed a numerical simulation of the angle-resolved reflectivity from the fabricated structure using the transfer-matrix method [7].

The simulation results are shown in Fig. 1, *c*. As observed in Fig. 1, *c*, *d* the experimental results show qualitative agreement with the numerical simulations, with Rabi splitting values on the order of tens of meV.

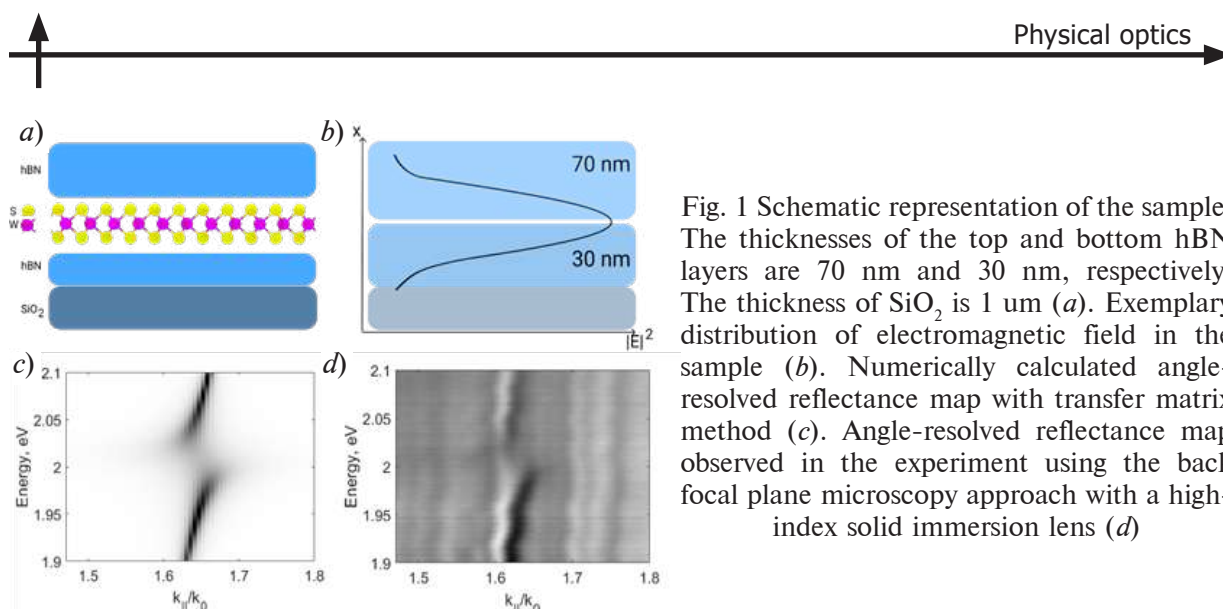


Fig. 1 Schematic representation of the sample. The thicknesses of the top and bottom hBN layers are 70 nm and 30 nm, respectively. The thickness of SiO₂ is 1 μm (a). Exemplary distribution of electromagnetic field in the sample (b). Numerically calculated angle-resolved reflectance map with transfer matrix method (c). Angle-resolved reflectance map observed in the experiment using the back focal plane microscopy approach with a high-index solid immersion lens (d)

Conclusion

We experimentally demonstrate waveguide polaritons in an hBN waveguide with an embedded TMDC monolayer in ambient conditions. Our results pave the way towards miniature and chip-compatible room-temperature polaritonic devices based entirely on 2D materials.

REFERENCES

1. **Mak K. F., Shan J.**, Photonics and optoelectronics of 2D semiconductor transition metal dichalcogenides. *Nature Photonics*. 10.4 (2016) 216–226.
2. **Akinwande D., et al.**, Graphene and two-dimensional materials for silicon technology. *Nature*. 573 (7775) (2019) 507–518.
3. **Dufferwiel S., et al.**, Exciton–polaritons in van der Waals heterostructures embedded in tunable microcavities. *Nature Communications*. 6 (8579) (2015) 1–7.
4. **Munkhbat Battulga, et al.**, Electrical control of hybrid monolayer tungsten disulfide-plasmonic nanoantenna light–matter states at cryogenic and room temperatures. *ACS Nano* 14 (1) (2020) 1196–1206.
5. **Kravtsov V., et al.**, Nonlinear polaritons in a monolayer semiconductor coupled to optical bound states in the continuum. *Light: Science & Applications*. 9 (56) (2020) 1–8.
6. **Permyakov D. V., et al.**, Probing Optical Losses and Dispersion of Fully Guided Waves through Critical Evanescent Coupling. *JETP Letters*. 113 (12) (2021) 780–786.
7. **Mackay Tom G., Akhlesh Lakhtakia**, The transfer-matrix method in electromagnetics and optics. *Synthesis lectures on electromagnetics*. 1 (1) (2020) 1–126.

THE AUTHORS

KONDRATIEV Valeriy I.
valeriy.kondratiev@metalab.ifmo.ru

IVANOVA Tatyana
tatyana.ivanova@metalab.ifmo.ru

TYUGAEV Mikhail D.
mikhail.tiugaev@metalab.ifmo.ru

SAMUSEV Anton K.
a.samusev@metalab.ifmo.ru
ORCID: 0000-0002-3547-6573

KRAVTSOV Vasily
vasily.kravtsov@metalab.ifmo.ru
ORCID: 0000-0002-3555-1027

Received 15.08.2022. Approved after reviewing 19.08.2022. Accepted 15.09.2022.

Conference materials
UDC 621.382.088
DOI: <https://doi.org/10.18721/JPM.153.344>

Measurement of the internal quantum efficiency of emission in the local region of the LED chip

I. V. Frolov ¹✉, O. A. Radaev ¹, V. A. Sergeev ^{1, 2}

¹ Ulyanovsk Branch of Kotelnikov Institute of Radio-Engineering and Electronics
of Russian Academy of Sciences, Ulyanovsk, Russia;

² Ulyanovsk State Technical University, Ulyanovsk, Russia

✉ ufire@mv.ru

Abstract. A method for measuring the internal quantum efficiency in local areas of the LED chip is presented. The method is based on measuring the emission brightness distribution profiles and 3 dB frequencies of the electroluminescence of the LED at two low values of currents with a digital CMOS camera and calculating the internal quantum efficiency for each image pixel using the formula obtained in accordance with the ABC model of charge carrier recombination in a heterostructure. The measurement method was tested on the example of commercial blue InGaN LEDs. It is shown that the degree of homogeneity of the internal quantum efficiency distribution profile is significantly higher than the degree of homogeneity of the emission brightness distribution profile, which is due to the inhomogeneity of the distribution of the light extraction efficiency coefficient in different areas of the LED chip. The presented measurement method can be used to diagnose defects in local areas of the LED heterostructure.

Keywords: LED, light-emitting heterostructure, internal quantum efficiency, measurements

Funding: The work was carried out within the framework of the state task and partially was supported by the Russian Foundation for Basic Research and Ulyanovsk region, project No. 19-47-730002.

Citation: Frolov I. V., Radaev O. A., Sergeev V. A., Measurement of the internal quantum efficiency of emission in the local region of the LED chip. St. Petersburg State Polytechnical University Journal. Physics and Mathematics, 15 (3.3) (2022) 226–229. DOI: <https://doi.org/10.18721/JPM.153.344>

This is an open access article under the CC BY-NC 4.0 license (<https://creativecommons.org/licenses/by-nc/4.0/>)

Материалы конференции
УДК 621.382.088
DOI: <https://doi.org/10.18721/JPM.153.344>

Измерение внутреннего квантового выхода излучения в локальных областях кристалла светодиода

И. В. Фролов ¹✉, О.А. Радаев ¹, В.А. Сергеев ^{1, 2}

¹ Ульяновский филиал Института радиотехники и электроники
им. В. А. Котельникова Российской академии наук, Ульяновск, Россия;

² Ульяновский государственный технический университет, Ульяновск, Россия

✉ ufire@mv.ru

Аннотация. Представлен способ измерений внутреннего квантового выхода излучения в локальных областях кристалла светодиода. Способ основан на измерении цифровой КМОП камерой профилей распределения яркости излучения и граничных частот электролюминесценции светодиода при двух малых значениях тока и расчете внутреннего квантового выхода для каждого пикселя изображений по формуле, полученной в соответствии с ABC моделью рекомбинации носителей заряда в гетероструктуре. Способ измерений апробирован на примере коммерческих синих InGaN гетероструктурных



светодиодах. Показано, что степень однородности профиля распределения внутреннего квантового выхода существенно выше, чем степень однородности профиля распределения яркости излучения, что обусловлено неоднородностью распределения коэффициента вывода излучения по площади кристалла светодиода. Представленный способ измерений может быть использован для диагностики дефектов локальных областей гетероструктуры светодиода.

Ключевые слова: светодиод, светоизлучающая гетероструктура, внутренний квантовый выход, измерения

Финансирование: Работа выполнена в рамках государственного задания при частичной финансовой поддержке Российского фонда фундаментальных исследований и Правительства Ульяновской области, проект № 19-47-730002 р-а.

Ссылка при цитировании: Фролов И. В., Радаев О. А., Сергеев В. А. Измерение внутреннего квантового выхода излучения в локальных областях кристалла светодиода // Научно-технические ведомости СПбГПУ. Физико-математические науки. 2022. Т. 15. № 3.3. С. 226–229. DOI: <https://doi.org/10.18721/JPM.153.344>

Статья открытого доступа, распространяемая по лицензии CC BY-NC 4.0 (<https://creativecommons.org/licenses/by-nc/4.0/>)

Introduction

The internal quantum efficiency (IQE) is the most important parameter of LEDs, which determines the efficiency of converting electric current into optical emission. According to the ABC model of charge carrier recombination in a heterostructure, the IQE is defined as the ratio of the radiative recombination rate to the sum of the radiative and nonradiative recombination rates [1]. Since the rate of nonradiative recombination is directly related to the defects density in the heterostructure, the IQE can be used as a parameter characterizing the quality of the structure. The investigation of factors affecting the internal quantum efficiency of InGaN/GaN LEDs and methods to increase it is an important task [2, 3].

Most of the known methods for measuring the IQE are based on measuring the photoluminescence [4] or electroluminescence [5] parameters of the LED at temperatures of 4–10 K. The application of these measurement methods in the conditions of input or output control in production is difficult.

Defects and indium concentration fluctuations in InGaN-based light-emitting heterostructures are responsible for the inhomogeneous distribution of electroluminescence parameters over the chip area. The presence in the structure of local regions with an increased defects density can cause accelerated degradation of the LED characteristics. In this regard, the development of new methods and means for measuring the electro-optical parameters of local regions of LED chips at room temperatures is an actual task from the point of view of increasing the efficiency of detecting and rejecting defective and potentially unreliable LEDs.

The purpose of the work was to develop and experimentally test a method for measuring the IQE of emission from local regions of the InGaN LED chip.

Materials and Methods

The method for measuring the IQE of emission presented in [6] was used as a basis. The measurement method is based on the ABC model of charge carrier recombination in the InGaN heterostructure of the LED, which establishes the relationship between the IQE of the LED emission and the concentration of charge carriers in the active region through recombination coefficients: defect-related SRH recombination coefficient A , radiative recombination coefficient B , and Auger non-radiative recombination coefficient C . At low currents the effect of Auger recombination can be neglected. The ABC model also establishes a relationship between the recombination coefficients and the 3 dB frequency of the electroluminescence of the LED. Based on the ABC model in [6] an expression was obtained for calculating the IQE η at the LED current I_1 from the results of measurements of the emission power and 3dB frequencies of the electroluminescence of the LED at two low values of currents:

$$\eta(I_1) = \left[\frac{f_{3dB}(I_2) / f_{3dB}(I_1) - 1}{\sqrt{P(I_2) / P(I_1) - 1}} \right] / \left[2 - \frac{f_{3dB}(I_2) / f_{3dB}(I_1) - 1}{\sqrt{P(I_2) / P(I_1) - 1}} \right]. \quad (1)$$

where $f_{3dB}(I_1)$ and $f_{3dB}(I_2)$ are 3 dB frequencies of LED electroluminescence measured at current I_1 and I_2 , respectively; $P(I_1)$ и $P(I_2)$ are LED emission power at current I_1 and I_2 , respectively.

To measure the IQE of emission in local region of the LED chip, a hardware-software complex [7] was used. The hardware-software complex includes a Levenhuk D320L microscope, which includes an FL-20BW digital camera with a maximum resolution of 5472×3648, a DG4162 pulse generator, and a LED supply mode setting unit. The LED is fixed on the microscope stage. A direct pulsed current with amplitude I_1 , duty cycle 50% and pulse repetition rates of 1 kHz and 500 kHz is alternately passed through the LED, and then a direct pulsed current with amplitude I_1 and a frequency of 500 kHz is passed through the LED with the reverse polarity voltage applied to the LED at the end of the current pulse. The images of the LED chip obtained by a digital camera are stored in the computer memory in the form of a matrix, the elements of which have a 16-bit capacity. That is, the brightness of a pixel can take values in the range from 0 to 65535 arbitrary units (a. u). Then the measurements are repeated at a pulsed current with amplitude I_2 . For each pixel of the LED chip image, a 3 dB frequency is calculated and the IQE is calculated by formula (1).

Results and Discussion

Approbation of the method was performed on a commercial blue InGaN LED TO-3216BC-BF. The profiles of $f_{3dB}(I)$ and $P(I)$ were measured at currents $I_1 = 50 \mu\text{A}$ and $I_2 = 100 \mu\text{A}$. Fig. 1 shows the profile of the distribution of the brightness over the chip area of one of the investigated LEDs, measured at a current of 50 μA with a digital camera exposure time of 5 ms. The brightness range was divided into eight subranges. Areas of the chip, the brightness of which is within one of the subranges are highlighted in color in accordance with the color scale. It can be seen from the Fig. 1 that the profile contains local areas with increased brightness.

Fig. 2 shows the distribution profile of the IQE over the LED chip area, measured at a current of 50 μA . The average of IQE is 0.56 a. u. This profile is more uniform than the brightness profile shown in Fig. 1.

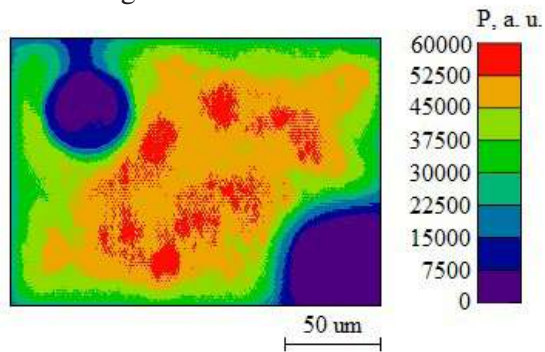


Fig. 1. The profile of the distribution of the brightness over the area of the LED chip at 50 μA

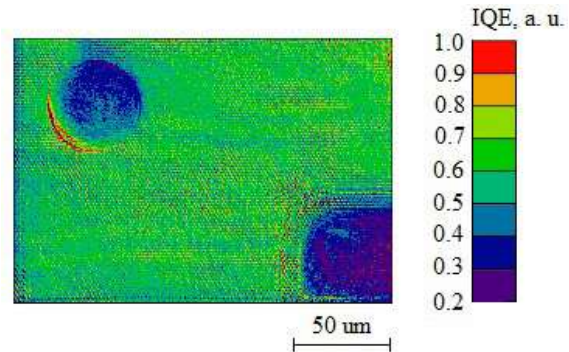


Fig. 2. IQE distribution profile over LED chip area at 50 μA

The degree of homogeneity of the distribution profiles was assessed as follows. We calculated the average value of the brightness \bar{P} and internal quantum efficiency IQE over the area of the active region of the chip (the area occupied by the electrodes was subtracted from the total area of the chip), the standard deviations of values σ_p and σ_{IQE} , and the coefficients $k_p = S_p/S$ and $k_{IQE} = S_{IQE}/S$ were calculated, where S_p is the LED chip area within which the brightness is in the range $(\bar{P} - \sigma_p; \bar{P} + \sigma_p)$; S_{IQE} is the chip area within which IQE is in the range $(\overline{IQE} - \sigma_{IQE}; \overline{IQE} + \sigma_{IQE})$; S is the areas of the active region of the LED chip. According to the obtained estimates, for the investigated LED $k_p = 0.44$, $k_{IQE} = 0.69$. This means that the distribution of IQE is more homogeneous and close to the normal distribution law, that is, in the predominant part of the LED chip area, IQE takes values close to the average value. The brightness distribution is less



uniform and differs from the normal distribution law; a significant part of the LED chip area is occupied by areas with a brightness significantly exceeding the average value.

Differences in the distribution profiles of brightness and IQE are explained by the uneven distribution of the light emission extraction coefficient over the LED chip area. This may be due to the inhomogeneity of the optically transparent layers above the heterostructure. Thus, the obtained results show that to assess the uniformity of the parameters of a light-emitting heterostructure, it is necessary to use the IQE values, since they characterize the heterostructure and do not depend on the light emission extraction coefficient.

Conclusion

The results of experimental testing of the method for measuring the internal quantum efficiency in local regions of the LED chip are presented. The method is based on measuring the distribution profiles of brightness and 3 dB frequencies at two low values of currents and calculating the IQE value from the functional dependence obtained on the basis of the ABC model of charge carriers recombination in a heterostructure. The measurement method can be implemented on standard radio measuring equipment under normal conditions and does not require cryogenic temperature. It is shown that the distribution profiles of brightness and IQE are different. This difference is due to the inhomogeneity of the distribution of the light emission extraction coefficient. The measurement method can be used to control the parameters of the light-emitting heterostructure, including in its local areas.

REFERENCES

1. **Schubert E. F.**, Light Emitting Diodes, Cambridge University Press, Cambridge, 2006.
2. **Anchal N., Sahoo B. K.**, Effect of strain on internal quantum efficiency of InGaN/GaN blue LED, Materials Today: Proceedings. 28 (1) (2020) 311–313.
3. **Zhou Q., Xu M., Wang H.**, Internal quantum efficiency improvement of InGaN/GaN multiple quantum well green light-emitting diodes, Opto-Electronics Review. 24 (1) (2016) 1–9.
4. **Chen G., Craven M., Kim A., Munkholm A., Watanabe S., Camras M., Gutz W., Steranka F.**, Performance of high-power III-nitride light emitting diodes, Phys. stat. sol. (a). 205 (5) (2008) 1086.
5. **Wang Y., Pan M., Li T.**, Comprehensive study of internal quantum efficiency of highbrightness GaN-based light-emitting diodes by temperature-dependent electroluminescence method, Proc. of SPIE. 9003 (2014) 90030D.
6. **Frolov I. V., Sergeev V. A., Radaev O. A.**, A Method for Measuring the Internal Quantum Efficiency of InGaN LED Emission, Technical Physics. 66 (8) 2021 1230–1233.
7. **Frolov I. V., Sergeev V. A., Radaev O. A.**, Measurement of the Distribution Profile of Electroluminescence Cutoff Frequencies over the Area of a Light-Emitting Heterostructure. Instruments and Experimental Techniques. 64 (2) (2021) 259–263.

THE AUTHORS

FROLOV Ilya V.
ilya-frolov88@mail.ru
ORCID: 0000-0003-0608-4754

SERGEEV Viacheslav A.
sva@ulstu.ru
ORCID: 0000-0003-4854-2813

RADAEV Oleg A.
oleg.radaev.91@mail.ru
ORCID: 0000-0002-8156-9412

Received 12.07.2022. Approved after reviewing 14.07.2022. Accepted 14.07.2022.

Conference materials

UDC 538.945

DOI: <https://doi.org/10.18721/JPM.153.345>

New design of a waveguide integrated photon number resolving superconducting detector with micron-wide strips

M. A. Dryazgov^{1, 2, ✉}, Yu. P. Korneeva², A. A. Korneev^{1, 2, 3}

¹ National Research University Higher School of Economics, Moscow, Russia;

² Institute of Nanotechnology of Microelectronics of the Russian Academy of Sciences, Moscow, Russia;

³ Moscow State Pedagogical University, Moscow, Russia

✉ mdryazgov@hse.ru

Abstract. We report on the development of a design for a waveguide integrated photon number resolving superconducting detector with micron-wide strips. The detector is designed for a 1550-nm-wavelength single-mode waveguide. Using the planarization operation, it is possible to cover the waveguide and the entire area around it with a dielectric layer, producing a flat surface for the superconducting detector fabrication. The detector is formed in a shape of a straight line directly above the waveguide. The length and width of the superconducting detector are chosen to absorb maximum of the radiation from the waveguide. In the same superconductor layer, the Klopfenstein taper impedance transformer is designed as a non-uniform coplanar line. The use of impedance matching Klopfenstein tapers makes it possible to distinguish the resistances of several hot spots, that is, to distinguish the number of absorbed photons. The detector should absorb almost all radiation and be capable to distinguish up to 3 photons in an optical pulse.

Keywords: superconductivity, photon number resolving detector, integrated photonic, Klopfenstein taper

Funding: This study was funded by the Russian Science Foundation (RSF) grant No. 20-12-00287.

Citation: Dryazgov M. A., Korneeva Yu. P., Korneev A. A., New design of a waveguide integrated photon number resolving superconducting detector with micron-wide strips. St. Petersburg State Polytechnical University Journal. Physics and Mathematics, 15 (3.3) (2022) 230–234. DOI: <https://doi.org/10.18721/JPM.153.345>

This is an open access article under the CC BY-NC 4.0 license (<https://creativecommons.org/licenses/by-nc/4.0/>)

Материалы конференции

УДК 538.945

DOI: <https://doi.org/10.18721/JPM.153.345>

Новый дизайн интегрированного на волновод детектора с разрешением числа фотонов на основе сверхпроводниковых полосок микронной ширины

М. А. Дрязгов^{1, 2, ✉}, Ю. П. Корнеева², А. А. Корнеев^{1, 2, 3}

¹ Национальный исследовательский университет «Высшая школа экономики», Москва, Россия;

² Институт нанотехнологий микроэлектроники Российской академии наук, Москва, Россия;

³ Московский педагогический государственный университет, Москва, Россия

✉ mdryazgov@hse.ru

Аннотация. Мы сообщаем о разработке дизайна сверхпроводящего детектора с разрешением числа фотонов на основе полосок микронной ширины интегрированного на оптический волновод. Детектор помещается на волновод после операции планаризации диэлектрика. Разрешение числа фотонов достигается путем согласования



импедансов коаксиальной линии и сопротивления детектора, зависящего от количества одновременно поглощенных фотонов. В качестве трансформатора импедансов мы предлагаем использовать сверхпроводящую копланарную линию переменной ширины в форме конуса Клопфенштейна.

Ключевые слова: сверхпроводимость, детектор с разрешением числа фотонов, интегральная фотоника, конус Клопфенштейна

Финансирование: Работа выполнена при поддержке Российского Научного Фонда грант № 20-12-00287.

Ссылка при цитировании: Дрязгов М. А., Корнеева Ю. П., Корнеев А. А. Новый дизайн интегрированного на волновод детектора с разрешением числа фотонов на основе сверхпроводниковых полосок микронной ширины // Научно-технические ведомости СПбГПУ. Физико-математические науки. 2022. Т. 15. № 3.3. С. 230–234. DOI: <https://doi.org/10.18721/JPM.153.345>

Статья открытого доступа, распространяемая по лицензии CC BY-NC 4.0 (<https://creativecommons.org/licenses/by-nc/4.0/>)

Introduction

Superconducting Single Photon Detectors (SSPD) have proven to be excellent for detecting single photons [1] in quantum information applications. However, the challenges of quantum optics require detectors capable to resolve the number of photons [2]. Moreover, present development of quantum computers is directed towards integrated circuits [3]. All this suggests that superconducting photon-number resolving (PNR) detectors should be compatible with the integration on a photonic chip [4–6].

Traditionally, SSPDs are made as 100-nanometer-wide strips, which does not allow them to effectively absorb the radiation from the waveguide. This problem can be solved using micron-wide superconducting strips [7], planarized [8] and integrated with impedance matching Klopfenstein tapers [9].

The planarization makes it possible to cover the waveguide and the entire area around it with a dielectric layer, producing a flat surface for the superconductor deposition. Then a micron-wide superconducting strip can be placed above the waveguide, even if the strip is wider than the waveguide. The use of impedance matching Klopfenstein tapers makes it possible to distinguish the resistances of several hot spots, that is, to distinguish the number of absorbed photons.

We propose a new design of the PNR with a Klopfenstein taper on the waveguide and determine its parameters for manufacturing.

Waveguide and SSPD

The following parameters were chosen for modeling: the waveguide material is Si_3N_4 ($n = 1.9894$) surrounded by SiO_2 ($n = 1.444$) medium, waveguide width $w_{\text{wg}} = 1.68 \mu\text{m}$, waveguide height $d_{\text{wg}} = 0.5 \mu\text{m}$. Modeling in the COMSOL environment demonstrates that it will be a single-mode waveguide for a wavelength of $\lambda = 1550 \text{ nm}$. A strip of NbN (with refraction index $n = 5.20685 - 5.82i$) 5 nm thick is placed above the waveguide. The ground contacts of the coplanar line are placed far enough away so as not to affect the absorption of radiation from the waveguide. The width of the superconducting strip w_{strip} and the thickness of the dielectric layer (d_{diel}) between the waveguide and superconductor are selected to ensure maximum radiation absorption (Fig. 1, a).

The simulation results in the COMSOL environment are shown in Fig. 1, b. It is clearly visible that for maximum absorption, the thickness of the dielectric layer between the waveguide and superconductor should be as small as possible: for example, the absorption of $1.4 \text{ dB}/\mu\text{m}$ is achieved for $d_{\text{diel}} = 0 \text{ nm}$, and for $d_{\text{diel}} = 100 \text{ nm}$ the absorption is only $0.7 \text{ dB}/\mu\text{m}$. Absorption increases with increasing width of the superconducting strip. However, as shown in the inset in Fig. 1, b, for strips wider than 2 micrometers, the increase in absorption is extremely small and does not give any improvement.

Thus, it is necessary to place 2- μm -wide superconducting strip directly on the waveguide. Even

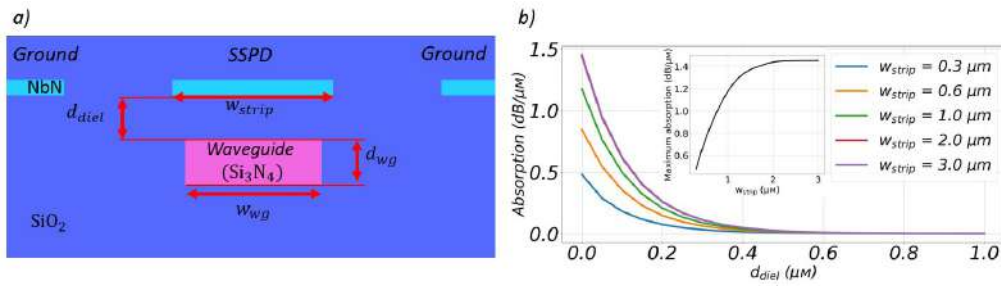


Fig. 1. A cross-section showing the waveguide with an SSPD on top (a). The dependence of the absorption on the thickness d_{diel} of the dielectric layer between the waveguide and SSPD (b). The red and purple curves (for $w_{strip} = 2$ and $3 \mu m$) are indistinguishable due to the similar absorption values. In insert: dependence of the maximum absorption (at $d_{diel} = 0$) on the width of the superconducting strip

though the width of the superconducting strip is greater than the width of the waveguide, this is possible if the waveguide is covered with a thick dielectric layer and, using the planarization operation, the dielectric layer is removed along the upper boundary of the waveguide.

To achieve the maximum absorption of $1.4 \text{ dB}/\mu\text{m}$, the length l_{strip} of the superconducting strip required to absorb 99% of the radiation from the waveguide is $14 \mu\text{m}$.

Klopfenstein taper

A normal domain with a resistance of about $1 \text{ k}\Omega$ is formed, when a photon is absorbed in a superconducting strip. Accordingly, when two or more photons are absorbed, the number of normal domains increases proportionally. However, the resistance of a different number of normal domains is indistinguishable against the coaxial line impedance of 50Ω . To solve this problem impedance matching is necessary which will ensure distinguishing between resistances of normal domains, that is, the number of absorbed photons.

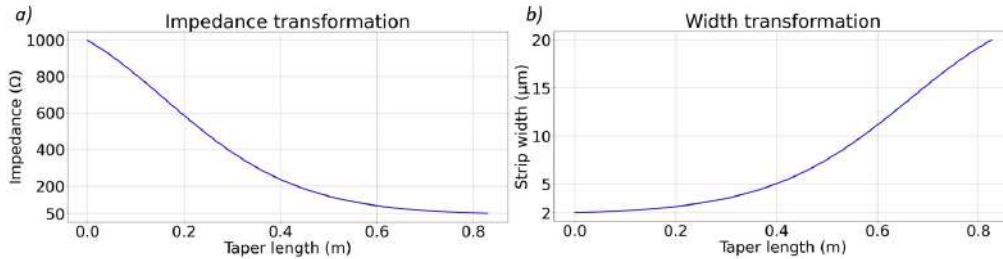


Fig. 2. Smooth transformation of impedance along the length of the co-planar line calculated using Klopfenstein's formulas (a). The width of the signal contact vs line length (b)

The matching of the impedances of the coaxial line and the normal domain is carried out using the Klopfenstein taper. First, determine the reflection coefficient without impedance matching according to formula:

$$\Gamma_0 = \frac{1}{2} \ln \frac{Z_0}{Z_1} \quad (1)$$

here $Z_1 = 50 \Omega$ is the characteristic impedance of the coaxial line, $Z_0 = 1 \text{ k}\Omega$ is the resistance of the normal domain. Then $\Gamma_0 = 1.5$.

Taking the maximum permissible reflection coefficient $\Gamma_m = 0.1$, the constant A , which is responsible for a smooth change in the impedance, can be found by (2):

$$A = \cosh^{-1}(\Gamma_0 / \Gamma_m) \quad (2)$$

Then $A = 3.4$. The length of the Klopfenstein taper is found by formula:

$$L = \frac{Ac}{2\pi f_{\min} \sqrt{\epsilon}} \quad (3)$$

here $c = 3 \cdot 10^8 \text{ m/s}$ is the speed of light in the vacuum, $\epsilon = 3.9$ is the absolute permittivity of the

SiO₂, $f_{min} = 100$ MHz is the minimum frequency of the transmitted signal. Then $L = 83.4$ cm. To achieve a smooth change in the impedance, formula (4) is used:

$$\varphi(x, A) = \int_0^x \frac{I_1(A\sqrt{1-y^2})}{A\sqrt{1-y^2}} dy, |x| \leq A \quad (4)$$

here $I_1(x)$ is the modified Bessel function of the 1st order.

Finally, the change in impedance according to the Klopfenstein formula (5) is shown in Fig. 2, a.

$$\ln Z(z) = \frac{1}{2} \ln Z_0 Z_l + \frac{A^2}{\cosh A} \Gamma_0 \varphi\left(\frac{2z}{L} - 1, A\right), 0 \leq z \leq L \quad (5)$$

Impedance matching is performed by using nonuniform transmission line with varying a coplanar line impedance. A smooth change in the width of the superconducting strip (Fig. 2, b) acting as a signal contact from 2 μm to 20 μm with a constant gap width of 20 μm over $L = 83$ cm will provide a smooth change in impedance according to the Klopfenstein formula.

Now it becomes possible to distinguish the resistance of one normal domain from two, three or more. That is, to distinguish the number of photons in an optical pulse.

Design concept

We suggest photonic integrated circuit which has transmission lines with ground-signal-ground (GSG) probing pad which matched to the RF probe impedance of 50 Ω. The Klopfenstein taper is used for matching between SSPD and GSC probing pad. On a SiO₂ dielectric substrate there is a silicon nitride (Si₃N₄) waveguide. The waveguide is covered with a dielectric layer (SiO₂) with subsequent planarization, which will allow placing a detector on top with impedance matching transformer in the form of a Klopfenstein taper. The detector is made in the form of a straight 2-μm-wide strip of NbN 14 μm long. After all, the structure is covered with a dielectric layer to prevent radiation scattering (Fig. 3).

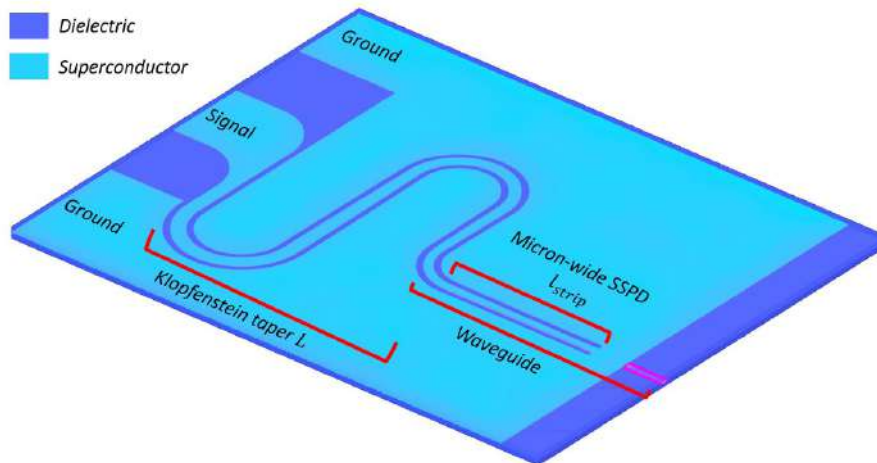


Fig. 3. The design concept of the PNR-SSPD with a Klopfenstein taper integrated on the optical waveguide (not to scale)

The described detector absorbs 99% of the radiation from the optical waveguide and is able to distinguish up to three photons in an optical pulse due to impedance matching.

Conclusion

We have proposed a design for a waveguide integrated PNR superconducting detector with micron-wide strips connected to Klopfenstein taper. The optimal parameters were calculated for absorbing 99% of the radiation and matching the impedance of the coaxial line and the superconductor in the normal state: $w_{strip} = 2$ μm, $l_{strip} = 14$ μm, $w_{wg} = 1.68$ μm, $d_{wg} = 0.5$ μm, $L = 83.4$ cm.

REFERENCES

1. **You L.**, Superconducting nanowire single-photon detectors for quantum information, *Nanophotonics*. 9 (9) (2020) 2673–2692.
2. **Zhang Zh., Zhao Qi, Razavi M., Ma X.**, Improved key-rate bounds for practical decoy-state quantum-key-distribution systems, *Physical Review A*. A95 (2017) 012333.
3. **Schnauber P., Singh A., Schall J., Park S. I., Dong Song J., Rodt S., Srinivasan K., Reitzenstein S., Davanco M.**, Indistinguishable Photons from Deterministically Integrated Single Quantum Dots in Heterogeneous GaAs/Si₃N₄ Quantum Photonic Circuits, *Nano Letters*. 19 (10) (2019) 7164–7172.
4. **Sahin D., Gaggero A., Zhou Z., Jahanmirinejad S., Mattioli F., Leoni R., Beetz J., Lermer M., Kamp M., Hufiling S., Fiore A.**, Waveguide photon-number-resolving detectors for quantum photonic integrated circuits, *Applied Physics Letters*. 103 (2013) 111116.
5. **McDonald C., Moody G., Nam S. W., Mirin R. P., Shainline J.M., McCaughan A., Buckley S., Silverman K. L.**, III-V photonic integrated circuit with waveguide-coupled light-emitting diodes and WSi superconducting single-photon detectors, *Applied Physics Letters*. 115 (2019) 081105.
6. **Xiang Ch., Jin W., Bowers J. E.**, Silicon nitride passive and active photonic integrated circuits: trends and prospects, *Photonics Research*. 10 (6) (2022) A82-A96.
7. **Korneeva Yu. P., Vodolazov D. Yu., Semenov A. V., Florya I. N., Simonov N. O., Baeva E., Korneev A. A., Goltsman G. N., Klapwijk T. M.**, Optical Single-Photon Detection in Micrometer-Scale NbN Bridges, *Physical Review Applied*. 9 (2018) 064037.
8. **Muench J. E., Ruocco A., Giambra M. A., Miseikis V., Zhang D., Wang J., Watson H. F. Y., Park G. C., Akhavan Sh., Sorianello V., Midrio M., Tomadin A., Coletti C., Romagnoli M., Ferrari A. C., Goykhman I.**, Waveguide-Integrated, Plasmonic Enhanced Graphene Photodetectors, *Nano Letters*. 19 (11) (2019) 7632–7644.
9. **Zhu D., Colangelo M., Chen Ch., Korzh B. A., Wong F. N. C., Shaw M. D., Berggren K. K.**, Resolving photon numbers using a superconducting tapered nanowire detector, *Nano Letters*. 20 (5) (2020) 3858–3863.

THE AUTHORS

DRYAZGOV Mikhail A.
mdryazgov@hse.ru
ORCID: 0000-0002-6280-4667

KORNEEV Alexander A.
alex.korneev78@gmail.com
ORCID: 0000-0002-0116-9591

KORNEEVA Yuliya P.
korneeva_yuliya@mail.ru
ORCID: 0000-0003-1576-265X

Received 14.07.2022. Approved after reviewing 14.07.2022. Accepted 18.07.2022.

Conference materials

UDC 621.373.826

DOI: <https://doi.org/10.18721/JPM.153.346>

The effect of mesa-stripe design parameters on the 975 nm laser diode output characteristics

A. V. Fomin ¹, E. M. Filonenko ¹✉, S. A. Kryukov ¹, S. Kh. Nazhmetov ¹

¹ FSUE "RFNC-VNIITF named after Academ. E. I. Zababakhin", Snezhinsk, Russia

✉ dep5@vniitf.ru

Abstract. The present work is devoted to evaluating the effect of mesa-stripe design parameters on the output characteristics of 975 nm InGaAs/GaAs/AlGaAs laser diodes with the emitting stripe width $W = 100 \mu\text{m}$ and the cavity length $L = 4 \text{ mm}$. The output power, threshold current, central wavelength, and full spectral width at half maximum values were analyzed when comparing the two variants of mesa-stripe design to determine the optimal etching depth of semiconductor structure. Two variants of the mesa-stripe design were obtained by plasma-chemical etching to different depths of the heterostructure. According to the results of the study for the mesa-stripe design formed by etching to the p-cladding layer of the laser heterostructure, a less scatter of the controlled parameters within a group of fabricated laser diodes and effective suppression of parasitic lateral modes in the LD cavity were revealed.

Keywords: optoelectronics, laser diode, optical confinement, mesa-stripe design, etching depth, electrooptical parameters

Citation: Fomin A. V., Filonenko E. M., Kryukov S. A., Nazhmetov S. Kh., The effect of mesa-stripe design parameters on the 975 nm laser diode output characteristics. St. Petersburg State Polytechnical University Journal. Physics and Mathematics, 15 (3.3) (2022) 235–238. DOI: <https://doi.org/10.18721/JPM.153.346>

This is an open access article under the CC BY-NC 4.0 license (<https://creativecommons.org/licenses/by-nc/4.0/>)

Материалы конференции

УДК 621.373.826

DOI: <https://doi.org/10.18721/JPM.153.346>

Исследование влияния параметров мезаполосковой конструкции лазерных диодов спектрального диапазона 975 нм на характеристики излучения

А. В. Фомин ¹, Е. М. Филоненко ¹✉, С. А. Крюков ¹, С. Х. Нажметов ¹

¹ ФГУП «РФЯЦ-ВНИИТФ им. академ. Е.И. Забабахина», Снежинск, Россия

✉ dep5@vniitf.ru

Аннотация. В настоящей работе приведены результаты оценки влияния конструкции чипа на выходные характеристики лазерных диодов InGaAs/GaAs/AlGaAs спектрального диапазона 975 нм с шириной полоска $W = 100 \text{ мкм}$ и длиной резонатора $L = 4 \text{ мм}$. При сравнении двух вариантов мезаполосковой конструкции анализировались значения выходной мощности, порогового тока, центральной длины волны и ширины спектра на полувысоте с целью определения оптимальной глубины травления полупроводниковой гетероструктуры. Два варианта мезаполосковой конструкции были получены плазмохимическим травлением канавок на разную глубину гетероструктуры. По результатам исследования для конструкции мезаполоска, образованного травлением до слоя р-эмиттера лазерной гетероструктуры, был выявлен меньший разброс контролируемых параметров внутри группы изготовленных лазерных диодов и продемонстрировано эффективное подавление паразитных латеральных мод в резонаторе ЛД.

Ключевые слова: оптоэлектроника, лазерный диод, оптическое ограничение, мезаполосковая конструкция, глубина травления, электрооптические характеристики

Ссылка при цитировании: Фомин А. В., Филоненко Е. М., Крюков С. А., Нажметов С. Х. Исследование влияния параметров мезаполосковой конструкции лазерных диодов спектрального диапазона 975 нм на характеристики излучения // Научно-технические ведомости СПбГПУ. Физико-математические науки. 2022. Т. 15. № 3.3. С. 235–238. DOI: <https://doi.org/10.18721/JPM.153.346>

Статья открытого доступа, распространяемая по лицензии CC BY-NC 4.0 (<https://creativecommons.org/licenses/by-nc/4.0/>)

Introduction

Today, high-power laser diodes (LDs) emitting at 975 nm are widely used for fiber laser pumping [1, 2]. In the LD design, a stimulated emission is generated in quantum well region between waveguide layers which, in turn, are surrounded by claddings. The plane-parallel Fabry-Perot cavity is formed by two cleaved facets of semiconductor crystal [3]. Optical confinement of LD radiation in the vertical direction is formed directly during epitaxial growth of laser heterostructure waveguide layers, while the formation of a waveguide necessary to create a lateral direction of LD radiation is considered to be a crucial design problem to be solved in the course of post-stage operations of high-power LD technology along with the development of optical and contact coatings.

Lateral confinement of radiation in a laser heterostructure can be attained by creating an effective refractive-index step, Δn_{eff} , at the boundary with radiation region or be achieved due to a difference in gain in this direction [3, 4]. An appropriate LD design in the first case can be formed by etching the heterostructure down to the n-type cladding, the walls of the etching profile optically constraining the radiation in the lateral direction (Fig. 1, *a*). A gain step, Δg , can be similarly achieved by forming an LD mesa-stripe by etching the heterostructure, yet with the etch front reaching only the p-type cladding (Fig. 2, *b*). In this case, the concentration of charge carriers is sufficiently high only in a limited region under the stripe creating conditions to overcome optical loss [3, 4].

This work was aimed at considering the above-mentioned design solutions and was devoted to evaluating the effect of the etching depth of the grooves forming the mesa-stripe on the output parameters of the LDs emitting at 975 nm in order to determine the optimal mesa-stripe geometry for the existing design of InGaAs/GaAs/AlGaAs laser heterostructure.

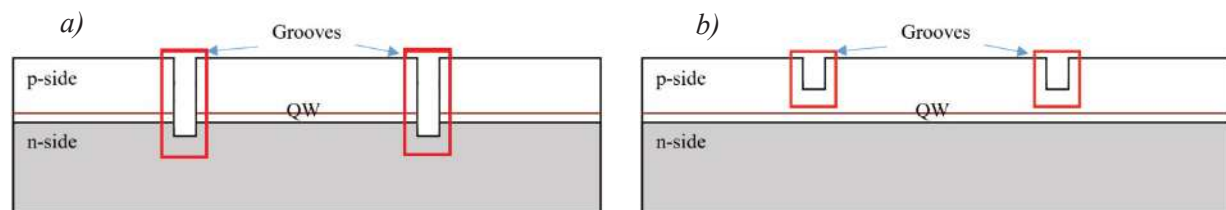


Fig. 1. Mesa-stripe designs with etching to the n-type cladding (*a*) and etching to the p-type cladding (*b*)

Materials and Methods

The InGaAs/GaAs/AlGaAs heterostructure samples to be studied were grown by metalorganic chemical vapour deposition (MOCVD) method. The topology of the produced LDs was a mesa-stripe design with different depths of etched grooves defining mesas, denoted further as deep and shallow ones. In the first case, the etch front reached the n-cladding region. In the second case, the etch front reached the p-cladding without affecting the laser heterostructure waveguide and the active region. The etching depth was controlled by profilometry and SEM analysis. In the course of this work, laser diodes of two types of mesa-stripe designs were fabricated having the emitting stripe width $W = 100 \mu\text{m}$ and the cavity length $L = 4 \text{ mm}$. For output characteristics measurements the LDs with different mesa-stripe designs were mounted on heatsinks with thin-film AuSn solder [5].



Results and discussion

The output characteristics of two groups of LDs without applied cavity mirrors and with different mesa design depths for QCW generation mode of up to a current of 3 A are shown in Fig. 2. Table 1 shows the average values of wavelength, λ , full width at half maximum, FWHM, output power, P, threshold current, I_{th} , and estimated scatter of parameters for each LD group. A greater scatter of spectral characteristics and of output power values is observed within the group of deep mesa LDs, while the scatter of threshold current values is identical for both groups (Fig. 2, *a*, *b*). Thus, the manufactured shallow mesa LD design is characterized by more stable values obtained for the controlled parameters.

Table 1

Average values of controlled parameters and scatter estimation for two groups of LDs with different mesa-stripe designs

Design	Number of LDs	Average value				Standard deviation			
		λ , nm	FWHM, nm	I_{th} , A	P, W	λ , nm	FWHM, nm	I_{th} , A	P, W
Deep mesa	43	974.3	3.3	0.34	1.2	0.5	0.6	0.02	0.1
Shallow mesa	43	975.1	3.1	0.34	1.2	0.2	0.2	0.01	0.0

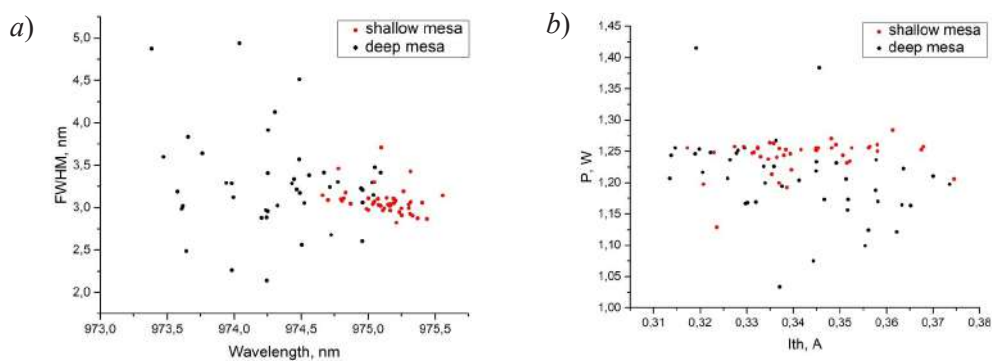


Fig. 2. Correlation plots of FWHM and central wavelength λ (*a*) and LDs output power and threshold current for two groups of LDs with shallow and deep mesas (*b*)

The output characteristics were also measured in the CW mode for LDs with applied mirrors (Fig. 3). The typical value of the external differential efficiency for deep mesa LDs was $\eta = 0.95$ W/A, that for shallow mesa LDs being $\eta = 1.05$ W/A. Typical values of FWHM for deep mesa LDs can reach 10 nm at the current of 12 A provided that several local maxima are present in the spectrum (Fig. 3, *a*). At the same time, typical values of FWHM for shallow mesa LDs made up 3.7–5 nm at the current of 12 A (Fig. 3, *b*).

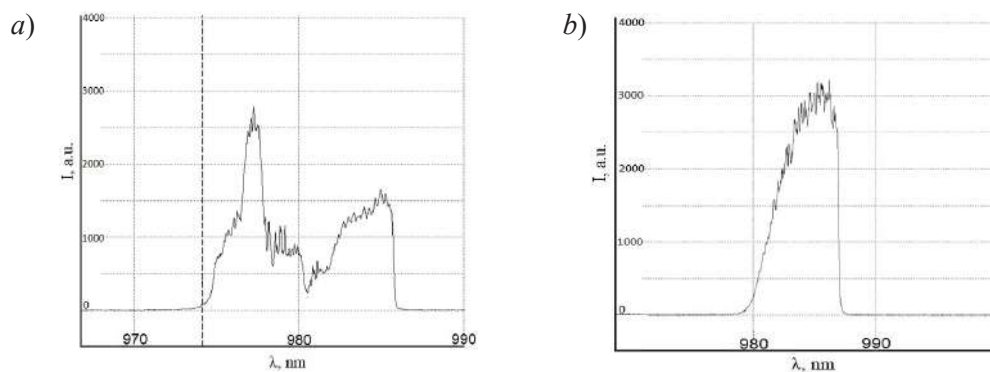


Fig. 3. Typical spectra for LDs with mirrors obtained in CW mode at 12 A current: deep (*a*) and shallow mesa-stripe designs (*b*)

Conclusion

The studies of the output characteristics for two groups of LDs allowed establishing the advantage of the shallow mesa design, which is characterized by obtaining more reproducible values of the controlled LD parameters. Lower values of differential efficiency, as well as the presence of several local maxima in the spectrum of deep mesa-stripe LDs may indicate the formation of conditions suitable for amplification of higher order modes in this type of design. In turn, the shallow mesa design allows effectively suppressing the parasitic lateral modes in the resonator, as evidenced by the presence of a single local maximum in the LD spectrum.

REFERENCES

1. **Duesterberg R., Xu L., Skidmore J. A., Guo J., Cheng J., Du J., Zucker E. P.**, 100W high-brightness multi-emitter laser pump. High-Power Diode Laser Technology and Applications IX, edited by Mark S. Zediker, Proc. of SPIE. 7918 (2011) 79180V.
2. **Skidmore J., Peters M., Rossin V., Guo J., Xiao Y., Cheng J., Zucker E.**, Advances in high-power 9XXnm laser diodes for pumping fiber lasers. High-Power Diode Laser Technology and Applications XIV, edited by Mark S. Zediker, Proc. of SPIE. 9733 (2016) 97330B.
3. **Zhukov A. E.**, Lasers based on semiconductor nanostructures [in Russian], Elmor, Saint-Petersburg, 2007.
4. **Diehl R.**, High-Power Diode Lasers: Fundamentals, Technology, Applications with Contributions by Numerous Experts, Applied Physics. 78 (2000).
5. **Filonenko E. M., Fomin A. V., Ivanov V. V.**, Features of Au(80)Sn(20) thin film solder manufacturing technology, IOP Conference Series: Materials Science and Engineering. 781 (2020) 012019.

THE AUTHORS

FILONENKO Elena M.

dep5@vniitf.ru

ORCID: 0000-0002-9477-612X

FOMIN Alexey V.

dep5@vniitf.ru

KRYUKOV Sergey A.

dep5@vniitf.ru

NAZHMETOV Salavat Kh.

dep5@vniitf.ru

Received 24.07.2022. Approved after reviewing 25.07.2022. Accepted 25.07.2022.

PHYSICAL MATERIALS TECHNOLOGY

Conference materials

UDC 546.06, 546.05

DOI: <https://doi.org/10.18721/JPM.153.347>

TEM contrast enhancement by adsorption of erbium ions on the inner surface of micro-mesoporous silica particles

D. A. Eurov¹✉, E. A. Volkova¹, D. A. Kirilenko¹, D. A. Kurdyukov¹, E. Yu. Stovpiaga¹

¹ Ioffe Institute, St. Petersburg, Russia

✉ eurov@gvg.ioffe.ru

Abstract. A simple and facile method is proposed for treatment of the inner surface of micro-mesoporous spherical particles of amorphous silica with the solutions of heavy element salts, which allows direct visualization of the particles' porous structure by the transmission electron microscopy (TEM) technique. The method is based on the adsorption of ions of heavy elements (on the example of Er³⁺ ions) by the surface of the pores, which makes it possible to enhance the contrast in the TEM image. The particles before and after erbium ions adsorption are characterized by means of TEM, nitrogen porosimetry and energy dispersive X-ray spectroscopy. It is demonstrated that the developed method for the particles' surface functionalization allows implementing erbium adsorption without affecting the morphology and inner structure of particles. It is shown that erbium content after the adsorption procedure does not exceed 0.1 at.% and the pore structure of silica particles remains the same – the specific surface area, volume and pore size do not change.

Keywords: porous silica, adsorption, transmission electron microscopy, erbium ions, microporosity

Funding: This work was funded by the Russian Science Foundation, project No. 22-23-20104 and by the St. Petersburg Science Foundation, agreement No. 27/2022 (14.04.2022).

Citation: Eurov D. A., Volkova E. A., Kirilenko D. A., Kurdyukov D. A., Stovpiaga E. Yu., Tem contrast enhancement by adsorption of erbium ions on the inner surface of micro-mesoporous silica particles. St. Petersburg State Polytechnical University Journal. Physics and Mathematics, 15 (3.3) (2022) 239–243. DOI: <https://doi.org/10.18721/JPM.153.347>

This is an open access article under the CC BY-NC 4.0 license (<https://creativecommons.org/licenses/by-nc/4.0/>)

Материалы конференции

УДК 546.06, 546.05

DOI: <https://doi.org/10.18721/JPM.153.347>

Увеличение контраста ПЭМ изображений микро-мезопористого кремнезема за счет адсорбции ионов эрбия внутренней поверхностью частиц

Д. А. Еуров¹✉, Е. А. Волкова¹, Д. А. Кириленко¹, Д. А. Курдюков¹, Е. Ю. Стовпяга¹

¹ Физико-технический институт им. А. Ф. Иоффе, Санкт-Петербург, Россия

✉ eurov@gvg.ioffe.ru

Аннотация. Предложен простой и технологичный метод обработки внутренней поверхности микро-мезопористых сферических частиц аморфного кремнезема, позволяющий визуализировать их пористую структуру методом просвечивающей электронной микроскопии (ПЭМ). Метод основан на адсорбции ионов тяжелых элементов (на примере ионов эрбия) поверхностью пор частиц, что позволяет увеличить контраст на ПЭМ изображениях. Показано, что адсорбция ионов эрбия не влияет на внутреннюю структуру частиц кремнезема – удельная поверхность, объем и размер пор не меняются.

Ключевые слова: пористый кремнезем, адсорбция, просвечивающая электронная микроскопия, ионы эрбия, микропористость

Финансирование: Работа выполнена при финансовой поддержке Российского научного фонда грант №22-23-20104 и гранта Санкт-Петербургского научного фонда в соответствии с соглашением от 14.04.2022 г. № 27/2022.

Ссылка при цитировании: Еуров Д. А., Волкова Е. А., Кириленко Д. А., Курдюков Д. А., Стовпяга Е. Ю. Увеличение контраста ПЭМ изображений микро-мезопористого кремнезема за счет адсорбции ионов эрбия внутренней поверхностью частиц // Научно-технические ведомости СПбГПУ. Физико-математические науки. 2022. Т. 15. № 3.3. С. 239–243. DOI: <https://doi.org/10.18721/JPM.153.347>

Статья открытого доступа, распространяемая по лицензии CC BY-NC 4.0 (<https://creativecommons.org/licenses/by-nc/4.0/>)

Introduction

Porous silica particles are of great interest due to their inertness, biocompatibility and high adsorption capacity and are used in a wide variety of applications [1]. The porosity is one of the main characteristics of the particles in practical use. It determines the significance of the detailed study of the porous structure in order to fabricate materials with the required properties such as specific surface area, size, morphology and volume of pores. A number of methods are used to study the porous structure, in particular, adsorption porosimetry, small-angle X-ray scattering, transmission and scanning electron microscopy (TEM and SEM) [2–4]. Direct visualization of nanosize pores within the submicron particles by microscopic methods is quite intricate due to the low contrast (because of a low atomic numbers of silicon and oxygen). In ordered channel-like materials (e.g. SBA-15) mesopores can be observed due to their regular spatial arrangement and orientation of the channels along a certain axis, while micropores in the channel walls are not visible. The introduction of a contrast agent (NaCl) into the reaction mixture during synthesis made it possible to visualize micropores in SBA-15 by SEM [4]. When studying the micro-mesoporous particles of amorphous silica synthesized earlier by us [5], the study of the porous structure by the TEM method becomes even more complicated due to the fact that the pores inside the particles are disordered. In this case, the interpretation of TEM images, which are, in some approximation, the projection of the density of a complex three-dimensional structure, is significantly difficult. To enhance the TEM contrast, we developed a method for the adsorption of heavy metal ions by the surface of pores, which made it possible to directly visualize their porous structure.

Materials and Methods

Materials. Cetyltrimethylammonium bromide (CTAB), $C_{16}H_{33}N(CH_3)_3Br$, 99+% (Acros); aqueous ammonia (NH_3), 24% wt., $\geq 99.99\%$; ethanol (C_2H_5OH), 95% wt.; deionized water (H_2O) 10 M Ω ; tetraethoxysilane (TEOS), $Si(OC_2H_5)_4$, 99+% (Acros); [3-(methacryloyloxy)propyl] trimethoxysilane (MPTMOS), $H_2C=C(CH_3)CO_2(CH_2)_3Si(OCH_3)_3$, 98% (Aldrich); hydrochloric acid (HCl), 37% wt., ACS reagent grade; erbium sulfate octahydrate ($Er_2(SO_4)_3 \cdot 8H_2O$), 99.9%, (Acros); nitric acid (HNO_3), 60% (Aldrich).

Methods. In the present study we used spherical micro-mesoporous silica particles (MMSP) with a diameter of 405 ± 25 nm. MMSP were synthesized according to the method developed by us via basic hydrolysis of (80% mol. TEOS + 20% mol. MPTMOS) in $NH_3-H_2O-C_2H_5OH$ -surfactant mixture [5]. The molar ratio of the reagents (TEOS+MPTMOS): $NH_3:H_2O:C_2H_5OH$:CTAB was 1:60:370:230:0.2. The temperature of the reaction mixture was 65 °C, the synthesis duration – 1 h. To remove organics, the particles were washed with an alcoholic solution of HCl (0.01 M) and then were annealed in a flow of O_2 at a temperature of 400 °C for 5 h.

The functionalization of the inner surface with Er^{3+} ions was carried out by the method of capillary impregnation of particles with an erbium sulfate solution. The process technology was based on the technique developed by us previously for the adsorption of Ni^{2+} ions by mesoporous silica particles [6]. In this case, a weighed portion (0.5 g) of particles was added to 5 ml of

0.01M $\text{Er}_2(\text{SO}_4)_3$ solution and subjected to ultrasonic treatment for 2 h, after which the resulting suspension was left for a day. During the impregnation, erbium ions were adsorbed by active silanol groups on the inner surface of cylindrical silica nanochannels within MMSP [5, 6]. To remove excess $\text{Er}_2(\text{SO}_4)_3$, the particles were sedimented by centrifugation, and the supernatant was separated. After that, the particles were dried in air at 60 °C and then subjected to heat treatment at 200 °C for 30 min. To remove bulk erbium compounds from the outer surface of the MMSP and nanocrystallites from their pores, the particles were immersed with a 5M HNO_3 and kept for 2 h, after which the particles were centrifuged and the supernatant was poured off. The procedure was repeated twice. The resulting particles were then washed twice with deionized water.

Transmission electron microscopic measurements were performed using a Jeol JEM-2100F microscope (accelerating voltage 200 kV, point-to-point resolution 0.19 nm) equipped with Bruker XFlash 6T-30 energy dispersive X-ray (EDX) spectrometer. The nitrogen adsorption was performed using a Micromeritics 3FLEX at a temperature of 77 K. The specific surface area was calculated by the Brunauer – Emmett – Teller (BET) method, and the pore size distribution was found using the nonlocal density functional theory (NLDFT).

Results and Discussion

Fig. 1 shows TEM images with different magnifications of MMSP before (Fig. 1, *a*) and after (Fig. 1, *b*) adsorption of Er^{3+} ions. It can be seen that adsorption of erbium does not affect the size and the shape of the particles which remain the same. At the same time the porous structure of the particles becomes much more clearly visible due to the presence of an element with high Z number on the pore surface. One can see features with the sizes of 2.5 nanometers on the high-resolution TEM images of the particles' surface region (Fig. 1, *b*), which are indistinguishable in the case of untreated particles (Fig. 1, *a*). This value corresponds to the inner diameter of the nanochannels calculated from the results of nitrogen porosimetry (see below). Thus, the proposed technique for treatment of micro-mesoporous silica particles with Er^{3+} ions made it possible to visualize pores on high-resolution TEM images.

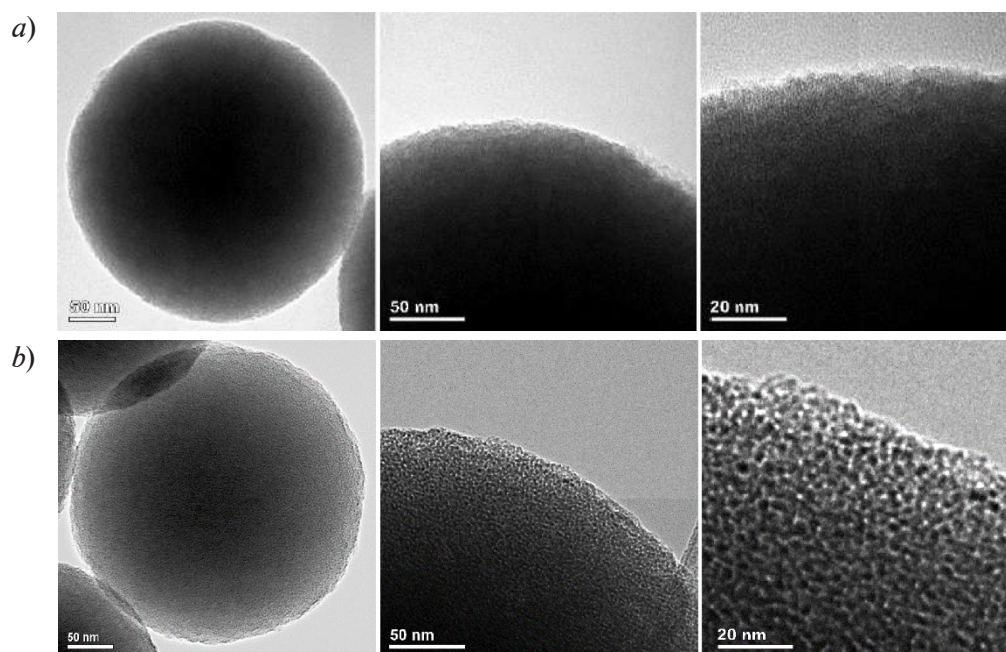


Fig.1. TEM images of micro-mesoporous silica particles before (*a*) and after (*b*) functionalization with erbium ions

The nitrogen adsorption and desorption isotherms of the MMSP we synthesized are shown in Fig. 2, *a*. The isotherms have a step-like form characteristic of M41S silica materials and belong to type IV [7]. The specific surface area of the particles was calculated in the pressure range $0.05 \leq p/p_0 \leq 0.20$ by the BET method. According to the results of adsorption structural analysis, the specific surface area and pore volume of particles before and after treatment with erbium

sulfate solution also remained practically unchanged and were found to be $1630 \text{ m}^2\text{g}^{-1}$, $0.72 \text{ cm}^3\text{g}^{-1}$ and $1610 \text{ m}^2\text{g}^{-1}$, $0.71 \text{ cm}^3\text{g}^{-1}$, respectively (Fig. 2).

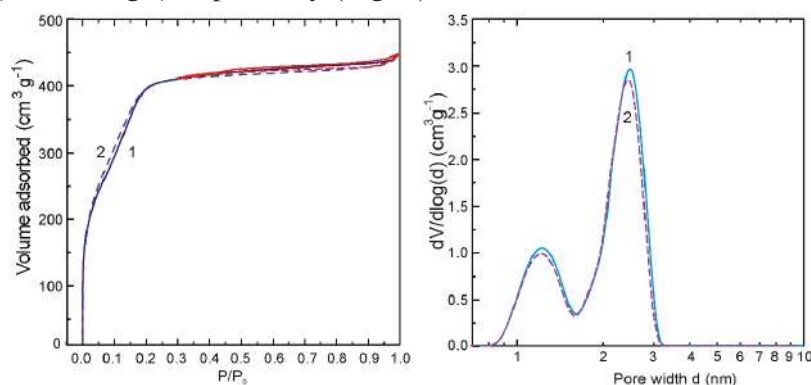


Fig. 2. N_2 adsorption and desorption isotherms at 77 K (a) and pore size distribution for particles before (1) and after (2) treatment with erbium sulfate solution (b)

The pore size distribution (Fig. 2, b curve 1) demonstrates that the synthesized MMSP contain pores ranging from 0.7 to 3.2 nm, which is in good agreement with the TEM data (Fig. 1, b). The adsorption of Er^{3+} ions does not change the diameter of the pores compared to the initial particles, which indirectly confirms a small content of erbium on the surface of pores. This also agrees with the EDX data (Fig. 3). There are no peaks corresponding to erbium observed on the spectrum, which indicates that its content does not exceed 0.1 % at. Peaks corresponding to Cu and C on the spectrum (Fig. 3) are due to the specimen support grid.

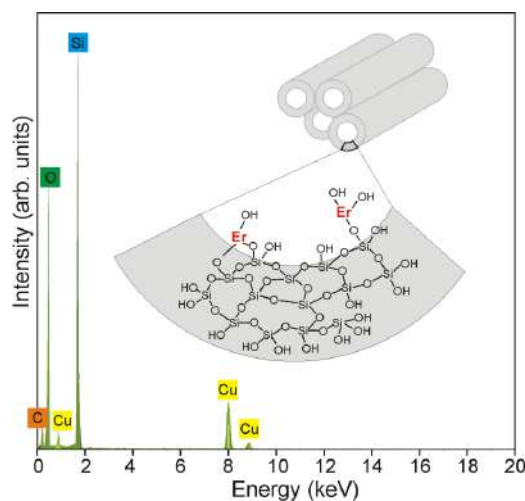


Fig. 3. EDX spectrum of MMSP after Er^{3+} adsorption. *Inset*: schematic representation of silica nanochannels with erbium ions adsorbed on the inner surface

Erbium was introduced into the pores of the MMSP so that erbium atoms were probably chemically bonded to the pore surface. The silanols on the inner surface of silica nanochannels demonstrate acidic behavior while erbium exhibits to a greater extent basic properties. Erbium oxy- and hydroxy silicates may form on the pore surface during the annealing. The similar compounds were observed in the MMSP/ Gd_2O_3 : Eu^{3+} composite [8]. After washing the MMSP/Er with concentrated HNO_3 only erbium atoms bonded to the surface silanols were present within the particles (Fig. 3, *inset*). The abundant erbium dissolved by acid was removed from the pores and the outer surface of the particles. Thus, as a result of treatment erbium-decorated inner surface of silica nanochannels were obtained.

Conclusion

A method is proposed for functionalization of the inner surface of silica with Er^{3+} ions in order to visualize pores inside micro-mesoporous particles by TEM. The proposed approach made



it possible to significantly enhance the contrast in TEM images of MMSP. It was shown that the adsorption of erbium ions does not affect the porous structure of particles. The developed technique is simple, easily reproducible, inexpensive, and can be applied to most porous materials in which it is required to study the internal structure.

Acknowledgments

The TEM study was carried out on equipment of the Federal Joint Research Center “Material science and characterization in advanced technology”.

REFERENCES

1. Narayan R., Nayak U. Y., Raichur A. M., Garg S., Mesoporous silica nanoparticles: a comprehensive review on synthesis and recent advances. *Pharmaceutics*, 10 (3) (2018) 118.
2. Imp rator-Clerc M., Davidson P., Davidson A., Existence of a microporous corona around the mesopores of silica-based SBA-15 materials templated by triblock copolymers *Journal of the American Chemical Society*, 122 (48) (2000) 11925–11933.
3. Liu J., Zhang X., Direct observation of nanorange ordered microporosity within mesoporous molecular sieves. *Chemistry of Materials*, 14 (2002) 25362–2540.
4. Kjellman T., Asahina S., Schmitt J., Imp rator-Clerc M., Terasaki O., Alfredsson V., Direct observation of plugs and intrawall pores in SBA-15 using low voltage high resolution scanning electron microscopy and the influence of solvent properties on plug-formation. *Chemistry of Material*, 25 (20) (2013) 4105–4112.
5. Kurdyukov D. A., Eurov D. A., Kirilenko D. A., Kukushkina J. A., Sokolov V. V., Yagovkina M. A., Golubev V. G., High-surface area spherical micro-mesoporous silica particles. *Microporous and Mesoporous Materials*, 223 (2016) 225–229.
6. Kurdyukov D. A., Chernova E. N., Russkikh Y. V., Eurov D.A., Sokolov V.V., Bykova A. A., Shilovskikh V. V., Keltsieva O. A., Ubyivovk E. V., Anufrikov Y. A., Fedorova A. V., Selyutin A. A., Sukhodolov N. G., Podolskaya E. P., Golubev V. G., Ni-functionalized submicron mesoporous silica particles as a sorbent for metal affinity chromatography, *Journal of Chromatography A*, 1513 (1) (2017) 140–148.
7. Gregg S. J., Sing. K. S. W., Adsorption, Surface Area and Porosity. 2nd Ed. Academic Press, London, 1982.
8. Feofilov S. P., Kulinkin A. B., Eurov D. A., Kurdyukov D. A., Golubev V.G., Fluorescence spectroscopy study of mesoporous SiO₂ particles containing Gd₂O₃:Eu³⁺, *Material Research Express*, 1 (2) (2014) 025019.

THE AUTHORS

EUROV Daniil A.

edan@mail.ru

ORCID: 0000-0002-7471-4028

VOLKOVA Ekaterina A.

starosta194volkova@gmail.com

KIRILENKO Demid A.

zumsisai@gmail.com

ORCID: 0000-0002-1571-209X

KURDYUKOV Dmitry A.

kurd@gvg.ioffe.ru

ORCID: 0000-0002-3041-9609

STOVPIAGA Ekaterina Yu.

kattrof@gvg.ioffe.ru

ORCID: 0000-0003-0434-5252

Received 11.07.2022. Approved after reviewing 14.07.2022. Accepted 15.07.2022.

Conference materials

UDC 538.958

DOI: <https://doi.org/10.18721/JPM.153.348>

Optical absorption and Raman scattering mapping of nanoparticles patterns formed in glass by nanosecond laser in UV, VIS and IR

E. S. Babich ^{1,2✉}, V. P. Kaasik ^{1,2}, A. V. Redkov ³, A. A. Lipovskii ^{1,2}

¹ Alferov University, St. Petersburg, Russia;

² Peter the Great St. Petersburg Polytechnic University, St. Petersburg, Russia;

³ Institute of Problems of Mechanical Engineering RAS, St. Petersburg, Russia

✉ babich_es@spbstu.ru

Abstract. The paper is devoted to optical study of silver nanoparticles formed in a glass enriched with silver ions upon irradiation with nanosecond laser in UV, VIS and IR. The silver ions were introduced in glass by ion-exchange procedure. The silver nanoparticles were patterned to form spot-like (irradiation with individual laser pulses) and lines-like (laser pulses overlap on the glass surface) ensembles. Obtained optical absorption maps of spot-like and lines-like ensembles subjected to additional chemical etching of the glass reveal the impact of laser wavelength, fluence and pulse frequency on the spatial (lateral and depth) arrangement of the nanoparticles in the ensembles. The applicability of the etched and non-etched spot-like and lines-like ensembles in surface enhanced Raman scattering spectroscopy was demonstrated, and Raman scattering maps of the ensembles were obtained. The homogeneity of the signal along the ensembles and Raman enhancement factor were evaluated and compared with ones of silver nanostructures formed by other techniques.

Keywords: silver nanoparticles, glass, nanosecond laser

Funding: E.S. Babich thanks the Council for Grants of the President of the Russian Federation project SP-1491.2021.4. V. P. Kaasik and A. A. Lipovskii thank the Ministry of Science and Higher Education of the Russian Federation project FSRM-2020-001.

Citation: Babich E. S., Kaasik V. P., Redkov A. V., Lipovskii A. A., Optical absorption and Raman scattering mapping of nanoparticles patterns formed in glass by nanosecond laser in UV, VIS and IR. St. Petersburg State Polytechnical University Journal. Physics and Mathematics, 15 (3.3) (2022) 244–249. DOI: <https://doi.org/10.18721/JPM.153.348>

This is an open access article under the CC BY-NC 4.0 license (<https://creativecommons.org/licenses/by-nc/4.0/>)

Материалы конференции

УДК 538.958

DOI: <https://doi.org/10.18721/JPM.153.348>

Оптическое и рамановское картирование структур из наночастиц, сформированных в стекле под действием наносекундного УФ, ВИД и ИК лазерного излучения

Е. С. Бабич ^{1,2✉}, В. П. Каасик ^{1,2}, А. В. Редьков ³, А. А. Липовский ^{1,2}

¹ Академический университет им. Ж.И. Алфёрова РАН, Санкт-Петербург, Россия;

² Санкт-Петербургский Политехнический университет Петра Великого, Санкт-Петербург, Россия;

³ Институт проблем машиноведения РАН, Санкт-Петербург, Россия

✉ babich_es@spbstu.ru

Аннотация. Работа посвящена разработке и исследованию серебряных наночастиц, сформированных в обогащенном ионами серебра стекле под действием наносекундного лазерного излучения. Установлено влияние длины волны и плотности энергии лазерного излучения, а также частоты следования импульсов, на пространственное распределение



и оптические характеристики формируемых частиц. Продемонстрирована возможность применения наночастиц в спектроскопии поверхностно-усиленного рамановского рассеяния света.

Ключевые слова: серебряные наночастицы, стекло, наносекундный лазер

Финансирование: Е. С. Бабич благодарит Совет по грантам Президента РФ, стипендия СП-1491.2021.4. Исследования В. П. Каасика и А. А. Липовского выполнены в рамках Государственного задания «Исследование структур микро- и нанопластики, формируемых в аморфных диэлектриках под действием сильных локальных полей» (код темы FSRM-2020-001).

Ссылка при цитировании: Бабич Е. С., Каасик В. П., Редьков А. В., Липовский А. А. Оптическое и рамановское картирование структур из наночастиц, сформированных в стекле под действием наносекундного УФ, ВИД и ИК лазерного излучения // Научно-технические ведомости СПбГПУ. Физико-математические науки. 2022. Т. 15. № 3.3. С. 244–249. DOI: <https://doi.org/10.18721/JPM.153.348>

Статья открытого доступа, распространяемая по лицензии CC BY-NC 4.0 (<https://creativecommons.org/licenses/by-nc/4.0/>)

Introduction

Metal nanoparticles (NPs) are known for their extraordinary optical properties. Their resonance light absorption at the wavelength of localized surface plasmon resonance (LSPR) is accompanied by giant enhancement of electric field nearby surface. This enhancement intensifies light-matter interaction allowing, in particular, detection of single molecules via surface enhanced Raman scattering (SERS) [1]. The developing approach to the formation of NPs is reduction of metal ions, which are embedded into a glass, by irradiation of UV-IR short pulse lasers. Commonly, silver ions are introduced in glass via ion-exchange [2] or ion implantation [3]. The laser irradiation reduces embedded silver ions due to the glass heating by absorbed light [4] (similarly to the reduction of silver ions in thermally heated glasses [5]) and generation of free electrons by multiphoton absorption or avalanche ionization followed by the reaction $\text{Ag}^+ + e^- \rightarrow \text{Ag}^0$ [6]. Clustering of silver atoms in heated/softened glass results in the formation of silver NPs. One of the advantages of the described approach, similarly to using profiled electrodes and thermal poling [7] is patterning of NPs distribution according to a given template, which opens up possibilities to integrate NPs in microfluidic chips and create lab-on chip devices based on SERS [8]. However, to imply NPs in SERS one should ensure that they meet criteria of sufficient Raman enhancement and homogenous signal distribution along the active area. In this study, we reveal impact of laser wavelength, fluence and pulse frequency on spatial arrangement and SERS-activity of silver NPs ensembles laser-drawn on the glass surface.

Materials and Methods

In the experiments we used soda-lime silicate glass and introduced silver ions in the subsurface glass layer via $\text{Na}^+ \leftrightarrow \text{Ag}^+$ ion-exchange [9]: the glass was immersed into the melt of $(\text{AgNO}_3)_{5\text{wt.}\%}(\text{NaNO}_3)_{95\text{wt.}\%}$ at 325 °C for 20 min. We irradiated the glass with 6 ns pulses of Nd:YAG laser (Litron Nano L) at wavelength, λ , of 1.06, 0.53 and 0.35 μm . Moving the glass in the plane perpendicular to the laser beam at the speed of 200 $\mu\text{m/s}$ and varying laser pulse frequency we patterned NPs to draw “lines” (pulses overlapping on the glass surface) and “spots” (individual pulses). The frequencies were chosen for each wavelength individually considering the diameter of the laser beam, which was 90, 160 and 250 μm for $\lambda = 0.35, 0.53$ and 1.06 μm , respectively. The parameters of the patterning are presented in Table 1.

Both “lines” and “spots” showed characteristic yellowish coloration induced by optical absorption at ~ 450 nm (silver NPs LSPR [10]). To map the LSPR intensity distribution we used homemade setup that included a halogen lamp (Ocean Optics HL-2000-FHSA-LL), a modular spectrometer (Solar LS SC82), a translation stage and a camera. Normally incident white light was focused by 10x/0.25 objective on the glass surface to the spot of the diameter of 80 μm , 90% of the light passed through the glass was collected by a second 10x/0.25 objective and analyzed

Table 1

The parameters of the laser patterning of silver ions-enriched glass

Laser wavelength, μm	Laser fluence, J/cm^2		
	5.4	10.3	12.6
1.06	–	0.5 Hz / 2 Hz	0.5 Hz / 2 Hz
0.53	–	1 Hz / 2 Hz	1 Hz / 2 Hz
0.35	1 Hz / 3 Hz	1 Hz / 3 Hz	–

with the spectrometer, while 10% was directed to the camera, which allowed precise positioning of the glass using the stage. Absorption spectra were measured along the “lines” and “spots” with $40\ \mu\text{m}$ step by moving the stage in the plane perpendicular to optical axis of the setup.

To reveal NPs spatial arrangement we obtained LSPR intensity distributions for the glass subjected to the laser irradiation and additional chemical etching in $\text{HF}(5\mu\text{l}):\text{NH}_4\text{F}(5\text{g}):\text{H}_2\text{O}(40\text{g})$ for 2, 4, 6 and 8 min. We characterized the glass surface with optical profilometer (Zygo NewView 6000) before and after 8 min etching.

Etched and non-etched laser-irradiated glasses were tested in SERS of 1,2-di(4-pyridyl) ethylene (BPE) using confocal Raman microscope (Witec Alpha 300R) with $10\times/0.25$ objective and $532\ \text{nm}$ excitation laser. The droplet of BPE water solution was dried on the glass surface, the molecular coverage being several monolayers, $\sim 10^{-11}\ \text{mol}/\text{mm}^2$. To evaluate Raman enhancement we also tested BPE crystallites ($\sim 10^{-8}\ \text{mol}/\text{mm}^2$) placed on the surface of the virgin glass (plain Raman measurements). The spectra acquisition time was 1 s and laser power was 0.7 and 33 mW for SERS and Raman measurements, respectively.

Result and discussion

The glass surface characterization demonstrated that the laser drawing of “lines” and “spots” results in formation of craters which lateral size corresponds to the size of laser spot. The crater profile does not change in the course of the etching, and therefore, etching rate of the laser-irradiated glass corresponds to one of the pristine glass, being $\sim 23\ \text{nm}/\text{min}$. Considering this, we analyzed optical and SERS maps obtained for the glass subjected to the laser irradiation and additional 2–8 min etching.

Typical LSPR intensity distribution across laser-drawn “spot” before and after the etching is illustrated with Fig. 1, *a*. One can see, the maximal absorption corresponds to the center of the “spot”, which evidences formation of higher number of silver NPs in this region. The absorption decreases in the course of the etching, which indicates removal of NPs. The derivatives of functions of maximal absorption on thickness of the etched glass layer for the “spots” irradiated at different laser wavelengths and laser fluencies are presented in Fig. 1, *b–d*. One can see, NPs form within thin subsurface glass layer, $< 150\ \text{nm}$, the maximal concentration being at $\sim 50\text{--}100\ \text{nm}$ under the surface for all the wavelengths. Note, for $\lambda = 1.06\ \mu\text{m}$ the increase in the laser fluence results in the appearance of two regions enriched with NPs - they form near the surface and deeper in the glass bulk (see Fig. 1, *b*) that is two-layer ensemble. For $\lambda = 0.35$ and $0.53\ \mu\text{m}$ (Fig. 1, *c*, *d*) the increase in the laser fluence results in formation of NPs deeper in glass and closer to the surface, respectively.

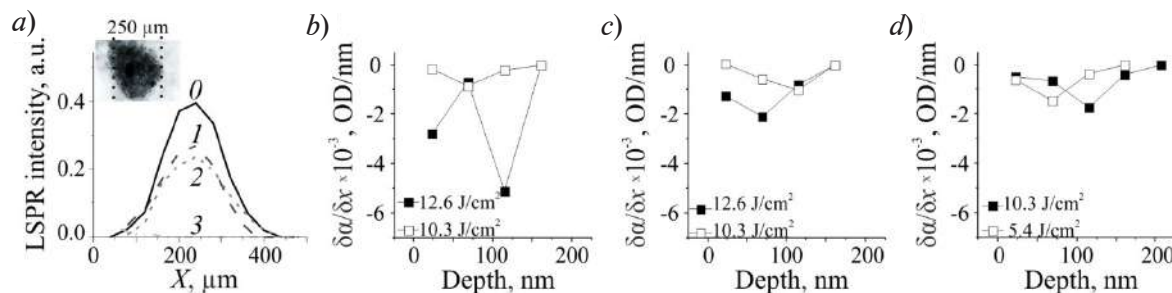


Fig. 1. Typical LSPR intensity distribution across laser-drawn “spot” before (0) and after etching off 45 (1), 90 (2) and 140 nm (3) of glass (*a*). The derivatives of functions of maximal absorption on thickness of etched glass $\delta\alpha/\delta x$ for the “spots” irradiated at 1.06 (*b*), 0.53 (*c*) and 0.35 μm (*d*) laser wavelengths. Fig. 1, *a* corresponds to the “spot” formed at 1.06 μm , 12.6 J/cm^2 and 0.5 Hz.



Fig. 2, *a* presents typical LSPR intensity distribution along etched and non-etched laser-drawn “line”. One can see, the overlapping of the laser pulses on the glass surface results in formation of silver NPs that are uniformly distributed along the “line” - the relative standard deviation (RSD) of the absorption is only 6% for the non-etched “line” presented in Fig. 2, *a*. For $\lambda = 1.06$ and $0.35 \mu\text{m}$ the derivatives of functions of the average absorption on thickness of the etched off glass layer demonstrate relatively uniform depth distribution of NPs within ~ 200 nm (see Fig. 2, *b*, *d*). For $\lambda = 0.53 \mu\text{m}$ NPs concentrated at ~ 50 nm under the glass surface (see Fig. 2, *c*).

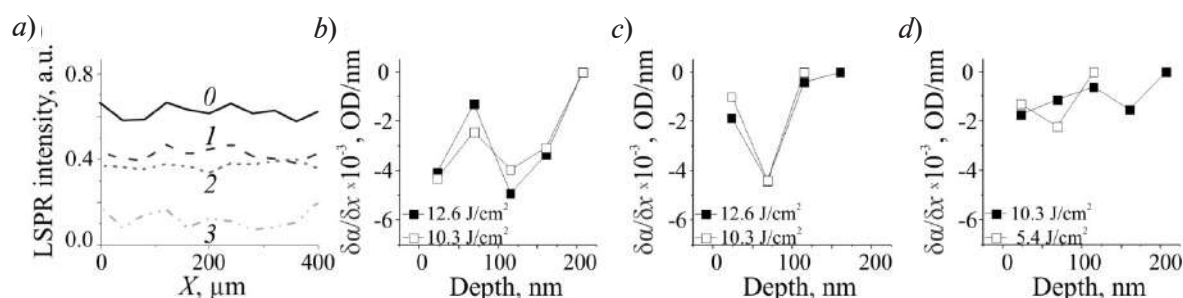


Fig. 2. Typical LSPR intensity distribution across laser-drawn “line” before (0) and after etching off 45 (1), 90 (2) and 140 nm (3) of glass (*a*). The derivatives of functions of average absorption on thickness of etched glass $\delta\alpha/\delta x$ for the “lines” irradiated at 1.06 (*b*), 0.53 (*c*) and 0.35 μm (*d*) laser wavelengths.

Fig. 1, *a* corresponds to the “line” formed at 1.06 μm , 12.6 J/cm^2 and 2 Hz

Thus, in most cases of laser-drawing, concentration of NPs is maximal at ~ 50 nm under the glass surface. Indeed, NPs formation is governed by glass heating [4], and the heat penetration depth determined by laser pulse duration and glass thermal diffusivity [11] is ~ 55 nm.

We tested formed NPs in SERS before and after removal of ~ 50 nm of glass. The SERS signal was undetectable for the non-etched samples, which evidences that NPs are completely covered with glass. Typical SERS signal distributions along etched “spot” and “line” are presented in Fig. 3, *a*, *b* respectively. One can see, SERS maps are similar to optical ones: maximal signal is detected in the center of the “spot”, and signal is relatively uniform along the “line”. Note, at the fixed laser fluence the decrease of the wavelength results in decreasing RSD of SERS signal along the “line” from 102% to 41%. For $\lambda = 0.35$ and $0.53 \mu\text{m}$ the increase in the fluence results in decreasing RSD, the minimal RSD being 29% for $\lambda = 0.53 \mu\text{m}$. The “line” drawn at 1.06 μm and high fluence demonstrates the highest RSD, 225%.

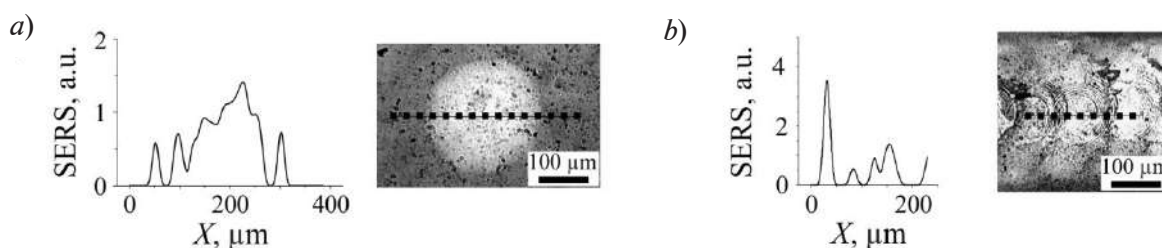


Fig. 3. Typical SERS signal distributions along etched “spot” (*a*) and “line” (*b*)

Fig. 1, *a*, *b* correspond to the “spot” and “line” formed at 1.06 μm , 12.8 J/cm^2 , 0.5 and 2 Hz, respectively

We evaluated enhancement factor (EF) provided by NPs ensembles using the procedure described in Ref. [12]. We used maximal and average SERS signal for evaluation of “spot” and “line” EFs, respectively. The “spot” and “line” EFs are in $\sim 2\text{--}4 \cdot 10^5$ and $\sim 0.6\text{--}4 \cdot 10^5$ range, respectively. The maximal EF is for the “spot” drawn at 0.53 μm and 12.6 J/cm^2 , and for the “line” drawn at 0.35 μm and 5.4 J/cm^2 . The minimal EF is for the “spot” and “line” formed at 1.06 μm , 12.6 and 10.3 J/cm^2 , respectively. The tendency is clear: the ensembles provided maximal EF have maximal concentration of NPs at ~ 50 nm under the surface (see Fig. 1 and 2). The patterns formed at 1.06 μm provide minimal EF because of the two-layer ensemble of NPs – the peaks of their concentrations are at ~ 25 and ~ 100 nm under the surface.

Thus, one can expect higher EF by etching NPs ensembles obtained at 1.06 μm shorter or longer time. Nevertheless, obtained EFs are comparable with ones demonstrated by nanostructures formed, for example, by laser nanostructuring of soda-lime glass with the subsequent deposition of thin silver film [13], by femtosecond laser sintering of silver NPs paste [14] or by femtosecond laser induced plasma assisted ablation of silicon wafer followed by deposition of thin silver film [15].

Conclusion

We demonstrated that the irradiation of silver ions-enriched soda-lime glass with 6 ns-long laser pulse at 1.06, 0.53 and 0.35 μm wavelength results in formation of silver nanoparticles in the area corresponded to the size of laser spot. The maximal concentration of nanoparticles is in the center of the spot, and ~ 50 nm under the glass surface for 0.35 and 0.53 μm irradiation and at ~ 25 nm and ~ 100 nm for 1.06 μm irradiation. The irradiation of the glass with the pulses overlapping on the glass surface (“line”), which was provided by moving the glass in the course of the irradiation, results in formation of nanoparticles that are uniformly distributed along the “line”. After the removal of ~ 50 nm glass surface layer, formed ensembles of silver nanoparticles are applicable in SERS. The Raman enhancement provided by the nanoparticles is in $\sim 6 \cdot 10^4 - 4 \cdot 10^5$ range, depending on the laser wavelength, fluence and pulse frequency. Distribution of Raman signal along active area is close to uniform for the ensembles formed under 0.35 and 0.53 μm irradiation, the minimal relative standard deviation of signal being 29%.

REFERENCES

1. Li C., Huang Y., Li X., Zhang Y., Chen Q., Ye Z., Alqarni Z., Bell S. E. J., Xu Y., Towards practical and sustainable SERS: a review of recent developments in the construction of multifunctional enhancing substrates, *Journal of Materials Chemistry C*. 9 (2021) 11517–11552.
2. Berger A., Concentration and size depth profile of colloidal silver particles in glass surfaces produced by sodium-silver ion-exchange, *Journal of Non-Crystalline Solids*. 151 (1992) 88–94.
3. Vytkačova S., Svecova B., Nekvindova P., Spirkova J., Mackova A., Miksova R., Buttger R., The formation of silver metal nanoparticles by ion implantation in silicate glasses, *Nuclear Instruments and Methods in Physics Research, Section B: Beam Interactions with Materials and Atoms*. 371 (2016) 245–250.
4. Wackerow S., Abdolvand A., Generation of silver nanoparticles with controlled size and spatial distribution by pulsed laser irradiation of silver ion-doped glass, *Optics Express*. 22 (2014) 5076.
5. Zhang J., Dong W., Sheng J., Zheng J., Li J., Qiao L., Jiang L., Silver nanoclusters formation in ion-exchanged glasses by thermal annealing, UV-laser and X-ray irradiation, *Journal of Crystal Growth*. 310 (2008) 234–239.
6. Blondeau J., Pellerin S., Vial V., Dzierżęga K., Pellerin N., Andreazza-Vignolle C., Influence of pulsed laser irradiation on precipitation of silver nanoparticles in glass, *Journal of Crystal Growth*. 311 (2008) 172–184.
7. Chervinskii S., Sevriuk V., Reduto I., Lipovskii A., Formation and 2D-patterning of silver nanoisland film using thermal poling and out-diffusion from glass, *Journal of Applied Physics* 114 (2013) 224301.
8. Stankevičius E., Garliauskas M., Laurinavičius L., Trusovas R., Tarasenko N., Pauliukaitė R., Engineering electrochemical sensors using nanosecond laser treatment of thin gold film on ITO glass, *Electrochimica Acta*. 297 (2019) 511–522.
9. Babich E., Kaasik V., Reduto I., Scherbak S., Lipovskii A., Kinetics of nanoparticles formation under UV, VIS and IR nanosecond laser irradiation of a silver-ions-enriched glass, *Journal of Laser Micro/Nanoengineering*. 16 (2021) 88–93.
10. Amendola V., Bakr O., Stellacci F., A study of the surface plasmon resonance of silver nanoparticles by the discrete dipole approximation method: effect of shape, size, Structure, and assembly, *Plasmonics*. 5 (2010) 85–97.
11. Jacinto C., Messias D., Andrade A., Lima S., Baesso M., Catunda T., Thermal lens and Z-scan measurements: Thermal and optical properties of laser glasses - A review, *Journal of Non-Crystalline Solids*. 352 (2006) 3582–3597.



12. **Babich E., Kaasik V., Redkov A., Maurer T., Lipovskii A.**, SERS-active pattern in silver-ion-exchanged glass drawn by infrared nanosecond laser, *Nanomaterials*. 10 (2020) 1849.
13. **Aleknavičienė I., Pabrėža E., Talaikis M., Jankunec M., Račiukaitis G.**, Low-cost SERS substrate featuring laser-ablated amorphous nanostructure, *Applied Surface Science*. 571 (2022) 151248.
14. **Kurnoothala R., Muthukumar S., Vishnubhatla K.**, Facile fabrication of integrated microfluidic SERS substrate by femtosecond laser sintering of silver nano particles, *Optical Materials*. 111 (2021) 110518.
15. **Xu L., Liu H., Chua T., Hong M., Zhou H.**, Fabrication of SERS substrates by femtosecond LIPAA for detection of contaminants in foods, *Optics and Laser Technology*. 151 (2022) 107954.

THE AUTHORS

BABICH Ekaterina S.
babich_es@spbstu.ru
ORCID: 0000-0003-4970-2591

REDKOV Alexey V.
red-alex@mail.ru
ORCID: 0000-0002-2748-6966

KAASIK Vladimir P.
vkaasik@yandex.ru
ORCID: 0000-0002-9976-6721

LIPOVSKII Andrey A.
lipovskii@mail.ru
ORCID: 0000-0001-9472-9190

Received 11.07.2022. Approved after reviewing 17.07.2022. Accepted 18.07.2022.

Conference materials
UDC 539.23, 620.3
DOI: <https://doi.org/10.18721/JPM.153.349>

Langmuir-Blodgett technology to obtain semi-magnetic photosensitive materials

S. V. Stetsyura ¹, P. G. Kharitonova ¹✉, E. G. Glukhovskoy ¹

¹ Saratov State University, Saratov, Russia

✉ haritonovapg@gmail.com

Abstract. We studied the technological modes of obtaining of nanoscale coatings containing a controlled number of iron atoms on a semiconductor substrate by Langmuir-Blodgett technology. We determined the regime of obtaining a monolayer of iron arachinate with the maximum content of iron atoms into monolayer. The analysis of compression isotherms made it possible to determine the surface density of the of iron atoms. Modeling the processes of diffusion taking into account the limited solubility Fe in CdS makes it possible to estimate the number of iron arachinate monolayers required to form a heterophase material that exhibits magnetic properties. The diffusion coefficient of Fe atoms in CdS was determined experimentally from the profile of iron distribution in CdS obtained using secondary ion mass spectrometry. The model allows to predict the density and depth of the occurrence of the nanosized iron -containing phases. It was obtained that 30 monolayers of iron arachinate obtained at pH = 5.83 provide the formation of nanosized phases at a depth of up to 300 μm. The annealing was for 30 minutes at a temperature of 450 °C.

Keywords: Langmuir-Blodgett technology, heterophase material, ferromagnetic phase, semi-magnetic material, monolayer, diffusion

Funding: The work was carried out at the expense of the Russian Science Foundation (project No. 22-22-00194, <https://rscf.ru/en/project/22-22-00194/>).

Citation: Stetsyura S. V., Kharitonova P. G., Glukhovskoy E. G., Langmuir-Blodgett technology to obtain semi-magnetic photosensitive materials. St. Petersburg State Polytechnical University Journal. Physics and Mathematics, 15 (3.3) (2022) 250–254. DOI: <https://doi.org/10.18721/JPM.153.349>

This is an open access article under the CC BY-NC 4.0 license (<https://creativecommons.org/licenses/by-nc/4.0/>)

Материалы конференции
УДК 539.23, 620.3
DOI: <https://doi.org/10.18721/JPM.153.349>

Технология Ленгмюра-Блоджетт для получения полумагнитных фоточувствительных материалов

С. В. Стецюра ¹, П. Г. Харитоновна ¹✉, Е. Г. Глуховской ¹

¹ Саратовский государственный университет имени Н. Г. Чернышевского, Саратов, Россия

✉ haritonovapg@gmail.com

Аннотация. Проведено исследование и апробация технологических режимов получения на полупроводниковой подложке наноразмерных покрытий, содержащих контролируемое количество атомов железа, по технологии Ленгмюра-Блоджетт. Моделирование процессов диффузии атомов Fe позволяет прогнозировать с высокой точностью плотность и глубину залегания наноразмерных железосодержащих фаз.

Ключевые слова: технология Ленгмюра-Блоджетт, гетерофазный материал, ферромагнитная фаза, полумагнитный материал, монослой, диффузия

Финансирование: Исследование выполнено за счет гранта Российского научного фонда № 22-22-00194, <https://rscf.ru/project/22-22-00194/>.



Ссылка при цитировании: Стецюра С. В., Харитонов П. Г., Глуховской Е. Г. Технология Ленгмюра-Блоджетт для получения полумагнитных фоточувствительных материалов // Научно-технические ведомости СПбГПУ. Физико-математические науки. 2022. Т. 15. № 3.3. С. 250–254. DOI: <https://doi.org/10.18721/JPM.153.349>

Статья открытого доступа, распространяемая по лицензии CC BY-NC 4.0 (<https://creativecommons.org/licenses/by-nc/4.0/>)

Introduction

Of special interest are the materials whose properties can be controlled by various external effects (for example, a magnetic field and an optical range radiation). This possibility increases the functionality of devices made on the basis of these materials. Such materials are soft magnetic homogeneous and semi-magnetic heterophase materials [1], which have a perspective for use in modern industries and are interesting for science due to the variety of their properties. Previously, massive monocrystals of solid solutions were mainly investigated [2]. But in recent years, significant attention is paid to the study of the film and nanolayer [3] of soft magnetic materials and structures. Heterophase semi-magnetic photosensitive materials are not enough studied due to the lack of reproducible (proven) technology and modelling views about obtaining such material with optimal and reproducible characteristics. Cadmium sulfide (CdS) can be used as a semiconductor matrix to create soft magnetic structures, because CdS has high photosensitivity, and its technology is well detailed for film polycrystalline forms and monocrystalline substrates. We have demonstrated [4] that the Fe-doping of CdS makes it possible to obtain heterophase structures based on a paramagnetic matrix of a solid solution CdS:Fe with ferromagnetic inclusions of FeS and Fe₂O₃, which are formed as a result of the processes of self-organization and decomposition of a supersaturated solid solution due to the limited solubility of Fe in CdS.

Previously, we created a semi-magnetic heterophase material based on a CdS:Fe solid solution by thermal evaporation of all components of this material [4]. As a result, a film sample with the properties of a semi-magnetic material was obtained. However, the method of thermal evaporation does not allow us to obtain materials with a predictable arrangement of nanoscale phases and to control the size of these phases.

The aim of this work is the study and testing of technological modes and conditions for producing of nanoscale coatings containing a controlled number of iron atoms on a semiconductor substrate by Langmuir-Blodgett technology. The modeling of diffusion processes of Fe atoms in a photosensitive substrate allows us to predict density and depth of the occurrence of nanoscale iron-containing phases to high precision.

Materials and Methods

The Langmuir-Blodgett technology makes it possible to form multilayer nanoscale layers of surface-active substances at the liquid-gas interface with a thickness of each monolayer of one molecule. Monolayers play the role of an organic matrix, which can include various functional elements. This feature of the formation of monolayers is used for dosed transfer of metal atoms onto a solid substrate. It is possible to obtain clusters of a size-defined by changing the mode and conditions of filming process.

In our work, arachic acid (AA) C₁₉H₃₉COOH was used as an organic matrix. We have chosen arachic acid because the length of the carbon chain ensures its almost complete insolubility in water. This circumstance determines the production of a monolayer stable in time with a high ordering of molecules in the layer, which makes it possible to obtain high reproducibility of the processes of formation and transfer of monolayers. FeCl₃ salt was used as a source of iron. To obtain Langmuir-Blodgett films we used equipment of monolayer deposition KSV-Nima LBThrough Medium KN 2002 (KSV-Nima, Finland). This trough is equipped with two moving barriers that provide symmetrical bilateral compression, with an accuracy of positioning the barriers and determining the area occupied by the monolayer, up to 0.1%. The measurement of surface tension was carried out by weighing the Wilhelmy plate, while the accuracy of determining the surface pressure was 0.01 mN/m.

The arachic acid was diluted in chloroform to a concentration of 0.001 mol/L and injected in a volume of 50 μl onto the surface of an aqueous solution of FeCl_3 to obtain monolayers. The amount of iron and its the distribution density in the layer of a surface-active substances depend on the pH of the subphase where films were formed and the concentration of FeCl_3 . In our experiments, the concentration of FeCl_3 was 10^{-3} mol/L. To develop the most efficient regime for obtaining an iron-containing coating, the pH value of the aqueous subphase was varied in the range from 3.7 to 8.

After preparing the solution and introducing the surfactant, the monolayer was compressed by a moving barrier at a rate of 1 cpm until a close-packed layer was formed, which was recorded by the π - A isotherm. The monolayer was transferred to the substrate surface by the Langmuir-Schaeffer method. The temperature, surface pressure π of the monolayer, and the average area A per molecule in the monolayer were controlled during the process of obtaining a close-packed monolayer. The optimal technological parameters are air and subphase temperature -23 ± 1 $^{\circ}\text{C}$, surface pressure -18 mN/m, which were kept constant in the process of obtaining the layer. Under these conditions, iron-containing monolayers were transferred onto a solid substrate.

Semiconductor single-crystal wafers (CdS) were used as solid substrates for transferring the obtained iron-containing films. The surface quality of the wafers and low specific resistivity made it possible to comprehensively study the resulting nanoscale coatings.

Auger electron spectroscopy combined with layer-by-layer ion etching of the substrate was used to characterize the distribution of Fe in the obtained heterophase samples “organic coating-semiconductor substrate”, annealed at a temperature of 450 $^{\circ}\text{C}$ for 30 minutes. The bombardment was by argon atoms with an energy of 3 keV, which made it possible to introduce minimal distortions into the chemical composition of the measured layer.

Results and Discussion

Fig. 1 shows the π - A isotherms of iron arachinate monolayers obtained at different pH values of an aqueous FeCl_3 solution and for an impurity-free arachic acid monolayer.

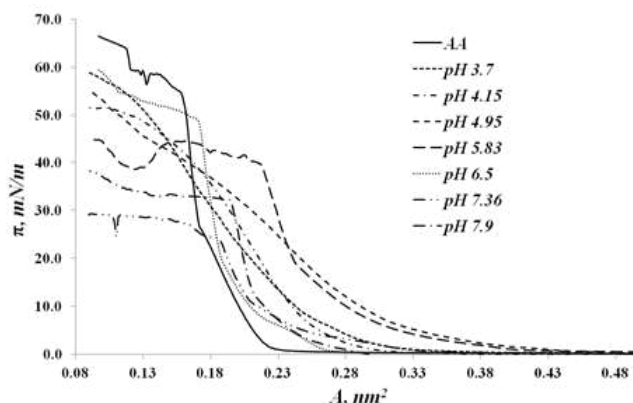


Fig. 1. Dependences of the surface pressure π of a monolayer on the area A per one molecule for arachic acid (AA) and its salts at different pH values of the solution

The values of the average area per molecule were determined in monolayers of iron arachinate obtained at different pH values by approximating the sections on the compression isotherms corresponding to the solid-crystalline state (Fig. 2).

The area per molecule for an arachic acid monolayer is 0.22 nm^2 . For iron arachinate films, the packing density of molecules was varied across the entire range of pH values. Changes in the area per molecule A ranged from 0.25 nm^2 to 0.32 nm^2 . Moreover, at pH from 3.7 to 5.8, the value of A increased, then practically stabilized at a value of 0.32 nm^2 . Starting from pH = 6.5 the area per molecule began to decrease and at pH = 7.36 it reached a minimum value of 0.22 nm^2 .

Most researchers explain the increase in the area per molecule with the incorporation of metal atoms into the surfactant monolayer. The proportion of acid molecules converted to salt changes with pH variation: the larger this proportion, the greater the average area per molecule

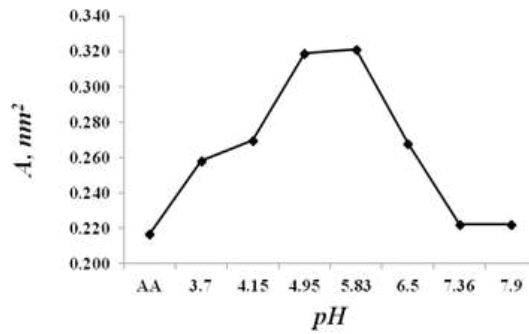


Fig. 2. Average area per molecule in monolayers of arachic acid (AA) and its salts at different pH values

in the monolayer. In an alkaline medium, metal clusters can attach to the film and metal can precipitate. In the first case, there is an increase in the area per molecule A , and in the second case, the value of A can decrease almost to the value corresponding to arachic acid without metal inclusions. Analysis of Fig. 2 shows that the maximum number of Fe atoms is incorporated into the monolayer in the range of pH values from 5 ± 0.2 to 6 ± 0.2 . The stabilization of the maximum value of the area per molecule suggests that all acid molecules in the monolayer have attached Fe and converted to salt.

Fig. 3 shows the iron distribution profiles in single-crystal CdS wafers with 30 deposited monolayers of iron arachinate, obtained at pH = 5.83. The measurements were carried out before and after high-temperature annealing at a temperature of 450 °C.

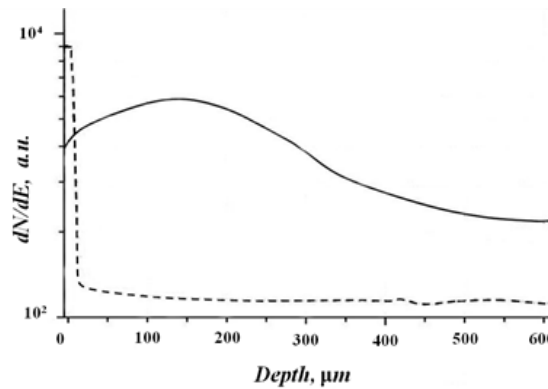


Fig. 3. Iron distribution profiles before (dashed lines) and after high-temperature annealing (solid lines)

It follows from the graph that the thickness of the Fe layer is less than 10 µm for an unannealed sample that corresponds to the film thickness of iron arachinate. After annealing, Fe is recorded over the entire thickness of the substrate (600 µm), but an increased content of Fe is observed in the layer up to 300 µm. If before annealing the profile was a step function, then after annealing it is a part of the Gaussian function. Therefore, the Gaussian equation can be used to describe diffusion:

$$N(x, t) = \frac{nN_s}{\sqrt{\pi Dt}} \exp\left(-\frac{x^2}{4Dt}\right) \quad (1)$$

where $N(x, t)$ is the impurity concentration at a depth x from the surface after diffusion for time t ; N_s is the surface density of Fe atoms in a monolayer; n is the number of monolayers; D is the diffusion coefficient (in this case, iron atoms).

The value of N_s was calculated based on the area per molecule of iron arachinate, on the basis of π - A isotherms. The calculated average area per one molecule was 0.32 nm², then $N_s = 3.125 \cdot 10^{14}$ cm⁻². Annealing time $t = 1800$ s. The diffusion coefficient D obtained using these parameters is $0.16 \cdot 10^{-10}$ cm²/s, which corresponds to the literature data.

The model of the diffusion of metal atoms in a semiconductor substrate taking into account the limited solubility [5] allows us to confirm the formation of iron solid solutions over the entire thickness of the substrate and the possible precipitation of iron atoms at the depth up to 300 μm with the formation of a ferromagnetic phase.

Conclusion

The researched technology allows us to obtain a heterophase nanostructured photoconductor with ferromagnetic phases. The use of organic nanoscale coatings structured by iron ions as a source of impurity makes it possible to set the required depth of formation of the ferromagnetic phase. Model of diffusion of metal atoms in a semiconductor photosensitive substrate taking into account the limited solubility Fe in CdS makes it possible to estimate the number of iron arachinate monolayers required to form a heterophase material that exhibits magnetic properties.

Acknowledgments

The work was carried out at the expense of the Russian Science Foundation (project No. 22-22-00194, <https://rscf.ru/en/project/22-22-00194/>).

REFERENCES

1. Jindal S., Sharma P., Ferromagnetic transition metal-doped CdS nanoparticles: a comparative study, *Journal of Materials Science: Materials in Electronics*. 31 (2020) 20295–20302.
2. Ivanchik I. I., Khokhlov D. R., De Visser A., Characteristic features of the magnetoresistance of $\text{Pb}_{1-x}\text{Sn}_x\text{Te}(\text{In})$ and $\text{Pb}_{1-x}\text{Mn}_x\text{Te}(\text{In})$ alloys in ultrastrong magnetic fields, *Semiconductors*. 30 (8) (1996) 732–742.
3. Nuriyev I. R., Mehrabova M. A., Nazarov A. M., Hasanov N. H., Sadigov R. M., Farzaliyev S. S., Farajov N. V., Structure and surface morphology of $\text{Cd}_{1-x}(\text{Mn}, \text{Fe})_x\text{Se}$ epitaxial films, *Journal of Surface Investigation: X-ray, Synchrotron and Neutron Techniques*. 13 (6) (2019) 1083.
4. Stetsyura S. V., Kharitonova P. G., Malyar I. V., Semi-magnetic film coating based on a photosensitive semiconductor, *Applied Physics*. 5 (2020) 66–72.
5. Stetsyura S. V., Malyar I. V., Serdobintsev A. A., Klimova S. A., Effect of parameters of narrow-gap inclusions on the type and intensity of secondary-ion photoeffect in heterophase photosensitive semiconductors, *Semiconductors* 43 (8) (2009) 1064–1070.

THE AUTHORS

STETSYURA Svetlana V.
stetsyurasv@mail.ru
ORCID: 0000-0002-4337-012X

GLUKHOVSKOY Evgeny G.
glukhovskoy@gmail.com
ORCID: 0000-0002-8282-3638

KHARITONOVA Polina G.
haritonovapg@gmail.com
ORCID: 0000-0003-0591-9908

Received 25.07.2022. Approved after reviewing 26.07.2022. Accepted 02.08.2022.

Conference materials
UDC 546.05; 538.975
DOI: <https://doi.org/10.18721/JPM.153.350>

The effect of the seed layer on the TiO₂ nanotubes coatings quality grown on the glass substrates by hydrothermal synthesis

M. G. Volkova ^{1, 2}✉, A. P. Ivanishcheva ², V. V. Petrov ², E. M. Bayan ¹

¹ Southern Federal University, Rostov-on-Don, Russia;

² Research and Education Centre "Microsystem technics and multisensor monitoring systems", Southern Federal University, Taganrog, Russia

✉ mvol@sfedu.ru

Abstract. Coatings of titanium dioxide nanotubes were obtained on glass substrates by hydrothermal synthesis method. The influence of the seed layer synthesis method on the coatings quality was studied. The synthesized materials are nanoscale, crystallized in a mixed anatase-rutile modification. It was shown that for seed layers deposited by low-temperature solid-phase pyrolysis technique, the coatings are more homogeneous than for seed layers deposited by sol-gel method. In addition, a tendency to agglomeration was noted for nanotubes grown on a seed layer deposited by the sol-gel method. The electrophysical properties study showed that for materials with a seed layer obtained by the sol-gel method, the resistance is an order of magnitude higher than for materials with a seed layer synthesized by low-temperature pyrolysis technique. The activation energy (E_a) for titanium dioxide nanotubes (seed layer is applied by sol-gel method) was 0.74 eV, and for the sample obtained by low-temperature pyrolysis E_a was 0.68 eV.

Keywords: titanium dioxide, thin films, hydrothermal synthesis, seed layer, nanotubes

Funding: This work was financially supported by the RFBR, project No. 20-07-00653 A.

Citation: Volkova M. G., Ivanishcheva A. P., Petrov V. V., Bayan E. M., The effect of the seed layer on the TiO₂ nanotubes coatings quality grown on the glass substrates by hydrothermal synthesis. St. Petersburg State Polytechnical University Journal. Physics and Mathematics, 15 (3.3) (2022) 255–259. DOI: <https://doi.org/10.18721/JPM.153.350>

This is an open access article under the CC BY-NC 4.0 license (<https://creativecommons.org/licenses/by-nc/4.0/>)

Материалы конференции
УДК 546.05; 538.975
DOI: <https://doi.org/10.18721/JPM.153.350>

Влияние затравочного слоя на качество покрытий из нанотрубок TiO₂ выращенных на стеклянных подложках гидротермальным методом

М. Г. Волкова ^{1, 2}✉, А. П. Иванищева ², В. В. Петров ², Е. М. Баян ¹

¹ Южный федеральный университет, Ростов-на-Дону, Россия;

² НОЦ «Микросистемная техника и мультисенсорные мониторинговые системы», Южный федеральный университет, Таганрог, Россия

✉ mvol@sfedu.ru

Аннотация. Покрытия из нанотрубок диоксида титана были получены на стеклянных подложках гидротермальным методом. В ходе работы было изучено влияние метода синтеза затравочного слоя на получаемые покрытия. Синтезированные материалы наноразмерны, кристаллизуются в смешанной анатазно-рутильной модификации. Показано, что для затравочных слоев, нанесенных методом низкотемпературного твердофазного пиролиза, покрытия более однородные, чем для затравочных слоев, нанесенных золь-гель методом. Кроме того, для нанотрубок выращенных на

затравочном слое, нанесенном золь-гель методом, была отмечена склонность к агломерации. Изучение электрофизических свойств показало, что для материалов с затравочным слоем, полученным золь-гель методом, сопротивление на порядок выше, чем для материалов с затравочным слоем синтезированным низкотемпературным пиролизом. Энергия активации (E_a) для нанотрубок диоксида титана, где затравочный слой нанесен золь-гель методом составила 0.74 эВ, а для образца, полученного методом низкотемпературного пиролиза – 0.68 эВ.

Ключевые слова: диоксид титана, тонкие пленки, гидротермальный синтез, затравочный слой, нанотрубки

Финансирование: Работа выполнена при финансовой поддержке гранта РФФИ № 20-07-00653 А.

Ссылка при цитировании: Волкова М. Г., Иванищева А. П., Петров В. В., Баян Е. М. Влияние затравочного слоя на качество покрытий из нанотрубок TiO_2 , выращенных на стеклянных подложках гидротермальным методом // Научно-технические ведомости СПбГПУ. Физико-математические науки. 2022. Т. 15. № 3.3. С. 255–259. DOI: <https://doi.org/10.18721/JPM.153.350>

Статья открытого доступа, распространяемая по лицензии CC BY-NC 4.0 (<https://creativecommons.org/licenses/by-nc/4.0/>)

Introduction

Semiconductor oxide materials are the most commonly used in almost all areas of modern industry. Thin films nanomaterials coatings based on zinc oxide, tin dioxide or titanium dioxide can be used as gas-sensitive sensors [1], photocatalysts [2], optical devices [3], etc. The simultaneous use of various oxides and the creation of composite materials based on them also leads to properties improvement of the target products [4]. For example, the use of zinc and tin (IV) oxides leads to a significant improvement in gas-sensitive properties due to the appearance of a potential barrier at the boundary of the ZnO/SnO_2 heterojunction [5].

The study of film materials with a certain structure, such as nanorods, nanotubes, nanocubes, etc., is of particular interest, since such materials will have a larger surface area and a concentration of defects, which in turn can lead to improved gas-sensitive or photocatalytic properties [6]. However, smooth nanowires adsorb gases only on their surfaces, which creates serious obstacles to achieving highly sensitive properties, therefore porous nanowires are most interesting to study because of their high surface-to-volume ratio and porous structure, which allows gases to be absorbed not only on the surface, but also throughout the volume. Despite the fact that nanotubes and nanorods have similar morphology, nanotubes will have greater porosity and surface area, which is also more preferable for obtaining promising functional nanomaterials [7].

Nanostructured titanium dioxide is one of the most promising multifunctional inorganic materials due to its unique physical and chemical properties. TiO_2 coatings can be used in a wide range of applications, including catalysis, self-cleaning surfaces, gas sensors, solar cells, etc. [8]. There are various methods for producing TiO_2 films, among which are chemical (sol-gel, pyrolysis methods, deposition methods) and mixed physico-chemical methods (electrodeposition, atomic layer deposition, etc.) [9]. However, using hydrothermal synthesis, it is possible to obtain high-purity nanostructures with a given morphology at a relatively low temperature.

Obtaining high-quality coatings from nanotubes is possible in the presence of a seed layer without pores and cracks, therefore, the most important step in the nanostructure's growth is the choice of the seed layer synthesis method [10]. The most common synthesis methods are pyrolysis technique and sol-gel method, as the simplest and most cost-effective. Spray pyrolysis methods are widely known and most commonly used, but the solid-phase pyrolysis method is less common. In the course of previous studies, the authors developed and successfully applied film materials synthesis method based on zinc and tin (IV) oxides [11], therefore, the production of film materials based on titanium dioxide by this method seemed to be the most preferable. The sol-gel method is also a relatively simple technology, but a serious disadvantage may be poor reproducibility and the inability to obtain homogeneous coatings [12]. Therefore, the purpose of this work was to study the effect of the seed layer synthesis method on the quality of TiO_2 nanotubes coatings obtained by hydrothermal synthesis.

Materials and Methods

Titanium tetrachloride, titanium butoxide, organic acid, 1,4-dioxane, sodium hydroxide and distilled water were selected as precursors to produce TiO_2 -nanotubes films coatings. Nanostructured film coatings were obtained in two stages. The first stage included the preparation of a seed layer using sol-gel method or low-temperature solid-phase pyrolysis technique. In the first case, the titanium tetrachloride hydrolysis product was applied once to pre-prepared glass substrates.

In the second case, the seed layer was synthesized in the melt by the interaction of titanium butoxide and organic acid. The resulting melt was cooled, crushed, and after dissolution in 1,4-dioxane, it was also applied once to the prepared substrates. The substrates with the applied solutions were subjected to temperature treatment in a muffle furnace for two hours at a temperature of 550 °C. Cooling was carried out in air together with a muffle furnace, which allows us to obtain homogeneous coatings without cracks.

At the second stage, TiO_2 nanotubes were obtained by hydrothermal synthesis. To achieve this, the substrates with the applied seed layer were placed in a cell for hydrothermal synthesis, a solution of 10 M sodium hydroxide and titanium dioxide powder were added (the cell load did not exceed 80%). Hydrothermal treatment was carried out for 24 hours at a temperature of 160 °C. At the end of the nanostructure growth procedure, the samples were washed with distilled water to the neutral medium of the solution and dried in air. The synthesized materials were examined by X-ray diffraction analysis (XRD, ARLX'TRA diffractometer, Thermo ARL, $\text{CuK}\alpha$ radiation) and scanning electron microscopy (SEM, scanning electron microscope Nova Nanoab 600). The study of the electrical resistance dependence on the reverse temperature was carried out according to the previously described method [1].

Results and Discussion

According to the results of XRD, for film materials obtained by low-temperature pyrolysis at the first stage of synthesis, a mixed structure of anatase and rutile is shown. Calculations of the crystallite sizes according to the Scherrer equation showed that the average size is 9 and 13 nm for the anatase and rutile phases, respectively. XRD patterns of materials after hydrothermal treatment do not have clearly crystallized peaks, which allow us to indirectly judge the presence of nanoscale titanium dioxide materials (Fig. 1).

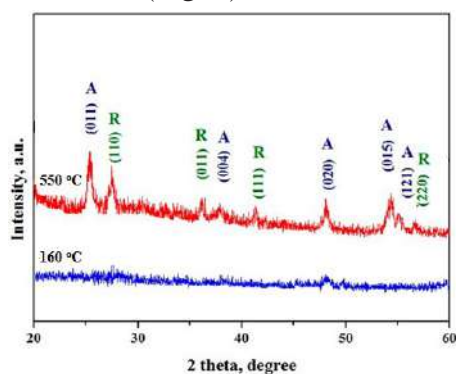


Fig. 1. XRD patterns of TiO_2 -materials obtained by low-temperature pyrolysis (red curve) and hydrothermal method (blue curve), anatase is A, rutile is R

According to SEM data, nanostructured titanium dioxide coatings obtained by hydrothermal method (the seed layer is applied by pyrolysis) are nanotubes with a diameter of about 10 nm, a length of several microns; the tubes are extended, sometimes curved, rolled into balls of 3–5 microns in size (Fig. 2, *a*). For nanostructures synthesized by the hydrothermal method with a seed layer applied using sol-gel technology, a slightly different nature of the nanotubes growth is shown. The resulting structures are thin nanotubes with a diameter of several tens of nanometers, extended, and sometimes curved, with a length of several microns. On the tubes surface there are island agglomerates consisting of tubes tangles (Fig. 2, *b*), which may be due to the uneven application of the seed layer as a result of an imperfect synthesis method.

The electrophysical properties of the obtained film were measured using a software and hardware measuring complex that allows detecting the dependence of resistance on temperature,

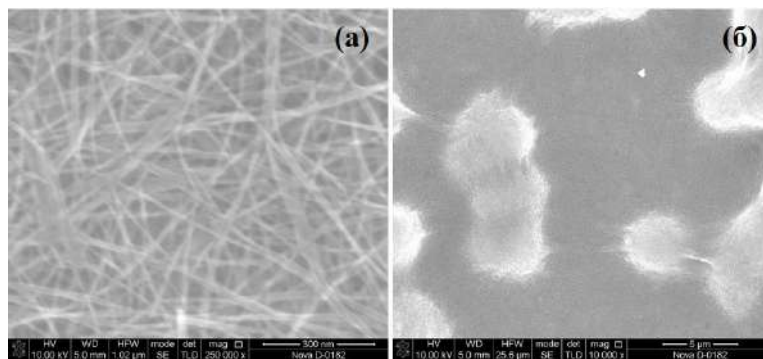


Fig. 2. SEM-image of TiO_2 -nanotubes (seed layer was deposited using low-temperature pyrolysis (a) and sol-gel method (b))

as well as the activation energy of conductivity [13]. To achieve this, V-Ni contacts were formed on top of nanotubes by thermal vacuum evaporation. The dependence of the electrical resistance on the reverse temperature is shown in Fig. 3.

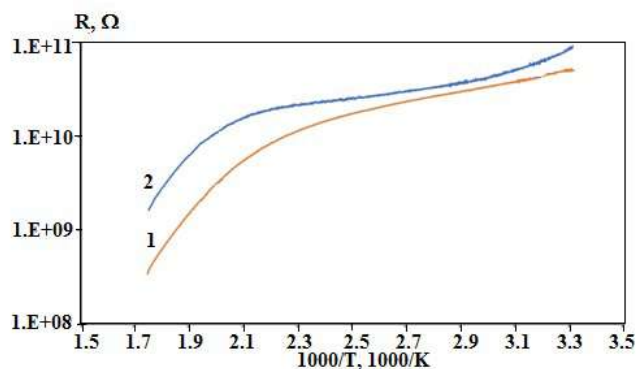


Fig. 3. R - $1000/T$ dependence of TiO_2 -nanotubes (seed layer was deposited using low-temperature pyrolysis (curve 1) and sol-gel method (curve 2))

Titanium dioxide nanotubes grown on the seed layer synthesized by low-temperature pyrolysis (Fig. 3, curve 1) and sol-gel method (curve 2), have a similar character and high nonlinearity. With an increase in the heating temperature in the temperature range of 30–130 °C, a slight decrease in the resistance is observed. In the temperature range of 150–300 °C, there is a sharp decrease in resistance by 1.5 orders of magnitude. The structure with TiO_2 nanotubes grown on the seed layer deposited by the sol-gel method has a resistance an order of magnitude higher than TiO_2 nanotubes grown on the seed layer synthesized by low-temperature pyrolysis. This may be a consequence of the amorphous structure of TiO_2 nanotubes with a seed layer deposited by the sol-gel method. The same conclusions are confirmed by the calculation of the activation energy of conductivity (E_a) carried out in the temperature range of 200–300 °C. For titanium dioxide nanotubes, grown on the seed layer applied by sol-gel method, the E_a was 0.74 eV, and for the sample with seed layer obtained by low-temperature pyrolysis, the E_a was 0.68 eV.

Conclusion

Coatings of titanium dioxide nanotubes were obtained by hydrothermal method. It was shown that when a seed layer was applied by low-temperature pyrolysis technique, it is possible to obtain smaller diameter tubes and a better coating, without the presence of agglomerates. The presence of a large number of “stuck together” particles in the material with sol-gel seed layer application can be explained by the uneven distribution of nanotube growth centers. The study of electrophysical properties showed that for materials with a seed layer obtained by the sol-gel method, the resistance is an order of magnitude higher than for materials with a seed layer synthesized by low-temperature pyrolysis. This can be explained by the more amorphous structure of materials with a seed layer obtained by the sol-gel method, which confirms the calculation of the activation energy – for these materials it is higher than for materials with a seed layer



deposited by low-temperature pyrolysis.

Acknowledgments

The authors are grateful to the Laboratory for Technology of Functional Nanomaterials of the Institute of Nanotechnology, Electronics and Equipment Engineering of the Southern Federal University for SEM studies conducting.

REFERENCES

1. Petrov V. V., Ivanishcheva A. P., Volkova M. G., Storozhenko V. Yu., Gulyaeva I. A., Pankov I. V., Volochaev V. A., Khubezhov S. A., Bayan E. M., High Gas Sensitivity to Nitrogen Dioxide of Nanocomposite ZnO-SnO₂ Films Activated by a Surface Electric Field Nanomaterials. 12 (12) (2022) 2025.
2. Bayan E. M., Pustovaya L. E., Volkova M. G., Recent advances in TiO₂-based materials for photocatalytic degradation of antibiotics in aqueous systems, Environ. Technol. Innov. 24 (2021) 101822.
3. Granqvist C. G., Electrochromics for smart windows: Oxide-based thin films and devices, Thin solid films. 564 (2014) 1–38.
4. Lia T., Zenga W., Wang, Z., Quasi-one-dimensional metal-oxide-based heterostructural gas-sensing materials: A review, Sensors and Actuators B. 221 (2015) 1570–1585.
5. Mirzaei A., Leonardi S. G. Neri G., Detection of hazardous volatile organic compounds (VOCs) by metal oxide nanostructures-based gas sensors: A review, Ceramics International. 42 (2016) 15119–15141.
6. Sun Y. F., Liu S. B., Meng F. L., Liu J. Y., Jin Z., Kong L. T., Liu J. H., Metal oxide nanostructures and their gas sensing properties: a review, Sensors. 12 (3) (2012) 2610–2631.
7. Levy-Clement C., Elias J., Tena-Zaera R., ZnO/CdSe nanowires and nanotubes: Formation, properties and applications, Phys. Status Solidi C. 6 (2009) 1596–1600.
8. Varshney G., Kanel S. R., Kempisty D. M., Varshney V., Agrawal A., Sahle-Demessie E., Varma R. S., Nadagouda M. N., Nanoscale TiO₂ films and their application in remediation of organic pollutants, Coordination Chemistry Reviews. 306(1) (2016) 43–64.
9. Malekshahi Byranvand M., Nemati Kharat A., Fathollahi L., Malekshahi Beiranvand Z., A review on synthesis of nano-TiO₂ via different methods, Journal of nanostructures. 3 (1) (2013) 1–9.
10. Pant B., Park M., Park S. J., Recent advances in TiO₂ films prepared by sol-gel methods for photocatalytic degradation of organic pollutants and antibacterial activities, Coatings. 9 (10) (2019) 613.
11. Bayan E. M., Petrov V. V., Volkova M. G., Storozhenko V. Yu., Chernyshev A. V., SnO₂-ZnO nanocomposite thin films: The influence of structure, composition and crystallinity on optical and electrophysical properties, J. Adv. Dielectr. 11 (05) (2021) 2160008.
12. Faustini M., Louis B., Albouy P. A., Kuemmel M., Grosso D., Preparation of sol-gel films by dip-coating in extreme conditions, The Journal of Physical Chemistry C. 114 (17) (2010) 7637–7645.
13. Petrov V. V., Varzarev Yu. N., Bayan E. M., Storozhenko V. Yu., Rozhko A. A., Study of the electrophysical properties of thin films of mixed zinc and tin oxides, Proceedings of the 2019 IEEE International Conference on Electrical Engineering and Photonics (EExPolytech). October 17–18, 2019, Publ.: Peter the Great St. Petersburg Polytechnic University. (2019) 242–243.

THE AUTHORS

VOLKOVA Maria G.
mvol@sfedu.ru
ORCID: 0000-0001-9483-162X

PETROV Viktor V.
vvpetrov@sfedu.ru
ORCID: 0000-0003-3725-6053

IVANISHCHEVA Alexandra P.
starnikova@sfedu.ru
ORCID: 0000-0002-3779-8242

BAYAN Ekaterina M.
ekbayan@sfedu.ru
ORCID: 0000-0002-8445-9139

Received 13.07.2022. Approved after reviewing 15.07.2022. Accepted 15.07.2022.

Conference materials

UDC 538.958

DOI: <https://doi.org/10.18721/JPM.153.351>

Optical studies of InP nanostructures monolithically integrated in Si (100)

I. A. Melnichenko ¹✉, N. V. Kryzhanovskaya ¹, Yu. S. Berdnikov ^{1,2},
E. I. Moiseev ¹, I. S. Makhov ¹

¹ Higher School of Economics University, St. Petersburg, Russia;

² St. Petersburg State University, St. Petersburg, Russia

✉ imelnichenko@hse.ru

Abstract. We present a photoluminescence study of InP nanostructures monolithically integrated to Si (100) substrate. The InP nanostructures were grown in pre-formed pits in the silicon substrate using an original approach by metal–organic vapor phase epitaxy via selective area growth driven by molten alloy. The obtained InP/Si nanostructures have submicron size above and below substrate surface. InP nanostructures were investigated by photoluminescence spectroscopy at temperatures in the range of 5–300 K and at different pump power. Room temperature photoluminescence spectra of the studied structures exhibit the peak corresponding to zinc blende InP band gap. The obtained results show high crystalline quality of the InP material.

Keywords: III-V nanostructures, InP monolithically integrated on silicon, near IR radiation

Funding: This study was supported by Russian Science Foundation grant No. 22-22-20057, <https://rscf.ru/project/22-22-20057/> and by St. Petersburg Science Foundation grant 66/2022 dated 15 April 2022.

Citation: Melnichenko I. A., Kryzhanovskaya N. V., Berdnikov Yu. S., Moiseev E. I., Makhov I. S., Optical studies of InP nanostructures monolithically integrated in Si (100). St. Petersburg State Polytechnical University Journal. Physics and Mathematics, 15 (3.3) (2022) 260–264. DOI: <https://doi.org/10.18721/JPM.153.351>

This is an open access article under the CC BY-NC 4.0 license (<https://creativecommons.org/licenses/by-nc/4.0/>)

Материалы конференции

УДК 538.958

DOI: <https://doi.org/10.18721/JPM.153.351>

Изучение оптических характеристик InP нановключений интегрированных на Si (100)

И. А. Мельниченко ¹✉, Н. В. Крыжановская ¹, Ю. С. Бердников ^{1,2},
Э. И. Моисеев ¹, И. С. Махов ¹

¹ Национальный исследовательский университет «Высшая школа экономики», Санкт-Петербург, Россия;

² Санкт-Петербургский государственный университет, Санкт-Петербург, Россия

✉ imelnichenko@hse.ru

Аннотация. Мы представляем исследование фотолюминесценции нановключений InP, монолитно интегрированных в подложку Si (100). Нановключения InP были выращены в предварительно сформированных отверстиях в кремниевой подложке с использованием нового подхода, основанного на селективном росте и капельном осаждении на базе метода металлоорганической газофазной эпитаксии. Отдельные нановключения InP/Si были исследованы методом спектроскопии фотолюминесценции в диапазоне температур 5–300 К при различной мощности накачки. Спектры фотолюминесценции исследованных структур при комнатной температуре демонстрируют максимум интенсивности, соответствующий ширине запрещенной зоны InP в конфигурации



сфалерита. Полученные результаты свидетельствуют о высоком кристаллическом качестве нановключений InP.

Ключевые слова: III-V наноструктуры, интеграция InP на кремний, излучение в ближнем ИК диапазоне

Финансирование: Работа выполнена при поддержке гранта РФФИ № 22-22-20057, <https://rscf.ru/project/22-22-20057/> и гранта Санкт-Петербургского научного фонда в соответствии с соглашением от 15 апреля 2022 г. № 66/2022.

Ссылка при цитировании: Мельниченко И. А., Крыжановская Н. В., Бердников Ю. С., Моисеев Э. И., Махов И. С. Изучение оптических характеристик InP нановключений, интегрированных на Si (100) // Научно-технические ведомости СПбГПУ. Физико-математические науки. 2022. Т. 15. № 3.3. С. 260–264. DOI: <https://doi.org/10.18721/JPM.153.351>

Статья открытого доступа, распространяемая по лицензии CC BY-NC 4.0 (<https://creativecommons.org/licenses/by-nc/4.0/>)

Introduction

Seamless integration of optically active A3B5 materials on silicon is the key challenge in creation of integrated light sources, which are highly demanded for further development of quantum computing, communications, and sensing [1, 2]. Compatibility with the well-developed silicon-based fabrication is crucial for scalability of new generation of compact and power-efficient light sources [3, 4]. The desired structures therefore can combine A3B5 materials (with high electron mobility and direct band gap) and the highly optimized processing of Si (001) platform.

However, integration the III-V-based light emitting devices with Si substrates is difficult because of the lattice mismatch between most of A3B5 materials and silicon, as well as the difference in polarity and thermal expansion coefficients, which typically lead to high defect density in the structures. Meanwhile, low number of defects and dislocations is critical for optical devices due to the detrimental impact of non-radiative recombination of charge carriers on the efficiency of light emission.

In this work we study InP nanostructures epitaxially grown in the pits of Si (100) substrates using the recently developed method of selective area metal–organic vapor phase epitaxy (MOVPE) driven by molten alloy, which allows obtaining InP/Si nanostructures with low crystal defect density and sharp interfaces between the grown InP and hosting Si [5]. Here we study the optical properties of the formed InP/Si nanostructures using microphotoluminescence (PL) measurements correlated with scanning electron microscopy and surface mapping by confocal microscopy.

Materials and Methods

Nanostructure fabrication started with the deposition of SiN_x mask on top of Si (100) surface and formation of the array of 200 nm wide openings in the mask spaced 800 nm apart each other. Then, the inverted-pyramidal pits in Si were etched within the mask openings using KOH aqueous solution. The substrate patterning was followed by deposition of the droplets of indium-rich melt inside the etched pits, which is then was annealed in phosphine (PH₃). The structures with the optimal crystal quality formation were obtained after annealing under PH₃ flux of 2.2·10⁻² mol min⁻¹ and substrate temperature of 600 °C More details of the fabrication procedure can be found in [5].

PL maps and spectra were measured using an Integra Spectra NT-MDT confocal microscope at room temperature. The Nd:YLF laser operating in continuous mode (527 nm wavelength) was used for excitation. The excitation laser beam was focused using a 100x objective (Mitutoyo, M Plan APO NIR) with a numerical aperture NA = 0.5. The same objective was used to collect the photoluminescence signal of InP nanostructures. The radiation was directed to the entrance slits of the monochromator (Sol Instruments MS5204i) using mirrors. Detection was performed using a cooled InGaAs CCD array (iDus). To acquire the PL spectra at low temperatures, the structures were placed into the closed-cycle helium cryostation Montana Instruments Cryostation s50.

Results and Discussion

Fig. 1 shows typical spectra obtained from single InP nanostructure with a single peak at 915 nm (corresponding to InP in the zinc blende crystal phase) and the full width at half maximum (FWHM) of about 55 nm. SEM image of the array of InP nanostructures is also shown in the inset to Fig. 1.

The nanostructure marked with the red circle in the inset to Fig. 1 was also explored in depth. PL scanning over the depth of this nanostructure was performed using mirror optics of the confocal microscope and tunable holder. Obtained results show the homogeneity of InP peak shape and a gradual decrease of PL intensity in the depth of the substrate. This decline in the PL intensity is related to the inverted pyramidal shape of the etched pits which implies the reduction of InP volume with the depth.

Photoluminescence at room temperature is observed from almost every single nanostructure, indicating the formation of InP crystals without threading dislocations. Also, we observed significant variation of the PL intensity from different nanostructures, that may be due to the different amount of InP material inside the pits and. Meanwhile the spectra have similar shape and position of the peak.

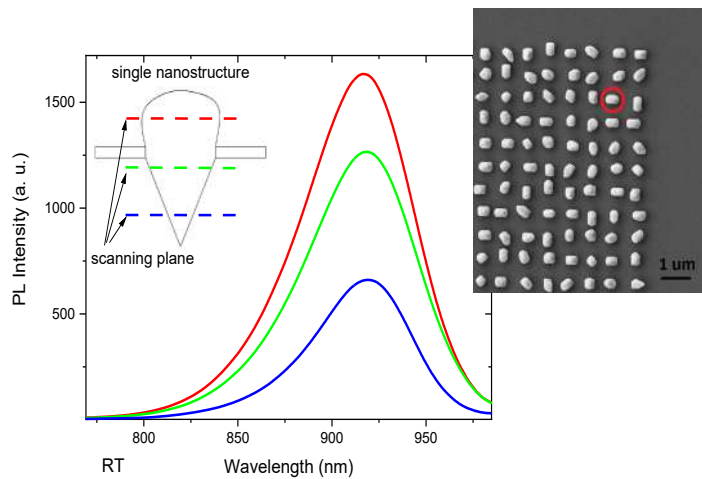


Fig. 1. PL spectrum from highlighted InP nanostructure, measured at room temperature over the depth. SEM image on inset

Next, we studied low temperature photoluminescence spectra of the nanostructure (Fig. 2). At 5 K we observe three spectral lines assigned to zinc blende InP free exciton (FE) at 1.417 eV, bound exciton (BE) at 1.412 eV and donor-valence band transition (1.404 eV) [6]. As temperature rising, the high energy processes increase. The donor-valence band line disappears at ~ 20 K and the bound exciton line does at ~ 30 K. As the temperature is increased further, the intensity of free exciton band emission increases and dominates the spectrum.

Most of the scanned nanostructures have similar low-temperature spectra in wavelength range of 870–900 nm. In contrast, the shorter-wavelength series of lines (840–860 nm or 1.48–1.44 eV) have different intensity and wavelengths in each nanostructure. These lines are probably caused by twinning defects in InP/Si nanostructures that were observed by transmission electron microscopy [5].

Twins are often found in III-V nanostructures and can be considered as monolayer phase of wurtzite (WZ) in zinc blende (ZB) material. This kind of defects does not form dangling bonds and thus not affect drastically the intensity of radiative recombination. The existence of heterointerfaces due to ZB/WZ polytypism causes the appearance of type II band alignment. The contribution from recombination on the type II band transitions can be observed in the long decay of shortwave tail, shown in figure 3 [7]. Thus, high energy PL lines at low temperatures (Fig. 2) may be caused by appearance of wurtzite InP phase (1.486 eV). Nevertheless, these lines have very low intensity and even disappear in some studied nanostructures, so we can conclude that the most of nanostructures have a zinc blende structure of high crystalline quality.

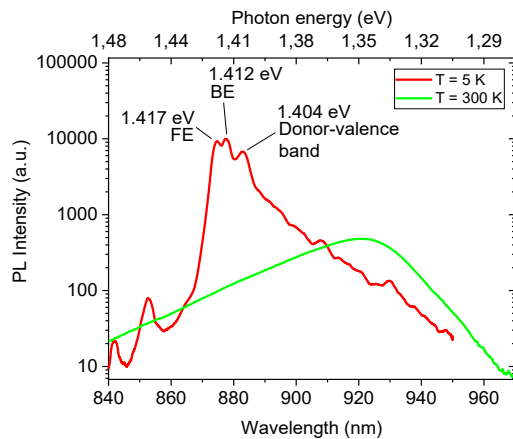


Fig. 2. PL spectra of single InP nanostructure, measured at 5K and room temperature

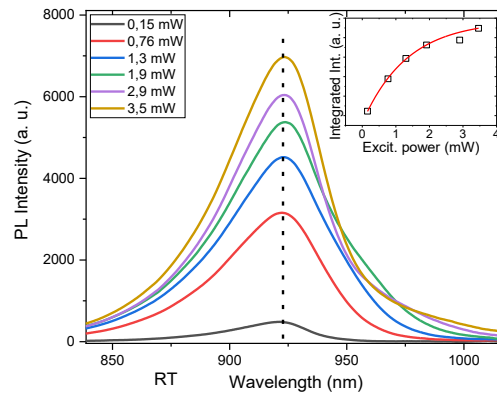


Fig. 3. Dependence of InP nanostructure PL intensity on pumping power

Fig. 3 illustrates the variation of room temperature PL intensity with the excitation power. With the pump power increase from 0.15 to 3.5 mW the FWHM of the PL peak increases from 37 nm (55 meV) to 50 nm (73.5 meV). The peak wavelength remains nearly constant and only shifts slightly to the longer wavelengths at high excitation power due to the structure heating. The shape of the peak (the long wavelength tail) strongly depends on the position on the sample, the crystal quality of individual InP structures. Slowdown of integral intensity growth with the pump power can be fitted with an exponential function. Such behavior can be explained by the saturation of radiative recombination in the volume of a single nanostructure.

Conclusion

We investigated the optical properties of the InP nanostructures monolithically integrated into Si (100) synthesized via this original epitaxial method. Obtained InP nanostructures show PL emission in the near-infrared range (PL peak at ~ 920 nm) at room temperature. Their intensity varies from each other due to different volume of InP. PL scanning over the depth of nanostructures shows the homogeneity of InP peak and a gradual decrease of PL intensity with depth. Low temperature measurements showed spectral lines assigned to zinc blende InP transitions and low peaks in shorter wavelengths, that can be associated with twinning defects in InP nanostructures. The obtained results demonstrate high crystalline quality of the integrated InP zinc blende nanostructures and their optical characteristics.

Acknowledgments

The authors are thankful to E. Semenova and D. Viazmitinov for the provided structures.

REFERENCES

1. Liu S., Khope A., Latest advances in high-performance light sources and optical amplifiers on silicon, *Journal of Semiconductors* 42 (2021) 041307.
2. Sun K., Gao J., Jung D., Bowers J., Beling A., 40 Gbit/s waveguide photodiode using III–V on silicon heteroepitaxy, *Optics Letters*. 45 (11) (2020) 2954–2956.
3. Bettotti P., Hybrid materials for integrated photonics. *Advances in Optics*. 2014 (2014).
4. Roelkens G., Abassi A., Cardile P., Dave U., De Groote A., De Koninck Y., Van Thourhout D., et al., III-V-on-silicon photonic devices for optical communication and sensing, In *Photonics, Multidisciplinary Digital Publishing Institute*. 2 (3) (2015) 969–1004.
5. Viazmitinov D. V., Berdnikov Y., Kadkhodazadeh S., Dragunova A., Sibirev N., Kryzhanovskaya N. V., Radko I., Huck A., Yvind K., Semenova E., Monolithic integration of InP on Si by molten alloy driven selective area epitaxial growth, *Nanoscale*. 12 (46) (2020) 23780–23788.
6. Heim U., Röder O., Queisser H. J., Pilkuhn M., Photoluminescence of InP, *Journal of Luminescence*. 1 (1970) 542–551.

7. Alouane M. H., Chauvin N., Khmissi H., Naji K., Ilahi B., Maaref H., Bru-Chevallier C., Excitonic properties of wurtzite InP nanowires grown on silicon substrate, Nanotechnology. 24 (3) (2012) 035704.

THE AUTHORS

MELNICHENKO Ivan A.

imelnichenko@hse.ru

ORCID: 0000-0003-3542-6776

KRYZHANOVSKAYA Natalia V.

nataliakryzh@gmail.com

ORCID: 0000-0002-4945-9803

BERDNIKOV Yury S.

yuryberdnikov@gmail.com

ORCID: 0000-0002-1630-1559

MOISEEV Eduard I.

emoiseev@hse.ru

ORCID: 0000-0003-3686-935X

MAKHOV Ivan S.

makhoviv@gmail.com

ORCID: 0000-0003-4527-1958

Received 13.07.2022. Approved after reviewing 21.07.2022. Accepted 22.07.2022.

Conference materials
UDC 546.05; 538.975
DOI: <https://doi.org/10.18721/JPM.153.352>

Surface and electrophysical properties study of thin TiO₂-SnO₂ nanocomposite films

I. A. Gulyaeva ¹✉, A. P. Ivanishcheva ¹, M. G. Volkova ², E. M. Bayan ², V. V. Petrov ¹

¹ Research and Education Centre "Microsystem technics and multisensor monitoring systems", Southern Federal University, Taganrog, Russia;

² Southern Federal University, Rostov-on-Don, Russia

✉ tenirka@mail.ru

Abstract. Thin nanocomposite films based on pure tin dioxide with a low content of titanium oxide (0, 1, 3, and 5 mol %) were obtained by solid-phase low-temperature pyrolysis. The thickness of the films obtained was up to 200 nm. The particle size of the TiO₂-SnO₂ nanomaterial lies in the range of 7–13 nm. Atomic force microscopy (AFM) showed that the films have a granular structure with a height difference of 11–114 nm. The surface of the film with a Ti concentration of 5 mol.% has a higher roughness compared to other samples. Force microscopy with a Kelvin probe (KPFM) revealed a surface potential, indicating the existence of a strong surface electric field. A small addition of titanium dioxide (1%) to the tin dioxide structure leads to the appearance of peak values of the surface potential, the value of which reaches 1325 mV. Studies of the temperature dependences of the obtained samples showed that the pure SnO₂ film has the maximum resistance values and high nonlinearity. However, with a small addition of titanium dioxide (1%) to tin dioxide, the electrical resistance of the nanosized material sharply decreases and has indicators 4–5 orders of magnitude lower than those of pure SnO₂ films.

Keywords: nanomaterials, thin films, pyrolysis, tin dioxide, titanium dioxide, surface potential, electrical properties

Funding: This work was financially supported by the RFBR, project No. 20-07-00653 A.

Citation: Gulyaeva I. A., Ivanishcheva A. P., Volkova M. G., Bayan E. M., Petrov V. V., Surface and electrophysical properties study of thin TiO₂-SnO₂ nanocomposite films. St. Petersburg State Polytechnical University Journal. Physics and Mathematics, 15 (3.3) (2022) 265–270. DOI: <https://doi.org/10.18721/JPM.153.352>

This is an open access article under the CC BY-NC 4.0 license (<https://creativecommons.org/licenses/by-nc/4.0/>)

Материалы конференции
УДК 546.05; 538.975
DOI: <https://doi.org/10.18721/JPM.153.352>

Исследование поверхностных и электрофизических свойств тонких нанокompозитных пленок состава TiO₂-SnO₂

И. А. Гуляева ¹✉, А. П. Иванищева ¹, М. Г. Волкова ², Е. М. Баян ², В. В. Петров ¹

¹ Научно-образовательный центр «Микросистемная техника и мультисенсорные системы мониторинга», Южный федеральный университет, Таганрог, Россия;

² Южный федеральный университет, Ростов-на-Дону, Россия

✉ tenirka@mail.ru

Аннотация. Методом твердофазного низкотемпературного пиролиза были получены тонкие нанокompозитные пленки на основе чистого диоксида олова с низким содержанием оксида титана (0, 1, 3 и 5 мол. %). Атомно-силовой микроскопией (АСМ) показано, что пленки имеют зернистую структуру с перепадом высот 11–114 нм. Методом Кельвин-зондовой силовой микроскопии (КЗСМ) на поверхности TiO₂-SnO₂

пленок с молярным соотношением Ti:Sn равным 1:99 обнаружен высокий поверхностный потенциал (V_b = 1325 мВ), показывающий существование сильного поверхностного электрического поля.

Ключевые слова: наноматериалы, тонкие пленки, пиролиз, диоксид олова, диоксид титана, поверхностный потенциал, электрофизические свойства

Финансирование: Работа выполнена при финансовой поддержке РФФИ, проект № 20-07-00653 А.

Ссылка при цитировании: Гуляева И. А., Иванищева А. П., Волкова М. Г., Баян Е. М., Петров В. В., Исследование поверхностных и электрофизических свойств тонких нанокompозитных пленок состава TiO₂-SnO₂ // Научно-технические ведомости СПбГПУ. Физико-математические науки. 2022. Т. 15. № 3.3. С. 265–270. DOI: <https://doi.org/10.18721/JPM.153.352>

Статья открытого доступа, распространяемая по лицензии CC BY-NC 4.0 (<https://creativecommons.org/licenses/by-nc/4.0/>)

Introduction

Inorganic oxide nanomaterials based on tin and titanium dioxides are widely used to create electronic devices, photocatalysts, solar cell electrodes and gas sensors [1–3]. Titanium dioxide is the most commonly used as a photocatalyst, but the width of its band gap does not allow it to be used when irradiated with visible light, so various modifying additives are used for this purpose [4]. One of these additives is tin ions (4+), since the close radius allows you to replace titanium in the crystal lattice [5–6]. Tin dioxide has chemical and thermal stability, and due to the combination of high conductivity and high potential for the release of excess oxygen, Electrodes based on SnO₂ also contribute to the complete oxidation of organic compounds [7]. Another reason for the combined use of these oxides may be a similar type of crystallization, since both tin dioxide and titanium dioxide can be crystallized in the structure of rutile [8].

Modification of SnO₂ films with titanium dioxide allows to improve various properties of the nanocomposite material, including electrophysical [9–10]. For example, the work [11] describes the properties of nanostructures based on Ti-SnO₂ films, among the factors that ensure the success of the use of these materials as electrodes are listed: (1) The structure of the core-shell of the Ti-SnO₂ network are listed: (1) The structure of the core-shell of the Ti-SnO₂ network, consisting of Ti inside a shell of SnO₂ nanocrystals, is favorable for the diffusion of lithium ions during cyclic charge-discharge. (2) The Ti in the composite acts as an effective mechanical support for relieving the stress caused by the intercalation–deintercalation of lithium, which can play a crucial role in the excellent lithium storage capacity and the cyclic capacity of the electrode. (3) Mesopores formed by 3D microstructures also contribute to the improvement of the electrochemical characteristics of the electrode, possibly because they facilitate the diffusion of the electrolyte or lithium ions during charge-discharge processes.

The purpose of this work was to study surface (surface morphology and surface electric potential) and electrophysical (temperature dependence of electrical resistance) properties synthesized by solid-phase low-temperature pyrolysis of thin films TiO₂-SnO₂.

Materials and Methods

To obtain thin film materials TiO₂-SnO₂ with a ratio of Ti:Sn = 0:100, 1:99, 3:97, 5:95 by the method of solid-phase low-temperature pyrolysis, tin salts (SnCl₄·5H) were used as precursors for the synthesis of thin films TiO₂-SnO₂ and titanium ((C₄H₉O)₄Ti). The resulting salts were dissolved in 1,4-dioxane and applied three times to the prepared silicon and polycore substrates. Each layer was dried in air and in a drying oven at a temperature of 120 °C. The final temperature treatment was carried out in a muffle furnace at a temperature of 600 °C for two hours. The synthesis conditions were selected according to previous studies [12].

According to X-ray phase analysis, the resulting films have a crystal structure of cassiterite, regardless of the concentration of the additives administered. The resulting reflexes are somewhat expanded, which is typical for film nanocrystalline materials. Diffraction maxima of other phases



are not detected. Synthesized $\text{TiO}_2\text{-SnO}_2$ is characterized by a decrease in both particle sizes from 36 to 22 nm and the degree of crystallization from 68% to 45% with an increase in the concentration of titanium from 0 to 5 mol. %, which may be due to an increase in the concentration of defects and a less “ideal” crystal structure.

The study of the surface morphology and surface potential of the obtained films was carried out using the Ntegra probe nanolaboratory (NT-MDT SI, Russia). For this purpose, the samples were first examined using atomic force microscopy, and then Kelvin-probe force microscopy was used. In the study, the AFM and KPFM methods used the NSG10/Pt cantilever with a force constant of 11.2 N/m (TipsNano, Estonia) and a radius of curvature of about 25 nm.

To process the results of AFM measurements, the Image Analysis (NT-MDT) program was used, with the help of which the roughness parameters were estimated, the root value of roughness (S_q , Root Mean Square) and the maximum height difference (S_y , Peak-to-peak). On the basis of the KPFM measurements, the values of the surface potential V_b were determined. To compare the surface potentials on different film samples, the difference between the maximum and minimum values ΔV_b was used, the values of which were averaged according to the sample.

Studies of the electrophysical properties of the obtained film samples were carried out on a software and hardware measuring complex that allows measuring the dependence of resistance on temperature [13].

Results and Discussion

Fig. 1 shows AFM scans of studied samples of $\text{TiO}_2\text{-SnO}_2$ films with a Ti:Sn ratio of 0:100, 1:99, 3:97, 5:95 mol.% with a size of $3 \times 3 \mu\text{m}^2$.

Table 1 shows roughness (S_y , nm), maximum elevation differences (S_q , nm), as well as surface potential values (V_b , mV) and its average values (ΔV_b , mV) for each of the samples obtained.

Table 1

Surface characteristics of $\text{TiO}_2\text{-SnO}_2$ films

Ti:Sn, mol.%	S_y , nm	S_q , nm	V_b , mV	ΔV_b , mV
0:100	11.0	1.4	4	4
1:99	34.3	4.1	1325	141
3:99	60.2	7.4	326	39
5:99	114.6	12.6	126	17

AFM studies have shown that $\text{TiO}_2\text{-SnO}_2$ films have a granular structure, and the roughness of films increases with increasing concentration of titanium dioxide. The least roughness has a film SnO_2 ($S_y = 11.0$ nm), and $\text{TiO}_2\text{-SnO}_2$ film with a concentration of Ti 5 mol.% has the highest roughness ($S_y = 114.6$ nm).

Studies of KPFM have shown that the lowest value of the surface potential ($V_b = 4$ mV) is characteristic of the tin oxide film – Fig. 1, *h*. This is due to the fact that the contact of two crystallites of tin dioxide contributes to the formation of a low surface potential. However, a small addition (1 mol.%) of titanium dioxide to the structure of tin dioxide leads to the appearance of peak values of the surface potential, the value of which reaches 1325 mV. It is known that the electron output work of titanium dioxide (4.7 eV) [14] is somewhat less than that of tin oxide (4.8–4.9 eV). [15, 16].

When the crystallites TiO_2 and SnO_2 come into contact, electrons will pass from titanium dioxide to tin dioxide, and regions with large local surface potential values of V_b should arise. The latter indicates the existence on the surface of such a film of a strong (up to 10^7 V/cm) electric field, which can significantly affect the transfer of charge carriers in it and the processes occurring on its surface [17].

Fig. 2 shows the dependence of electrical resistance on inverse temperature.

Pure SnO_2 film has maximum resistance values and high nonlinearity. However, with a small addition of titanium dioxide (1%) to tin dioxide, the electrical resistance of the nanoscale material is sharply reduced and has indicators 4–5 orders of magnitude lower than pure SnO_2 films. This may also be a consequence of the presence of a high surface electric field in $\text{TiO}_2\text{-SnO}_2$ films

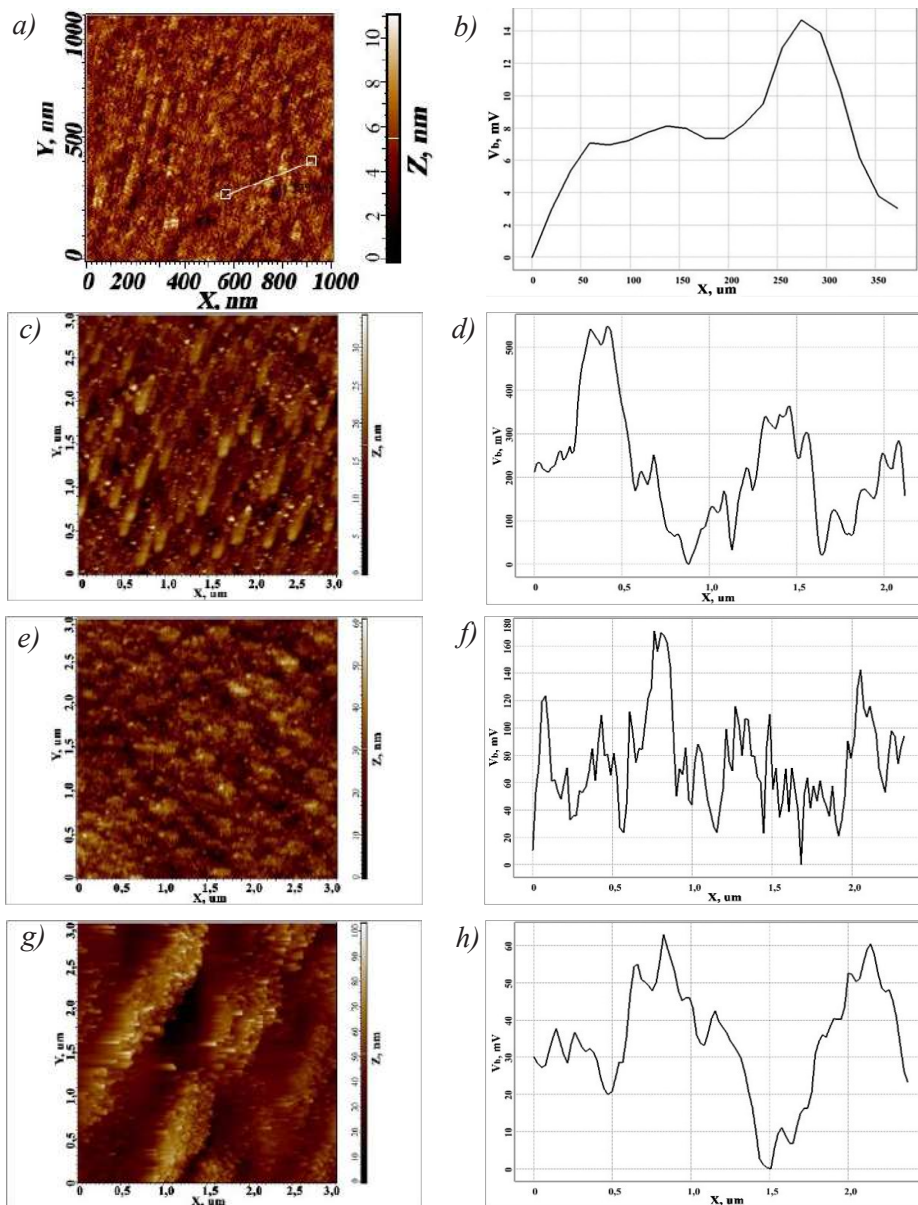


Fig. 1. AFM elevation scans (*a, c, e*) and their corresponding surface potential distribution (*b, d, f*) over the surface $\text{TiO}_2\text{-SnO}_2$ films with a Ti:Sn mole ratio of 0:100 (*a, b*), 1:99 (*c, d*), 3:97 (*e, f*) and 5:95 (*g, h*) mol. %

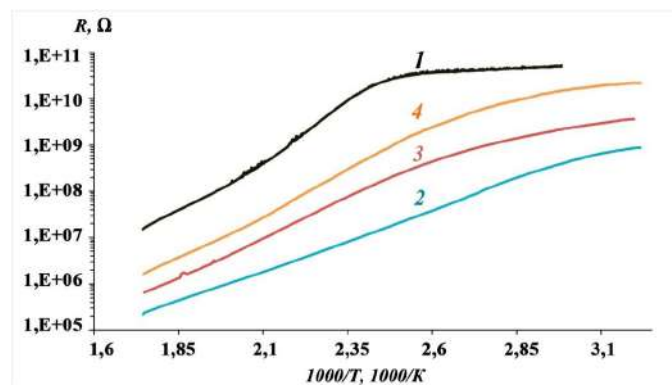


Fig. 2. Dependence of R on $1000/T$ for $\text{TiO}_2\text{-SnO}_2$ films with a molar ratio of Ti:Sn equal to 0:100 (curve 1), 1:99 (curve 2), 3:97 (curve 3) and 5:95 (curve 4) mol. %



with a Ti:Sn molar ratio of 1:99. A higher content of titanium dioxide additives (3 and 5%) shows a higher resistance than that of sample c (1%). At the same time, the dependence of electrical resistance on the reverse temperature for the resulting films is close to linear.

Conclusion

Nanoscale films of TiO_2 - SnO_2 composition with controlled thickness were formed by solid-phase low-temperature pyrolysis. The KPFM method detected a surface potential on their surface, showing the existence of a high surface electric field. The resulting TiO_2 - SnO_2 films can be used as solar cell electrodes and gas-sensitive materials for gas sensors.

Acknowledgments

We would like to express our gratitude to the staff of the Laboratory for Technology of Functional Nanomaterials of the Institute of Nanotechnology, Electronics and Equipment Engineering of the Southern Federal University for their help in conducting AFM and KFM studies.

REFERENCES

1. Li Z., Li H., Wu Z., Wang M., Luo J., Torun H., Hu P., Yang C., Grundmann M., Liu X., Fu Y., Advances in designs and mechanisms of semiconducting metal oxide nanostructures for high-precision gas sensors operated at room temperature, *J Mater. Horizons*. 6 (3) (2019) 470–506.
2. Tiwana P., Docampo P., Johnston M. B., Snaith H. J., Herz, L. M., Electron mobility and injection dynamics in mesoporous ZnO, SnO₂, and TiO₂ films used in dye-sensitized solar cells, *ACS nano*. 5 (6) (2011) 5158–5166.
3. Korotcenkov G., Han S. H., Cho B. K., Metal oxide nanocomposites: advantages and shortcomings for application in conductometric gas sensors, In *Materials Science Forum*, Trans Tech Publications Ltd. 872 (2016) 223–229.
4. Zaleska A., Doped-TiO₂: a review, *Recent patents on engineering*, 2 (3) (2008) 157–164.
5. Bayan E. M., Lupeiko T. G., Pustovaya L. E., Volkova M. G., Synthesis and photocatalytic properties of Sn–TiO₂ nanomaterials, *J. Adv. Dielectr.* 10 (1,2) (2020) 2060018.
6. Sulaiman S. N. A., Noh M. Z., Adnan N. N., Bidin N., Ab Razak S. N., Effects of photocatalytic activity of metal and non-metal doped TiO₂ for hydrogen production enhancement—a review, *Journal of Physics: Conference Series*, IOP Publishing. 1027 (1) (2018) 012006.
7. Sharma A., Ahmed A., Singh A., Oruganti S. K., Khosla A., Arya S., Review—Recent Advances in Tin Oxide Nanomaterials as Electrochemical/Chemiresistive Sensors, *J Electrochem. Soc.* 168 (2021) 027505.
8. Shanthi S., Kumar D., Synthesis, structural and optical properties of alloyed Ti(1-x)SnxO₂ nanoparticles, *Superlattices and Microstructures*. 85 (2015) 139–148.
9. Das S., Jayaraman V., SnO₂: A comprehensive review on structures and gas sensors, *Progress in Materials Science*. 66 (2014) 112–255.
10. Volkova M. G., Storozhenko V. Yu., Gulyaeva I. A., Starnikova A. P., Petrov V. V., Bayan E. M., TiO₂-SnO₂ films: Synthesis by low-temperature pyrolysis and electrophysical properties, *Materials Today: Proceedings*. 52 (2) (2022) 187–190.
11. Zhou H., Zhong Y., He Z., Zhang L., Wang J., Zhang J., Cao C., Highly porous Ti/SnO₂ network composite film as stable binder-free anode materials for lithium ion batteries, *Applied Surface Science*. 314 (2014) 1–6.
12. Bayan E. M., Lupeiko T. G., Pustovaya L. E., Fedorenko A. G., Effect of synthesis conditions on the photocatalytic activity of titanium dioxide nanomaterials, *Nanotechnologies in Russia*. 12 (5) (2017) 269–275.
13. Petrov V. V., Sysoev V. V., Starnikova A. P., Volkova M. G., Kalazhokov Z. Kh., Storozhenko V. Yu., Khubezhov S. A., Bayan E. M., Synthesis, Characterization and Gas Sensing Study of ZnO-SnO₂ Nanocomposite Thin Films, *Chemosensors*. 9 (6) (2021) 124.
14. Fomenko V. S., Emission properties of elements and chemical compounds. Ed. Academy of Sciences of the USSR, Kiev, 1961. (In Russ).
15. Firas K. M. A., Noor J. R., Synthesis and characterization of ZnO/SnO₂ nanorods core-shell arrays for high performance gas sensors, *Applied Physics A*. 127 (203) (2021).

16. **Sahm T., Gurlo A., Barsan N., Weimar U.**, Basics of oxygen and SnO₂ interaction; work function change and conductivity measurements, *Sens. Actuators B Chem.* 118 (1–2) (2006) 78–83.

17. **Petrov V. V.**, Investigation of the gas molecules interaction features with the oxide gas-sensitive materials surface, *Nano- and microsystem technology.* 1 (2007) 24–27.

THE AUTHORS

GULYAEVA Irina A.

tenirka@mail.ru

ORCID: 0000-0001-9364-1007

IVANISHCHEVA Alexandra P.

a.starnikova@mail.ru

ORCID: 0000-0002-3779-8242

VOLKOVA Maria G.

mvol@sfedu.ru

ORCID: 000000019483162X

BAYAN Ekaterina M.

ekbayan@sfedu.ru

ORCID: 0000-0002-8445-9139

PETROV Victor V.

vvp2005@inbox.ru

ORCID: 0000-0003-3725-6053

Received 13.07.2022. Approved after reviewing 25.07.2022. Accepted 26.07.2022.

Conference materials
UDC 546.05; 538.975
DOI: <https://doi.org/10.18721/JPM.153.353>

Study of structural properties and photoconductivity of Co_3O_4 -ZnO thin films

I. A. Gulyaeva ¹✉, I. O. Ignatieva ², E. M. Bayan ², V. V. Petrov ¹

¹ Southern Federal University, Taganrog, Russia;

² Southern Federal University, Rostov-on-Don, Russia

✉ tenirka@mail.ru

Abstract. In this work, we study the photoconductivity parameters of Co_3O_4 -ZnO thin films formed on polycortex substrates. Co_3O_4 -ZnO nanocomposite films were deposited on substrates by solid-phase pyrolysis with a Co:Zn molar ratio of 10:90, 5:95, 3:97, and 1:99 and annealed at a temperature of 600 °C. The film thickness was 150–200 nm. The crystal structure of the films was studied, and the SEM images were analyzed. After application of contact metallization, the parameters of photoconductivity were measured under the action of light from an LED with a wavelength of 400 nm.

Keywords: nanomaterials, thin films, solid-state pyrolysis, photoconductivity

Funding: The study was supported by the Russian Science Foundation grant No. 22-29-00621, <https://rscf.ru/en/project/22-29-00621/> at the Southern Federal University.

Citation: Gulyaeva I. A., Ignatieva I. O., Bayan E. M., Petrov V. V., Study of structural properties and photoconductivity of Co_3O_4 -ZnO thin films. St. Petersburg State Polytechnical University Journal. Physics and Mathematics, 15 (3.3) (2022) 271–275. DOI: <https://doi.org/10.18721/JPM.153.353>

This is an open access article under the CC BY-NC 4.0 license (<https://creativecommons.org/licenses/by-nc/4.0/>)

Материалы конференции
УДК 546.05; 538.975
DOI: <https://doi.org/10.18721/JPM.153.353>

Исследование структурных свойств и фотопроводимости тонких пленок Co_3O_4 -ZnO

И. А. Гүляева ¹✉, И. О. Игнатъева ², Е. М. Баян ², В. В. Петров ¹

¹ Южный федеральный университет, Таганрог, Россия;

² Южный федеральный университет, Ростов-на-Дону, Россия

✉ tenirka@mail.ru

Аннотация. В данной работе изучаются параметры фотопроводимости тонких пленок Co_3O_4 -ZnO, образованных на поликорковых подложках. Нанокompозитные пленки Co_3O_4 -ZnO наносили на подложки методом твердофазного пиролиза с молярным соотношением Co:Zn 10:90, 5:95, 3:97, 1:99 и отжигали при температуре 600 °C. Толщина пленок составляла 50–100 нм. Изучена кристаллическая структура пленок и проанализированы СЭМ изображения. После нанесения контактной металлизации были измерены параметры фотопроводимости Co_3O_4 -ZnO пленок при воздействии излучения светодиода с длиной волны 400 нм.

Ключевые слова: наноматериалы, тонкие пленки, твердофазный пиролиз, фотопроводимость

Финансирование: Работа выполнена при поддержке гранта РФФ № 22-29-00621, <https://rscf.ru/ru/project/22-29-00621/> в Южном федеральном университете.

Ссылка при цитировании: Гуляева И. А., Игнатъева И. О., Баян Е. М., Петров В. В., Исследование структурных свойств и фотопроводимости тонких пленок $\text{Co}_3\text{O}_4\text{-ZnO}$ // Научно-технические ведомости СПбГПУ. Физико-математические науки. 2022. Т. 15. № 3.3. С. 271–275. DOI: <https://doi.org/10.18721/JPM.153.353>

Статья открытого доступа, распространяемая по лицензии CC BY-NC 4.0 (<https://creativecommons.org/licenses/by-nc/4.0/>)

Introduction

Nowadays the development of new materials promising for alternative energy sources is attracting more and more attention from researchers. The most studied multifunctional material is zinc oxide, which is a wide-band n-type conductor ($E_g = 3.37$ eV [1]) with chemical and thermal stability, low toxicity, and cost. Significant interest is caused by such properties as structural [2], optical [3], electrical [4], gas-sensitive [5] and photocatalytic [6]. It is noted that the execution of materials in the form of thin films with nanoscale particles is the most desirable, since it is such materials that make it possible to obtain effective devices with unique properties.

There are many physical and chemical synthesis methods. The most frequently used methods, such as pulsed laser deposition [7], chemical vapor deposition [8], magnetron sputtering [9], sol-gel [10] and spray pyrolysis [11]. It has been established that the various properties of zinc oxide films are significantly affected by the additives introduced. So, doping with group III elements (Al, Ga, In) and transition metal elements (Co, Ni, Mn and Cu) it can change the optical and electrical properties of film materials. It is known that the cobalt additive is able to increase the photoreclick of ZnO in the visible spectral range, which allows such materials to become useful for converting solar energy into chemical or electrical potentials [12].

The paper [13] reports on the study of the photoconductivity of a broadband semiconductor ZnO doped with cobalt ions ($\text{Zn}_{1-x}\text{Co}_x\text{O}$). The photoconductivity of materials demonstrates a strong dependence on the cobalt content. Thus, the data show that an increase in x increases the energy of the edge of the conduction band, which increases the ionization energy of $\text{Co}^{2+}/\text{Co}^{3+}$.

In this paper, we report on the structural properties and photoconductivity parameters of $\text{Co}_3\text{O}_4\text{-ZnO}$ thin films obtained by solid-phase pyrolysis. The results showed that the materials obtained are promising candidates for alternative energy sources.

Materials and Methods

Zinc (II) acetate dihydrate $\text{Zn}(\text{CH}_3\text{COO})_2 \cdot 2\text{H}_2\text{O}$, cobalt (II) acetate tetrahydrate $\text{Co}(\text{CH}_3\text{COO})_2 \cdot 4\text{H}_2\text{O}$, and organic acid were used as precursors in the solid-phase pyrolysis. The process of forming thin films consisting of two stages conducted according to the previously described method [14]. During the first stage, a mixture of zinc and cobalt salts were melted in organic acid, and intermediate product was obtained. During the second stage, a solution of the produced product in a dioxane was applied to substrates previously prepared substrates. Then the resulting films were annealed at 600°C during 2 hours.

We have studied the phase composition of the film materials and crystalline quality by X-ray phase analysis (XRD) on an ARL'XTRA diffractometer. In the future, a counter-pin V-Ni metallization was applied to the $\text{Co}_3\text{O}_4\text{-ZnO}$ film by the method of thermal vacuum evaporation through the mask and a flat photoresistor with an initial "dark" resistance R_0 was formed.

To investigate the surface morphology and structure of the films, $\text{Co}_3\text{O}_4\text{-ZnO}$ was carried out by scanning electron microscopy (SEM) using a microscope NovaNanoLab 600 (FEI, Holland).

Results and Discussion

Fig. 1 demonstrates X-ray diffraction patterns of thin films based on zinc oxide doped with different concentration of cobalt ions (1–10%) in the 2θ range $20\text{--}80^\circ$. It was established that the obtained materials are polycrystalline in nature and two-phase. In addition to the peaks of the hexagonal structure of wurtzite of zinc oxide, there are peaks characteristic of Co_3O_4 . Moreover, the intensity of the peaks of zinc oxide wurtzite is much more pronounced than the peaks of cobalt oxide.

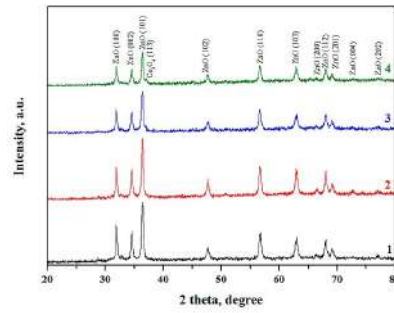


Fig. 1. X-ray images of Co_3O_4 -ZnO films with a ratio of Co:Zn of 1:99 (1), 3:97 (2), 5:95 (3), 10:90 (4)

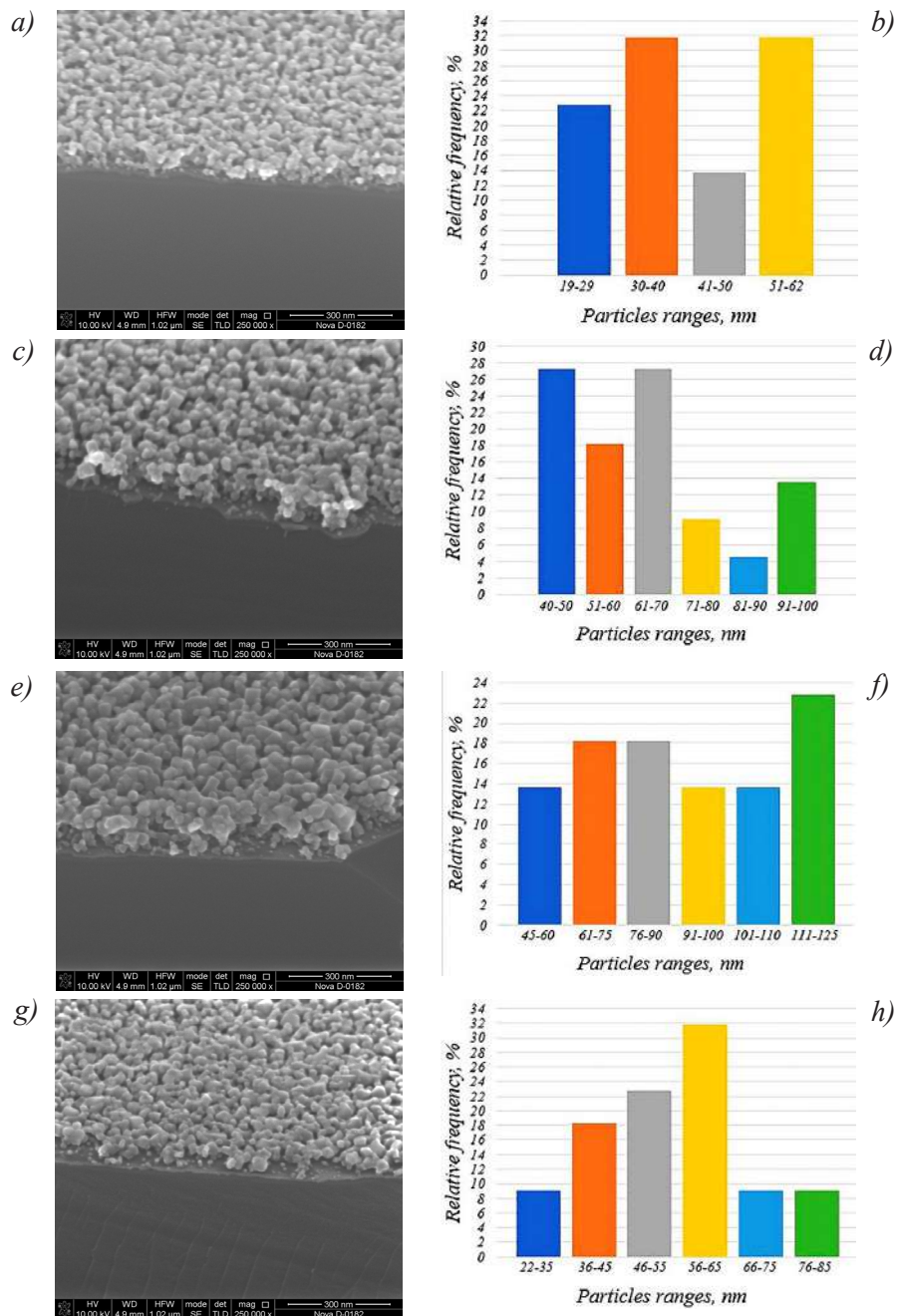


Fig.2 SEM image of Co_3O_4 -ZnO films with a ratio of Co:Zn of 1:99 (a, b), 3:97 (c, d), 5:95 (e, f), 10:90 (g, h)

SEM studies showed (Fig. 2) that the thickness of the resulting films was 40–100 nm. Statistical processing of the results of EMS analysis is presented on the histograms below. It can be seen that the films have a developed relief and consist of nanoparticles, the sizes of which vary for Co_3O_4 -ZnO films with a ratio of Co:Zn of 1:99 (*a, b*) from 19–65 nm, 40–100 nm for 3:97 (*c, d*), for 5:95 (*e, f*) it was 45–125 nm and 22–81 nm for 10:90 (*g, h*). Co_3O_4 -ZnO films have the largest particle size with a Co:Zn of 3:97 and 5:95 ratio. Co_3O_4 particle size is reduced to 19 nm.

In order to study the parameters of the photoconductivity of thin semiconductor films and heterostructures formed on opaque substrates, a stand was designed and manufactured. The work of the stand is based on measuring the kinetics of the photoconductivity of a resistive structure based on the film under study when it is irradiated with a LED with a given wavelength. Eight LEDs with a maximum radiation wavelength of 940, 660, 625, 525, 470 and 400 nm were chosen for the research. In addition, the design of the stand includes a pulsed constant voltage power supply AKIP-1101 (Russia), which makes it possible to regulate the energy characteristics of the radiation. To measure the characteristics of radiation, an ultraviolet radiation intensity meter CENTER 532 (China) and an illumination meter (luxmeter) CENTER 530 (China) are used. The electrical contact is provided by tungsten probes, and the photoconductivity is monitored with a Tektronix DMM 4050 digital multimeter (China). There was a direct change in photoconductivity under the action of light from an LED with a peak wavelength of 400 nm.

When the LED was turned on, a photoresistance was observed in all film samples. The measurement was carried out before the beginning of the “unfolding” of the dependencies. Subsequently, the time constant for the generation of charge carriers under the action of light was calculated.

Fig. 3 shows a timeline of the time change in normalized photoresistance under the action of light for films with a molar ratio of Co:Zn of 10:90, 5:95, 3:97, 1:99.

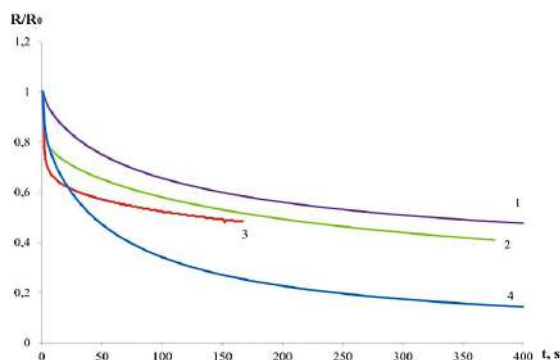


Fig. 3. Graph of the temporal change in normalized photoresistance under the action of light for Co_3O_4 -ZnO films with a molar ratio Co:Zn of 1:99 (1), 3:97 (2), 5:95 (3), 10:90 (4)

Studies have shown that a film with an additive of 1% cobalt has the longest constant time equal to 70 s. Adding cobalt oxide of 3% and 10% drastically reduces the constant duration to 37 and 60 s. The fastest response time of 25 s was found in a sample with a Co:Zn ratio of 5:95. This behavior of photoconductivity parameters is associated with the nanocomposite structure of the film material, and lower values of the constant time are associated with a higher concentration of charge carrier generation centers at the Co_3O_4 -ZnO interface at a Co:Zn ratio of 5:95. It can also be noted that the response kinetics for all films were similar, which indicates the same generation mechanisms - recombination of charge carriers in ZnO sol-gel films with the addition of CoO.

Conclusion

Based on the X-ray diffraction results, it was found that the resulting material is two-phase, which is confirmed by the presence of peaks characteristic of ZnO and Co_3O_4 . It is noted that the intensity of the wurtzite peaks of zinc oxide is much more pronounced than the peaks of cobalt oxide. Thus, in this work, thin films of Co_3O_4 -ZnO were synthesized by a new method of solid-phase pyrolysis, in which the phase composition and the measured kinetics of photoconductivity were investigated. that the Co_3O_4 -ZnO film with a Co:Zn ratio of 5:95 has the lowest value of the time constant (25 s). At the same time, this film has the largest particle size, which may be a consequence of its speed.



REFERENCES

1. Cranton W. M., Kalfagiannis N., Hou X., Ranson R., Koutsogeorgis D. C., Enhanced electrical and optical properties of room temperature deposited Aluminium doped Zinc Oxide (AZO) thin films by excimer laser annealing, *Optics and Lasers in Engineering*. 80 (2016) 45–51.
2. Ondo-Ndong R., Pascal-Delannoy F., Boyer A., Giani A., Foucaran A., Structural properties of zinc oxide thin films prepared by rf magnetron sputtering, *Materials Science and Engineering: B*. 97 (1) (2003) 68–73.
3. Bayan E. M., Petrov V. V., Volkova M. G., Storozhenko V. Yu., Chernyshev A. V., SnO₂–ZnO nanocomposite thin films: The influence of structure, composition and crystallinity on optical and electrophysical properties, *Journal of Advanced Dielectrics*. 11 (2021) 4–5.
4. Guziewicz E., Godlewski M., Wachnicki L., Krajewski T. A., Luka G., Gieraltowska S., Jablonski A., ALD grown zinc oxide with controllable electrical properties, *Semiconductor Science and Technology*. 27 (7) (2012) 074011.
5. Petrov V. V., Ivanishcheva A. P., Volkova M. G., Storozhenko V. Yu., Gulyaeva I. A., Pankov I. V., Volochaev V. A., Khubezhov S. A., Bayan E. M., High Gas Sensitivity to Nitrogen Dioxide of Nanocomposite ZnO-SnO₂ Films Activated by a Surface Electric Field, *Nanomaterials* 12 (2022) 2025.
6. Fouad O. A., Ismail A. A., Zaki Z. I., Mohamed R. M., Zinc oxide thin films prepared by thermal evaporation deposition and its photocatalytic activity, *Applied Catalysis B: Environmenta*. 62 (1-2) (2006) 144–149.
7. Wisz G., Virt I., Sagan P., Potera P., Yavorskyi R., Structural, optical and electrical properties of zinc oxide layers produced by pulsed laser deposition method, *Nanoscale Research Letters*. 12 (1) (2017) 1–7.
8. Waugh M. R., Hyett G., Parkin I. P., Zinc oxide thin films grown by aerosol assisted CVD, *Chemical Vapor Deposition*. 14 (11-12) (2008) 366–372.
9. Song D., Effects of rf power on surface-morphological, structural and electrical properties of aluminium-doped zinc oxide films by magnetron sputtering, *Applied surface science*. 254 (13) (2008) 4171–4178.
10. Kamaruddin S. A., Chan K. Y., Yow H. K., Zainizan Sahdan M., Saim H., Knipp D., Zinc oxide films prepared by sol–gel spin coating technique, *Applied Physics A*. 104 (1) (2011) 263–268.
11. Aoun Y., Benhaoua B., Gasmi B., Benramache S., Structural, optical and electrical properties of zinc oxide thin films deposited by a spray pyrolysis technique, *Journal of Semiconductors*. 36 (1) (2015) 013002.
12. Kaphle A., Echeverria E., Mellroy D. N., Roberts K., Hari, P., Thermo-optical properties of cobalt-doped zinc oxide (ZnO) nanorods, *Journal of Nanoscience and Nanotechnology*. 19 (7) (2019) 3893–3904.
13. Johnson C. A., Cohn A., Kaspar T., Chambers S. A., Salley G. M., Gamelin D. R., Visible-light photoconductivity of Zn_{1-x}Co_xO and its dependence on Co²⁺ concentration, *Physical Review B*. 84 (12) (2011) 125203.
14. Petrov V. V., Sysoev V. V., Starnikova A. P., Volkova M. G., Kalazhokov Z. Kh., Storozhenko V. Yu., Khubezhov S. A., Bayan E. M., Synthesis, characterization and gas sensing study of ZnO-SnO₂ nanocomposite thin films, *Chemosensors*. 9 (6) (2021) 124.

THE AUTHORS

GULYAEVA Irina A.
tenirka@mail.ru
ORCID: 0000-0001-9364-1007

BAYAN Ekaterina M.
ekbayan@sfedu.ru
ORCID: 0000-0002-8445-9139

IGNATIEVA Irina O.
iignateva@sfedu.ru
ORCID: 0000-0002-8528-4537

PETROV Victor V.
vvpetrov@sfedu.ru
ORCID: 0000-0003-3725-6053

Received 13.07.2022. Approved after reviewing 17.07.2022. Accepted 17.07.2022.

Conference materials

UDC 544.7

DOI: <https://doi.org/10.18721/JPM.153.354>

Aluminum nanostructures produced by aerosol dry printing for ultraviolet photoluminescence enhancement

D. Malo ^{1,2}✉, A. A. Lizunova ¹, M. Nouraldeen ^{1,3}, V. I. Borisov ¹, V. V. Ivanov ¹

¹ Moscow Institute of Physics and Technology, Dolgoprudny, Moscow Region, Russia;

² Damascus University, Damascus, Syria;

³ Tartous University, Tartous, Syria

✉ malo.dana@mail.ru

Abstract. Aluminum nanoparticles and nanostructures characterized by plasmon resonance in the ultraviolet (UV) range became a subject of intense research. Fluorescence is considered an important phenomenon in catalysis, UV photonics and in clinical medicine, for example, in cell imaging, medical diagnostics and biophysical studies. This work demonstrates metal-enhanced luminescence in the UV region of zinc oxide nanoparticles deposited on films of aluminum nanoparticles formed by dry aerosol printing on quartz substrates. Two different conditions of metal aluminum nanoparticles (Al NPs) production in spark discharge method were used to obtain aluminum nanoparticles with an average size 9.5 ± 5.6 and 15.5 ± 8.9 nm. At an excitation wavelength of 325 nm, the photoluminescent enhancement factor at 377 nm was about 1.3 for zinc oxide nanoparticles (ZnO NPs) with mean size 26.6 ± 7.4 nm. This study is a perspective step to confirm the benefits and focus attention on the plasmonic properties of Al nanostructures in UV range.

Keywords: metal enhanced luminescence, ultraviolet region (UV), aluminum nanostructures, aluminum nanoparticles, zinc oxide nanoparticles, films, spark discharge method, dry aerosol printing

Funding: This work was financially supported by Russian Science Foundation (project No. 22-19-00311, <https://rscf.ru/en/project/22-19-00311/>).

Citation: Malo D., Lizunova A. A., Nouraldeen M., Borisov V. I., Ivanov V. V., Aluminum nanostructures produced by aerosol dry printing for ultraviolet photoluminescence enhancement. St. Petersburg State Polytechnical University Journal. Physics and Mathematics, 15 (3.3) (2022) 276–280. DOI: <https://doi.org/10.18721/JPM.153.354>

This is an open access article under the CC BY-NC 4.0 license (<https://creativecommons.org/licenses/by-nc/4.0/>)

Материалы конференции

УДК 544.7

DOI: <https://doi.org/10.18721/JPM.153.354>

Наноструктуры алюминия полученные методом сухой аэрозольной печати для усиления ультрафиолетовой фотолюминесценции

Д. Мало ^{1,2}✉, А. А. Лизунова ¹, М. Нуралдин ^{1,3}, В. И. Борисов ¹, В. В. Иванов ¹

¹ Московский физико-технический институт, Долгопрудный, Московская область, Россия;

² Дамасский университет, Дамаск, Сирия;

³ Тартусский университет, Тартус, Сирия

✉ malo.dana@mail.ru

Аннотация. Эта работа демонстрирует усиленную люминесценции в ультрафиолетовой (УФ) области наночастиц оксида цинка, нанесенных на пленки из наночастиц алюминия, сформированных методом сухой аэрозольной печати. Металлические наночастицы алюминия со средними размерами 9.5 ± 5.6 и 15.5 ± 8.9 нм были получены



в газовом разряде при двух различных условиях синтеза. Коэффициент усиления фотолюминесценции частиц оксида цинка со средним размером 26.6 ± 7.4 нм на длине волны 377 нм (при возбуждении на 325 нм) в присутствии частиц алюминия составлял около 1.3.

Ключевые слова: усиление люминесценции, ультрафиолетовая область (УФ), наноструктуры алюминия, наночастицы алюминия, наночастицы оксида цинка, пленки, метод газового разряда, сухая аэрозольная печать

Финансирование: Исследование выполнено за счет гранта Российского научного фонда (проект № 22-19-00311, <https://rscf.ru/en/project/22-19-00311/>).

Ссылка при цитировании: Мало Д., Лизунова А. А., Нуралдин М., Борисов В. И., Иванов В. В., Наноструктуры алюминия полученные методом сухой аэрозольной печати для усиления ультрафиолетовой фотолюминесценции // Научно-технические ведомости СПбГПУ. Физико-математические науки. 2022. Т. 15. № 3.3. С. 276–280. DOI: <https://doi.org/10.18721/JPM.153.354>

Статья открытого доступа, распространяемая по лицензии CC BY-NC 4.0 (<https://creativecommons.org/licenses/by-nc/4.0/>)

Introduction

The photoluminescence enhancement is considered one of the most intense research fields at the present time, especially in ultraviolet region [1–3]. Aluminum is attractive metal for commercial applications owing to low-cost, high plentiful, high stability due to the presence of the shell natural oxide, and easy inclusion into fabrication processes [4, 5]. Additionally, aluminum nanoparticles have plasmon resonance in the UV region [6, 7] that make this metal as a promising material for creating plasmonic structures with enhancing luminescence in the UV region of the spectrum for many applications in medicine and technologies as solar cells [8], ultraviolet light-emitting diodes [9,10], and chemical and biological sensors [5, 11, 12].

Several chemical and physical methods are used to synthesize aluminum nanoparticles [13]. One of them is spark discharge synthesis [6, 14] which allows to produce spherical nanoparticles with varies morphology and optical parameters as well as it can be used for the film fabrication.

There are a lot of expensive methods for the nanostructures' and film fabrication, for example: molecular beam epitaxy [15] and electron beam lithography [16]. However, several simple, cheap and easily scalable methods exist for the films' production based on metal nanoparticles and semiconductor phosphors. Dry aerosol printing is known to be a promising method to deposit chemically pure nanoparticles (NPs), produced by spark discharge, on substrate in real time for manufacturing planar microstructures and films [17].

At present, zinc oxide nanoparticles are used as the most widespread semiconductor material for verification the phenomena of metal-enhance luminescence in ultraviolet range near plasmonic nanostructures based on noble metal [18], and aluminium [19, 20].

Therefore, the purpose of our research is to investigate the metal-enhanced luminescence of ultraviolet phosphor, namely zinc oxide nanoparticles, in the presence of aluminum nanoparticles produced in our laboratory by spark discharge and deposited on quartz substrate by dry aerosol printing. It is shown that metal-enhanced luminescence of ZnO NPs was achieved using two samples of Al NPs with different average sizes at an excitation wavelength of 325 nm.

Materials and Methods

Suspension of zinc oxide was prepared from a dispersion of ZnO Sigma Aldrich (40 wt. %) by 10-times dilution using chromatographically pure isopropyl alcohol (Macron), ultrasonic treatment for 5 minutes and centrifugation (Sigma 3–30K) for 5 minutes at 25 000 rpm. The obtained suspension of ZnO NPs was diluted with chromatographically pure isopropyl alcohol to obtain suspension with concentration 2.2 g/l. To obtain Al NPs, the spark discharge generator [6] was used in atmosphere of argon of purity 6.0 with aluminum electrodes, capacitor 40 nF, discharge voltage 1.5 kV, pulse repetition rate 0.5 kHz and gas flow 1 L/min, for Al_I sample, 7 degrees of bevel of the electrodes were used, while for Al_{II} sample additional in-flow thermal treatment (600 °C) of NPs in tube furnace was applied.

To form thin films, Al NPs were deposited ($4 \times 4 \text{ mm}^2$) on a quartz substrate ($2 \times 2 \text{ cm}^2$) by dry aerosol printing [17]. Focusing nozzle with an outlet diameter of 300 nm, the internal channel of the nozzle is characterized by a smooth wall and a gradual decrease in the diameter of the channel. At the end of the nozzle there is a hole with a diameter D_{nn} , (Al NPs were depositing through a coaxial nozzle with an outlet hole of 300 μm located at 1 mm from the substrate surface. For studying the luminescence enhancement, the ZnO NPs (2.2 g/l) were disposed on the surface of Al NPs film.

The size and crystal structure of primary nanoparticles were received by transmission electron microscope (TEM) Jeol JEM 2100 (200 kV). The UV-vis-NIR spectra and luminescence emission of films were obtained using JASCO V-770 and JASCO FP-8300 spectrometers, correspondingly.

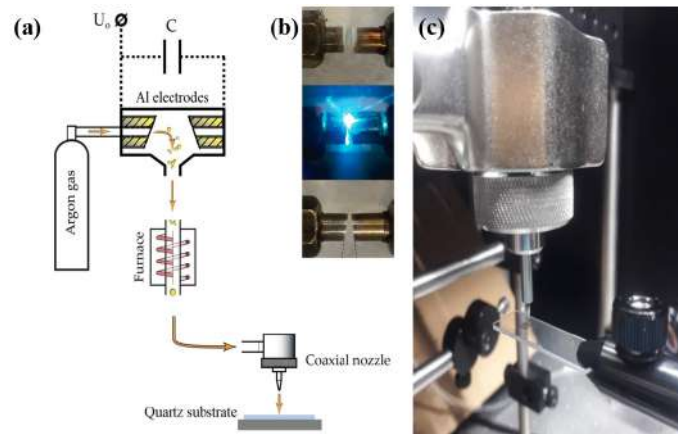


Fig. 1. Scheme of Al NPs synthesis by spark discharge generator with printing on quartz substrate (a); photograph of a spark between parallel (the upper photo) Al electrodes and with bevel (the bottom photo) electrodes (b); the dry aerosol printing of Al film (c)

Results and Discussion

TEM and electron diffraction images presented in Fig. 2 show that the Al nanoparticles have spherical shape and metal crystal structure, the average primary particle size of NPs synthesized with 7 degrees of bevel of the electrodes (Al_I) was $9.5 \pm 5.6 \text{ nm}$ while $15.5 \pm 8.9 \text{ nm}$ for particles synthesized with additional sintering at 600°C (Al_{II}). ZnO NPs were with mean size $26.6 \pm 7.4 \text{ nm}$.

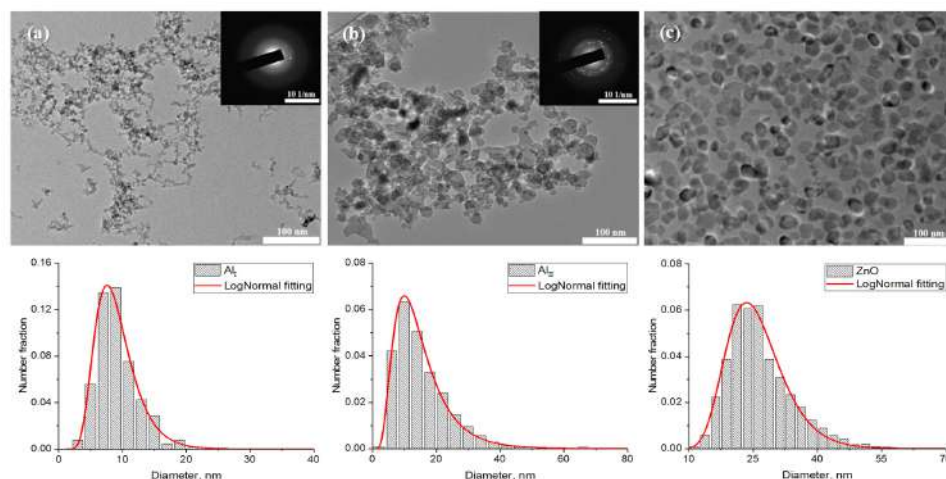


Fig. 2. Typical TEM images with corresponding SAED patterns (on the insert) for Al_I (a); Al_{II} (b); ZnO (c) and their histograms of the particle size distribution, approximated by a lognormal function

The measurements of the Al NPs films absorption spectra showed a uniformly decreasing function of wavelength and the presence of weak absorption peak in the UV region with peak position approximately at 245 nm for Al samples and for ZnO film approximately at 360 nm (Fig. 3, a). As shown in Fig. 3, b luminescence enhancement was achieved on quartz substrate

using two of Al NPs samples where ZnO layer was deposited above the Al layer (ZnO/Al) and the peak position was at 377 nm at an excitation wavelength of 325 nm. The photoluminescent enhancement factor was about 1.3 for (ZnO/Al) films when compared to bare ZnO film.

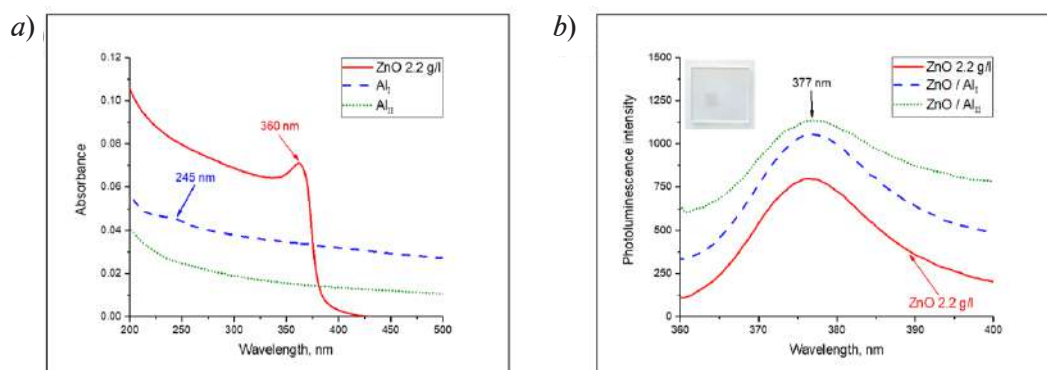


Fig. 3. Absorption spectra of films: ZnO 2.2 g/l, Al_I and Al_{II} (a); Photoluminescence emission spectra of films: ZnO 2.2 g/l, ZnO layer on Al_I layer and ZnO on Al_{II} at an excitation wavelength 325 nm (b)

The results mentioned above are considered acceptable for micro-nanostructure of ZnO nanoparticles in the presence of Al NPs. For example, in [21] the peak position of photoluminescence emission spectrum was at 375 nm with enhancement ratio 2.5 whereas another group achieved the enhancement ratio 170 at 389 nm [20]. Moreover, on array of oval Al NPs, the photoluminescence of ZnO nanocrystal increased 9.7 times at about 380 nm [19].

Conclusion

The spark discharge method is considered to be a simple and promising method for synthesis of metal Al NPs with plasmon resonance in the UV region. In this research, we presented experimental studies showing the effect of aluminum nanoparticles on the emission of fluorophores in the UV region of the spectrum. Metal-enhanced luminescence of ZnO NPs with mean size (26.6 ± 7.4 nm) was achieved using two samples of Al NPs with different average sizes (9.5 ± 5.6 and 15.5 ± 8.9 nm) at an excitation wavelength of 325 nm. Absorption peak position was detected at 245 nm for Al films, while for ZnO it was approximately at 360 nm.

At an excitation wavelength of 325 nm, the photoluminescence intensity of ZnO NPs in the UV region at wavelength 377 nm increased by 30 % in the presence of Al film based on metal NPs synthesized by spark discharge method and deposited on quartz substrate by dry aerosol printing when compared to bare ZnO film was shown. These promising results presented aluminum nanostructures as functional substrates for metal-enhanced luminescence applications in imaging, biosensing, catalysis and UV photonics.

REFERENCES

1. Guzatov D. V., Gaponenko S. V., Demir H. V., Plasmonic enhancement of electroluminescence, *AIP Advances*. 8 (1) (2018) 015324.
2. Yu H., Peng Y., Yang Y., Li Z.-Y., Plasmon-enhanced light–matter interactions and applications, *npj Computational Materials*. 5 (1) (2019) 1-14.
3. Gaponenko S. V., Demir H. V., *Applied nanophotonics*, Cambridge University Press: (2018).
4. Knight M. W., King N. S., Liu L., Everitt H. O., Nordlander P., Halas N. J., Aluminum for plasmonics, *ACS nano*. 8 (1) (2014) 834-840.
5. Gérard D., Gray S. K., Aluminium plasmonics, *Journal of Physics D: Applied Physics*. 48 (18) (2014) 184001.
6. Borisov V. I., Lizunova, A. A., Mazharenko A. K., Malo, D., Ramanenka A. A., Shuklov I. A., Ivanov V. V., Aluminum nanoparticles synthesis in spark discharge for ultraviolet plasmonics, *Journal of Physics: Conference Series*, IOP Publishing. 1695 (2020) 012021.
7. Martin J., Khlopin D., Zhang F., Schuermans S., Proust J., Maurer T., Gérard D., Plain J., Aluminum nanostructures for ultraviolet plasmonics, *UV and Higher Energy Photonics: From Materials to Applications 2017*, International Society for Optics and Photonics.10351(2017) 103510D.

8. **Zhang Y., Cai B., Jia B.**, Ultraviolet plasmonic aluminium nanoparticles for highly efficient light incoupling on silicon solar cells, *Nanomaterials*. 6 (6) (2016) 95.
9. **Honda, M., Kumamoto Y., Taguchi A., Saito Y., Kawata S.**, Plasmon-enhanced UV photocatalysis, *Applied Physics Letters*. 104 (6) (2014) 061108.
10. **Huang K., Gao N., Wang C., Chen X., Li J., Li S., Yang X., Kang J.**, Top-and bottom-emission-enhanced electroluminescence of deep-UV light-emitting diodes induced by localised surface plasmons, *Scientific reports*. 4 (1) (2014) 1–7.
11. **Li W., Ren K., Zhou J.**, Aluminum-based localized surface plasmon resonance for biosensing, *TrAC Trends in Analytical Chemistry*. 80 (2016) 486–494.
12. **Akbay N., Lakowicz J. R., Ray K.**, Distance-dependent metal-enhanced intrinsic fluorescence of proteins using polyelectrolyte layer-by-layer assembly and aluminum nanoparticles, *The Journal of Physical Chemistry C*. 116 (19) (2012) 10766–10773.
13. **Ghorbani H. R.**, A review of methods for synthesis of Al nanoparticles, *Orient journal of chemistry*. 30 (4) (2014) 1941–1949.
14. **Meuller B. O., Messing M. E., Engberg D. L., Jansson A. M., Johansson L. I., Norl n, S. M., Tureson N., Deppert K.**, Review of spark discharge generators for production of nanoparticle aerosols. *Aerosol Science and Technology*. 46 (11) (2012) 1256–1270.
15. **Aggarwal V., Ramesh C., Tyagi P., Gautam S., Sharma A., Husale S., Kumar M. S., Kushvaha S.**, Controlled epitaxial growth of GaN nanostructures on sapphire (11–20) using laser molecular beam epitaxy for photodetector applications. *Materials Science in Semiconductor Processing*. 125 (2021) 105631.
16. **Yue W., Wang Z., Yang Y., Chen L., Syed A., Wong K., Wang X.**, Electron-beam lithography of gold nanostructures for surface-enhanced Raman scattering, *Journal of Micromechanics and Microengineering*. 22 (12) (2012) 125007.
17. **Khabarov K. M., Nouraldeen M., Lizunova A. A., Urazov M. N., Ivanov V. V.**, Formation of planar plasmon microstructures by dry aerosol printing, *Journal of Physics: Conference Series*, IOP Publishing. 2086 (2021) 012147.
18. **Guidelli E. J., Baffa O., Clarke D. R.**, Enhanced UV emission from silver/ZnO and gold/ZnO core-shell nanoparticles: photoluminescence, radioluminescence, and optically stimulated luminescence, *Scientific reports*. 5 (1) (2015) 1–11.
19. **Muravitskaya A., Gokarna A., Movsesyan A., Kostcheev S., Rumyantseva A., Couteau C., Lerondel G., Baudrion A.-L., Gaponenko S., Adam P.-M.**, Refractive index mediated plasmon hybridization in an array of aluminium nanoparticles, *Nanoscale*. 12 (11) (2020) 6394–6402.
20. **Lu J., Li J., Xu C., Li Y., Dai J., Wang Y., Lin Y., Wang S.**, Direct resonant coupling of Al surface plasmon for ultraviolet photoluminescence enhancement of ZnO microrods. *ACS Applied Materials & Interfaces*. 6 (20) (2014) 18301–18305.
21. **Wu K., Lu Y., He H., Huang J., Zhao B., Ye Z.**, Enhanced near band edge emission of ZnO via surface plasmon resonance of aluminum nanoparticles, *Journal of Applied Physics*. 110 (2) (2011) 023510.

THE AUTHORS

MALO Dana
 malo.dana@mail.ru
 ORCID: 0000-0001-6310-9183

BORISOV Vladislav I.
 borisov.vi@phystech.edu
 ORCID: 0000-0001-7186-5050

LIZUNOVA Anna A.
 lizunova.aa@mipt.ru
 ORCID: 0000-0002-2895-4696

IVANOV Victor V.
 ivanov.vv@mipt.ru
 ORCID: 0000-0002-9149-0468

NOURALDEEN Messan
 messannouraldeen@phystech.edu
 ORCID: 0000-0001-5437-0021

Received 14.07.2022. Approved after reviewing 14.07.2022. Accepted 15.07.2022.

Conference materials

UDC 538.975

DOI: <https://doi.org/10.18721/JPM.153.355>

Physical properties of GaN/InGaN nanowires grown by PA-MBE on silicon substrate

D. N. Bondarenko ^{1,2✉}, V. O. Gridchin ^{1,2,3}, K. P. Kotlyar ¹, A. I. Baranov ²,
A. A. Maksimova ², R. R. Reznik ^{1,2,3,4}, G. E. Cirlin ^{1,2,3,4}

¹ St. Petersburg State University, St. Petersburg, Russia;

² Alferov University, St. Petersburg, Russia;

³ IAI RAS, St. Petersburg, Russia;

⁴ ITMO University, St. Petersburg, Russia

✉ bondarenko.dariya.spb@gmail.com

Abstract. The paper presents an approach to growth of GaN nanowires with thick core-shell InGaN insertions with a high indium content for creation of LED structure. The study of the electrical properties shows typical diode dependence. The results obtained can make a significant contribution to the development of light emitting diodes on silicon substrates.

Keywords: micro light-emitting diodes, molecular beam epitaxy, GaN/InGaN nanowires, silicon substrates, thick core-shell InGaN insertions

Funding: The growth of experimental samples was carried out under financial support of the research grant of IAI RAS No. 075-00761-22-00, FFZM-2022-0008. The morphology of grown samples was studied under financial support of the Russian Science Foundation Grant No. 21-72-00099. Electro-physical properties studies of grown samples were done under financial support of the Ministry of Science and Higher Education of the Russian Federation, research project No. 2019-1442.

Citation: Bondarenko D. N., Gridchin V. O., Kotlyar K. P., Baranov A. I., Maksimova A. A., Reznik R. R., Cirlin G. E., Physical properties of GaN/InGaN nanowires grown by PA-MBE on silicon substrate. St. Petersburg State Polytechnical University Journal. Physics and Mathematics, 15 (3.3) (2022) 281–284. DOI: <https://doi.org/10.18721/JPM.153.355>

This is an open access article under the CC BY-NC 4.0 license (<https://creativecommons.org/licenses/by-nc/4.0/>)

Материалы конференции

УДК 538.975

DOI: <https://doi.org/10.18721/JPM.153.355>

Физические свойства GaN/InGaN нитевидных нанокристаллов выращенных методом МПЭ с плазменной активацией на кремнии

Д. Н. Бондаренко ^{1,2✉}, В. О. Гридчин ^{1,2,3}, К. П. Котляр ¹, А. И. Баранов ²,
А. А. Максимова ², Р. Р. Резник ^{1,2,3,4}, Г. Э. Цырлин ^{1,2,3,4}

¹ Санкт-Петербургский государственный университет, Санкт-Петербург, Россия;

² Санкт-Петербургский академический университет им. Ж. И. Алферова РАН, Санкт-Петербург, Россия;

³ Институт аналитического приборостроения РАН, Санкт-Петербург, Россия;

⁴ Национальный исследовательский университет ИТМО, Санкт-Петербург, Россия

✉ bondarenko.dariya.spb@gmail.com

Аннотация. В данной работе представлен подход к синтезу светоизлучающей структуры на основе нитевидных нанокристаллов GaN с объемными вставками структуры «core-shell» InGaN с высоким содержанием индия. Изучение электрических свойств показывает типичную диодную зависимость. Полученные результаты могут внести весомый вклад для разработки светоизлучающих диодов на кремниевых подложках.

Ключевые слова: микросветодиоды, молекулярно-пучковая эпитаксия, нитевидные нанокристаллы GaN/InGaN, кремниевые подложки, объемные вставки структуры «core-shell» InGaN

Финансирование: Экспериментальные образцы были синтезированы при поддержке государственного задания ИАП РАН № 075-00761-22-00, FFZM-2022-0008. Исследования морфологических свойств выращенных образцов были выполнены при финансовой поддержке Российского Научного Фонда грант № 21-72-00099. Электро-физические свойства выращенных образцов были исследованы при финансовой поддержке Министерства науки и высшего образования Российской Федерации, проект тематики научных исследований № 2019-1442.

Ссылка при цитировании: Бондаренко Д. Н., Гридчин В. О., Котляр К. П., Баранов А. И., Максимова А. А., Резник Р. Р., Цырлин Г. Э. Физические свойства GaN/InGaN нитевидных нанокристаллов выращенных методом МПЭ с плазменной активацией на кремнии // Научно-технические ведомости СПбГПУ. Физико-математические науки. 2022. Т. 15. № 3.3. С. 281–284. DOI: <https://doi.org/10.18721/JPM.153.355>

Статья открытого доступа, распространяемая по лицензии CC BY-NC 4.0 (<https://creativecommons.org/licenses/by-nc/4.0/>)

Introduction

Nowadays, the area of research of the development of micro light-emitting diodes (LEDs) based on InGaN ternary compounds is strictly relevant [1]. Since these semiconductors with a direct band gap have unique properties, from which one can distinguish the ability to control the emission wavelength from near UV to near IR by changing the chemical composition [1]. However, during the synthesis of homogeneous InGaN layers with different chemical compositions, internal strains and phase separation (“miscibility gap”) appear, associated with a large lattice mismatch between InN and GaN [2]. Also, the problem of the synthesis such layers with high crystalline quality is the lack of lattice-matched substrates compared to InGaN. As shown earlier, one of the ways to solve the problems described above is the synthesis of nanowires (NWs) [3]. One of the advantages of NWs is the possibility of obtaining practically defect-free structures on substrates with different lattice parameters and different thermal expansion coefficients [4]. Due to this, it is possible to use silicon wafers as substrates for growing NWs. Also, it is possible to circumvent of “miscibility gap” due to which it is possible to obtain an InGaN solid solution with any required chemical composition [5]. In this case, InGaN NWs grown with a high In content can have a spontaneously formed core-shell structure [6]. In this connection, at present, a large number of studies are aimed at creating light-emitting devices in the visible range based on GaN/InGaN NWs, where thick core-shell InGaN serves as the active region.

In this work, we study the structural and optoelectronic properties of GaN NWs with a thick core-shell InGaN active region grown on n-Si (111) substrates by plasma-activated molecular beam epitaxy (PA-MBE).

Materials and Methods

The GaN/InGaN NWs were grown by PA-MBE using a Riber Compact 12 MBE setup equipped with Ga, In, Mg, and Si effusion cells and a nitrogen plasma source. We used n-Si(111) substrates with 0.002–0.004 Ω·cm electrical resistivity. The growth process consists of major steps. The pretreatment of the substrates, necessary for the removal native silicon oxide layer, was carried out using an aqueous solution of hydrofluoric acid. After treatment, the substrates were transferred to a growth chamber and subjected to thermal treatment at a temperature of 950 °C. Then the temperature was lowered to a value of 600 °C, and Ga droplets were formed on the surface of the substrate for 15 sec. Then the substrate temperature was raised to 820 °C. After stabilization of the temperature, a nitrogen plasma source with a power of 450 W was ignited, the flux of which was set at 0.4 sccm. At this stage, GaN NWs with n-type conductivity were formed due to the simultaneous opening of Ga and Si effusion cells. After that, InGaN active regions were formed. Finally, p-type GaN NWs were formed by doping with Mg. The total growth time was 17 h.



The morphological properties of the sample were studied using scanning electron microscopy (SEM supra 25 Zeiss). The electrical properties of the NWs were studied by measuring the current–voltage (I-V) curves at room temperatures.

Results and Discussion

Fig. 1, *a, b* show typical SEM images of grown GaN/InGaN NWs and a schematic representation of GaN/InGaN NWs. As can be seen from figure 1, the morphology of the grown structures is close-packed GaN/InGaN NWs with an average length of 1.5 μm and the diameters at the base and top of about 90 nm and 350 nm, respectively. Also, it can be seen that the sample consists of both separated and partially coalesced NWs.

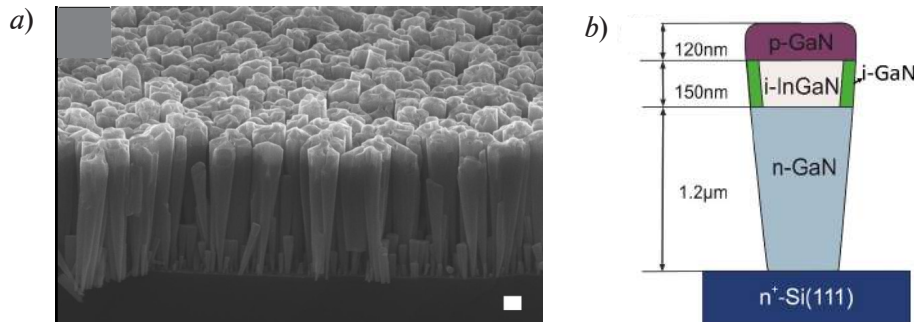


Fig. 1. SEM images of GaN/InGaN NWs: isometric view (*a*) and schematic image of the NW structure (*b*). The scale bars correspond to 200 nm

Before measuring the I-V curves the aluminum ohmic bottom contacts were formed on the n-Si substrate, and contacts were formed face top contacts on the p-GaN NWs by coating Ag paste (Fig. 2, *a*). Fig. 2, *b* shows the results of the measurements of I-V curves. As can be seen from the figure, the sample demonstrates typical diode behavior with an opening voltage of about 8V. High opening voltage can be caused by the Schottky barrier at the p-GaN/Ag interface [7]. The insertion to Fig. 2, *b* shows a photograph of the glow of the created structure.

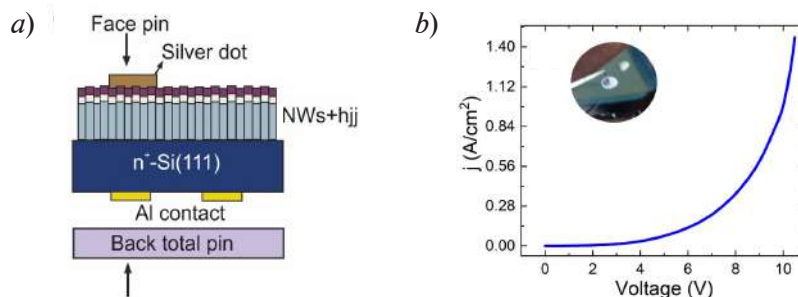


Fig. 2. Scheme of an LED based on an array of GaN/InGaN NWs on the n-Si(111) substrate (*a*); The current-voltage curve of GaN/InGaN NWs LED (*b*)

Conclusion

In summary, the growth of the GaN/InGaN nanowires on the n-Si(111) substrate by the PA-MBE method was demonstrated. The results of grown NWs morphological properties showed that the morphology of both samples is a close-packed array of cone-shaped NWs with an average length of about 1.5 μm . The I–V curves of the samples show typical diode characteristics. The preliminary results showed the glow of the created structure when voltage is applied.

REFERENCES

1. Bui H. Q. T., Velpula R. T., Jain B., Aref O. H., Nguyen H. -D., Lenka T. R., Nguyen H. P. T., Full-Color InGaN/AlGaIn Nanowire Micro Light-Emitting Diodes Grown by Molecular Beam Epitaxy: A Promising Candidate for next Generation Micro Displays, Micromachines. 10 (8) (2019) 492.

2. **Ho I., Stringfellow G. B.**, Solid phase immiscibility in GaInN, *Applied Physics Letters*. 69 (18) (1996) 2701–2703.
3. **Yan R., Gargas D., Yang P.**, Nanowire photonics, *Nature Photonics*. 3 (10) (2009) 569.
4. **Dubrovskii V. G., Cirlin G. E., Ustinov V. M.**, Semiconductor nanowhiskers: Synthesis, properties, and applications, *Semiconductors*. 43 (12) (2009) 1539–1584.
5. **Roche E., Andre Y., Avit G., Bougerol C., Castelluci D., R  veret F., Gil E., M  dard F., Leymarie J., Jean T., Dubrovskii V. G., Trassoudaine A.**, Circumventing the Miscibility Gap in InGaN Nanowires Emitting from Blue to Red, *Nanotechnology*. 29 (46) (2018) 465602.
6. **Gridchin V. O., Kotlyar K. P., Reznik R. R., Dragunova A. S., Kryzhanovskaya N. V., Lendyashova V. V., Kirilenko D. A., Soshnikov I. P., Shevchuk D. S., Cirlin G. E.**, Multi-colour light emission from InGaN nanowires monolithically grown on Si substrate by MBE, *Nanotechnology*. 32 (33) (2021) 335604.
7. **Picozzi S., Continenza A., Satta G., Massidda S., Freeman A. J.**, Metal induced gap states and Schottky barrier heights at non-reactive GaN/noble-metal interfaces, *Physical Review B*. 61 (24) (2000) 16736.

THE AUTHORS

BONDARENKO Daria N.
bondarenko.dariya.spb@gmail.com
ORCID: 0000-0003-4537-069X

MAKSIMOVA Alina A.
deer.blackgreen@yandex.ru
ORCID: 0000-0002-3503-7458

GRIDCHIN Vladislav O.
gridchinfo@yandex.ru
ORCID: 0000-0002-6522-3673

REZNIK Rodion R.
moment92@mail.ru
ORCID: 0000-0003-1420-7515

KOTLYAR Konstantin P.
konstantin21kt@gmail.com
ORCID: 0000-0002-0305-0156

CIRLIN George E.
george.cirlin@mail.ru
ORCID: 0000-0003-0476-3630

BARANOV Artem I.
baranov_art@spbau.ru
ORCID: 0000-0002-4894-6503

Received 21.07.2022. Approved after reviewing 08.08.2022. Accepted 19.08.2022.

Conference materials
UDC 621.317.39.084.2
DOI: <https://doi.org/10.18721/JPM.153.356>

Modification of the optical and electrical properties of NiO films by thermal annealing

Ya. B. Enns^{1, 2}✉, A. N. Kazakin^{1, 2}, I. M. Komarevtsev^{1, 2},
E. A. Vyacheslavova¹, A. S. Kondrateva¹, M. V. Mishin¹

¹ Alferov University, St. Petersburg, Russia;

² Peter the Great St.Petersburg Polytechnic University, St. Petersburg, Russia

✉ ennsjb@gmail.com

Abstract. This paper presents the results of studying the effect of thermal annealing on the optical and electrical characteristics of NiO films. NiO layers were synthesized using DC magnetron sputtering from a Ni target. The films were deposited in an Ar/O₂ gas mixture with a ratio of 70%/30%, respectively. The deposition power was 100 W. The resulting films had low transparency and high conductivity, which is associated with a high content of oxygen vacancies in the NiO structural layer. The influence of thermal annealing on the characteristics of NiO films was studied on films obtained by magnetron sputtering. Annealing was carried out in an oxygen-containing environment at temperatures from 200 °C to 550 °C and an annealing duration from 5 to 120 minutes. The results of optical studies have shown that annealing at temperatures up to 550 °C leads to an increase in transparency from 5% to 80% at a wavelength of 700 nm. In this case, an increase in the temperature and duration of the process is accompanied by an increase in the optical band gap. A similar trend was observed in the study of film conductivity, where an increase in the annealing temperature leads to an increase in resistivity from 0.2 Ω cm to 1460 Ω cm.

Keywords: nickel oxide, transparency, thermal annealing, resistivity, optical band gap

Funding: The work was done as a part of the state assignment (No. FSRM-2020-0011) of the Ministry of Education.

Citation: Enns Ya. B., Kazakin A. N., Komarevtsev I. M., Vyacheslavova E. A., Kondrateva A. S., Mishin M. V., Modification of the optical and electrical properties of NiO films by thermal annealing. St. Petersburg State Polytechnical University Journal. Physics and Mathematics, 15 (3.3) (2022) 285–289. DOI: <https://doi.org/10.18721/JPM.153.356>

This is an open access article under the CC BY-NC 4.0 license (<https://creativecommons.org/licenses/by-nc/4.0/>)

Материалы конференции
УДК 621.317.39.084.2
DOI: <https://doi.org/10.18721/JPM.153.356>

Модификация оптических и электрических свойств пленок NiO с применением термического отжига

Я. Б. Эннс^{1, 2}✉, А. Н. Казакин^{1, 2}, И. М. Комаревцев^{1, 2},
Е. А. Вячеславова¹, А. С. Кондратьева¹, М. В. Мишин¹

¹ Санкт-Петербургский национальный исследовательский Академический университет имени Ж. И. Алферова, Санкт-Петербург, Россия;

² Санкт-Петербургский государственный университет, Санкт-Петербург, Россия

✉ ennsjb@gmail.com

Аннотация. В данной работе представлены результаты исследования влияния термического отжига на оптические и электрические характеристики пленок NiO. Слои NiO были синтезированы с использованием DC магнетронного напыления из мишени Ni. Напыление пленок осуществлялось в газовой смеси Ar/O₂ соотношением 70%/30%,

соответственно. Мощность напыления составила 100 W. Полученные пленки имели низкую прозрачность и высокую проводимость, что связано с высоким содержанием кислородных вакансий в структурном слое NiO. Влияние термического отжига на характеристики пленок NiO изучалось на пленках, полученных методом магнетронного напыления. Отжиг осуществлялся в кислородосодержащей среде при температурах от 200 °С до 550 °С и длительностью отжига от 5 до 120 минут. Результаты оптических исследований показали, что отжиг при температурах до 550 °С приводит к увеличению прозрачности с 5 % до 80 % на длине волны 700 нм. При этом увеличение температуры и длительности процесса сопровождается с увеличением оптической ширины запрещенной зоны. Подобная тенденция наблюдалась при исследовании проводимости пленок, где повышение температуры отжига приводит к увеличению удельного сопротивления с 0.2 Ом·см до 1460 Ом·см.

Ключевые слова: оксид никеля, прозрачность, термический отжиг, удельное сопротивление, оптическая запрещенная зона

Финансирование: Работа выполнена в рамках Государственного задания (№ FSRM-2020-0011).

Ссылка при цитировании: Эннс Я. Б., Казакин А. Н., Комаревцев И. М., Вячеславова Е. А., Кондратьева А. С., Мишин М. В. Модификация оптических и электрических свойств пленок NiO с применением термического отжига // Научно-технические ведомости СПбГПУ. Физико-математические науки. 2022. Т. 15. № 3.3. С. 285–289. DOI: <https://doi.org/10.18721/JPM.153.356>

Статья открытого доступа, распространяемая по лицензии CC BY-NC 4.0 (<https://creativecommons.org/licenses/by-nc/4.0/>)

Introduction

There is an increase in attention to transition metal oxides such as TiO₂, MoO₃, WO₃, CuO, ZnO, NiO and others. These materials can be used both for manufacturing power diode structures [1] and for optoelectronic applications [2]. Nickel oxide (NiO) is the most prominent representative of this class of substances. At the moment, there are several models for the conductivity of semiconductor nickel oxide, but all of them are based on the fact that NiO is a direct-gap material, has its own hole conductivity, and has a band gap of 3.6–4.0 eV. Thus, this oxide semiconductor has a high prospect in optoelectronic devices.

NiO films can be synthesized by various methods, among which the method of magnetron sputtering is highly promising, due to the high quality of the film, low cost, and high speed of coating formation. Films are deposited using both RF magnetrons and targets made of high-purity Ni or stoichiometric NiO [3] and DC magnetrons with Ni targets [4]. In both cases, deposition occurs by adding O₂ to the working gas mixture. A high concentration of acceptors can be obtained due to spontaneously formed Ni vacancies [5], which is achieved by choosing the reactive sputtering technological parameters. At the same time, it is rather difficult to achieve a high quality of NiO films after magnetron sputtering, where films can mainly have low crystallinity, low mobility, and low transparency. This is due to the high concentration of point defects inside the film due to the high oxygen content [6]. The simplest method for modifying the resulting film coatings is high-temperature annealing. Annealing can lead to an increase in the structural perfection of the material and, as a consequence, to a decrease in the concentration of point defects inside the film, an increase in the width of the optical band gap, and an increase in resistivity.

In this work, we study in detail the effect of high-temperature annealing on the optical and electrical characteristics of magnetron sputtered NiO films.

Materials and Methods

In the study, NiO films were formed on a glass substrate (Corning 0211) using DC magnetron sputtering from a Ni (99.95%) nickel target. Magnetron sputtering was carried out in a mixture of working gases 30% O₂ / 70% Ar at a working pressure of 3 mTorr. The gas flow rate was 6 sccm and 14 sccm for O₂ and Ar, respectively. The magnetron sputtering power was 100W.

After deposition, the glass substrates were divided into 10×10 mm chips using a circular saw and NiO films were subjected to thermal annealing in an oxygen-containing controlled environment. A series of annealings were carried out in the temperature range of 200–550 °C with a duration of 5–120 min.

Film thicknesses were determined using an Ambios XP-1 contact profilometer. The optical and electrical parameters of the resulting films were measured. The optical transmission and reflectance spectra were measured applying an AvaSpec-ULS2048XL-EVO-RS spectrometer and a xenon lamp in the wavelength range of 300–800 nm. Electrical measurements were carried out using a probe station and semiconductor device analyzer (Keysight B1500A) to determine the current-voltage characteristics.

Results and Discussion

The thickness of the NiO layer was about 150 nm, which corresponds to a deposition rate of 1.6 nm/min. The resulting NiO films had high conductivity and low transparency. The results obtained after thermal annealing showed an increase in the transparency of the films with an increase in the temperature and duration of the annealing of the films. Fig. 1, *a* shows examples of optical spectral characteristics of NiO films with different annealing conditions. The trend of increasing the transparency of films can be traced in Fig. 1, *b*. Thus, after annealing at 550 °C, the transmission of the films increased from 5% to 80% at a wavelength of 700 nm.

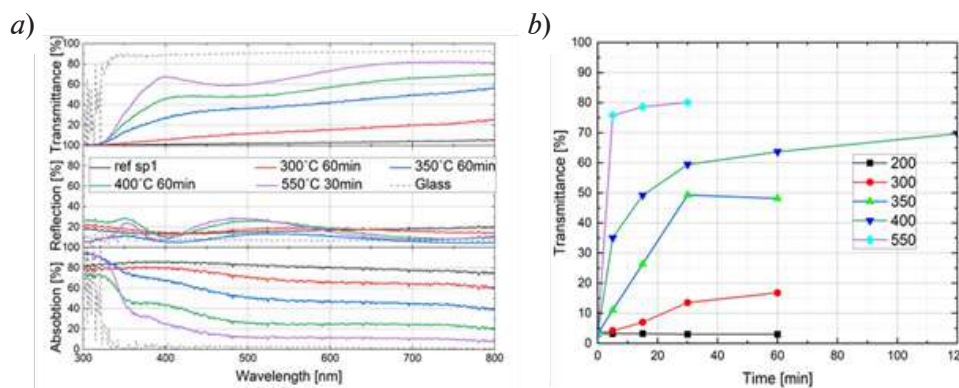


Fig. 1. Optical transmission, reflection and absorption spectra of samples obtained by annealing at different temperatures (*a*); Dependence of the transmittance (700 nm) on the annealing time (*b*)

The increase in the transparency of the films to a greater extent may be due to a decrease in optical absorption, a decrease in the concentration of carriers, and an increase in the crystallinity of the film.

The optical bandgap (E_g) of each sample was extracted from the absorption edge. According to the theory of optical absorption, the absorption coefficient is calculated as follows:

$$(\alpha h\nu)^k = A(h\nu - E_g)$$

where A is a constant, α is the absorption coefficient, and $h\nu$ is the photon energy. Since NiO is a direct band gap material, the exponent k is set to 2. The Tauc plot was used to determine the optical band gap and is shown in Fig. 2, *a*. E_g of NiO films can be obtained by extrapolating the linear part $(\alpha h\nu)^2$ to the $h\nu$ axis. It was found that an increase in the temperature and duration of annealing is accompanied by an increase in the width of the optical band gap. Fig. 2, *b* shows the trend in optical band gap versus annealing time for different process temperatures. The oxygen interstices in NiO films can either act as a lattice defect, scattering and/or absorbing incident light, or it can introduce some energy levels of impurities into the band gap and reduce the optical band gap [3]. Annealing of NiO films can promote the diffusion of interstitial oxygen atoms from NiO films, which appear itself in an increase in the optical band gap.

In addition, it has been found that an increase in the transparency of the films is accompanied by a significant increase in resistivity from 0.2 Ω cm to 1460 Ω cm. Fig. 3 shows the trend in the

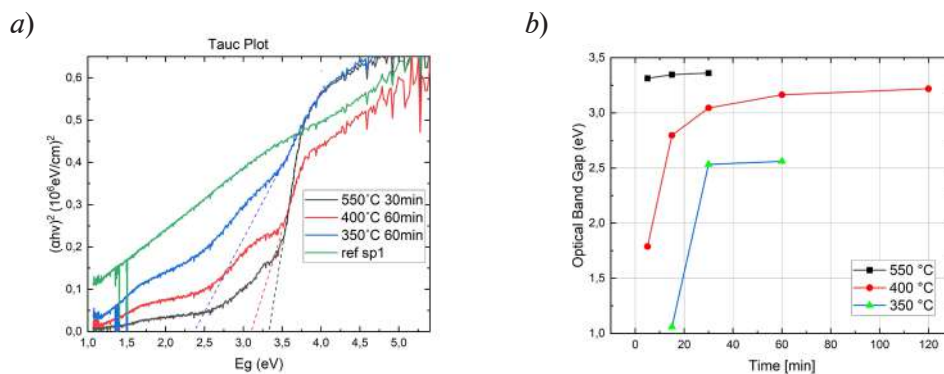


Fig. 2. The plot of $(\alpha h\nu)^2$ versus photon energy $h\nu$ (a); dependence of the optical band gap on the annealing time for different process temperatures (b)

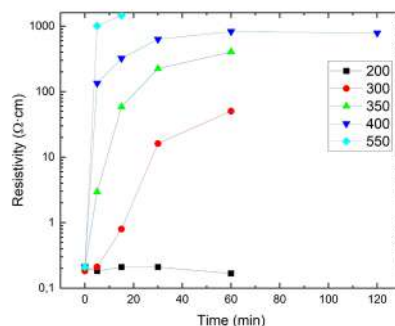


Fig. 3. Dependence of the resistivity of NiO films on the annealing time for various temperature processes

change in the resistivity of NiO films as a function of the annealing time for various temperature processes. This can also be a consequence of the relaxation of interstitial oxygen atoms as a result of annealing.

Conclusion

The NiO layer was synthesized using DC magnetron sputtering from a Ni metal target, which is a simple, scalable and inexpensive method. The effect of annealing the obtained films on the optical and electrical characteristics was studied. Conductivity measurements show that the resistivity of the NiO films increases significantly with the annealing temperature from 0.2 $\Omega \cdot \text{cm}$ (initial) to 1460 $\Omega \cdot \text{cm}$ (annealing at 550 °C). In addition, an increase in resistivity is accompanied by an increase in the transparency of the films and an increase in the optical band gap after annealing of the films. This may be due to a decrease in the density of point defects inside NiO after annealing due to the diffusion of oxygen interstices.

REFERENCES

1. Mistrya B. V., Bhattb P., Bhavsara K. H., Trivedia S. J., Trivedib U. N., Joshi U. S., Growth and properties of transparent p-NiO/n-ITO ($\text{In}_2\text{O}_3:\text{Sn}$) p-n junction thin film diode, *Thin Solid Films*. 519 (11) (2011) 3840–3843.
2. Warasawa M., Watanabe Y., Ishida J., Murata Y., Chichibu S. F., Sugiyama M., Fabrication of Visible-Light-Transparent Solar Cells Using p-Type NiO Films by Low Oxygen Fraction Reactive RF Sputtering Deposition, *Japanese Journal of Applied Physics*. 52 (2R) (2013) 021102.
3. Ren Y., Li L., Liu N., Zhang K., Li Ch., Chen Zh., Zhang B., Quasi-vertical GaN heterojunction diodes with p-NiO anodes deposited by sputtering and post-annealing, *Vacuum*. 182 (2020) 109784.



4. **Li L., Wang X., Liu Y., Ao J-P.**, NiO/GaN heterojunction diode deposited through magnetron reactive sputtering, *Journal of Vacuum Science & Technology A*. 34 (2016) 02D104.
5. **Lany S., Osorio-Guillren J., Zunger A.**, Origins of the doping asymmetry in oxides: hole doping in NiO versus electron doping in ZnO, *Phys. Rev. B Condens. Matter*. 75 (2007) 1–4.
6. **Kim S.-K., Yang H., Kim Y.-S.**, Effects of double heat treatment of NiO hole transport layer on the performance of QLEDs, *Journal of Materials Science*. 55 (2020) 17046–17060.

THE AUTHORS

ENNS Yakov B.

ennsjb@gmail.com

ORCID: 0000-0003-4396-2368

KAZAKIN Alexey N.

kazakin75@gmail.com

ORCID: 0000-0001-8762-1587

KOMAREVTSEV Ivan M.

mail.nikitina@mail.ru

ORCID: 0000-0002-6800-9218

VYACHESLAVOVA Ekaterina A.

cate.viacheslavova@yandex.ru

ORCID: 0000-0001-6869-1213

KONDRATEVA Anastasia S.

Kondrateva_n@spbau.ru

ORCID: 0000-0003-3915-9329

MISHIN Maxim V.

mishinm@spbau.ru

ORCID: 0000-0003-3250-1515

Received 25.07.2022. Approved after reviewing 26.07.2022. Accepted 27.07.2022.

Conference materials
UDC 537.632.4, 537.635
DOI: <https://doi.org/10.18721/JPM.153.357>

Synthesis and properties of nanostructure composites based on barium titanate and 3D metals

A. V. Kurilova ¹✉, A. L. Sukhachev ², K. V. Shulga ³, K. V. Bogdanov ¹,
I. V. Nemtsev ², A. Yu. Dubavik ¹, A. E. Sokolov ^{2,3}

¹ University ITMO, St. Petersburg, Russia;

² Kirensky Institute of Physics Siberian Branch, Russian Academy of Sciences, Krasnoyarsk, Russia;

³ Siberian Federal University, Krasnoyarsk, Russia

✉ ankurilova@niuitmo.ru

Abstract. We report the production of a hybrid nanostructure combining ferroelectric and antiferromagnetic ordering based on toroidal nanoparticles of barium titanate and an iron-cobalt nanoalloy. The methods of optical and magneto-optical spectroscopy revealed a change in the coordination of 3D metal ions in the composition of FeCo after high-temperature annealing in the presence of barium titanate, and a study of the magnetic properties showed a change in the predominant alignment of spins from superparamagnetic to antiferromagnetic type. In addition, the sample exhibits optically nonlinear properties.

Keywords: antiferromagnetism, magnetoelectric, magnitooptic

Funding: This study was funded by RFBR grant No. 20-32-90144 (investigation of magnetic and magnitooptical properties).

Citation: Kurilova A. V., Sukhachev A. L., Shulga K. V., Bogdanov K. V., Nemtsev I. V., Dubavik A. Yu., Sokolov A. E., Synthesis and properties of nanostructure composites based on barium titanate and 3D metals. St. Petersburg State Polytechnical University Journal. Physics and Mathematics, 15 (3.3) (2022) 290–294. DOI: <https://doi.org/10.18721/JPM.153.357>

This is an open access article under the CC BY-NC 4.0 license (<https://creativecommons.org/licenses/by-nc/4.0/>)

Материалы конференции
УДК 537.632.4, 537.635
DOI: <https://doi.org/10.18721/JPM.153.357>

Синтез и свойства наноструктурного композита на основе титаната бария и 3D металлов

А. В. Курилова ¹✉, А. Л. Сухачев ², К. В. Шульга ³, К. В. Богданов ¹,
И. В. Немцев ², А. Ю. Дубовик ¹, А. Э. Соколов ^{2,3}

¹ Национальный исследовательский университет ИТМО, Санкт-Петербург, Россия;

² Институт физики им. Л. В. Киренского Сибирского отделения
Российской академии наук, Красноярск, Россия;

³ Сибирский федеральный университет, Красноярск, Россия

✉ ankurilova@niuitmo.ru

Аннотация. Мы сообщаем о получении гибридной наноструктуры, сочетающей сегнетоэлектрическое и антиферромагнитное упорядочение, на основе тороидальных наночастиц титаната бария и наносплава железо-кобальт. Методами оптической и магнитооптической спектроскопии было выявлено изменение координации ионов 3D металлов в составе FeCo после высокотемпературного обжига в присутствии титаната бария, а исследование магнитных свойств показало изменение преимущественного выстраивания спинов с суперпарамагнитного на антиферромагнитный тип.

Ключевые слова: антиферромагнетизм, магнитоэлектрики, магнитооптика

Финансирование: Работа выполнена в рамках гранта РФФИ № 20-32-90144.

Ссылка при цитировании: Курилова А. В., Сухачев А. Л., Шульга К. В., Богданов К. В., Немцев И. В., Дубовик А. Ю., Соколов А. Э. Синтез и свойства наноструктурного композита на основе титаната бария и 3D металлов // Научно-технические ведомости СПбГПУ. Физико-математические науки. 2022. Т. 15. № 3.3. С. 290–294. DOI: <https://doi.org/10.18721/JPM.153.357>

Статья открытого доступа, распространяемая по лицензии CC BY-NC 4.0 (<https://creativecommons.org/licenses/by-nc/4.0/>)

Introduction

Ferroelectromagnetics (electromagnetics) are materials and multiphase heterostructures with simultaneous presence ferroelectric and ferromagnetic ordering. They have great potential for practical use in magneto- and optoelectronics, as elements of various sensors, tunable optical elements, and memory devices with magnetic reading or electrical recording [1, 2].

In our work, we investigated a composite that coincides with a combination of lead-free ferroelectric perovskite, BaTiO₃ (BTO), and cobalt-iron alloy nanoparticles FeCo.

The BTO nanoparticles are the most studied perovskite-type ferroelectrics because of their excellent optical and electrical properties [3]. But a little part is known about bimetallic nanoparticles. Example, the crystal structure of the Fe_{100-x}Co_x alloy depends on the temperature of the synthesis and the related to ratio of Co and Fe, the ideal stoichiometry with high saturation and the least coercive force belongs to Fe₆₀Co₄₀ etc. How are the cations in this nanocrystal interconnected between themselves without oxidation in air? In standard case there is a shell which passivates the surface after calcination [4].

In a report [5] analogy structure (CoFe films on BTO substrates) shows significant change properties during structural phase transitions of BTO. Starting from 300 K, cooling through the tetragonal to orthorhombic phase transition leads to a sharp 90° magnetic switching in the magnetic strip domains, an increase in magnetoelastic anisotropy while preserving the overall structure of the magnetic domains. But the influence of morphology and the ratios of BTO to FeCo and Fe to Co on the current processes is not yet known.

Materials and Methods

Synthesis of BTO nanoparticles. The first step of our composite is based on [6]. 1.26 g of BaCl₂·2H₂O and 0.15 g H₂C₂O₄ (oxalic acid) were dissolved in 10 mL of distilled water. After that 2.5 mL butyl titanate and 2.5 mL H₂O were added into the mixture system. Then, 2.25 g NaOH was added into the solution with continuous ultrasonication. The as-prepared mixture was put into a Teflon-lined stainless-steel autoclave (25 mL) and conducted at 160 °C for 12h.

The solution was finally washed with distilled water and absolute methanol for three times.

Synthesis of FeCo/C alloy nanoparticles. As in paper [7], 16 ml of paraffin oil, 50 µl of oleic acid, and 50 µl of oleyl amine were collected and the mixture was degassed with heating to 140 °C and N₂ for 2 h. At the same time, 4 ml of paraffin oil was degassed at room temperature, and we raised the temperature to 275 °C and kept it at this temperature for 1 h in argon flux. 103.3 mg of Co(oleate)₂ and 137 mg of Fe(CO)₅ were added in the 4 ml paraffin oil. Following this, this mixture was injected dropwise to the hot reaction mixture for 7 minutes and the reaction was completed after 10 minutes and cooled slowly at room temperature. The sample was washed several times with a mixture of hexane/alcohols and purified by magnetic separation.

Accordingly, we expect to obtain nanoparticles with the formula Fe₄₅Co₅₅.

Synthesis of BTO-FeCo/C nanocomposite. We took two solutions of BTO (methanol) and FeCo (hexane) with equal concentrations and volume and placed them together in a preheated oven (~ 500 °C) for 15 minutes. Some part of the sample demonstrated diamagnetic properties (black precipitate), the other was ferromagnetic (beige precipitate) and hydrophilic.

The morphology and microstructure of the NPs were investigated using scanning electron microscope Quantex 70, Bruker, USA with accelerating voltage 3000 V and emission current 10100 nA.

Optical and magneto-optical spectra were registered on spectrometer of circle dichroism Jasco J-1500 with electromagnet MCD-581. Measurements were carried out in the range 200–800 nm in field 1.5T.

The magnetic properties were measured with the vibrating sample magnetometer Lakeshore 7400 series VSM (Lake Shore Cryotronics, Inc., Westerville, OH, USA).

Results and Discussion

As a result of SEM (Quantex 70, Bruker, USA), the mean size of the completed sample is 0.5 μm . Its form and dimensions in Fig. 1 can be explained by agglomeration during the heat treatment. Another reason is the specifics of hydrothermal processing of BaTiO_3 nanotorus synthesis.

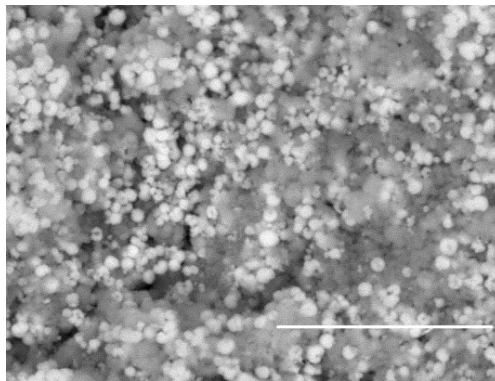


Fig. 1. Bright-field SEM image of the FeCo-enveloped BTO nanoparticles. Scale – 10 μm

Since the absorption spectra do not show any significant features, magnetic circular dichroism spectra were studied to study the excited electronic states of iron and cobalt ions. The MCD spectra of the initial sample of FeCo nanoparticles undergo a significant shape change, apparently associated with the interaction of FeCo and BTO nanoparticles. To identify the energies of electronic transitions and study the redistribution of band intensities, the MCD spectra of the initial FeCo nanoparticles and the composite were decomposed into Gaussian components (Fig. 2). As a result of decomposition, the transitions presented in Table 1 were identified. Similar to those observed in works [7–10]. In the same way, the bands were defined on 1) 1.8, 2) 1.95, 3) 2.1, 4) 2.3, 5) 2.4, 6) 2.6, 7) 2.85, 8) 3, 9) 3.3, 10) 4, 11) 4.3 eV in the $\text{BaTiO}_3/\text{FeCo}$ spectrum (Fig. 2, a). The main spectral feature is transitions at 1.8 eV (peak 1), which are not observed for FeCo/C and change intensity during each measurement. It can also be a splitting band with a center of 1.5 eV as an effect arising in a magnetic field [7]. In addition, there are bands that can belong to BTO nanoparticles: 3, 4 or 5, 9, 10, 11.

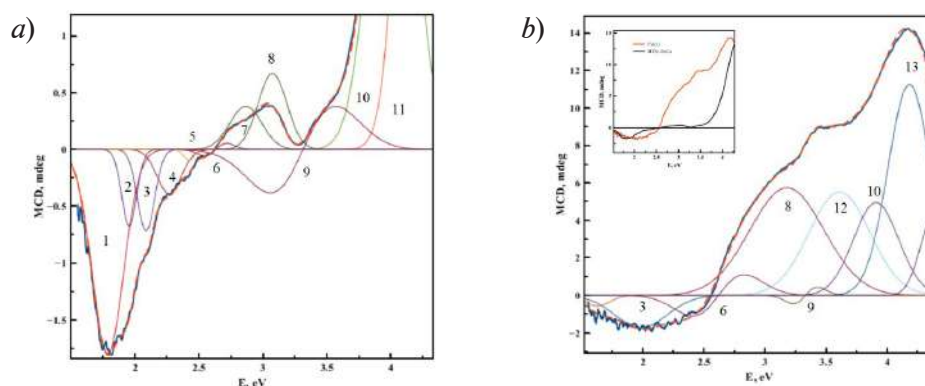


Fig. 2. MCD spectrum of $\text{BaTiO}_3/\text{FeCo}$ nanostructure (a) and FeCo/C nanoparticles (b)

Fig. 3, a, shows that a loop of FeCo nanoparticles behaves like a classical superparamagnetic one with a saturation magnetization of 1.35 emu/g and a complete absence of coercivity. In a composite consisting of magnetic and non-magnetic nanoparticles, the M_s value is 5 times

Table 1

Transitions indicated in Fig. 2

Peaks	Designation	Peaks	Designation
1	-	6	$p(O^{2-}) \rightarrow e_g(Co^{3+})$ or ${}^6A_g({}^6S) \rightarrow {}^4A_g, {}^4E_g({}^4G)(Fe^{3+}, O_h)$
2	${}^6A_{1g}({}^6S) \rightarrow {}^4T_2({}^4G)(Fe^{3+}, O_h)$ or ${}^4T_{1g}(F) \rightarrow {}^4A_{2g}(F)(Co^{2+}, O_h)$	7	${}^6A_{1g}({}^6S) \rightarrow {}^4T_{2g}({}^4D)(Fe^{3+}, O_h)$
3	-	8	${}^1A_{1g}(I) \rightarrow {}^1T_{1g}(I)(Co^{3+}, O_h)$
4	${}^4T_{1g}(F) \rightarrow {}^4T_{1g}(P)(Co^{2+}, O_h)$ or $p(O^{2-}) \rightarrow t_{2g}(Co^{2+})$	9	${}^6A_{1g}({}^6S) \rightarrow {}^4T_{2g}({}^4D)(Fe^{3+}, O_h)$
5	${}^1A_{1g}(I) \rightarrow {}^1T_{2g}(I)(Co^{3+}, O_h)$	10	${}^6A_{1g}({}^6S) \rightarrow {}^4T_1({}^4D)(Fe^{3+}, O_h)$

smaller, this can be explained by the fact that we cannot accurately take into account which part of the sample is the mass of magnetic nanoparticles. At the same time, the question remains why the composite has a coercive force of 60 Oe, apparently due to an increase in the size of the initial FeCo nanoparticles, or a strong interparticle interaction of magnetic and non-magnetic particles. The temperature dependences of magnetization Fig. 3, *b* also show a rather strange increase in the blocking temperature of nanoparticles from 210 K to 250 K, respectively for FeCo and BaTiO₃/FeCo.

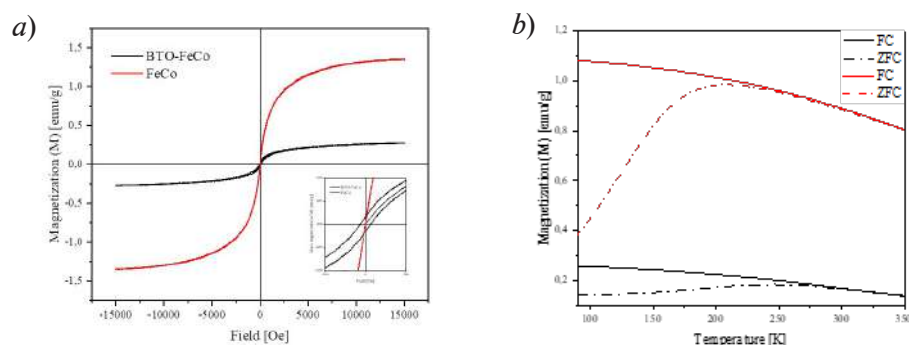


Fig. 3. Magnetic hysteresis loops of BaTiO₃/FeCo nanostructure and FeCo nanoalloy at 300K (*a*) and temperature dependences of magnetization for BaTiO₃/FeCo (black) and FeCo (red) in the field 2 kOe (*b*)

Conclusion

Ferroelectromagnetics composites BaTiO₃/FeCo were obtained and a preliminary study of their magnetic and magneto-optical properties was carried out. It has been demonstrated that dilution of the initial FeCo magnetic nanoparticles with perovskite-like ferroelectric BTO nanoparticles leads to strong interparticle interaction and, apparently, to a violation of the surface layer of magnetic nanoparticles, which significantly affects their properties. In any case, the resulting composite requires further investigation.

Acknowledgments

The authors would like to express their special thanks to Krasnoyarsk Regional Center of Research Equipment of Federal Research Center “Krasnoyarsk Science Center SB RAS”

REFERENCES

1. Kalashnikova A. M., Pisarev R. V., Bezmaternykh L. N., Temerov V. L., Kirilyuk A., Rasing T., Optical and magneto-optical studies of a multiferroic GaFeO₃ with a high Curie temperature. Journal of Experimental and Theoretical Physics Letters. 81 (9) (2005) 452–457.
2. Pyatakov A. P., Zhdanov A. G., Zvezdin A. K., Nonlinear magneto-optical effect in multiferroic material bismuth ferrite. In ICONO 2005: Nonlinear Optical Phenomena. 6259 (2006) 35–44.
3. Yashima M., Hoshina T., Ishimura D., Kobayashi S., Nakamura W., Tsurumi T., Wada S., Size effect on the crystal structure of barium titanate nanoparticles. Journal of applied physics. 98 (1) (2005) 014313.
4. Ferrando R., Jellinek J., Johnston R. L., Nanoalloys: from theory to applications of alloy clusters and nanoparticles. Chemical reviews. 108 (3) (2008) 845–910.
5. Lahtinen T. H., van Dijken S., Temperature control of local magnetic anisotropy in multiferroic CoFe/BaTiO₃. Applied Physics Letters. 102 (11) (2013) 112406.
6. El Kabouss K., Kacimi M., Ziyad M., Ammar S., Ensuque A., Piquemal J. Y., Bozon-Verduraz F., Cobalt speciation in cobalt oxide-apatite materials: structure-properties relationship in catalytic oxidative dehydrogenation of ethane and butan-2-ol conversion. Journal of Materials Chemistry. 16 (25) (2006) 2453–2463.
7. Lafrentz M., Brunne D., Kaminski B., Pavlov V. V., Rodina A. V., Pisarev R. V., Bayer M., Magneto-Stark effect of excitons as the origin of second harmonic generation in ZnO. Physical review letters. 110 (11) (2013) 116402.
8. Kim K. J., Park Y. R., Hyun D. H., Lee S. H., Optical properties of normal spinel M_xCo_{3-x}O₄ (M=Cr and Cu): Coexistence of charge-transfer and crystal-field transitions. Journal of applied physics. 96 (4) (2004) 1975–1978.
9. Parkinson G. S., Iron oxide surfaces. Surface Science Reports. 71 (1) (2016) 272–365.
10. Ivantsov R., Ivanova O., Zharkov S., Molochev M., Krylov A., Gudim I., Edelman I., Magnetic circular dichroism in the canted antiferromagnet α-Fe₂O₃: Bulk single crystal and nanocrystals. Journal of Magnetism and Magnetic Materials. 498 (2020) 166208.
11. Alshammari M. S., Alqahtani M. S., Albargi H. B., Alfihed S. A., Alshetwi Y. A., Alghihab A. A., Gehring, G. A., Magnetic properties of In₂O₃ containing Fe₃O₄ nanoparticles. Physical Review B. 90 (14) (2014) 144433.

THE AUTHORS

KURILOVA Anastasiia V.
ankurilova@niuitmo.ru
ORCID: 0000-0003-1419-8508

NEMTSEV Ivan V.
nemtsev@iph.krasn.ru
ORCID: 0000-0002-4222-3099

BOGDANOV Kirill V.
kirw.bog@itmo.ru

DUBAVIK Alexey Yu.
adubavik@itmo.ru

SHULGA Karina V.
tabakaewa-karina@mail.ru
ORCID: 0000-0002-7034-0591

SOKOLOV Alexey E.
alexeys@iph.krasn.ru
ORCID: 0000-0002-8426-1982

SUKHACHEV Alexander L.
sanya@iph.krasn.ru
ORCID: 0000-0003-4644-8823

Received 28.07.2022. Approved after reviewing 21.08.2022. Accepted 30.08.2022.

Conference materials
UDC 538.911, 538.953
DOI: <https://doi.org/10.18721/JPM.153.358>

Optimizing deposition regimes to fabricate vanadium dioxide film for active metasurfaces

M. E. Kutepov ¹✉, I. K. Domaratskiy ², S. S. Zhukov ², E. M. Kaidashev ¹,
I. V. Lisnevskaya ¹, K. G. Abdulvakhidov ¹, V. E. Kaydashev ¹

¹ Southern Federal University, Rostov-on-Don, Russia;

² Moscow Institute of Physics and Technology (MIPT), Dolgoprudny, Russia

✉ kutepov.max@yandex.ru

Abstract: Several deposition protocols to obtain epitaxial VO₂ films from metallic vanadium and VO₂ targets are compared. Films obtained from VO₂ target showed much smoother and droplet free surface compared to those prepared from V target. The samples prepared from oxide target in average showed larger middle IR reflection of 55–67% in conducting state compared to ~ 56% for samples obtained from metal V target.

Keywords: vanadium dioxide, metal-to-isolator transition, pulsed laser deposition

Funding: This study was funded by SFU project No. 07/2020-06-MM, RSF project No. 21-79-00209 and RSF project No. 22-29-01037.

Citation: Kutepov M. E., Domaratskiy I. K., Zhukov S. S., Kaidashev E. M., Lisnevskaya I. V., Abdulvakhidov K. G., Kaydashev V. E., Optimizing deposition regimes to fabricate vanadium dioxide film for active metasurfaces. St. Petersburg State Polytechnical University Journal. Physics and Mathematics, 15 (3.3) (2022) 295–299. DOI: <https://doi.org/10.18721/JPM.153.358>

This is an open access article under the CC BY-NC 4.0 license (<https://creativecommons.org/licenses/by-nc/4.0/>)

Материалы конференции
УДК 538.911, 538.953
DOI: <https://doi.org/10.18721/JPM.153.358>

Оптимизация режимов осаждения пленки диоксида ванадия для активных метаповерхностей

М. Е. Кутепов ¹✉, И. К. Домарацкий ², С. С. Жуков ², Е. М. Кайдашев ¹,
И. В. Лисневская ¹, К. Г. Абдулвахидов ¹, В. Е. Кайдашев ¹

¹ Южный федеральный университет, Ростов-на-Дону, Россия;

² Московский физико-технический институт, Долгопрудный, Россия

✉ kutepov.max@yandex.ru

Аннотация. Проведено сравнение нескольких протоколов напыления эпитаксиальных пленок VO₂ из мишени металлического ванадия и VO₂. В отличие от пленок изготовленных из металлической мишени пленки из оксидной мишени показали поверхность свободную от капель. Образцы, синтезированные из оксидной мишени, в среднем показали большее среднее ИК-отражение 55–67% в проводящем состоянии по сравнению с ~ 56% для образцов, полученных из металлической ванадиевой мишени.

Ключевые слова: диоксид ванадия, переход металл-изолятор, импульсное лазерное напыление

Финансирование: Работа выполнен в рамках гранта ЮФУ № 07/2020-06-MM, гранта РФФИ № 21-79-00209, гранта РФФИ № 22-29-01037.

Ссылка при цитировании: Кутепов М. Е., Домарацкий И. К., Жуков С. С., Кайдашев Е. М., Лисневская И. В., Абдулвахидов К. Г., Кайдашев В. Е. Оптимизация

режимов осаждения пленки диоксида ванадия для активных метаповерхностей // Научно-технические ведомости СПбГПУ. Физико-математические науки. 2022. Т. 15. № 3.3. С. 295–299. DOI: <https://doi.org/10.18721/JPM.153.358>

Статья открытого доступа, распространяемая по лицензии CC BY-NC 4.0 (<https://creativecommons.org/licenses/by-nc/4.0/>)

Introduction

THz/middle IR imaging techniques for biology and medicine as well as sixth generation (6G) of mobile communication systems urgently need new tools to in-situ manipulate a front of a plane wave in sub-THz range of 0.1–1 THz and middle IR range of 10–60 THz. By exploiting “static” metasurfaces made of metallic antenna array one may already fabricate a great variety of devices to filter mid-IR/THz waves, modulate its intensity or manipulate a wavefront, i.e. focus radiation [1], obtain beam steering to a given angle [2], alter polarization [1, 3], filter wavelength [4] or achieve ultrafast modulation [5]. Due to use of metallic elements the functions of these devices are pre-defined by their design. VO₂-based metasurfaces whose mid-IR/THz transmission/reflection are dynamically altered due to isolator-to-metal transition (IMT) do offer a great flexibility in programming device characteristics by local heating [6], electric current [7], mechanical stress [8] or laser light exposure [9]. Some progress in this direction has already been achieved recently [10, 11]. However, to obtain an advanced performance of a metasurface several characteristics of VO₂ film should be engineered in proper manner. These properties of VO₂ film should be simultaneously optimized, namely, isolator-to-metal state resistance alteration ratio, abruptness of a resistance versus temperature characteristics, lower phase transition temperature and reduced photo- and/or electrically induced switching times. Earlier we obtained VO₂ films from metallic V target. However large amount of droplets is observed on the surface of the VO₂ film deposited by pulsed laser deposition from metallic vanadium target. Poor surface smoothness still makes it challenging to manufacture devices by e-beam lithography.

In this report we optimized PLD protocols to obtain VO₂ films on c-Al₂O₃ substrates with droplet free surface as well as high crystallinity, abrupt and narrow electrical hysteresis loop and large dynamic range of middle IR reflection alteration. Characteristics of samples obtained by ablation V and VO₂ targets in different regimes are compared.

Experimental

VO₂ films were prepared by pulsed laser deposition method. KrF laser beam (248 nm, 15ns, 10 Hz) was focused on the surface of rotating VO₂ or metallic vanadium target to give a fluence of 2 J/cm². The c-Al₂O₃ substrate was positioned at 5 cm from the target. The substrate temperature was maintained at 550 °C. The films were deposited in oxygen ambient for 4000 laser pulses. Samples in the first series were deposited by ablating a vanadium oxide target using the same laser fluence of 2 J/cm² and varied oxygen pressure in the range of 1.5×10⁻² – 5×10⁻² mbar. Another series of samples was deposited from metallic V target at substrate temperature of T = 650 °C oxygen pressure of 6×10⁻² mbar and laser fluence of 2.3 J/cm²

Results and discussion

VO₂ films obtained from VO₂ target showed much smoother surface in contrast to those prepared by ablating metallic target whose surface suffers from droplets condensed in plasma plume.

X-ray diffraction patterns for both series of samples reveal characteristic reflexes of monocline VO₂ lattice with VO₂ (002) || c-Al₂O₃ (006) as shown in Fig. 2 *a, b*. FWHM of (020) and (040) reflexes are 0.17° and 0.19° for samples prepared from VO₂ target and 0.18° and 0.20° correspondingly for samples obtained from metallic one. The XRD spectra for series of samples prepared from VO₂ target reveal several additional reflexes (not assigned yet) evidencing the presence of some extra phases. In contrast the XRD spectra of samples prepared from metallic vanadium target showed much better crystalline homogeneity without any structural impurities as shown in Fig. 2, *b*.

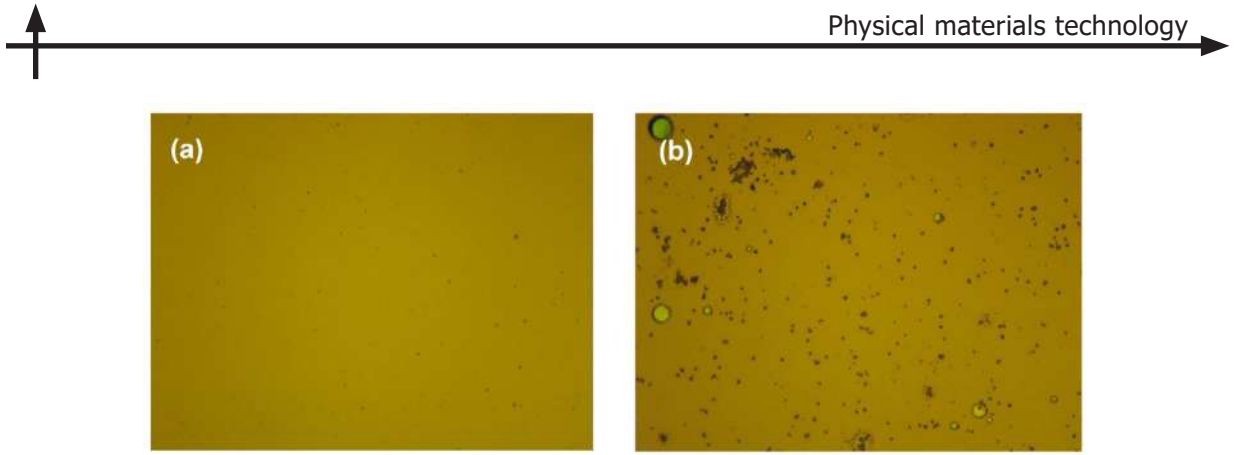


Fig.1 Morphology of VO_2 film prepared from vanadium dioxide (a) and metallic vanadium (b) target. Field of view $100 \times 134 \mu\text{m}$

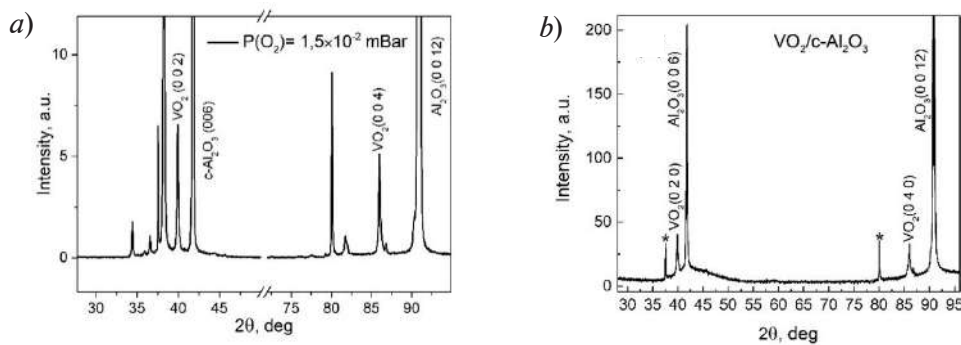


Fig. 2 XRD spectra of $\text{VO}_2/\text{c-Al}_2\text{O}_3$ films prepared from oxide VO_2 (a) and metallic V (b) targets

Resistance versus temperature related MIT hysteresis loops are varied for VO_2 samples deposited from oxide target at different oxygen pressure as shown in Fig. 3, a. The temperature of phase transition, resistance change ratio and hysteresis loop width may be slightly tuned by choosing oxygen pressure during the deposition. In particular the curve with narrowest hysteresis of 4.5°C and maximal isolator-to-metallic phase resistance change ratio of 2.4×10^3 was recorded for films deposited at 4×10^{-2} mbar as shown in Fig. 3, b. Note, that $R(T)$ curve for VO_2 film prepared from metallic target shows even narrower loop width of 3.3°C .

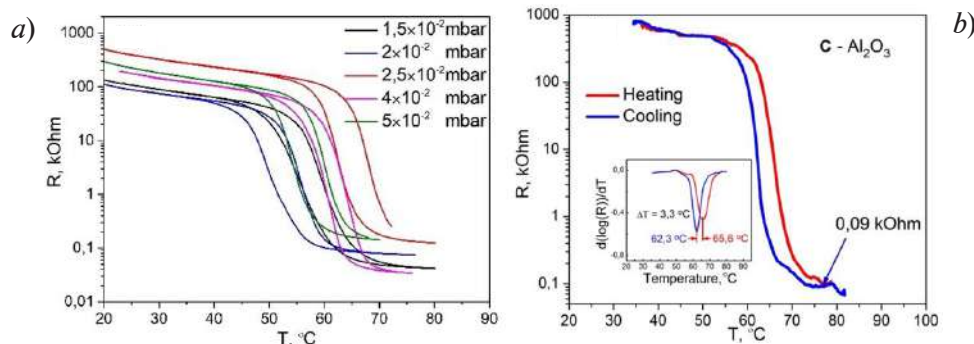


Fig.3 $R(T)$ hysteresis loop of VO_2 samples obtained from VO_2 target at different oxygen pressures (a) and from metallic V target (b). Example of derivative curve $d(\lg(R(T)))/dT$ of VO_2 film fabricated from metallic V target is shown in inset

The quality of electrical switching hysteresis loop readily analyzed from the derivative of $\lg_{10}(R(T))$ value plotted as function of film temperature. The features of electrical switching of VO_2 films prepared at different oxygen pressure, namely the phase transition temperature T_{PT} , hysteresis loop width ΔT and film resistance in isolator and conducting states are summarized in Table 1. Abruptness of $R(T)$ characteristics can be estimated by $FWHM$ and minimum value of $d(\lg(R(T)))/dT$ curve.

Table 1

The features of electrical switching of VO₂ films prepared at different oxygen pressure

$P(O_2)$, mbar	T_{PT} , °C	$FWHM$	$d(\lg R(T))/dT$ min	R_{RT} , kΩ	R_{min} , kΩ	ΔT , °C	$R_{isolator}/R_{metallic}$
1.5×10^{-2}	59.5	8	-0.31	89.7	0.042	7.1	2.1×10^3
2×10^{-2}	55.5	6	-0.37	74.8	0.042	5.8	1.8×10^3
4×10^{-2}	64	6.8	-0.42	145	0.034	4.5	4.3×10^3
5×10^{-2}	59.9	5.5	-0.41	180	0.142	5.9	1.3×10^3

Reflection spectra in the middle and near IR were studied using Bruker Vertex 80V FTIR spectrometer equipped with a Hyperion 2000 microscope. The spectra were recorded from a spot of $\sim 40 \mu\text{m}^2$ from the homogeneous surface free of droplets. Optical reflection spectra in the middle infrared range reveal drastic change upon film heating above the isolator-metal transition due to its conductivity alteration as shown in Fig. 4. The characteristic shape of reflection spectra is altered at the temperature of structural phase transition T_{TR} evidencing the change of VO₂ lattice symmetry as well as electronic structure. Notably that films prepared from VO₂ target show greater reflection variation as shown in Fig. 4, a compared to the ones deposited from metallic vanadium target (Fig. 4, b). In particular, VO₂ temperature alteration from 30 °C to 80 °C results in mid IR reflection (at 10μm) increase of 55–67% for samples obtained at different oxygen pressure from VO₂ target. Samples obtained from metal V target showed $\sim 56\%$ mid IR reflection change. Note that samples synthesised from VO₂ target at oxygen pressure of 2×10^{-2} mbar in series shown in Fig. 4, a reveal greatest dynamic range of mid IR transmission alteration.

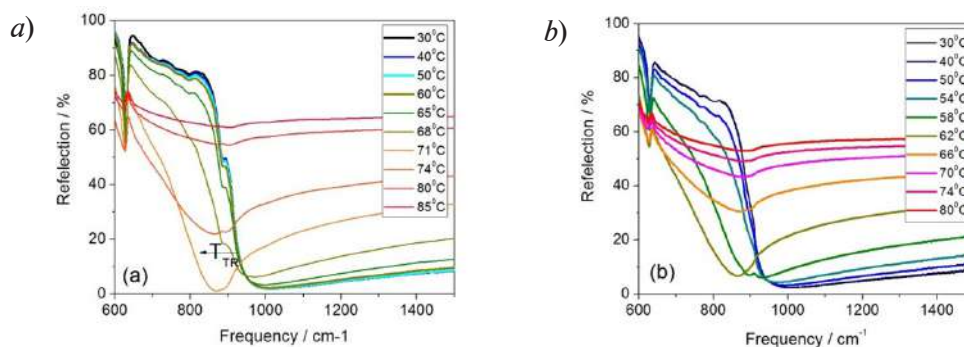


Fig. 4 Temperature dependent middle IR reflection spectra of VO₂ film prepared by ablating VO₂ (a) and metallic V target (b)

Conclusion

Several pulsed laser deposition regimes to obtain quality VO₂ films are discussed. Samples obtained from VO₂ target show smooth surface whereas the ones obtained by ablating metallic vanadium target reveal a lot of droplets. Both types of films reveal high electrical, structural and optical switching characteristics, however the samples obtained from VO₂ target show some extra crystalline orientations/phases, which is a subject of further studies. The samples prepared from oxide target in average showed larger middle IR reflection of 55–67% in conducting state compared to $\sim 56\%$ for samples obtained from metal V target. The sample synthesized at 4×10^{-2} had the smallest difference of 4.5° between the hysteresis heating and cooling curves, as well as the greatest resistance change abruptness.

REFERENCES

1. Zhang X., Tian Z., Yue W., Gu J., Zhang S., Han J., Zhang W., Broadband Terahertz Wave Deflection Based on C-shape Complex Metamaterials with Phase Discontinuities, Adv. Mater. 25 (33) (2013) 4567.



2. Wang T., He J., Guo J., Wang X., Feng S., Kuhl F., Becker M., Polity A., Klar P. J., Zhang Y., Thermally switchable terahertz wavefront metasurface modulators based on the insulator-to-metal transition of vanadium dioxide, *Opt. Express*. 27 (15) (2019) 20347.
3. Liu L., Zhang X., Kenney M., Su X., Xu N., Ouyang C., Shi Y., Han J., Zhang W., Zhang S., Broadband metasurfaces with simultaneous control of phase and amplitude, *Adv. Mater.* 26 (2014) 5031.
4. Edgar M. P., Gibson G. M., Padgett M. J., Principles and prospects for single-pixel imaging, *Nature Photonics*. 13 (2019) 13.
5. Gingras L., Jaber A., Maleki A., Reshef O., Dolgaleva K., Boyd R. W., Ménard J. M., Ultrafast modulation of the spectral filtering properties of a THz metasurface, *Optics Express*. 28 (2020) 20296.
6. Lei D. Y., Appavoo K., Ligmajer F., Sonnefraud Y., Haglund R. F., Maier S. A., Optically-Triggered Nanoscale Memory Effect in a Hybrid Plasmonic-Phase Changing Nanostructure, *ACS Photonics*, 2 (9) (2015) 1306.
7. Qazilbash M. M., Li Z. Q., Podzorov V., Brehm M., Keilmann F., Chae B.G., Kim H. T., Basov D. N., Electrostatic modification of infrared response in gated structures based on VO₂, *Appl. Phys. Lett.*, 92 (2008) 241906.
8. Wei J., Wang Z., Chen W., Cobden D. H., New aspects of the metal-insulator transition in single-domain vanadium dioxide nanobeams, *Nature Nanotechnology*. 4 (2009) 420.
9. Cavalleri A., Dekorsy Th., Chong H. H. W., Kieffer J. C., Schoenlein R. W., Evidence for a structurally-driven insulator-to-metal transition in VO₂: A view from the ultrafast timescale, *Phys. Rev. B*, 70 (2004) 161102 (R).
10. Cuffe S., John J., Zhang Z., Parra J., Sun J., Orobtcouk R., Ramanathan S., Sanchis P., VO₂ nanophotonics, *APL Photon.* 5 (11) (2020) 110901.
11. He J., Dong T., Chi B., Zhang Y., Metasurfaces for Terahertz Wavefront Modulation: a Review, *J. Infrared, Millimeter, and Terahertz Waves*. 41 (2020) 607.

THE AUTHORS

KUTEPOV Maxim E.
kutepov.max@yandex.ru
ORCID: 0000-0002-3805-5416

DOMARATSKIY Ivan K.
Domaratskiy@phystech.edu
ORCID: 0000-0002-8036-8301

ZHUKOV Sergey S.
zhukov.ss@mipt.ru
ORCID: 0000-0001-7268-8666

KAIDASHEV Evgeni M.
emkaydashev@sfedu.ru
ORCID: 0000-0002-5886-6443

LISNEVSKAYA Inna V.
liv@sfedu.ru

ABDULVAKHIDOV Kamaludin G.
kgabdulvahidov@sfedu.ru

KAYDASHEV Vladimir E.
kaydashev@gmail.com
ORCID: 0000-0003-1913-591X

Received 01.09.2022. Approved after reviewing 15.09.2022. Accepted 19.09.2022.

Conference materials

UDC 29.19.22

DOI: <https://doi.org/10.18721/JPM.153.359>

Thermoelectric properties of graphenylene nanotubes with encapsulated fullerenes

E. V. Morozova ¹✉, D. A. Timkaeva ¹

¹ Ulyanovsk State University, Ulyanovsk, Russia

✉ morozovaev@ulsu.ru

Abstract. Thermoelectric properties of graphenylene nanotubes with encapsulated C₆₀ fullerenes are studied by means of the DFT-based calculations. The electrical and thermal conductivities, Peltier and Seebeck coefficients, and thermoelectric figure of merit ZT are estimated for different distances between fullerenes and various chirality of graphenylene nanotubes.

Keywords: graphenylene nanotubes, fullerene, thermoelectric figure of merit

Funding: This study is supported by the Ministry of Science and Higher Education of the Russian Federation (grant No. 0830-2020-0009).

Citation: Morozova E. V., Timkaeva D. A., Thermoelectric properties of graphenylene nanotubes with encapsulated fullerenes. St. Petersburg State Polytechnical University Journal. Physics and Mathematics, 15 (3.3) (2022) 300–305. DOI: <https://doi.org/10.18721/JPM.153.359>

This is an open access article under the CC BY-NC 4.0 license (<https://creativecommons.org/licenses/by-nc/4.0/>)

Материалы конференции

УДК 29.19.22

DOI: <https://doi.org/10.18721/JPM.153.359>

Термоэлектрические свойства графениленовых нанотрубок с инкапсулированными фуллеренами

Е. В. Морозова ¹✉, Д. А. Тимкаева ¹

¹ Ульяновский государственный университет, Ульяновск, Россия

✉ morozovaev@ulsu.ru

Аннотация. Термоэлектрические свойства графениленовых нанотрубок с инкапсулированными фуллеренами C₆₀ изучены с помощью расчетов на основе теории функционала плотности. Электро- и теплопроводность, коэффициенты Пельтье и Зеебека и термоэлектрическая добротность ZT рассчитаны для различных расстояний между фуллеренами и различной хиральности графениленовых нанотрубок.

Ключевые слова: графениленовые нанотрубки, фуллерен, термоэлектрическая добротность

Финансирование: Работа выполнена при поддержке Министерства науки и высшего образования Российской Федерации (грант № 0830-2020-0009).

Ссылка при цитировании: Морозова Е. В., Тимкаева Д. А. Термоэлектрические свойства графениленовых нанотрубок с инкапсулированными фуллеренами // Научно-технические ведомости СПбГПУ. Физико-математические науки. 2022. Т. 15. № 3.3. С. 300–305. DOI: <https://doi.org/10.18721/JPM.153.359>

Статья открытого доступа, распространяемая по лицензии CC BY-NC 4.0 (<https://creativecommons.org/licenses/by-nc/4.0/>)



Introduction

In recent years, a large number of new two-dimensional carbon structures have been proposed and studied for use in nanoelectronics and hydrogen energy storage. Such two-dimensional materials, in particular, include graphenylene [1]. Graphenylene is the first example of a two-dimensional non-delocalized sp^2 -carbon network consisting of cyclohexatriene units with two completely different C–C bonds within the C_6 ring. It has periodically arranged pores with a diameter of 3.2 Å. Graphenylene is a semiconductor with a narrow direct band gap. Optimization and calculation of the electronic structure of graphenylene were carried out in [2, 3]. The values of the band gap obtained differ from each other, sometimes by an order of magnitude. This is because since the band gap is rather narrow, the value E_g is extremely sensitive to the position of atoms in the optimized structure and strongly depends on the choice of calculation method. In graphenylene, the distribution of electron density is completely different from graphene, since there is a certain alternation between neighboring bonds. Graphenylene nanoribbons were studied in [4]. Electronic spectra indicate that all considered nanoribbons could be classified as direct bandgap semiconductors. The calculated dependencies of bandgap on nanoribbon width show the identical scaling rules for armchair and zigzag graphenylene ribbons. A family-based classification used for the electronic structure of armchair graphene nanoribbons can not be extended to the case of graphenylene ones.

In [5, 6], new van der Waals heterostructures based on graphenylene were proposed and analyzed. In a recent work [7], the optical and thermoelectric properties of graphenylene and octagraphene nanotubes were studied using first-principles calculations. In the present work, the thermoelectric properties of graphenylene nanotubes with encapsulated fullerenes C_{60} for various types of nanotube chirality and different distances between fullerenes. Such structures are promising for thermoelectric power generators. We optimize and study the armchair graphenylene nanotube of 12.99 Å in diameter and zigzag graphenylene nanotube of 11.24 Å in diameter with encapsulated C_{60} fullerenes.

Materials and Methods

Calculations of the thermoelectric properties of the investigated semiconductor graphenylene nanotubes (Fig. 1) were carried out by means of the density functional theory (DFT) and the method of nonequilibrium Green's functions implemented in Quantum ATK [8]. We use the DFT to calculate the electron transmission and the force field method to estimate the phonon transmission. In the force field method, we use Tersoff's optimized empirical potential of the molecular dynamics of carbon systems. We used the PseudoDojo pseudopotential with a linear combination of atomic orbitals (LCAO) basis sets. HybridGGA was chosen as the exchange-correlation functional. The criteria for reliable convergence for the total energy and force are 10^{-6} eV and 0.01 eV/Å. The vacuum region 35 Å is used to eliminate boundary effects.

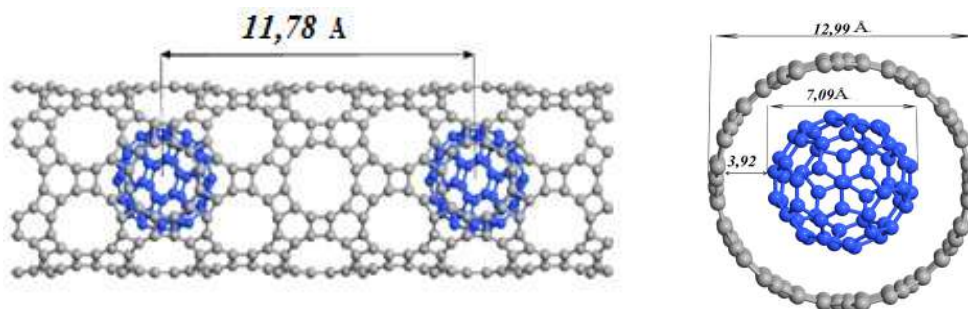


Fig. 1. Structure of a graphenylene nanotube with encapsulated C_{60} fullerenes

A density cut-off grid of 75 Ha (1 Ha = 27.21 eV) was applied, and the Monkhorst-Pack method [9] with a set of k points was used to generate k points in the Brillouin zone $1 \times 1 \times 27$. The calculations were carried out for room temperature ($T = 300$ K). The maximum efficiency of the

energy conversion process in a thermoelectric material is determined by its thermoelectric figure of merit ZT , defined by the expression

$$ZT = \frac{S^2GT}{\lambda} \quad (1)$$

where S is the Seebeck coefficient, G is the electrical conductivity, T is the absolute temperature, λ is the thermal conductivity coefficient, which is equal to the sum of the electron λ_e and phonon λ_{ph} thermal conductivities.

The nonequilibrium Green's function method (NEGF), DFT, and nonequilibrium molecular dynamics were used to calculate the thermoelectric coefficients and the Peltier coefficient. We used the standard model, in which the central part of the tube is connected to the semi-infinite left and right parts. QuantumATK [8] calculates the indicated thermoelectric coefficients and the Peltier coefficient in accordance with the linear response theory. The following relationships are used:

$$G_e = \left. \frac{dI}{dV_{bias}} \right|_{dT=0} ; S = - \left. \frac{dV_{bias}}{dT} \right|_{I=0} ; \lambda_e = \left. \frac{dI_Q}{dT} \right|_{I=0} ; \Pi = \left. \frac{I_Q}{I} \right|_{dT=0} = SV_{bias}. \quad (2)$$

The parameters of the system are given in Table 1.

Table 1

Parameters of the studied structures

Distance between fullerenes, R , Å	Tube diameter, D , Å
13.60	11.24
11.78	12.99
23.56	12.99

Results and Discussion

Obtaining materials with high thermoelectric figure of merit ZT is complicated by the requirement of independent control of electrical conductivity, thermal conductivity and Seebeck coefficient, which are often interrelated. A thermoelectric material with a high ZT must have low thermal conductivity λ , high electrical conductivity G , and high Seebeck coefficient S . In this paper, we investigate the effect of encapsulation of fullerenes in the cavity of a graphenylene nanotube on the above properties, taking into account chirality of nanotubes and distance between neighboring encapsulated fullerenes.

Fig. 2 shows the calculated thermoelectric properties (electrical and thermal conductivities, Peltier and Seebeck coefficients, thermoelectric figure of merit) of the armchair graphenylene nanotube system with encapsulated C_{60} fullerenes.

Thus, we observe that the introduction of fullerenes into the cavity of a graphenylene nanotube makes it possible to increase the electrical conductivity of the device, but significantly reduces its thermoelectric efficiency by reducing the Seebeck coefficient and increasing the thermal conductivity.

Fig. 3 shows the thermoelectric characteristics of two graphenylene nanotube- C_{60} fullerene systems with zigzag and armchair chirality types. The systems were selected with the closest possible nanotube diameter (a graphenylene nanotube with an "armchair" chirality has a diameter of 12.99 Å, and with a "zigzag" chirality, a diameter of 11.24 Å) and the distance between the centers of neighboring fullerenes (11.78 Å for an armchair nanotubes and 13.60 Å for a zigzag nanotube).

The graphenylene armchair nanotube- C_{60} fullerene system demonstrates higher electrical and thermal conductivities at zero and near-zero energies, but a low Seebeck coefficient.

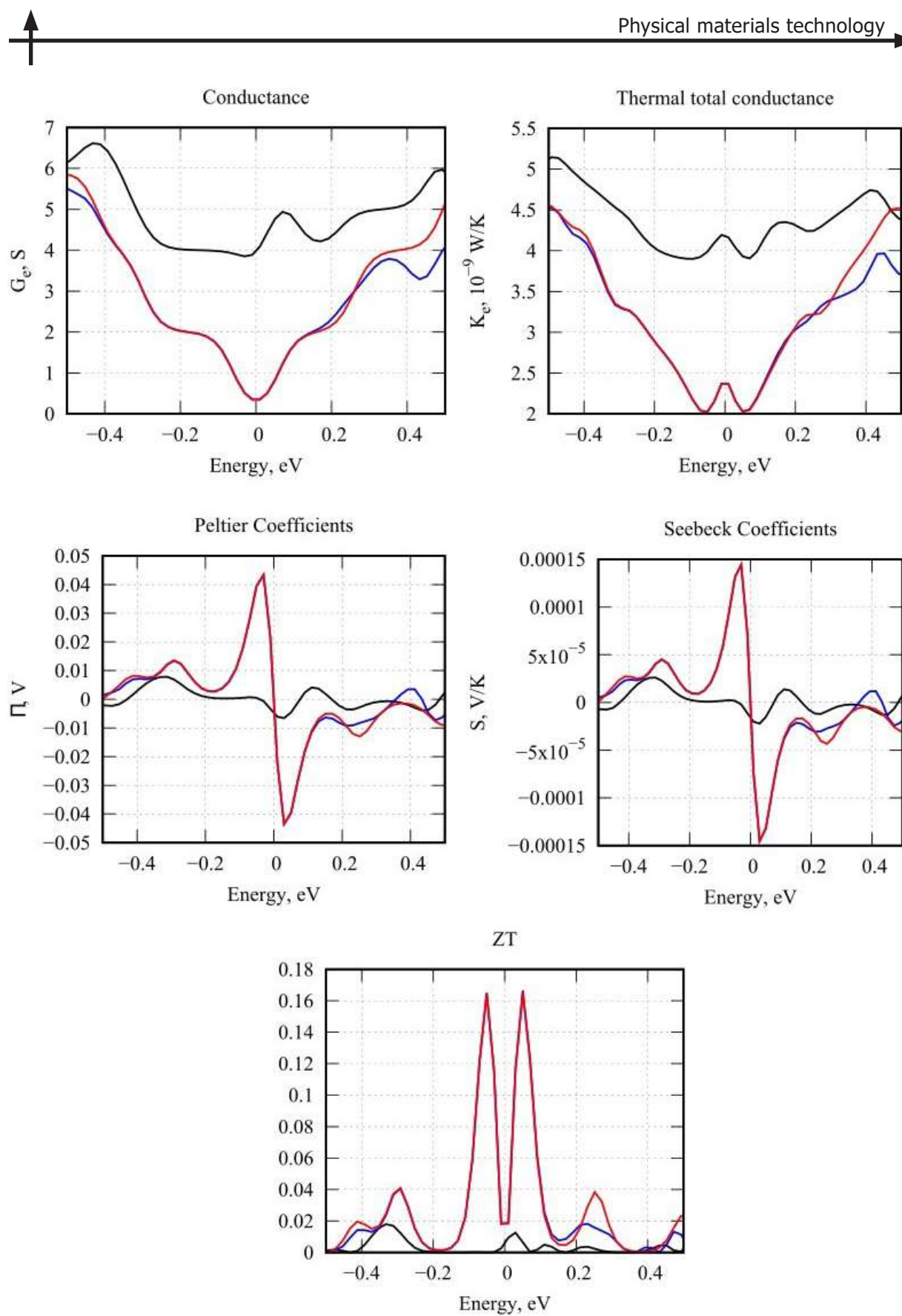


Fig. 2. The results of calculations of the thermoelectric coefficients for a graphenylene nanotube (red line) and graphenylene nanotube- C_{60} fullerene systems with a distance between the centers of two neighboring fullerenes of 11.78 Å (black line) and 23.56 Å (blue line)

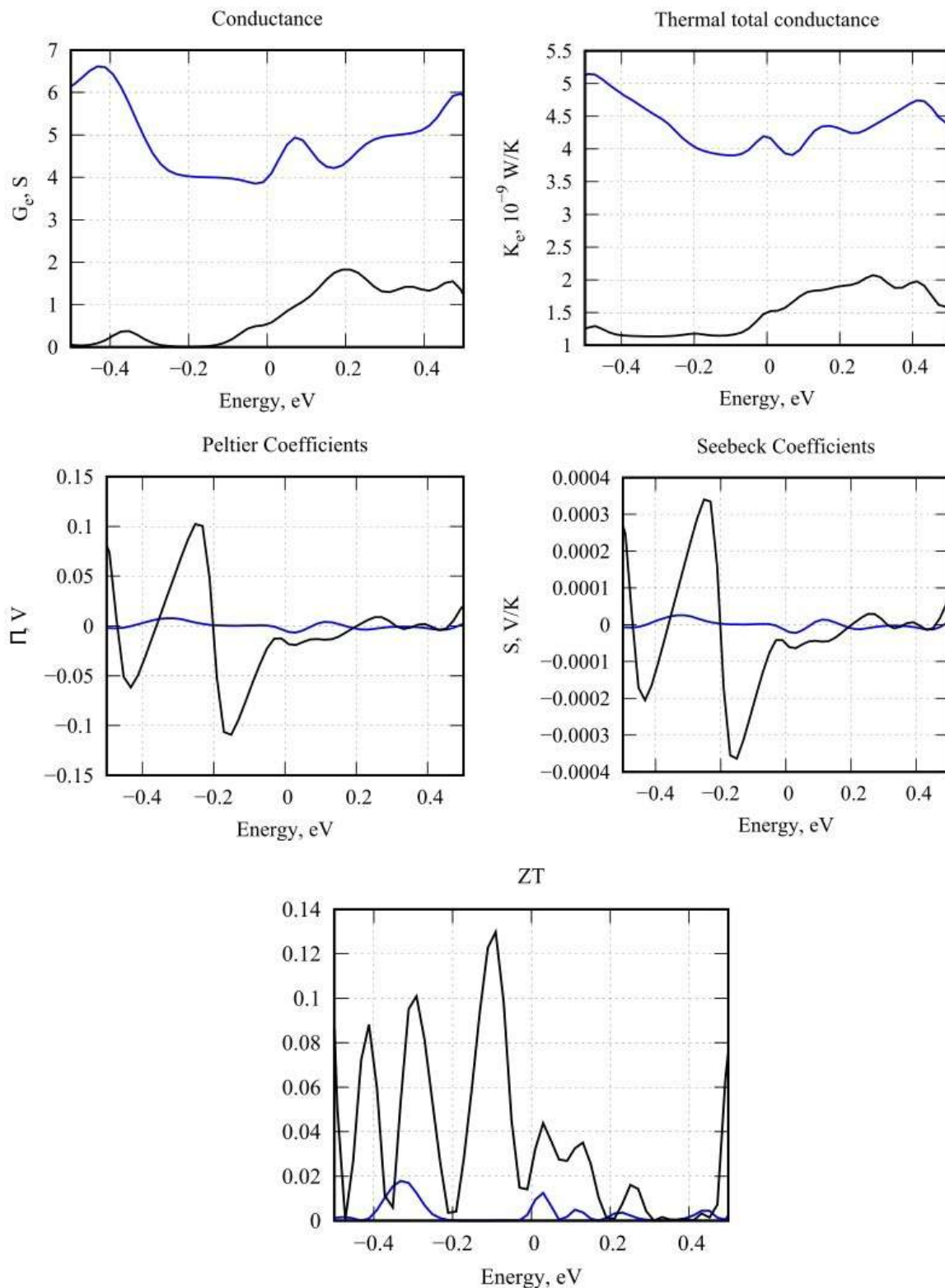


Fig. 3. Thermoelectric properties of graphenylene nanotube with zigzag chirality with encapsulated C_{60} fullerenes located inside the tube at a distance between their centers of 13.60 Å (black line) and a graphenylene nanotube system with an armchair chirality with encapsulated C_{60} fullerenes located inside the tube at a distance between their centers 11.78 Å (blue line)



Conclusion

Using DFT, NEGF and the molecular dynamics method, the thermoelectric properties of graphenylene nanotubes with encapsulated fullerenes are calculated. The thermoelectric figure of merit is significantly higher for the system of “zigzag” graphenylene C_{60} nanotubes than for the armchair graphenylene C_{60} nanotube system due to low thermal conductivity and high Seebeck coefficient. The introduction of fullerenes into the cavity of a graphenylene nanotube makes it possible to increase the electrical conductivity of the device, but, with an increase in the number of fullerenes in the tube, it significantly reduces its thermoelectric efficiency by reducing the Seebeck coefficient and increasing the thermal conductivity.

REFERENCES

1. Koch A. T., Khoshaman A. H., Fan H. D., Sawatzky G. A., Nojeh A., Graphenylene nanotubes, The journal of physical chemistry letters, 6 (19) (2015) 3982–3987.
2. Brunetto G., Autreto P. A. S., Machado L. D., Santos B. I., Dos Santos R. P., Galvao D. S., Nonzero gap two-dimensional carbon allotrope from porous grapheme, The Journal of Physical Chemistry C, 116 (23) (2012) 12810–12813.
3. Enyashin A. N., Ivanovskii A. L., Graphene allotropes, physica status solidi (b), 248 (8) (2011) 1879–1883.
4. Brazhe R. A., Meftakhutdinov R. M., Electronic and optical properties of carbon supracrystalline sp-2 nanoallotropes, Technical Physics, 61 (5) (2016) 750–755.
5. Cai J., Ruffieux P., Jaafar R., Bieri M., Braun T., Blankenburg S., Muoth M., Seitsonen A. P., Saleh M., Feng X., Fasel R., Atomically precise bottom-up fabrication of grapheme nanoribbons, Nature, 466 (7305) (2010) 470–473.
6. Meftakhutdinov R. M., Sibatov R. T., Kochaev A. I., Graphenylene nanoribbons: electronic, optical and thermoelectric properties from first-principles calculations, Journal of Physics: Condensed Matter, 32 (34) (2020) 345301.
7. Kochaev A. I., Meftakhutdinov R. M., Sibatov R. T., Timkaeva D. A., Optical and thermoelectric properties of graphenylene and octagraphene nanotubes from first-principles calculations, Computational Materials Science, 186 (2021) 109999.
8. Smidstrup S., Stradi D., Wellendorff J., Khomyakov P. A., Vej-Hansen U. G., Lee M. E., Stokbro K., First-principles Green's-function method for surface calculations: A pseudopotential localized basis set approach, Physical Review B, 96 (19) (2017) 195309.
9. Monkhorst H. J., Pack J. D., Special points for Brillouin-zone integrations, Physical review B, 13 (12) (1976) 5188.

THE AUTHORS

MOROZOVA Ekaterina V.
morozovaev@ulsu.ru
ORCID: 0000-0002-7530-3933

TIMKAEVA Diana A.
timkaevada@ulsu.ru
ORCID: 0000-0003-3748-0696

Received 14.07.2022. Approved after reviewing 20.07.2022. Accepted 08.09.2022.

Conference materials

UDC 535.327

DOI: <https://doi.org/10.18721/JPM.153.360>

Temperature-dependent exciton-polaritons in perovskite photonic crystal slab

M. A. Masharin ¹✉, S. V. Makarov ¹, A. K. Samusev ¹

¹ ITMO University, St. Petersburg, Russia

✉ mikhail.masharin@metalab.ifmo.ru

Abstract. Exciton-polaritons are perspective platform for realizing ultrafast and strong optical modulations, which are necessary for the plant of applications. However, exciton-polaritons are studied mostly for semiconductor quantum wells inside vertical Bragg cavities, which limits it to the cryogenic temperatures and prevents planar realizations, which can be a problem for real-world applications. Recently, perovskites become one of the perspective materials for room-temperature strong light-matter coupling regime due to their unique physical properties. In this work, we experimentally demonstrate for the first-time room-temperature exciton-polaritons in planar halide perovskite photonic crystal slab fabricated by a nanoimprint lithography method. We experimentally measured polariton dispersion from angle-resolved photoluminescence spectra and confirm the strong light-matter coupling regime at room temperature and lower. Also, we studied the temperature dependence of the exciton energy level in MAPbBr₃ and the light-matter coupling coefficient. The obtained dependences can be attributed to polaron effects in this material. The results can become the basis of further research on perovskite exciton-polaritons in planar photonic cavities.

Keywords: halide perovskites, exciton-polaritons, photonic crystal slab

Funding: The work was funded by Russian Science Foundation, grant No. 21-12-00218 and by RPMA grant of School of Physics and Engineering of ITMO University.

Citation: Masharin M. A., Makarov S. V., Samusev A. K., Temperature-dependent exciton-polaritons in perovskite photonic crystal slab. St. Petersburg State Polytechnical University Journal. Physics and Mathematics, 15 (3.3) (2022) 306–310. DOI: <https://doi.org/10.18721/JPM.153.360>

This is an open access article under the CC BY-NC 4.0 license (<https://creativecommons.org/licenses/by-nc/4.0/>)

Материалы конференции

УДК 535.327

DOI: <https://doi.org/10.18721/JPM.153.360>

Температурная зависимость экситон-поляритонов в перовскитной фотонно-кристаллической пластине

М. А. Машарин ¹✉, С. В. Макаров ¹, А.К. Самусев ¹

¹ Университет ИТМО, Санкт-Петербург, Россия

✉ mikhail.masharin@metalab.ifmo.ru

Аннотация. В данной работе мы впервые экспериментально демонстрируем сильную связь свет-вещество в планарной фотонно-кристаллической пластине, сделанной из поликристаллической пленки органо-неорганического перовскита MAPbBr₃ методом nanoimprint литографии. В работе мы рассказываем о методах фабрикации, морфологии образца, а также демонстрируем экспериментально измеренный углоразрешенный спектр фотолюминесценции, содержащий ветки поляритонной дисперсии при комнатной температуре. Варьируя температуру образца, мы получили зависимость экситонного уровня, а также коэффициента связи свет-вещество от температуры.



Ключевые слова: органо-неорганические перовскиты, экситон-поляритоны, фотонно-кристаллическая пластина

Финансирование: Работа была сделана при поддержке Российского Научного Фонда № 21-12-00218, а также при финансовой поддержке гранта НИРМА ФТ МФ Университета ИТМО.

Ссылка при цитировании: Машарин М. А., Макаров С. В., Самусев А. К. Температурная зависимость экситон-поляритонов в перовскитной фотонно-кристаллической пластине // Научно-технические ведомости СПбГПУ. Физико-математические науки. 2022. Т. 15. № 3.3. С. 306–310. DOI: <https://doi.org/10.18721/JPM.153.360>

Статья открытого доступа, распространяемая по лицензии CC BY-NC 4.0 (<https://creativecommons.org/licenses/by-nc/4.0/>)

Introduction

One of the most critical problems in photonics is the searching for the material base with high optical nonlinearities in an ultrashort time. Part-light, part-matter quasiparticles exciton-polaritons represent a perspective platform to solve this problem, thanks to its hybrid properties. Since the first works about exciton-polaritons in GaAs quantum well (QW) implemented in a Bragg cavity [1], there already have been shown several concepts of polariton devices, such as polariton transistors, switchers, and lasers [2, 3]. Despite the huge progress in this field at this moment, most of the exciton-polariton designs are limited to cryogenic temperatures, due to low exciton binding energy. Also, large Bragg cavity vertical sizes are still the obstacle for the further development. To overcome it new materials with room-temperature exciton and planar photon cavities designs are needed.

One of the possible implementations of planar photon cavities, which can be experimentally studied, is leaky modes of a photonic crystal slab. This approach was already used for exciton-polaritons with monolayer of MoSe₂ [4]. However, 2D materials are very sensitive to defects and limited to monolayer lateral sizes. In our work, we present a photonic crystal slab based on the halide perovskite MAPbBr₃, fabricated by the nanoimprint lithography method. Such approach has several advantages: large scale of the polariton cavity (> 1 cm²) due to the perovskite synthesis methods and nanoimprint lithography [5]; room-temperature exciton in MAPbBr₃ around 40 meV [6], easy and cheap to fabricate, and huge cavity photon mode localization, because photonic cavity simultaneously plays the role of the exciton material.

In this work, we demonstrate for the first-time room temperature exciton-polariton dispersions in the planar photon cavity. We show the fabrication method of the MAPbBr₃ photonic crystal slab and its morphology. Also, we show the angle-resolved photoluminescence (PL) spectrum at room temperature with exciton-polariton branch, calculated from the two-coupled oscillator model [7], and the dependence of exciton level and Rabi splitting on the temperature, calculated from the noted model.

Materials and Methods

MAPbBr₃ perovskite is one of the most interesting materials for exciton-polariton systems because it has room-temperature exciton with high oscillator strength, defect tolerance, synthesis from solutions, enough softness for nanoimprint lithography and observed polaron effects, which affect exciton-polariton states [5].

First, we prepare the perovskite solution by dissolving 33.59 mg of MABr (Sigma Aldrich) and 110,1 mg of PbBr₂ (TCI) in the mixture of DMF:DMSO in a relation equal to 3:1. Resulting 0.3M solution is steered for 24 hours at room temperature. After we filter it by PTFE filter to avoid small crystallites.

Second, we wash SiO₂ substrates (12×12 cm²) with sonication in the deionized water, acetone and 2-propanol for 10 minutes consecutively, and afterwards clean it in an oxygen plasma cleaner for 10 minutes. Afterwards we transfer substrates in the dry glovebox with nitrogen atmosphere.

Next, we fabricate MAPbBr₃ polycrystalline films by spin-coating method in the nitrogen dry glovebox. (Fig. 1, a). We depose 40 uL of prepared MAPbBr₃ solution on the cleaned substrate

and place it on the spin-coater. After, it is spinning at 3000 rpm for 40 seconds. At the 20 second after the start we drip 300 uL of toluene, which plays the role of the antisolvent, on the top of the rotating substrate.

After the spinning we take out the substrate with MAPbBr₃ polycrystalline film from the glovebox for the nanoimprint lithography. We put a large-scale cleaned DVD disk mold on the top of the MAPbBr₃ film and apply 15 MPa pressure for 10 minutes. After we remove the mold and put the sample in the nitrogen atmosphere the further annealing at 90 °C for 10 minutes. The resulting sample slowly degrades under ambient conditions and therefore it is stored in the dry glovebox with an inert atmosphere (Fig. 1, a).

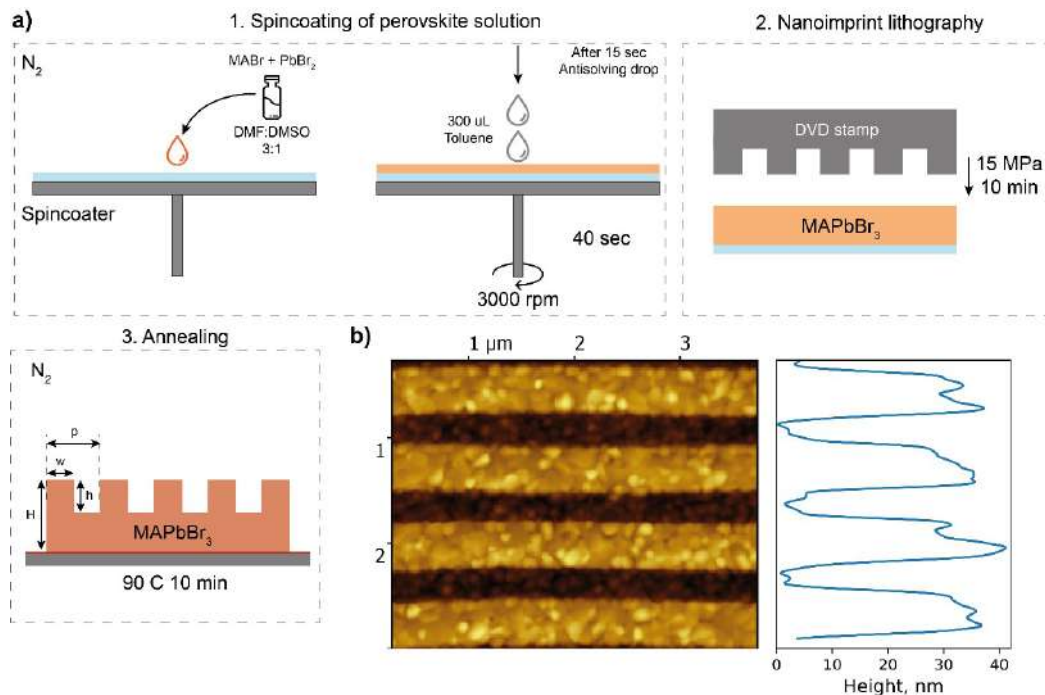


Fig. 1. Sketch of the main steps of the MAPbBr₃ crystal slab fabrication (a) AFM scan of the perovskite crystal slab morphology and its vertical profile (b)

We studied the resulting sample morphology by the atomic force microscopy (AFM) method (Fig. 1, b). The periodic structure has a pronounced rectangular shape with a period of 750 nm, a modulation depth of 35 nm, and a comb width of 450 nm. The roughness of the sample is lower than 5 nm, which points to the high quality of the resulting photonic crystal slab.

To confirm the strong light-matter coupling regime and measure exciton-polariton dispersion we used the angle-resolved spectroscopy method. The experimental setup is shown in Fig. 2. Femtosecond laser (220 fs) at 490 nm (Pharos + Orpheus-F, Light Conversion) was used as an incident pump of PL. A repetition rate of 10 kHz was chosen to avoid thermal effects. Half-wave plate and Glan prism were used to filter laser polarization and attenuate laser fluence. Lens L1 was used to focus incident emission to the back focal plane (BFP) of the objective (Mitutoyo NIR HR 50x with N.A. = 0.65) to realize the pump spot of 30 um on the sample placed in the closed-cycle helium cryostat (Advanced Research Systems). A large pump spot for a high N.A. objective is required to pump the area with a large number of the grating period.

The emission from the sample gets into the objective and then into the 4f scheme, realized by the lenses L2, L3, and spatial filtering. The information on the emission angle distribution contains in BFP, which is imaged by dashed lines in Fig. 2. Lens L4, located at the focal distance from BFP, makes Fourier transform (focus each particular emission angle to its point on BFP), and then the BFP image goes to the slit spectrometer at $k_y = 0$, which is coupled to the imaging CCD (Princeton Instruments SP2500+PyLoN). Image from the spectrometer, coupled to the imaging CCD represents colormap with angle distribution on the one axis and light wavelength on the other (example in Fig. 3, a).

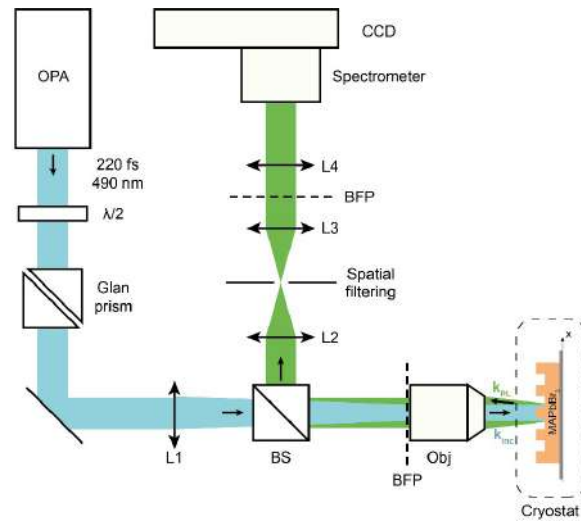


Fig. 2. Scheme of the experimental setup of angle-resolved PL measurements. L – Lens, BS – beam splitter, obj – objective, BFP – back focal plane

Results and Discussion

We measured the angle-resolved spectrum of the MAPbBr₃ photonic crystal slab, fabricated by the nanoimprint lithography method at room temperature (Fig. 3, *a*). We extract the polariton mode from the spectrum, determine an exciton level from the PL and reflection spectra, and estimate uncoupled cavity photon mode by linear approximation of the mode far from the exciton resonance. From the well-known two-coupled oscillator model, described strong light-matter regime (Eq. 1) [7], we fitted polariton dispersion (solid yellow line in Fig. 3, *a*) with varying parameter coupling coefficient g . At room temperature, the coupling coefficient is equal to 109.5 meV, which is much larger than the half-difference of exciton and cavity photon linewidths, which is around 4 meV, that confirms the strong light-matter coupling regime [7].

$$E_{LP}(k_x) = \frac{E_X + E_C(k_x)}{2} - \frac{1}{2} \sqrt{(E_X - E_C(k_x))^2 + g^2} \quad (1)$$

where E_{LP} , E_X , E_C are complex energy of lower polariton, exciton and uncoupled cavity photon respectively; g is coupling coefficient.

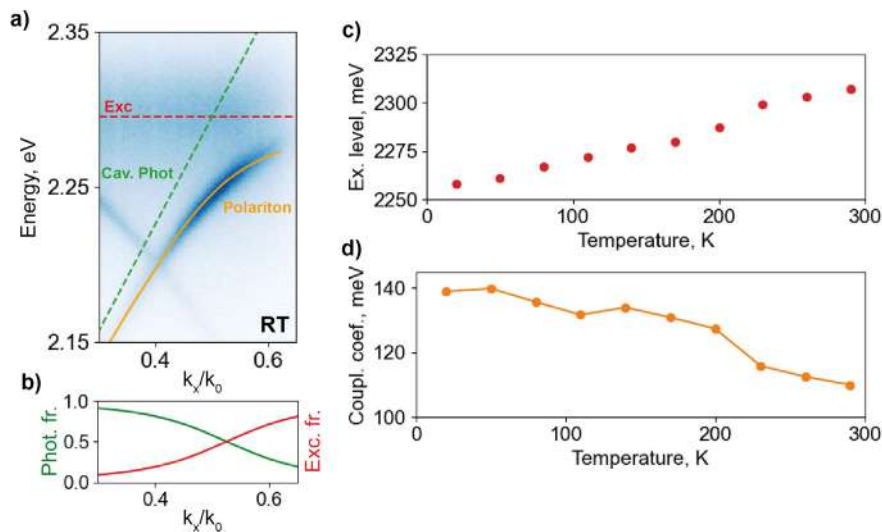


Fig 3. Angle-resolved PL spectrum measured at room temperature. Red dashed line – exciton level, green dashed line – uncoupled cavity photon dispersion, solid yellow line is fitted by two-coupled oscillator model polariton dispersion (*a*). Hopfield coefficients of polariton at room temperature, extracted from the model (*b*); Exciton level as a function of the temperature (*c*); Rabi splitting, calculated from the measured angle-resolved spectra and two-coupled oscillator model (*d*)

In Fig. 3, *b* Hopfield coefficients of the polariton brunch are shown, which reveal to the photon and exciton fractions in polariton as a function of angle emission. There should be noted, that when the exciton fraction reaches the value around 0.7, polariton brunch dissipates due to the strong exciton absorption. As the exciton and band-to-band absorption is strong, the upper polariton branch does not exist in the system.

With lowering the temperature we measured angle-resolved spectra and extracted from it exciton level and polariton coupling coefficients (Fig. 3, *c*, *d*). Shifting of the exciton level with lowering the temperature can be attributed to polarons in the perovskite [6]. In this work there are no other polaron effects, however, it should play a significant role under a polariton resonance pump [5]. Also, with lowering temperature coupling coefficient increases due to the increase of exciton concentration and decrease of the nonradiative losses in the system.

Conclusion

In our work, we experimentally demonstrate for the first-time exciton-polariton dispersion in the planar photonic crystal slab based on halide perovskite MAPbBr₃. Thanks to the unique properties of perovskites, we succeeded to realize the periodic structure on the polycrystalline perovskite film by nanoimprint lithography and confirm a strong light-matter coupling regime of exciton and photonic crystal slab leaky modes. We also reveal the dependence of the exciton level and light-matter coupling coefficients with temperature. These results confirm the opportunity for room temperature exciton-polaritons in the planar cavity and can form the basis of further perovskite exciton-polariton studies.

REFERENCES

1. Weisbuch C., et al., Observation of the coupled exciton-photon mode splitting in a semiconductor quantum microcavity, *Phys. Rev. Lett.* 69 (23) (1992) 3314–3317.
2. Liew T. C. H., Shelykh I. A., Malpuech G., Polaritonic devices, *Phys. E Low-Dimensional Syst. Nanostructures.* Elsevier, 43 (9) (2011) 1543–1568.
3. Kasprzak J., et al., Bose-Einstein condensation of exciton polaritons, *Nature.* 443 (7110) (2006) 409–414.
4. Kravtsov V., et al., Nonlinear polaritons in a monolayer semiconductor coupled to optical bound states in the continuum, *Light Sci. Appl. Springer US*, 9 (1) (2020).
5. Masharin M. A., et al., Polaron-enhanced polariton nonlinearity in lead halide perovskites. 2022.
6. Soufiani A. M., et al., Polaronic exciton binding energy in iodide and bromide organic-inorganic lead halide perovskites, *Appl. Phys. Lett.* 107 (23) (2015).
7. Hopfield J. J., Theory of the contribution of excitons to the complex dielectric constant of crystals, *Phys. Rev.* 112 (5) (1958) 1555–1567.

THE AUTHORS

MASHARIN Mikhail A.
mikhail.masharin@metalab.ifmo.ru
ORCID: 0000-0003-0687-8706

SAMUSEV Anton K.
a.samusev@metalab.ifmo.ru
ORCID: 0000-0002-3547-6573

MAKAROV Sergey V.
s.makarov@metalab.ifmo.ru
ORCID: 0000-0002-9257-6183

Received 18.07.2022. Approved after reviewing 20.07.2022. Accepted 23.07.2022.

Conference materials

UDC 538.975

DOI: <https://doi.org/10.18721/JPM.153.361>

Plasma assisted molecular beam epitaxy growth of InGaN nanostructures on Si substrates

V. O. Gridchin^{1, 2, 3}✉, R. R. Reznik^{1, 2, 3}, K. P. Kotlyar³, T. M. Shugabaev¹,
A. S. Dragunova⁴, N. V. Kryzhanovskaya⁴, G. E. Cirlin^{1, 2, 3}

¹ Alferov University, St. Petersburg, Russia;

² IAI RAS, St. Petersburg, Russia;

³ St. Petersburg State University, St. Petersburg, Russia;

⁴ National Research University Higher School of Economics, St. Petersburg, Russia

✉ gridchinfo@gmail.com

Abstract. In this work, we study the influence of the substrate temperature on the structural and optical properties of InGaN nanostructures synthesized by plasma-assisted molecular beam epitaxy. We show that ternary InGaN alloys with a chemical composition within the miscibility gap can be synthesized under N-rich growth conditions at the substrate temperatures from 600 to 670 °C. The results can be used to create visible and white light-emitting diodes on Si substrates.

Keywords: InGaN, silicon, structural properties, optical properties, plasma-assisted molecular beam epitaxy

Funding: The samples were grown under financial support of RSF grant (project No.19-72-30010). The structural properties were studied under financial support of the research grant of St. Petersburg State University No. 93020138. The study of photoluminescence was implemented in the framework of the Basic Research Program at the National Research University Higher School of Economics (HSE University).

Citation: Gridchin V. O., Reznik R. R., Kotlyar K. P., Shugabaev T. M., Dragunova A. S., Kryzhanovskaya N. V., Cirlin G. E., Plasma assisted molecular beam epitaxy growth of InGaN nanostructures on Si substrates. St. Petersburg State Polytechnical University Journal. Physics and Mathematics, 15 (3.3) (2022) 311–314. DOI: <https://doi.org/10.18721/JPM.153.361>

This is an open access article under the CC BY-NC 4.0 license (<https://creativecommons.org/licenses/by-nc/4.0/>)

Материалы конференции

УДК 538.975

DOI: <https://doi.org/10.18721/JPM.153.361>

Молекулярно-пучковая эпитаксия с плазменной активацией азота InGaN наноструктур на кремнии

В. О. Гридчин^{1, 2, 3}✉, Р. Р. Резник^{1, 2, 3}, К. П. Котляр³, Т. М. Шугабаев¹,
А. С. Драгунова⁴, Н. В. Крыжановская⁴, Г. Э. Цырлин^{1, 2, 3}

¹ Санкт-Петербургский академический университет им. Ж. И. Алферова РАН, Санкт-Петербург, Россия;

² Институт аналитического приборостроения РАН, Санкт-Петербург, Россия;

³ Санкт-Петербургский государственный университет, Санкт-Петербург, Россия;

⁴ Национальный исследовательский университет «Высшая школа экономики», Санкт-Петербург, Россия

✉ gridchinfo@gmail.com

Аннотация. В работе представлены результаты исследования влияние температуры подложки на структурные и оптические свойства наноструктур InGaN, синтезированных методом молекулярно-пучковой эпитаксии с плазменной активацией азота. Показано, что тройной раствор InGaN с химическим составом в зоне разрыва смешиваемости

может быть синтезирован в азот-обогащенных ростовых условиях при температурах подложки от 600 до 670 °С. Полученные результаты могут представлять интерес для создания оптоэлектронных устройств на кремниевых подложках в видимом диапазоне.

Ключевые слова: InGaN, кремний, структурные свойства, оптические свойства, молекулярно-пучковая эпитаксия с плазменной активацией азота

Финансирование: Ростовые эксперименты проведены при поддержке Российского научного фонда (проект № 19-72-30010). Исследования структурных свойств проведены при поддержке гранта СПбГУ № 93020138. Исследования фотолюминесценции проведены в рамках Программы фундаментальных исследований НИУ ВШЭ.

Ссылка при цитировании: Гридчин В. О., Резник Р. Р., Котляр К. П., Шугабаев Т. М., Драгунова А. С., Крыжановская Н. В., Цырлин Г. Э. Молекулярно-пучковая эпитаксия с плазменной активацией азота InGaN наноструктур на кремнии // Научно-технические ведомости СПбГПУ. Физико-математические науки. 2022. Т. 15. № 3.3. С. 311–314. DOI: <https://doi.org/10.18721/JPM.153.361>

Статья открытого доступа, распространяемая по лицензии CC BY-NC 4.0 (<https://creativecommons.org/licenses/by-nc/4.0/>)

Introduction

Ternary InGaN alloys are promising semiconductor materials for visible solid-state lighting [1] and renewable energy sources [2, 3] due to the direct band gap with the energy from 3.37 (GaN) to 0.7 eV (InN). However, the growth of InGaN alloys with the high In content ($x_{\text{In}} > 0.3$) and high crystal quality is an extremely challenging task due to the large difference in interatomic spacing between InN and GaN [4]. Plasma-assisted molecular beam epitaxy (PA-MBE) technique possesses a great potential for growing high-quality InGaN epitaxial structures. In particular, relatively low growth pressures and consumptions of the high purity nitrogen and group-III materials (7N) allow one to reduce contamination of the epitaxial structures. The PA-MBE growth process may proceed far from thermodynamic equilibrium that can potentially contribute to grow of InGaN over the entire compositional range. One of the possible approaches to obtain InGaN alloys with the high In content and high crystal quality is the growth of InGaN nanowires (NWs) [5, 6]. It has recently been shown that InGaN NWs with the In content of about 35% can be grown on silicon substrates by the PA-MBE [7, 8]. However, the influence of the growth conditions in the PA-MBE on the physical properties of ternary InGaN alloys is still poorly studied. This work is devoted to studying the substrate temperature influence on the physical properties of ternary InGaN alloys grown by plasma-assisted molecular beam epitaxy on Si substrates.

Materials and Methods

The InGaN nanostructures were grown directly on p-type Si(111) substrates using Riber Compact 12 MBE setup, equipped with Ga, In effusion cells, and the nitrogen plasma source. Initially, the substrate was transferred to the growth chamber and heated to 950 °C for thermal treatment. Next, the substrate temperature was decreased to the desired value allowing the growth of InGaN nanostructures. We carried out several experiments at growth temperatures from 600 °C to 670 °C. An atomically clean silicon surface was observed by the reflection high-energy electron diffraction (RHEED) at all growth temperatures. After the stabilization of the growth temperature, the nitrogen plasma source was ignited at 450 W and the N flux was set to 0.4 sccm. At this moment, the growth chamber pressure was $7.4 \cdot 10^{-6}$ Torr. Finally, In and Ga effusion cells were simultaneously opened and the InGaN structure was grown during 20 hours. The growth was performed under N-rich conditions. The fluxes of In and Ga, measured by Bayard-Alpert vacuum gauge before the growth, were equal to $1 \cdot 10^{-7}$ Torr.

The morphology of the samples was studied by scanning electron microscopy (SEM Supra 25 Zeiss). The measurements of photoluminescence were performed at room temperature (RT PL) under a helium–cadmium (He-Cd) metal-vapor laser with a wavelength of 325 nm at 15.5 mW. The PL signal was detected using a DK480 Spectral products monochromator and a single-channel silicon detector using synchronous detection (SRS 510 “Stanford Research Systems”).

Results and Discussion

Fig. 1 shows the SEM images of the samples grown at: (a) 600 °C; (b) 650 °C; (c) 670 °C. As can be seen from Fig. 1, *a*, the ternary InGaN alloy is synthesized in the three-dimensional structure consisted of a nanocolumn layer near the substrate and “nanoflowers” formed above. The structural properties of this sample were studied in detail in [9]. The average height of nanostructures is about 4.8 μm. The InGaN NWs separated from each other are grown at the substrate temperature of about 650 °C (see Fig. 1, *b*). The average height of NWs is 2.9 μm and their average diameter is 100 nm. The InGaN compact layer with an average height of 1.6 μm is formed at 670 °C (see Fig. 1, *c*).

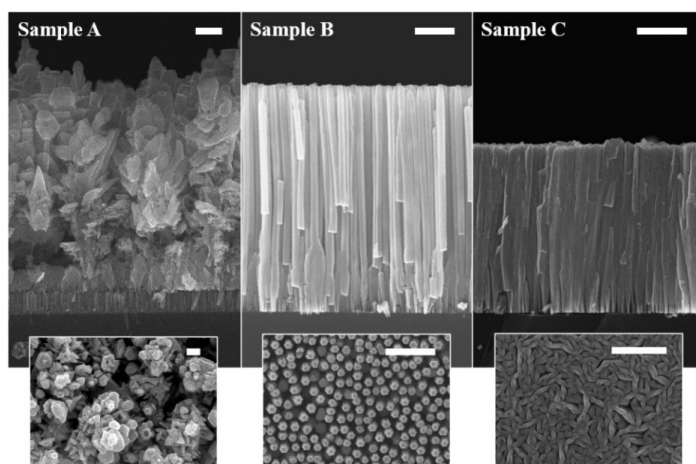


Fig. 1. Typical cross-section SEM images of the samples grown at (a) 600 °C, (b) 650 °C, (c) 670 °C. The insertions demonstrate corresponding plan-view SEM images. The scale bars are 500 nm

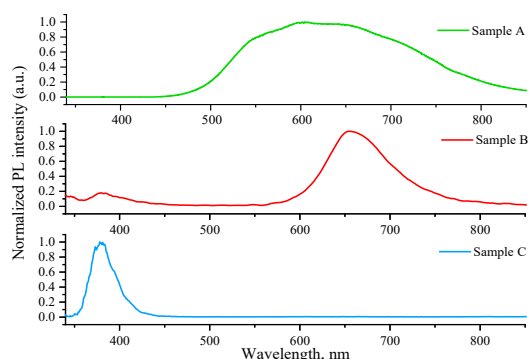


Fig. 2. RT PL spectra of the InGaN nanostructures grown at various substrate temperatures. The green line is the PL of sample A. The red line is the PL of sample B. The blue line is the PL of sample C

Fig. 2 shows the normalized RT PL spectra of the samples. The green line is the RT PL spectrum of sample A grown at the lowest temperature. The sample exhibits a broad emission spectrum in the range from 450 to 850 nm which is explained by the inhomogeneous distribution of In atoms within the structure [9]. In the case of sample B (see the red line in Fig. 2), the RT PL spectrum demonstrates two emission areas: the first with the maximum at 380 nm and the second with the maximum at 656 nm. In the work [7] we have shown that InGaN NWs exhibit spontaneously formed core-shell structure with the In content in the core of about 30–35% and in the shell of about 0–4%. As has been shown, the use of RT PL from the core-shell InGaN NWs can be converted into the actual chemical composition by the Vegard's law with a bowing parameter of 1.43 eV. In this

regard, the InGaN NWs of sample B consist of a spontaneously formed core-shell structure. The first area of RT PL corresponds to the emission from the shell with the In content of about 0–4% and the second area corresponds to the core with the In content of about 44%. The blue line in Fig. 2 is the emission of sample C. The spectrum has a maximum centered at 380 nm that corresponds to an In content of 4%. This indicates that indium adatoms practically do not incorporate into the growing structure under these growth conditions, which is explained by the predominance of the InN thermal decomposition instead of the formation of InGaN nanostructures.

Conclusion

To conclude, we have investigated the influence of the substrate temperature on the structural and optical properties of ternary InGaN alloys. The three-dimensional InGaN nanostructures

with an inhomogeneously distributed In content was grown at 600 °C. The InGaN NWs with the In content of about 40% were grown at 650 °C. The InGaN compact layer with the In content of about 4% was grown at 670 °C. The results can be used to create visible and white light-emitting diodes directly on Si substrates.

REFERENCES

1. Bui H. Q. T., Velpula R. T., Jain B., Aref O. H., Nguyen H.-D., Lenka T. R., Nguyen H. P. T., Full-Color InGaN/AlGaIn Nanowire Micro Light-Emitting Diodes Grown by Molecular Beam Epitaxy: A Promising Candidate for next Generation Micro Displays, *Micromachines*. 10 (8) (2019) 492.
2. Chu S., Li W., Yan Y., Hamann T., Shih I., Wang D., Mi Z., Roadmap on Solar Water Splitting: Current Status and Future Prospects, *Nano Futures*. 1 (2) (2017) 022001.
3. Lin J., Wang W., Li G., Modulating Surface/Interface Structure of Emerging InGaN Nanowires for Efficient Photoelectrochemical Water Splitting, *Advanced Functional Materials*. 30 (52) (2020) 2005677.
4. Ho I., Stringfellow G., Solid Phase Immiscibility in GaInN, *Applied Physics Letters*. 69 (18) (1996) 2701–2703.
5. Kuykendall T., Ulrich P., Aloni S., Yang P., Complete Composition Tunability of InGaN Nanowires Using a Combinatorial Approach, *Nature materials*. 6 (12) (2007) 951–956.
6. Roche E., Andre Y., Avit G., Bougerol C., Castellucci D., Réveret, F., Gil E., Médard F., Leymarie J., Jean T., Dubrovskii V. G., Trassoudaine A., Circumventing the Miscibility Gap in InGaN Nanowires Emitting from Blue to Red, *Nanotechnology*. 29 (46) (2018) 465602.
7. Gridchin V. O., Kotlyar K. P., Reznik R. R., Dragunova A. S., Kryzhanovskaya N. V., Lendyashova V. V., Kirilenko D. A., Soshnikov I. P., Shevchuk D. S., Cirlin G. E., Multi-Colour Light Emission from InGaN Nanowires Monolithically Grown on Si Substrate by MBE, *Nanotechnology*. 32 (33) (2021) 335604.
8. Tabata T., Paek J., Honda Y., Yamaguchi M., Amano H., Growth of InGaN Nanowires on a (111) Si Substrate by RF-MBE, *physica status solidi c*. 9 (3-4) (2012) 646–649.
9. Gridchin V. O., Kotlyar K. P., Reznik R. R., Shevchuk D. S., Kirilenko D. A., Bert N. A., Soshnikov I. P., Cirlin G. E., Peculiarities of the Structural Properties of In_xGa_{1-x}N Polytotype Nanostructures Grown by Molecular-Beam Epitaxy, *Journal of Physics: Conference Series – IOP Publishing*. 1482 (1) (2020) 012014.

THE AUTHORS

GRIDCHIN Vladislav O.
gridchinfo@gmail.com
ORCID: 0000-0002-6522-3673

DRAGUNOVA Anna S.
anndra@list.ru
ORCID: 0000-0002-0181-0262

REZNIK Rodion R.
moment92@mail.ru
ORCID: 0000-0003-1420-7515

KRYZHANOVSKAYA Natalia V.
nataliakryzh@gmail.com
ORCID: 0000-0002-4945-9803

KOTLYAR Konstantin P.
konstantin21kt@gmail.com
ORCID: 0000-0002-0305-0156

CIRLIN George E.
george.cirlin@mail.ru
ORCID: 0000-0003-0476-3630

SHUGABAEV Talgat M.
talgashugabaev@mail.ru
ORCID: 0000-0002-4110-1647

Received 20.07.2022. Approved after reviewing 22.07.2022. Accepted 23.07.2022.

Conference materials

UDC 538.9.

DOI: <https://doi.org/10.18721/JPM.153.362>

Independent control of size and shape of GaAs nanostructures during droplet epitaxy using ultra-low arsenic flux

S. V. Balakirev ¹, E. A. Lakhina ¹✉, D. V. Kirichenko ¹, N. E. Chernenko ¹,
N. A. Shandyba ¹, M. M. Eremanko ¹, M. S. Solodovnik ¹

¹ Southern Federal University, Taganrog, Russia

✉ lakhina@sfedu.ru

Abstract. GaAs nanostructures are promising candidates for use in future nanoelectronics and quantum photonics. However, technology of their controllable fabrication with precisely predefined size, shape and surface density still requires further improvement. In this paper, we reveal a possibility to reduce a size of gallium droplets using exposure to the arsenic flux of ultra-low values. The control of size and shape of droplets is implemented independently of their surface density that enables formation of low-density arrays of small-sized quantum dots. Based on droplet arrays with trimodal size distribution, we demonstrate that droplets with larger sizes are less influenced by the low arsenic flux whereas smaller droplets may reduce in volume or decay completely resulting in the formation of nanoholes. The technique under consideration can be used for the fabrication of single quantum dot devices with specified characteristics.

Keywords: droplet epitaxy, GaAs, nanostructures, arsenic flux

Funding: This study was supported by the Russian Science Foundation Grant No. 21-79-00310, <https://rscf.ru/project/21-79-00310/>, at the Southern Federal University.

Citation: Balakirev S. V., Lakhina E. A., Kirichenko D. V., Chernenko N. E., Shandyba N. A., Eremanko M. M., Solodovnik M. S., Independent control of size and shape of GaAs nanostructures during droplet epitaxy using ultra-low arsenic flux. St. Petersburg State Polytechnical University Journal. Physics and Mathematics, 15 (3.3) (2022) 315–319. DOI: <https://doi.org/10.18721/JPM.153.362>

This is an open access article under the CC BY-NC 4.0 license (<https://creativecommons.org/licenses/by-nc/4.0/>)

Материалы конференции

УДК 538.9.

DOI: <https://doi.org/10.18721/JPM.153.362>

Независимое управление размером и формой наноструктур GaAs при капельной эпитаксии с помощью ультрамалого потока мышьяка

С. В. Балакирев ¹, Е. А. Лахина ¹✉, Д. В. Кириченко ¹, Н. Е. Черненко ¹,
Н. А. Шандыба ¹, М. М. Еременко ¹, М. С. Солодовник ¹

¹ Южный федеральный университет, Таганрог, Россия

✉ lakhina@sfedu.ru

Аннотация. В данной работе демонстрируется возможность уменьшения размера капель галлия за счет воздействия на них потока мышьяка ультрамалых значений. Управление размером и формой капель осуществляется независимо от их поверхностной плотности, что позволяет формировать массивы квантовых точек малого размера с низкой поверхностной плотностью. Основываясь на массивах капель с тримодальным распределением по размерам, мы демонстрируем, что капли большего размера в меньшей степени подвержены влиянию малого потока мышьяка, в то время как капли меньшего размера могут уменьшаться в объеме или полностью распадаться, приводя к формированию наноглублений.

Ключевые слова: капельная эпитаксия, GaAs, наноструктуры, поток мышьяка

Финансирование: Исследование выполнено за счет гранта Российского научного фонда № 21-79-00310, <https://rscf.ru/project/21-79-00310/>, в Южном федеральном университете.

Ссылка при цитировании: Балакирев С. В., Лахина Е. А., Кириченко Д. В., Черненко Н. Е., Шандыба Н. А., Ерёменко М. М., Солодовник М. С. Независимое управление размером и формой наноструктур GaAs при капельной эпитаксии с помощью ультрамалого потока мышьяка // Научно-технические ведомости СПбГПУ. Физико-математические науки. 2022. Т. 15. № 3.3. С. 315–319. DOI: <https://doi.org/10.18721/JPM.153.362>

Статья открытого доступа, распространяемая по лицензии CC BY-NC 4.0 (<https://creativecommons.org/licenses/by-nc/4.0/>)

Introduction

Semiconductor nanostructures, including A3B5 quantum dots, have recently attracted increasing attention due to the intensification of the transition of micro- and optoelectronic devices to principles based on quantum effects [1]. GaAs/AlGaAs quantum dots have proven themselves particularly well as potential quantum light sources because of their negligible fine structure splitting and short exciton lifetimes [2]. However, quantum dots in lattice-matched systems are impossible to obtain via the traditional Stranski-Krastanov growth mechanism [3]. An alternative method that has been widely used recently is a droplet epitaxy which makes it possible to form Ga droplets and then transform them into GaAs nanostructures independently in two main stages [4].

In order to fabricate high-efficiency emitters of single photons and entangled photon pairs, single quantum dots are usually required [5], which can be realized by the formation of low-density arrays of nanostructures with their further division into separate device elements [6]. A difficulty lies in the fact that achieving a low surface density requires a high substrate temperature leading to the droplet enlargement or a decrease in the amount of deposited material (deposition thickness) [7]. However, the deposition thickness cannot be reduced to near-zero values because of the presence of a critical thickness of droplet formation which increases with decreasing temperature [8, 9].

Previously, we demonstrated that large In droplets obtained at temperatures providing their low surface density can be reduced in volume due to the phenomenon of diffusion decay under a low arsenic flux [10, 11]. In this paper, we reveal the same process concerning Ga droplets on the GaAs(001) surface. Although nanorings are observed at the place of original perimeters of droplets, droplets shrink by almost 1.3 times, which can be extended by further alterations of technological parameters. We also demonstrate that small droplets reduce in volume more intensively than large droplets. This fact can be used as well to provide a flexible control of the droplet size with their surface density kept at the same level.

Materials and Methods

SemiTEq STE35 molecular beam epitaxy equipment was used to grow samples on epi-ready GaAs(001) substrates. Calibration of the growth rates and *in situ* monitoring of the growth processes were carried out using a reflection high-energy electron diffraction system.

After standard procedure of the native oxide removal at a substrate temperature (T) of 600 °C under an A_{As} pressure $P = 4 \cdot 10^{-5}$ Pa, 250 nm of GaAs buffer layer was grown at $T = 580$ °C with a growth rate of 1 monolayer (ML) per second. Then, a deposition temperature $T = 500$ °C was set on the substrate in the absence of the arsenic vapor in the growth chamber.

After the background pressure was reduced below $2 \cdot 10^{-7}$ Pa, 3 equivalent ML of gallium was deposited on the GaAs surface at a nominal growth rate of 0.25 ML/s. Then, the substrate temperature was decreased to a value $T_{\text{ULF}} = 300$ °C at which the exposure of droplets to the ultra-low arsenic flux was carried out. The flux values corresponded to increments ΔP of the pressure in the chamber which ranged from $3 \cdot 10^{-8}$ to $5 \cdot 10^{-7}$ Pa. An additional exposure to the flux



increment $\Delta P = 6 \cdot 10^{-8}$ Pa at $T_{ULF} = 400$ °C was carried out on one of the samples. In 5 minutes after closing the arsenic valve, each of samples was transferred out of the chamber and delivered to FEI Nova Nanolab scanning electron microscope (SEM) and NT-MDT NTEGRA atomic force microscope (AFM) for the nanostructure characterization.

Results and Discussion

It is well-known that Ga droplets formed on the Ga(Al)As(001) surface can be converted into GaAs dots [12] or transformed into GaAs rings and ring-hole complexes [13] when exposed to the arsenic flux. However, a very low arsenic flux which is traditionally used for droplet etching of the surface [14] can lead to a different phenomenon at a relatively low temperature, namely the diffusion decay of droplets [10, 11]. This phenomenon consists in the outflow of atoms from the droplet due to the metal concentration gradient between the droplet and the surface enriched in arsenic. If the rate of this event is higher than the rate of crystallization or etching, the droplet can reduce in volume before its arsenization while the surface density of droplets retains its initial value. As one can see in Fig. 1 and 2, an increase in the arsenic pressure increment ΔP from $3 \cdot 10^{-8}$ to $5 \cdot 10^{-7}$ Pa leads to a decrease in the average diameter of droplets obtained after deposition of 3 ML of gallium on GaAs surface from 71 nm to 56 nm.

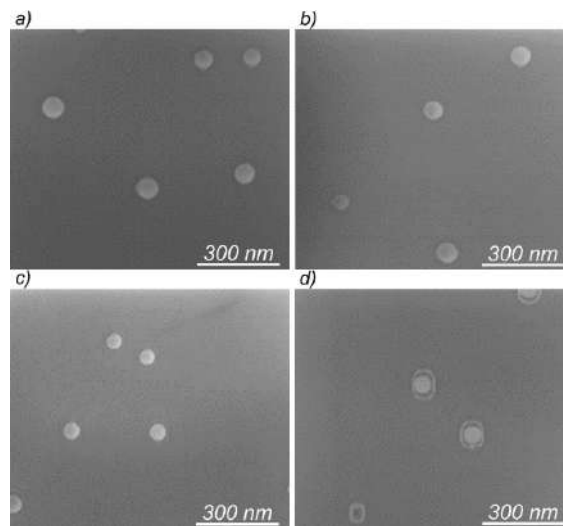


Fig. 1. SEM images of nanostructures obtained after deposition of 3 ML of gallium on the GaAs surface and subsequent exposure to the low arsenic flux at $T_{ULF} = 300$ °C: $\Delta P = 3 \cdot 10^{-8}$ Pa (a), $\Delta P = 6 \cdot 10^{-8}$ Pa (b), $\Delta P = 5 \cdot 10^{-7}$ Pa (c), $\Delta P = 1 \cdot 10^{-6}$ Pa (d)

A further increase in the pressure increment ΔP to $1 \cdot 10^{-6}$ leads to a larger change in the droplet diameter as a percentage of the original droplet diameter (26% for the sample with $\Delta P = 1 \cdot 10^{-6}$ and 24% for the sample with $\Delta P = 5 \cdot 10^{-7}$), determined by the droplet boundaries or the diameter of the crystallized ring retained around the droplet. Although the change in the droplet size is not very significant, it can be increased by various techniques including the alterations of exposure time and flux values, substrate temperature during the exposure, multistage exposure with interruptions etc. The surface density of droplets in a range of the pressure increments from $3 \cdot 10^{-8}$ to $1 \cdot 10^{-6}$ Pa is around $4.5 \cdot 10^8$ cm⁻².

It is also worth noting that the average diameter of droplets obtained after deposition of 3 ML of gallium and exposed to the ultra-low arsenic flux $\Delta P = 6 \cdot 10^{-8}$ Pa at $T_{ULF} = 300$ °C have a trimodal distribution (Fig. 3, a, c) with one peak corresponding to large droplets and two small peaks related to smaller droplets appearing on the surface due to the secondary nucleation [10]. The peak positions representing the average diameter of droplets of each group are at 37, 49 and 69 nm (Fig. 3, c).

The exposure of droplets to the arsenic flux at a higher temperature of 400 °C leads to the complete decay of smaller droplets with their transformation into rings and holes whereas larger droplets retain on the surface (Fig. 3, b). The peak position of large droplets shifts from 69 to 64 nm (Fig. 3, d), which indicates a decrease of the droplet size as a result of the arsenic exposure.

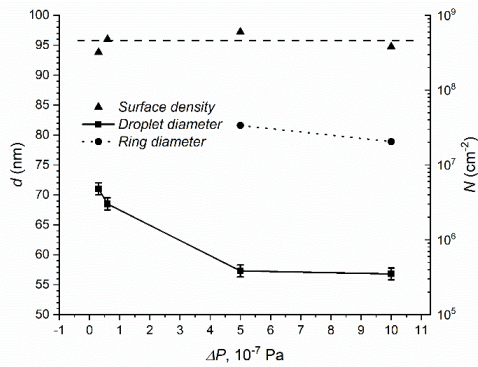


Fig. 2. Arsenic pressure dependences of the average diameter of nanostructures obtained after deposition of 3 ML of gallium on the GaAs surface at $T = 500\text{ }^{\circ}\text{C}$ and subsequent exposure to the low arsenic flux at $T_{ULF} = 300\text{ }^{\circ}\text{C}$

Droplets of smaller sizes transform into nanorings with a peak position of their diameter at 50 nm.

Within some of the rings, small holes with an average diameter of 14 nm are also observed (Fig. 3, *b, d*). Holes are formed on the surface because of the droplet etching which is a typical process occurred at relatively high temperatures and low arsenic fluxes [15]. However, large droplets reduce in volume without the ring and hole formation which indicates that droplets with near-critical sizes are more influenced by the arsenic flux. This phenomenon can be used to decrease the surface density of nanostructures after initial formation of high-density droplet arrays.

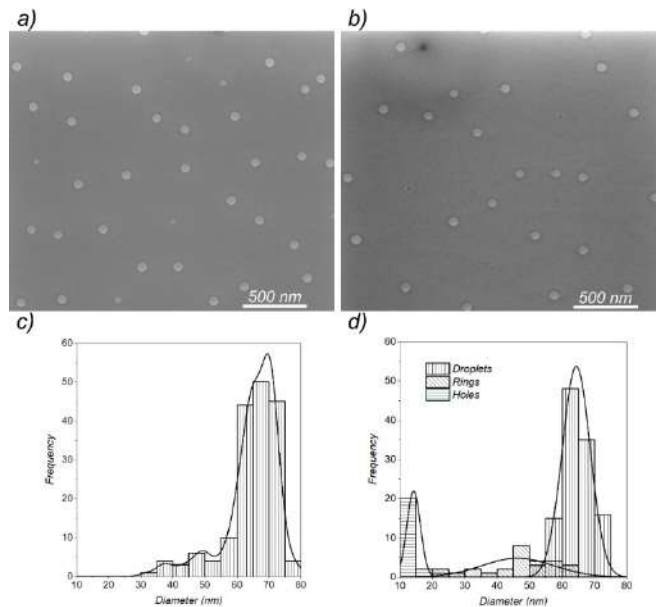


Fig. 3. SEM images (*a, b*) and histograms of size distributions (*c, d*) of nanostructures obtained after deposition of 3 ML of gallium and subsequent exposure to the ultra-low arsenic flux $\Delta P = 6 \cdot 10^{-8}\text{ Pa}$ at: (*a, c*) $T_{ULF} = 300\text{ }^{\circ}\text{C}$; (*b, d*) $T_{ULF} = 400\text{ }^{\circ}\text{C}$

Conclusion

We reported, for the first time, the possibility of reducing the gallium droplet size using the ultra-low arsenic flux to obtain low-density arrays of small-sized nanostructures. The droplet diameter decreases with increasing arsenic flux whereas the surface density remains approximately at the same value. Droplet arrays obtained after deposition of 3 ML of gallium at $T = 500\text{ }^{\circ}\text{C}$ with subsequent exposure to the arsenic flux are shown to have a trimodal size distribution. We revealed that gallium droplets of a large size exposed to the arsenic flux at $T_{ULF} = 400\text{ }^{\circ}\text{C}$ reduce in volume or transform into dot-and-ring complexes while droplets with smaller sizes decay completely leaving behind nanorings or nanoholes formed because of the droplet etching.

REFERENCES

1. Lu C.-Y., Pan J.-W., Quantum-dot single-photon sources for the quantum internet, Nat. Nanotechnol. 16 (2021) 2019–2021.



2. Silva da S. F. C., Undeutsch G., Lehner B., Manna S., Krieger T. M., Reindl M., Schimpf C., Trotta R., Rastelli A., GaAs quantum dots grown by droplet etching epitaxy as quantum light sources, *Appl. Phys. Lett.* 119 (2021) 120502.
3. Joyce B. A., Vvedensky D. D., Self-organized growth on GaAs surfaces, *Mater. Sci. Eng. R Reports.* 46 (2004) 127–176.
4. Sanguinetti S., Watanabe K., Tateno T., Gurioli M., Werner P., Wakaki M., Koguchi N., Modified droplet epitaxy GaAs/AlGaAs quantum dots grown on a variable thickness wetting layer, *J. Cryst. Growth.* 253 (2003) 71–76.
5. Ahn D. H., Jang Y. D., Baek J. S., Schneider C., Höfling S., Lee D., A broad-band planar-microcavity quantum-dot single-photon source with a solid immersion lens, *Appl. Phys. Lett.* 118 (2021).
6. Huang X., Su R., Yang J., Rao M., Liu J., Yu Y., Yu S., Wafer-scale epitaxial low density inas/gaas quantum dot for single photon emitter in three-inch substrate, *Nanomaterials.* 11 (2021).
7. Heyn C., Feddersen S., Modeling of al and ga droplet nucleation during droplet epitaxy or droplet etching, *Nanomaterials.* 11 (2021) 1–13.
8. Lee J. H., Wang Z. M., Salamo G. J., Observation of change in critical thickness of in droplet formation on GaAs(100), *J. Phys. Condens. Matter.* 19 (2007).
9. Balakirev S. V, Solodovnik M. S., Eremenko M. M., Konoplev B. G., Ageev O. A., Mechanism of nucleation and critical layer formation during In/GaAs droplet epitaxy, *Nanotechnology.* 30 (2019) 505601.
10. Balakirev S. V., Chernenko N. E., Eremenko M. M., Ageev O. A., Solodovnik M. S., Independent Control Over Size and Surface Density of Droplet Epitaxial Nanostructures Using Ultra-Low Arsenic Fluxes, *Nanomaterials.* 11 (2021) 1184.
11. Balakirev S. V., Kirichenko D. V., Chernenko N. E., Shandyba N. A., Eremenko M. M., Ageev O. A., Solodovnik M. S., Low-density arrays of ultra-small InAs nanostructures obtained by two-stage arsenic exposure during droplet epitaxy, *Appl. Surf. Sci.* 578 (2022) 152023.
12. Mano T., Abbarchi M., Kuroda T., Mastrandrea C. A., Vinattieri A., Sanguinetti S., Sakoda K., Gurioli M., Ultra-narrow emission from single GaAs self-assembled quantum dots grown by droplet epitaxy, *Nanotechnology.* 20 (2009).
13. Heyn C., Stemmann A., Klingbeil M., Strelow C., Köppen T., Mendach S., Hansen W., Mechanism and applications of local droplet etching, *J. Cryst. Growth.* 323 (2011) 263–266.
14. Heyn C., Stemmann A., Eiselt R., Hansen W., Influence of Ga coverage and As pressure on local droplet etching of nanoholes and quantum rings, *J. Appl. Phys.* 105 (2009) 054316.
15. Fuster D., González Y., González L., Fundamental role of arsenic flux in nanohole formation by Ga droplet etching on GaAs(001), *Nanoscale Res. Lett.* 9 (2014) 1–6.

THE AUTHORS

BALAKIREV Sergey V.
sbalakirev@sfedu.ru
ORCID: 0000-0003-2566-7840

SHANDYBA Nikita A.
shandyba@sfedu.ru
ORCID: 0000-0001-8488-9932

LAKHINA Ekaterina A.
lakhina@sfedu.ru
ORCID: 0000-0002-9326-2418

EREMENKO Mikhail M.
eryomenko@sfedu.ru
ORCID: 0000-0002-7987-0695

KIRICHENKO Danil V.
dankir@sfedu.ru
ORCID: 0000-0001-7476-2778

SOLODOVNIK Maxim S.
solodovnikms@sfedu.ru
ORCID: 0000-0002-0557-5909

CHERNENKO Natalia E.
nchernenko@sfedu.ru
ORCID: 0000-0001-8468-7425

Received 19.07.2022. Approved after reviewing 27.07.2022. Accepted 31.07.2022.

Conference materials

UDC 541.1

DOI: <https://doi.org/10.18721/JPM.153.363>

Low-adhesive silicone rubbers for flexible light-emitting devices

A. S. Miroshnichenko ^{1, 2, 3✉}, K. V. Deriabin ¹, I. S. Mukhin ^{2, 3, 4}, R.M. Islamova ¹

¹ St. Petersburg State University, St. Petersburg, Russia;

² ITMO University, St. Petersburg, Russia;

³ Alferov University, St. Petersburg, Russia;

⁴ Peter the Great St. Petersburg Polytechnic University, St. Petersburg, Russia

✉ anna.miroshnichenko.sergeevna@gmail.com

Abstract. In this work, 2-phenylethyl-functionalized (SSR) and 2-methyl-3-methoxy-3-oxopropyl-functionalized silicone rubbers (MSR) were obtained via the platinum(0)-catalyzed hydrosilylation reaction between styrene/methyl methacrylate and polymethylhydrosiloxane. SSR exhibits both sufficient elongation at break ($\epsilon = 45 \pm 5\%$), tensile strength ($\sigma = 1.5 \pm 0.4$ MPa) and Young's modulus, ($E = 3.4 \pm 0.7$ MPa), which is higher than for Sylgard 184 ($E = 1.1 \pm 0.3$ MPa). SSR and MSR are optically transparent and exhibit a low adhesion to a Si substrate. However, MSR possesses lower tensile strength ($\sigma = 0.6 \pm 0.1$ MPa, $E = 0.6 \pm 0.1$ MPa) comparing to SSR. Thus, SSR was applied as a supporting polymer matrix for encapsulation of inorganic NWs arrays for flexible optoelectronics.

Keywords: catalytic hydrosilylation, polysiloxanes, nanowires, light-emitting diodes

Funding: this study was supported by the Russian Science Foundation (grant No. 20-19-00256). The NW samples were grown under the support of the Ministry of Science and Higher Education of the Russian Federation (state task No. 0791-2020-0005).

Citation: Miroshnichenko A. S., Deriabin K. V., Mukhin I. S., Islamova R. M., Low-adhesive silicone rubbers for flexible light-emitting devices. St. Petersburg State Polytechnical University Journal. Physics and Mathematics, 15 (3.3) (2022) 320–325. DOI: <https://doi.org/10.18721/JPM.153.363>

This is an open access article under the CC BY-NC 4.0 license (<https://creativecommons.org/licenses/by-nc/4.0/>)

Материалы конференции

УДК 541.1

DOI: <https://doi.org/10.18721/JPM.153.363>

Низко-адгезионные силиконовые резины для гибких светоизлучающих устройств

А. С. Мирошниченко ^{1, 2, 3✉}, К. В. Дерябин ¹, И. С. Мухин ^{2, 3, 4}, Р. М. Исламова ¹

¹ Санкт-Петербургский государственный университет, Санкт-Петербург, Россия;

² Университет ИТМО, Санкт-Петербург, Россия;

³ Академический университет им. Ж. И. Алфёрова, Санкт-Петербург, Россия;

⁴ Санкт-Петербургский политехнический университет Петра Великого, Санкт-Петербург, Россия

✉ anna.miroshnichenko.sergeevna@gmail.com

Аннотация. В работе представлены 2-фенилэтил- (SSR) и 2-метил-3-метокси-3-оксопропил-функционализованные силиконовые резины (MSR). SSR и MSR были получены с помощью реакции каталитического гидросилилирования между стиролом или метилметакрилатом и полиметилгидросилоксаном в присутствии комплекса платины(0). SSR демонстрирует требуемые относительное удлинение при разрыве ($\epsilon = 45 \pm 5\%$), предел прочности при растяжении ($\sigma = 1.5 \pm 0.4$ МПа) и модуль Юнга ($E = 3.4 \pm 0.7$ МПа), значения которого превышают значения для Syl-



gard 184 ($E = 1.1 \pm 0.3$ МПа). SSR и MSR являются оптически прозрачными в видимой спектральной области, а также обладают уменьшенной адгезией к ростовой кремниевой подложке. Однако MSR имеет более низкую механическую прочность ($\sigma = 0.6 \pm 0.1$ МПа, $E = 0.6 \pm 0.1$ МПа) по сравнению с SSR. Таким образом, SSR был использован в качестве поддерживающей полимерной матрицы для гибких светоизлучающих устройств на основе полупроводниковых нитевидных нанокристаллов.

Ключевые слова: каталитическое гидросилилирование, полисилоксаны, светодиоды

Финансирование: Работа выполнена в рамках гранта РФФИ № 20-19-00256. Образцы нитевидных нанокристаллов были выращены при финансовой поддержке в рамках государственного задания (№ 0791-2020-0005) Министерства науки и высшего образования РФ.

Ссылка при цитировании: Мирошниченко А. С., Дерябин К. В., Мухин И. С., Исламова Р. М. Низко-адгезионные силиконовые резины для гибких светоизлучающих устройств // Научно-технические ведомости СПбГПУ. Физико-математические науки. 2022. Т. 15. № 3.3. С. 320–325. DOI: <https://doi.org/10.18721/JPM.153.363>

Статья открытого доступа, распространяемая по лицензии CC BY-NC 4.0 (<https://creativecommons.org/licenses/by-nc/4.0/>)

Introduction

Commercial silicone rubbers on the base of polydimethylsiloxanes (PDMSs) such as Dow Corning Sylgard 184 usually are employed as supporting flexible transparent membrane for flexible nanowires (NWs)-based light-emitting devices [1–3] due to the transparency and relatively good elastic properties [4]. However, the commercial PDMS product Sylgard 184 demonstrates a high adhesion to a silicon substrate hampering the membrane release. These factors determine the high demand for development of new durable transparent polymer materials for manufacturing technology of thin membrane/NWs-based devices.

Modification of polysiloxanes by their reaction with various vinyl monomers leads to the increased mechanical strength and reduced adhesion to Si [5].

Materials and Methods

Materials: polymethylhydrosiloxane (PMHS) (number average molecular weight $M_n = 1700–3200$ g·mol⁻¹, viscosity 12–45 cSt, Sigma-Aldrich, St. Louis, USA), α,ω -di(dimethylvinylsiloxy)polydimethylsiloxane (ν -PDMS) (weight-average molecular weight $M_w = 25000$ g·mol⁻¹, viscosity 850–1150 cSt at 25 °C, Sigma Aldrich, St. Louis, USA), Karstedt's catalyst (platinum(0)-1,3-divinyl-1,1,3,3-tetramethyldisiloxane complex) solution 0.1 M in xylene (ABC R GmbH, Karlsruhe, Germany), styrene and methyl methacrylate (ReagentPlus®, contains 4-tert-butylcatechol as stabilizer, $\geq 99\%$), SYLGARD™ 184 Silicone Elastomer Kit (Dow Corning, Midland, Michigan, USA), and dimethyl sulfoxide (DMSO, $\geq 99\%$, Vekton, Saint Petersburg, Russia) were purchased from commercial suppliers and their purity was checked by ¹H and ¹³C NMR spectroscopy before usage. Anhydrous toluene (Vekton, Saint Petersburg, Russia) was distilled over sodium-benzophenone ketyl prior to use.

Methods:

Details about molecular beam epitaxy (MBE) of GaP NWs, CsPbBr₃ perovskite layer fabrication and SWCNT film synthesis are precisely described in the following reference [6].

Spectroscopy equipment and studies

The NMR spectra were recorded on Bruker AVANCE III 400 spectrometers in CDCl₃ at 25 °C at 400 MHz for ¹H, 100 MHz for ¹³C, 80 MHz for ²⁹Si NMR spectra, respectively.

Swelling measurements

The empty pycnometer was preliminarily rinsed with distilled water, dried, and its weight was measured. The pycnometer was filled up to the mark with distilled water and its mass with water was determined. The mass of silicone rubber (m) was estimated as follows: pieces of silicone rubber were placed in a pycnometer with water, and excess water was removed using filter paper, and the mass of the pycnometer was determined together with water and a sample. The density

of polymer sample (ρ) was determined by the following equation:

$$\rho = \frac{m}{m_1 + m - m_3} \cdot \rho_0, \quad (1)$$

where $\rho_0 = 0.997 \text{ g}\cdot\text{cm}^{-3}$ is density of distilled water at room temperature (20, RT).

Samples (rectangles 10 mm long and 3 mm width) were weighed to estimate the initial dry weight (m_{unex}). Toluene (approximately 270 mL) was added to a round bottom flask that was attached to a Soxhlet extractor and reflux condenser. The sample was loaded into a Soxhlet extractor. The solvent was boiled under reflux in a heating mantle for 2 h. After stopping boiling, the sample was removed and immediately weighed (m_s). Sample swelling percentage was calculated using the following equation:

$$s(\%) = \frac{m_s}{m_{unex}} \cdot 100, \quad (2)$$

Then the sample was dried overnight at RT, then dried for 12 h at 120 °C and reweighed (m_{ex}). Soluble fraction (w_{sol}) and polymer fraction (v) in the swollen sample were calculated as follows:

$$w_{sol}(\%) = \frac{m_{unex} - m_{ex}}{m_{unex}} \cdot 100, \quad (3)$$

$$v = \left[1 + \frac{m_s - m_{ex}}{m_{ex}} \cdot \frac{\rho_p}{\rho_s} \right]^{-1}, \quad (4)$$

where ρ_s and ρ_p – densities of the solvent (toluene, $0.87 \text{ g}\cdot\text{cm}^{-3}$) and polymers, respectively.

Tensile properties studies and instruments

Tension tests were conducted on a Shimadzu EZ-L-5kN universal testing machine at a constant cross-head speed of 40 mm/min. At least five measurements were made on each polymer sample according to the ISO 37 type 3 standard.

Thin film processing

Thin membranes of SSR25/GaP NWs and MSR25/GaP NWs were obtained with G-coating.

Adhesion study

Adhesion properties were studied with atomic force microscopy (AFM) approach/retract curves analysis. AFM approach/retraction curves were measured and analyzed on Bruker AFM with standard Si cantilevers (TipsNano HA_CNC B, Cantilever length $184 \pm 2 \mu\text{m}$, Cantilever width $34 \pm 3 \mu\text{m}$).

Results and Discussion

The transparent SSR were obtained by a two-step procedure of the platinum(0)-catalyzed hydrosilylation reaction between styrene and polymethylhydrosiloxane giving poly(methylhydrosiloxane-*co*-methyl(2-phenylethyl)siloxane) (S-PMHS). The molar ratios of Si-H (PMHS) and styrene vinyl groups (1:1) were selected to achieve the content of phenylethyl substituents 50%. In order to obtain transparent phenylethyl-functionalized silicone rubber (SSR) S-PMHS was cross-linked with ν -PDMS. The content of phenylethyl groups in the formed SSR is 25 mol.% (SSR25). Synthesis procedure along with structure and cross-links determination are presented in [6].

The transparent functionalized silicone rubber with the content of 2-methyl-3-methoxy-3-oxopropyl groups equal 25 mol.% (MSR25) was obtained analogously via described above method. The swelling data indicates a correlation between values of a swelling percentage (s), a soluble fraction content (w_{sol}), and a fraction of the polymer in the swollen sample (v) (Table 1). SSR25 exhibits a lower s and w_{sol} , but higher v in comparison with MSR25. Therefore, SSR25 is characterized by a larger amount of the cross-links (because of higher content of the starting Si-H groups in S-PMHS in the polymer network). Sylgard 184 and SSR25 demonstrated comparable swelling values.

The tensile properties of the studied rubbers are shown in Table 1. SSR25 exhibits a lower elongation at break (ϵ), but higher tensile strength (σ) in comparison with MSR25, which is in good agreement with the swelling data for the samples. SSR25 has comparable to Sylgard 184



Table 1

Swelling and tensile properties of silicone rubbers

Silicone rubber	Swelling properties				Tensile properties		
	ρ , g·cm ⁻³	s , %	w_{sol} , %	ν	ϵ , %	σ , MPa	E , MPa
SSR25	1.21 ±0.32	166 ±2	3.0 ±0.7	0.50 ±0.01	45 ±5	1.5 ±0.4	3.4 ±0.7
MSR25	1.05 ±0.01	281 ±13	10 ±0.6	0.30 ±0.01	90 ±19	0.6 ±0.1	0.6 ±0.1
Sylgard 184	1.00 ±0.01	190 ±21	4.1 ±0.4	0.48 ±0.01	92 ±8	2.4 ±0.6	1.1 ±0.3

tensile strength σ and higher Young's modulus (E). Thus, SSR25 can be more preferable as polymer matrix material than MSR25.

The adhesion to the silicon substrate was determined by analyzing the AFM approach/retraction curves. The adhesion force of cantilever to polymer layers can be estimated as the product of the distance between A and B points on corresponding retract curves and the constant spring value of the used AFM tip (Fig. 1). SSR25 exhibits the lowest adhesion among the studied silicone rubbers with corresponding value of 0.55 of Sylgard 184 adhesion value. MSR25 possesses a slightly higher adhesion (0.66 of Sylgard 184 adhesion value), but still more advantageous than commercial Sylgard 184.

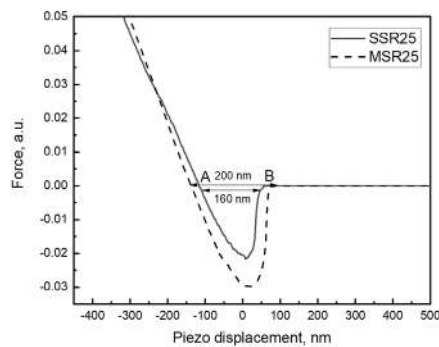


Fig. 1. AFM approach/retract curves of SSR25 and MSR25

UV-Vis spectra of functionalized silicone rubbers indicate no absorption in visible spectral range (see inserts in Fig. 2). According to scanning electron microscopy (SEM) study MSR25 and SSR25 have uniform morphology (Fig. 2) and no spherical structure formation.

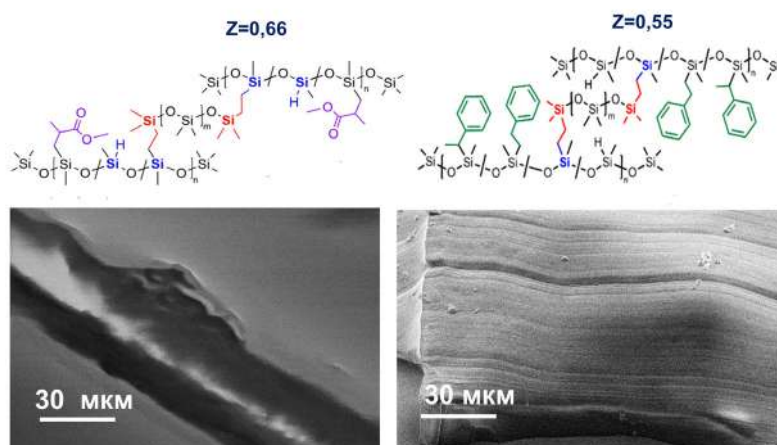


Fig. 2. SEM image of MSR25(left) and SSR25(right) films and their UV-Vis spectra

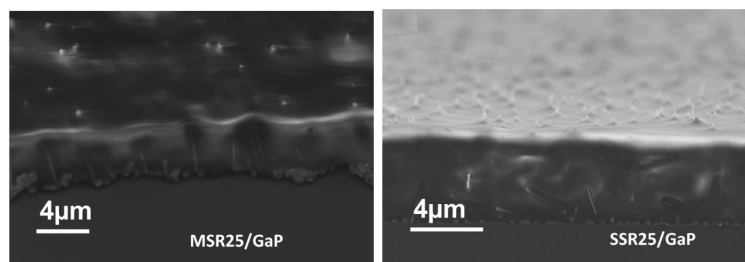


Fig. 3. SEM image of MSR25 and SSR25 films with encapsulated NWs array SSR25 has advantages in tensile properties and was chosen as supporting polymer matrix for GaP/CsPbBr₃ based flexible green LED

Thus, transparency and film uniformity along with the reduced adhesion allows to use these polymers for NWs encapsulation. MSR25 and SSR25 both display sufficient encapsulation properties of NWs array (Fig. 3). GaP NWs arrays were encapsulated into MSR25 and SSR25 with G-coating method [5].

Due to the advantages in tensile properties, SSR25/GaP was chosen over MSR25/GaP and employed as flexible transparent contacts for green air-stable perovskite-based LED [6].

Conclusion

Transparent functionalized silicone rubbers SSR25 and MSR25 were obtained via the platinum(0)-catalyzed hydrosilylation reaction between styrene/methyl methacrylate and polymethylhydrosiloxane and cross-linked with ν -PDMS. SSR25 and MSR25 show lower adhesion to Si substrate in comparison with Sylgard 184 value ($Z = 1$) – 0.55 and 0.66, respectively. SSR25 exhibits both sufficient elongation at break ($\epsilon = 45 \pm 5\%$) and tensile strength ($\sigma = 1.5 \pm 0.4$ MPa, $E = 3.4 \pm 0.7$ MPa), which is the main advantage over MSR25. The combination of these useful properties determines the applicability of SSR25 as a supporting polymer matrix for encapsulation arrays of inorganic NWs for flexible optoelectronics.

Acknowledgments

Physicochemical measurements were performed at the Center for Magnetic Resonance, Center for Chemical Analysis and Materials Research, and Thermogravimetric and Calorimetric Research Center (all belonging to Saint Petersburg State University).

REFERENCES

1. Kochetkov F. M., Neplokh V., Mastaliev V. A., Mukhangali S., Vorob'ev A. A., Uvarov A. V., Komissarenko F. E., Mitin D. M., Kapoor A., Eymery J., Amador-Mendez N., Durand C., Krasnikov D., Nasibulin A. G., Tchernycheva M., Mukhin I. S., Stretchable Transparent Light-Emitting Diodes Based on InGaN/GaN Quantum Well Microwires and Carbon Nanotube Films, *Nanomaterials*. 11 (2021) 1503.
2. Neplokh V., Fedorov V., Mozharov A., Kochetkov F., Shugurov K., Moiseev E., Amador-Mendez N., Statsenko T., Morozova S., Krasnikov D., Nasibulin A. G., Islamova R., Cirlin G., Tchernycheva M., Mukhin I., Red GaPAs/GaP Nanowire-Based Flexible Light-Emitting Diodes, *Nanomaterials*. 11 (2021) 2549.
3. Dai X., Messanvi A., Zhang H., Durand C., Eymery J., Bougerol C., Julien F. H., Tchernycheva M., Flexible Light-Emitting Diodes Based on Vertical Nitride Nanowires, *Nano Lett.* 15 (2015) 6958–6964.
4. Ren Z., Yan S., Polysiloxanes for optoelectronic applications, *Progress in Materials Science*. 83 (2016) 383–416.
5. Neplokh V., Kochetkov F. M., Deriabin K. V., Fedorov V. V., Bolshakov A. D., Eliseev I. E., Mikhailovskii V. Y., Ilatovskii D. A., Krasnikov D. V., Tchernycheva M., Cirlin G. E., Nasibulin A. G., Mukhin I. S., Islamova R. M., Modified silicone rubber for fabrication and contacting of flexible suspended membranes of n-/p-GaP nanowires with a single-walled carbon nanotube transparent contact, *J. Mater. Chem. C*. 8 (2020) 3764–3772.



6. Miroshnichenko A. S., Deriabin K. V., Baeva M., Kochetkov F. M., Neplokh V., Fedorov V. V., Mozharov A. M., Koval O. Yu., Krasnikov D. V., Sharov V. A., Filatov N. A., Gets D. S., Nasibulin A. G., Makarov S. V., Mukhin I. S., Kukushkin V. Yu., Islamova R. M., Flexible Perovskite CsPbBr₃ Light Emitting Devices Integrated with GaP Nanowire Arrays in Highly Transparent and Durable Functionalized Silicones, J. Phys. Chem. Lett. (2021) 9672–9676.

THE AUTHORS

MIROSHNICHENKO Anna S.
pll1921@mail.ru
ORCID: 0000-0002-3125-8317

MUKHIN Ivan S.
imukhin@yandex.ru
ORCID: 0 0000-0001-9792-045X

DERIABIN Konstantin V.
deriabin.k@yahoo.com
ORCID: 0000-0002-3055-6865

ISLAMOVA Regina M.
r.islamova@spbu.ru
ORCID: 0000-0003-1180-6539

Received 15.08.2022. Approved after reviewing 15.08.2022. Accepted 15.08.2022.

PHYSICS OF MOLECULES

Conference materials

UDC 535.37

DOI: <https://doi.org/10.18721/JPM.153.364>

Photoluminescence from lead halide perovskite superlattices

P. A. Tonkaev ¹✉, E. V. Grechaninova ¹, A. P. Pushkarev ¹, S. V. Makarov ¹

¹ ITMO University, St. Petersburg, Russia

✉ pavel.tonkaev@metalab.ifmo.ru

Abstract. Lead halide perovskites are a new class of materials with promising optoelectronic properties. Bulk halide perovskites have been applied as solar cells, light-emitting diodes, photodetectors, and nanolasers. Colloidal lead halide perovskite nanocrystals have shown high quantum efficiency of photoluminescence. Moreover, perovskite nanocrystals can be assembled in an ordered 3D array or superlattice to demonstrate superfluorescence emission. In this work, we synthesized CsPbBr₃ superlattices with the linear size of several micrometers and studied their photoluminescence properties at room temperature and 6 K. We demonstrated that the photoluminescence spectra of perovskite nanocrystals are preserved in superlattices at both temperatures. We also found a small spectral shift, which we attribute to a more uniform size distribution of nanocrystals in the superlattice.

Keywords: halide perovskites, nanocrystals, superlattice, photoluminescence, Mie resonance, Purcell effect

Funding: This work was performed with financial support of the Russian Science Foundation (project No. 22-22-20077).

Citation: Tonkaev P. A., Grechaninova E. V., Pushkarev A. P., Makarov S. V., Photoluminescence from lead halide perovskite superlattices. St. Petersburg State Polytechnical University Journal. Physics and Mathematics, 15 (3.3) (2022) 326–329. DOI: <https://doi.org/10.18721/JPM.153.364>

This is an open access article under the CC BY-NC 4.0 license (<https://creativecommons.org/licenses/by-nc/4.0/>)

Материалы конференции

УДК 535.37

DOI: <https://doi.org/10.18721/JPM.153.364>

Фотолюминесценция сверхрешеток свинцово-галогенидного перовскита

П. А. Тонкаев ¹✉, Е. В. Гречанинова ¹, А. П. Пушкарёв ¹, С. В. Макаров ¹

¹ Университет ИТМО, Санкт-Петербург, Россия

✉ pavel.tonkaev@metalab.ifmo.ru

Аннотация. В работе были синтезированы сверхрешетки CsPbBr₃ с линейным размером в несколько микрометров, их фотолюминесцентные свойства были исследованы при комнатной температуре и 6 К. Было показано, что спектры фотолюминесценции нанокристаллов перовскита сохраняются в сверхрешетках при обеих температурах.

Ключевые слова: галогенидные перовскиты, нанокристаллы, сверхрешетки, фотолюминесценция, резонансы Ми, эффект Парселла

Финансирование: Исследование выполнено за счет гранта Российского научного фонда № 22-22-20077.

Ссылка при цитировании: Тонкаев П. А., Гречанинова Е. В., Пушкарёв А. П., Макаров С. В. Фотолюминесценция сверхрешеток свинцово-галогенидного перовскита // Научно-технические ведомости СПбГПУ. Физико-математические науки. 2022. Т. 15. № 3.3. С. 326–329. DOI: <https://doi.org/10.18721/JPM.153.364>



Статья открытого доступа, распространяемая по лицензии CC BY-NC 4.0 (<https://creativecommons.org/licenses/by-nc/4.0/>)

Introduction

Lead halide perovskites are a class of new materials with outstanding properties and low-cost fabrication methods that have been applied in the field of photovoltaics [1], light-emitting diodes [2], and photodetectors [3]. Moreover, due to relatively high refractive index, perovskite nanostructures support Mie resonances in the optical and near-infrared ranges which enhance photoluminescence [4], increase nonlinear absorption [5], and lower the lasing threshold [6]. Meanwhile, lead halide perovskite nanocrystals with quantum confinement have high photoluminescence quantum yield [7]. Furthermore, perovskite nanocrystals can assemble in the ordered 3D arrays or superlattices. These structures allow additional control of emission properties and provide the opportunity to develop new effective optical nanosources. Herein, we aim to study the photoluminescence of unordered perovskite nanocrystals and single CsPbBr₃ superlattices with linear dimensions of several micrometers at room temperature and 6 K.

Materials and Methods

The CsPbBr₃ perovskite nanocrystals were obtained by the hot injection method. The resulting nanocrystals were separated by centrifugation and dispersed in toluene to obtain a colloidal solution. Superlattices were formed from these colloidal nanocrystals. The CsPbBr₃ superlattices were fabricated on a silicon substrate. The transverse dimensions of individual superlattices ranged from 1 μm to 10 μm, while some of them agglomerated to form clusters of superlattices, and some remained spatially isolated, which made it possible to measure photoluminescence for individual objects.

The photoluminescence spectra of the samples were measured using a pump provided by a femtosecond laser with the wavelength of 400 nm for the temperature of 6 K and 350 nm for room temperature. The 150 fs pulses with a repetition rate of 100 kHz were focused onto the sample surface at normal incidence by a 50x microscope objective. The emission was collected in transmission for room temperature and in reflection for the cryogenic one.

Results and Discussion

The normalized photoluminescence spectra measured at room temperature are shown on the Fig. 1, *a*. The emission spectrum of unordered perovskite nanocrystals (dash-dotted curve) has a maximum at wavelength of 518 nm, whereas the superlattice assembled from these nanocrystals (a curve with circles) demonstrates a maximum at 517 nm. We attribute this slight difference to the smaller size distribution of perovskite nanocrystals. Meanwhile, the spectral shift between the bulk perovskite film and nanocrystal structures is significant due to quantum confinement. At room temperature, the photoluminescence maximum of the bulk perovskite thin film is approximately at 525 nm (curve with squares). All three spectra have comparable widths at half-height, which are 19.4 nm for the bulk film, 17.6 nm for unordered nanocrystals, and 20 nm for the superlattice. These results demonstrate that superlattices assembled from perovskite nanocrystals preserve quantum confinement and do not transit into the bulk material state.

The photoluminescence spectra obtained from perovskite structures at cryogenic temperature are illustrated in the Fig. 1, *b*. All three structures demonstrate redshift with the decrease of temperature to 6K. Thus, the perovskite superlattice has a photoluminescence maximum at a wavelength of 530 nm, whereas unordered nanocrystals and the bulk perovskite film have their maxima at 532 nm and 538 nm, respectively. All three emission spectra become narrower than they were at room temperature due to reduction of non-radiative losses. The photoluminescence spectra of the film and the superlattice still have comparable widths, which are 2.2 nm and 2.7 nm, respectively. However, for unordered perovskite nanocrystals this value is several times larger and equals to 6.7 nm. This difference between widths correlates with the previous assumption that unordered perovskite nanocrystals have wider size distribution than nanocrystals in the superlattice.

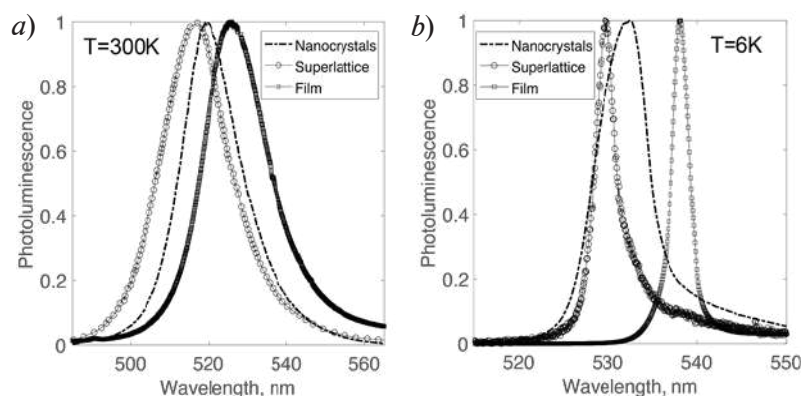


Fig. 1. Photoluminescence spectra from the thin perovskite film, not ordered nanocrystals and the superlattice at room temperature (a) and cryogenic temperature (b)

In addition, we conducted measurements of superlattice photoluminescence via pump power. The results are shown in Fig. 2. The lowest spectrum represents pump power of 4 μW . The next spectra correspond to the gradual increase of the power pump to 140 μW , whereas the top spectrum corresponds to the power of 9 μW returned back after high power. With the pump power increase, the second peak appears gradually at the wavelength of 532 nm. Consider that with switching back to low pump power the position of the second peak is preserved. Thus, the change that has taken place is irreversible. We assume that by laser-induced heating part of perovskite nanocrystals agglomerate to nanocrystals with bigger size and lower quantum confinement, which have longer emission wavelength.

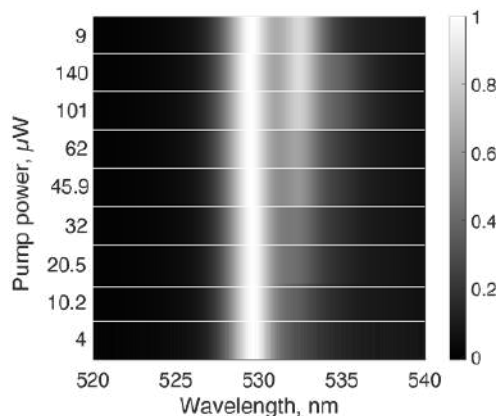


Fig. 2. Photoluminescence spectra from the superlattice at the temperature of 6K for different pump power, which starts from 4 μW , go to 140 μW , and back to 9 μW

Conclusion

The photoluminescence properties of superlattices assembled from CsPbBr_3 nanocrystals at room temperature and 6K were studied. It was demonstrated that photoluminescence spectra of perovskite superlattices are similar to emission spectra of initial colloidal nanocrystals, but have a slight blueshift which we attributed to uniform size distribution of nanocrystals. These structures allow modification of optoelectronic properties of perovskite nanocrystals at 3D level. In addition, perovskite superlattices are promising structures for micro- and nanolasers and photodetectors.

REFERENCES

1. **Snaith H. J.**, Present status and future prospects of perovskite photovoltaics, *Nature Materials*. 17 (5) (2018) 372–376.
2. **Lin K. et al.**, Perovskite light-emitting diodes with external quantum efficiency exceeding 20 per cent. *Nature*. 562 (7726) (2018) 245–248.



3. **Marunchenko A. A. et al.**, Single-Walled Carbon Nanotube Thin Film for Flexible and Highly Responsive Perovskite Photodetector, *Advanced Functional Materials*. 32 (12) (2022) 2109834.
4. **Tiguntseva E. Y., Zograf G. P., Komissarenko F. E., Zuev D. A., Zakhidov A. A., Makarov S. V., Kivshar Y. S.**, Light-emitting halide perovskite nanoantennas, *Nano Letters*. 18 (2) (2018) 1185–1190.
5. **Tiguntseva E. et al.**, Room-temperature lasing from Mie-resonant nonplasmonic nanoparticles, *ACS Nano*. 14 (7) (2020) 8149–8156.
6. **Fan Y. et al.**, Enhanced Multiphoton Processes in Perovskite Metasurfaces, *Nano Letters*. 21 (17) (2021) 7191–7197.
7. **Protesescu L. et al.**, Nanocrystals of cesium lead halide perovskites (CsPbX₃, X= Cl, Br, and I): novel optoelectronic materials showing bright emission with wide color gamut, *Nano Letters*. 15 (6) (2015) 3692–3696.

THE AUTHORS

TONKAEV Pavel A.

pavel.tonkaev@metalab.ifmo.ru
ORCID: 0000-0003-1849-0653

GRECHANINOVA Evgeniia V.

e.grechaninova@metalab.ifmo.ru
ORCID: 0000-0003-4087-8224

PUSHKAREV Anatoly P.

anatoly.pushkarev@metalab.ifmo.ru
ORCID: 0000-0002-1793-6812

MAKAROV Sergey V.

s.makarov@metalab.ifmo.ru
ORCID: 0000-0002-9257-6183

Received 11.07.2022. Approved after reviewing 14.07.2022. Accepted 15.07.2022.

Conference materials

UDC 538.97

DOI: <https://doi.org/10.18721/JPM.153.365>

Plasmonic structures for sensors

V. V. Zhurikhina ¹✉

¹ Peter the Great St. Petersburg Polytechnic University, St. Petersburg, Russia

✉ zhurikhina_vv@spbstu.ru

Abstract. The article provides a brief overview of the use of surface plasmon resonance in optical sensors of various types. Such sensors are widely used in healthcare, security, food safety and environmental monitoring. The physical basis and design of plasmon-enhanced sensors, such as colorimetric sensors, sensors based on plasmon-enhanced fluorescence, and surface-enhanced Raman sensors, are considered.

Keywords: plasmons, sensors, resonance, field enhancement, Raman scattering

Funding: The research is partially funded by the Ministry of Science and Higher Education of the Russian Federation as part of World-class Research Center program: Advanced Digital Technologies (contract No. 075-15-2022-311 dated 20.04.2022).

Citation: Zhurikhina V. V., Plasmonic structures for sensors. St. Petersburg State Polytechnical University Journal. Physics and Mathematics, 15 (3.3) (2022) 330–334. DOI: <https://doi.org/10.18721/JPM.153.365>

This is an open access article under the CC BY-NC 4.0 license (<https://creativecommons.org/licenses/by-nc/4.0/>)

Материалы конференции

УДК 538.97

DOI: <https://doi.org/10.18721/JPM.153.365>

Плазмонные структуры для сенсоров

В. В. Журихина ¹✉

¹ Санкт-Петербургский политехнический университет Петра Великого, Санкт-Петербург, Россия

✉ zhurikhina_vv@spbstu.ru

Аннотация. В статье представлен краткий обзор использования поверхностного плазмонного резонанса в оптических сенсорах различных типов. Такие сенсоры широко используются в здравоохранении, системах безопасности и мониторинге окружающей среды. Рассмотрены физические основы и конструкция сенсоров с плазмонным усилением, таких как колориметрические сенсоры, сенсоры на основе плазмонно усиленной флуоресценции и сенсоры на основе поверхностно усиленного комбинационного рассеяния.

Ключевые слова: плазмоны, сенсоры, резонанс, усиление поля, рамановское рассеяние

Финансирование: Работа выполнена при финансовой поддержке Минобрнауки России в рамках реализации программы Научного центра мирового уровня по направлению «Передовые цифровые технологии» СПбПУ (соглашение от 20.04.2022 № 075-15-2022-311).

Ссылка при цитировании: Журихина В. В. Плазмонные структуры для сенсоров // Научно-технические ведомости СПбГПУ. Физико-математические науки. 2022. Т. 15. № 3.3. С. 330–334. DOI: <https://doi.org/10.18721/JPM.153.365>

Статья открытого доступа, распространяемая по лицензии CC BY-NC 4.0 (<https://creativecommons.org/licenses/by-nc/4.0/>)



Introduction

Surface plasmon resonance (SPR) is a phenomenon caused by collective oscillations of conduction electrons in metallic nanostructures [1]. Both the intensity and position of the SPR are highly dependent on the size, shape, and composition of the nanostructures, as well as the dielectric properties of the environment [2–4]. The latter makes it possible to create optical sensors using plasmonic metal nanostructures.

There are two different forms of plasmon resonance: nanoparticle localized plasmon resonance (LSPR) and propagating surface plasmon polaritons (SPP) [5]. LSPR is observed if the dimensions of the metal nanostructure are smaller than the wavelength of the incident light. In this case, collective nonpropagating oscillations of surface electrons arise in a metallic nanostructure. The LSPR frequency ω_α along the α axis in an ellipsoidal nanoparticle is determined by the formula [6]

$$\omega_\alpha = \omega_p / \sqrt{1 + \varepsilon_{diel} (1/L_\alpha - 1)} \quad (1)$$

where ω_p is Drude plasma frequency, ε_{diel} is dielectric constant of surrounding media, L_α is geometrical factor for a given axis (for a sphere $L_\alpha = 1/3$). As can be seen from (1), the resonant frequency depends on the refractive index of the environment, which is the basis for plasmonic sensors. Also known is the phenomenon of high concentration of the incident electromagnetic (EM) field around the nanostructure due to LSPR. A local EM field influences optical processes such as nonlinear optical effects, fluorescence, and Raman scattering.

In contrast to LSPR, SPPs are propagating electron oscillations on a metal/dielectric surface, in particular, on the surface of thin metal films. The wave vector SPP can be written as [6]

$$k_{SPP} = \frac{\omega}{c} \sqrt{\frac{\varepsilon_{Me} \cdot \varepsilon_{diel}}{\varepsilon_{Me} + \varepsilon_{diel}}} \quad (2)$$

where ε_{Me} is dielectric function of metal. Due to the mismatch between the momentum of the incident light and the propagating plasmon-polariton, the SPP cannot be excited by radiation in free space. To excite the SPP, momentum matching is required, for example, due to attenuated total internal reflection or a periodic structure. As can be seen from (2), the propagation of SPP depends on the refractive index of the environment, which is used when creating sensors.

SPP Based Plasmonic Sensors

Surface propagating SPPs or mixed mode SPP/LSPR can be used to detect changes in the refractive index of the environment. Since an additional pulse must be provided to excite the SPP, prism or grating circuits are used. The classic setup for SPP excitation is the Kretschmann configuration [7]. In this configuration, a metal film deposited on the prism (usually a noble metal, most often gold) almost completely reflects the incident radiation, except at a certain angle when the SPP is excited, called the SPR angle. This angle depends on the refractive index of the environment, which makes it possible to detect changes with a high degree of accuracy. For example, if molecules (an analyte) in an aqueous solution bind to ligands immobilized on a plasmonic metal film, the SPP band is redshifted due to the higher refractive index of the molecules [8, 9]. In this way, the concentration of analyte molecules in solution can be detected.

LSPR Based Plasmonic Sensors

Noble metal nanoparticles such as Au, Ag and Cu exhibit LSPR in the optical range and are widely used to create plasmonic sensors [10]. According to (1), the position of the LSPR depends on the shape of the nanoparticle and the dielectric environment: the wavelength of the LSPR peak shifts when the analyte binds to the functionalized surface of the nanoparticle, changing the local refractive index. Colorimetric plasmonic sensors based on the shift of the LSPR peak in colloidal solutions with nanoparticles are a simple and convenient method for detecting analytes in solution, since this technique provides direct visualization of the analyte concentration. For example, functionalized gold nanoparticles have been used for the colorimetric detection of heavy metals, small biological molecules, and biomacromolecules [11–13].

Plasmon-Enhanced Fluorescence (PEF) Sensors

The enhancement of the EM field near the surface of nanoparticles due to LSPR can be used for plasmon-enhanced fluorescence spectroscopy. Enhancement of the fluorescence of sensors based on LSPR is possible due to the enhancement of excitation and/or emission [14]. In both cases, stronger local electromagnetic fields will lead to higher enhancement. According to (1), the enhancement of the EM field near a sharp tip will be higher due to the geometric factor (the effect of a needle or lightning rod); thus, nanorods and prolate ellipsoids will have an increased PEF effect compared to nanospheres. The plasmonic fluorescence enhancement factor is usually in the range of 10–100, but can be higher in optimized plasmonic nanostructures, reaching even 10^3 [15]. Xie et al utilized a Ag nano-triangle array to enhance the fluorescence of near-infrared (NIR) dyes [16]. They obtained that the fluorescence of a low quantum-yield (4%) NIR dye can be enhanced by two orders of magnitude using the Ag triangle array pattern.

Surface-Enhanced Raman Scattering Sensors

Surface enhanced Raman scattering (SERS) is one of the most powerful and promising analytical methods for bio- and chemical analysis due to a number of advantages: (1) high selectivity of the method due to the unique spectral characteristics of analytes, (2) high sensitivity up to the detection of single molecules, (3) ease of operation, (4) the possibility of detecting multicomponent compounds with a single excitation laser due to narrow spectral bands [17–20]. Raman scattering itself is ineffective due to the small scattering cross section ($10^{-28} \sim 10^{-30}$ cm²/molecule). However, amplification of the local EM field in plasmonic nanostructures gives Raman signal amplification from 10^4 to 10^8 [21]. Maximization of the plasmonic electromagnetic field is crucial for the development of a sensitive SERS probe, so much effort has been devoted to the development of SERS substrates [22–24].

In our experiments, we use both self-organizing silver nanoisland films on the glass surface and dendritic structures as SERS substrates [25–28]. The advantages of dendritic structures are the high amplification of the local field compared to nanospheres, as well as stability and resistance to external influences. In our work, we obtained an enhancement of the Raman signal up to 10^6 – 10^7 on the basis of silver dendritic structures [27]. The formation of nanoislands by out-diffusion technique in combination with glass polarization and etching can be carried out in microchannels in glass, which is very promising for microfluidics [29, 30].

Conclusion

Structures exhibiting plasmon resonances can be easily adapted to various sensory applications through the choice of material and structure. This provides flexibility for the development of plasmon-enhanced sensors and opens up great opportunities for the use of such devices. In the future, plasmonics will be developed to enhance the sensor signal and to develop new detection devices based on fluorescence and SERS. At the same time, the efficiency of plasmon-enhanced sensors directly depends on the design of plasmonic structures and the development of new methods for their fabrication.

REFERENCES

1. **Bohm D., Pines D.**, A Collective Description of Electron Interactions: III. Coulomb Interactions in a Degenerate Electron Gas, *Phys. Rev.* 92 (1953) 609–625.
2. **Albella P., Garcia-Cueto B., González F., Moreno F., Wu P. C., Kim T.-H., Brown A., Yang Y., Everitt H. O., Videen G.**, Shape Matters: Plasmonic Nanoparticle Shape Enhances Interaction with Dielectric Substrate, *Nano Lett.* 11 (2011) 3531–3537.
3. **Jain P. K., El-Sayed M. A.**, Surface Plasmon Resonance Sensitivity of Metal Nanostructures: Physical Basis and Universal Scaling in Metal Nanoshells, *J. Phys. Chem. C.* 111 (2007) 17451–17454.
4. **Scherbak S. A., Shustova O. V., Zhurikhina V. V., Lipovskii A. A.**, Electric Properties of Hemispherical Metal Nanoparticles: Influence of the Dielectric Cover and Substrate, *Plasmonics.* 10 (2015) 519–527.
5. **Zayats A. V., Smolyaninov I. I.**, Near-field photonics: surface plasmon polaritons and localized surface plasmons, *J. Opt. A Pure Appl. Opt.* 5 (2003) 16–50.



6. Klimov V., Nanoplasmonics, Jenny Stanford Publishing, 2014.
7. Zayats A. V., Smolyaninov I. I., Maradudin A. A., Nano-optics of surface plasmon polaritons, *Phys. Rep.* 408 (2005) 131–314.
8. Bolduc O. R., Pelletier J. N., Masson J.-F., SPR Biosensing in Crude Serum Using Ultralow Fouling Binary Patterned Peptide SAM, *Anal. Chem.* 82 (2010) 3699–3706.
9. Homola J., Yee S. S., Gauglitz G., Surface plasmon resonance sensors: review, *Sensors Actuators B Chem.* 54 (1999) 3–15.
10. Mayer K. M., Hafner J. H., Localized Surface Plasmon Resonance Sensors, *Chem. Rev.* 111 (2011) 3828–3857.
11. Daniel W. L., Han M. S., Lee J.-S., Mirkin C. A., Colorimetric Nitrite and Nitrate Detection with Gold Nanoparticle Probes and Kinetic End Points, *J. Am. Chem. Soc.* 131 (2009) 6362–6363.
12. Zhang J., Wang L., Pan D., Song S., Boey F. Y. C., Zhang H., Fan C., Visual Cocaine Detection with Gold Nanoparticles and Rationally Engineered Aptamer Structures, *Small.* 4 (2008) 1196–1200.
13. Storhoff J. J., Elghanian R., Mucic R. C., Mirkin C. A., Letsinger R. L., One-Pot Colorimetric Differentiation of Polynucleotides with Single Base Imperfections Using Gold Nanoparticle Probes, *J. Am. Chem. Soc.* 120 (1998) 1959–1964.
14. Li M., Cushing S. K., Wu N., Plasmon-enhanced optical sensors: a review, *Analyst.* 140 (2015) 386–406.
15. Kinkhabwala A., Yu. Z., Fan S., Avlasevich Y., Müllen K., Moerner W. E., Large single-molecule fluorescence enhancements produced by a bowtie nanoantenna, *Nat. Photonics.* 3 (2009) 654–657.
16. Xie F., Pang J. S., Centeno A., Ryan M. P., Riley D. J., Alford N. M., Nanoscale control of Ag nanostructures for plasmonic fluorescence enhancement of near-infrared dyes, *Nano Res.* 6 (2013) 496–510.
17. Vo-Dinh T., SERS chemical sensors and biosensors: new tools for environmental and biological analysis, *Sensors Actuators B Chem.* 29 (1995) 183–189.
18. Zhurikhina V., Skvortsov A., Babich E., Redkov A., Raman Spectroscopy of Amino Acids Using Metal Nanoisland Films on Glass, in: 2021 Int. Conf. Electr. Eng. Photonics, IEEE, 2021: pp. 168–170.
19. Li M., Cushing S. K., Zhang J., Lankford J., Aguilar Z. P., Ma D., Wu N., Shape-dependent surface-enhanced Raman scattering in gold–Raman-probe–silica sandwiched nanoparticles for biocompatible applications, *Nanotechnology.* 23 (2012) 115501.
20. Zong S., Wang Z., Chen H., Yang J., Cui Y., Surface Enhanced Raman Scattering Traceable and Glutathione Responsive Nanocarrier for the Intracellular Drug Delivery, *Anal. Chem.* 85 (2013) 2223–2230.
21. Ko E., Hwang J., Kim J. H., Lee J. H., Lee S. H., Tran V.-K., Chung W. S., Park C. H., Choo J., Seong G. H., Electrochemical Fabrication of Nanostructures on Porous Silicon for Biochemical Sensing Platforms, *Anal. Sci.* 32 (2016) 681–686.
22. Babich E., Scherbak S., Lubyankina E., Zhurikhina V., Lipovskii A., Power Spectral Density Analysis for Optimizing SERS Structures, *Sensors.* 22 (2022) 593.
23. Batista E., Dos Santos D., Andrade G. S., Sant’Ana A., Brolo A., Temperini M. A., Using Polycarbonate Membranes as Templates for the Preparation of Au Nanostructures for Surface-Enhanced Raman Scattering, *J. Nanosci. Nanotechnol.* 9 (2009) 3233–3238.
24. Miller E. N., Palm D. C., De Silva D., Parbatani A., Meyers A. R., Williams D. L., Thompson D. E., Microsphere Lithography on Hydrophobic Surfaces for Generating Gold Films that Exhibit Infrared Localized Surface Plasmon Resonances, *J. Phys. Chem. B.* 117 (2013) 15313–15318.
25. Zhurikhina V. V., Brunkov P. N., Melehin V. G., Kaplas T., Svirko Y., Rutckaia V. V., Lipovskii A. A., Self-assembled silver nanoislands formed on glass surface via out-diffusion for multiple usages in SERS applications, *Nanoscale Res. Lett.* 7 (2012) 1–5.
26. Babich E., Scherbak S., Asonkeng F., Maurer T., Lipovskii A., Hot spot statistics and SERS performance of self-assembled silver nanoisland films, *Opt. Mater. Express.* 9 (2019) 4090.
27. Babich E., Raskhodchikov D., Redkov A., Hmima A., Nashchekin A., Lipovskii A., Dendritic structures by glass electrolysis: Studies and SERS capability, *Curr. Appl. Phys.* 24 (2021) 54–59.

28. Skvortsov A., Babich E., Redkov A., Lipovskii A., Zhurikhina V., Stable in Biocompatible Buffers Silver Nanoisland Films for SERS, Biosensors. 11 (2021) 448.

29. Babich E., Reduto I., Redkov A., Reshetov I., Zhurikhina V., Lipovskii A., Thermal poling of glasses to fabricate masks for ion exchange, J. Phys. Conf. Ser. 1695 (2020) 012107.

30. Babich E. S., Gangrskiaia E.S., Reduto I. V., Béal J., Redkov A. V., Maurer T., Lipovskii A. A., Self-assembled silver nanoparticles in glass microstructured by poling for SERS application, Curr. Appl. Phys. 19 (2019) 1088–1095.

THE AUTHORS

ZHURIKHINA Valentina V.

zhurikhina_vv@spbstu.ru

ORCID: 0000-0003-0685-9409

Received 12.07.2022. Approved after reviewing 14.07.2022. Accepted 14.07.2022.

RADIOPHYSICS

Conference materials

UDC 621.3

DOI: <https://doi.org/10.18721/JPM.153.366>

A seesaw-type MEMS switch with Pt and Ru contacts

I. V. Uvarov ¹✉, V. V. Naumov ¹, A. N. Kupriyanov ¹, M. O. Izyumov ¹, I. I. Amirov ¹

¹ Valiev Institute of Physics and Technology of Russian Academy of Sciences, Yaroslavl, Russia

✉ i.v.uvarov@bk.ru

Abstract. Microelectromechanical systems (MEMS) switches have outstanding working characteristics and a wide range of possible applications, but suffer from the lack of reliability. The main reason of failure is the degradation of metal contacts, which increases the on-resistance or leads to stiction. A proper choice of the contact material may solve the problem. In this work, the performance of Pt-Pt and Ru-Ru contacts is investigated. The study is performed using a recently proposed stiction-protected MEMS switch. The contact resistance and lifecycle in the cold switching regime are measured and compared.

Keywords: MEMS switch, electrostatic actuation, contact resistance, lifecycle

Funding: This work is supported by the grant of President of the Russian Federation no. MK-945.2021.4 and the program no. FFNN-2022-0017 of the Ministry of Science and Higher Education of Russia for Valiev Institute of Physics and Technology of RAS.

Citation: Uvarov I. V., Naumov V. V., Kupriyanov A. N., Izyumov M. O., Amirov I. I., A seesaw-type MEMS switch with Pt and Ru contacts. St. Petersburg State Polytechnical University Journal. Physics and Mathematics, 15 (3.3) (2022) 335–339. DOI: <https://doi.org/10.18721/JPM.153.366>

This is an open access article under the CC BY-NC 4.0 license (<https://creativecommons.org/licenses/by-nc/4.0/>)

Материалы конференции

УДК 621.3

DOI: <https://doi.org/10.18721/JPM.153.366>

МЭМС-переключатель с контактами из платины и рутения

И. В. Уваров ¹✉, В. В. Наумов ¹, А. Н. Куприянов ¹, М. О. Изюмов ¹, И. И. Амиров ¹

¹ Ярославский филиал Физико-технологического института им. К. А. Валиева

Российской академии наук, Ярославль, Россия

✉ i.v.uvarov@bk.ru

Аннотация. Переключатели, изготовленные по технологии микроэлектромеханических систем (МЭМС), обладают выдающимися рабочими характеристиками и представляют интерес для множества применений. Недостатком этих устройств является невысокая надежность, обусловленная деградацией металлических контактов. Подбор материала контактов может решить проблему. В этой работе исследуются рабочие характеристики контактов из платины и рутения. Выполнены измерения сопротивления и ресурса контактов в холодном режиме.

Ключевые слова: МЭМС-переключатель, электростатическое управление, контактное сопротивление, ресурс

Финансирование: Грант Президента Российской Федерации № МК-945.2021.4, государственное задание ФТИАН им. К. А. Валиева РАН Минобрнауки РФ по теме № FFNN-2022-0017.

Ссылка при цитировании: Уваров И. В., Наумов В. В., Куприянов А. Н., Изюмов М. О., Амиров И. И. МЭМС-переключатель с контактами из платины и рутения // Научно-

Introduction

Wireless communication and radar systems demonstrate significant progress in recent years. The evolution is achieved due to advanced electronic components, including switches for routing of radio frequency and microwave signals. However, the development of electromagnetic and semiconductor relays has almost exhausted, and new approaches are required to support the trend. MEMS switches are considered as a promising alternative to conventional devices. They provide superior radio frequency characteristics in combination with small size, low power consumption and capability of integration with CMOS circuits [1]. An important characteristic of the switch is the lifecycle, which is mainly determined by the durability of contacts. Metallic surfaces degrade during operation due to friction, contamination and other phenomena [2]. The degradation is considered as the main reason for the switch failure, because it increases the contact resistance or leads to stiction. Several methods to overcome the problem are known, including elimination of the contact bounce [3], two-stage switching [4] and refreshing the contact point [5]. But more straight way is the selection of contact materials. Typically, the contacts are made of noble metals due to their chemical inertness and low resistivity. In this paper we compare working characteristics of Pt-Pt and Ru-Ru contacts. The study is performed at the recently developed seesaw-type MEMS switch [6]. The modified design provides enhanced contact force at a reasonable driving voltage. The on-resistance and lifecycle for both materials are analyzed and compared.

Materials and Methods

The switch is shown in Fig 1, *a*. A source electrode is a 100 μm long and 45 μm wide beam made of aluminium. It is suspended by torsion springs above two pairs of gate and drain electrodes. The gap between the beam and electrodes is of 1.5 μm . The beam has contact bumps on the bottom side. When the driving voltage is applied to the gate, the electrostatic force tilts the beam, and the bump touches the drain turning the switch on. When the voltage is removed, the switch returns to the off state under the elastic force of the springs. In case of stiction, the voltage is applied to the opposite gate, which creates the recovery force that breaks the contact. The beam and electrodes have an optimized shape that ensures several times higher contact force in comparison with the previous design [6].

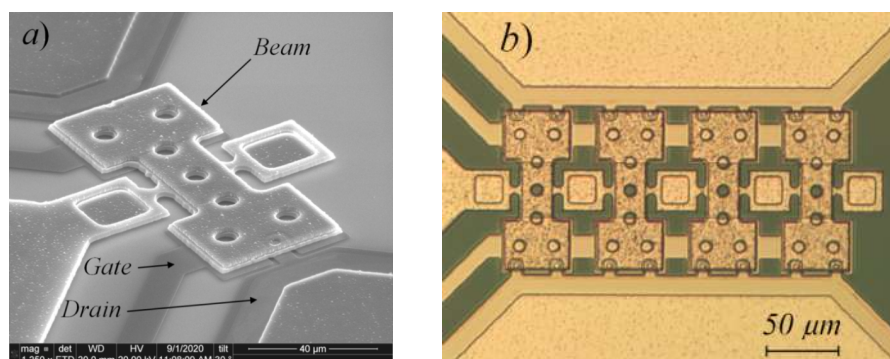


Fig. 1. MEMS switch under investigation: scanning electron microscope image of the basic single-beam device (*a*); optical image of the four-beam switch, each beam contains four contact bumps (*b*)

The switch is fabricated by surface micromachining on an oxidized silicon wafer using the five-mask process described previously [7]. The bumps and electrodes are made of platinum or ruthenium, so the switch provides Pt-Pt and Ru-Ru contact. Each arm of the beam contains one or two contact bumps. In addition, we fabricate the switch with four beams, which are connected

to each other and actuated simultaneously by the common gate, see Fig. 1, *b*. Both one- and four-beam switches are fabricated in one- and two-bump versions.

The switches are tested in standard laboratory conditions without packaging. Measuring equipment is connected to the sample according to Fig. 2. Rectangular pulses of the gate voltage V_{G1} and V_{G2} are applied to both sides of the switch alternately with the frequency of about 1 Hz. The device has a pull-in voltage of 27 V, so the gate voltage of 30 V should be enough for actuation. However, both Pt-Pt and Ru-Ru contacts are prone to stiction. To recover the switch, an increased voltage is applied. Two values of 55 and 80 V are chosen to test the device at various contact force. The DC signal $V_S = 5$ V is fed to the beam. In order to prevent the damage of contacts by electric arcing, the switch operates in a cold regime. The source voltage is applied to the beam after the contacts are closed and is removed before they are opened. Load resistors $R_1 = R_2 = 5$ kOhm limit the drain current I_D by 1 mA, which is controlled at the left channel by a multimeter. Thus, the transmitted power does not exceed 5 mW. Contact resistance R_C is calculated at each actuation cycle using the resistive divider circuit, which contains R_C and the corresponding load resistor.

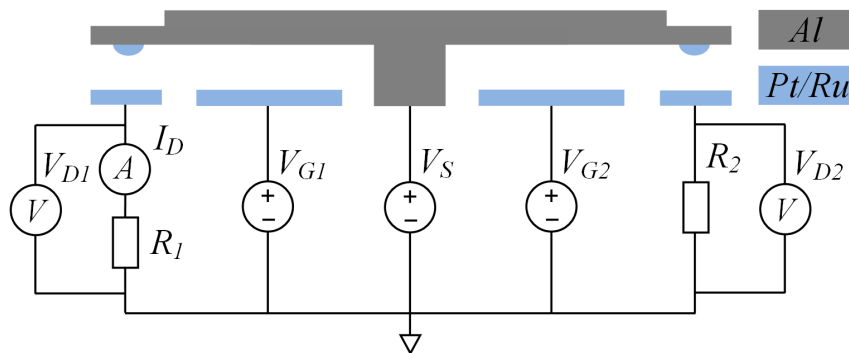


Fig. 2. Schematic illustration of the experimental setup

Results and Discussion

First of all, we test the basic switch with one beam and one bump per arm. A typical graph of the contact resistance throughout the first thousand cycles is shown in Fig. 3, *a*. The switch with Pt-Pt contacts demonstrates rather unstable R_C . It varies from 66 to 619 Ohm and has the average value of 281 Ohm. Ruthenium provides more stable resistance of 76–199 V with the average value of 157 Ohm, which is 44% lower compared to platinum. To all appearance, the instability is caused by accumulation of carbon-containing contaminants on the contact surfaces, as was observed for the Pt-based switch of the previous design [8]. Such contamination called “frictional polymerization” is a feature of platinum group metals due to their electron structure [9]. It was demonstrated that Pt adsorbs carbon from the ambient air and forms nonvolatile carbon contamination [10]. However, the surface of ruthenium may undergo a slight oxidation during fabrication. The layer of RuO_2 prevents the accumulation of carbon [11]. This is a probable reason for the more stable behavior of the Ru-based device.

The contact resistance during the long-term test is shown in Fig. 3, *b*. The switches fail due to the sharp increase of R_C to the megaohm level. Platinum-contact devices have a lifetime below $4 \cdot 10^4$ working cycles, while ruthenium-based switches withstand more than $3 \cdot 10^5$ actuations. High durability of Ru contacts is explained by low contamination rate and high hardness, although the jumps of the resistance are also observed. The sharp decrease of R_C to 20–60 Ohm takes place when the contamination film is damaged by a mechanical impact or electrical breakdown.

Further, we test several samples of each type in order to collect statistical data. Only the ruthenium-based devices are considered. The basic switch provides the average contact resistance of 209 Ohm at $V_G = 55$ V. Increasing the voltage up to 80 V rises the contact force F_C from 38 to 84 μN , according to a finite element simulation [6]. When the force equals to several tens of micronewtons, asperities of the contact surfaces experience elastic deformation. The resistance depends on the force as $R_C \sim F_C^{-1/3}$ [2]. Therefore, at $V_G = 80$ V one can expect $R_C \approx 160$ Ohm. However, the switch demonstrates somewhat higher value of 195 Ohm. To all appearance, tribopolymers make a contribution.

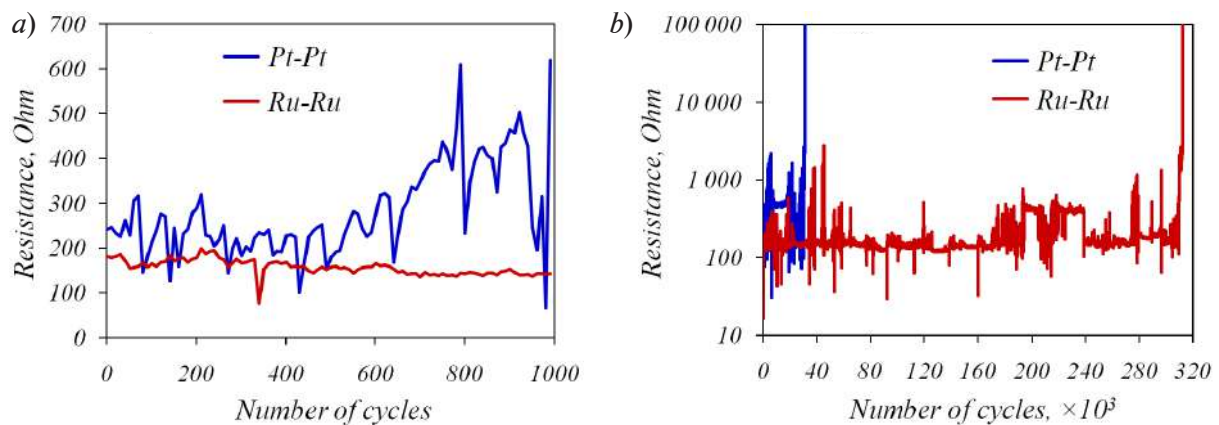


Fig. 3. Contact resistance of switches with Pt-Pt and Ru-Ru contacts during the first thousand of working cycles (a) and throughout the whole lifecycle (b)

The use of two bumps per arm increases the tendency to stiction. For the one-bump switch the gate voltage of 50–55 V is enough to overcome stiction, while the two-bump device requires 70–75 V. This is explained by the growth of adhesion force with the larger contact area. In addition, the average resistance is increased to 223 Ohm at $V_G = 80$ V. Apparently, the contact force is divided between two bumps, thereby reducing the contact pressure. It is worth noting that the use of four beams connected in parallel also does not improve the performance. This result disagrees with expectations, because the four-beam switch provides larger contact area at the same F_C per bump. Additional measurements are required to verify this result.

Conclusion

The paper reports the first measurements of the performance for a recently proposed seesaw-type MEMS switch. The device is fabricated by surface micromachining using the five-mask process. In order to select the optimal contact material, the switch is equipped by Pt-Pt and Ru-Ru contacts. The tests are performed in the cold regime without packaging. The input voltage equals to 5 V, while the current does not exceed 1 mA. The platinum-based switch demonstrates a rather high and unstable contact resistance, which is determined by the formation of tribopolymers. Ruthenium provides more stable and low resistance, probably, due to oxidation of the contacts during fabrication. Increasing the contact force reduces the resistance, although a stronger effect is expected. Using two contact bumps per arm instead of one bump does not improve the performance, but increases the probability of stiction. Increasing the number of beams connected in parallel also does not improve working characteristics, but this result needs further analysis. Ruthenium contacts provide almost ten times longer lifecycle compared to platinum contacts. Thus, Ru is more preferable material for the demonstrated switch.

This work is supported by the grant of President of the Russian Federation no. MK-945.2021.4 and the program no. FFNN-2022-0017 of the Ministry of Science and Higher Education of Russia for Valiev Institute of Physics and Technology of RAS. The study is performed using the equipment of Facilities Sharing Centre “Diagnostics of Micro- and Nanostructures”.

REFERENCES

1. Rebeiz G. M., RF MEMS: Theory, Design, and Technology, John Wiley & Sons, Hoboken, New Jersey, 2003.
2. Toler B. F., Coutu R. A., McBride J. W., A review of micro-contact physics for microelectromechanical systems (MEMS) metal contact switches, Journal of Micromechanics and Microengineering. 23 (2013) 103001.
3. Czaplewski D. A., Dyck C. W., Sumali H., Massad J. E., Koppers J. D., Reines I., Cowan W. D., Tigges C. P., A soft-landing waveform for actuation of a single-pole single-throw ohmic RF MEMS switch, Journal of Microelectromechanical Systems. 15 (2006) 1586–1594.



4. Liu Y., Bey Y., Liu X., Extension of the hot-switching reliability of RF-MEMS switches using a series contact protection technique, IEEE Transactions on Microwave Theory and Techniques. 64 (2016) 3151–3162.
5. Song Y.-H., Ko S.-D., Yoon J.-B., A highly reliable two-axis MEMS relay demonstrating a novel contact refresh method, Journal of Microelectromechanical Systems. 24 (2015) 1495–1502.
6. Uvarov I. V., Marukhin N. V., A seesaw-type MEMS switch with enhanced contact force: the first results, Journal of Physics: Conference Series. 2086 (2021) 012069.
7. Uvarov I. V., Migration of adhesive material in electrostatically actuated MEMS switch, Microelectronics Reliability. 125 (2021) 114372.
8. Uvarov I. V., Kupriyanov A. N., Stiction-protected MEMS switch with low actuation voltage, Microsystem Technologies. 25 (2019) 3243–3251.
9. Czaplewski D. A., Nordquist C. D., Dyck C. W., Patrizi G. A., Kraus G. M., Cowan W. D., Lifetime limitations of ohmic, contacting RF MEMS switches with Au, Pt and Ir contact materials due to accumulation of ‘friction polymer’ on the contacts, Journal of Micromechanics and Microengineering. 22 (2012) 105005.
10. Cumpson P. J., Seah M. P., Stability of reference masses. IV: Growth of carbonaceous contamination on platinum-iridium alloy surfaces, and cleaning by UV/ozone treatment, Metrologia. 33 (1996) 5072–532.
11. Czaplewski D. A., Nordquist C. D., Patrizi G. A., Kraus G. M., Cowan W. D., RF MEMS switches with RuO₂-Au contacts cycled to 10 billion cycles, Journal of Microelectromechanical Systems. 22 (2013) 655–661.

THE AUTHORS

UVAROV Ilia V.

i.v.uvarov@bk.ru

ORCID: 0000-0002-6882-0625

NAUMOV Victor V.

vnau@rambler.ru

KUPRIYANOV Alexander N.

shurik7777@mail.ru

IZYUMOV Mikhail O.

mikhail-izyumov@yandex.ru

AMIROV Ildar I.

ildamirov@yandex.ru

Received 13.07.2022. Approved after reviewing 15.07.2022. Accepted 19.07.2022.

Conference materials
UDC 621.396.67.012.12
DOI: <https://doi.org/10.18721/JPM.153.367>

A mmWave rod antenna array compatible with a PCB prototyping technology

A. N. Lyubchak ^{1,2}✉, A. N. Prikhodko ^{1,2}, V. S. Andreev ^{1,2},
A. S. Shurakov ^{1,2,3}, G. N. Goltsman ^{1,2}

¹ National Research University Higher School of Economics, Moscow, Russia;

² Moscow Pedagogical State University, Moscow, Russia;

³ National University of Science and Technology MISiS, Moscow, Russia

✉ anlyubchak@miem.hse.ru

Abstract. A mmWave communication is becoming a reality. Nowadays, 5G networks are at the stage of commercial implementation while numerous studies around the world are devoted to investigating practical issues of switching to the 6G standard. Next generation communication systems should rely on highly directive transceivers, which potentially suffer from a micromobility issue. In this paper, we report on the design of a mmWave rod antenna array compatible with a PCB prototyping technology. The array makes use of a dielectric multimode interference power splitter integrated with four weakly coupled dielectric rod antennas at its output. It is cheap to fabricate and has a half-power beamwidth of 11° with a corresponding side lobe level of -11 dB at 135 GHz. Thus, the proposed design seems suitable for prototyping mmWave transceivers within lab studies of a micromobility issue in 6G networks. The design is adaptable for high permittivity PCB laminates and, therefore, is potentially compatible with Si platform. All together suggests efficient operation of dielectric rod antenna arrays in the mmWave band and beyond.

Keywords: millimeter waves, dielectric rod antenna, multimode interference power splitter, antenna array, PCB laminate, direct machining

Funding: Support from the Basic Research Program of the National Research University Higher School of Economics in the development of experimental setup and methods is gratefully acknowledged. Experimental samples were fabricated under the support of the Russian Science Foundation grant No. 21-72-10119, <https://rscf.ru/project/21-72-10119/>.

Citation: Lyubchak A. N., Prikhodko A. N., Andreev V. S., Shurakov A. S., Goltsman G. N., A mmWave rod antenna array compatible with a PCB prototyping technology. St. Petersburg State Polytechnical University Journal. Physics and Mathematics, 15 (3.3) (2022) 340–344. DOI: <https://doi.org/10.18721/JPM.153.367>

This is an open access article under the CC BY-NC 4.0 license (<https://creativecommons.org/licenses/by-nc/4.0/>)

Материалы конференции
УДК 621.396.67.012.12
DOI: <https://doi.org/10.18721/JPM.153.367>

Решетка штыревых антенн миллиметрового диапазона совместимая с технологией прототипирования печатных плат

А. Н. Любчак ^{1,2}✉, А. Н. Приходько ^{1,2}, В. С. Андреев ^{1,2},
А. С. Шураков ^{1,2,3}, Г. Н. Гольцман ^{1,2}

¹ Национальный исследовательский университет «Высшая школа экономики», Москва, Россия;

² Московский педагогический государственный университет, Москва, Россия;

³ Национальный университет науки и технологий «МИСиС», Москва, Россия

✉ anlyubchak@miem.hse.ru

Аннотация. В настоящее время сети связи 5G находятся на стадии коммерческого внедрения, а научные исследования во всем мире направлены на изучение практических



аспектов перехода на стандарт 6G. Системы связи следующего поколения должны иметь в своем составе узконаправленные приемопередатчики, которые потенциально подвержены негативному влиянию микроподвижности. В данной статье мы сообщаем о разработке решетки штыревых антенн миллиметрового диапазона, совместимой с технологией прототипирования печатных плат. Ключевую роль в устройстве решетки играет делитель мощности на основе многомодовой интерференции, интегрированный по выходу с четырьмя слабосвязанными диэлектрическими штыревыми антеннами. Геометрия решетки проста в изготовлении и обеспечивает ширину пучка 11° с уровнем боковых лепестков -11 дБ на частоте 135 ГГц. Таким образом, предлагаемая конструкция хорошо подходит для создания прототипов приемопередатчиков миллиметрового диапазона в рамках лабораторных исследований эффекта микроподвижности в сетях 6G. Конструкция может быть также адаптирована к использованию ламинатов для печатных плат с высокой диэлектрической проницаемостью и, следовательно, потенциально совместима с кремниевой платформой. Все вышесказанное позволяет сделать вывод об эффективности использования решеток диэлектрических штыревых антенн как в миллиметровом волновом диапазоне, так и за его пределами.

Ключевые слова: миллиметровые волны, диэлектрическая штыревая антенна, делитель мощности на основе многомодовой интерференции, антенная решетка, ламинат для печатной платы, механическая обработка

Финансирование: Выражается благодарностью Программе фундаментальных исследований НИУ ВШЭ за поддержку в разработке экспериментальной установки и методик. Экспериментальные образцы изготовлены при поддержке гранта Российского научного фонда № 21-72-10119, <https://rscf.ru/project/21-72-10119/>.

Ссылка при цитировании: Любчак А. Н., Приходько А. Н., Андреев В. С., Шураков А. С., Гольцман Г. Н. Решетка штыревых антенн миллиметрового диапазона, совместимая с технологией прототипирования печатных плат // Научно-технические ведомости СПбГПУ. Физико-математические науки. 2022. Т. 15. № 3.3. С. 340–344. DOI: <https://doi.org/10.18721/JPM.153.367>

Статья открытого доступа, распространяемая по лицензии CC BY-NC 4.0 (<https://creativecommons.org/licenses/by-nc/4.0/>)

Introduction

Nowadays, millimeter waves (mmWaves) attract close attention of both the scientific community and the communication industry. The society needs for fast and reliable data transfer eminently grew in the coronavirus pandemic era. A mmWave communication is becoming a reality. 5G networks are at the stage of commercial implementation while numerous studies around the world are devoted to investigating practical issues of switching to the 6G standard. Next generation communication systems should rely on transceivers equipped with high directivity antennas [1] causing potential loss of connection upon slight displacement of a mobile device. This is referred to as a micromobility issue and is of high practical importance [2].

Conventional way to implement a high directivity input optics of a receiver/transmitter is to use an antenna array. Since there is a variety of antenna array technologies, the choice is always a trade-off between performance of the array and its fabrication complexity. In this paper, we report on the design of a mmWave rod antenna array compatible with a PCB prototyping technology. The design is inspired by that of a W-band fully dielectric rod antenna array with integrated power divider [3], but it relies on a low-cost PCB laminate (FSD255G series, 1 mm thick [4]). Fabrication details and outcome of performance tests are provided further in the text.

Fabrication and Evaluation Details

Referring to Fig. 1, *a*, the proposed antenna array is fully dielectric and makes use of a multimode interference (MMI) power splitter integrated with four weakly coupled dielectric rod antennas (DRAs) at its output. Dimensions of the antenna array key elements are summarized in Table 1. It is worth mentioning that the chosen PCB laminate is intrinsically fibrous, and,

therefore, the fabricated array structure has no sharp edges along perimeter which complicates inspection of its actual linear dimensions. The geometry is implemented with the aid of a MITS Eleven Lab PCB prototyping machine [5], metallization on both sides of the PCB laminate is removed via wet etching. The array is designed for operation at 135 GHz, where it has a half-power beamwidth (*HPBW*) of 11° and a side lobe level (*SLL*) of -11 dB. It is also well matched with a feeding WR6.5 rectangular waveguide: we measure return loss (*RL*) of 17.5 dB at 135 GHz.

As shown in figure 1b, during the beam profile measurements, we used a membrane-integrated planar Schottky diode (PSD) [6] as a core of direct-detection receiver (Rx). The PSD WR6.5 input was loaded by the proposed DRA array. Transmitter (Tx) made use of a backward wave oscillator (BWO) providing CW AM signal over the frequency range of 126.5–145.5 GHz. Tx was equipped with input optics identical to that of Rx. The measurements were conducted at the Tx-to-Rx distance of 35 cm, which approaches a Fraunhofer distance (D_F) defined by equation 1 for chosen geometry of the DRA array. Despite noticeable absorption loss in the array elements, we observed peak value of a signal-to-noise ratio (*SNR*) of ~ 670 during all the measurements. This *SNR* value was achieved for the Rx time constant of 100 ms. Given that power at the array input can be increased from 1.5 to 120 mW if BWO is replaced by a commercially available solid state mmWave source, insertion loss of the array is acceptable from a practical point of view. Outcome of the beam profile measurements is provided in Fig. 2.

$$D_F = 2D^2\lambda^{-1}, \tag{1}$$

where D is the largest dimension of the DRA array aperture and λ is the free space wavelength.

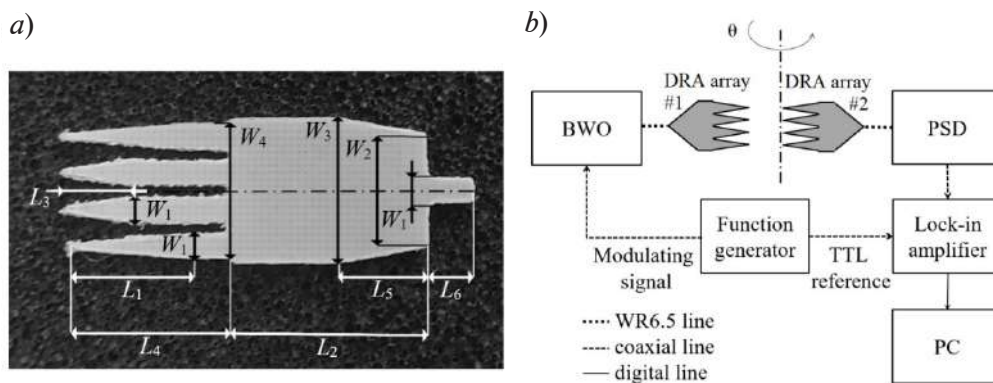


Fig. 1. Geometry of the proposed DRA array in H-plane (a); (b) diagram of the experimental setup for measuring the beam profiles in H- and E-planes (b)

Table 1

Dimensions of the antenna array key elements

Geometric parameter	Nominal value	Measured value	
		DRA array #1	DRA array #2
L_1	7.72 mm	7.44±0.36 mm	7.65±0.14 mm
L_2	11.74 mm	11.73±0.14 mm	11.73±0.14 mm
L_3	4.15 mm	4.15±0.14 mm	4.14±0.14 mm
L_4	10.80 mm	10.65±0.21 mm	10.58±0.22 mm
L_5	5.35 mm	5.36±0.14 mm	5.29±0.14 mm
L_6	2.86 mm	2.86±0.14 mm	2.86±0.14 mm
W_1	1.29 mm	1.29±0.14 mm	1.28±0.14 mm
W_2	6.86 mm	6.79±0.14 mm	6.79±0.14 mm
W_3	8.75 mm	8.79±0.14 mm	8.80±0.14 mm
W_4	8.14 mm	8.15±0.14 mm	8.15±0.14 mm

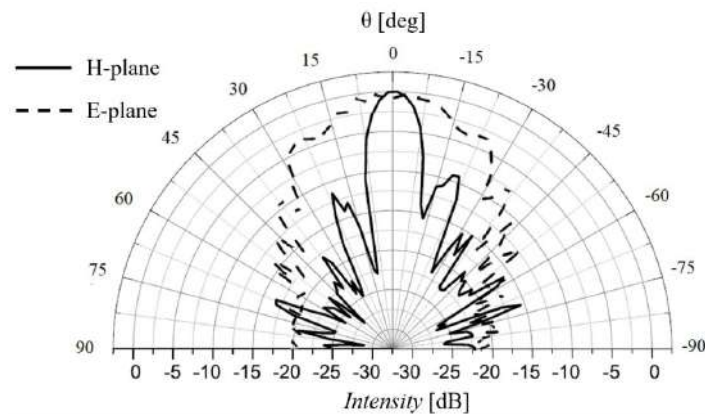


Fig. 2. Measured H- and E-plane beam profiles of the proposed DRA array

Fig. 3 provides frequency profiles of return losses measured for the DRA arrays #1 and #2. During the measurements, we used a solid state mmWave source providing up to 120 mW of output power over the frequency range from 132 to 162 GHz. The source and the array under study were connected through a waveguide directional coupler with a coupling factor of -15 dB and an isolation of 30 dB. For a given frequency of the source (F_{ss}), the RL value was calculated with the aid of equation 2.

$$RL = 10 \log_{10} (P_1 P_2^{-1}), \quad (2)$$

where P_1 and P_2 are the mmWave powers at the input and transmitted ports of the directional coupler, respectively. The power values were consequently measured by a precision waveguide power meter while the source was permanently connected to the coupled port of the directional coupler.

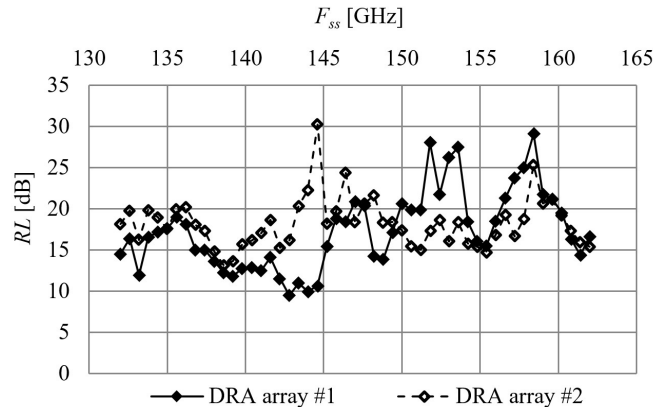


Fig. 3. Measured return losses of the DRA arrays

Both DRA arrays demonstrated decent match with a WR6.5 rectangular waveguide over the entire range of 132–162 GHz and at $F_{ss} = 135$ GHz specifically. Together with the beam profile frequency dependence [3], this suggests that the proposed design provides fractional input frequency bandwidth of at least 20%. Moreover, the design is adaptable for high permittivity laminates. Switching to a material with relative permittivity of 4.4 provides reduction in the array dimensions by $\sim 50\%$ [7]. Thus, we plan to further reduce aperture size of the array via switching to FSD1020T series laminate [8]. In addition to shortening a Fraunhofer distance, this aids to minimize propagation losses due to absorption in the array elements. Remaining compliant with a 2D PCB machinery, the design becomes even more attractive for implementation of highly directive mmWave transceivers as part of a lab measurement equipment.

Conclusion

In this paper, we propose design of a linear DRA array integrated with MMI power splitter developed for operation in the mmWave band. Low-cost PCB laminate and 2D CNC machining

are used to implement the array geometry. The proposed design is evaluated via both the beam profile and return loss measurements conducted in the frequency range from 132 to 162 GHz. We measure the H-plane $HPBW = 11^\circ$ with $SLL = -11$ dB and $RL \geq 17.5$ dB at 135 GHz. The design is adaptable for high permittivity PCB laminates and Si platform. In addition to shortening a Fraunhofer distance, switching to them aids to minimize propagation losses due to absorption in the array elements. All together suggests efficient operation of DRA arrays in the mmWave band and far beyond it.

REFERENCES

1. Ning, B., Tian, Z., Chen, Z., Han, C., Yuan, J., Li, S., Prospective beamforming technologies for ultra-massive MIMO in terahertz communications: A tutorial, arXiv preprint arXiv:2107.03032 (2021).
2. Stepanov N. V., Moltchanov D., Begishev V., Turlikov A., Koucheryavy Y., Statistical analysis and modeling of user micromobility for THz cellular communications. IEEE Transactions on Vehicular Technology. 71(1) (2021) 725–738.
3. Tesmer H., Reese R., Polat E., Nickel M., Jakoby R., Maune H., Fully dielectric rod antenna arrays with integrated power divider. Frequenz, 73(11-12) (2019) 367–377.
4. ElecTrade-M. URL: http://www.elm.ru/attach/catalog/v_2464_253.pdf. Accessed June 05, 2022.
5. MITS. URL: <http://www.mitspcb.com/edoc/11lab.htm>. Accessed June 05, 2022.
6. Shurakov A., Belikov I., Prikhodko A., Mikhailov D., Gol'tsman G., Membrane-integrated planar schottky diodes for waveguide mmwave detectors. Microwave & telecommunication technology, 3 (2021) 34.
7. Reese R., Polat E., Tesmer H., Strobl J., Schuster C., Nickel M. Maune H., Liquid crystal based dielectric waveguide phase shifters for phased arrays at W-band. IEEE Access, 7, (2019) 127032-127041.
8. ElecTrade-M. URL: http://www.elm.ru/attach/catalog/v_2464_253.pdf. Accessed June 05, 2022.

THE AUTHORS

LYUBCHAK Anastasia N.
 anyubchak@miem.hse.ru
 ORCID: 0000-0002-4861-2466

SHURAKOV Alexander S.
 alexander@rplab.ru
 ORCID: 0000-0002-4671-7731

PRIKHODKO Anatoliy N.
 anprikhodko@hse.ru
 ORCID: 0000-0002-4859-8975

GOLTSMAN Gregory N.
 goltsman@rplab.ru
 ORCID: 0000-0002-1960-9161

ANDREEV Vladislav S.
 AndrejeffVS@yandex.ru
 ORCID: 0000-0003-2604-5496

Received 13.08.2022. Approved after reviewing 17.08.2022. Accepted 09.09.2022.

Conference materials

UDC 52-77

DOI: <https://doi.org/10.18721/JPM.153.368>

Millimeter wave photonic crystal waveguides fabricated via direct machining

A. N. Prikhodko^{1,2}✉, I. I. Belikov^{1,2}, A. V. Lvov¹,
A. S. Shurakov^{1,2,3}, G. N. Goltsman^{1,3}

¹ Moscow Pedagogical State University, Moscow, Russia;

² National Research University Higher School of Economics, Moscow, Russia;

³ National University of Science and Technology MISiS, Moscow, Russia

✉ anprikhodko@hse.ru

Abstract. At the moment, millimeter waves attract close attention not only of the scientific community, but also of the communication industry. Number of studies worldwide are currently focused on finding efficient solutions for the transceiver technologies compatible with beamforming and carrier frequencies beyond 100 GHz. It was recently demonstrated that the technology of integrated silicon photonic crystals provides decent propagation loss and low fabrication complexity upon implementation of waveguide components for the sub-mmWave band. In this paper, we report on the millimeter wave photonic crystal waveguides fabricated from high permittivity PCB laminate by the means of direct machining. Inspection of the fabricated waveguide samples reveals no violation of the photonic crystal geometry due to the fabrication tolerances. The photonic crystals are designed for operation at frequencies 140–160 GHz, and we measure the power attenuation coefficient attributed to the waveguide geometry of 0.02 dB/mm at 145 GHz. The design considerations, including justification of the laminate choice, and detailed results of performance tests are presented in the paper.

Keywords: millimeter waves, photonic crystal waveguide, high permittivity PCB laminate, direct machining, 2D CNC machining

Funding: Support from the Basic Research Program of the National Research University Higher School of Economics in the development of experimental setup and methods is gratefully acknowledged. Experimental samples were fabricated under the support of the Russian Science Foundation grant No. 21-72-10119, <https://rscf.ru/project/21-72-10119/>.

Citation: Prikhodko A. N., Belikov I. I., Lvov A. V., Shurakov A. S., Goltsman G. N., Millimeter wave photonic crystal waveguides fabricated via direct machining. St. Petersburg State Polytechnical University Journal. Physics and Mathematics, 15 (3.3) (2022) 345–349. DOI: <https://doi.org/10.18721/JPM.153.368>

This is an open access article under the CC BY-NC 4.0 license (<https://creativecommons.org/licenses/by-nc/4.0/>)

Материалы конференции

УДК 52-77

DOI: <https://doi.org/10.18721/JPM.153.368>

Фотонно-кристаллический волновод миллиметрового диапазона, изготовленный методом механической обработки

А. Н. Приходько^{1,2}✉, И. И. Беликов^{1,2}, А. В. Львов¹,
А. С. Шураков^{1,2,3}, Г. Н. Гольцман^{1,3}

¹ Московский педагогический государственный университет, Москва, Россия;

² Национальный исследовательский университет «Высшая школа экономики», Москва, Россия;

³ Национальный исследовательский технологический университет «МИСиС», Москва, Россия

✉ anprikhodko@hse.ru

Аннотация. В настоящий момент миллиметровый волновой диапазон привлекает внимание не только научного сообщества, но и отрасли связи. Большое число исследований по всему миру сосредоточено на поиске эффективных решений для технологий приемопередатчиков, совместимых с функцией управления пучком при несущих частотах выше 100 ГГц. Недавно было показано, что технология интегрированных кремниевых фотонных кристаллов обеспечивает простоту изготовления и низкие вносимые потери при создании волноводных компонентов субмиллиметрового диапазона. В данной статье мы сообщаем о фотонно-кристаллических волноводах миллиметрового диапазона, изготовленных методом механической обработки из ламината для печатных плат с высокой диэлектрической проницаемостью. При контроле качества изготовленных образцов волноводов не выявлено нарушения заданной геометрии фотонного кристалла вследствие погрешности изготовления. Фотонные кристаллы спроектированы для использования в полосе частот 140–160 ГГц: измеренное на частоте 145 ГГц значение коэффициента ослабления мощности, связанного с геометрией волновода, составило 0.02 дБ/мм. Подробные результаты измерений технических характеристик, а также ключевые аспекты проектирования, включая обоснование выбора ламината, представлены далее в тексте статьи.

Ключевые слова: миллиметровые волны, фотонно-кристаллический волновод, ламинат для печатных плат с высокой диэлектрической проницаемостью, механическая обработка, 2D ЧПУ обработка

Финансирование: Выражается благодарностью Программе фундаментальных исследований НИУ ВШЭ за поддержку в разработке экспериментальной установки и методик. Экспериментальные образцы изготовлены при поддержке гранта Российского научного фонда № 21-72-10119, <https://rscf.ru/project/21-72-10119/>.

Ссылка при цитировании: Приходько А. Н., Беликов И. И., Львов А. В., Шураков А. С., Гольцман Г. Н. Фотонно-кристаллический волновод миллиметрового диапазона, изготовленный методом механической обработки // Научно-технические ведомости СПбГПУ. Физико-математические науки. 2022. Т. 15. № 3.3. С. 345–349. DOI: <https://doi.org/10.18721/JPM.153.368>

Статья открытого доступа, распространяемая по лицензии CC BY-NC 4.0 (<https://creativecommons.org/licenses/by-nc/4.0/>)

Introduction

At the moment, the millimeter wave (mmWave) band attracts close attention not only of the scientific community, but also of the communication industry. Progress in a mmWave communication is in line with the society needs for the speed and quality of data transfer which drastically enlarged in the coronavirus pandemic era. Next generation communication networks should rely on the transceiver technologies compatible with beamforming and carrier frequencies beyond 100 GHz [1]. This may potentially result in a fatal increase of their complexity, fabrication and operational costs. Thus, number of studies worldwide are currently focused on finding efficient software and hardware solutions.

It was recently proposed that the technology of integrated silicon photonic crystals is beneficial compared to that of conventional hollow metallic rectangular waveguides at sub-millimeter waves [2]. The benefits are mainly related to the reduction of propagation loss and fabrication complexity upon implementation of a single-mode waveguide and simple passive components. In this paper, we report on the technology of a mmWave photonic crystal waveguide (PCWG) fabricated by the means of direct machining. PCWG utilizes high permittivity laminate [3]. The geometry of photonic crystal is implemented with the aid of a PCB prototyping machine [4]. Metallization on both sides of the laminate is removed via wet etching at the final step of the fabrication process. The waveguide is designed for a single-mode operation at frequencies 140–160 GHz. The design considerations and results of performance tests are presented further in the text.

Evaluation of Fabricated Samples

Our designs make use of FSD1020T series laminate, which attributes relative permittivity (ϵ_r) of 10.2 and loss tangent ($\tan\delta$) of 0.002 at 10 GHz according to the manufacturer specifications.



Suitability of the laminate for our task is justified by evaluation of its dielectric properties in the mmWave band. This is achieved by measuring return (RL) and insertion losses (IL) of a WR6.5 rectangular waveguide section with an FSD1020T insert installed in it. The lengths of the waveguide section (l_{ws}) and the dielectric insert (l_{di}) are 25 and 6.4 mm, respectively; other their linear dimensions are identical. During the return loss measurement, we use a solid state mmWave source providing up to 120 mW of output power over the frequency range from 133 to 162 GHz. The source and the waveguide under study are connected through a waveguide directional coupler with a coupling factor of -15 dB and an isolation of 30 dB. The dielectric insert inside the waveguide is placed next to its flange facing the directional coupler, i.e., the front flange. For a given frequency of the source (F_{ss}), the RL value is calculated with the aid of equation 1.

$$RL = 10 \log_{10} (P_1 P_2^{-1}), \quad (1)$$

where P_1 and P_2 are the mmWave powers at the input and transmitted ports of the directional coupler, respectively. The power values are consequently measured by a precision waveguide power meter while the source is permanently connected to the coupled port of the directional coupler. During the insertion loss measurement, the source is disconnected from the latter port and is attached to the rear flange of the waveguide under study. This is to keep electric length of the transmission line constant which is useful in further analysis of the measured frequency profiles. At given F_{ss} , the IL value is defined by ratio of power provided by the source (P_{ss}) to that measured by the power meter (P_{pm}) in accordance with equation 2. Results of both the return and insertion loss measurements are provided in Fig. 1.

$$IL = 10 \log_{10} (P_{ss} P_{pm}^{-1}). \quad (2)$$

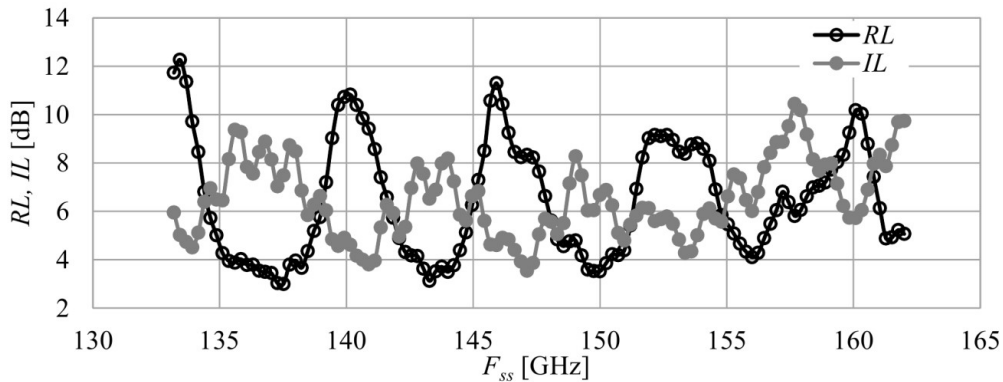


Fig. 1. Return and insertion losses measured for a WR6.5 rectangular waveguide section with an FSD1020T insert installed in it

Measured frequency profiles of the return and insertion losses are used to evaluate dielectric properties of the FSD1020T insert. This is achieved with the aid of math provided in equations 3–5 accompanied by S-parameter simulations for the studied transmission lines in QUCS [5]. Degree of agreement between the measured and simulated frequency profiles is used as a feedback parameter. In the end, we obtain $\epsilon_r \approx 10.6$ and $\tan \delta = 0.011$ at 145 GHz. This corresponds to the laminate power attenuation coefficient (α) of 0.47 dB/mm. These values are used to develop geometry of the photonic crystal intended for the implementation of a single-mode waveguide.

$$A = 1 - 10^{-0.1RL} - 10^{-0.1IL}, \quad (3)$$

$$\tan \delta = -\ln(A) c (2\pi F_{ss} \epsilon_r^{0.5} l_{di})^{-1}, \quad (4)$$

$$\alpha = -10 \log_{10} (A) l_{di}^{-1}. \quad (5)$$

Here A is the absorptance and c is the speed of light in vacuum.

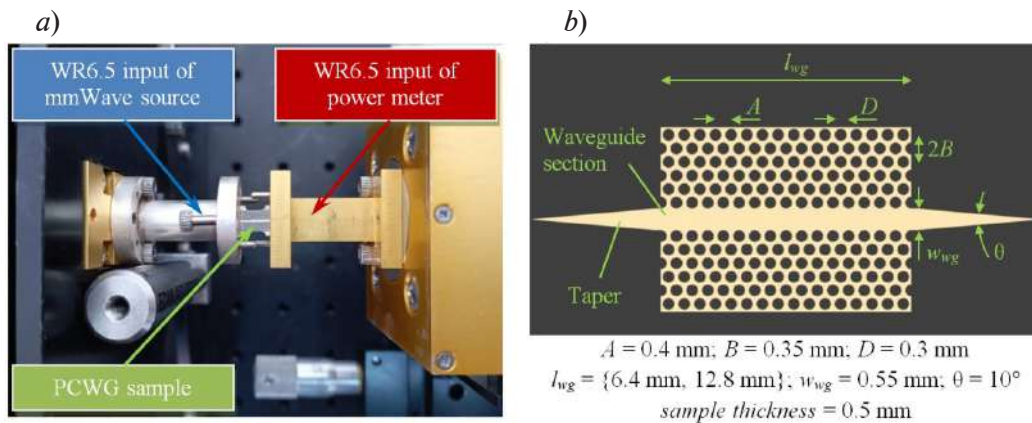


Fig. 2. Measurement setup with a PCWG sample installed (a); (b) geometry of the samples (b)

We fabricate PCWG samples with waveguide sections of several lengths (l_{wg}) to evaluate insertion losses due to the energy leakage into a free space (L_{wg}) and those due to the input/output coupling elements (L_{ce}). Thus, total insertion loss (L_{tot}) can be explicitly presented as a function of l_{wg} as $L_{tot}(l_{wg}) = 2L_{ce} + (\alpha + \alpha_{wg}) l_{wg}$ if measured in decibels. Here $\alpha_{wg} = L_{wg} / l_{wg-1}$ is the power attenuation coefficient attributed to the waveguide geometry.

Fig. 2, a provides photo of the fabricated PCWG sample installed between WR6.5 inputs of a solid state mmWave source and precision power meter. Referring to Fig. 2, b, PCWG section is integrated with input/output tappers, which ensure coupling with the TE₁₀ mode when inserted into a WR6.5 waveguide. Positioning of the sample together with the power meter with respect to the mmWave source is maintained with the aid of a precision 3D translation stage.

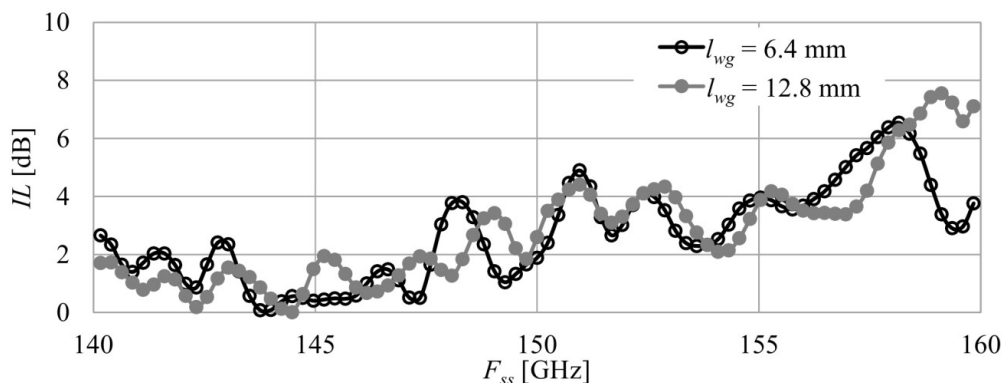


Fig. 3. Insertion losses of the fabricated PCWG samples (dielectric losses are calibrated out)

We measure $\alpha_{wg} = 0.02$ dB/mm and $L_{ce} = 0.2$ dB at 145 GHz. Detailed inspection of the fabricated PCWG samples reveals no violation of the photonic crystal geometry due to the fabrication tolerances. As provided in Fig. 3, frequency profiles of the samples insertion losses agree well, once absorption and scattering in FSD1020T are calibrated out. All together proves suitability of a 2D CNC machining for implementation of mmWave PCWG components.

Conclusion

In this paper, we report on the development and fabrication of a mmWave PCWG making use of an FSD1020T series PCB laminate. Dielectric properties of the laminate were preliminary evaluated by measuring reflection and transmission spectra of a WR6.5 rectangular waveguide section with a dielectric insert made of it. We measured $\epsilon_r \approx 10.6$ and $\tan\delta = 0.011$ at 145 GHz compared to those of 10.2 and 0.002 specified by the manufacturer at 10 GHz, respectively. The measured values were used to develop geometry of the photonic crystal intended for the implementation of a single-mode waveguide. Study of the PCWG samples fabricated via 2D CNC machining revealed power attenuation coefficient of 0.02 dB/mm attributed to the waveguide geometry. Frequency profiles of the samples insertion losses agreed well, and we observed no



violation of the developed geometry upon fabrication. All together proves suitability of a 2D direct machining, i.e., drilling and milling, for implementation of mmWave PCWG components.

REFERENCES

1. Ning, B., Tian, Z., Chen, Z., Han, C., Yuan, J., Li, S., Prospective beamforming technologies for ultra-massive MIMO in terahertz communications: A tutorial, arXiv preprint arXiv:2107.03032 (2021).
2. Withayachumnankul, W., Fujita, M., Nagatsuma, T., Integrated silicon photonic crystals toward terahertz communications, *Advanced Optical Materials*. 6 (16) (2021) 1800401.
3. ElecTrade-M. URL: http://www.eltm.ru/attach/catalog/v_2464_349.pdf. Accessed June 05, 2022.
4. MITS. URL: <http://www.mitspcb.com/edoc/11lab.htm>. Accessed June 05, 2022.
5. QUCS. URL: <http://qucs.sourceforge.net/index.html>. Accessed June 05, 2022.

THE AUTHORS

PRIKHODKO Anatoliy N.
anprihodko@hse.ru
ORCID: 0000-0002-4859-8975

SHURAKOV Alexander S.
alexander@rplab.ru
ORCID: 0000-0002-4671-7731

BELIKOV Ivan I.
ibelikov@hse.ru
ORCID: 0000-0002-7175-3451

GOLTSMAN Gregory N.
goltsman@rplab.ru
ORCID: 0000-0002-1960-9161

LVOV Andrey V.
andrei.lvov1707@yandex.ru
ORCID: 0000-0002-2969-7695

Received 15.08.2022. Approved after reviewing 15.08.2022. Accepted 05.09.2022.

Conference materials

UDC 537.86

DOI: <https://doi.org/10.18721/JPM.153.369>

Controlling asymmetric reflection of metasurfaces with loss

T. S. Vosheva¹, N. O. Bulatov¹, V. D. Burtsev¹✉, A. A. Khudykin¹, D. S. Filonov¹

¹ Moscow Institute of Physics and Technology (National Research University), Dolgoprudny, Russia

✉ burtsev.vd@phystech.edu

Abstract. Optical theorem, being the manifestation of the energy conservation law, relates the total scattering cross-section of a structure with its scattering in the forward direction. However, there are no fundamental restrictions on other directions. Strong asymmetric reflection and backscattering can be achieved in structures with magneto-electric coupling, taking place between constitutive elements. Here scattering properties of single meta-particles, based on near-field coupled electric and magnetic dipoles, and their arrays are analyzed. It is shown that dissipation is the key mechanism, responsible for the asymmetric backscattering behavior. While far-field scattering can serve as a sufficient loss mechanism in the case of single structures, ohmic dissipation should be added in the case of periodic arrays (metasurfaces). In this case, the practical realization is based on split-ring resonators, loaded with resistance, and wires, both printed on a PC board.

Keywords: metasurfaces, metamaterials, scattering, asymmetric responses

Funding: The research was supported by the Federal Academic Leadership Program “Priority 2030”.

Citation: Vosheva T. S., Bulatov N. O., Burtsev V. D., Khudykin A. A., Filonov D. S., Controlling asymmetric reflection of metasurfaces with loss. St. Petersburg State Polytechnical University Journal. Physics and Mathematics, 15 (3.3) (2022) 350–353. DOI: <https://doi.org/10.18721/JPM.153.369>

This is an open access article under the CC BY-NC 4.0 license (<https://creativecommons.org/licenses/by-nc/4.0/>)

Материалы конференции

УДК 537.86

DOI: <https://doi.org/10.18721/JPM.153.369>

Управление асимметричным отражением метаповерхностей с потерями

Т. С. Вошева¹, Н. О. Булатов¹, В. Д. Бурцев¹✉, А. А. Худыкин¹, Д. С. Филонов¹

¹ Московский физико-технический институт (национальный
исследовательский университет), Долгопрудный, Россия

✉ burtsev.vd@phystech.edu

Аннотация. Оптическая теорема, являющаяся частным случаем закона сохранения энергии, связывает полное сечение рассеяния структуры с ее рассеянием в направлении падающей волны. Однако для других направлений не существует фундаментальных ограничений. Здесь анализируются рассеивающие свойства одиночных метачастиц, через ближнее поле электрических и магнитных диполей, и их массивов. В частности, показано, что диссипация является ключевым механизмом, ответственным за асимметричное поведение обратного рассеяния. В то время как рассеяние в дальнем поле может служить достаточным механизмом потерь в случае одиночных структур, в случае периодических массивов (метаповерхностей) необходимо добавить омическую диссипацию. В данном случае практическая реализация основана на резонаторах с разрезным кольцом, нагруженных сопротивлением, и проводках, оба напечатаны на плате ПК.



Ключевые слова: метаповерхности, метаматериалы, рассеяние, асимметричные отклики

Финансирование: Исследование выполнено при поддержке федеральной программы академического лидерства «Приоритет 2030».

Ссылка при цитировании: Вошева Т. С., Булатов Н. О., Бурцев В. Д., Худыкин А. А., Филонов Д. С. Управление асимметричным отражением метаповерхностей с потерями // Научно-технические ведомости СПбГПУ. Физико-математические науки. 15 (3.3) (2022) 350–353. DOI: <https://doi.org/10.18721/JPM.153.369>

Статья открытого доступа, распространяемая по лицензии CC BY-NC 4.0 (<https://creativecommons.org/licenses/by-nc/4.0/>)

Introduction

Metamaterials have gained broad interest in the past decade, as they hold the promise for delivering new types of devices [1]. The basic functionalities of metamaterials are achieved by carefully designing the constitutive elements (meta-atoms) that govern the composite's behavior. Split ring resonators (SRR) and thin wires are often employed as the building blocks in many realizations, owing both to the fact that these structures are well understood theoretically [2], as well as the relative ease of their manufacturing. In order to achieve complex properties, meta-atoms often consist of more than one structure [3]. One of the desired functionalities that could be achieved with metamaterials is an asymmetric response. For example, asymmetric properties (and especially transmission) could find use in a range of applications, such as anti-reflection coatings [4] and many others.

Scattering characteristics of individual elements could be controlled by engineering their multipolar responses. For example, the so-called Huygen's elements rely on interference between electric and magnetic dipolar responses that suppress the backward scattering [5, 6]. Properties of magnetic and electric resonances could be tailored by particle's shape, e.g. core-shell geometry [7]. Meta-particles with nonsymmetrical scattering are discussed in detail in [8, 9, 10] where a few structures were studied analytically, including the omega, omega-Tellegen, and the chiral-moving particle. It was shown that periodic structures constructed from such meta-atoms could be used to create thin films with tunable nonsymmetrical transmission and reflection, e.g. [11, 12] and references therein. Here another example of an asymmetric meta-particle is proposed, putting an emphasis on reflection characteristics and its balance with the forward scattering.

The optical theorem [13] relates the forward scattering from an object with its total radar cross-section (RCS) and is a manifestation of the fundamental principle of causality. Remarkably, the theorem favors the forward direction over all the rest and there is no simple relation between the total RCS and the backward scattering, for example. Here a special type of meta-atom, having a symmetric forward and asymmetric backward scattering is studied. The hybrid magneto-electric particle (HMEP), consisting of a SRR and a thin wire (Fig. 1, *a*) is considered analytically, numerically and experimentally. The HMEP is shown to have asymmetric backscattering when illuminated by a plane wave from opposite directions. At the next stage, arrays of HMEPs are analyzed and asymmetric reflection characteristics are studied.

Results

Single HMEP particle was analyzed first. The theoretical description is based on coupled dipole model, which addresses the scattering phenomenon self-consistently. The key mechanism for the asymmetric scattering relies on peculiar coupling dynamics, where magnetic field of electric dipole, induces currents on the SRR, and electric field of the SRR is coupled to the wire (Fig. 1, *b*) [14]. Fig. 1, *c-f*, shows the numerical values of forward and total scattering cross sections of the HMEP. Blue and red lines correspond to opposite directions of the incident plane wave. For both positive and negative incident directions the scattering remains the same. Those numerical results underline the validity of the optical theorem, relating forward scattering to the RCS. As it could be explicitly seen, the theorem is satisfied and no distinction on the propagation

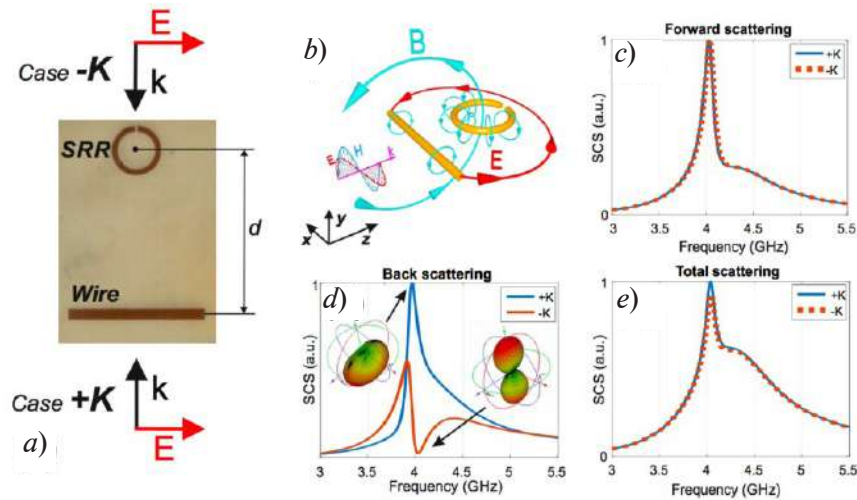


Fig. 1. Work [14], Fig. 1 (b), Fig. 3: Photograph of the HMEP particle (a). Schematics of magneto-electric coupling (b). Total and forward scattering spectra (c), (e). Asymmetric backscattering spectra (d)

direction could be made. Fig. 1, *d* is the main result, showing that the backscattering on the z-axis at a large distance away from the HMEP, strongly depends on the direction of incident field propagation. In the forward direction (+*k*) the field is strongly reflected around 4GHz while in the backward direction (-*k*) there is almost no backscattering at all in the same frequency range. To satisfy optical theorem, the scattered radiation should be redistributed along other directions in space. It is worth noting, that retarded Green's functions should be used for the accurate description of the asymmetric backscattering phenomenon. As the result, the relation to the radiation losses can be traced back.

To underline the impact of the loss mechanism on the asymmetric backscattering phenomenon, arrays of HMEPs were analyzed. In periodically structured subwavelength surfaces the diffraction losses plays a minor role, hence true Joule losses should be incorporated. This was done by attaching lumped resistive elements within the split rings. Characteristics of the arrays with different resistive loads were analyzed and the results appear in Fig. 2. Panel (a) shows the forward scattering (transmission) of the structure. It can be seen that exactly the same spectra are obtained for both incident directions, as it is expected from the reciprocity theorem. The backward scattering (reflection), on the other hand, strongly depends on the value of the lumped resistors.

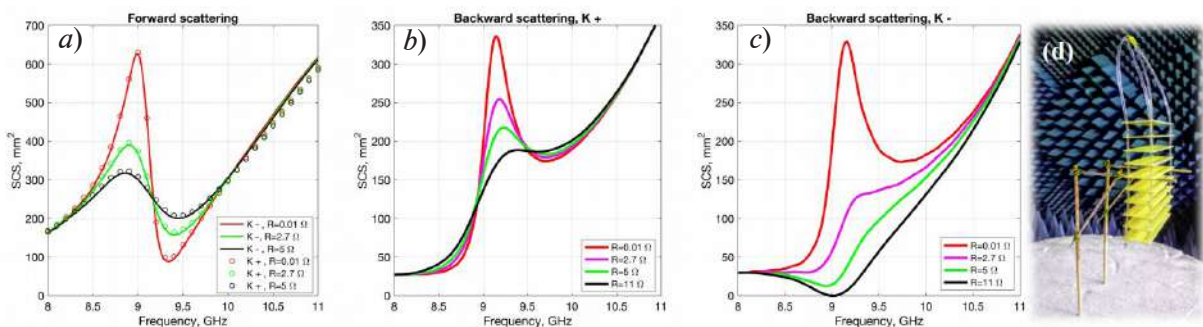


Fig. 2. Scattering cross-section of HMEP array (transmission) spectra (a). Reflection spectra for opposite directions of the incidence (b), (c). Colored lines correspond to different values of lumped resistors. (d) Photograph of the fabricated HMEP array

Fig. 2, *b* and *c* show the reflection spectra, obtained for opposite incident directions. While for the small value of the resistors the spectra are almost identical, strong asymmetry develops with the increase of the values. This behavior clearly demonstrates the nature of the effect – dissipation-inspired asymmetric reflection. Fig. 2, *d* shows the photograph of the fabricated HMEP array.



Conclusion

The effect of asymmetric backscattering and reflection was demonstrated analytically and numerically. It was shown that the radiation loss is responsible for the effect in the case of single meta-particle with a sufficient level of magneto-electric coupling between two constitutive elements. In the case of the array, composed of such particles, the effect of asymmetric reflection is inspired by Joule losses, which were implemented via inclusion of additional resistive elements within the split rings, forming the array.

REFERENCES

1. Engheta N., Ziolkowski R. W., *Metamaterials: Physics and Engineering Explorations*. Wiley-IEEE Press; 1 edition, 2006.
2. Sauviac B., Simovski C. R., Tretyakov S. A., Double split-ring resonators: Analytical modeling and numerical simulations, *Electromagnetics*, 24 (5) (2004) 317–338.
3. Karilainen A. O., Tretyakov S. A., Isotropic chiral objects with zero backscattering, *IEEE Trans. Antennas Propag.*, 60 (9) (2012) 4449–4452.
4. Wang K. X., Yu Z., Sandhu S., Liu V., Fan S., Condition for perfect antireflection by optical resonance at material interface, in *Optica*, 1 (6) (2014) 388.
5. Krasnok A. E., Miroshnichenko A. E., Belov P. A., Kivshar Y. S., All-dielectric nanoantennas, in *Proc. of SPIE*, 8806 (2013) 880626.
6. Karilainen A. O., Alitalo P., Tretyakov S. A., Chiral antenna element as a low backscattering sensor, *Proc. 5th Eur. Conf. Antennas Propag.*, 2011, pp. 1865–1868.
7. Liu W., Miroshnichenko A. E., Neshev D. N., Kivshar Y. S., Broadband Unidirectional Scattering by Magneto-Electric Core–Shell Nanoparticles, *ACS Nano*, 6 (6) (2012) 5489–5497.
8. Ra'di Y., Asadchy V., Tretyakov S., Total Absorption of Electromagnetic Waves in Ultimately Thin Layers, *IEEE Trans. Antennas Propag.*, 61 (9) (2013) 4606–4614.
9. Ra'di Y., Asadchy V. S., Tretyakov S. A., Tailoring Reflections From Thin Composite Metamirrors, *IEEE Trans. Antennas Propag.*, 62 (7) (2014) 3749–3760.
10. Ra'di Y., Asadchy V. S., Tretyakov S. A., One-way transparent sheets, *Phys. Rev. B*, 89 (7) (2014) 075109.
11. Pfeiffer C., Grbic A., Metamaterial Huygens' surfaces: Tailoring wave fronts with reflectionless sheets, *Phys. Rev. Lett.*, 110 (19) (2013) 197401.
12. Yazdi M., et al., A Bianisotropic Metasurface With Resonant Asymmetric Absorption, *IEEE Trans. Antennas Propag.*, 63 (7) (2015) 3004–3015.
13. Jackson J. D., *Classical Electrodynamics*, 3d ed. p. 500.
14. Kozlov V., Filonov D., Shalin A. S., Steinberg B. Z., Ginzburg P., Asymmetric Backscattering from the Hybrid Magneto-Electric Meta Particle, <http://arxiv.org/abs/1608.05980>, Aug. 2016.

THE AUTHORS

VOSHEVA Tatyana S.
Vosheva.ts@mipt.ru
ORCID: 0000-0002-5786-4972

KHUDYKIN Anton A.
khudykin.aa@mipt.ru
ORCID: 0000-0001-7992-7981

BULATOV Nikita O.
nikita.bulatov@phystech.edu
ORCID: 0000-0003-1145-3075

FILONOV Dmitry S.
dimfilonov@gmail.com
ORCID: 0000-0002-5394-8677

BURTSEV Vladimir D.
burtsev.vd@phystech.edu
ORCID: 0000-0002-7988-5213

Received 30.08.2022. Approved after reviewing 01.09.2022. Accepted 08.09.2022.

Conference materials

UDC 537.86

DOI: <https://doi.org/10.18721/JPM.153.370>

Features of microwave excitation signal formation in a quantum frequency standard

R. A. Dmitriev ¹✉, A. S. Grevtseva ¹, V. V. Davydov ²

¹ The Russian Institute of Radionavigation and Time, St. Petersburg, Russia;

² Peter the Great St. Petersburg Polytechnic University, St. Petersburg, Russia

✉ Rusher.official@gmail.com

Abstract. The necessity of upgrading the quantum frequency standard based on rubidium-87 atoms is substantiated. So in the design of quantum frequency standards, individual blocks are mainly upgraded. A solution is proposed to improve the design of the rubidium frequency standard. A block diagram of the part of the standard that is being upgraded is presented. The results of mathematical modeling of the output characteristics of the frequency converter are presented. A forecast of improvement of the metrological characteristics of the quantum frequency standard is obtained.

Keywords: quantum frequency standard, rubidium standard, satellite navigation systems, phase locked loop

Citation: Dmitriev R. A., Grevtseva A. S., Davydov V. V., Features of microwave excitation signal formation in a quantum frequency standard. St. Petersburg State Polytechnical University Journal. Physics and Mathematics, 15 (3.3) (2022) 354–359. DOI: <https://doi.org/10.18721/JPM.153.370>

This is an open access article under the CC BY-NC 4.0 license (<https://creativecommons.org/licenses/by-nc/4.0/>)

Материалы конференции

УДК 537.86

DOI: <https://doi.org/10.18721/JPM.153.370>

Особенности формирования сигнала СВЧ возбуждения в квантовом стандарте частоты

Р. А. Дмитриев ¹✉, А. С. Гревцева ¹, В. В. Давыдов ²

¹ Российский институт радионавигации и времени, Санкт-Петербург, Россия;

² Санкт-Петербургский политехнический университет Петра Великого, Санкт-Петербург, Россия

✉ Rusher.official@gmail.com

Аннотация. Обоснована необходимость модернизации квантового стандарта частоты на атомах рубидия-87. Отмечено, что в конструкции квантовых стандартов частоты в основном модернизации подвергаются отдельные блоки. Предлагается решение по усовершенствованию конструкции рубидиевого стандарта частоты. Представлена структурная схема части стандарта, которая подвергается модернизации. Представлены результаты математического моделирования выходных характеристик преобразователя частоты. Получен прогноз улучшения метрологических характеристик квантового стандарта частоты.

Ключевые слова: квантовый стандарт частоты, рубидиевый стандарт, системы спутниковой навигации, фазовая автоподстройка частоты

Ссылка при цитировании: Дмитриев Р. А., Гревцева А. С., Давыдов В. В. Особенности формирования сигнала СВЧ возбуждения в квантовом стандарте частоты. // Научно-технические ведомости СПбГПУ. Физико-математические науки. 2022. Т. 15. № 3.3. С. 354–359. DOI: <https://doi.org/10.18721/JPM.153.370>

Статья открытого доступа, распространяемая по лицензии CC BY-NC 4.0 (<https://creativecommons.org/licenses/by-nc/4.0/>)

Introduction

In a world without reference sources of timestamps and frequencies, it is now impossible to transmit large amounts of information, conduct long-term physical experiments, and others [1-10]. Increased attention is paid to determining the exact time in coordinate determination systems [11-15], especially in satellite navigation systems, where the mismatch of satellite time scales leads to large measurement errors [16-21]. These systems are the main ones in determining the coordinates of objects when solving various tasks of navigation, environmental monitoring and others [16-19, 21-27].

The operating satellite navigation constellations (Russian GLONASS, European GALILEO, American (USA) GPS and Chinese BSD) actively use quantum frequency standards (QFS) to determine the exact time [1, 17, 18, 27-30]. Among quantum standards in satellite communication systems, rubidium QFSs are most widely used due to their small size and low cost in comparison with other types of standards.

At present, with the development of electronic equipment, the requirements for the accuracy of satellite navigation systems are constantly increasing, which makes the task of their modernization especially urgent [30-32]. This paper discusses one of the possible solutions for modernizing the design of a quantum frequency standard based on rubidium-87 atoms.

Modernization a part to design of the rubidium frequency standard

The principle of the QFS operation is based on automatic tuning of the crystal oscillator (CO) frequency to the value of the quantum transition frequency in optically oriented Rb-87 atoms. To implement the tuning of the CO frequency, the working cell of the atomic discriminator (DA) is irradiated with a microwave signal, the frequency of which corresponds to the frequency of the quantum transition of excited rubidium-87 atoms. In the case of a deviation of the frequency of the microwave signal from the value of the frequency of the resonant transition, an error signal (ES) is generated, according to which the CO is adjusted. Therefore, one of the important points in the functioning of the QFC is the formation of a microwave signal.

In this paper, a microwave signal with a frequency of 6834.7 MHz is proposed to be synthesized using a two-ring phase locked loop (PLL) system.

The PLL system uses the principle of comparing the phase of the output signal of a voltage-controlled oscillator (VCO) with the signal of a reference oscillator. When they deviate, the phase detector generates an error signal proportional to the phase difference. The signal from the

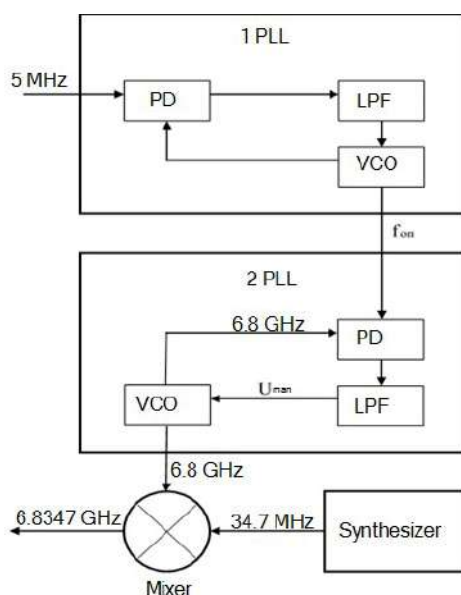


Fig. 1. Frequency converter circuit for quantum frequency standard based on rubidium-87 atoms

PD goes to the low-pass filter and then to the VCO, adjusting it so that the phase difference is zero.

The phase detector operates at the comparison frequency f_{cp} , for this the frequencies of the reference and output signals are preliminarily divided by the required coefficients. By selecting the division coefficients, the required frequency is obtained at the input of the phase detector (PD). The output frequency is determined by the formula:

$$F_{out} = \frac{F_{ref} \times K}{K_{ref}}, \quad (1)$$

where F_{out} is the output frequency, F_{ref} is reference signal frequency, K is the division factor of the input frequency, K_{ref} is the division factor of reference frequency.

The block diagram of the formation of a microwave signal (Fig. 1) consists of several parts (blocks). The first part is a 100 MHz controlled oscillator with phase locked loop. The output signal of this generator is then used as a reference. The second part is a miniature VCO module with a PLL with a frequency of 6.8 GHz. To create the exact value of the quantum transition frequency at the final stage, it is necessary to add a fractional component equal to 34.7 MHz to the output signal. The fractional component of 34.7 MHz is created using a special synthesizer (the third part of the circuit) and mixed with a mixer to the 6.8 GHz output signal.

New shaping circuitry includes a 6.8 GHz voltage-controlled oscillator. To reduce the weight and size characteristics, the use of a VCO with a PLL in the form of a compact microwave module was chosen. An electrical circuit was developed for its operation and control.

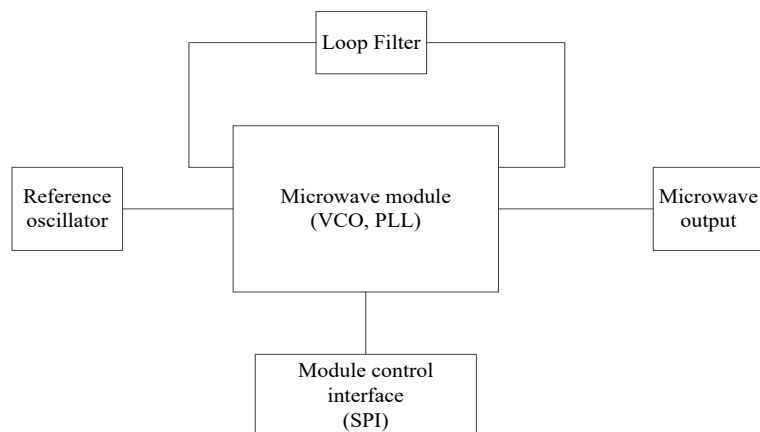


Fig. 2. Frequency converter circuit for quantum frequency standard based on rubidium-87 atoms

This scheme is shown in Fig. 2.

The scheme in Fig. 2 includes:

- 100 MHz reference oscillator (previously developed),
- loop filter
- Microwave module (VCO with PLL) at 6.8 GHz.

The microwave module is controlled by SPI.

Frequency converter simulation

The frequency converter circuit shown in Fig. 2 was modeled in the ADIsim PLL program. For this, the optimal VCO (VCO) was selected from the catalog of this program, and the characteristics of the reference signal were also set (the layout of the reference frequency generator was developed earlier). As a result of the simulation, the elements of the loop filter were selected.

The ADIsim PLL program allows you to evaluate the phase noise of individual functional units of the circuit, as well as the overall level of phase noise of the entire system. The simulation results are shown in Table 1 and in Fig. 3. The Total column estimates the total phase noise level of the system.



Table 1

Phase Noise Table

Arequency	Total	VCO	Ref	Chip	Filter
100	-89.76	-143.8	-93.39	-92.23	-159.0
1.00k	-101.2	-123.8	-113.3	-101.5	-139.0
10.0k	-102.1	-103.9	-130.1	-107.3	-119.0
100k	-89.94	-90.15	-131.5	-107.2	-105.6
1.00M	-111.8	-111.8	-165.0	-140.9	-134.5

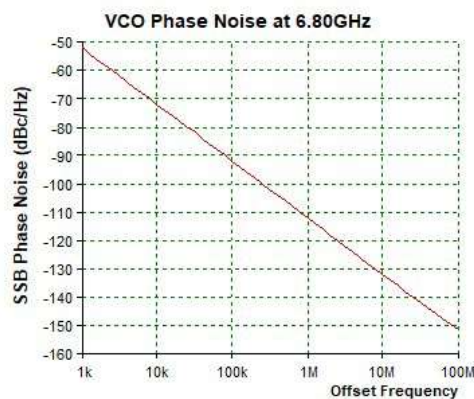


Fig. 3. The simulation results

Conclusion

The developed design of the QFS has several significant advantages. First, the use of an indirect synthesis method, namely a phase-locked loop system, allows a cleaner spectrum of the output signal to be obtained. Secondly, the formation of the microwave signal at all stages of the new circuit is controlled; it is possible to precisely adjust the signal frequency to the frequency of the quantum transition of rubidium-87 atoms. This makes it possible to reduce the error in establishing the actual value of the frequency of the output signal of the rubidium RFS, which improves the stability of the device.

REFERENCES

1. Wang D., Rud V. Y., Prospective directions for the development of microwave frequency standards for satellite navigation systems, *Journal of Physics: Conference Series*. 2086 (1) (2021) 012073.
2. Semenov V. V., Nikiforov N. F., Ermak S. V., Calculation of stationary magnetic resonance signal in optically oriented atoms induced by a sequence of radio pulses, *Soviet journal of Communications Technology and Electronics*. 36 (4) (1991) 59–63.
3. Lukashev N. A., Davydov R. V., Glinushkin A. P., Rud' V. Y., Improving characteristics of microwave frequency standard on Hg-199 ions for telecommunication systems, *Journal of Physics: Conference Series*. 1326 (1) (2019) 012046.
4. Mihov E. D., Nepomnyashchiy O. V., Selecting informative variables in the identification problem *Journal of Siberian Federal University – Mathematics and Physics*. 9 (4) (2016) 473–480.
5. Ryzhenko I. N., Lutsenko A. E., Varygin O. G., Nepomnyashchiy O. V., Carrier compensation mode implementation in satellite communication channels. In: *Proceedings of 2019 International Siberian Conference on Control and Communications, SIBCON 2019*, vol. 8729665 (2019) 23–29.
6. Davydov R., Antonov V., Moroz A., Parameter Control System for a Nuclear Power Plant Based on Fiber-Optic Sensors and Communication Lines, In: *IEEE International Conference on*

Electrical Engineering and Photonics (EExPolytech), Saint-Petersburg, Russia, 13-15 October 2019. vol. 8906791 (2019) 295–297.

7. **Petrov A. A., Myazin N. S., Kaganovskiy V. E.**, Rubidium atomic clock with improved metrological characteristics for satellite communication system, *Lecture Notes in Computer Science (including subseries Lecture Notes in Artificial Intelligence and Lecture Notes in Bioinformatics)*. 10531 LNCS (2017) 561–568.

8. **Popovskiy N., Gureeva I., Rud V. Y.**, Development to high-rate fiber optic communication line with code division multiplexing, *ACM International Conference Proceeding Series*. 2021 (2021) 527–531.

9. **Popovskiy N. I., Rud V. Yu.** Features of the construction of photonic integrated circuits for communication systems *Journal of Physics: Conference Series*. 2086(1) (2021) 012163.

10. **Davydov V. V., Kruzhalov S. V., Vologdin V. A.**, Concerning some features of studying the flow of liquid media by a Doppler method: *Journal of Optical Technology (A Translation of Opticheskii Zhurnal)*. 84 (8) (2017) 568–573.

11. **Fadeenko V. B., Pchelkin G. A., Davydov V. V., Rud V. Yu.**, Features of the transmission of microwave signals in the range of 8-12 GHz in the maritime radar station over fiber-optic communication line, *Journal of Physics: Conference Series*. 1400 (4) (2019) 044010.

12. **Ermak S. V., Karseev A. U., Velichko E. N.**, Fiber-optic super-high-frequency signal transmission system for sea-based radar station *Lecture Notes in Computer Science (including subseries Lecture Notes in Artificial Intelligence and Lecture Notes in Bioinformatics)*. 8638 LNCS (2014) 694–702.

13. **Sharova N. V., Fedorova E. V., Vologdin V. A.**, Fiber-optics system for the radar station work control, *Lecture Notes in Computer Science (including subseries Lecture Notes in Artificial Intelligence and Lecture Notes in Bioinformatics)*. 9247 (2015) 712–721.

14. **Lenets V. A., Tarasenko M. Yu., Rodygina N. S.**, New method for testing of antenna phased array in X frequency range, *Journal of Physics: Conference Series*. 1038 (1) (2018) 012037.

15. **Tarasenko M. Yu., Lenets V. A., Malanin K. Yu., Akulich N. V.**, Features of use direct and external modulation in fiber optical simulators of a false target for testing radar station, *Journal of Physics: Conference Series*. 1038 (1) (2018) 012035.

16. **Arinushkina K. G., Valov A. P.**, Digital processing of optical signals in the frequency standard based in rubidium atoms – 87, In: *Proceedings of ITNT 2021 - 7th IEEE International Conference on Information Technology and Nanotechnology, 2021 Samara, Russia, 20-24 September 2021*. vol. 44026298 (2021) 44–49.

17. **Bandi T., Affolderbach C., Calosso C. E., et al.**, High-performance laser-pumped rubidium frequency standard for satellite navigation, *Electron. Lett.* 47 (2001) 698–699.

18. **Grevtseva A., Rud V.**, Method of processing velocity increase of measuring results of quantum frequency standard parameters for information transfer velocity increase in satellite communication systems, *CEUR Workshop Proceedings*. 2667 (2020) 15–18.

19. **Petrov A. A.**, New scheme of the microwave signal formation for quantum frequency standard on the atoms of caesium-133 *Journal of Physics: Conference Series*. 769(1) (2016) 012065.

20. **Kuzmin M. S., and Rogov S. A.**, On the use of a multi-raster input of one-dimensional signals in two-dimensional optical correlators, *Computer Optics*. 43 (3) (2019) 391–396.

21. **Lukashev N. A., Moroz A. V.**, Compact microwave frequency standard on Hg-199 ions for navigation systems, *Journal of Physics: Conference Series*. 1236 (1) (2019) 012068.

22. **Valov A. P., Arinushkina K. G.**, The use of digital data processing to improve the metrological characteristics of the rubidium frequency standard, *Journal of Physics: Conference Series*. 2086 (1) (2021) 012070.

23. **Petrov A. A., Grebenikova N. M.**, Some Directions of Quantum Frequency Standard Modernization for Telecommunication Systems, *Lecture Notes in Computer Science (including subseries Lecture Notes in Artificial Intelligence and Lecture Notes in Bioinformatics)*. 11118 LNCS (2018) 641–648.

24. **Petrov A. A.**, Improvement frequency stability of caesium atomic clock for satellite communication system, *Lecture Notes in Computer Science (including subseries Lecture Notes in Artificial Intelligence and Lecture Notes in Bioinformatics)*. 9247 (2015) 739–744.



25. **Lukashev N. A., Rud V. Yu.**, Microwave frequency standard on Hg-199 ions for space stations and vehicles *Journal of Physics: Conference Series*. 1400 (2) (2019) 022050.
26. **Petrov A. A.**, Digital Frequency Synthesizer for ¹³³Cs-Vapor Atomic Clock, *Journal of Communications Technology and Electronics*. 62 (3) (2017) 289–293.
27. **Petrov A. A., Shabanov V. E., Zalyotov D. V., Bulyanitsa A. L., Shapovalov D. V.**, Modernization of the frequency synthesizer of cesium atomic clock, *IEEE International Conference on Electrical Engineering and Photonics, EExPolytech 2018, Saint-Petersburg, October 2018*. vol. 8564389 (2018) 52–55.
28. **Riehle F.**, Frequency standard. Basic and applications. WILEY-VCH Verlag GmbH Co. KGaA: New-York, 2008.
29. **Petrov A. A., Zaletov D. V., Shapovalov D. V.**, Peculiarities of Constructing a Scheme for Formation of a Microwave Excitation Signal in a Cesium Atomic Clock, *Journal of Communications Technology and Electronics*. 66 (3) (2021) 295–299.
30. **Grevtseva A. S., Dmitriev R. A.**, Features of the formation of the frequency of the microwave excitation signal in the quantum frequency standard on rubidium atoms – 87, *Journal of Physics: Conference Series*. 2086 (1) (2021) 012055.
31. **Zalyotov D. V., Shabanov V. E., Shapovalov D. V.**, Features of direct digital synthesis applications for microwave excitation signal formation in quantum frequency standard on the atoms of cesium, *Journal Physics: Conference Series*. 1124 (1) (2018) 041004.
32. **Valdv A. P., Lukashev N. A., Grebenikova N. M.**, Improving performance of quantum frequency standard with laser pumping, *Proceedings of 18th International conference of Laser Optics ICLO-2018, Saint-Petersburg, Vol. 8435889 (2019) 271*.

THE AUTHORS

DMITRIEV Roman A.
Rusher.official@gmail.com
ORCID: 0000-0002-2964-1165

DAVYDOV Vadim V.
davydov_vadim66@mail.ru

GREVTSEVA Anna S.
annagrevtseva@mail.ru
ORCID: 0000-0001-6308-4035

Received 14.07.2022. Approved after reviewing 26.07.2022. Accepted 26.07.2022.

THEORETICAL PHYSICS

Conference materials

UDC 535.14

DOI: <https://doi.org/10.18721/JPM.153.371>

Dynamics of the uncertainty value of quadratures for bosonic quantum states

S. S. Medvedeva ¹✉, A. A. Gaidash ^{1,2}, G. P. Miroshnichenko ¹,
A. D. Kiselev ^{1,3}, A. V. Kozubov ^{1,2}

¹ ITMO University, St. Petersburg, Russia;

² Steklov Mathematical Institute of Russian Academy of Sciences, Moscow, Russia;

³ St. Petersburg State University, St. Petersburg, Russia

✉ ss_medvedeva@itmo.ru

Abstract. In this work we consider the time evolution of the mean values of the first and second moments of the quadrature operators for an arbitrary bosonic quantum state in a single mode transmitted through an optical fiber channel. We utilize the density matrix formalism and the open quantum systems theory and investigate Lindblad master equation in order to derive expressions for the dynamics of mentioned field observables. Obtained expressions contain terms characterized by high frequency oscillations. For the purpose of elimination of these terms we find the envelope functions for the values of the first and second moments of the quadrature operators.

Keywords: quantum optics, open quantum systems theory, quadratures, single mode

Funding: This study was funded by the Ministry of Science and Education of the Russian Federation project title “Quantum dynamics and correlation measurements of multimode photonic systems and topologically nontrivial polarization states” grant No. 2019-0903.

Citation: Medvedeva S. S., Gaidash A. A., Miroshnichenko G. M., Kiselev A. D., Kozubov A. V., Dynamics of the uncertainty value of quadratures for bosonic quantum states. St. Petersburg State Polytechnical University Journal. Physics and Mathematics, 15 (3.3) (2022) 360–364. DOI: <https://doi.org/10.18721/JPM.153.371>

This is an open access article under the CC BY-NC 4.0 license (<https://creativecommons.org/licenses/by-nc/4.0/>)

Материалы конференции

УДК 535.14

DOI: <https://doi.org/10.18721/JPM.153.371>

Динамика неопределенности квадратур бозонных квантовых состояний

С. С. Медведева ¹✉, А. А. Гайдаш ^{1,2}, Г. П. Мирошниченко ¹,
А. Д. Киселёв ^{1,3}, А. В. Козубов ^{1,2}

¹ Университет ИТМО, Санкт-Петербург, Россия;

² Математический институт им. В. А. Стеклова РАН, Москва, Россия;

³ Санкт-Петербургский государственный университет, Санкт-Петербург, Россия

✉ ss_medvedeva@itmo.ru

Аннотация. В работе рассматривается временная эволюция первых и вторых моментов квадратур одномодовых фотонных квантовых состояний, передаваемых по оптоволоконному каналу. При использовании формализма матриц плотности и теории открытых квантовых систем выведены выражения, описывающие динамику указанных выше полевых наблюдаемых. Для исключения из анализируемых выражений членов, характеризующихся высокочастотными осцилляциями, были найдены огибающие значений.



Ключевые слова: квантовая оптика, теория открытых квантовых систем, квадратуры, одномодовый случай

Финансирование: Работа выполнена в рамках Государственного задания «Квантовая динамика и корреляционные изменения многомодовых фотонных систем и топологически нетривиальных поляризационных состояний» (код темы 2019-0903).

Ссылка при цитировании: Медведева С. С., Гайдаш А. А., Мирошниченко Г. П., Киселёв А. Д., Козубов А. В. Динамика неопределенности квадратур бозонных квантовых состояний // Научно-технические ведомости СПбГПУ. Физико-математические науки. 2022. Т. 15. № 3.3. С. 360–364. DOI: <https://doi.org/10.18721/JPM.153.371>

Статья открытого доступа, распространяемая по лицензии CC BY-NC 4.0 (<https://creativecommons.org/licenses/by-nc/4.0/>)

Introduction

One of the main constraints on the technological utilization of the unique quantum features such as superposition or squeezing lies in decoherence: the detrimental influence of environment leads any quantum system to the loss of its beneficial quantum features [1]. A theory that may be employed to investigate the evolution of quantum systems considering decoherence is open quantum systems approach [2]. Within this theory different methods are being used; in our research we focus on solving a master equation for a density matrix of a quantum state.

Materials and Methods

In order to give a description of a nonunitary dynamics of a bosonic quantum state study the Liouville master equation that is a special case of the Gorini–Kossakowski–Sudarshan–Lindblad (GKSL) master equation [3]:

$$\begin{cases} \frac{\partial}{\partial t} \hat{\rho}(t) = -i[\hat{H}, \hat{\rho}(t)] + \hat{\Gamma} \hat{\rho}(t), \\ \hat{\rho}(t)|_{t=0} = \hat{\rho}_0 \end{cases}, \quad (1)$$

where Hamiltonian of the system is

$$\hat{H} = \omega \left(\hat{a}^\dagger \hat{a} + \frac{1}{2} \right), \quad (2)$$

here \hat{a} , (\hat{a}^\dagger) are the annihilation (creation) operator, ω is the frequency of the optical mode, and relaxation superoperator acting on a density matrix of a state has the form:

$$\hat{\Gamma} \hat{\rho}(t) = -\frac{\gamma}{2} (n_T + 1) (\hat{a}^\dagger \hat{a} \hat{\rho}(t) + \hat{\rho}(t) \hat{a}^\dagger \hat{a} - 2\hat{a} \hat{\rho}(t) \hat{a}^\dagger) - \frac{\gamma n_T}{2} (\hat{a} \hat{a}^\dagger \hat{\rho}(t) + \hat{\rho}(t) \hat{a} \hat{a}^\dagger - 2\hat{a}^\dagger \hat{\rho}(t) \hat{a}), \quad (3)$$

where γ denotes the thermalization rate, n_T denotes the mean number of thermal photons.

The explicit solution to this equation may be found, for example, with the use of SU(1,1) algebra formalism [4], Jordan mapping [5]. In this investigation we act by the quadrature operators [6]:

$$\begin{aligned} \hat{q} &= \frac{1}{\sqrt{2}} (\hat{a}^\dagger + \hat{a}), \\ \hat{p} &= \frac{i}{\sqrt{2}} (\hat{a}^\dagger - \hat{a}), \end{aligned} \quad (4)$$

of interest on the master equation, apply the trace operation and then solve the resulting equation to obtain the time-dependence of a mean value of an operator [7, 8].

Results and Discussion

Firstly, utilizing the method described in the above, we obtain evolutionary equations for the first moment of quadratures operators:

$$\begin{aligned}\langle q \rangle &= e^{-\frac{\gamma}{2}t} (\langle q_0 \rangle \cos \omega t + \langle p_0 \rangle \sin \omega t), \\ \langle p \rangle &= e^{-\frac{\gamma}{2}t} (\langle p_0 \rangle \cos \omega t - \langle q_0 \rangle \sin \omega t),\end{aligned}\tag{5}$$

where q_0, p_0 are the mean values of the quadrature operators at the initial time moment:

$$\begin{aligned}\langle q_0 \rangle &\equiv Tr \{ \hat{q} \hat{\rho}_0 \}, \\ \langle p_0 \rangle &\equiv Tr \{ \hat{p} \hat{\rho}_0 \}.\end{aligned}\tag{6}$$

Eqs. (5) show that the time dependence of both quadrature operators' mean values has the form of high frequency (optical frequency ω) damped oscillations. However, the part of steady-state oscillations does not provide the essential information concerning the dynamics of the quadratures. Thus we find the envelope function:

$$f_{env.}(t) = \pm \sqrt{\langle q_0 \rangle^2 + \langle p_0 \rangle^2} e^{-\frac{\gamma}{2}t},\tag{7}$$

that has an identical form for both $q(t)$ and $p(t)$.

Secondly, keeping in mind that some quantum states, for example, squeezed vacuum states, possess unique qualities which can be observed through the use of the second order of an operator, we derive the equations for the squares $\langle q^2 \rangle, \langle p^2 \rangle$:

$$\begin{aligned}\langle q^2 \rangle &= \frac{1}{2} (e^{-\gamma t} (c_0 + a_0 \cos 2\omega t + b_0 \sin 2\omega t - d_0) + d_0), \\ \langle p^2 \rangle &= \frac{1}{2} (e^{-\gamma t} (c_0 - a_0 \cos 2\omega t - b_0 \sin 2\omega t - d_0) + d_0),\end{aligned}\tag{8}$$

and variances $\Delta q(t), \Delta p(t)$ of the quadratures:

$$\begin{aligned}\Delta q &= \frac{1}{2} (e^{-\gamma t} (C_0 + A_0 \cos 2\omega t + B_0 \sin 2\omega t - d_0) + d_0), \\ \Delta p &= \frac{1}{2} (e^{-\gamma t} (C_0 - A_0 \cos 2\omega t - B_0 \sin 2\omega t - d_0) + d_0),\end{aligned}\tag{9}$$

where coefficients are

$$\begin{aligned}a_0 &= \langle q_0^2 \rangle - \langle p_0^2 \rangle, & A_0 &= \Delta q_0 - \Delta p_0, \\ b_0 &= \langle qp_0 \rangle + \langle pq_0 \rangle, & B_0 &= \langle qp_0 \rangle + \langle pq_0 \rangle - 2\langle q_0 \rangle \langle p_0 \rangle, \\ c_0 &= \langle q_0^2 \rangle + \langle p_0^2 \rangle, & C_0 &= \Delta q_0 + \Delta p_0, \\ d_0 &= 2n_T + 1,\end{aligned}\tag{10}$$

$\Delta q_0, \Delta p_0$ are the mean value variances of the quadrature operators at the initial moment of time:

$$\begin{aligned}\Delta q_0 &\equiv \langle q_0^2 \rangle - \langle q_0 \rangle^2, \\ \Delta p_0 &\equiv \langle p_0^2 \rangle - \langle p_0 \rangle^2,\end{aligned}\tag{11}$$

and $\langle q_0^2 \rangle, \langle qp_0 \rangle$ and $\langle pq_0 \rangle, \langle p_0^2 \rangle$ are the constituents of the covariance matrix:

$$\begin{bmatrix} \langle q_0^2 \rangle & \langle qp_0 \rangle \\ \langle pq_0 \rangle & \langle p_0^2 \rangle \end{bmatrix} \equiv \begin{bmatrix} Tr \{ \hat{q}^2 \hat{\rho}_0 \} & Tr \{ \hat{q} \hat{p} \hat{\rho}_0 \} \\ Tr \{ \hat{p} \hat{q} \hat{\rho}_0 \} & Tr \{ \hat{p}^2 \hat{\rho}_0 \} \end{bmatrix}\tag{12}$$



It can be seen that the dynamics of both the squares and variances incorporates high frequency (optical frequency) damped oscillations likewise. Thus, we proceed to determine the envelope function of the dynamics. We find bend points for multiplier of $e^{-\gamma t}$ from, for example, Eqs. (9):

$$\begin{aligned}\frac{\partial}{\partial t}(C_0 + A_0 \cos 2\omega t + B_0 \sin 2\omega t - d_0) &= 0, \\ \frac{\partial}{\partial t}(C_0 - A_0 \cos 2\omega t - B_0 \sin 2\omega t - d_0) &= 0,\end{aligned}\tag{13}$$

After a simplification we obtain the following envelope functions of the dynamics of the squares F_{env} :

$$F_{env.}(t) = \frac{1}{2} \left(\left(c_0 \pm \sqrt{a_0^2 + b_0^2} - d_0 \right) e^{-\gamma t} + d_0 \right),\tag{14}$$

and variances Δf_{env} of the quadratures:

$$\Delta f_{env.}(t) = \frac{1}{2} \left(\left(C_0 \pm \sqrt{A_0^2 + B_0^2} - d_0 \right) e^{-\gamma t} + d_0 \right).\tag{15}$$

Obtained expressions are of a more utility considering technical realisation of the quadratures detection [9].

Conclusion

Utilizing the method of solving GKSL master equation for a mean value of a particular operator we obtain the expressions of time evolution for the first and second moments of the quadrature operators for an arbitrary bosonic quantum state in a single mode transmitted through an optical fiber channel. Moreover, we find the envelope functions for the obtained expressions for the purpose of detection that are of a more utility considering technical realisation.

REFERENCES

1. **Breuer H.-P., Petruccione F.**, The theory of open quantum systems. Oxford University Press on Demand. (2002).
2. **Joos E., Zeh H. D., Kiefer C., Giulini D. J., Kupsch J., Stamatescu I. O.**, Decoherence and the appearance of a classical world in quantum theory. Springer Science & Business Media. (2013).
3. **Carmichael H.**, An open systems approach to quantum optics: lectures presented at the Université Libre de Bruxelles, October 28 to November 4, 1991. Springer Science & Business Media. 18 (2009).
4. **Gaidash A. A., Kozubov A. V., Miroschnichenko G. P.**, Dissipative dynamics of quantum states in the fiber channel. Physical Review A. 102 (2) (2020) 023711.
5. **Gaidash A. A., Kozubov A.V., Miroschnichenko G.P., Kiselev A.D.**, Quantum dynamics of mixed polarization states: effects of environment-mediated intermode couplings. Optical Society of America. 38 (9) (2021) 2603–2611.
6. **Scully M. O., Zubairy M. S.**, Quantum optics. American Association of Physics Teachers. (1999).
7. **Gaidash A. A., Kozubov A. V., Medvedeva S. S., Miroschnichenko G. P.**, The Influence of Signal Polarization on Quantum Bit Error Rate for Subcarrier Wave Quantum Key Distribution Protocol. Multidisciplinary Digital Publishing Institute. 22 (12) (2020) 1393.
8. **Medvedeva S. S., Gaidash A. A., Kozubov A. V., Miroschnichenko G. P.**, Dynamics of field observables in quantum channels. IOP Publishing. 1984 (1) (2021) 012007.
9. **Laudenbach F., Pacher C., Fung C. H. F., Poppe A., Peev M., Schrenk B., Hübel H.** Continuous-variable quantum key distribution with Gaussian modulation—the theory of practical implementations. Advanced Quantum Technologies, 1 (1) (2018) 1800011.

THE AUTHORS

MEDVEDEVA Svetlana S.

ss_medvedeva@itmo.ru

ORCID: 0000-0001-5249-5955

KISELEV Alexei D.

adkiselev@itmo.ru

ORCID: 0000-0002-1023-3284

GAIDASH Andrei A.

andrei_gaidash@itmo.ru

ORCID: 0000-0001-9870-9285

KOZUBOV Anton V.

avkozubov@itmo.ru

ORCID: 0000-0002-4468-5406

MIROSHNICHENKO George M.

gpmiroshnichenko@itmo.ru

ORCID: 0000-0002-4265-8818

Received 18.07.2022. Approved after reviewing 18.07.2022. Accepted 18.07.2022.

Conference materials

UDC 530.145

DOI: <https://doi.org/10.18721/JPM.153.372>

Phase-time-encoding MDI QKD tolerant to detector imperfections

I. V. Petrov ¹✉, D. D. Menskoy ¹, A. S. Tayduganov ¹

¹ National University of Science and Technology MISiS, Moscow, Russia

✉ i.petrov@goqrates.com

Abstract. Measurement-device-independent quantum key distribution (MDI QKD) allows to eliminate the single-photon detector (SPD) vulnerabilities, increase the communication distance limits, and construct a multiple users key distribution network. Nevertheless, detector imperfections are able to decrease the secret key rate and maximum distance by orders of magnitude. In this work we propose a model of large SPD's dead time for the phase-time-encoding MDI QKD. We also propose a modified measurement device (Charlie) scheme with four detectors which is able to partially restore the sifted key loss caused by dead time.

Keywords: quantum cryptography, MDI QKD, single-photon detector, dead time

Funding: This research was ordered by JSCo “RZD”.

Citation: Petrov I. V., Menskoy D. D., Tayduganov A. S., Phase-time-encoding MDI QKD tolerant to detector imperfections. St. Petersburg State Polytechnical University Journal. Physics and Mathematics, 15 (3.3) (2022) 365–370. DOI: <https://doi.org/10.18721/JPM.153.372>

This is an open access article under the CC BY-NC 4.0 license (<https://creativecommons.org/licenses/by-nc/4.0/>)

Материалы конференции

УДК 530.145

DOI: <https://doi.org/10.18721/JPM.153.372>

Протокол КРК с НЦУ с фазово-временным кодированием, устойчивый к неидеальности детекторов

И. В. Петров ¹✉, Д. Д. Менской ¹, А. С. Тайдуганов ¹

¹ Национальный исследовательский технологический университет МИСиС, Москва, Россия

✉ i.petrov@goqrates.com

Аннотация. Квантовое распределение ключа с независимым центральным узлом (КРК с НЦУ), позволяет устранить уязвимости детектора одиночных фотонов (ДОФ). Тем не менее, несовершенство детектора может снизить скорость секретного ключа и максимальное расстояние на порядки. В этой работе мы предлагаем модель большого мертвого времени ДОФ для фазово-временного кодирования КРК с НЦУ. Мы также предлагаем модифицированную схему измерительного устройства (Чарли) с четырьмя детекторами, которая способна частично восстановить потерю просеянного ключа, вызванную мертвым временем.

Ключевые слова: квантовая криптография, КРК с НЦУ, MDI QKD, однофотонный детектор, мертвое время

Финансирование: Исследовательская работа выполнена по заказу ОАО «РЖД».

Ссылка при цитировании: Петров И. В., Менской Д. Д., Тайдуганов А. С. Протокол КРК с НЦУ с фазово-временным кодированием, устойчивый к неидеальности детекторов // Научно-технические ведомости СПбГПУ. Физико-математические науки. 2022. Т. 15. № 3.3. С. 365–370. DOI: <https://doi.org/10.18721/JPM.153.372>

Статья открытого доступа, распространяемая по лицензии CC BY-NC 4.0 (<https://creativecommons.org/licenses/by-nc/4.0/>)

Introduction

Similar to conventional prepare-and-measure QKD, dead time τ of a single-photon detectors (SPD) do not affect on the MDI QKD performance as long as τ is less than pulse-to-pulse time interval in a quantum channel. This condition imposes a severe limitation on the secret key rate: dead time limits the detection frequency from above by the $1/\tau$ value. Meanwhile, widely used gated-mode single-photon avalanche photodiodes (SPAD) are characterized by the large dead time $\tau \sim 0.1\text{--}10 \mu\text{s}$ [1]. For typical pulse preparation frequency $f = 10^8 \text{ Hz}$ this means decrease in detection frequency by the 3 orders of magnitude ($1/\tau \sim 10^5$). This indicates the problem of practical MDI QKD with imperfect detectors, which we attempt to solve. In this work we consider the phase-time-encoding MDI QKD protocol with decoy-state technique and propose slight modifications to the measurement device, which improves the protocol performance. First, we explain how detectors' dead time affects the Bell state measurement. Second, we provide a theoretical model for the sifted key rate, which is useful for the optimal parameters search, and analyze the protocol performance.

Influence on Bell measurement output

In MDI QKD the untrusted node Charlie performs Bell measurement of the Alice-Bob joint quantum state and declares the result [2]. Events of the form $A_i \cap A_j$ are considered *successful*, where A_i and A_j denote detector's click in the corresponding time and space mode $i \in \{c_E, d_E\}$, $j \in \{c_L, d_L\}$ (c and d stand for space modes, E and L stand for time modes – see Fig. 1, a). As far as standard measurement scheme (see Fig. 1, a) contains only one SPD at each beam splitter (BS) output, the events $A_{c_E} \cap A_{c_L}$ and $A_{d_E} \cap A_{d_L}$ cannot be detected in the case, when dead time overlaps the second pulse in a time-encoded pair, i.e. $\tau \geq 1/f$. Using the theoretical formula of signal gain from [3], one can draw a simple conclusion: the loss of half of the events leads to double decrease in the gain, and hence the speed of the sifted key.

Alternative schemes:

1. We propose the *scheme with four detectors* (see Fig. 1, b) which contains two detectors at every BS output (c, d). As a result, one half of the previously discarded successful events can be detected, which for infinite key limit gives 25% restore of the sifted key rate in comparison with the two-detector scheme.

2. The scheme with four detectors can be upgraded in order to detect all the successful events with equal probabilities (see Fig. 1, c). One can send a pulse in each half of the time slots from previous schemes, provided that in each pair of detectors there is one that is gated in the first half of the time slot, while another is gated in the second half. Further we refer to this scheme as a *scheme with time-divided measurement*. Unfortunately, using passive beam splitters results in no profit in sifted key rate.

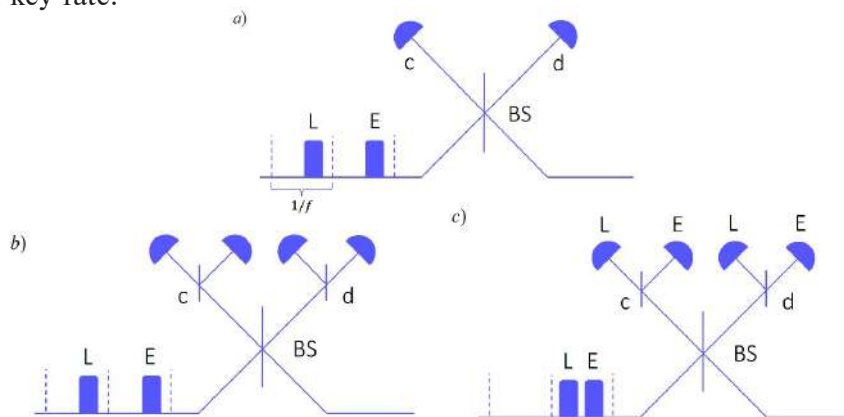


Fig. 1. Measurement schemes for phase-time-encoding MDI QKD: (a) – two detectors [3], (b) – four detectors, (c) – time-divided measurement. BS – beam splitter, (c, d) – output channels of BS, E, L – time slots of pulse preparation and detection gates



Sifted key rate model

The above result is valid for the sifted key rate estimation only in the case when the dead time overlaps every second pulse ($\tau \approx 1/f$). Otherwise, the result obtained in the limit $\tau \gg 1/f$ and under conditions of synchronous dead time and infinite statistics is additionally applied [4]:

$$R_{sift}^{\tau \neq 0} = \frac{R_{sift}^{\tau=0}}{1 + \tau R_{tot}} \quad (1)$$

where $R_{sift}^{\tau=0} = f p_Z^2 p_\mu^2 Q_{\mu_a \mu_b}^Z$ is sifted key rate for zero dead time (drawn out of signal gain $Q_{\mu_a \mu_b}^Z$ estimated in Z-basis for $\mu_{(a(b))}$ Alice (Bob) intensities [3]), $p_\mu = 0.5$ and $p_Z = 0.5$ are signal pulse and basis choice probabilities respectively, R_{tot} is the overall signal gain for BB84 protocol. In the case of MDI QKD, we have to estimate overall count rate when at least one detector clicks considering $\tau = 0$.

The simple estimation of R_{tot} that considers the two-detectors Charlie scheme, dark counts and multi-photon pulses is

$$R_{tot}^{(1)} = f (\Pr(n_{ph} > 0) + 2p_{dc}) \quad (2)$$

where

$$\Pr(n_{ph} > 0) = (1 - e^{-\mu_a \eta_a}) + (1 - e^{-\mu_b \eta_b}) - (1 - e^{-\mu_a \eta_a})(1 - e^{-\mu_b \eta_b}) \approx 4\mu \eta_{ch} \quad (3)$$

is a probability of nonzero-photon pulses pass through the channel, μ is mean photon number per pulse, η_{ch} is quantum channel transmittance. This prediction does not take into account Hong-Ou-Mandel interference on the beam splitter. Such a 'naïve' estimation close to the one from [4]. Note, when the decoy-state technique is used, the probability above must be summarized over all intensity pairs.

In general, for the decoy-state MDI protocol all detection events must be taken into account, and one has to sum up all click probabilities. We consider clicks from two incoming coherent states, prepared in different bases and of different intensities, and clicks due to dark counts. This estimation is referred to as $R_{tot}^{(2)}$:

$$R_{tot}^{(2)} = f \sum_{b_1, b_2, i, j, \mu_a, \mu_b} \Pr(n_{click} \geq 1 | \psi_{a,b}, \mu_a, \mu_b) \cdot p(\psi_{a,b}) \quad (4)$$

$$p(\psi_{a,b}) = p_{i,j} p_\mu p_{basis} = \frac{1}{4} p_{\mu_a} p_{\mu_b} p_{b_1} p_{b_2},$$

$$\text{args} : b_1, b_2 \in \{X, Z\}; i, j \in \{0, 1\}; \mu_a, \mu_b \in \{\mu, \nu, \omega\}$$

Here every joint Alice-Bob quantum state $\psi_{a,b}$ is defined by the basis $\{p_{b_1}, p_{b_2}\}$ and intensity $\{p_{\mu_a}, p_{\mu_b}\}$ choice probabilities. General formula for $\Pr(n_{click} \geq 1 | \psi_{a,b}, \mu_a, \mu_b)$ can be derived from a detector independent click probabilities D_i , averaged over the global phase:

$$\Pr(n_{click} \geq 1 | \psi_{a,b}, \mu_a, \mu_b) = 1 - \int_0^{2\pi} \frac{d\phi}{2\pi} \prod_i (1 - D_i) = 1 - p_{no}^{b_1 b_2} \quad (5)$$

where $i \in \{c_E, c_L, d_E, d_L\}$, $b_1, b_2 \in \{Z, X\}$. One can consider $p_{no}^{b_1 b_2}$ as a probability of 'no clicks' on the detector. In the case of XX and ZZ basis choice (D_i^{ZZ}, D_i^{XX} are defined in [3])

$$p_{no}^{XX} = (1 - p_{dc})^4 e^{-2\mu'},$$

$$p_{no}^{ZZ} = (1 - p_{dc})^4 e^{-\mu'}. \quad (6)$$

Here $\mu' = \mu_a \eta_a + \mu_b \eta_b$.

It is left to calculate the probabilities for the cases XZ and ZX (it is worth noting that these

cases are connected through the replacing μ_a to μ_b and vice versa). One has to consider a state

$$\left| e^{i\phi_a} \sqrt{\mu_a} \right\rangle_{a_E} \left| e^{i(\phi_a+\theta_a)} \sqrt{\mu_a} \right\rangle_{a_L} \left| 0 \right\rangle_{b_E} \left| e^{i\phi_b} \sqrt{\mu_b} \right\rangle_{b_L} \quad (7)$$

After passing through the channel and beam splitter this state becomes

$$\begin{aligned} & \left| e^{i\phi_a} \sqrt{\frac{\eta_a \mu_a}{2}} \right\rangle_{c_E} \left| e^{i(\phi_a+\theta_a)} \sqrt{\frac{\eta_a \mu_a}{2}} + e^{i\phi_b} \sqrt{\frac{\eta_b \mu_b}{2}} \right\rangle_{c_L} \otimes \\ & \otimes \left| e^{i\phi_a} \sqrt{\frac{\eta_a \mu_a}{2}} \right\rangle_{d_E} \left| e^{i(\phi_a+\theta_a)} \sqrt{\frac{\eta_a \mu_a}{2}} - e^{i\phi_b} \sqrt{\frac{\eta_b \mu_b}{2}} \right\rangle_{d_L} \end{aligned} \quad (8)$$

In this case the detection probabilities are equal to

$$\begin{aligned} D_{c_E} &= D_{d_E} = 1 - (1 - p_{dc}) e^{-\frac{\eta_a \mu_a}{2}}, \\ D_{c_L} &= 1 - (1 - p_{dc}) e^{-1/2(\eta_a \mu_a + \eta_b \mu_b + 2\sqrt{\eta_a \mu_a \eta_b \mu_b} \cos(\Delta_\phi + \theta_a))}, \\ D_{d_L} &= 1 - (1 - p_{dc}) e^{-1/2(\eta_a \mu_a + \eta_b \mu_b - 2\sqrt{\eta_a \mu_a \eta_b \mu_b} \cos(\Delta_\phi + \theta_a))}. \end{aligned} \quad (9)$$

As a result, we derive that

$$p_{no}^{XZ} = (1 - p_d)^4 e^{-\mu_a} e^{-\mu'}, p_{no}^{ZX} = (1 - p_d)^4 e^{-\mu_b} e^{-\mu'}. \quad (10)$$

Thus, we can accurately estimate $R_{sift}^{\tau \neq 0}$ for a two-detector measurement scheme. To compare sifted key rate with proposed alternatives, consider $R_{sift}^{\tau=0} = r(\eta_d)$ as a function of an SPD quantum efficiency η_d .

Alternative schemes:

1. In the scheme with four detectors, when one detector in an arm of the first BS clicks, the left detector in the same arm and the second BS can be regarded together as a detector with $\eta_d/2$ efficiency. In order to predict the sifted key rate, we can use the same equations, but instead of $R_{sift}^{\tau=0} = r(\eta_d)$ we consider $R_{sift}^{\tau=0} = r(\eta_d) + r(\eta_d/2)$;

2. In the scheme with time-divided measurement one doesn't have to throw away the half of successful events in the Bell measurement, but all the detectors always have constant decrease in efficiency ($\eta_d/2$). Therefore, we consider $R_{sift}^{\tau=0} = r(\eta_d/2)$ and $R_{tot} = r'(\eta_d/2)$.

We note that $R_{sift}^{\tau \neq 0}$ formulas for alternative schemes are numerically accurate only in single-photon approximation and the limit of $\tau \gg 0$. Otherwise, they provide estimative results.

Simulation

In Fig. 2 we compare the computed secret key generation rate $R_{sift}^{\tau \neq 0}$ for three presented detection schemes as a function of detector's dead time τ . Other model parameters are listed in Tab. 1. Four-detector scheme shows only partial restore, which is about 1.25 times of the measurement scheme with two detectors. Meanwhile, even considering double preparation frequency, time-divided scheme shows no restore of the key rate loss due to undetected successful events, as expected. Nevertheless, the dead time $\tau \leq 10 \mu s$ slows down MDI QKD by up to 3 times, regardless of the measurement scheme. One can also note the significant difference between 'naïve' sifted key rate estimation $R^{(1)}$ and accurate model $R^{(2)}$.



Table 1

Key model parameters

μ	ν	ω	p_z	p_μ	p_ν	L_{ab} , km	η_d	P_{dc}	f
0.3	$\mu/50$	$\mu/100$	0.5	0.5	0.25	160	10%	10^{-6}	3×10^8

Notations: $\{\mu, \nu, \omega\}$ are signal, weak decoy and vacuum intensities (average number of photons per pulse), $\{p_z, p_\mu, p_\nu\}$ are basis and pulse intensity choice probabilities, L_{ab} – total line length (0.2 dB/km fiber loss), η_d, P_{dc} – detector quantum efficiency and dark count probability, f – pulse repetition frequency.

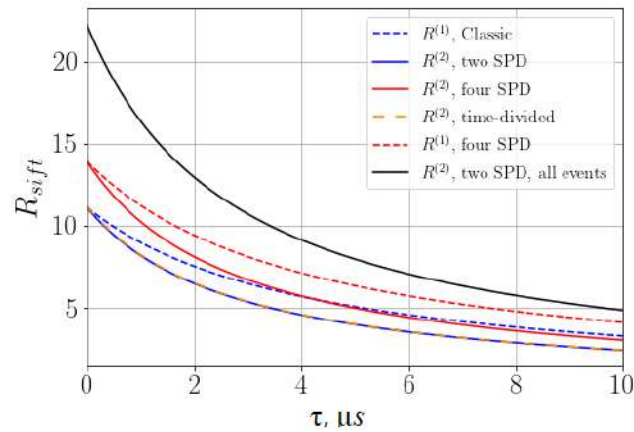


Fig. 2. Dependence of sifted key rate R_{sift} from dead time τ of a single photon detector (SPD). Three measurement schemes are compared (see Fig. 1). $R^{(1)}$ – ‘naïve’ estimation, $R^{(2)}$ – our general theoretical result

Conclusion

Dead time of a single-photon avalanche photodiode causes the dramatic decrease in the sifted key rate of a QKD setup. Phase-time-encoding MDI protocol is even more vulnerable for dead time $\tau \geq 1/f$, because it leads to the loss of a half of successful events in the Bell measurement. We proposed the theoretical model in order to predict the total number of detection events in the measurement scheme. We also proposed and compared measurement schemes with four detectors and with time-divided measurement, where the former is able to compensate for 25% of losses due to previously undetected events. This theoretical result needs further confirmation either by numerical or natural experiment. Meanwhile, the proposed sifted key model is applicable to accurate parameter optimization [5], compared to often used ‘naïve’ estimations of the total number of events.

Acknowledgments

This research was ordered by JSCo «RZD». The authors would also like to acknowledge Aleksander Duplinsky for thoughtful and productive discussions.

REFERENCES

1. **Hadfield R. H.**, Single-photon detectors for optical quantum information applications. *Nature Photonics*, 3 (12) (2009) 696–705.
2. **Lo H. K., Curty M., Qi B.**, Measurement-device-independent quantum key distribution. *Physical review letters*, 108 (13) (2012) 130503.
3. **Ma X., Razavi M.**, Alternative schemes for measurement-device-independent quantum key distribution. *Phys. Rev. A*, 86 (2012) 062319.
4. **Burenkov V., Qi B., Fortescue B., Lo H.-K.**, Security of high-speed quantum key distribution with finite detector dead time, 2010. DOI:10.48550/ARXIV.1005.0272
5. **Xu, F., Curty M., Qi B., Lo H.-K.**, Practical aspects of measurement-device-independent quantum key distribution. *New Journal of Physics*, 15 (11) (2013) 113007.

THE AUTHORS

PETROV Ivan V.
i.petrov@goqrte.com
ORCID: 0000-0002-5422-2886

TAYDUGANOV Andrey S.
a.tayduganov@goqrte.com

MENSKOY Daniil D.
d.meskoy@goqrte.com

Received 19.08.2022. Approved after reviewing 24.08.2022. Accepted 08.09.2022.

EXPERIMENTAL TECHNIQUE AND DEVICES

Conference materials

UDC 538.9

DOI: <https://doi.org/10.18721/JPM.153.373>

Integrated optical transceiver based on III-V microdisk laser and photodiode

N. V. Kryzhanovskaya ^{1,2}✉, E. I. Moiseev ^{1,2}, A. S. Dragunova ^{1,2}, M. V. Maximov ²,
S. A. Mintairov ³, N. A. Kaluzhnyy ³, F. I. Zubov ², M. M. Kulagina ³,
J. A. Guseva ³, A. I. Likhachev ³, A. E. Zhukov ¹

¹ National Research University Higher School of Economics, St Petersburg, Russia;

² Alferov University, St. Petersburg, Russia;

³ Ioffe Institute, St. Petersburg, Russia

✉ nkryzhanovskaya@hse.ru

Abstract. In this work, we study III-V p-i-n photodetectors and disk microlasers in terms of their static and small-signal modulation frequency response. InGaAs/GaAs quantum well-dots (QWDs) are used as the active region of the devices to provide operation wavelength around 1.1 μm , high optical and frequency response and temperature stability of characteristics. 30 μm -in-diameter microdisk lasers revealed CW output power level of 15–22 mW and error-free 10 Gbit/s data transmission at 30 $^{\circ}\text{C}$ without temperature stabilization. The microdisk laser and the p-i-n photodiode were heterogeneously integrated on a silicon substrate by Au-Au thermocompression bonding to form a compact transceiver. Detection of microlaser emission by the closely placed p-i-n photodiode is studied. The absolute value of the responsivity of the waveguide detector as high as 0.68 A/W for the unbiased device is demonstrated. The efficiency of the optical link at the level of 1.4% is achieved. Approaches to obtain higher efficiency of the optical link are discussed.

Keywords: microdisk laser, waveguide detector, transceiver, quantum well-dots

Funding: The fabrication of the microlaser and photodiode is supported by the Russian Science Foundation grant 18-12-00287, <https://rscf.ru/project/18-12-00287/>. The study of the laser's output power was implemented in the framework of the Basic Research Program at the National Research University Higher School of Economics (HSE University).

Citation: Kryzhanovskaya N. V., Moiseev E. I., Dragunova A. S., Maximov M. V., Mintairov S. A., Kaluzhnyy N. A., Zubov F. I., Kulagina M. M., Guseva J. A., Likhachev A. I., Zhukov A. E., Integrated optical transceiver based on III-V microdisk laser and photodiode. St. Petersburg State Polytechnical University Journal. Physics and Mathematics, 15 (3.3) (2022) 371–375. DOI: <https://doi.org/10.18721/JPM.153.373>

This is an open access article under the CC BY-NC 4.0 license (<https://creativecommons.org/licenses/by-nc/4.0/>)

Материалы конференции

УДК 538.9

DOI: <https://doi.org/10.18721/JPM.153.373>

Интегральный оптический трансивер на базе III-V микродискового лазера и фотодиода

Н. В. Крыжановская ^{1,2}✉, Э. И. Моисеев ^{1,2}, А. С. Драгунова ^{1,2}, М. В. Максимов ²,
С. А. Минтаиров ³, Н. А. Калужный ³, Ф. И. Зубов ², М. М. Кулагина ³,
Ю. А. Гусева ³, А. И. Лихачев ³, А. Е. Жуков ¹

¹ Национальный исследовательский университет «Высшая школа экономики», Санкт-Петербург, Россия;

² Академический университет им. Ж. И. Алфёрова, Санкт-Петербург, Россия;

³ Физико-технический институт им. А.Ф. Иоффе, Санкт-Петербург, Россия

✉ nkryzhanovskaya@hse.ru

Аннотация. В данной работе мы исследуем p-i-n фотодетекторы III-V и дисковые микролазеры с точки зрения их статических характеристик и возможности малосигнальной частотной модуляции. Микродисковый лазер и p-i-n фотодиод были интегрированы на кремниевой подложке с помощью термокомпрессионного соединения Au-Au для формирования компактного приемопередатчика. Исследовано детектирование излучения микролазера с помощью близко расположенного p-i-n фотодиода.

Ключевые слова: микродисковый лазер, волноводный детектор, приемопередатчик, квантовые яма-точки

Финансирование: Изготовление микролазера и фотодиода выполнено при поддержке гранта РФФИ 18-12-00287, <https://rscf.ru/project/18-12-00287/>. Исследование выходной мощности лазера выполнено в рамках Программы фундаментальных исследований НИУ ВШЭ.

Ссылка при цитировании: Крыжановская Н. В., Моисеев Э. И., Драгунова А. С., Максимов М. В., Минтаиров С. А., Калюжный Н. А., Зубов Ф. И., Кулагина М. М., Гусева Ю. А., Лихачев А. И., Жуков А. Е. Интегральный оптический трансивер на базе III-V микродискового лазера и фотодиода // Научно-технические ведомости СПбГПУ. Физико-математические науки. 2022. Т. 15. № 3.3. С. 371–375. DOI: <https://doi.org/10.18721/JPM.153.373>

Статья открытого доступа, распространяемая по лицензии CC BY-NC 4.0 (<https://creativecommons.org/licenses/by-nc/4.0/>)

Introduction

Semiconductor resonators with disk geometry supporting whispering gallery modes (WGMs) are a promising basis for creating energy-efficient and small-sized coherent light sources suitable for various applications [1]. For a number of practical applications, it is desirable to combine a semiconductor WGM microlaser with a photodetector to form a transceiver. For example, such transceivers with an open optical channel available for external action can be used as various types of microsensors (biosensor, nanoparticle detection), galvanic isolation, contactless control, etc [2]. Such an optical component that includes a laser source, a photodetector, and (optionally) an additional passive element (e.g., optical waveguide) should be fabricated on silicon-on-insulator substrates using complementary metal–oxide–semiconductor (CMOS) technologies for further signal processing. Formation of photonic waveguides and optical modulators integrated over CMOS circuits have been already demonstrated [3, 4]. III–V semiconductor lasers have been grown directly on silicon substrate [5], but rather high growth temperature (above 500 °C) is not compatible with CMOS processing. Direct bonding of III–V active devices on silicon platform offers an acceptable low temperature process that is compatible with CMOS fabrication. Moreover, III-V devices can be transferred onto pre-determined sites on the Si-based wafer without selective-area overgrowth. In this work, we report on the design, fabrication and characterization of an optical transceivers based on III-V microdisk lasers and photodetector bonded onto silicon substrate.

Materials and Methods

In this work, we use semiconductor microdisk (MD) laser as a light source for a compact transceiver. MD lasers demonstrate low energy-to-data ratio (1.5 pJ/bit for the 10- μ m in diameter laser) and in the plane output emission, which facilitates the integration of such microlasers with other planar optoelectronic elements even in the far field. For light detection we used a waveguide p-i-n photodiode. Metal-organic vapor phase epitaxy was used to grow the epitaxial structures of the p-i-n photodiode and the laser on an $n\pm$ GaAs substrate misoriented by 6° toward [111] direction. The active region of the photodiode consists of ten stacked InGaAs/GaAs quantum

well-dots structures, with a plane quantum dot density in excess of $1 \times 10^{11} \text{ cm}^{-2}$. MD laser with a mesa diameter D of $30 \mu\text{m}$ were formed by photolithography and dry etching (STE ICPe68). The photodiode was made in the form of a parallelepiped cleaved along $\{110\}$ crystallographic planes. The length and the width of the photodiode were $200 \mu\text{m}$ and $50 \mu\text{m}$, respectively. Top p-contact was formed using a $0.1 \mu\text{m}$ thick AgMn/Ni/Au alloy. As an n-contact, we used the metallization of the AuGe and Ni alloy, deposited by thermal evaporation on the back side of the substrate. The light-absorbing edges of the photodiode structures were formed by cleaving crystals without applying additional anti-reflective coatings.

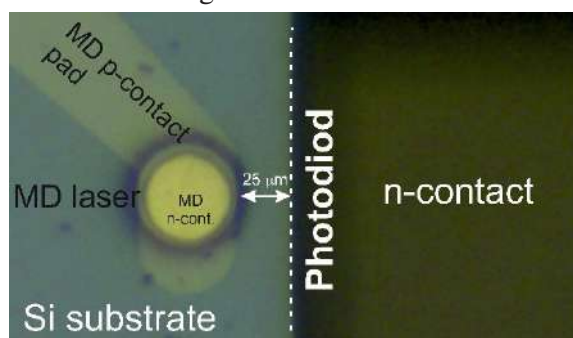


Fig. 1. Photo of the microlaser and photodiode bonded onto the Si substrate

Microlaser and photodiode were bonded onto Si substrate using Au-Au thermocompressive bonding (Fig. 1). The distance between the MD sidewall and the PD was as small as $25 \mu\text{m}$.

Results and Discussion

First, the microdisk laser and the p-i-n photodiode were fabricated and studied separately. The microlaser demonstrates single-mode emission near $1.1 \mu\text{m}$. As detected by an external Ge power meter, the free space output optical power increases almost linearly up to 12 mW limited by the thermal roll-over at 120 mA (Fig. 2). In $30 \mu\text{m}$ in diameter bonded microdisk laser the maximum -3-dB modulation frequency of 8.2 GHz was found. The InGaAs/GaAs QWDs p-i-n photodiodes with low dark current ($2.1 \mu\text{A}/\text{cm}^2$) and sensitivity up to $1.12 \mu\text{m}$ spectral range were demonstrated.

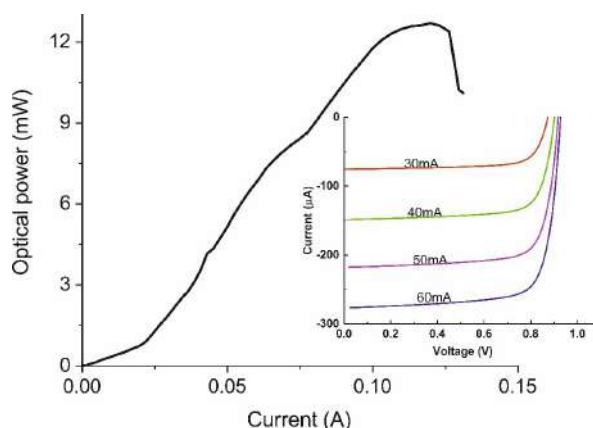


Fig. 2. Light-current characteristic of the bonded $30 \mu\text{m}$ in diameter disk microlaser obtained at 20°C . Inset: photocurrent of the photodiode integrated with microlaser at different laser pumping current

Next, the microlaser and photodetector were integrated onto Si substrate using Au-Au thermocompressive bonding. Epi-side down bonding of the microdisk laser to a silicon substrate significantly (~ 2 times) decreases the thermal resistance and improves continuous-wave and dynamic characteristics. The photocurrent of the photodiode integrated with microlaser versus the MD pumping current and PD reverse bias were studied (inset in Fig. 2). The maximum link efficiency determined as the ratio of the photodiode photocurrent increment to the increment of the microlaser bias current was up to 1.4% .

Since the active region of the photodiode consists of ten stacked InGaAs/GaAs quantum well-dots structures it can be used as an amplifying medium for the light transferring in the photodiode waveguide. We have measured the photocurrent of the PD integrated with the microlaser versus the MD pumping current also applying pumping current to PD. To test the amplification effect, we excluded photocurrent induced by the PD emission itself (Fig. 3). We observe the increase of the photodiode photocurrent with the maximum photocurrent increment value $\sim 40 \mu\text{A}$. Obviously, such a small increment is caused not so much by amplification as by the gradual transparency of the InGaAs/GaAs quantum well-dots active region.

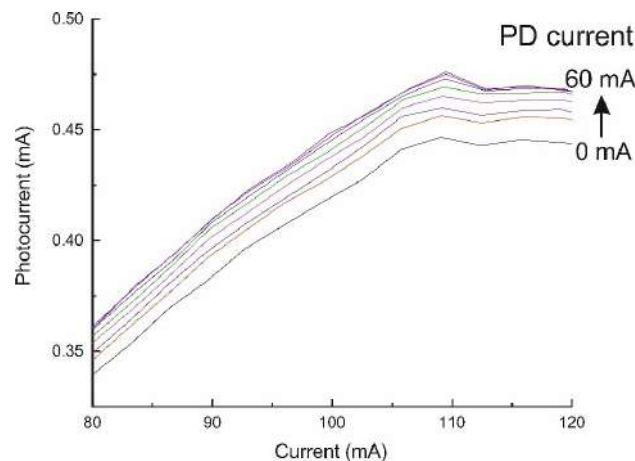


Fig. 3. Photocurrent of the PD integrated with microlaser versus the MD pumping current obtained at various PD photocurrents

Conclusion

To conclude, we have studied microdisk laser and the p-i-n photodiode heterogeneously integrated on a silicon substrate by Au-Au thermocompression bonding to form a compact transceiver. The maximum link efficiency determined as the ratio of the photodiode photocurrent increment to the increment of the microlaser bias current was up to 1.4%. Due to complicate far-field intensity distribution of the microdisk laser only a small fraction of the emission falls on the receiving area of the photodetector. The response can be improved by the directional MD laser emission output and proper vertical alignment of the MD laser and the waveguide PD.

Acknowledgments

Electron-microscopy studies were performed using the equipment of the “Materials Science and Diagnostics in Advanced Technologies” Federal Center for Collective Use.

REFERENCES

1. Wong W. W., Jagadish C., Tan H. H., III-V Semiconductor Whispering-Gallery Mode Micro-Cavity Lasers: Advances and Prospects, *IEEE Journal of Quantum Electronics*, (2022). DOI: 10.1109/JQE.2022.3151082.
2. Toropov N., Cabello G., Serrano M. P., Gutha R. R., Vollmer F., Review of biosensing with whispering-gallery mode lasers, *Light: Science and Application*. 10 (2021) article number 42.
3. Vlasov Y. A., McNab S. J., Losses in single-mode silicon-on-insulator strip waveguides and bends, *Optics Express*. 12 (8) (2004) 1622–1631.
4. Liu A., Jones R., Liao L., Samara-Rubio D., Rubin D., Cohen O., Nicolaescu R., Paniccia M., A high-speed silicon optical modulator based on a metal-oxide-semiconductor capacitor, *Nature*. 427 (2004) 615–618.
5. Cao V., Park J.-S., Tang M., Zhou T., Seeds A., Chen S, Liu H., Recent Progress of Quantum Dot Lasers Monolithically Integrated on Si Platform, *Frontiers in Physics: Optics and photonics*. 10 (2022) 839953. doi: 10.3389/fphy.2022.839953.

THE AUTHORS

KRYZHANOVSKAYA Natalia V.
nataliakryzh@gmail.com
ORCID: 0000-0002-4945-9803

MOISEEV Eduard I.
emoiseev@hse.ru
ORCID: 0000-0003-3686-935X

DRAGUNOVA Anna S.
anndra@list.ru
ORCID: 0000-0002-0181-0262

MAXIMOV Mikhail V.
maximov.mikh@gmail.com
ORCID: 0000-0002-9251-226X

KALYUZHNYI Nikolay A.
Nickk@mail.ioffe.ru
ORCID: 0000-0001-8443-4663

MINTAIROV Sergey A.
mintairov@scell.ioffe.ru
ORCID: 0000-0002-6176-6291

ZUBOV Fedor I.
fedyazu@mail.ru
ORCID: 0000-0002-3926-8675

KULAGINA Marina M.
Marina.Kulagina@mail.ioffe.ru
ORCID: 0000-0002-8721-185X

GUSEVA Yulia A.
Guseva.Julia@mail.ioffe.ru
ORCID: 0000-0002-7035-482X

LIKHACHEV Alexey I.
lihachev_alexey@bk.ru
ORCID: 0000-0003-1639-3382

ZHUKOV Alexey E.
zhukale@gmail.com
ORCID: 0000-0002-4579-0718

Received 08.08.2022. Approved after reviewing 21.08.2022. Accepted 24.08.2022.

Conference materials

UDC 53.06

DOI: <https://doi.org/10.18721/JPM.153.374>

Fabrication of a micropump based on the fast electrochemical actuator with the PDMS membrane

I. V. Uvarov ^{1,2}, P. S. Shlepakov ^{1,2}✉, A. M. Abramychev ^{1,2}, V. B. Svetovoy ³

¹ Valiev Institute of Physics and Technology RAS, Yaroslavl Branch, Yaroslavl, Russia;

² P. G. Demidov Yaroslavl State University, Yaroslavl, Russia;

³ A. N. Frumkin Institute of Physical Chemistry and Electrochemistry RAS, Moscow, Russia

✉ p.shlepakov@bk.ru

Abstract. Microfluidic systems can deliver drugs to a human body in small accurate doses. For this purpose, they have to be equipped by a compact, energy-efficient and microtechnology-compatible pump. A recently proposed micropump based on the fast electrochemical actuator meets these requirements. It contains three actuators operating in a peristaltic manner. The first version of the pump was not completely functional due to the shortcomings of the fabrication process. In this work, we proposed a modified technological route. The flexible membranes of the actuators are made of polydimethylsiloxane (PDMS) instead of SiN_x, which increases the fabrication yield. The route includes the formation of the PDMS membrane on a polyester film and two steps of bonding of the membrane to a photoresist SU-8, which are the most critical operations. Details of the fabrication process are reported and optimal bonding conditions are found.

Keywords: microfluidics, micropump, electrochemical actuator, nanobubbles, bonding

Funding: This work is supported by the Russian Science Foundation, Grant No. 18-79-10038.

Citation: Uvarov I. V., Shlepakov P. S., Abramychev A. M., Svetovoy V. B., Fabrication of a micropump based on the fast electrochemical actuator with the PDMS membrane. St. Petersburg State Polytechnical University Journal. Physics and Mathematics, 15 (3.3) (2022) 376–380. DOI: <https://doi.org/10.18721/JPM.153.374>

This is an open access article under the CC BY-NC 4.0 license (<https://creativecommons.org/licenses/by-nc/4.0/>)

Материалы конференции

УДК 53.06

DOI: <https://doi.org/10.18721/JPM.153.374>

Изготовление микронасоса на основе быстрого электрохимического актюатора с ПДМС-мембраной

И. В. Уваров ^{1,2}, П. С. Шлепаков ^{1,2}✉, А. М. Абрамычев ^{1,2}, В. Б. Световой ³

¹ Ярославский филиал Физико-технологического института имени К.А. Валиева Российской академии наук, Ярославль, Россия;

² Ярославский государственный университет им. П. Г. Демидова, Ярославль, Россия;

³ Институт физической химии и электрохимии им. А. Н. Фрумкина Российской академии наук, Москва, Россия

✉ p.shlepakov@bk.ru

Аннотация. Микрофлюидные устройства способны выполнять прецизионную доставку лекарств в тело человека. Для этой задачи они должны быть оснащены компактным и энергоэффективным микронасосом. Предложенный ранее микронасос на основе быстрого электрохимического актюатора отвечает этим требованиям. Он содержит три актюатора, работающих в перистальтическом режиме. Первая версия



насоса функционировала неудовлетворительно вследствие недостатков технологии изготовления. В этой работе предложен модифицированный технологический маршрут. В качестве материала мембраны актюатора используется полидиметилсилоксан (ПДМС), что увеличивает выход годных образцов. Технология включает нанесение ПДМС на гибкую пленку и два процесса сращивания мембраны с фоторезистом SU-8.

Ключевые слова: микрофлюидика, микронасос, электрохимический актюатор, нанопузыри, сращивание

Финансирование: Работа выполнена при финансовой поддержке РФФ, проект № 18-79-10038

Ссылка при цитировании: Уваров И. В., Шлепаков П. С., Абрамычев А. М., Световой В. Б. Изготовление микронасоса на основе быстрого электрохимического актюатора с ПДМС-мембраной // Научно-технические ведомости СПбГПУ. Физико-математические науки. 2022. Т. 15. № 3.3. С. 376–380. DOI: <https://doi.org/10.18721/JPM.153.374>

Статья открытого доступа, распространяемая по лицензии CC BY-NC 4.0 (<https://creativecommons.org/licenses/by-nc/4.0/>)

Introduction

Microfluidic systems are attractive for many applications. They operate with small amount of fluid and are fabricated by the means of microtechnology. A tiny microfluidic chip can do the same as bulky equipment. Labs on chip are widely used in biology and medicine for manipulation with cells [1, 2], virus and pathogen detection [3, 4], diseases diagnostics [5, 6], and other purposes. Promising microfluidic systems are small modules that deliver drugs to human body [7] or to a target organ or tissue [8]. Drug delivery modules require a compact, energy-efficient and microtechnology-compatible pump. A recently proposed micropump based on the fast electrochemical actuator satisfies these criteria [9]. The main part of the pump has a size of about of 3 mm, which is an order of magnitude smaller compared to the conventional micropumps. The pump is designed to have a flow rate of 1.5 $\mu\text{L}/\text{min}$ with a dosage accuracy of 0.25 nL. The first version of the pump was not completely functional due to fabrication problems. The device has been equipped with the SiN_x membrane that was bonded to the channels made of SU-8 photoresist. The quality of bonding was sensitive to the surface imperfections, contaminants and process conditions, which led to a rather low fabrication yield. To solve this problem, we propose to make the membrane of polydimethylsiloxane (PDMS). This soft material envelopes particles and defects on the surface of SU-8, thereby preventing leakage. Here we describe a modified fabrication process of the micropump based on the fast electrochemical actuator. The most critical steps related to the formation of the PDMS membrane and its bonding to SU-8 are described in detail.

Design of the pump

The micropump contains three working chambers formed on a glass substrate in a layer of the photoresist SU-8 as shown in Fig. 1. Each chamber has a diameter of 500 μm and a height of 16 μm . The chambers are covered by a 60 μm thick PDMS membrane and filled with an electrolyte that is a molar solution of Na_2SO_4 in distilled water. Two electrodes are located inside the chamber. The electrode material is a 500 nm thick aluminium conductive layer covered by a 150 nm thick working layer of ruthenium, which ensures high durability of the electrodes. The electrodes have a circular shape that provides large deflection of the membrane compared to other designs [10]. One electrode is grounded, while a series of alternating polarity voltage pulses is applied to another electrode. Nanobubbles of hydrogen and oxygen are generated in the chamber and push the membrane up. The membrane blocks the channel with the liquid to be pumped, which is formed above the chambers. When the pulses are turned off, the nanobubbles recombine in milliseconds due to spontaneous combustion reaction [11], and the membrane returns to the initial position. Driving signals are applied in such a way that the actuators operate peristaltically and push the liquid from the inlet to the outlet [9].

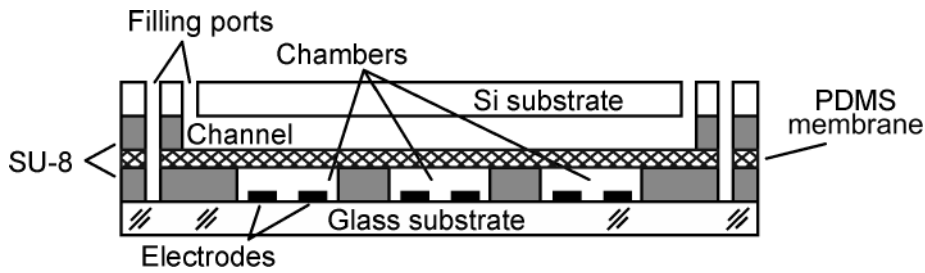


Fig. 1. A schematic cross-section of the micropump

Fabrication

A newly proposed fabrication process is shown in Fig. 2. At the first step, the electrodes are deposited on a glass substrate by magnetron sputtering. The chambers and channels for the electrolyte are formed in the SU-8 layer by spin-coating and photolithography. The soft bake and post exposure bake are carried out at 95 and 80 °C during 20 and 10 min, respectively. The hard bake is not performed in order to eliminate final cross-linking of the SU-8. Dividing trenches of 80 μm in depth are made in the substrate by a dicing saw.

Next, PDMS is spin-coated at 1000 rpm onto the polyester film (step 2). A 60 μm thick PDMS layer is obtained, which is further bonded to the SU-8 layer on the glass substrate. The adhesion between PDMS and polyester is significantly lower than that for PDMS and SU-8. The film is detached from the PDMS layer manually and openings for the channels and contact pads are punched (step 3).

Further, a silicon wafer is processed. The channels for working fluid are formed in the SU-8 layer (step 4) followed by the plasma etching of filling ports and dividing trenches from the backside (step 5). Finally, the wafer is bonded to the PDMS layer (step 6). The transparency of the glass substrate allows alignment of the substrates and observation of the meniscus during pumping. The bonded wafers are divided to separate chips by breaking along the trenches.

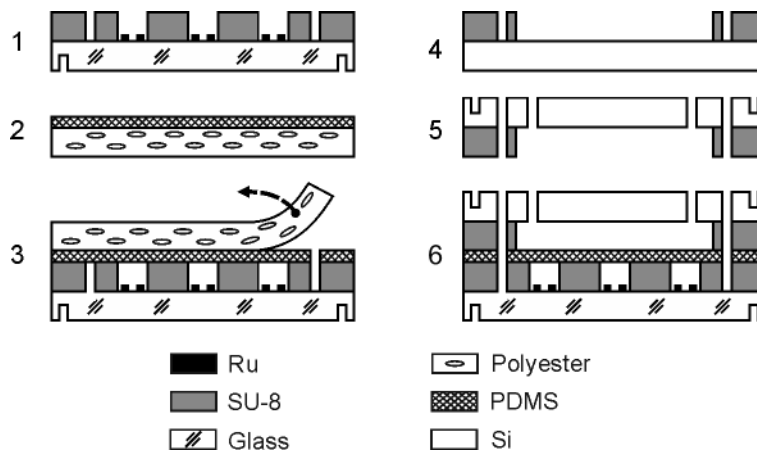


Fig. 2. Fabrication process for the micropump

The proposed route includes two steps of bonding PDMS to SU-8. The bonding is carried out by N₂ plasma treatment of the PDMS layer followed by pressing it manually to the SU-8 surface and heating the sample to initiate the N-C bond [12]. This process is the most critical part of the route. Too high pressure and too high power of the plasma produce cracks on the PDMS surface, while too low values are not enough for activation of amino groups. Both cases lead to poor adhesion and leaks of the liquids. Therefore, optimal parameters for the bonding process must be found.

The optimal parameters for the treatment have been chosen. A piece of PDMS with a size of 1×1×1 cm³ is bonded to the SU-8 layer spin-coated on a Si substrate. Plasma treatment of PDMS is performed using the Diener Atto low-pressure plasma cleaner. Plasma power, nitrogen



pressure and treatment duration are varied for reaching the strongest adhesion between PDMS and SU-8. The power takes the value from 50 to 300 W, while the pressure is from the range of 0.1 to 0.4 mbar. The plasma exposure is performed during 120–1050 s. After the treatment the PDMS sample is put on the SU-8 layer. The stack is pressed to achieve a close contact of the surfaces. However, too high pressure may cause clogging the channels and chambers with PDMS, while too low pressure can leave air bubbles between the surfaces. The PDMS layer envelopes imperfections on the SU-8 surface and provides better adhesion than previously used SiN_x . The final step is the heating of the samples to 100 °C for 30 min in a drying chamber.

The bonding strength is estimated by manual detachment of PDMS from the substrate. The strongest adhesion is achieved at the pressure of 0.4 mbar, the power of 200 W, and the exposure time of 210 s. It was impossible to detach the samples without tearing the PDMS. Increasing of any treatment parameter leads to cracks on the PDMS surface. Reduction of the plasma power below 150 W leads a significant decrease of the adhesion.

Further, the optimal treatment is applied to a 60 μm thick PDMS layer fabricated on a polyester film. The layer is exposed to plasma and pressed to a Si wafer with the chambers formed in SU-8. In order to achieve an intimate contact of the surfaces, we use a 3D-printed roller made of thermo plastic urethane for pressing the samples. Gradual pressing from one edge of the stack to another avoids air bubbles. After the bonding the film is successfully detached from the PDMS layer, leaving the membrane above the chambers. In order to verify the adhesion strength, a piece of PDMS is bonded to the membrane layer using the well-known oxygen plasma treatment [13]. The detachment is impossible without tearing PDMS. Thus, the formation of the membrane is established, making us ready for the fabrication of the micropump.

Conclusions

The modified fabrication process of the peristaltic micropump based on the fast electrochemical actuator is described. The flexible membranes of the actuators are made of PDMS instead of SiN_x , which increases the fabrication yield. This soft material envelopes particles and defects on the surface of SU-8, thereby preventing leakage. The bonding of PDMS to SU-8 is the most critical operation of the route. It is performed by N_2 plasma treatment of PDMS, pressing it to SU-8, and heating the stack. Optimal parameters for the plasma exposure are found using the trial samples. The highest bonding strength is achieved at the nitrogen pressure of 0.4 mbar, plasma power of 200 W and treatment duration of 210 s. Using these parameters, a 60 μm thick PDMS membrane fabricated on a polyester film is successfully bonded to the wafer with chambers and channels. Thus, the formation of the membrane is established, making the fabrication of the micropump possible.

REFERENCES

1. Tang W., Jiang D., Li Z., Zhu L., Shi J., Yang J., Xiang N., Recent advances in microfluidic cell sorting techniques based on both physical and biochemical principles. *Electrophoresis*. 40 (6) (2019) 930–954.
2. Xu X., Huang X., Sun J., Wang R., Yao J., Han W., Yin M., Recent progress of inertial microfluidic-based cell separation. *Analyst*. (2021).
3. Basiri A., Heidari A., Nadi M. F., Fallahy M. T. P., Nezamabadi S. S., Sedighi M., Rezaei N., Microfluidic devices for detection of RNA viruses. *Reviews in medical virology*. 31 (1) (2021) 1–11.
4. Kant K., Shahbazi M. A., Dave V. P., Ngo T. A., Chidambara V. A., Than L. Q., Wolff A., Microfluidic devices for sample preparation and rapid detection of foodborne pathogens. *Biotechnology advances*. 36 (4) (2018) 1003–1024.
5. Garcia-Cordero J. L., Maerkl S. J., Microfluidic systems for cancer diagnostics. *Current Opinion in Biotechnology*. 65 (2020) 37–44.
6. Luan Q., Macaraniag C., Zhou J., Papautsky I., Microfluidic systems for hydrodynamic trapping of cells and clusters. *Biomicrofluidics*. 14 (3) (2020) 031502.
7. Riahi R., Tamayol A., Shaegh S. A. M., Ghaemmaghami A. M., Dokmeci M. R., Khademhosseini A., Microfluidics for advanced drug delivery systems. *Current Opinion in Chemical Engineering*. 7 (2015) 101–112.

8. **Pons-Faudoa F. P., Ballerini A., Sakamoto J., Grattoni A.**, Advanced implantable drug delivery technologies: transforming the clinical landscape of therapeutics for chronic diseases. *Biomedical microdevices*. 21 (2) (2019) 1–22.

9. **Uvarov I. V., Shlepakov P. S., Melenev A. E., Ma K., Svetovoy V. B., Krijnen G. J.**, A Peristaltic Micropump Based on the Fast Electrochemical Actuator: Design, Fabrication, and Preliminary Testing. *Actuators*. – Multidisciplinary Digital Publishing Institute. 10 (3) (2021) 62.

10. **Shlepakov P. S., Uvarov I. V., Naumov V. V., Melenev A. E., Svetovoy V. B.**, Optimization of electrodes for the fast electrochemical actuator. *Journal of Physics: Conference Series*. – IOP Publishing. 1410 (1) (2019) 012197.

11. **Svetovoy V., Postnikov A., Uvarov I., Sanders R., Krijnen G.**, Overcoming the fundamental limit: Combustion of a hydrogen-oxygen mixture in micro-and nano-bubbles. *Energies*. 9 (2) (2016) 94.

12. **Zhang Z., Zhao P., Xiao G., Watts B. R., Xu C.**, Sealing SU-8 microfluidic channels using PDMS. *Biomicrofluidics*. 5 (4) (2011) 046503.

13. **Eddings M. A., Johnson M. A., Gale B. K.**, Determining the optimal PDMS–PDMS bonding technique for microfluidic devices. *Journal of Micromechanics and Microengineering*, 18 (6) (2008) 067001.

THE AUTHORS

UVAROV Ilia V.

i.v.uvarov@bk.ru

ORCID: 0000-0002-6882-0625

ABRAMYCHEV Andrey M.

irumiantsieva@bk.ru

ORCID: 0000-0002-3914-4875

SHLEPAKOV Pavel S.

p.shlepakov@bk.ru

ORCID: 0000-0002-1255-791X

SVETOVOY Vitaliy B.

svetovoy@yandex.ru

ORCID: 0000-0002-9649-5663

Received 14.07.2022. Approved after reviewing 08.08.2022. Accepted 08.09.2022.

Conference materials
UDC 544.344.015.22
DOI: <https://doi.org/10.18721/JPM.153.375>

TEM use for the study of chitosan microspheres and nanospheres obtained from its salts with several acids

A. A. Khakimova ¹✉, V. V. Pominov ¹, T. S. Babicheva ¹, S. L. Shmakov ¹,
A. M. Zakharevich ¹, A. B. Shipovskaya ¹

¹ Saratov State University, Saratov, Russia

✉ konduktorova.anastasiya@gmail.com

Abstract. Aminopolysaccharide-containing dispersed systems were obtained by coacervation based on a water–oil emulsion of a chitosan solution in glycolic or tartaric acid (a salt water-soluble form of the polymer) followed by neutralization of the salt form of the polymer with triethanoamine. Morphology was studied and the size of dispersed chitosan particles was estimated by the methods of transmission electron and polarization microscopy. The spherical shape of the solid-phase constituent of the dispersed system was established, whose size varied from 50 nm to 115 μm. The influence of the acid nature on the morphological structure, size and fineness of the formed chitosan-containing particles is shown. The disperse system formed using glycolic acid was unstable. The use of tartaric acid was found to contribute to the stabilization of a highly dispersed system. The effect of the component ratio of the dispersed system on the morphology and size of spherical chitosan-containing structures was studied.

Keywords: transmission electron microscopy, polarizing microscopy, chitosan, microspheres, nanospheres, chitosan tartrate, chitosan glycolate

Citation: Khakimova A. A., Pominov V. V., Babicheva T. S., Shmakov S. L., Zakharevich A. M., Shipovskaya A. B., TEM use for the study of chitosan microspheres and nanospheres obtained from its salts with several acids. St. Petersburg State Polytechnical University Journal. Physics and Mathematics, 15 (3.3) (2022) 381–385. DOI: <https://doi.org/10.18721/JPM.153.375>

This is an open access article under the CC BY-NC 4.0 license (<https://creativecommons.org/licenses/by-nc/4.0/>)

Материалы конференции
УДК 544.344.015.22
DOI: <https://doi.org/10.18721/JPM.153.375>

Применение ПЭМ для изучения микро- и наносфер хитозана, полученных из его солей с разными кислотами

А. А. Хакимова ¹✉, В. В. Поминов ¹, Т. С. Бабичева ¹, С. Л. Шмаков ¹,
А. М. Захаревич ¹, А. Б. Шиповская ¹

¹ Саратовский национальный исследовательский государственный университет имени Н. Г. Чернышевского, Саратов, Россия

✉ konduktorova.anastasiya@gmail.com

Аннотация. Методом коацервации на основе водно-масленной эмульсии раствора хитозана в гликолевой или винной кислоте (солевая водорастворимая форма полимера) с последующей нейтрализацией солевой формы полимера триэтаноамином получены полисахаридсодержащие дисперсные системы. Методами просвечивающей электронной и поляризационной микроскопии изучены морфология и определен размер дисперсных частиц хитозана. Установлена сферическая форма твердофазной составляющей дисперсной системы, размер которой варьируется от 50 нм до 115 мкм. Показано влияние природы кислоты на морфологическую структуру, размер и дисперсность сформированных хитозансодержащих частиц. Дисперсная система, сформованная с использованием гликолевой кислоты нестабильна. Обнаружено, что применение винной

кислоты способствует стабилизации высокодисперсной системы. Исследовано влияние соотношения компонентов дисперсной системы на морфологию и размер сферических хитозансодержащих структур.

Ключевые слова: просвечивающая электронная микроскопия, поляризационная микроскопия, хитозан, микросферы, наносферы, тартрат хитозана, гликолят хитозана

Ссылка при цитировании: Хакимова А. А., Поминов В. В., Бабичева Т. С., Шмаков С. Л., Захаревич А. М., Шиповская А. Б. Применение ПЭМ для изучения микро- и наносфер хитозана, полученных из его солей с разными кислотами // Научно-технические ведомости СПбГПУ. Физико-математические науки. 2022. Т. 15. № 3.3. С. 381–385. DOI: <https://doi.org/10.18721/JPM.153.375>

Статья открытого доступа, распространяемая по лицензии CC BY-NC 4.0 (<https://creativecommons.org/licenses/by-nc/4.0/>)

Introduction

Currently, much attention is paid to obtaining materials with efficient targeted delivery of biologically active substances on polymer matrices. In particular, the use of a matrix based on a chitosan-containing material may help stabilize a drug substance, prevent its biodegradation, and increase its biological activity [1–4]. The formation of dispersed chitosan particles is often based on the formation of a complex colloidal system, resulting in a wide range of sizes (microspheres and nanospheres) [5–9]. The multistage nature of the process of their obtaining is also undesirable [10, 11]. In this regard, it is necessary to control both the size of the resulting spheres and the structure of their walls, which transmission electron microscopy (TEM) can be successfully applied for. It is also noteworthy that, despite active research, chitosan-containing materials are still obtained on the basis of aqueous acetic solutions of chitosan [12–14]. The use of biologically active acids in combination with chitosan would make it possible to expect a synergistic effect and expand the application scope of spherical structures of microspheres and nanospheres [15, 16].

In this work, the effect of the acid nature on the formation of microspheres and nanospheres obtained in the course of the interfacial reaction of the polymer-analogous chitosan salt → base transformation was studied by the TEM method.

Materials and Methods

We used chitosan with an average viscosity molecular weight of 700 kDa, a deacetylation degree of 80 mol.% produced by CJSC Bioprogress (RF), 1.5% aqueous solution of glycolic acid (Sigma-Aldrich, USA), 6% aqueous solution of tartaric acid (KhimReaktiv SIAB, China), 50% aqueous solution of triethanolamine (CJSC Baza No. 1 Khimreaktivov, RF), vegetable oil (MEZ Yug Rusi Ltd., RF).

The objects of our study were microspheres and nanospheres obtained from chitosan solutions in glycolic and tartaric acids. Polymer solutions with a concentration of 3 wt % were prepared by dissolving an air-dry sample of the polymer in the calculated volume of an aqueous acid solution with stirring on a magnetic stirrer at $22 \pm 2^\circ\text{C}$ for ~ 5–7 h. The polymer in solution was in the salt form (chitosan glycolate or tartrate). The conversion of chitosan into its basic form was carried out by treatment with an aqueous TEA solution. Particles were obtained by coacervation in two stages. First, an emulsion was prepared by mixing vegetable oil with a chitosan solution in glycolic or tartaric acid under stirring (1,000 rpm) and keeping the emulsion on a stirrer for 3 min. At the second stage, a neutralizing agent (TEA) was added and the system was kept for an hour on a stirrer until dispersion was formed. The mass ratio of all three components was varied.

Before microscopy, sample preparation was carried out by centrifugation (12,000 rpm) of the resulting dispersed system for 5 min, followed by removal of the upper oil part and dispersion with water. The procedure was repeated 5 times. Next, the aqueous dispersion was applied onto an aluminum substrate with a formvar coating and dried under vacuum on a K450X Carbon Coater for 5 min. The size of solid-phase nanoobjects was estimated by TEM using a MIRA\\LMU microscope at an accelerating voltage of 30 kV and a conducting current of 400 pA with a dark and bright field detector (TED/TEB). The size of solid-phase microobjects was assessed on a



LaboPol-2 polarizing microscope (RF) with crossed nicols and $\times 10$ magnification. The photos were taken with a DMC 300, 3 MPx USB camera (China). Microsphere size calculations were performed from digital photos using image analysis software.

Gravimetric measurements were carried out on an Ohaus Discovery analytical balance (USA), weighing accuracy ± 0.01 mg.

Results and Discussion

The study of our disperse system in a polarizing microscope at several magnifications made it possible to observe clear solid-phase structures of micron size and spherical shape with a thin dark shell (Fig. 1). There was some difference in the morphology of the spherical particles formed from chitosan solutions in glycolic and tartaric acids. E.g., the use of tartaric acid made it possible to obtain particles with an almost ideal spherical shape. The use of glycolic acid led to some distortion of the spherical shape of the microparticles and their aggregation. It turned out that the acid nature affects not only the morphology, but also the dispersion degree of the resulting systems. For example, the size of the solid-phase spherical structures varied within ~ 50 nm – 115 μm and ~ 2.7 – 33 μm for chitosan tartrate and chitosan glycolate, respectively.

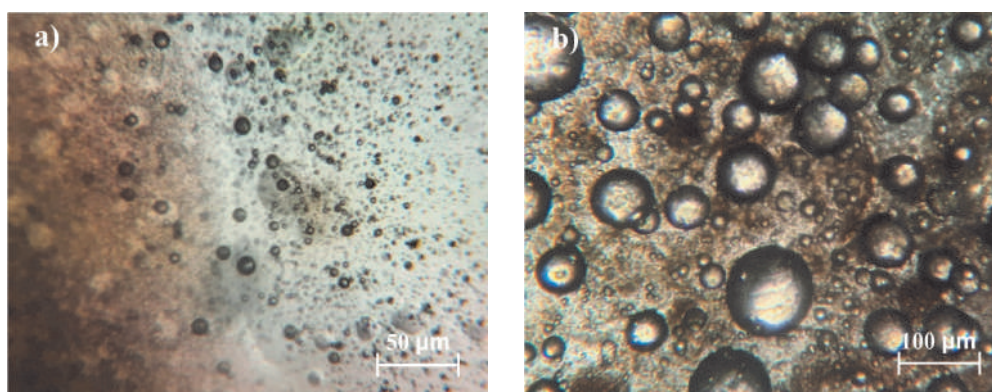


Fig. 1. Optical photos of spherical structures obtained from a chitosan solution in glycolic (a) acid and tartaric (b) acid

The TEM method made it possible to establish that the obtained dispersions also contain nanometer-sized particles (Fig. 2). Nanoparticles based on chitosan tartrate, like microparticles obtained from a similar polymer solution, predominantly had a spherical shape. The size of the spherical chitosan structures depended on the volume ratio of the aqueous (chitosan solution and TEA solution) and oil media. Such sizes are comparable with currently known analogues obtained using chitosan acetate and NaOH (~ 0.5 – 10 μm) [7].

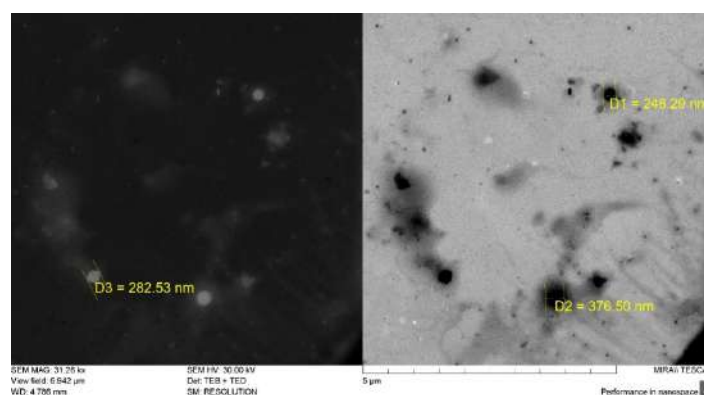


Fig. 2. TEM photo of the spherical structures obtained from a chitosan solution in tartaric acid

At the next stage, the kinetic stability of our resulting disperse systems was assessed. The objects were kept at room temperature ($22 \pm 2^\circ\text{C}$) for 30 days. During the experiment, it was found that dispersions of chitosan-containing microparticles and nanoparticles with a variable

mass ratio of the components (oil: aqueous solution of the salt form of chitosan: TEA) were unstable and delaminated into few layers, namely: oil layers without and with some content of a small fraction of dispersed particles, and a layer of solid white precipitate. The dispersed systems of chitosan glycolate particles obtained at component ratios of 1:2:2 and 2:1:1 underwent phase separation within 30 min, while those obtained at component ratios of 1:1:1, 1:1:2, 1:2:1 and 2:1:2 did within 24 h. The dispersed system of chitosan tartrate particles was kinetically more stable. No phase separation was observed within a month for the 1:2:1 oil:chitosan tartrate:TEA system.

Conclusion

Thus, it was found that the nature of the acid-solvent, other things being equal, affects the size and structure of the resulting microspheres and nanospheres. Spherical particles obtained from a chitosan solution in tartaric acid had a wider range of sizes, in contrast to those obtained from a chitosan solution in glycolic acid. Using the PM and TEM methods, a relationship was found between the size of the obtained chitosan microspheres and nanospheres and the ratio of aqueous (chitosan solution and TEA solution) and oil media, which

REFERENCES

1. Ji X. Shao, H., Li X., Ullah M. W., Luo G., Xu Z., Zhang Y., *Biomaterials*. 285 (2022) 121530.
2. Fonseca D. R., Moura A., Leiro V., Silva-Carvalho R., Estevinho B. N., Seabra C. L., Martins M. C. L., *Acta Biomaterialia*. 137 (2022) 186–198.
3. Atila D., Chen C. Y., Lin C. P., Lee Y. L., Hasirci V., Tezcaner A., Lin F. H., *Carbohydrate Polymers*. 278 (2022) 118976.
4. Yan S., Zhu J., Wang Z., Yin J., Zheng Y., Chen X., *European journal of pharmaceutics and biopharmaceutics*. 78 (3) (2011) 336–345.
5. Butstraen C., Salaün F., Preparation of microcapsules by complex coacervation of gum Arabic and chitosan, *Carbohydrate polymers*. 99 (2014) 608–616.
6. Valente J. F. A., Gaspar V. M., Antunes B. P., Countinho P., Correia I. J., *Polymer*. 54 (1) (2013) 5–15.
7. Tokumitsu H., Ichikawa H., Fukumori Y., Block L. H., *Chemical and pharmaceutical bulletin*. 47 (6) (1999) 838–842.
8. Li Y., Wu C., Wu T., Wang L., Chen S., Ding T., Hu Y., Preparation and characterization of citrus essential oils loaded in chitosan microcapsules by using different emulsifiers, *Journal of Food Engineering*. 217 (2018) 108–114.
9. Prego C., Fabre M., Torres D., Alonso M. J., Efficacy and mechanism of action of chitosan nanocapsules for oral peptide delivery, *Pharmaceutical research*. 23 (3) (2006) 549–556.
10. Song W., Zhao G., Zheng H., He G., Li J., Zhang J., Wang Y., *Materials Letters*. 278 (2020) 128348.
11. Lyu S. Y., Kwon Y. J., Joo H. J., Park W. B., Preparation of alginate/chitosan microcapsules and enteric coated granules of mistletoe lectin, *Archives of pharmacal research*. 27 (1) (2004) 118–126.
12. Li H., Wang F., Core-shell chitosan microsphere with antimicrobial and vascularized functions for promoting skin wound healing, *Materials & Design*. 204 (2021) 109683.
13. Ceryn A. A., Nascife L., Norte S., Costa S. A., do Nascimento J. H. O., Morisso F. D. P., Costa S. M., *International Journal of Biological Macromolecules*. (185) (2021) 572–581.
14. El-Gibaly I., Development and in vitro evaluation of novel floating chitosan microcapsules for oral use: comparison with non-floating chitosan microspheres, *International journal of pharmaceutics*. 249 (1-2) (2002) 7–21.
15. Lugovitskaya T. N., Shipovskaya A. B., Shmakov S. L., Shipenok X. M., Formation, structure, properties of chitosan aspartate and metastable state of its solutions for obtaining nanoparticles, *Carbohydrate Polymers*, 277 (2022) 118773.
16. Rossi S., Vigani B., Puccio A., Bonferoni M. C., Sandri G., Ferrari F., Chitosan ascorbate nanoparticles for the vaginal delivery of antibiotic drugs in atrophic vaginitis, *Marine Drugs*. 15 (10) (2017) 319.



THE AUTHORS

KHAKIMOVA Anastasia A.
konduktorova.anastasiya@gmail.com
ORCID: 0000-0002-3756-2803

POMINOV Vladislav V.
vladislav.razer@mail.ru
ORCID: 0000-0002-8113-3248

BABICHEVA Tatiana S.
tatyana.babicheva.1993@mail.ru
ORCID: 0000-0002-6655-8483

SHMAKOV Sergey L.
ShmakovSL@mail.ru
ORCID: 0000-0001-8019-0083

ZAKHAREVICH Andrei M.
lab-15@mail.ru
ORCID: 0000-0002-3813-5870

SHIPOVSKAYA Anna B.
Shipovskayaab@yandex.ru
ORCID: 0000-0003-1916-4067

Received 17.07.2022. Approved after reviewing 27.07.2022. Accepted 18.08.2022.

Journal

**ST. PETERSBURG STATE POLYTECHNICAL UNIVERSITY
JOURNAL: PHYSICS AND MATHEMATICS**

Vol. 15, No. 3.3, 2022

Founder and publisher: Peter the Great St. Petersburg Polytechnic University

The journal is registered with the Federal Service for Supervision of Communications,
Information Technology and Mass Media (Roskomnadzor).
Certificate ПИИ ФС77-51457 issued 19.10.2012.

Editorial Office

Dr. Prof. *V.K. Ivanov*, Editor-in-Chief
Dr. Prof. *A.E. Fotiadi*, Deputy Editor-in-Chief
Dr. Prof. *V.V. Dubov*
Dr. Prof. *P.A. Karaseov*
Dr. Assoc. Prof. *V.M. Kapralova*
A.S. Kolgatina, translator
N.A. Bushmanova, editorial manager

*All papers presented are final author versions
Peer review is under responsibility of the Organizing Committee*

Phone 8 (812) 294-22-85

Website <https://physmath.spbstu.ru/>

E-mail: physics@spbstu.ru

Typesetting by *N.A. Bushmanova, A.S. Kolgatina*

Published 30.10.2022. Format 60x84/8. Digital print.

Printer's sheets

Print circulation 1000. Order ID .
